MEDICAL RADIOLOGY

Diagnostic Imaging

A. L. Baert
K. Sartor

Diagnostic Nuclear Medicine

2nd Revised Edition

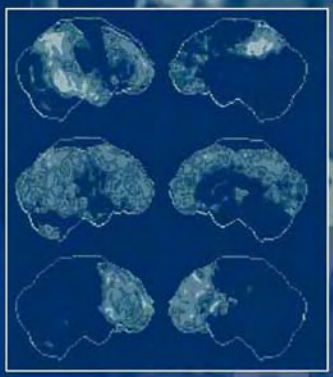

Christiaan Schiepers
Editor

Springer

MEDICAL RADIOLOGY
Diagnostic Imaging

Christiaan Schiepers (Ed.)

Diagnostic Nuclear Medicine

2nd Revised Edition

With Contributions by

M. Allen-Auerbach · R. Barone · D. Bequé · C. P. Bleeker-Rovers · G. Bormans · R. Campisi
J. Czernin · M. Dahlbom · J. J. Frost · S. S. Gambhir · G. Goerres · D. A. Hillier · C. Hoh
F. Jamar · F. Y. J. Keng · G. Lucignani · H. R. Nadel · J. Nuyts · W. J. G. Oyen · H. J. J. M. Rennen
H. D. Royal · H. R. Schelbert · C. Schiepers · M. L. Schipper · H. C. Steinert · M. E. Stilwell
T. Traub-Weidinger · M. Tulchinsky · J.-L. C. P. Urbain · K. Verbeke · A. Verbruggen · I. Virgolini
G. K. von Schulthess · S. I. Ziegler

Foreword by
A. L. Baert

With 142 Figures in 235 Separate Illustrations, 11 in Color and 32 Tables

Springer

Christiaan Schiepers, MD, PhD
Department of Molecular and Medical Pharmacology
David Geffen School of Medicine at UCLA
10833 Le Conte Avenue, AR-144 CHS
Los Angeles, CA 90095-6942
USA

Medical Radiology · Diagnostic Imaging and Radiation Oncology
Series Editors: A. L. Baert · L. W. Brady · H.-P. Heilmann · M. Molls · K. Sartor

Continuation of Handbuch der medizinischen Radiologie
Encyclopedia of Medical Radiology

Library of Congress Control Number: 2004106812

ISBN 3-540-42309-5 Springer Berlin Heidelberg New York
ISBN 978-3-540-42309-6 Springer Berlin Heidelberg New York

Springer is part of Springer Science+Business Media

http//www.springeronline.com

Printed in Germany

Medical Editor: Dr. Ute Heilmann, Heidelberg
Desk Editor: Ursula N. Davis, Heidelberg
Production Editor: Kurt Teichmann, Mauer
Cover-Design and Typesetting: Verlagsservice Teichmann, Mauer

Printed on acid-free paper – 21/3151xq – 5 4 3 2 1 0

Foreword

Since the publication of the first edition of "Diagnostic Nuclear Medicine" rapid progress has occurred in the field of nuclear medicine imaging.

Multimodality imaging, image fusion and molecular imaging techniques are being developed at a swift pace and some of these new methods, such as PET/CT scanning, have already had a major impact on the detection and staging of malignant tumors in daily clinical practice.

The second edition of this successful volume offers a comprehensive and completely updated overview of the current applications of modern nuclear medicine imaging and a fascinating perspective on future developments in this field.

The editor, Christiaan Schiepers, is a leading international expert in the field. He has been able to recruit several other widely known specialists, each dealing with his specific area of expertise.

It is my great privilege to congratulate the editor and all of the authors for their excellent contributions to this superb volume.

I am convinced that all specialists involved in clinical imaging as well as those concerned with the clinical care of oncological patients will benefit greatly from this book, which will help them to maintain their high standards of good clinical practice.

I wish this volume the same success as the first edition.

Leuven

Albert L. Baert

Preface

The number of diagnostic nuclear medicine procedures has grown in the first few years of the new century. Nuclear cardiology has diversified, stimulating development of new equipment and imaging protocols. Gated myocardial perfusion imaging completed with quantification is now a standard procedure. Faster computers have led to improved reconstruction techniques, higher image quality, increased patient throughput and more automated acquisition and processing protocols. In addition, automated processing and reporting and tele-radiology have made higher workloads possible despite the decreasing amount of money available.

In this volume of the Medical Radiology series, imaging procedures in the nuclear medicine field are presented and put in perspective. The success of the first edition has led to this revised book, with updates and additions. The influence of molecular biology is readily appreciable and a move from functional to molecular imaging is in progress. Gene imaging is promising and initial results are visible on the horizon, although gene therapy for human disease has stalled temporarily because of unanticipated side effects.

The predicted demise of nuclear medicine as a separate imaging specialty has not come true. On the contrary, multi-modality and molecular imaging are now in vogue. The introduction of PET/CT in the work-up of patients with cancer is a prominent new feature of this edition. Pharmacological interventions and new radiopharmaceuticals have broadened the number of applications and increased the accuracy of available tests. Hepato-biliary scintigraphy is now covered in a separate chapter.

This volume documents many of the advances around the turn of the century and provides an update of the diagnostic nuclear medicine field. It is organized into three sections: clinical applications, basics and future prospects. The publishers and I are grateful to the many participants who devoted their time to the chapters, enabling the readers – students and professionals – to get an overview. Radiologists, nuclear medicine specialists and technologists, and interested physicians will find this book useful.

Los Angeles, California — Christiaan Schiepers

Contents

1 Introduction

Christian Schiepers

CONTENTS

In the present revised volume of *Diagnostic Nuclear Medicine*, the advancements in the field of nuclear medicine (NM) are presented with an emphasis on progress in the beginning of this millennium. The name 'molecular imaging' is used more frequently for diagnostic NM imaging, but is not commonplace. We will use the traditional term NM. The various contributions in this imaging field such as new tracers and equipment, modifications of existing tests, diagnostic algorithms, and general applications for whole body imaging are discussed. Major achievements during the last decade of the 20th century were the contribution of FDG in positron imaging, receptor and peptide imaging, pharmacological augmentation to enhance the accuracy of neuro-, cardiac, renal and hepatobiliary imaging. This progress has broadened the field and strengthened NM as a functional and molecular imaging modality.

The re-focusing of NM on imaging of biological processes had its effects on the selection of topics in this revised edition. Dual modality imaging with combined PET/CT is featured in Chap. 12 from the Zurich group in Switzerland and Chap. 13 from the UCLA group in California. Topics selected were considered representative of the mainstream events. In addition to the new chapters on PET/CT, hepatobiliary imaging was introduced as a separate chapter. Other chapters were completely re-written or underwent major revisions. A few were updated and had only minor revisions (Chaps. 4, 7 and 15,) and two were left unchanged and re-printed from the first edition. Our selection is aimed at elucidating key processes in cellular mechanisms of the human body, under normal conditions as well as in disease.

1.1 Perspective

NM started as a field where radioactive products were put to use for the benefit of mankind, e.g. thyroid scintigraphy and therapy. The performed studies in the field have fluctuated tremendously since those early years. Flow imaging of the brain was a frequent procedure in the NM clinic until CT was introduced. Later on, sophisticated triggering techniques were developed and true functional imaging of cardiac function became a reality. At present, we take the results of these pioneering efforts for granted. The next major step was introduction of tomography and multi-head camera systems in NM facilities. The ever increasing speed of computers allowed for reconstruction within minutes, and permitted standardization of imaging protocols for acquisition, processing and review. Image interpretation and reporting, as well as database management, PACS and teleradiology became easy tasks with the help of computers.

The equipment was tuned for Tc-99m as the radionuclide of choice, and radiochemistry was geared toward the Tc-99m pharmaceuticals. Kits that could easily be labeled at room temperature replaced many of the older products.

The main achievement, in my view, is the shift that occurred at the end of the last century, when NM changed from functional to biological imaging, with a major change of focus to the cellular and molecular level. The enormous strides of molecular biology, and awareness that defective genes cause disease, have revived mechanistic models of study-

C. Schiepers, MD, PhD
Department of Molecular and Medical Pharmacology, David Geffen School of Medicine at UCLA, 10833 Le Conte Avenue, AR-144 CHS, Los Angeles, CA 90095-6942

ing nature, a trend similar to the one that propelled modern physics at the turn of the 19th century. Two factors played an important part: the advancements in immunology, and the glucose analogue FDG as tracer for metabolic imaging.

In the present volume the interdisciplinary nature of NM imaging is emphasized: the view of clinicians, radiologists, nuclear medicine specialists, engineers and molecular biologists, will be put forward to highlight their view on development and implementation of tests to study organ function in vivo.

1.2 Objectives

This volume is meant for the general NM practitioner, who wants to keep abreast of the latest clinical developments as well as the interested student and professional. This volume was not meant as a textbook, but as an addition to these readily available texts. There are three different sections, the first of which deals with clinical applications. Contrary to other volumes, the clinical point of view is central and comes first, and the state of the art in the major fields is presented. In the second section, the principles upon which these scintigraphic imaging techniques are based will be discussed and new trends outlined. The progress in radiopharmaceuticals, image acquisition and processing is the main subject of this second section of the book. In the last section, the horizon of genetic imaging is explored and early results in the clinical arena are presented. Selection of topics in the preparation of this volume is one of the prerogatives of an editor. The emphasis has been put on clinical progress in the field as well as on new modalities that are likely to stay. The typical radiological format was chosen, i.e. review by topology, and mixed with the classic internal medicine approach of organ system description.

In the clinical section, standard tests in neurological, cardiac, pulmonary, gastrointestinal, renal, and skeletal scintigraphy are being dealt with. In addition, typical multi-organ fields such as oncology, infection and inflammation are subjects of detailed review. As in any volume, choices have to be made. In this volume, monoclonal antibodies are not presented in a separate chapter. Although there are some very effective therapy protocols with antibodies, just a few diagnostic imaging applications are in use, such as granulocyte imaging, tumor antigen imaging, and thrombosis detection. The switch to smaller molecules such as peptides looks far more promising (see Chaps. 10 and 15).

Positron imaging will be discussed interspersed with single photon imaging for neurologic, cardiac and oncologic applications (Chaps. 2, 3, 6 ,7). Three chapters deal exclusively with positron imaging (Chaps. 11–13).

1.3 Clinical Overview

In the first section, the main organ systems are presented. In Chap. 2 brain imaging is reviewed for clinical entities such as stroke, epilepsy, and degenerative disorders. Neuro-receptors and their potential in neuro-degenerative disease as well as applications in psychiatric illness will be discussed. The use of emission tomography allows assessment of cerebral blood flow, glucose utilization, oxygen metabolism, rate of incorporation of amino acids into proteins, and rate of transport of substrates into the brain. Measurement of the rate of neurotransmitter storage, release, and binding to specific receptors is possible, but is not used in clinical practice yet. This possibility has raised high expectations among clinical neurologists and psychiatrists for future developments.

Dysfunctional myocardium in patients with poor left ventricular function can be caused by several mechanisms. The concepts of ”hibernation” and ”stunning”, both representing viable myocardium, are discussed in Chap. 3. Distinction of viable myocardium from scar tissue is crucial to determine whether revascularization is a therapeutic option. The available clinical evidence to assess myocardial viability prior to coronary revascularization is presented. Various techniques are highlighted indicating that viability assessment will lead to the correct use of resources, with the potential of decreasing health care costs.

Pulmonary embolism is a common clinical entity, and the imaging diagnosis remains a topic of fierce debate. The emphasis on evidence-based medicine and outcome significantly affects our thinking about diagnosis and treatment. ”Do we need to treat all pulmonary emboli?” and ”How do we identify the patient in whom the risk of treatment is less than the risk of no treatment?” are questions posed in Chap. 4. It is the authors’ firm belief that only new reasoning will allow us to make progress with diagnosis and management of pulmonary embolism.

Studies of the urinary tract are directed to quantification of renal flow and function. Various tracers are discussed and compared, a detailed analysis is given of how they affect the measured parameters. The addition of pharmacological augmentation became popular for several existing tests of the GI and the GU tract. These topics are dealt with in Chap. 5 and 8. Hepatobiliary imaging and augmentation are now incorporated in a new Chap. 9. Specific applications for pediatric NM are given in Chap. 14.

Bone scintigraphy has been around for a long time. It remains an exclusively sensitive procedure for evaluating a variety of skeletal disorders. Main referrals are detection of metastases, trauma, and orthopedic problems. Sports injuries also appear a major indication for performing bone scans. Some 40 years ago ^{18}F-fluoride was introduced as a bone imaging agent. This radiopharmaceutical has been revived since PET systems have become commonplace in the NM clinic. The PET technique allows for true regional quantification of bone blood flow (Chap. 6).

Wolfgang Becker, who wrote the previous chapter on infection and inflammation, passed away unexpectedly. The group of Nijmegen, Netherlands has prepared the text of Chap. 7 for the current edition. In order to localize an infectious process, we need procedures with high sensitivity for all body regions. The studies available and their clinical effectiveness are discussed. A typical diagnostic dilemma, posed daily, is the differential diagnosis of inflammation versus infection, e.g. after a surgical procedure. A variety of tracers and clinical conditions are presented, as well as interpretation and reporting of the image findings.

The field of receptor imaging came back in vogue in the 1990s with the introduction of new peptides. Receptors are proteins, which bind specific ligands, and subsequently respond with a well-defined event. Historically, these radioligands have evolved from monoclonal antibodies, which are large proteins, via "molecular recognition units" to small peptides. Recognition of tumor-specific properties can be used to detect cancers, and peptide receptors appear highly expressed on tumor cells. Chapter 10 illustrates that peptides have proven effective in clinical practice.

In the field of oncology, the 1990s showed an emerging role for the glucose analog FDG (2-^{18}F-fluoro-2-deoxy-D-glucose), which is the most frequently used PET radiopharmaceutical. High rates of glycolysis are found in many malignant tumor cells with increased membrane transporters. The uptake of FDG varies greatly for different tumor types. High uptake is usually associated with a high number of viable tumor cells and/or rapidly proliferating cells. Increased FDG uptake is not specific for neoplasms and many inflammatory processes have increased uptake. An overview for the common cancers in the Western world is given in Chap. 11.

The main addition in the current volume is dual modality imaging with PET/CT. The pioneering work of the Zurich group is well known and they present their experience in lung, and head and neck cancer in Chap. 12. The PET/CT experience in lymphoma, breast, GI, and GYN cancers is discussed in Chap. 13.

Pediatric nuclear medicine has special needs, because of the size and age of the patients. A selection of topics is presented in Chap. 14.

1.4 Basics of Diagnostic Nuclear Medicine

The second section of the book deals with the basics in radiopharmaceuticals, instrumentation and image processing. The potential variety of radiopharmaceuticals which may be developed is unlimited, keeping nuclear medicine in the forefront of clinical imaging. Chapter 15 provides an overview of the developments and trends for the near future.

The technological improvements of the standard gamma camera include higher spatial resolution, better uniformity, higher count rate performance, and multi-detector geometry. New hybrid devices were manufactured for both single photon and coincidence imaging, bringing the advantages of PET to the general nuclear medicine clinic. These hybrid devices have been discontinued, and the new trend is merging of standard imaging equipment, e.g. PET with CT, and SPECT with CT. Combining both imaging modalities in one system, which appeared promising in the previous version of the book, has become reality. CT not only provides images of diagnostic quality, but is also used for attenuation correction, greatly reducing acquisition time. Clinical applications of dual modality imaging are discussed in Chaps. 12 and 13. Chapter 16 provides a text on instrumentation and data acquisition.

Computer speed tends to double per year, an exponential growth curve that will continue up to the limit set by physics. New reconstruction techniques will be discussed and compared, leading to improved image quality. Iterative reconstruction techniques, and correction for attenuation and scatter are the standard

in tomographic NM imaging. The effects on quantification of tracer distribution will be touched upon. In addition, simple and handy techniques for image enhancement are presented (Chap. 17).

1.5 Future Perspective

The third section of this volume provides an introduction and progress report on gene imaging. The advances in molecular biology have made it possible to image specific molecular processes, and by inference the expression of gene(s) controlling these processes may be visualized. Conventional nuclear imaging techniques can be used by manufacturing a radio-labeled substrate that interacts with the protein of the gene of interest. General methods are emerging to image gene expression, which will be the subject of Chap. 18. Many phenomena in disease are leading to altered cellular functions, which can be imaged with molecular biology assays in living animals and humans.

Clinical Applications

2 Neurochemical Imaging with Emission Tomography: Clinical Applications

Giovanni Lucignani and James J. Frost

CONTENTS

G. Lucignani, MD
Unit of Molecular Imaging, Division of Radiation Oncology, European Institute of Oncology, and Institute of Radiological Sciences, University of Milan, Via Ripamonti 435, 20141 Milan, Italy
J. J. Frost, PhD, MD
Departments of Radiology and Radiological Services and Neuroscience, The Johns Hopkins University School of Medicine, JHOC 3225, 601 North Carolina Street, Baltimore, MD 21287, USA

2.1 Introduction

The assessment of neurochemical and neurophysiological variables by emission tomography can be based on two strategies in relation to the goal to be achieved. A first approach is aimed at the assessment of basic variables related to brain functional activity and energy metabolism, such as blood flow, rates of glucose and oxygen metabolism, and incorporation of amino acids into proteins. This first approach allows us the assessment of brain function in a broad manner, often without previous knowledge of the location, if any, to look for a specific function or an abnormal function. A second approach is based on the measurement of neurotransmitter synthesis and reuptake, receptor density and enzyme activity, i.e., variables related to the function of the chemically heterogeneous neuronal populations that compose the central nervous system. This second approach requires a more solid prior hypothesis on the system and on the neurochemical variable to be assessed, among many, and on the construction of the experimental approach. The two approaches are complementary and can be used for the assessment of regional derangements of cerebral energy metabolism and chemical transmission. As most CNS disorders entail neurochemical alterations involving the synthesis of neurotransmitters and the disruption of synaptic function, imaging of neurotransmitters and neuroreceptors has become crucial in helping to understand the intrinsic neurochemical basis of neurologic and psychiatric diseases.

The first studies aimed at the in vivo assessment of cerebral function by using radioactive tracers and external monitoring by gamma-rays detectors were focused on measuring cerebral hemodynamics and energy metabolism (Ingvar and Lassen 1961; Hoedt-Rasmussen et al. 1966; Obrist et al. 1975; Phelps et al. 1979; Reivich et al. 1979; Frackowiak et al. 1980; Herscovitch et al. 1983). This work was a tremendous stimulus in the development of tracer methods for the assessment of regional cerebral blood flow in clinical practice, a goal that has been readily achieved in the mid 1980s following the development of SPECT perfusion tracers labeled with Iodine-123 and most important with Technetium-99m. Following these milestones in the development of brain perfusion imaging in humans, there has been further development of methods and tracers over the last two decades that permit the assessment of neurotransmission. The first images of brain receptors were those of dopamine (D_2) receptors (Wagner et al. 1983) with PET, and those of muscarinic cholinergic receptors (Eckelman et al. 1984) with SPECT. An historical overview of the development in the field of neurotransmitter imaging has recently been published by Frost (2003). Following this seminal work many tracers have been developed (Mason and Mathis 2003) and are currently used. Basic neuroscientists and clinical neuropsychiatrists use these methods for the assessment of regional cerebral functional activity and of neurochemical transmission under physiologic or pharmacologic conditions. Currently, the use of emission tomography allows assessment of cerebral blood flow, glucose utilization, oxygen metabolism, oxygen extraction ratio, rate of incorporation of amino acids into proteins, and rate of transport of substrates across the brain capillaries into the brain, as well as of the rate of neurotransmitter storage, release, and binding to specific receptors. The assessment of neurotransmission by emission tomography has attracted the interest of neuroscientists with an expertise in nuclear medicine and has raised high expectations among clinical neurologists and psychiatrists, many of which have been realized.

2.2 Physiologic and Biochemical Basis of Radionuclide Brain Imaging

The central nervous system is a heterogeneous entity composed of a number of neuronal systems for transferring signals along their own body surface and, by secreting highly selective chemical substances, transferring this information to down-stream neurons. This function requires a continuous supply of nutrients through the cerebral circulation. As nutrients are delivered to brain structures for their energy metabolism, the rate of delivery and their consumption is indicative of neuronal functional activity, and also of functional derangements when they occur. Since the function of the nervous system is based on the communication among its components, the characterization of the neuronal circuits and of neurotransmission constitute a primary goal of neuroscientists and neuropsychiatrists. A description of the fundamental body of knowledge is reported elsewhere (Feldman et al. 1997; Siegel et al. 1999).

Neuronal communication represents the ultimate function of the nervous system. It requires the integrated function of ion channels, classified according to the mechanism controlling their gating as either voltage-sensitive or receptor operated, and neurotransmitters, defined on their presence and release at the presynaptic sites and on the capability to evoke a response at the postsynaptic site. The sequence of events characterizing neurotransmission can be schematically summarized as follows. The propagation of an action potential in the presynaptic neuron activates voltage-sensitive channels at the nerve ending, which turn on the fusion and release of synaptic vesicles, containing the neurotransmitter, into the synaptic cleft; the neurotransmitter then binds to postsynaptic neuroreceptors and initiates a cascade of events, including the activation of second messengers, and by modifying the ionic permeability of the postsynaptic neuron. This event in turn may result in the excitation or inhibition of the postsynaptic neuron, by either depolarization or hyperpolarization states produced by changes in neuronal membranes' permeability to ions such as calcium, sodium, potassium and chloride. The depolarization results in an excitatory postsynaptic potential (EPSP), whereas the hyperpolarization results in an inhibitory postsynaptic potential (IPSP). EPSP and IPSP have a short duration, of the order of milliseconds, therefore they represent temporary states during which the threshold for neuronal response is either decreased (depolarization) or increased (hyperpolarization). The electrical impulses and the chemical messengers act sequentially and synergistically, the former for intraneuronal conduction, the latter for interneuronal communication.

2.2.1 Cerebral Blood Flow and Energy Metabolism

The normal energy metabolism of the nervous system is dependent on the obligatory consumption of oxygen and glucose. Due to the lack of significant storage of glycogen, the brain functions are sustained by a continuous supply of nutrients via blood. The rate of glucose and oxygen utilization throughout the brain is very heterogeneous and is tightly coupled to the rate of blood flow. Thus, the assessment of any of the three variables, i.e., blood flow, oxygen or glucose utilization, provides a measure of the degree of cerebral functional activity (Sokoloff 1960). Normal values of regional cerebral blood flow and metabolism and other neurophysiologic variables are listed in Table 2.1. Because of the close relation between blood flow, metabolism and brain function, the assessment of blood flow is currently performed not only with the aim of detecting cerebrovascular disorders, i.e., pathologic states originated by alterations of cerebral circulation, but also to assess other diseases of the nervous system that, due to neuronal death or to neuronal loss of function, require less blood supply compared to normal regions. In the latter case the reduction of blood flow is secondary to a reduced metabolic demand. The increase in blood flow is interpreted as a consequence of increased functional activity and this concept is the basis of the neuroactivation studies aimed at localizing areas and neuronal networks involved in functional processes.

Table 2.1. Normal values per 100 g brain tissue in a healthy resting young adult man. (Modified from Sokoloff 1960)

Cerebral blood flow	57 ml/min
Cerebral oxygen consumption	3.5 ml/min
Cerebral glucose utilization	5.5 mg/min
Cerebral blood volume	4.8 ml
Mean RBC volume	1.5 ml
Mean plasma volume	3.3 ml

2.2.2 Neurotransmission

The function of the different neuronal systems of the brain hinges on the synthesis and release of several neurotransmitters, each acting selectively on specific neuroreceptor types and subtypes. Thus, neurons, receptors, and entire neuronal networks, can be classified according to the neurotransmitter utilized. Neurotransmitters can range in size from small molecules such as amino acids and amines, to peptides. They are contained in small intracellular vesicles and are released in the synaptic cleft by exocytosis. Neurotransmitters act by influencing the excitability of target receptors, located either on postsynaptic neurons or effector organs. The mechanism of action of neurotransmitters depends on the features of the two types of receptor subfamilies. Ligand-gated receptors contain an intrinsic channel that is rapidly opened in response to transmitter binding, whereas G protein-coupled receptors activate G proteins in the membrane which then stimulate various membrane effector proteins. Membrane proteins act on the synthesis of second messengers (e.g. cAMP, cGMP, and Ca ions) which in turn act on intracellular protein kinases. The action of neurotransmitters may produce rapid and short-term changes, or initiate long term processes by modifying gene expression. The neurotransmitter action is terminated after metabolic degradation or cellular reuptake. Many neurons possess autoreceptors at their surface, which by responding to the cell's own transmitter initiate feedback mechanisms that reduce transmitter synthesis and release.

2.3 Methodology

The development and use of methods for brain radionuclide studies must take into account cerebral morphologic heterogeneity, neuronal circuitry complexity, neurotransmitter specificity, non-uniform blood flow and metabolism, and presence of the blood–brain barrier (BBB). Each experimental and diagnostic procedure must be tailored to examine the physiologic and biochemical process of interest.

The methodological research has been aimed at constructing instruments to detect and reconstruct the temporal distribution of tracer substances in three dimensions and at developing methods of data analysis for the transformation of the radioactivity distribution data into relevant neurophysiologic and neurochemical parameters.

2.3.1 Detection Instruments

The process of detecting photons emitted either as singles or in pairs, constitutes the basis of single photon emission computed tomography (SPECT) and

positron emission tomography (PET), respectively (Chap. 16). In order to appreciate the potentials and limitations of SPECT and PET with respect to their applications in brain studies, it is worth pinpointing some features of both techniques. Image quality in emission tomography results from a compromise between spatial resolution, which affects the ability to discriminate small structures, and count density, which depends on the system detection efficiency and determines the level of noise in the image. The temporal resolution of emission tomography, defined as the minimum time needed for acquisition of counts, even with recent increases in detection efficiency, remains on the order of seconds/minutes to obtain acceptable, i.e., low noise levels in the image. It should be noted that detection efficiency in PET is approximately 10–15 times higher than in SPECT. The features of state-of-the-art PET and SPECT scanners are defined according to their physical performances, including field of view, spatial resolution, system sensitivity, count rate (Chap. 16). Whereas PET remains for the brain an instrument primarily devoted to research with many opportunities for clinical applications still unexplored, SPECT is nowadays widely used for clinical purposes, and will mature as a research tool in time.

2.3.2 Dynamic and Static Acquisition Procedures

Two main approaches can be used for SPECT and PET brain data acquisition. One is based on the acquisition at one fixed time interval after tracer administration. The second approach is based on the measurement of changes in time of the brain radioactivity distribution. The two approaches are sometimes referred to as autoradiographic and dynamic imaging, respectively. Both methods may require sequential sampling of peripheral arterial or venous blood to determine the time course of radioactivity in blood. Blood sampling is usually necessary for quantitative assessment of physiologic or biochemical processes, whereas it is not required for assessing uptake ratios of radioactivity distribution between cerebral structures, also referred to as semiquantitative indices of function.

2.3.3 Data Analysis

Data analysis presents a major intellectual and practical challenge in SPECT and PET. Quantification is, in general, a requisite of research studies and is often a complex procedure that may require the assessment of the fractions of radioactive metabolites in blood by chromatography and scintillation counting, as well as scanning times in the order of hours. Data acquired for quantification must be analyzed by kinetic models; these are in general schematic representations of the behavior of tracers in the body spaces, i.e., compartments (Gjedde and Wong 1990). Kinetic models represent the basis to calculate the variables of interest, e.g., tracer rate of transfer across compartment boundaries or rate of tracer accumulation in a compartment. The application of these models requires measurement of radioactivity concentrations in blood and brain after tracer injection. These models may require the a priori knowledge of parameters that are applicable to any subject; two of such kinetic models are shown in Fig. 2.1. Models representing biological events never can fully account for all relevant factors and conditions that occur in vivo and consequently are imperfect. The experimental procedures must therefore be designed to minimize the possible errors arising from limitations and imperfections of the method. Semiquantitative assessment is considered adequate in most clinical studies with emission tomography, when only localization of phenomena is sought. Quantification may also not be required in activation studies, i.e., performed under baseline conditions (unstimulated) and then repeated under physiologic or pharmacologic stimuli, where localization of neuronal function is sought. For many studies that address clinical and research questions, location may be only a part of the information sought; the assessment of the magnitude of the alterations is also important. Furthermore, it is often impossible without quantification to make comparisons between individuals, e.g., patients, groups, and normal control subjects. Relative changes, as assessed by semiquantitative methods, may be inadequate because the reference region may be affected by the same process as the area under investigation. Nevertheless, semiquantitative assessments are in general preferred as they are less cumbersome for patients, physicians and technical staff, since blood sampling can generally be avoided and data acquisition can be performed in a shorter time span, with an acceptable tradeoff in accuracy.

Regional cerebral radioactivity is usually measured by drawing regions of interest (ROIs) of either regular or irregular shape on the images. This procedure is time consuming and can be biased as it is based on arbitrary subdivision of cerebral struc-

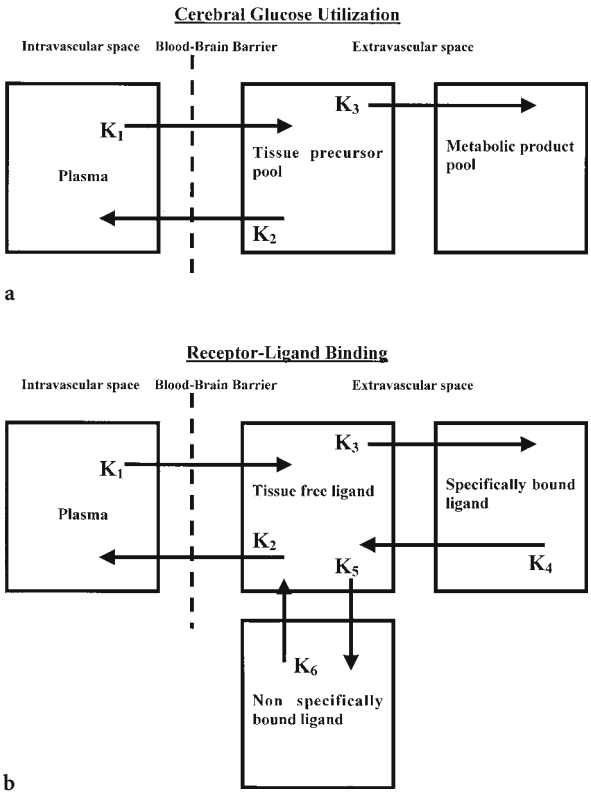

Fig. 2.1a,b. Compartmental models used to calculate physiologic and biochemical parameters for cerebral glucose utilization (**a**), and for receptor-ligand binding (**b**). The *K*'s are the rate constants or diffusion rates between compartments

tures into small discrete volumes. To overcome these problems non-interactive voxel by voxel-based techniques have been developed. One such method developed by Friston et al. (1995) for activation studies with PET and ^{15}O-labeled water, has become very popular, and is known as statistical parametric mapping (SPM). The use of this method has been extended to other tracers. It offers a series of non-interactive techniques that permit: (1) spatial normalization of brain images into a stereotactic space, (2) normalization for differences in global cerebral radioactivity distribution depending on intersubject variability, and (3) higher spatial resolution than that achieved with subjective ROIs based analysis.

Methods have been specifically developed for estimating in vivo regional variables of blood flow, metabolism, neurotransmitter synthesis and receptor binding. A selection of these methods is reported in Table 2.2.

Whereas numerous procedures for quantitative measurement of hemodynamic and metabolic variables have been established and fully validated, semiquantitative assessments are performed for clinical use. Methods developed for the assessment of neurotransmission function have been most often semiquantitative, although fairly simple quantitative methods exist for assessing the maximum concentration of binding sites (B_{max}) and the affinity of the ligand for the receptor (K_D). A frequently adopted

Table 2.2. Major neurotransmitters and receptors

Neurotransmitter	Receptors	Clinical application
Glutamic acid	NMDA,AMPA, kainate, quisqualate	Epilepsy Movement disorders Ischemia
Gamma-amino-butyric-acid linked to benzodiazepine receptors: $GABA_A$/BZD	$GABA_A$ and $GABA_B$	Movement disorders Mood disorders
Acetylcholine	Nicotinic (peripheral) Nicotinic (central), some abnormal in AD Muscarinic (central), five subtypes	Movement disorders Dementia Epilepsy
Dopamine	Five subtypes	Movement disorders Drug addiction Schizophrenia
Noradrenaline	Five subtypes	Vascular tone Movement control Mood control
Serotonin	Seven subtypes	Sleep Depression Food intake Pain
Opioid	Mu, delta, kappa	Drug addiction Pain syndromes Epilepsy Eating disorders

For details see: Feldman et al. 1997; Siegel et al. 1999

measure of the functional status of brain receptors is based on the assessment of the binding potential (BP), which is equal to the ratio of receptor density (B_{max}) to receptor affinity (K_D).

Analytical methods have also been developed that allow the assessment of the rate of uptake and storage of neurotransmitter precursors into neurons. One such method, which has interesting applications for the analysis of the behavior of any tracer and permits the assessment of volumes of distribution, as well as rate of trapping, has largely been applied (Patlak et al. 1985). However, there is a widespread use of semiquantitative methods based on the assessment of ratios of radioactivity concentration in target regions, i.e., known to contain specific receptors and in which there is specific tracer binding, to that of regions devoid of receptors, in which tracer uptake is non-specific. A comprehensive review on tracer kinetics has recently been published by Price (2003)

2.4 Tracers for Brain Imaging

Numerous tracers have been developed for studying the chemical processes in the brain (Mason and Mathis 2003). The availability of radiotracers for the in vivo assessment of biochemical variables, physiological, and pharmacological processes, is a major advantage of PET over SPECT, but the short half-life of the positron emitters makes the presence of a cyclotron mandatory in the proximity of the PET scanner, thus increasing the cost and limiting the diffusion of PET compared to SPECT. Indeed, in spite of the increased availability of PET scanners and cyclotrons, PET is mainly used for oncology and FDG is the only clinical tracer, produced in large amounts with automated industrial procedures. All other tracers used for PET brain scanning to assess the neurotransmitter system are still produced with often laborious semi-automated procedures, on demand, in centers where research is the primary goal. Moreover, their development presents in many cases a real challenge, even more so in view of the limited availability of experts and training programs in this field. Thus, while there are many examples of how molecular imaging has improved our understanding of brain function, examples of its use for diagnosis and treatment monitoring of neurologic diseases are less frequent. It is noteworthy that for some neurochemical studies, tracers labeled with single photon emitting radionuclides may be more suitable as they decay slowly and allow the assessment of tracer kinetics over several hours; this feature is particularly relevant for tracers with high affinity for receptors.

2.4.1 Cerebral Blood Flow and Metabolism Tracers

Cerebral blood flow can be measured both with SPECT or PET by using either diffusible or non-diffusible tracers. To the group of diffusible tracers belongs ^{133}Xe, a gas that decays by single photon emission and employed with SPECT (Kanno and Lassen 1979), as well as ^{15}O labeled water and ^{15}O labeled carbon dioxide (which is converted to ^{15}O-water in vivo), both decaying by positron emission and employed with PET. The use of molecular ^{15}O-oxygen, along with ^{15}O-water permits the assessment of oxygen extraction fraction, cerebral blood flow, and oxygen metabolism (Herscovitch et al. 1983; Frackowiak et al. 1980). To the group of the non-diffusible tracers belong the so-called chemical microspheres, i.e., tracers that cross the BBB after venous administration, and which are retained in the brain in proportion to blood flow dependent delivery; chemical microspheres are labeled with ^{99m}Tc and employed with SPECT (Leveille et al. 1992). The assessment of cerebral metabolism can be achieved by PET only, as for this purpose glucose, or its analogues, and oxygen itself can be used, which cannot be labeled with single photon emitting radionuclides. The measurement of glucose utilization is performed with ^{18}F-labeled 2-fluoro-2-deoxy-D-glucose (^{18}F-FDG) (Phelps et al. 1979; Reivich et al. 1979), since glucose itself, labeled with ^{11}C, undergoes a rapid metabolic degradation to water and carbon dioxide, which are partially lost during the measurement of the radioactivity concentration. ^{18}F-FDG instead remains trapped as ^{18}F-labeled fluorodeoxyglucose-6-phosphate, and accumulation is a function of the glucose metabolic rate.

2.4.2 Neurotransmission Function Tracers

The dopaminergic system has been extensively investigated in terms of both presynaptic and postsynaptic processes by means of selective positron emitting radiotracers. The large number of studies performed has also facilitated the development of

methods and procedures for studying other neurotransmitter systems. ^{18}F-Fluoro-DOPA has been extensively used as a probe of the presynaptic dopaminergic system, is transported across the BBB and incorporated into the sequence of processes for dopamine synthesis and subsequent conversion of dopamine to homovanillic acid and 3,4-dihydroxyphenylacetic acid (DOPAC) (Cumming and Gjedde 1998). Although this tracer does not permit the measurement of endogenous dopamine synthesis, turnover, and storage, it has been used as a probe of amino acid decarboxylase activity (the rate limiting enzyme in the synthesis of dopamine) and thus of nigrostriatal neuron density and presynaptic function.

The dopaminergic system has also been studied with tracers binding to the presynaptic dopamine reuptake system (DAT), such as ^{11}C-nomifensine, ^{18}F-GBR 13,119, ^{11}C-cocaine, ^{11}C-CFT, ^{11}C-WIN 35,428, and ^{11}C-FE–CIT. WIN 35,428 (Dannals et al. 1993) and ^{123}I-β–CIT (Neumeyer et al. 1991) are the tracers that are being used currently. The particular interest in DAT is related to the assessment of dopaminergic neuronal loss in Parkinson's disease and parkinsonian syndromes. The first agent for assessing dopamine reuptake labeled with ^{99m}Tc, TRODAT-1, has been synthesized and tested in human subjects (Kung et al. 1997).

The activity of the mitochondrial enzyme monoamine oxidase B (MAO-B) can be investigated by using ^{11}C-L-deprenyl, a so-called suicide inactivator, since it covalently binds to the MAO-B flavoprotein group, which results in the labeling of the enzyme itself. Following i.v. administration of this tracer, there is significant uptake and retention of radioactivity in the striatum and thalamus. This tracer can be used to measure the effect of therapy in patients under treatment with MAO-B inhibitors as well as the rate of turnover of MAO-B (Arnett et al. 1987; Fowler et al. 1987, 1993).

The type-2 vesicular monoamine transporter (VMAT-2) are cytoplasmic proteins of the presynaptic nerve terminal for monoamine transport from the cytoplasm into synaptic storage vesicles. Also this transporter has been imaged by using ^{11}C labeled DTBZ (Frey et al. 1996). In the brain, VMAT-2 is expressed exclusively by monoaminergic neurons, i.e., those using dopamine, serotonin, norepinephrine, or histamine, yet mainly by dopaminergic neurons.

Dopamine receptors can be grouped into two major families: one including D_1 and D_5 receptors, and the other including the D_2, D_3 and D_4 receptors. PET tracers to measure D_2 and D_1 receptors have been developed; however, there are currently no specific PET ligands to differentially evaluate D_3, D_4 and D_5 receptors

The first visualization of dopamine receptors in live human subjects with PET was reported by Wagner et al. (1983) using ^{11}C-N-methyl-spiperone, a D_2 receptor antagonist. Subsequently, several other D_2-receptor tracers have been synthesized including ^{11}C-raclopride and ^{18}F-fluoro-ethyl-spiperone (Coenen et al. 1987). For SPECT studies of the D_2 receptors ^{123}I-Iodobenzamide has been used (Kung et al. 1988, 1990). The specific D_1 ligands SCH 23,390, SCH 39,166 and NNC 112 labeled with ^{11}C have allowed investigation of D_1-receptor subtypes in human subjects with PET (Halldin et al. 1986, 1990, 1998; Abi-Dargham et al. 2000).

The cholinergic system includes two major receptor classes, nicotinic and muscarinic. Tracers have been developed for the assessment of cholinergic presynaptic function including acetylcholinesterase activity, by N-[^{11}C]methylpiperidin-4-yl propionate (Kuhl et al. 1996), and vesicular acetylcholine transporter, by vesamicol and benzovesamicol labeled with either ^{11}C or ^{18}F or ^{123}I (Kilbourn et al. 1990). Nicotinic receptor function assessment has been pursued with ^{11}C labeled nicotine, however the use of this tracer has been dropped due to high levels of non-specific binding. The limits of nicotine have been overcome by the development of 6-[^{18}F]fluoro-3-(2(S)-azetidinylmethoxy)pyridine (Dolle et al. 1999; Scheffel et al. 2000; Ding et al. 2000).

Muscarinic receptor function assessment has been evaluated with ^{123}I-quinuclinidylbenzilate (QNB) (Eckelman et al. 1984), ^{11}C-scopolamine, ^{11}C-tropanylbenzilate, ^{11}C-N-methyl-piperydilbenzilate (Mulholland et al. 1992, 1995; Koeppe et al. 1994), and recently by an M_2-selective agonist [^{18}F]FP-TZTP (Podruchny et al. 2003).

The opiate receptor system is comprised of three major receptor subtypes: mu, delta, and kappa; each subtype is composed of several subclasses. Opiate receptors have been studied with two ligands: ^{11}C-carfentanil, a potent opiate agonist that is highly selective for mu receptors, and ^{11}C-diprenorphine, a partial agonist of the same system but with no specificity for the opiate receptors subtypes: mu, delta, and kappa (Frost et al. 1986, 1990; Jones et al. 1988). This lack of specificity limits the use of diprenorphine due to its widespread uptake in the cortex, whereas the uptake of carfentanil is more selective to the areas that contain mu receptors. Delta receptors can be imaged using and ^{11}C-methyl-naltrin-

dole (Madar et al. 1996). ^{18}F-cyclofoxy is another opiate antagonist with high affinity for both the mu and kappa opiate receptor subtypes.

There are two classes of benzodiazepine (BZD) receptors that are relevant to the nervous system. The central BZD receptors, which are post synaptic membrane receptor ionophore complexes with a $GABA_A$ receptor (BZD/$GABA_A$), and the peripheral BZD receptors located on activated micro-glial cells and other non-neuronal components. [^{11}C]flumazenil (Samson et al. 1985; Shinotoh et al. 1986) and ^{123}I-iomazenil (Persson et al. 1985; Beer et al. 1990; Dey et al. 1994) are central benzodiazepine antagonists, used mostly to assess patients with epilepsy and cerebral-vascular disease, whereas [^{11}C]PK 11195 is a peripheral benzodiazepine receptor antagonist used to assess microglial activation in several conditions including multiple sclerosis, Rasmussen's encephalitis and gliomas.

There are seven serotonin receptors subtypes, 5-HT1 through 5-HT7. All but the 5-HT3 subtype are transmembrane proteins that are coupled to G-proteins, the 5-HT3 subtype is a ligand-gated ion channel. For the assessment of the serotoninergic system only a few tracers are available, including ^{11}C-ketanserin, ^{18}F-setoperone, ^{18}F-altanserin, ^{11}C-MDL 100,907 (Berridge et al. 1983; Crouzel et al. 1988; Mathis et al. 1996; Halldin et al. 1996). Moreover, ^{11}C and ^{18}F labeled spiperone analogs bind not only to dopamine but also to serotonin receptors. Indeed, in spite of the higher affinity of spiperone analogs for D_2 than for 5-HT_{2A} receptors, the high density of 5-HT_{2A} receptors in the frontal cortex, relative to the density of D_2 receptors, permits imaging of the 5-HT_{2A} receptors in the cortex with spiperone derivatives. The serotonin transporter has been assessed with ^{11}C labeled-McN5652 and DASB, while ^{11}C labeled tryptophan has been used for the in vivo assessment of serotonin synthesis (Diksic et al. 2000)

2.5 Clinical Applications

Progressive increase in life expectancy is leading to an increase in the number of subjects with degenerative and cerebrovascular diseases. At the same time, there is an increasing demand for diagnosis and treatment of all neuropsychiatric diseases, due in part to increasing public health awareness. The investigations carried out over two decades by emission tomography, have permitted the in vivo assessment of physiologic and neurochemical processes in several clinically relevant conditions. PET and SPECT studies have been aimed at clarifying the natural history of cerebrovascular diseases, characterizing the metabolic features of neuronal degeneration in dementia syndromes, assessing the neurochemical impairment in movement disorders, establishing the neurochemical correlates of the clinical and electrical alterations in epilepsy, as well as a variety of syndromes and pathologic states (Table 2.3). PET and SPECT brain studies have also contributed significantly to a new vision in the area of mental illnesses. Methods originally developed for research are slowly entering the clinical domain.

The use of emission tomography for assessing brain function under clinical circumstances is somewhat overshadowed by its use in research investigations. This is in sharp contrast with the trend in other organs and systems, namely in cardiology, oncology, and endocrinology. On the one hand, this is due to the large number of unanswered questions in neuroscience stimulating research activities, and on the other hand to the limited therapeutic resources for the treatment of many CNS diseases. In particular, lack of effective neurologic therapies makes the in depth characterization of patients for whom there are only limited therapeutic resources of limited utility for many specialists, especially after a diagnosis has been established. Unfortunately, morphologic imaging and electrophysiology are also of little help for understanding the nature of the CNS diseases and remain largely descriptive techniques. Morphologic imaging can only depict advanced disease states, often characterized by gross neuronal loss and irreversible changes in the primary site of the lesion. Electrophysiologic studies can provide us with information having very high temporal resolution, but barely acceptable spatial resolution, unless based on invasive intracranial exploration. Both provide limited insight into the neurochemical basis of functional mechanisms in the CNS. Thus, the goal for the future is the characterization of biochemical abnormalities of the CNS at as early a stage as possible during the disease, and to treat each individual patient with the most appropriate and tailored treatment. In this respect, emission tomography is a unique tool.

2.6 Dementias

The term "neurodegenerative dementia" comprises various diseases, including Alzheimer's disease (AD),

Table 2.3. Synopsis of clinically relevant tracers

Physiologic variable	Method	Tracers
Blood flow (CBF)	PET	^{15}O-carbon dioxide; ^{15}O-water; ^{11}C-butanol; ^{18}F-fluoro-methyl-fluoride; ^{13}N-ammonia
	SPECT	^{133}Xe; ^{99m}Tc-hydroxy-methyl-propyleneamine oxime (HMPAO); ^{99m}Tc-ethyl-cysteinate-dimer (ECD)
Oxygen extraction fraction (OEF) and metabolism ($CMRO_2$)	PET	Molecular oxygen ($^{15}O_2$) ($CMRO_2$ is calculated by multiplying CBF by OEF)
Glucose metabolism	PET	^{18}F-fluoro-deoxy-glucose
Blood volume	PET	^{15}O-carbon monoxide-labeled RBC
	SPECT	^{99m}Tc-RBC
Protein synthesis and amino acid transport	PET	^{11}C-methionine, ^{18}F-fluoro-L-tyrosine
Tumor viability and proliferation	PET	^{18}F-fluoro-deoxy-glucose; ^{11}C-thymidine; ^{11}C-methionine; ^{18}F-fluoro-L-tyrosine
	SPECT	^{201}Thallium; ^{99m}Tc-methoxy-isobutyl-isonitrile (MIBI); ^{123}I-methyl-tyrosine
Gamma-amino-butyric-acid (GABA)	PET	^{11}C-flumazenil; ^{18}F-fluoro-ethyl-flumazenil
	SPECT	^{123}I-iomazenil
Acetylcholine	PET	Acetylcholine-esterase activity: ^{11}C-methyl-phenyl-piperidine Nicotinic receptors: ^{11}C-nicotine Muscarinic receptors: ^{18}F-fluoro-dexetimide; ^{11}C-N-methyl-piperidil-benzilate; ^{11}C-Tropanyl benzilate; ^{11}C-scopolamine
	SPECT	Acetylcholine transport: ^{123}I-iodo-benzovesamicol Muscarinic receptors: ^{123}I-iododexetimide; ^{123}I-QNB;
Dopamine	PET	MAO-B: ^{11}C-deprenyl Presynaptic function: ^{18}F-fluoro-L-DOPA; ^{18}F-fluoro-L-m-tyrosine Dopamine reuptake: ^{11}C-nomifensine; ^{11}C-cocaine; ^{11}C-WIN 35,428 D2-receptors: ^{11}C-raclopride; ^{18}F-fluoro-ethyl-spiperone; ^{18}F-N-methylspiperone; ^{18}F-fluoro-alkyl-benzamides D1-receptors: ^{11}C-SCH 23,390
	SPECT	Dopamine reuptake: ^{123}I-beta-CIT D2-receptors: ^{123}I-Iodobenzamide (IBZM)
Noradrenaline		^{18}F-Fluoro-norepinephrine
Serotonin		5HT reuptake: ^{11}C-McN5652 5HT receptors: ^{18}F-fluoro-ethyl-ketanserin; ^{18}F-setoperone; ^{18}F-altanserin
Opioid	PET	^{11}C carfentanil (mu selective); ^{11}C methylnaltrindole (delta selective); ^{11}C diprenorphine (mu, delta, and kappa selective); ^{18}F cyclofoxy (mu and delta selective)

Pick's disease (frontotemporal lobar atrophy), diffuse – or cortical – Lewy body disease (DLBD), and multiple system atrophies. The disease with the highest prevalence is AD. Degenerative dementias are classified on the basis of postmortem neuropathologic assessment. Thus, the in vivo diagnosis of AD by clinical and instrumental assessment is only a probabilistic statement based on evidence of progressive cognitive decline, and lack of an alternative diagnosis of intoxications, systemic metabolic disturbances, infection, cerebrovascular ischemic disease, cerebral mass lesions, and normal pressure hydrocephalus. Several imaging strategies have been applied to the study of dementias. From the perspective of clinical diagnosis, glucose metabolism and blood flow are key variables. The assessment of other neurochemical variables is crucial for testing pathophysiological hypotheses of the etiology of AD and to assess the efficacy of new drugs as they are developed and introduced into clinical practice (Frey et al. 1998).

2.6.1 Cerebral Blood Flow and Metabolism in Patients with Degenerative Dementias

Glucose metabolism imaging with ^{18}F-FDG is the most sensitive and specific imaging modality available today for the diagnosis of AD. Automatic analysis of PET images yields a sensitivity as high as 95%–97% and a specificity of 100%, in discriminating patients with probable AD from normal subjects (Minoshima et al. 1995). Probable AD patients have reduced glucose utilization in the posterior parietal and temporal lobe association cortex and posterior cingulate cortex (Benson et al. 1983; Friedland et al. 1983; Cutler et al. 1985). In moderate-to-severely affected individuals, the reductions of metabolism are bilateral, yet there is often an asymmetry of the severity or the extent of hypometabolism. Patients with more advanced clinical symptoms have reduced metabolism in the dorsal prefrontal association cortex as

well, although the typical AD pattern is characterized by more severe parietotemporal than frontal involvement. In AD patients, metabolism is relatively spared in cortical regions other than the above, including the primary somatomotor, auditory, and visual cortices and the anterior cingulate cortex (Fig. 2.2). Subcortical structures including the basal ganglia, thalamus, brain stem, and cerebellum are also relatively preserved in typical AD. The metabolism in the involved regions decreases with disease severity as shown by longitudinal studies that reveal an overall reduction of glucose metabolism throughout the brain in AD, with progressively decreasing metabolism in the association cortex. The region least affected by AD is the pons while the posterior cingulate cortex is the area in which the hypometabolism occurs in the earliest stage of the disease.

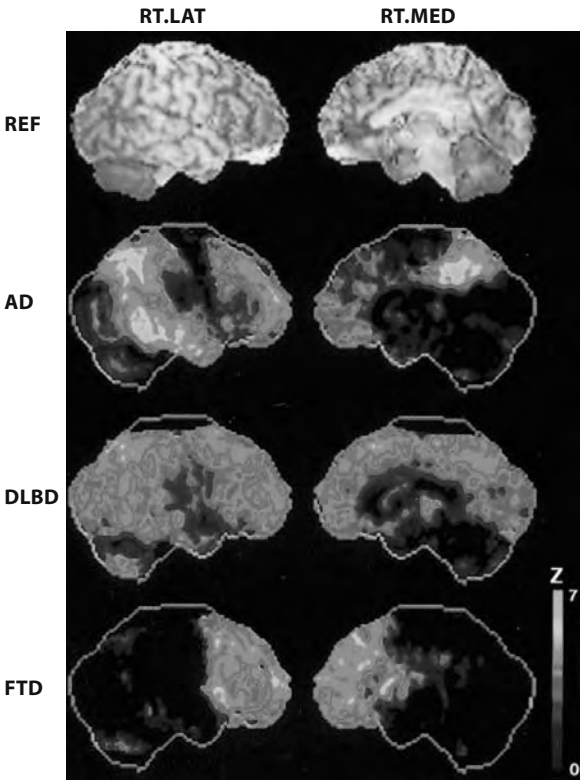

Fig. 2.2. Stereotaxic surface projection maps of glucose metabolism deficits in patients with dementia. Two columns of images are presented, representing the lateral (*left column*) and medial (*right column*) surface projections of the right cerebral hemisphere. The *top row* demonstrates surface-rendered MRI of a normal subject for anatomic reference (*REF*). The other rows of images depict stereotaxic surface projections of cerebral glucose metabolic decreases in individual demented patients, displayed in Z-score scale in comparison to an elderly normal database. The *second row* depicts a typical AD patient with prominent temporo-parietal and prefrontal hypometabolism on the lateral projection, and posterior cingulate hypometabolism on the medial projection. The third row depicts deficits in an autopsy-proven case of diffuse Lewy body disease (*DLBD*) with reductions in the association cortical areas as in AD, but with additional involvement of the occipital cortex on both medial and lateral projections. The *bottom row* depicts deficits in a patient with isolated frontal lobe hypometabolism (frontal lobe dementia, *FTD*). The metabolic decreases are depicted in Z-scores (standard deviations from normal) according to the color scale on the *right*, extending from *0* to *7*. From Frey et al. 1998

Several lines of evidence suggest the high sensitivity of ^{18}F-FDG PET in the early detection of AD. Many subjects with AD have already an abnormal PET on the initial examination performed for mild memory loss. These studies suggest that hypometabolism actually precedes both symptoms and the clinical diagnosis of AD. Thus, the ^{18}F-FDG PET scan appears to have excellent sensitivity in mildly-symptomatic patients and performs well in the diagnostic setting. Patients with frontal or frontotemporal dementia have also typical metabolic patterns. In instances of autopsy-proven Pick's disease, and in patients with a neuropsychometric suggestion of frontal dementia, ^{18}F-FDG PET reveals the greatest reduction in the frontal and anterior temporal association cortical regions, with the least reduction in the parietal association cortices (Kamo et al. 1987; Miller et al. 1997). Patients with pure AD and those with pure DLBD or mixed AD and DLBD, the so-called LB variant AD, can be distinguished (Fig. 2.2). In this latter group, the typical AD pattern of reduced temporoparietal and prefrontal hypometabolism is seen in association with additional hypometabolism of the primary visual cortices, whereas the metabolic patterns of DLBD and LBVAD do not, at this time, appear separable on the basis of cerebral glucose metabolism (Albin et al. 1996). The pattern assessed with PET ^{18}F-FDG in AD patients may also be detectable using SPECT and blood flow tracers. However, comparative studies of metabolism and flow have shown that SPECT may be a slightly less accurate methodology for the assessment of demented patients in the earliest stages of the disease (Messa et al. 1994).

2.6.2 Neurotransmission Function in Degenerative Dementias

Studies of the presynaptic function have been carried out by ^{123}I-iodobenzovesamicol (^{123}I-IBVM), which is a marker of the vesicular acetyl choline transporter (VAChT) (Kuhl et al. 1994, 1996; Hicks et al. 1991). Studies in normal subjects revealed modest reductions with advancing age, approximately 3%–4% per

decade. Application of the ^{123}I-IBVM SPECT method for studying AD revealed further losses of cholinergic cortical innervation. The average reductions are distinctly greater in AD patients with symptom onset before age 65 (30%) than in those with later age at onset (15%). These neocortical reductions were, however, less than the expected 50%–80% losses reported for choline acetyl transferase (CAT) enzyme activity in autopsy series. While CAT activity was reduced over 50% in the neocortex of AD, a parallel 15% reduction in VAChT was not statistically significant. Thus, there is the possibility that these two presynaptic cholinergic markers may be differentially regulated or differentially lost in AD. There may be upregulation of VAChT expression to compensate for cholinergic terminal losses, or alternatively, CAT expression may be reduced within otherwise intact presynaptic nerve terminals. Further studies are underway to explore each of these hypotheses. ^{11}C-N-methyl-piperidinil propionate (PMP) is a substrate for hydrolysis by acetyl choline esterase (AChE) (Kilbourn et al. 1996), thus, PET measurements of PMP hydrolysis, accomplished by measuring regional radiolabeled product retention in the brain, provide an index of AChE activity. Preliminary studies of patients with probable AD reveal approximately 20% reductions throughout the cerebral cortex (Namba et al. 1994; Irie et al. 1996; Iyo et al. 1997; Kuhl et al. 1999).

Postsynaptic cholinergic studies have also been carried out. Studies of muscarinic cholinergic receptors with ^{11}C-tropanyl benzilate (TRB) (Koeppe et al. 1994; Lee et al. 1996) and ^{11}C-N-methylpiperidyl benzilate (NMPB) (Mulholland et al. 1995; Zubieta et al. 1994) indicate minor losses of cholinergic receptors function with advancing age. In probable AD patients there is no evidence of significant neocortical losses of muscarinic receptors, whereas significant ligand delivery reduction is found in the association cortical areas, paralleling reductions in glucose. PET studies of the central benzodiazepine binding site on the $GABA_A$ receptor with the antagonist ligand ^{11}C-flumazenil are amenable for the assessment of neuronal viability. In patients with probable AD, a modest reduction of benzodiazepine binding sites has been observed in the association cortex only in the most clinically-advanced cases, thus indicating the presence of viable neurons in the early phases of the disease. As this reduction is of a lesser degree than glucose hypometabolism, it is conceivable that the reductions in glucose metabolism seen in the early stages of AD are not just a reflection of synapse and neuron losses, but a correlate of a synaptic dysfunction that precedes the structural losses (Meyer et al. 1995).

The development of acetylcholinesterase inhibitors for symptomatic treatment of AD is being pursued by several pharmaceutical companies. Development of PET imaging of the cholinergic system activity parallels this search to comply in due time with the need to assess the appropriateness of expensive treatments in the aging world population.

2.6.3 Amyloid and Microglial Activation Imaging in Alzheimer Disease

One of the major limitations in the diagnosis of AD is the lack of criteria that can exclude other illness that share with AD the same cognitive deterioration. Thus, AD can only be diagnosed at autopsy, when neuritic plaques and neurofibrillary tangles can be detected in the brain. To overcome this difficulty and to diagnose AD as early as possible, several attempts have been made to develop radiotracers that bind to the amyloid deposits in the brain; [^{18}F]FDDNP (2-(1-(6-[(2-[^{18}F]fluoro-ethyl)(methyl)amino]-2-naphthyl)ethylidene)malononitrile) is one such tracer and binds to amyloid senile plaques and neurofibrillary tangles (Shoghi-Jadid et al. 2002). However, this tracer presents some limitations, including low specificity, and in an effort to improve specific-to-non-specific amyloid binding ratios in vivo, a neutral ^{11}C-labeled derivative of thioflavin-T, 6-OH-BTA-1 or PIB, was developed. Imaging of amyloid plaques is still in the early stage, however the available results appear to be very promising.

Recently Cagnin et al. (2001) have reported the in-vivo detection of increased ^{11}C-PK11195 binding in AD of various degrees and suggested that microglial activation is an early event in the pathogenesis of the disease. Early detection of this process may ease the diagnosis of AD and allow an early neuroprotective treatment.

2.7 Movement Disorders

The balance between cholinergic and dopaminergic neuronal activity in the basal ganglia is required for normal motor function. Damage to dopaminergic nigrostriatal neurons is found in various forms of parkinsonism. In patients with Parkinson's Disease (PD) clinical symptoms occur when dopaminergic nigral neurons have undergone a loss of 40%–50%.

The neurons projecting to the putamen have been estimated to decline most, as compared to those innervating the caudate and those projecting to the nucleus accumbens. A reduction in dopamine metabolites 3,4-dihydroxyphenylacetic acid (DOPAC) and homovanillic acid (HVA), and the number of dopamine reuptake sites is also observed. The reduction in dopamine content occurs also in the mesocortical and mesolimbic projections of the ventral tegmental area (VTA) possibly as a consequence of the destruction of dopaminergic neurons in the VTA. Other neurotransmitter systems have been shown to be damaged in parkinsonism, including noradrenergic, cholinergic, opioidergic and serotonergic circuits (Dubois et al. 1983, 1987; Hornykiewicz and Kish 1984, 1986; Uhl et al. 1985; Baronti et al. 1991). Such alterations may explain the occurrence of depression, dementia and other symptoms in patients with PD.

2.7.1 Cerebral Blood Flow and Metabolism in Movement Disorders

In the early studies various patterns of flow and metabolism have been observed in movement disorders, related to the duration and degree of the disease. In the early phase of hemiparkinsonism an increased metabolism was found in the putamen and globus pallidus (Wolfson et al. 1985; Miletich et al. 1988), along with a decrease of metabolism in the frontal cortex, contralateral to the affected limbs (Perlmutter and Raichle 1985; Wolfson et al. 1985). In bilaterally affected patients the cortical alteration is more widespread; however, this effect could be due to concurrent degenerative processes (Kuhl et al. 1984). The significance of the cortical hypometabolism remains unclear. All studies have shown inconsistent and minor changes that have lead to abandon the use of ^{18}F-FDG and flow tracers to measure functional activity in the basal ganglia and cortex of patients with movement disorders. Overall, the assessment of flow and metabolism does not appear a useful approach in studying patients with movement disorders.

2.7.2 Neurotransmitter Function in Movement Disorders

The assessment of the dopaminergic presynaptic function has been pursued by two strategies: one aimed at assessing the incorporation of a metabolic substrate of dopamine synthesis in the nigrostriatal neuronal terminals, and another aimed at assessing the density of the presynaptic dopamine reuptake sites.

For the first goal the most used tracer is ^{18}F-6-fluoro-DOPA (^{18}F-DOPA) which is metabolized to ^{18}F-fluoro-dopamine by amino-acid decarboxylase (AADC) and subsequently stored in vesicles in the presynaptic nerve endings. Following ^{18}F-DOPA administration in patients with early PD and hemiparkinsonism, a reduced accumulation of tracer is observed, reflecting reduced-AADC-activity in the putamen contralateral to the affected limbs, with relative sparing of the caudate (Nahmias et al. 1985). Significant correlations between ^{18}F-DOPA uptake and motor symptoms have been reported (Leenders et al. 1988; Brooks et al. 1990a; Martin et al. 1988, 1989). These results are sustained by a lack of AADC activity due to a selective destruction of the ventrolateral nigrostriatal neurons projecting to the putamen in PD. However, the rate of ^{18}F-DOPA uptake is the expression of both the neuronal density as well as of the AADC activity. Whereas ^{18}F-DOPA has shown potential for the early and preclinical detection of PD, it must be noted that ^{18}F-DOPA uptake in the basal ganglia is not proportional to the degree of degeneration of the ventrolateral substantia nigra, due to adaptational increases in AADC function in the surviving cells. This is made evident by the observation that at the onset of symptoms, ^{18}F-DOPA uptake in the affected putamen is reduced by approximately 35%, with no significant reductions detected in the caudate. On the other hand, at symptom onset, putamen dopamine content is already decreased by 80% and at least 50% of pigmented nigra cells are lost. From these observations it can be concluded that the activity of DOPA decarboxylase, as assessed with ^{18}F-DOPA is a sensitive but inaccurate measure of dopaminergic neuronal loss. In fully symptomatic patients, reductions of ^{18}F-DOPA uptake range from 40%–60% in the posterior putamen, and 15%–40% in caudate and anterior putamen, respectively (Otsuka et al. 1991; Brooks et al. 1990b).

Functional imaging of the presynaptic transporter, aimed at assessing neuronal density by methods independent of dopamine synthesis, offers a more accurate alternative to ^{18}F-DOPA studies. This goal has been achieved by several cocaine analogues that bind to the presynaptic dopamine transporter (DAT) sites (Scheffel et al. 1992; Dannals et al. 1993; Lever et al. 1996). Among various tracers, ^{11}C-WIN 35,428 seems to be the most sensitive tracer for DAT imaging in PD, and PET studies have revealed

markedly reduced DAT levels in early PD (Frost et al. 1993). In patients with stage-2 PD, specific binding of ^{11}C-WIN 35,428 in the posterior putamen is reduced more than in the anterior putamen and the caudate nucleus (Fig. 2.3). SPECT imaging with ^{123}I-β-CIT also shows severe loss of striatal DA transporters in idiopathic PD compared to healthy human subjects, with markedly abnormal striatal uptake, more pronounced in the putamen than in the caudate nucleus. ^{123}I-β CIT uptake is related to clinical findings including degree of akinesia, rigidity, axial symptoms and activities of daily living. The striatal uptake is reduced by 35% in Hoehn-Yahr stage 1 to over 72% in stage 5 and is correlated to disease severity. In general, abnormalities of dopamine transporter binding are more pronounced than ^{18}F-DOPA abnormalities (Brucke et al. 1993; Seibyl et al. 1994; Marek et al. 1996). The assessment of presynaptic function may permit both the early detection of PD and a differential diagnosis between PD and progressive supranuclear palsy (PSP) in a single study since PSP is associated with a more uniform loss of DAT compared to PD which shows more specific loss in the posterior putamen (Fig. 2.2) (Ilgin et al. 1995). This goal can conveniently be achieved with SPECT tracers that selectively bind to the presynaptic dopamine transporters, such as ^{123}I-β-CIT (Messa et al. 1998). However, in early PD also DAT may not be directly related to the extent of neuronal loss. In fact, DAT may be downregulated as part mechanisms compensating for neuronal loss and reduced neurotransmitter availability.

The assessment of VMAT-2 may be a more reliable indicator of nigrostriatal nerve terminal density with minimal or no influence of regulatory changes. VMAT-2 density is in fact linearly related to the integrity of substantia nigra dopamine neurons and not subject to compensatory regulation as those apparently affecting the expression of DAT and the synthesis of DOPA (Lee et al. 2000). VMAT-2 specific binding using DTBZ and PET are greater in patients who have higher Hoehn and Yahr severity scores.

The role of methods for the assessment of presynaptic function is not diagnostic, except for patients who do not respond to dopaminergic treatment, or for experimental treatment definition and monitoring, including stem cell transplantation and electrical deep brain stimulation.

Ligands available for studying D_2 receptors with PET are ^{11}C-raclopride and spiperone derivatives labeled with ^{11}C and ^{18}F. D_2 receptors can also be assessed with SPECT and ^{123}I-IBZM (Giobbe et al. 1993; Nadeau et al. 1995). ^{123}I-IBZM SPECT and ^{11}C-raclopride PET findings in patients with PD are significantly correlated (Schwarz et al. 1994). In patients not treated with DOPA, either small increases or no changes in basal ganglia D_2 receptor density are observed (Rinne et al. 1990). In patients treated with L-DOPA, D_2 receptor density is reduced or unchanged (Hagglund et al. 1987). Longitudinal studies have shown that ^{11}C-raclopride uptake is increased in the putamen in the early stage of PD, compared to controls, whereas after 3–5 years ^{11}C-raclopride binding is significantly reduced in the putamen and caudate nucleus in these patients compared with baseline (Brooks et al. 1992a; Antonini et al. 1997). These results indicate long-term down-

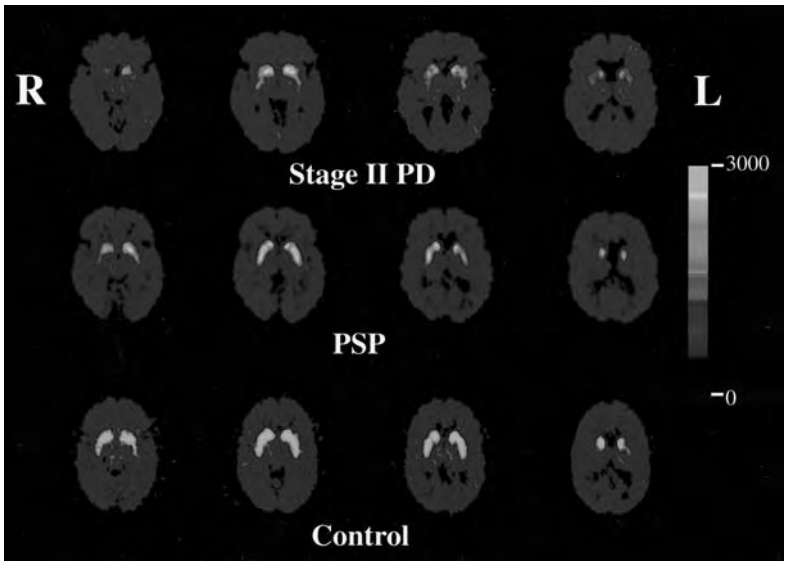

Fig. 2.3. Images of ^{11}C-WIN 35,428 binding at four different levels throughout the striatum of a healthy control, a stage-2 PD and a PSP patient. The images are obtained after averaging the data acquired from 35–82 min following administration of the tracer and are normalized for the administered activity. Higher binding in the basal ganglia is seen in the healthy age-matched control subject compared to patients diagnosed with PD and PSP. In PD, reduced ^{11}C-WIN 35,428 binding is seen predominantly in the posterior putamen while there is more uniform reduction throughout the entire striatum in PSP

regulation of striatal dopamine D_2 receptor binding in PD. Besides idiopathic Parkinson's disease there are other distinct diseases, such as progressive supranuclear palsy (PSP) and multiple system atrophy (MSA) may start with tremor, akinesia or rigidity. As the diagnosis may be difficult in some cases, hampering the adoption of a proper therapeutic strategy, tools for the early differential diagnosis of relevant and of clinical interest. PSP and MSA are characterized by a decrease of striatal D_2 dopamine receptor activity, as demonstrated by ^{123}I-IBZM uptake, compared to control subjects (van Royen et al. 1993). D_2 receptor density is less markedly reduced in the basal ganglia of patients with PSP, with frequent overlap with controls. The decrease in D_2 dopamine receptor activity in the early phase of PSP and MSA, contrary to the initial phases of PD, allows us to differentiate between idiopathic PD and parkinsonian syndromes (Buck et al. 1995). The differential diagnosis between essential tremor (ET) and PD is also crucial to implement an appropriate therapeutic strategy. This is a relevant issue as up to 1/3 of the patients presenting with tremor will eventually develop PD (Geraghty et al. 1985). Thus, the demonstration of reduced dopaminergic marker binding in the putamen of individual patients presenting with isolated postural tremor may provide the diagnosis and a targeted therapy. Familial essential tremor is characterized by putamen and caudate ^{18}F-DOPA uptake within the normal range, whereas ^{18}F-DOPA uptake in the basal ganglia appears reduced in patients with essential tremor that eventually develop typical PD (Brooks et al. 1992b).

The dopaminergic function is impaired in several syndromes including Huntington's chorea, tics, essential tremor, dystonia. The assessment of dopaminergic function in these diseases is of interest for research, however it is not of significant clinical relevance as observations are rather episodic. A detailed analysis of the use of functional imaging techniques for the assessment in the dopaminergic system has recently been published by Bohnen and Frey (2003).

2.8 Cerebrovascular Diseases

Patients with cerebrovascular disease (CVD) are conventionally studied after the onset of symptoms, by morphologic imaging techniques, such as CT and MRI. Morphologic imaging, although crucial for distinguishing between ischemia and hemorrhage, is not sufficient for the complete assessment of these patients. In particular, within the first 6 h after the onset of symptoms, CT and MRI T_2 sequences may be normal, as only MRI diffusion techniques (available only at a few sites) can indeed show the signs of early ischemia. Therefore, assessment of cerebral hemodynamics with emission tomography can be crucial for patient management in cases of transient ischemia and cerebral infarction, and for monitoring cerebrovascular reserve and reperfusion. The same methods can be used in patients with cerebral or subarachnoid hemorrhage. Local cerebral blood flow can conveniently be assessed with SPECT, while other key variables, such as glucose utilization, blood volume, oxygen extraction and oxygen metabolism can be assessed with PET. Although PET has permitted a detailed description of the natural history of CVD from a hemodynamic and metabolic standpoint, it is not easily amenable to individual patient assessment and management, due to the complexity of such studies. We will present a brief summary of the pathophysiology of stroke, with emphasis on CVD patient evaluation in clinical practice by SPECT with perfusion and viability tracers.

2.8.1 Cerebral Blood Flow and Metabolism in CVD Patients

Perfusion is determined by hemodynamic variables, including vessel patency, arterial blood pressure, cardiac output, as well as functional activity, i.e., the tissue metabolic demand. Thus, blood flow measurements represent the result of the balance between these two concurrent variables, i.e., delivery and demand.

With PET it has been shown that the regional cerebral metabolic rate of oxygen ($rCMRO_2$) is maintained by continuous oxygen delivery, adjusted to the metabolic demand by variations of regional blood flow (rCBF), regional oxygen extraction (rOER), and regional blood volume (rCBV). Reductions of perfusion pressure can be compensated by increases in rOER and rCBV. These compensatory mechanisms may leave the patient asymptomatic. Further reduction of perfusion pressure causes cerebral infarction (Frackowiak et al. 1980). The acute phase is followed by reperfusion and 1–3 weeks after the stroke by a marked increase of rCBF in the infarct area (Lassen 1966) without increase in $rCMRO_2$ (Wise

et al. 1983). Such changes in rCBF, uncoupled to the metabolic demand, are attributed to loss of vascular autoregulation mechanisms, capillary hyperplasia and tissue reperfusion and has been termed "luxury perfusion" by Lassen (1966). The assessment of perfusion in the postischemic phase may be relevant for prognostic evaluation as reperfusion within one week of stroke is suggestive of neurologic recovery, whereas delayed reperfusion, beyond 1 week is indicative of poor outcome (Jorgensen et al. 1994).

Another phenomenon that is observed in stroke patients, in the subacute and chronic phase, is the presence of reduced perfusion and metabolism in areas distant from the site of ischemia. Such reduction in neuronal function is attributed to deafferentation and is termed diaschisis. This phenomenon has been the object of several PET studies (Baron et al. 1981; Lenzi et al. 1982; Serrati et al. 1994). With respect to the location of the infarct region, the areas of diaschisis may be localized in the cerebellum contralateral and in the thalamus ipsilateral to a cortical lesion, in the cortex ipsilateral to a subcortical lesion and in the homotopic cortex contralateral to a cortical lesion.

With SPECT, one can study perfusion and assess the local hemodynamics in the ischemic territories, and the degree of focal neuronal dysfunction due to deafferentation and diaschisis in areas distant from the ischemic zone. In transient ischemic attacks (TIA), i.e., reversible episodes of temporary focal neuronal dysfunction caused by a transient cerebral hypoperfusion, SPECT perfusion studies within hours of the event demonstrate a persistent perfusion reduction, which in some cases may last for up to several days following the clinical recovery. This condition, i.e., persisting hypoperfusion with normal CT and complete clinical recovery termed "incomplete infarction", may be due to reduced vascular reserve, i.e., the capacity of the cerebral circulation to comply to increases in metabolic demand with vasodilatation. When this occurs, vascular reserve, an important predictor of stroke, can be measured in individual patients by assessing perfusion before and after pharmacologic challenge. Acetazolamide, 5% CO_2, or adenosine administration cause vasodilatation and increase blood volume and perfusion only in areas supplied by normal vessels (Vorstrup et al. 1986; Choksey et al. 1989). Lack of an increase of perfusion after challenge indicates a condition termed misery perfusion and is predictive of high risk of cerebral infarction. An alternative to pharmacologic challenge is the assessment of the rCBF/rCBV ratio. Due to the rapid modifications of the two variables they should be measured concurrently by using two tracers labeled with different radionuclides, i.e., either ^{133}Xe or ^{123}I-iodo-amphetamine for the assessment of rCBF and ^{99m}Tc-RBC for the assessment of rCBV (Sabatini et al. 1991).

The flow pattern at the time of cerebral infarction and thereafter is characterized by a high degree of spatial and temporal heterogeneity due to the imbalance of hemodynamic status and functional demand. In the acute phase of a stroke reduced uptake of the perfusion tracer is seen in an area corresponding to a vascular territory. The CT lesion that eventually develops is usually smaller than the area of the initial hypoperfusion, and at the same time areas of diaschisis are identifiable in cerebral and cerebellar territories. In the subacute phase of infarction, SPECT and CT studies show consistent volumes of ischemic tissue. As shown by SPECT, the core of the lesion is characterized by more severe tissue hypoperfusion than its periphery. Moreover, areas of hypoperfusion due to diaschisis can be observed in areas that are morphologically normal. The area of hypoperfusion surrounding the core lesion may show a response to the acetazolamide test and may reveal luxury perfusion. The chronic phase is characterized by an area of absent perfusion in the infarcted territory.

The clinical applications in cerebral ischemia are limited to SPECT both for diagnosis and prognosis due to the logistic difficulties. The use of SPECT for the early diagnosis of complete ischemic stroke is currently not considered necessary, in view of the fact that there is no substantial difference in the therapeutic approach, even though SPECT may provide information on the severity of hypoperfusion prior to the occurrence of morphologic alterations (Fieschi et al. 1989). On the other hand, the assessment of perfusion with SPECT is the only procedure that shows circulatory derangements underlying the occurrence of completely reversible symptoms in patients with TIA. The assessment of TIA by using a pharmacologic challenge, can provide useful information prior to EC-IC bypass surgery (Vorstrup et al. 1986).

As for the prognostic use of SPECT in stroke patients, it has been shown that the greater the perfusion deficit, the worse the outcome. This seems to hold particularly when the assessment is performed within 6 h of the onset of symptoms, but also up to 24 h post onset of symptoms (Giubilei et al. 1990; Limburg et al. 1991). The occurrence of diaschisis has been related to outcome, as permanent diaschisis 15–56 days after stroke is correlated with poor

outcome (Serrati et al. 1994). Although some hypotheses have been raised about the possibility of using this approach to select patients for thrombolysis with recombinant tissue plasminogen activator in acute stroke, many perplexities still remain and prospective studies are needed (Alexandrov et al. 1997).

Another frequent application of SPECT is the assessment of vasospasm in subarachnoid hemorrhage (SAH), an event that occurs 4–12 days after a SAH. SPECT can detect early the occurrence of ischemia, the worst complication of SAH in a non-invasive and reproducible manner (Davis et al. 1990; Soucy et al. 1990).

2.8.2 Imaging of Neuronal Viability by Assessment of Central Benzodiazepine Receptors

One limitation of SPECT perfusion studies is the inability to distinguish whether hypoperfusion is due to ischemia or to diaschisis, or to distinguish between glial and neuronal damage. The assessment of neuron-specific damage in CVD has become possible using ^{11}C-flumazenil and ^{123}I-iomazenil, two selective high affinity antagonists of the BZD/$GABA_A$ receptors. Biousse et al. (1993) have demonstrated reduced glucose metabolism with preserved distribution volume of flumazenil as a result of diaschisis, laying the groundwork for benzodiazepine $GABA_A$ (BZD/$GABA_A$) receptor studies in ischemia. In stroke patients, BZD/$GABA_A$ receptor imaging with ^{123}I-iomazenil and SPECT has been pursued. Hatazawa et al. (1995) have studied the relationship between iomazenil uptake, CBF, $CMRO_2$, morphologic and clinical findings (Fig. 2.4); they reported a decrease in iomazenil uptake beyond the CT hypodense area. This finding is suggestive of either a CT-negative ischemic damage in the area surrounding a complete infarction, or an inhibition of iomazenil binding due to the release of endogenous substances specifically binding to BZD receptors following ischemia. Perfusion reductions with a normal ^{123}I-iomazenil distribution indicate diaschisis, i.e., abnormalities in areas distant from the stroke region, due to deafferentation.

2.9 Epilepsy

Epilepsy is a heterogeneous group of neurological disorders characterized by recurrent seizures. Seizures may manifest as focal or generalized motor jerks, sensory or visual phenomena or more complex alterations in behavior, awareness and consciousness, and are influenced by the age of the patient, the degree of brain maturation, underlying focal lesions, and the electroencephalographic (EEG) correlates present at the time of seizures. Epilepsy is common, affecting 1% of the population with about 50 new cases per year per 100,000 people. Between 10% and 20% of these new cases will go on to have "medically intractable seizures" and therefore become candidates for surgical treatment if they can be shown to have a localized seizure focus. Non-invasive localization of seizure foci can be achieved in many patients with PET and SPECT imaging and these methods have a solid clinical role in management of epilepsy. Nonetheless, it is important to keep in mind that the diagnosis of epilepsy is made largely on clinical and electrophysiological grounds and accordingly, it is important to carefully integrate functional brain imaging studies into the diagnostic

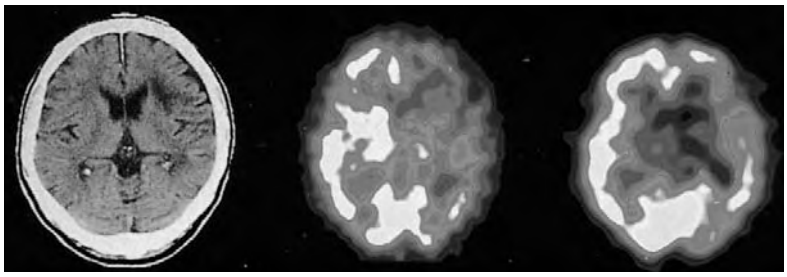

Fig. 2.4. ^{123}I-iomazenil SPECT study (*right*) in a 61-year-old patient with purely subcortical infarction 46 days after onset. CT scan (*left*) shows hypodensity in the frontal deep white matter with no involvement of the cortical area. Blood flow measured with ^{123}I-IMP (*center*) was reduced in the frontal and temporal cortices, basal ganglia, and thalamus ^{123}I-iomazenil image (*right*) demonstrated reduced uptake in the Broca area and milder reduction in the frontal and temporal lobes that were normal on the CT images. The patient presented with global aphasia

process in patients who have been determined to be candidates for seizure surgery.

2.9.1 Cerebral Blood Flow and Metabolism in Seizure Disorders

The cerebral metabolic consequences of epilepsy were first investigated using ^{18}F-FDG and PET (Kuhl et al. 1980; Engel et al. 1982a–c; Yamamoto et al. 1983; Theodore et al. 1984; Franck et al. 1986; Abou-Khalil et al. 1987). Following the development of blood flow tracers for SPECT imaging, many reports of blood flow abnormalities in epilepsy have appeared (Bonte et al. 1983; Sanabria et al. 1983; Lee et al. 1988; Stefan et al. 1987a; Lang et al. 1988). In recent years there has been a parallel recognition of the usefulness of PET and SPECT in evaluating patients for seizure surgery, but few systematic studies have been performed comparing these two modalities.

Most interictal PET studies demonstrate that approximately 70% of patients with severe partial seizures have reduced regional glucose utilization. Interictal hypometabolism is more common in patients with mesial temporal lesions such as hippocampal sclerosis, small tumors and hamartomas, but is less frequently seen in patients without radiographically visible lesions (Engel et al. 1982a; Henry et al. 1990). While the region of interictal hypometabolism corresponds grossly to the location of interictal EEG abnormalities, its size is consistently larger than the area of the EEG abnormality, as demonstrated in Fig. 2.5 (Engel et al. 1982a; Theodore et al. 1988; Henry et al. 1990). For example, in patients with seizure foci well localized in the temporal lobe, reduced metabolism is seen in the mesial and lateral temporal cortex and at times in the ipsilateral frontal and parietal cortex, basal ganglia and thalamus (Fig. 2.5) (Engel et al. 1982c; Henry et al. 1990; Sackelleras et al. 1990). However, subsequent studies indicated that within the temporal lobe the metabolic pattern may differ according to whether the patient has temporal lobe epilepsy of lateral neocortical or mesial basal origin (Hajek et al. 1993). Patients with temporal lobe epilepsy due to mesial gliosis display a generalized mesial and lateral hypometabolism, while patients with a lateral neocortical gliosis have relatively little mesial basal hypometabolism. Accordingly, PET may provide non-invasive information that helps stratify patients for mesial basal versus lateral neocortical selective temporal lobe surgery. Patients with bilateral hypometabolism have a worse surgical prognosis that those with unilateral hypometabolism (Blum et al. 1998). Interestingly, no quantitative relations have been observed between the presence and magnitude of regional hypometabolism and interictal or ictal electrical parameters (Engel 1988). Accordingly, ^{18}F-FDG metabolic studies appear to be measuring processes different than those reflected by regional electrical activity.

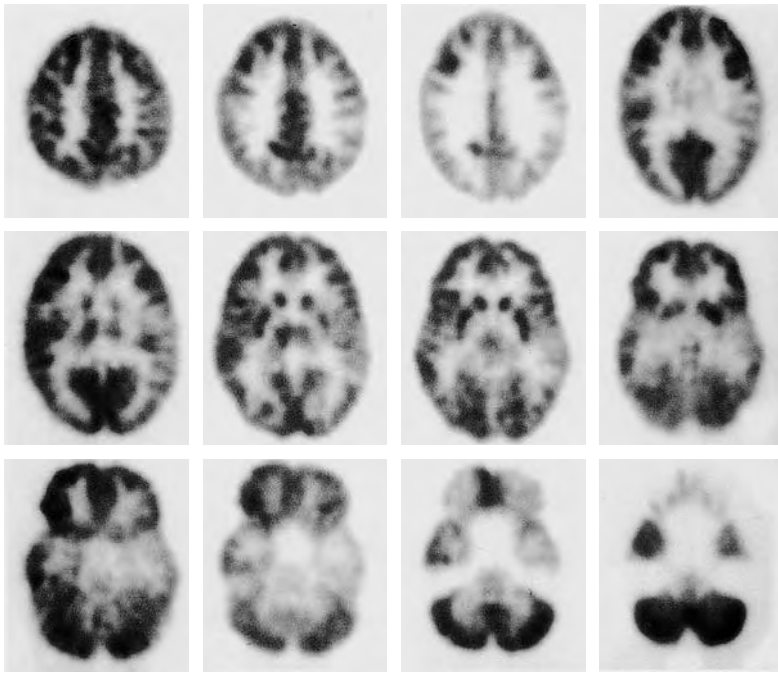

Fig. 2.5. ^{18}F-FDG-PET images of a patient with partial complex epilepsy. There is left temporal lobe interictal hypometabolism corresponding to the left temporal lobe seizure focus. In addition, the area of hypometabolism extends into the left frontoparietal region and ipsilateral thalamus, even though these areas were normal on the electroencephalogram

False positive identification of the side of a seizure focus by ^{18}F-FDG PET has been observed in only a few individuals and was attributed to artifacts resulting from depth electrode placement (Engel et al. 1982c; Engel 1984). Conversely, erroneous lateralization using scalp and sphenoidal EEG is observed in 10%–15% of patients (Engel 1984; Risinger et al. 1989). Accordingly, for clinical management of patients with intractable seizures ^{18}F-FDG PET is commonly used together with scalp EEG studies. Close correspondence of scalp EEG and ^{18}F-FDG PET results provides strong evidence for lateralization of epileptogenic tissue and in many instances patients undergo focal resections without invasive electrical monitoring. If ^{18}F-FDG PET and EEG data do not correspond then invasive electrical monitoring is needed (Engel et al. 1990). Although ^{18}F-FDG PET is clearly useful in non-invasive localization of epileptogenic tissue, there is no general correlation between the presence and degree of hypometabolism and the surgical outcome (Engel 1984). However, Swartz et al. (1992a) has demonstrated that patients with widespread areas of hypometabolism tend to have a worse postoperative prognosis. The lack of a clear relation between hypometabolism and outcome undoubtedly relates to the fact that ^{18}F-FDG PET overestimates the extent of epileptogenic tissue and conversely, extratemporal seizure foci may cause temporal lobe hypometabolism. Clearly new and more specific tracers are needed in order to identify epileptogenic tissue more precisely.

The site of interictal hypometabolism corresponds to sites of ictal onset as shown by EEG, but ictal PET studies are difficult to perform since the tracer may not be available due to its short half-life. Nonetheless, the fortuitous occurrence of seizures at the time of ^{18}F-FDG administration has provided ictal ^{18}F-FDG PET scans (Engel et al. 1982b, 1983; Theodore et al. 1984; Abou-Khalil et al. 1987). Due to the propagation of seizure activity beyond the focus and the problems in timing of the injection of ^{18}F-FDG, ictal PET scanning has received relatively little attention, particularly in the context of the clinical management of patients with intractable epilepsy. Additionally, images reflect average metabolic activity over an approximate 30-min time interval after injection. Accordingly, images reflect an admixture of interictal, ictal and postictal metabolism, which may be difficult to interpret. For example, some ^{18}F-FDG PET studies acquired during an ictus have shown global hypometabolism. In these instances it is thought that the ^{18}F-FDG PET image reflects predominantly postictal depression of metabolism when the actual seizure activity occurs during a small portion of the uptake period. Since some seizures may be subclinical it is important to monitor the EEG during the uptake period (Barrington et al. 1998). Ictal and postictal blood flow changes in epilepsy have been more extensively investigated with SPECT.

Although most ^{18}F-FDG PET studies have been performed in patients with complex partial seizures originating in the temporal lobe, the same methods can be used to localize frontal lobe lesions (Swartz et al. 1989; Franck et al. 1992; Henry et al. 1992; Robitaille et al. 1992). Interictal hypometabolism is observed in the region of frontal lobe seizure foci and, as in temporal lobe epilepsy, may extend beyond the areas of electrical abnormality (Henry et al. 1992; Swartz et al. 1989). The relation of PET to other imaging modalities in epilepsy has been recently reviewed (Duncan 1997).

SPECT imaging in epilepsy has employed ^{123}I-IMP and ^{123}HIPDM (Magistretti and Uren 1983; Lee et al. 1986, 1987, 1988) and subsequently ^{99m}Tc-HMPAO and related tracers (Stefan et al. 1987b; Andersen et al. 1988; Ryding et al. 1988; Devous and Leroy 1989; Rowe et al. 1989, 1991a; Grünwald et al. 1991; Krausz et al. 1991; Newton et al. 1992; Thomas et al. 1992). Overall, these results demonstrate the high sensitivity in localizing seizure foci comparable to that of ^{18}F-FDG PET (70%), but some studies have shown a lower sensitivity, stimulating the use of ictal SPECT scanning.

Due to the longer half-life of SPECT blood flow radiopharmaceuticals, the use of ictal and postictal scanning in patients with epilepsy has been explored in recent years (Magistretti and Uren 1983; Lee et al. 1987, 1988; Devous and Leroy 1989; Rowe et al. 1989; Marks et al. 1992; Newton et al. 1992; Ramsey et al. 1992). A number of studies have suggested that ictal imaging is more sensitive than interictal scanning in temporal lobe epilepsy (Rowe et al. 1989). In these studies a simultaneous EEG recording is obtained and the radiopharmaceutical injected within 1 or 2 min of the onset of seizure. Areas of interictal hypoperfusion convert to areas of hyperperfusion during the ictus. Ictal SPECT imaging has the potential to identify multiple and bilateral seizure foci, but carries with it the possibility of identifying areas of secondary seizure activity depending on the timing of the radiopharmaceutical injection and the rapidity of seizure spread. In addition, one study has provided evidence for an increase in regional blood flow prior to the initiation of seizure activity, implying that the blood

flow changes may not directly reflect regional seizure activity (Baumgartner et al. 1998). However, studies of localized simple partial seizures using ^{99m}Tc-HMPAO demonstrate well localized areas of hyperperfusion that correlate with the electrical and clinical localization. Ictal SPECT has also been applied to frontal lobe epilepsy, demonstrating a 91% sensitivity of correctly localizing lateralized seizure foci. Peri-ictal scanning in pediatric patients has been specifically evaluated and found to be beneficial (O'Brien et al. 1998; Shulkin 1997).

Post-ictal SPECT imaging (i.e., imaging within minutes after a seizure) has also been employed and the results demonstrate an improvement in sensitivity compared to interictal scanning (Rowe et al. 1989, 1991b; Duncan et al. 1993). The largest of these studies reported a sensitivity of 69% for post-ictal imaging compared to 38% for true interictal scans; the reasons for the low interictal sensitivity in this study are unclear. Within approximately 10 min after the completion of a seizure, the pattern of hyperperfusion in the antero-mesial temporal lobe and hypoperfusion in the remaining temporal lobe is often observed. After about 15 min the mesial hyperperfusion disappears and the hypoperfusion becomes less pronounced. Accordingly, the time from ictus is important in interpreting post-ictal SPECT images. It is important not to misinterpret severe post-ictal hypoperfusion ipsilateral to the seizure focus and hyperperfusion on the contralateral side. As with ^{18}F-FDG-PET imaging, SPECT perfusion imaging is more sensitive than MRI (Cordes et al. 1990). The presence of interictal hypoperfusion is similarly more common in patients with T_2-weighted MRI abnormalities, as compared to patients with normal MRI scans (Ryvlin et al. 1992).

Another application of ^{99m}Tc-HMPAO is to map the distribution of amobarbital in the intracarotid Wada test (Hietala et al. 1990; Jeffery et al. 1991; Hart et al. 1993). Administration of intracarotid amobarbital was first used to indicate hemispheric dominance for language in patients who were to undergo surgery for intractable epilepsy and is currently also used to identify patients at risk for amnesia following temporal lobe surgery. Subsequently, the WADA test has been used to aid in the lateralization of epileptogenic regions. A good correlation exists between interictal PET and intracarotid amobarbital administration in the lateralization of seizure foci (Salanova et al. 1998). Intracarotid amobarbital administration is used not only to localize language function, but also to predict memory disturbance following temporal lobectomy. In this regard, delivery of amobarbital to ipsilateral mesial lobe structures is the key. In 90% of individuals the posterior two-thirds of the hippocampus is supplied by the vertebrobasilar system via the posterior cerebral artery. Accordingly, administration of amobarbital via the intracarotid artery probably does not result in anesthesia of the entire hippocampus in many patients (Jeffery et al. 1991). If the amobarbital is not delivered to the hippocampus, false negative memory lateralization may occur. Co-administration of ^{99m}Tc-HMPAO and amobarbital via the internal carotid artery can be used to assess areas of perfusion during the WADA test. If present, contralateral hemispheric perfusion via the circle of Willis during the WADA test can also be identified.

Recent studies support the added value of PET over interictal SPECT studies (Lamusuo et al. 1997) and comparable accuracy with ictal SPECT and interictal PET (Markand et al. 1997). However, the final conclusions regarding the relative merits of PET and SPECT will have to await studies using state-of-the-art instrumentation for both modalities.

2.9.2 Neurotransmission Function in Seizure Disorders

Although scalp and invasive electroencephalography is the mainstay of diagnosis, classification, and lesion identification in epilepsy, PET and SPECT have advanced our understanding of the basic ictal and interictal blood flow and metabolic events that correlate with the electrical abnormalities. Flow-metabolism imaging alone is limited in its potential to elucidate the neurochemical mechanisms responsible for initiation and termination of seizures. More specific tracers are needed to further improve localization of the epileptogenic foci, predict prognosis following seizure surgery, and stratify patients for various drug therapies. New methods to image and quantitate neuroreceptors have provided the first approach to realizing these goals.

Studies using PET and SPECT have been conducted with tracers for opioid receptors: ^{11}C-carfentanil, ^{11}C-diprenorphine, ^{18}F-cyclofoxy, and ^{11}C-methylnaltrindole (Fig. 2.6) (Frost et al. 1988; Mayberg et al. 1991; Madar et al. 1997); benzodiazepine receptors: ^{11}C-flumazenil and ^{123}I-Iomazenil (Savic et al. 1988, 1990; Innis et al. 1991); muscarinic cholinergic receptors: ^{123}I-iododexetimide (Mueller-Gaertner et al. 1993); and histamine receptors: ^{11}C-doxepin (Iinuma et al. 1993). Increased levels of

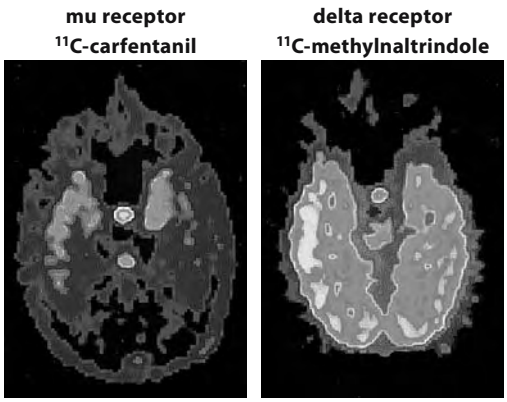

Fig. 2.6. Images of ^{11}C-carfentanil and ^{11}C-N-methyl-naltrindole binding in a patient with right-sided temporal lobe seizure focus. Both ^{11}C-carfentanil and ^{11}C-N-methyl naltrindole binding are increased in the right temporal neocortex

mu and delta opioid receptors (Fig. 2.6) and reduced benzodiazepine and muscarinic cholinergic receptors have been observed. In some, but not all, cases receptor imaging has provided additional localization information over flow/metabolism imaging alone. Comparison of ^{11}C-flumazenil (FMZ) and ^{18}F-FDG in patients with partial complex seizures has shown that ^{11}C-FMZ may provide improved localization of seizure foci (Savic et al. 1993; Koepp et al. 1997a,b; Richardson et al. 1997, 1998). However, another study showed that ^{11}C-flumazenil was less accurate (Debets et al. 1997). Changes in benzodiazepine receptors may vary as a function of seizure activity (Savic et al. 1998).

As FMZ binding depends on viability rather than metabolism and perfusion, it allows better identification of lesions and discrimination of areas of hypometabolism due to morphologic alterations from areas of hypometabolism extending beyond the area of the morphologic lesion, both in case of temporal and extratemporal epilepsy. Indeed FMZ circumscribes more restricted areas of decreased tracer binding relative to the extent of concurrent hypometabolism and hypoperfusion. Thus, FMZ PET is an excellent complementary imaging method in patients with inconclusive morphologic and functional studies.

Some studies have begun to examine the effect of seizure activity on ^{11}C-diprenorphine binding in patients with primary generalized absence seizures (Bartenstein et al. 1993) and seizures induced by reading (Koepp et al. 1998). These studies demonstrate that active seizure activity alters opioid receptor binding, probably due to release of endogenous opioid peptides. This demonstration of a functional change in opiate receptor binding following seizures introduces a new paradigm for investigation of the role of the opiate system in epilepsy.

2.10 Brain Tumors

For the last two decades the diagnostic work-up of brain tumors has been based on morphological imaging, first with CT and more recently with MRI (Atlas 1991; Fishbein 1988; Goldberg 1991). Contrast-enhanced CT is, in general, the first examination performed in patients with suspected brain tumor. It is possible with CT to make a differential diagnosis with other cerebral lesions and, to a limited extent also among different types of intracranial tumors. Investigations with CT and MRI, however, may yield partial answers, and must be complemented by biochemical imaging. Biochemical imaging of brain tumors may indeed be crucial for the early differential diagnosis, for a prognostic assessment and for differentiating between edema and gliosis, as well as between recurrence and radionecrosis, and is best achieved by emission tomography. The mechanisms of uptake and retention of each tracer in normal tissue, are frequently altered markedly in neoplastic tissue. Alterations in the normal pattern of tracer accumulation can either be due to secondary events, commonly detectable by morphologic imaging, such as the disruption of the BBB, or perfusion modifications due to compression and dislocation of the cerebral structures. However, most interesting is the tracer accumulation due to biochemical modifications of the neoplastic tissue itself, as alterations of metabolic processes and their rates may be related to the rate of growth and cell type of the tumor, while the expression of specific antigens or receptors by the tumor, may help in their histologic characterization and assist in treatment planning. Developments in morphologic imaging and concurrent advances in biochemical imaging have therefore completely modified the role of radiology and nuclear medicine in the assessment of patients with brain tumors.

The clinical use of radioactive tracers in neuro-oncology has followed their use for other purposes. This is the case of ^{18}F-fluorodeoxyglucose, developed for the assessment of neuronal functional activity, ^{11}C-methionine, developed for the assessment of amino acid transport and protein synthesis, followed by the development of ^{123}I-tyrosine. It also

holds for ^{201}Tl and ^{99m}Tc-methoxy-isobutil-isonitrile (MIBI), both extensively used in nuclear cardiology. All of these tracers are relatively non-specific, and some of them can also be used for the assessment of extracranial tumors. In other cases tracers have been developed for the assessment of tumors with very specific features, including the expression of antigens or receptors.

2.10.1 Imaging of Tumor Metabolic Processes

Tracers most commonly used for the assessment of cerebral tumors include ^{18}F-FDG, ^{11}C-methionine, ^{201}Tl and ^{99m}Tc-MIBI. In various manners their uptake is dependent on basic processes such as membrane permeability to electrolytes by active and passive mechanisms, Na^+, K^+, ATP-ase activity, energy metabolism and other metabolic variables such as protein synthesis, as well as on the presence of specific clearance mechanisms. The uptake and retention of tracer in tumor tissue depends also on cell type, extent of differentiation, immunogenicity, rate of growth, tissue mass perfusion pattern, BBB integrity, vascular neoformation and maturation.

^{18}F-FDG is the most important tracer for PET oncologic studies (see Chapters 11–13). Relatively simple synthesis and long half-life along with extensive knowledge of the mechanisms determining its uptake and retention have made it quite popular in neuro-oncology. Initial studies have related the grade of malignancy of gliomas to the rate of ^{18}F-FDG uptake, and have shown that while low grade astrocytomas have low ^{18}F-FDG uptake, anaplastic astrocytomas and glioblastomas have markedly elevated tracer uptake (di Chiro et al. 1982, 1988; di Chiro and Brooks 1988). In tumor cells there is an overexpression of glucose transporters and enzymes related to glucose metabolism and this causes an accumulation of tracer in tumor tissue that is generally higher than in normal tissue. As already stated, normal brain is avid of glucose and therefore the accumulation of ^{18}F-FDG in tumor may in some cases be very close to that of normal tissue causing difficulties in the interpretation of the study. Based on these premises ^{18}F-FDG has been used for the assessment of tumor malignancy and prognosis, but the most important use is follow-up of patients with low grade astrocytomas, possibly evolving into high grade malignancy, and the differentiation between radiation necrosis and tumor recurrence in patients presenting with relapse of neurologic symptoms and non-diagnostic CT and/or MRI after radiation therapy. Problems related to the tumor/non-tumor uptake ratio encountered with ^{18}F-FDG, and difficult differential diagnoses with other cerebral pathologies, i.e., infections, radiation necrosis, edema, that may cause abnormal ^{18}F-FDG uptake, can be avoided by using ^{11}C-methionine, the uptake of which is related to amino acid transport and metabolic rate of the tumor (Bergstrom et al. 1987; Ericson et al. 1985; Hatazawa et al. 1989).

An alternative to positron tracers in neuro-oncology is ^{201}Tl (Kaplan et al. 1987; Kim et al. 1990; Dierckx et al. 1994; Ricci et al. 1996). The discovery that ^{201}Tl accumulates in neoplastic tissue was serendipitous as it was observed in patients undergoing myocardial perfusion studies, who also had tumors. The uptake of ^{201}Tl in brain tumors is related to blood flow, BBB integrity and malignant cell density and is due to its similarities with potassium and thus on the Na^+,K^+, ATP-ase activity. ^{201}Tl uptake is also related to tumor type, as the rate of uptake differs, ^{201}Tl cannot be used as a partial substitute for histologic characterization and grading. It must be pointed out that, depending on the patient selection process ^{201}Tl sensitivity and specificity have been estimated to be about 70% and 80%, respectively, but sensitivity is lower in low grade gliomas, while specificity is lower in cases with hemorrhagic infarction. The highest sensitivities have been observed in glioblastoma multiforme and metastatic lesions.

Another tracer that is amenable for imaging cerebral tumors with SPECT is ^{99m}Tc-MIBI (O'Tuama et al. 1993; Soler et al. 1998; Maffioli et al. 1996), which was originally also developed for evaluating myocardial perfusion. This tracer is a cationic complex that is concentrated in cytoplasm and mitochondria as a result of passive diffusion across highly negative transmembrane potentials in relation to metabolic demand. Studies with this tracer have shown sensitivities similar to that of ^{201}Tl in malignant tumors and recurrence.

As for amino acid transport into tumor cells, the SPECT tracer ^{123}I-methyl-tyrosine, has been evaluated in small patient series with promising results (Biersack et al. 1989; Langen 1997).

2.10.2 Imaging of Cerebral Tumors by Antibodies and Receptor-Bound Tracers

Imaging modalities based on the use of SPECT and monoclonal antibodies is attracting increasing

interest, in particular for those aimed at the signal amplification by tumor pretargeting techniques. This is best achieved by the administration of biotinylated monoclonal antibody, followed by the administration of the radioactive tracer (two-step technique), or by the administration of avidin, after the monoclonal antibody, and then by the tracer administration (three-step technique). The additional steps are aimed at the enhancement of the signal-to-noise ratio, by allowing a longer time for the antibody localization on the tumor (two-step), and removal of free antibody by conjugation with avidin (three-step), prior to the administration of low doses of radioactive tracer.

The use of tracers, which specifically bind to receptors, has been applied mostly to pituitary adenomas, in particular in the assessment of non-secreting tumors. Non-functioning pituitary adenomas, as well as meningiomas and craniopharyngiomas, do not cause any specific endocrine syndrome; thus their presence is usually suggested by the evidence of compression of the parasellar nervous structures. Radiological differential diagnosis may occasionally be difficult in primary parasellar lesions with presentation in the parasellar region. Diagnostic uncertainty after MRI investigation occurs in up to 10% of patients with hormonally inactive tumors of the sellar region. In these selected cases, the in vivo characterization of the biochemical and functional properties of the tissue may provide useful information about the nature of the pituitary mass.

PET and SPECT have been used for the assessment of adenomas and other parasellar tumors with ^{18}F-FDG, ^{11}C-methionine, ^{11}C-tyrosine, ^{11}C-deprenyl, ^{11}C and ^{18}F labeled spiperone analogs, as well as ^{123}I-IBZM and ^{123}I-epidepride (Muhr et al. 1986; Daemen et al. 1991; Bergstrom et al. 1992; Pirker et al. 1996; Lucignani et al. 1997; de Herder et al. 1999). Some of the methods proposed for the assessment of sellar and parasellar tumors are based on measurements that are not specific to any particular type of neoplastic tissue, i.e., the rate of glucose metabolism or protein synthesis. These variables may indicate a neoplastic process when they are abnormally increased or decreased. Such methods have been shown to be useful for visualizing pituitary adenomas, for differentiating between viable neoplastic tissue and scar, and for assessing the response to pharmacological treatment. Other methods are based on the use of radiopharmaceuticals tracing processes in the normal and abnormal pituitary tissue, but neither in the other tumors of the sella nor in the nearest surrounding tissue.

Another approach to imaging pituitary adenomas is based on the presence of somatostatin receptors on pituitary tumors, which bind octreotide. For this purpose both ^{111}In-DTPA-pentetreotide and ^{123}I-Tyr3-octreotide have been used (Krenning et al. 1993; see Chap. 10).

2.10.3 Differential Diagnosis of Lymphoma and Infectious Diseases in AIDS

Neurological disorders occur in 40%–60% of patients with AIDS and approximately 10% develop focal lesions of the central nervous system. In these patients contrast enhancing brain lesions are most frequently caused by infectious diseases (50%–70% of patients), due to *Toxoplasma gondii*, *Candida albicans*, *Mycobacterium tuberculosis*, or by primary lymphomas (2%–10% of patients). Each type of lesion requires a timely, specific therapy, but it is a common practice to start anti-toxoplasmosis therapy based on empirical evidence. In patients who do not respond to therapy a non-invasive diagnostic procedure, i.e., alternative to biopsy, is required for an appropriate therapeutic planning. In these patients ^{201}Tl, ^{18}F-FDG or ^{99m}Tc-MIBI can be used to support the selection of a therapeutic approach, based on the evidence that in lymphomas the uptake of these tracers is generally higher than in focal infectious lesions (Costa et al. 1995; D'Amico et al. 1997).

2.11 Outlook for the Future

The state-of-the-art PET and SPECT techniques, which have been developed over the last 20 years, enable us to diagnose and evaluate CNS diseases, predominantly by measurement of cerebral blood flow and metabolism. Flow-metabolism methods make it possible to identify the areas of abnormal neuronal function and thus to differentiate distinct diseases due to cortical neuronal degeneration, such as the various forms of dementia that occur with cognitive impairment. However, as energy metabolism is a non-specific process with respect to the activity of the neuronal subpopulations, radionuclide imaging of the brain is under continuous evolution as new methods are developed and applied also for the assessment of

pre- and post-synaptic neurotransmitter function. These methods make it possible to differentiate syndromes occurring with motor impairment due to subcortical neuronal damage. Moreover, the use of neurochemical imaging, including the rate of synthesis and uptake of neurotransmitters, and their rate of binding to selective receptors appears crucial for the assessment of neuronal viability and damage in cerebral vascular diseases and epilepsy. Finally, the assessment of neurochemical derangements is the only key to the understanding of psychiatric diseases.

The future of brain radionuclide imaging hinges on the continuous development of devices to measure the radiotracer distribution, and on the search for new radiopharmaceuticals, along with improvements in the area of data processing. To this end, tomographic systems are being developed to improve the accuracy of measurements of radiotracer distribution with a concurrent reduction of the acquisition time, while radiopharmaceuticals that selectively tag the various receptor classes and subclasses are successfully manufactured. Last but not least, analytical procedures are being implemented for faster and more accurate image and data processing.

The strategy for the assessment of neurologic patients will soon include the use of activation tasks with pharmacologic challenge, and the use of dedicated instruments that combine state of the art X-ray computed tomography and emission tomography imaging. This synergistic approach will overcome the spatial resolution limitations of emission tomography and add the power of biochemical imaging to morphologic imaging.

References

Abi-Dargham A, Martinez D, Mawlawi O, Simpson N, Hwang DR, Slifstein M et al (2000) Measurement of striatal and extrastriatal dopamine D1 receptor binding potential with [^{11}C]NNC 112 in humans: validation and reproducibility. J Cereb Blood Flow Metab 20:225-243

Abou-Khalil BW, Siegel GJ, Sackellares JC, Gilman S, Hichwa R, Marshall R (1987) Positron emission tomography studies of cerebral glucose metabolism in chronic partial epilepsy. Ann Neurol 22:480-486

Albin RL, Minoshima S, D'Amato CJ, Frey KA, Kuhl DE, Sima AAF (1996) Fluoro-deoxyglucose positron emission tomography in diffuse Lewy body disease. Neurology 47:462-466

Alexandrov AV, Masdeu JC, Devous MD Sr, Black SE, Grotta JC (1997) Brain single-photon emission CT with HMPAO and safety of thrombolytic therapy in acute ischemic stroke. Proceedings of the meeting of the SPECT Safe Thrombolysis Study Collaborators and the members of the Brain Imaging Council of the Society of Nuclear Medicine. Stroke28:1830-1834

Andersen AR, Gram L, Kjaer L, Fuglsang-Frederiksen A, Herning M, Lassen NA, Dam M (1988) SPECT in partial epilepsy: identifying side of the focus. Acta Neurol Scand 78 [Suppl 117]:90-95

Antonini A, Schwarz J, Oertel WH, Pogarell O, Leenders KL (1997) Long-term changes of striatal dopamine D2 receptors in patients with Parkinson's disease: a study with positron emission tomography and [^{11}C]raclopride. Mov Disord 12:33-38

Arnett CD, Fowler JS, MacGregor RR (1987) Turnover of brain monoamine oxidase measured in vivo by positron emission tomography using L-^{11}C deprenyl. J Neurochem 49:522-527

Atlas SW (1991) Intraaxial brain tumours. In: Atlas SW (ed) Magnetic resonance imaging of the brain and spine. Raven, New York, pp 379-409

Baron JC; Bousser MG; Comar D; Soussaline F; Castaigne P (1981) Noninvasive tomographic study of cerebral blood flow and oxygen metabolism in vivo. Potentials, limitations, and clinical applications in cerebral ischemic disorders. Eur Neurol 20:273-284

Baronti F, Conant KE, Giuffra M, Davis TL, Brughitta G, Iadarola M, Berrettini WH, Chase TN, Mouradian MM (1991) Opioid peptides in Parkinson's disease: effects of dopamine repletion. Brain Res 560:92-96

Barrington SF, Koutroumanidis M, Agathonikou A, Marsden PK, Binnie CD, Polkey CE, Maisey MN, Panayiotopoulos CP (1998) Clinical value of "ictal" FDG-positron emission tomography and the routine use of simultaneous scalp EEG studies in patients with intractable partial epilepsies. Epilepsia 39:753-766

Bartenstein P, Ludolph A, Schober O, Lottes G, Scheidhauer K, Sciuk J, Beer H-F (1993) Benzodiazepine receptors and cerebral blood flow in partial epilepsy. Eur J Nucl Med 18:111-118

Baumgartner C, Serles W, Leutmezer F, Pataraia E, Aull S, Czech T, Pietrzyk U, Relic A, Podreka I (1998) Preictal SPECT in temporal lobe epilepsy: regional cerebral blood flow is increased prior to electroencephalography-seizure onset. J Nucl Med 39:978-982

Beer HF, Bläuenstein PA, Hasler PH, Delaloye B, Riccabona G, Bangerl I, Hunkeler W, Bonetti EP, Pieri L, Richards JG, Schubiger PA (1990) In vitro and in vivo evaluation of iodine-123-Ro16-0154: a new imaging agent for SPECT investigations of benzodiazepine receptors. J Nucl Med 31:1007-1014

Benson DF, Kuhl DE, Hawkins RA, Phelps ME, Cummings JL, Tsai SY (1983) The fluorodeoxyglucose-^{18}F scan in Alzheimer's disease and multi-infarct dementia. Arch Neurol 40:711-714

Bergstrom M, Muhr C, Lundberg PO, Berstrom K, Lundqvist H, Antoni G, Fasth K-G, Langstrom B (1987) In vivo study of amino acid distribution and metabolism in pituitary adenomas using positron emission tomography with ^{11}C-D-methionine and ^{11}C-L-methionine. J Comput Assist Tomogr 11:384-389

Bergstrom M, Muhr C, Jossan S, Lilja A, Nyberg G, Langstrom B (1992) Differentiation of pituitary adenoma and menin-

gioma: visualization with positron emission tomography and[^{11}C]-L-deprenyl. Neurosurgery 30:855-861

Berridge M, Comar D, Crouzel C, Baron JC (1983) ^{11}C-Labelled ketanserin: a selective serotonin S2 antagonist. J Label Compds Radiopharm 20:73

Biersack HJ, Coenen HH, Stocklin G, Reichmann K, Bockisch A, Oehr P, Kashab M, Rollmann O (1989) Imaging of brain tumors with L-3-[123I]iodo-alpha-methyl tyrosine and SPECT. J Nucl Med 30:110-112

Biousse V, Zilovicius M, De Recondo A, Woimant F, Amarenco P, Bousser MG et al (1993) PET study of central benzodiazepine receptors (BZR) with [^{11}C]-flumazenil (Cflu) distinguishes "functional" from structural hypometabolism in stroke. Neurology 43:A381

Blum DE, Ehsan T, Dungan D, Karis JP, Fisher RS (1998) Bilateral temporal hypometabolism in epilepsy. Epilepsia 39:651-659

Bohnen NI, Frey KA (2003) The role of positron emission tomography imaging in movement disorders. Neuroimag Clin North Am 13:791-803

Bonte FJ, Stokely EM, Devous MD Jr, Homan RW (1983) Single-photon tomographic study of regional cerebral blood flow in epilepsy. A preliminary report. Arch Neurol 40:267-270

Brooks DJ, Salmon EP, Mathias CJ, Quinn N, Leenders KL, Bannister R, Marsden CD, Frackowiak RSJ (1990a) The relationship between locomotor disability, autonomic dysfunction, and the integrity of the striatal dopaminergic system in patients with multiple system atrophy, pure autonomic failure, and Parkinson's disease, studied with PET. Brain 113:1539-1552

Brooks DJ, Ibanez V, Sawle GV, Quinn N, Lees AJ, Mathias CJ, Bannister R, Marsden CD, Frackowiak RSJ (1990b) Differing patterns of striatal ^{18}F-dopa uptake in Parkinson's disease, multiple system atrophy, and progressive supranuclear palsy (see comments). Ann Neurol 28:547-555

Brooks DJ, Ilbanez V, Sawle GV, Plaayford ED, Quinn N, Mathias CJ, Lees AJ, Marsden CD, Bannister R, Frackowiak RSJ (1992a) Striatal D2 receptor status in patients with Parkinson's disease, striatonigral degeneration, and progressive supranuclear palsy, measured with ^{11}C-raclopride and positron emission tomography. Ann Neurol 31:184-192

Brooks DJ, Playford ED, Ibanez V, Sawle GV, Thompson PD, Findley L, Marsden CD (1992b) Isolated tremor and disruption of the nigrostriatal system: an ^{18}F-dopa PET study (see comments). Neurology 42:1554-1560

Brucke T, Kornhuber J, Angelberger P, Asenbaum S, Frassine H, Podreka I (1993) SPECT imaging of dopamine and serotonin transporters with [^{123}I]beta-CIT. Binding kinetics in the human brain. J Neural Transm Gen Sect 94:137-146

Buck A, Westera G, Sutter M, Albani C, Kung HF, von Schulthess GKJ (1995) Iodine-123-IBF SPECT evaluation of extrapyramidal diseases. J Nucl Med 36:1196-1200

Cagnin A, Brooks DJ, Kennedy AM, Gunn RN, Myers R, Turkheimer FE et al (2001) In-vivo measurement of activated microglia in dementia. Lancet 358:461-467

Choksey MS, Costa DC, Iannotti F, Ell PJ, Chochard HA (1989) Tc-99m-HMPAO SPECT and cerebral blood flow: a study of CO2 reactivity. Nucl Med Commun 10:609-618

Coenen HH, Laufer P, Stocklin G, Wienhard K, Pawlik G, Bocker-Schwarz HG, Heiss WD (1987) 3-N-(2'[^{18}F]fluoroethyl)spiperone: a new ligand for cerebral dopamine receptor studies with PET. Life Sci 40:81-88

Cordes M, Christe W, Henkes H, Delavier U, Eichstädt H, Schörner W, Langer R, Felix R (1990) Focal epilepsies: HM-PAO SPECT compared with CT, MR, and EEG. J Comput Assist Tomogr 14:402-409

Costa DC, Gacinovic S, Miller RF (1995) Radionuclide brain imaging in acquired immunodeficiency syndrome (AIDS). Q J Nucl Med 39:243-249

Crouzel C, Venet M, Irie T, Sanz G, Boullais C (1988) Labelling of a serotonergic ligand with ^{18}F: [^{18}F]setoperone. J Label Compds Radiopharm 25:403

Cumming P, Gjedde A (1998) Compartmental analysis of dopa decarboxylation in living brain from dynamic positron emission tomograms. Synapse 29:37-61

Cutler NR, Haxby JV, Duara R, Grady CL, Kay AD, Kessler RM, Sundaram M, Rapoport SI (1985) Clinical history, brain metabolism, and neuropsychological function in Alzheimer's disease. Ann Neurol 18:298-309

Daemen BJ, Zwertbroek R, Elsinga PH, Paans AM, Doorenbos H, Vaalburg W (1991) PET studies with L-[^{11}C]tyrosine, L-[metyl-^{11}C]methionine and ^{18}F-fluorodeoxyglucose in prolactinomas in relation to bromocriptine treatment. Eur J Nucl Med 18:453-460

D'Amico A, Messa C, Castagna A, Zito F, Galli L, Pepe G, Lazzarin A, Lucignani G, Fazio F (1997) Diagnostic accuracy and predictive value of 201-Tl SPET for the differential diagnosis of cerebral lesions in AIDS patients. Nucl Med Commun 18:741-750

Dannals RF, Neumeyer JL, Milius RAJ, Ravert HT, Wilson AA, Wagner HN (1993) Synthesis of a radiotracer for studying dopamine uptake sites in vivo using PET: 2B-carbomethoxy-3B-(4-fluorophenyl)-[N-^{11}C-methyl]-tropane (^{11}C)CFT or (^{11}C)-WIN 35,428. J Label Compounds Radiopharmacol 33:147-152

Davis S, Andrews J, Lichenstein M, Kaye A, Tress B, Rossiter S, Salehi N, Binns D (1990) A Single-photon emission computed tomographay study of hypoperfusion after subarachnoid hemorrhage. Stroke 21:252-259

Debets RM, Sadzot B, van Isselt JW, Brekelmans GJ, Meiners LC, van Huffelen AO, Franck G, van Veelen CW (1997) Is ^{11}C-flumazenil PET superior to ^{18}FDG PET and 123I-iomazenil SPECT in presurgical evaluation of temporal lobe epilepsy. J Neurol Neurosurg Psychiatry 62:141-150

De Herder WWA, Reijs AEM, de Swart J, Kaandorp Y, Lamberts SWJ, Krenning EP, Kwekkeboom DJ (1999) Comparison of iodine-123 epidepride and iodine-123 IBZM for domapine D_2 receptor imaging in clinically non-functioning pituitary macroadenomas and macroprolactinomas. Eur J Nucl Med 26:46-50

Dey HM, Seibyl JP, Stubbs JB, Zoghbi SS, Baldwin RM, Smith EO, Zubal IG, Zea Ponce Y, Olson C, Charney DS (1994) Human biodistribution and dosimetry of the SPECT benzodiazepine receptor radioligand iodine-123 iomazenil. J Nucl Med 35:399-404

Devous MD Sr, Leroy RF (1989) Comparison of interictal and ictal regional cerebral blood flow findings with scalp and depth electrode seizure focus localization. J Cereb Blood Flow Metab 9 [Suppl]:S91

Di Chiro G, Brooks RA (1988) PET-FDG of untreated and treated cerebral gliomas. J Nucl Med 29:421-422

Di Chiro G, De LaPaz RL, Brooks RA, Sokoloff L, Kornblith PL, Smith BH, Patronas NJ, Kufta CV, Kessler RM, Johnson GS, Manning RG, Wolf AP (1982) Glucose utilization of cerebral gliomas measured by ^{18}F-fluorodeoxyglucose and positron emission tomography. Neurology 32:1323-1329

Di Chiro G, Oldfield E, Wright DC, de Michele G, Patronas N, Doppman JL, Larson SM, Masanori I, Kufta CV (1988) Cerebral necrosis after radiotherapy and/or intraarterial chemotherapy for brain tumours, PET and neuropathologic studies. Am J Roentgenol 150:189-197

Diksic M, Tohyama Y, Takada A (2000) Brain net unidirectional uptake of a-methyltryptophan. Neurochem Res 25:1537-1546

Dierckx RA, Martin JJ, Dobbeleir A, Crols R, Neetens I, de Deyn PP (1994) Sensitivity and specificity of thallium-201 single-photon emission tomography in the functional detection and differential diagnosis of brain tumours. Eur J Nucl Med 21:621-633

Ding Y, Liu N, Wang T, Marecek J, Garza V, Ojima I et al (2000) Synthesis and evaluation of 6-[^{18}F]fluoro-3-(2(S)-azetidiny lmethoxy)pyridine as a PET tracer for nicotinic acetylcholine receptors. Nucl Med Biol 27:381-389

Dolle F, Dolci L, Valette H, Hinnen F, Vaufrey F, Guenther I et al (1999) Synthesis and nicotinic acetylcholine receptor in vivo binding properties of 2-fluoro-3-[2(S)- 2-azetidiny lmethoxy]pyridine: a new positron emission tomography ligand for nicotinic receptors. J Med Chem 42:2251-2259

Dubois B, Ruberg M, Javoy-Agid F, Ploska A, Agid Y (1983) A subcortico-cortical cholinergic system is affected in Parkinson's disease. Brain Res 288:213-218

Dubois B, Danze F, Pillon B, Cusimano G, Lhermitte F, Agid Y (1987) Cholinergic-dependent cognitive deficits in Parkinson's disease. Ann Neurol 22:26-30

Duncan JS (1997) Imaging and epilepsy. Brain 120:339-377

Duncan R, Patterson J, Roberts R, Hadley DM, Bone I (1993) Ictal/postictal SPECT in the pre-surgical localization of complex partial seizures. J Neurol Neurosurg Psychiatry 56:141-148

Eckelman WC, Reba RC, Rzeszotarski WJ, Gibson RE, Hill T, Holman BL, Budinger T, Conklin JJ, Eng R, Grissom MP (1984) Cerebral imaging of acetylcholine muscarinic receptors. Science 223:291-293

Engel J Jr (1984) The use of positron emission tomographic scanning in epilepsy. Ann Neurol 15 [Suppl]:S180-191

Engel J Jr (1988) Comparison of positron emission tomography and electroencephalography as measures of cerebral function in epilepsy. In: Pfurtscheller G, Lopes da Silva FH (eds) Functional brain imaging. Huber, Bern, pp 229-238

Engel J Jr, Brown WJ, Kuhl DE, Phelps ME, Mazziotta JC, Crandall PH (1982a) Pathological findings underlying focal temporal lobe hypometabolism in partial epilepsy. Ann Neurol 12:518-528

Engel J Jr, Kuhl DE, Phelps ME, Crandall PH (1982b) Comparative localization of epileptic foci in partial epilepsy by PCT and EEG. Ann Neurol 12:529-537

Engel J Jr, Kuhl DE, Phelps ME (1982c) Patterns of human local cerebral glucose metabolism during epileptic seizures. Science 218:64-66

Engel J Jr, Kuhl DE, Phelps ME, Rausch R, Nuwer M (1983) Local cerebral metabolism during partial seizures. Neurology 33:400-413

Engel J Jr, Henry TR, Risinger MW, Mazziotta JC, Sutherling WW, Levesque MF, Phelps ME (1990) Presurgical evaluation for partial epilepsy: relative contributions of chronic depth-electrode recordings versus FDG-PET and scalp-sphenoidal ictal EEG. Neurology 40:1670-1677

Ericson K, Lilja A, Bergstrom M, Collins VP, Eriksson L, Ehrin E, von Holst H, Lundqvist H, Langsrom B B, Mosskin M (1985) Positron emission tomography with ([^{11}C]methyl)-L-methionine, [11C]D-glucose, and [68Ga]EDTA in supratentorial tumors. J Comput Assist Tomogr 9:683-689

Feldman RS, Meyer JS, Quenzer LF (1997) Principles of neuropsychopharmacology. Sinauer Associates, Sunderland

Fieschi C, Argentino C, Lenzi GL, Sacchetti ML, Toni D, Bozzao L (1989) Clinical and instrumental evaluation of patients with ischemic stroke within the first six hours. J Neurol Sci 91:311-321

Fishbein DS (1988) Neuroradiologic work-up of brain tumours. In: Theodore WH (ed) Clinical neuroimaging. Liss, New York, pp 111-137

Fowler JS, MacGregor RR, Wolf AP Arnett CD, Dewey SL, Schlyer D, Christman D, Logan J, Smith M, Sachs H et al (1987) Mapping human brain monoamine oxidase A and B with ^{11}C-labeled suicide inactivators and PET. Science 235:481-485

Fowler JS, Volkow ND, Logan J, Schlyer DJ, MacGregor RR, Wang GJ, Wolf AP, Pappas N, Alexoff D, Shea C (1993) Monoamine oxidase B (MAO B) inhibitor therapy in Parkinson's disease: the degree and reversibility of human brain MAO B inhibition by Ro 19 6327. Neurology 43:1984-1992

Frackowiak RSJ, Lenzi GL, Jones T, Heather JD (1980) Quantitative measurement of regional cerebral blood flow and oxygen metabolism in man using ^{15}O and positron emission tomography: theory, procedure and normal values. J Comput Assist Tomogr 4:727-736

Franck G, Sadzot B, Salmon E, Depresseux JC, Grisar T, Peters JM, Guillaume M, Quaglia L, Delfiore G, Delmotte D (1986) Regional blood flow and metabolic rates in human focal epilepsy and status epilepticus. In: Delgado-Escueta AV, Ward AA Jr, Woodbury DM, Porter RJ (eds) Basic mechanisms of the epilepsies. Molecular and cellular approaches. Advances in neurology, vol 44. Raven, New York, pp 935-948

Franck G, Maquet P, Sadzot B, Salmon E, Debets R, Dive D, Grisar T, Guillaume D, van Veelen C, van Huffelen A, van Emde Boas (1992) Contribution of positron emission tomography to the investigation of epilepsies of frontal lobe origin. In: Chauvel P, Delgado-Escueta AV et al (eds) Advances in neurology, vol 57. Raven, New York, pp 471-485

Frey KA, Koeppe RA, Kilbourn MR, Vander Borght TM, Albin RL, Gilman S et al (1996) Presynaptic monoaminergic vesicles in Parkinson's disease and normal aging. Ann Neurol 40:873-884

Frey KA, Minoshima S, Kuhl DE (1998) Neurochemical imaging of Alzheimer's disease and other degenerative dementias. Q J Nucl Med 42:166-178

Friedland RP, Budinger TF, Ganz E, Yano Y, Mathis CA, Koss B, Ober BA, Muesman RH, Derenzo SE (1983) Regional cerebral metabolic alterations in dementia of the Alzheimer type: positron emission tomography with [^{18}F]fluorodeoxyglucose. J Comput Assist Tomogr 7:590-598

Friston KJ, Holmes AP, Worsley KJ, Poline JB, Frith CD, Frackowiak RS (1995) Statistical parametric maps in functional imaging: a general linear approach. Human Brain Mapp 2:189-210

Frost JJ (1986) Measurement of neurotransmitter receptors by positron emission tomography: focus on the opiate receptor. NIDA Res Monogr 74:15-24

Frost JJ (2003) Molecular imaging of the brain: a historical perspective. Neuroimag Clin North Am 13:653-658

Frost JJ, Smith AC, Wagner HN Jr (1986) 3H-diprenorphine is selective for mu opiate receptors in vivo. Life Sci 38:1597-1606

Frost JJ, Mayberg HS, Fisher RS, Douglass KH, Dannals RF, Links JM, Wagner HN Jr (1988) Mu-opiate receptors measured by positron emission tomography are increased in temporal lobe epilepsy. Ann Neurol 23:231-237

Frost JJ, Mayberg HS, Sadzot B, Dannals RF, Lever JR, Ravert HT, Wilson AA, Wagner HN Jr, Links JM (1990) Comparison of [^{11}C]carfentanil binding to opiate receptors in humans by positron emission tomography. J Cereb Blood Flow Metab 10:484-492

Frost JJ, Rosier AJ, Reich SG, Smith JS, Ehlers MD, Snyder SH, Ravert HT, Dannals RF (1993) Positron emission tomographic imaging of the dopamine transporter with ^{11}C-WIN 35,428 reveals marked declines in mild Parkinson's disease. Ann Neurol 34:423-431

Geraghty JJ, Jankovic J, Zetusky WJ (1985) Association between essential tremor and Parkinson's disease. Ann Neurol 17:329-333

Giobbe D, Castellano GC, Podio V (1993) Dopamine D2 receptor imaging with SPECT using IBZM in 16 patients with Parkinson's disease. Ital J Neurol Sci 14:165-169

Giubilei F, Lenzi GL, di Piero V, Pozzilli C, Pantano P, Bastianello S, Argentino C, Fieschi C (1990) Predictive value of brain perfusion single-photon emission computed tomography in acute ischemic stroke. Stroke 21:895-900

Gjedde A, Wong DF (1990) Modeling neuroreceptor binding of radioligands in vivo. In: Frost JJ, Wagner HN Jr (eds) Quantitative imaging: neuroreceptors, neurotransmitters, and enzymes. Raven, New York, pp 51-79

Goldberg HI (1991) Extraaxial brain tumours. In: Atlas SW (ed) Magnetic resonance imaging of the brain and spine. Raven, New York, pp 327-377

Grünwald F, Durwen HF, Bockisch A, Hotze A, Kersjes W, Elger CE, Biersack HJ (1991) Technetium-99m-HMPAO brain SPECT in medically intractable temporal lobe epilepsy: a postoperative evaluation. J Nucl Med 32:388-394

Hagglund J, Aquilonius SM, Eckernas SA, Hartvig P, Lundquist H, Gullberg P, Langstrom B (1987) Dopamine receptor properties in Parkinson's disease and Huntington's chorea evaluated by positron tomography using ^{11}C-N-methylspiperone. Acta Neurol Scand 75:87-94

Hajek M, Antonini A, Leonhard K, Wieser HG (1993) Mesiobasal versus lateral temporal lobe epilepsy: metabolic differences in the temporal lobe shown by interictal ^{18}F-FDG positron emission tomography. Neurology 43:79-86

Halldin C, Stone-Elander S, Farde L, Ehrin E, Fasth KJ, Langstrom B, Sedvall G (1986) Preparation of ^{11}C-labelled SCH 23390 for the in vivo study of dopamine D-1 receptors using positron emission tomography. Appl Radiat Isot 37:1039-1043

Halldin C, Farde L, Barnett A, Sedvall G (1990) Preparation of [^{11}C]SCH 39166, a new selective D_1 dopamine receptor ligand for PET. J Nucl Med 31:737

Halldin C, Foged C, Chou YH, Karlsson P, Swahn CG, Sandell J et al (1998) Carbon-11-NNC 112: a radioligand for PET examination of striatal and neocortical D1-dopamine receptors. J Nucl Med 39:2061-2068

Hart J Jr., Lewis PJ, Lesser R, Fisher RS, Monsein LH, Schwerdt P, Bandeen-Roche K, Gordon B (1993) Anatomic correlates of memory from intracarotid amobarbital injections with technetium Tc-99m hexamethylpropyleneamine oxime SPECT. Arch Neurol 50:745-750

Hatazawa J, Ishiwata K, Itoh M, Kameyama M, Kubota K, Ido T, Matsuzawa T, Yoshimoto T, Watanuki S, Seo S (1989) Quantitative evaluation of L-[methyl-C-11] methionine uptake in tumor using positron emission tomography. J Nucl Med 30:1809-1813

Hatazawa J, Shimosegawa E, Okudera T, Inugami A, Ogawa T, Fujita H, Noguchi K, Kanno I, Miura S (1995) Evaluation of cerebral infarction with 123I-Iomazenil SPECT. J Nucl Med 36:2154-2161

Henry TR, Mazziotta JC, Engel J Jr, Christenson PD, Zhang JX, Phelps ME, Kuhl DE (1990) Quantifying interictal metabolic activity in human temporal lobe epilepsy. J Cereb Blood Flow Metab 10:748-757

Henry TR, Mazziotta JC, Engel J Jr (1992) The functional anatomy of frontal lobe epilepsy studied with PET. In: Chauvel P, Delgado-Escueta A, Holgren E, Bancaud J (eds) Advances in neurology, vol 57. Raven, New York, pp 449-463

Herscovitch P, Markham J, Raichle ME (1983) Brain blood flow measured with intravenous $H_2{}^{15}0$. I. Theory and error analysis. J Nucl Med 24:782-789

Hicks BW, Rogers GA, Parsons SM (1991) Purification and characterization of a nonvesicular vesamicol-binding protein from electric organ and demonstration of a related protein in mammalian brain. J Neurochem 57:509-519

Hietala S-O, Silfvenius H, Aasly J, Olivecrona M, Johnson L (1990) Brain perfusion with intracarotid injection of ^{99m}Tc-HM-PAO in partial epilepsy during amobarbital testing. Eur J Nucl Med 16:683-687

Hoedt-Rasmussen L, Sveinsdottir E, Lassen NA (1966) Regional cerebral blood flow in man determined by intra-arterial injection of radioactive inert gas. Circ Res 18:237-247

Hornykiewicz O, Kish SJ (1984) Neurochemical basis of dementia in Parkinson's disease. Can J Neurol Sci 11 [Suppl 1]:185-190

Hornykiewicz O, Kish SJ (1986) Biochemical pathophysiology of Parkinson's disease. Adv Neurol 45:19-34

Iinuma K, Yokoyama H, Otsuki T, Yanai K, Watanabe T, Ido T, Itoh M (1993) Histamine H_1 receptors in complex partial seizures. Lancet 341:238

Ilgin N, Zubieta JK, Reich SG, Ravert TH, Dannals RF, Frost JJ (1995) Differential diagnosis of Parkinson's disease and progressive supranuclear palsy with C11-WIN 35,248 PET imaging of the dopamine transporter. J Nucl Med 36:99

Ingvar DH, Lassen NA (1961) Quantitative determination of regional cerebral blood flow in man. Lancet 2:806-807

Innis RB, al-Tikriti MS, Zoghbi S, Baldwin RM, Sybirska EH, Laruelle MA, Malison RT, Seiby JP, Zimmermann RC, Johnson EW (1991) SPECT imaging of the benzodiazepine receptor: feasibility of in vivo potency measurements from stepwise displacement curves. J Nucl Med 32:1754-1761

Irie T, Fukushi K, Namba H, Iyo M, Tamagami H, Nagatsuka S et al (1996) Brain acetylcholinesterase activity: validation of a PET tracer in a rat model of Alzheimer's disease. J Nucl Med 37:649-655

Iyo M, Namba H, Fukushi K, Shinotoh H, Nagatsuka S, Suhara T, Nagatsuka S, Sumara T, Sudo Y, Suzuki K, Irie T (1997) Measurement of acetylcholinesterase by positron emission tomography in the brains of healthy controls and patients with Alzheimer's disease. Lancet 349:1805-1809

Jeffery PJ, Monsein LH, Szabo A, Hart JH, Fisher FS, Lesser RP, Debrun GM, Gordon B, Wagner HN Jr, Camargo EE (1991) Mapping the distribution of amobarbital sodium in the intracarotid Wada test by use of Tc-99m HMPAO with SPECT. Radiology 178:847-850

Jones AK, Luthra SK, Maziere B, Pike VW, Loc'h C, Crouzel C,

Syrota A, Jones T (1988) Regional cerebral opioid receptor studies with [^{11}C]diprenorphine in normal volunteers. J Neurosci Methods 2:121-129

Jorgensen HS, Sperling B, Nakayama H, Raaschow HO, Olsen TS (1994) Spontaneous reperfusion of cerebral infarcts in acute stroke patients. Incidence, time course and clinical outcome: the Copenhagen Stroke study. Arch Neurol 57:865-873

Kamo H, McGeer PL, Harrop R, McGeer EG, Calne DB, Martin WR, Pate BD (1987) Positron emission tomography and histopathology in Pick's disease. Neurology 37:439-445

Kanno I, Lassen NA (1979) Two methods for calculation of regional cerebral blood flow from emission computed tomography of emission tomography of inert gas concentration. J Comput Assist Tomogr 3:71-76

Kaplan WD, Takvorian T, Morris JH, Rumbaugh CL, Connolly BT, Atkins HL (1987) Thallium-201 brain tumor imaging: a comparative study with pathologic correlation. J Nucl Med 28:47-52

Kilbourn MR, Jung YW, Haka MS, Gildersleeve DL, Kuhl DE, Wieland DM (1990) Mouse brain distribution of a carbon-11 labeled vesamicol derivative: presynaptic marker of cholinergic neurons. Life Sci 47:1955-1963

Kilbourn MR, Snyder SE, Sherman PS, Kuhl DE (1996) In vivo studies of acetylcholinesterase activity using a labeled substrate, N-[^{11}C]methylpiperdin-4-yl propionate ([^{11}C]PMP). Synapse 22:123-131

Kim KT, Black KL, Marciano D, Mazziotta JC, Guze BH, Grafton S, Hawkins RA, and Becker DP. (1990) Thallium-201 SPECT imaging of brain tumors: methods and results. J Nucl Med 31:965-969

Koepp MJ, Labbe C, Richardson MP, Brooks DJ, van Paesschen W, Cunningham VJ, Duncan JS (1997a) Regional hippocampal [^{11}C]flumazenil PET in temporal lobe epilepsy with unilateral and bilateral hippocampal sclerosis. Brain 120:1865-1876

Koepp MJ, Richardson MP, Brooks DJ, Cunningham VJ, Duncan JS (1997b) Central benzodiazepine/gamma-aminobutyric acid A receptors in idiopathic generalized epilepsy: an [^{11}C]flumazenil positron emission tomography study. Epilepsia 38:1089-1097

Koepp MJ, Richardson MP, Brooks DJ, Duncan JS (1998) Focal cortical release of endogenous opioids during reading-induced seizures. Lancet 352:952-955

Koeppe RA, Frey KA, Mulholland GK, Kilbourn MR, Buck A, Lee KS, Kuhl DE (1994) [^{11}C]tropanyl benzilate-binding to muscarinic cholinergic receptors: Methodology and kinetic modeling alternatives. J Cereb Blood Flow Metab 14:85-99

Krausz Y, Cohen D, Konstantini S, Meiner Z, Yaffe S, Atlan H (1991) Brain SPECT imaging in temporal lobe epilepsy. Neuroradiology 33:274-276

Krenning EP, Kwekkeboom DJ, Bakker WH, Breman WAP, Kooij PPM, Oei HJ, wan Haen M, Postema PTE, de Jong M, Reubi JC, Visser TJ, Reijs AEM, Hofland LJ, Koper JW, Lamberts SWJ (1993) Somatostatin receptor scintigraphy with ^{111}In-DTPA-D-Phe and ^{123}I-Tyr3-octeotride: the Rotterdam experience in more than 1000 patients. Eur J Nucl Med 20:716-731

Kuhl DE, Engel J Jr, Phelps ME, Selin C (1980) Epileptic patterns of local cerebral metabolism and perfusion in humans determined by emission computed tomography of ^{18}FDG and $^{13}NH_3$. Ann Neurol 8:348-360

Kuhl DE, Metter EJ, Riege WH (1984) Patterns of local cerebral glucose utilisation determined in Parkinson's disease by the ^{18}F-fluorodeoxyglucose method. Ann Neurol 15:419-424

Kuhl DE, Koeppe RA, Fessler JA, Minoshima S, Ackermann RJ, Carey JE, Gildersleeve DL, Frey KA, Wieland DM (1994) In vivo mapping of cholinergic neurons in the human brain using SPECT and IBVM. J Nucl Med 35:405-410

Kuhl DE, Minoshima S, Fessler JA, Frey KA, Foster NL, Ficaro EP, Wieland DM, Koeppe RA (1996) In vivo mapping of cholinergic terminals in normal aging, Alzheimer's disease, and Parkinson's disease. Ann Neurol 40:339-410

Kuhl DE, Koeppe RA, Minoshima S, Snyder SE, Ficaro EP, Foster NL et al (1999) In vivo mapping of cerebral acetylcholinesterase activity in aging and Alzheimer's disease. Neurology 52:691-699

Kung HF, Kasliwal R, Pan SG, Kung MP, Mach RH, Guo YZ (1988) Dopamine D-2 receptor imaging radiopharmaceuticals: synthesis, radiolabeling, and in vitro binding of (R)-(+)- and (S)-(-)-3-iodo-2-hydroxy-6-methoxy-N-[(1-ethyl-2-pyrrolidinyl)methyl]benzamide. J Med Chem 31:1039-1043

Kung HF, Alavi A, Chang W, Kung MP, Keyes JW Jr, Velchik MG, Billings J, Pan S, Noto R, Rausch et al (1990) In vivo SPECT imaging of CNS D-2 dopamine receptors: initial studies with iodine-123-IBZM in humans. J Nucl Med 31:573-579

Kung MP, Stevenson DA, Plossl K, Meegalla SK, Beckwith A, Essman WD, Mu M, Lucki I, Kung HF (1997) [99mTc] TRODAT-1: a novel technetium-99m complex as a dopamine transporter imaging agent. Eur J Nucl Med 24:372-380

Lamusuo S, Ruottinen HM, Knuuti J, Harkonen R, Ruotsalainen U, Bergman J, Haaparanta M, Solin O, Mervaala E, Nousiainen U, Jaaskelainen S, Ylinen A, Kalviainen R, Rinne JK, Vapalahti M, Rinne JO (1997) Comparison of [^{18}F]FDG-PET, [99mTc]-HMPAO-SPECT, and [123I]-iomazenil-SPECT in localising the epileptogenic cortex. J Neurol Neurosurg Psychiatry 63:743-748

Lang W, Podreka I, Suess E, Müller C, Zeitlhofer J, Deecke L (1988) Single photon emission computerized tomography during and between seizures. J Neurol 235:277-284

Langen K (1997) Evaluation of 123-I-a-L-methyltyrosine as a SPECT tracer of amino acid uptake in brain tumours. In: De Deyn PP, Dierckx RA, Alavi A, Pickut BA (eds) SPECT in neurology and psychiatry. Libbey, London, pp 387-405

Lassen NA (1966) The luxury-perfusion syndrome and its possible relation to acute metabolic acidosis localized within the brain. Lancet 2:1113-1115

Lee BI, Markand ON, Siddiqui AR, Park HM, Mock B, Wellman HH, Worth RM, Edwards MK (1986) Single photon emission computed tomography (SPECT) brain imaging using N,N,N'-trimethyl-N'-(2 hydroxy-3-methyl-5-^{123}I-iodobenzil)-1,3-propanediamine 2 HCl (HIPDM): Intractable complex partial seizures. Neurology 36:1471-1477

Lee BI, Markand ON, Wellman HN, Siddiqui AR, Mock B, Krepshaw J, Kung H (1987) HIPDM single photon emission computed tomography brain imaging in partial onset secondarily generalized tonic-clonic seizures. Epilepsia 28:305-311

Lee BI, Markand ON, Wellman HN, Siddiqui AR, Park HM, Mock B, Worth RM, Edwards MK, Krepshaw J (1988) HIPDM-SPECT in patients with medically intractable complex partial seizures. Arch Neurol 45:397-402

Lee KS, Frey KA, Koeppe RA, Buck A, Mulholland GK, Kuhl DE (1996) In vivo quantification of cerebral muscarinic

receptors in normal human aging using positron emission tomography and [^{11}C]tropanyl benzilate. J Cereb Blood Flow Metab 16:303-310

Lee CS, Samii A, Sossi V, Ruth TJ, Schulzer M, Holden JE et al (2000) In vivo positron emission tomographic evidence for compensatory changes in presynaptic dopaminergic nerve terminals in Parkinson's disease. Ann Neurol 47:493-503

Leenders KL, Aquilonius SM, Bergstrom K, Bjurling P, Crossman AR, Eckernas SA, Gee AG, Hartuing P, Lundtquist H, Langstrom B (1988) Unilateral MPTP lesion in a rhesus monkey: effects on the striatal dopaminergic system measured in vivo with PET using various novel tracers. Brain Res 445:61-67

Lenzi GL, Frackowiak RSJ, Jones T (1982) Cerebral oxygen metabolism and blood flow in human cerebral ischemic infarction. J Cereb Blood Flow Metab 2:321-325

Leveille J, Demonceau G, Walovitch RC (1992) Intrasubject comparison between technetium-99m-ECD and technetium-99m-HMPAO in healthy human subjects. J Nucl Med 33:480-484

Lever JR, Scheffel U, Stathis M, Seltzman HH, Wyrick CD, Abraham P, Parkam K, Thomas BF, Boja JW, Fuhar MJ, Carroll FI (1996) Synthesis and in vivo studies of a selective ligand for the dopamine transporter: 3 beta-[4-(^{125}I)iodophenyl] tropan-2 beta-carboxylic acid isopropyl ester [(^{125}I)RTI-121]. J Nucl Med Biol 23:277-284

Limburg M, Royen EAV, Hijdra A, Verbeeten B Jr (1991) rCBF-SPECT in brain infarction: When does it predict outcome. J Nucl Med 3:382-387

Lucignani G, Losa M, Moresco RM, del Sole A, Matarrese M, Bettinardi V, Mortini P, Giovanelli M, Fazio F (1997) Differentiation of clinically non-functioning pituitary adenomas from meningiomas and craniopharyngiomas by positron emission tomography with [^{18}F]fluoro-ethyl-spiperone. Eur J Nucl Med 24:1149-1155

Lundkvist C, Halldin C, Ginovart N, Nyberg S, Swahn CG, Carr AA, Brunner F, Farde L (1996) [^{11}C]MDL 100907, a radioligand for selective imaging of 5-HT(2A) receptors with positron emission tomography. Life Sci 58:PL 187-192

Madar I, Lever JR, Kinter CM, Scheffel U, Ravert HT, Musachio JL, Mathews WB, Dannals RF, Frost JJ (1996) Imaging of delta opioid receptors in human brain by N1'-([^{11}C]methyl)naltrindole and PET. Synapse 24:19-28

Madar I, Lesser RP, Krauss G, Zubieta JK, Lever JR, Kinter CM, Ravert HT, Musachio JL, Mathews WB, Dannals RF, Frost JJ (1997) Imaging of delta- and mu-opioid receptors in temporal lobe epilepsy by positron emission tomography. Ann Neurol 41:358-367

Maffioli L, Gasparini M, Chiti A, Gramaglia A, Mongoj V, Pozzi A, Bombardieri E (1996) Clinical role of thechnetium-99m sestamibi single-photon emission tomography in evaluating pretreated patients with brain tumours. Eur J Nucl Med 23:308-311

Magistretti PL, Uren RF (1983) Cerebral blood flow patterns in epilepsy. In: Nistico G, DiPerri R, Meinardi H (eds) Epilepsy: an update on research and therapy. Liss, New York, pp 241-247

Marek KL, Seibyl JP, Zoghbi SS, Zea-Ponce Y, Baldwin RM, Fussell B, Charney DS, van Dyck C, Hoffer PB, Innis RP (1996) [123I] beta-CIT-SPECT imaging demonstrates bilateral loss of dopamine transporters in hemi-Parkinson's disease. Neurology 46:231-237

Markand ON, Salanova V, Worth R, Park HM, Wellman HN (1997) Comparative study of interictal PET and ictal SPECT in complex partial seizures. Acta Neurol Scand 95:129-136

Marks DA, Katz Am Hoffer P, Spencer SS (1992) Localization of extratemporal epileptic foci during ictal single photon emission computed tomography. Ann Neurol 31:250-255

Martin WRW, Stoessl AJ, Palmer M, Adam MJ, Ruth TJ, Grierson JR et al (1988) Positron emission tomography in Parkinson's disease: glucose and dopa metabolism. Adv Neurol 50:223-229

Martin WR, Palmer MR, Patlak CS, Calne DB (1989) Nigrostriatal function in humans studied with positron emission tomography. Ann Neurol 26:535-542

Mason NS, Mathis CA (2003) Positron emission tomography radiochemistry. Neuroimag Clin North Am 13:671-687

Mathis CA, Mahmood K, Huang Y, Simpson NR, Gerdes JM, Price JC (1996) Synthesis and preliminary in vivo evaluation of [^{11}C]MDL 100907: a potent and selective radioligand for the 5–HT2A receptor system. Med Chem Res 6:1–10

Mayberg HS, Sadzot B, Meltzer CC, Fisher RS, Lesser RP, Dannals RF, Lever JR, Wilson AA, Ravert HT, Wagner HN Jr, Bryan RN, Cromwell CC, Frost JJ (1991) Quantification of mu and non-mu opiate receptors in temporal lobe epilepsy using positron emission tomography. Ann Neurol 30:3-11

Messa C, Perani D, Lucignani G, Zenorini A, Zito F, Rizzo G, Grassi F, del Sole A, Franeschi M, Gilardi MC, Fazio F (1994) High resolution SPET/ [99mTc]HM-PAO in patients with probable Alzheimer's disease: comparison with PET/ [^{18}F]FDG. J Nucl Med 35:210-216

Messa C, Volonté MA, Fazio F, Zito F, Carpinelli A, d'Amico A, Rizzo G, Moresco RM, Paulesu E, Franceschi M, Lucignani G (1998) Differential distribution of striatal [^{123}I]βCIT in Parkinson's disease and progressive supranuclear palsy, evaluated with SPET. Eur J Nucl Med 25:1270-1276

Meyer M, Koeppe A, Frey KA, Foster NL, Kuhl DE (1995) Positron emission tomography measures of benzodiazepine binding in Alzheimer's disease. Arch Neurol 52:314-317

Miletich RS, Chan T, Gillespie M et al (1988) Contralateral basal ganglia metabolism in abnormal in hemiparkinsonian patients. An FDG-PET study. Neurology 38:S260

Miller BL, Darby A, Benson DF, Cummings JL, Miller MH (1997) Aggressive, socially disruptive and antisocial behaviour associated with fronto-temporal dementia. Br J Psychiatry 170:150-154

Minoshima S, Frey KA, Koeppe RA, Foster NL, Kuhl DE (1995) A diagnostic approach in Alzheimer's disease using three-dimensional stereotactic surface projections of fluorine-^{18}FDG PET. J Nucl Med 36:1238-1248

Mueller-Gaertner HW, Mayberg HS, Fisher RS, Lesser RP, Wilson AA, Ravert HT, Dannals RF, Wagner HN, Uematsu S, Frost JJ (1993) Decreased hippocampal muscarinic cholinergic receptor binding measured by ^{123}I-iododexetimide and SPECT in epilepsy. Ann Neurol 34:235-238

Muhr C, Bergstrom M, Lundberg PO, Bergstrom K, Hartving P, Lundqvist H, Antoni G, Langstom B (1986) Dopamine receptors in pituitary adenomas: PET visualization with (^{11}C)-N-methyl-spiperone. J Comput Assist Tomogr 10:175-180

Mulholland GK, Otto CA, Jewett DM, Kilbourn MR, Koeppe RA, Sherman PS, Petry NA, Carey JE, Atkinson ER, Archer S, Frey KA, Kuhl DE (1992) Synthesis, rodent biodistribution, dosimetry, metabolism, and monkey images of carbon-11 labeled (+)-2a-tropanyl benzilate: a central muscarinic receptor imaging agent. J Nucl Med 33:423-430

Mulholland GK, Kilbourn MR, Sherman P, Carey JE, Frey KA, Koeppe RA, Kuhl DE (1995) Synthesis, in vivo biodistribution and dosimetry of [^{11}C]N-methylpiperidyl benzilate ([^{11}C]NMPB), a muscarinic acetylcholine receptor antagonist. Nucl Med Biol 22:13-17

Nadeau SE, Couch MW, Devane CL, Shukla SS (1995) Regional analysis of D2 dopamine receptors in Parkinson's disease using SPECT and iodine-123-iodobenzamide. J Nucl Med 36:384-393

Nahmias C, Garnett ES, Firnau G, Long A (1985) Striatal dopamine distribution in parkinsonian patients during life. J Neurol Sci 69:223-230

Namba H, Irie T, Fukushi K, Iyo M (1994) In vivo measurement of acetylcholinesterase activity in the brain with a radioactive acetylcholine analog. Brain Res 667:278-282

Neumeyer JL, Wang S, Milius RA, Baldwin RM, Zea Ponce Y, Hoffer PB, Sybirska E, al Tikriti M, Charney DS, Malison RT (1991) Iodine-123-2-β-carboxymethoxy -3-β-(4-iodophenyl)tropane (βCIT): high affinity SPECT radiotracer of monoamine reuptake sites in brain. J Med Chem 34:3144-3146

Newton MR, Berkovic SF, Austin MC, Reutens DC, McKay WJ, Bladin PF (1992) Dystonia, clinical lateralization, and regional blood flow changes in temporal lobe seizures. Neurology 42:371-377

O'Brien TJ, Zupanc ML, Mullan BP, O'Connor MK, Brinkmann BH, Cicora KM, So EL (1998) The practical utility of performing peri-ictal SPECT in the evaluation of children with partial epilepsy. Pediatr Neurol 19:15-22

Obrist WD, Thompson HK Jr, Wang KS, Wilkinson WE (1975) Regional cerebral blood flow estimated by 133-Xenon inhalation. Stroke 6:245-256

Otsuka M, Ichiya Y, Hosokawa S (1991) Striatal blood flow, glucose metabolism, and ^{18}F-dopa uptake: difference in Parkinson's disease and atypical parkinsonism. J Neurol Neurosurg Psychiatry 54:898-904

Patlak C, Blasberg R, Fenstermacher J (1985) Graphical evaluation of blood-to-brain transfer constants from multiple-time uptake data. Generalizations. J Cereb Blood Flow Metab 5:584-590

Perlmutter JS, Raichle ME (1985) Regional blood flow in hemiparkinsonism. Neurology 35:1127-1134

Persson A, Ehrin E, Eriksson L, Farde L, Hedstrom CG, Litton JE, Mindus P, Sedvall G (1985) Imaging of [^{11}C]-labelled Ro 15-1788 binding to benzodiazepine receptors in the human brain by positron emission tomography. J Psychiatr Res 19:609-622

Phelps ME, Huang SC, Hoffman EJ, Selin C, Sokoloff L, Kuhl DE (1979) Tomographic measurement of local cerebral glucose metabolic rate in humans with (F-18)2-fluoro-2-deoxy-d-glucose: validation of method. Ann Neurol 6:371-388

Podruchny TA, Connolly C, Bokde A, Herscovitch P, Eckelman WC, Kiesewetter DO et al (2003) In vivo muscarinic 2 receptor imaging in cognitively normal young and older volunteers. Synapse 48:39-44

Pirker W, Riedl M, Luger A, Czech T, Rossler K, Asenbaum S, Angelberger P, Kornhuber J, Deecke L, Podreka I, Brucke T (1996) Dopamine D2 receptor imaging in pituitary adenomas using iodine-123-epidepride and SPECT. J Nucl Med 37:1931-1937

Price JC (2003) Principles of tracer kinetic analysis. Neuroimag Clin North Am 13:689-704

Ramsey SC, McLaughlin AF, Greenough R, Walsh J, Morris JG (1992) Comparison of independent aura, ictal and interictal cerebral perfusion. J Nucl Med 33:438-440

Reivich M, Kuhl D, Wolf A, Greenberg J, Phelps M, Ido T, Casella V, Fowler J, Hoffman E, Alavia A, Som P, Sokoloff L (1979) The ^{18}F-Fluoro-deoxyglucosemethod for the measurement of local cerebral glucose utilization in man. Circ Res 44:127-137

Ricci M, Pantano P, Pieralini A, di Stefano D, Santoro A, Bozzao L, Lenzi GL (1996) Relationship between thallium-201 uptake by supratentorial glioblastomas and their morphological characteristics on magnetic resonance imaging. Eur J Nucl Med 23:524-529

Richardson MP, Friston KJ, Sisodiya SM, Koepp MJ, Ashburner J, Free SL, Brooks DJ, Duncan JS (1997) Cortical grey matter and benzodiazepine receptors in malformations of cortical development. A voxel-based comparison of structural and functional imaging data. Brain 120:1961-1973

Richardson MP, Koepp MJ, Brooks DJ, Duncan JS (1998) ^{11}C-flumazenil PET in neocortical epilepsy. Neurology 51:485-492

Rinne JO, Laihinen A, Nagren K, Bergman J, Ruotsalainen U, Rinne UK (1990) PET demonstrates different behaviour of striatal dopamine D-1 and D-2 receptors in early Parkinson's disease. J Neurosci Res 27:494-499

Risinger MW, Engel J Jr, van Ness PL, Henry TR (1989) Ictal localization of temporal lobe seizures with scalp/sphenoidal recordings. Neurology 39:1288-1293

Robitaille Y, Rasmussen T, Dubeau, Tampieri D, Kemball K (1992) Histopathology of non-neoplastic lesions in frontal lobe epilepsy. Review of 180 cases with recent MRI and PET correlations. In: Chauvel P, Delgado-Escueta A, Holgren E, Bancaud J (eds) Advances in neurology, vol 57. Raven, New York, pp 499-513

Rowe CC, Berkovic SF, Sia STB, Austin M, McKay WJ, Kalnins RM, Bladin PF (1989) Localization of epileptic foci with postictal single photon emission computed tomography. Ann Neurol 26:660-668

Rowe CC, Berkovic SF, Austin MC, McKay WJ, Bladin PF (1991a) Patterns of postictal cerebral blood flow in temporal lobe epilepsy: qualitative and quantitative analysis. Neurology 41:1096-1103

Rowe CC, Berkovic SF, Austin MC, Saling M, Kalnins RM, McKay WJ, Bladin PF (1991b) Visual and quantitative analysis of interictal SPECT with technetium-99m-HMPAO in temporal lobe epilepsy. J Nucl Med 32:1688-1694

Ryding E, Rosen I, Elmqvist B, Ingvar DH (1988) SPECT measurements with 99mTc-HMPAO in focal epilepsy. J Cereb Blood Flow Metab 8:S95-S100

Ryvlin P, Garcia-Larrea L, Philippon B, Froment JC, Fischer C, Revol M, Mauguière F (1992) High signal intensity on T_2-weighted MRI correlates with hypoperfusion in temporal lobe epilepsy. Epilepsia 33:28-35

Sabatini U, Celsis P, Viallard G, Rascol A, Marc Vergnes JP (1991) Quantitative assessment of cerebral blood volume by single-photon emission computed tomography. Stroke 22:324-330

Sackellares JC, Siegel GJ, Abou-Khalil BW, Hood TW, Gilman S, McKeever PE, Hichwa RD, Hutchins GD (1990) Differences between lateral and mesial temporal metabolism interictally in epilepsy of mesial temporal origin. Neurology 40:1420-1426

Salanova V, Markand O, Worth R, Smith R, Wellman H, Hutchins G, Park H, Ghetti B, Azzarelli B (1998) FDG-PET

and MRI in temporal lobe epilepsy: relationship to febrile seizures, hippocampal sclerosis and outcome. Acta Neurol Scand 97:146-153

Samson Y, Hantraye P, Baron JC, Soussaline F, Comar D, Mazziere M (1985) Kinetics and displacement of ^{11}C-Ro 15=1788, a benzodiazepine antagonist, studied in human brain in vivo by positron emission tomography. Eur J Pharmacol 110:247-251

Sanabria E, Chauvel P, Askienazy S, Vignal JP, Trottier S, Chodkiewicz JP, Bancaud J (1983) Single photon emission computed tomography (SPECT) using ^{123}I-isopropyl-iodoamphetamine (IAMP) in partial epilepsy. In: Baldy-Moulinier M, Ingar D-H, Meldrum BS (eds) Current problems in epilepsy. vol 1. Cerebral blood flow, metabolism and epilepsy. Libbey, London, pp 82-87

Savic I, Persson A, Roland P, Pauli S, Sedvall G, Widen L (1988) In-vivo demonstration of reduced benzodiazepine receptor binding in human epileptic foci. Lancet 2:863-866

Savic I, Widen L, Thorell JO, Blomqvist G, Ericson K, Roland P (1990) Cortical benzodiazepine receptor binding in patients with generalized and partial epilepsy. Epilepsia 31:724-730

Savic I, Ingvar M, Stone-Elander S (1993) Comparison of [^{11}C]flumazenil and [^{18}F]FDG as PET markers of epileptic foci. J Neurol Neurosurg Psychiatry 56:615-621

Savic I, Blomqvist G, Halldin C, Litton JE, Gulyas B (1998) Regional increases in [^{11}C]flumazenil binding after epilepsy surgery. Acta Neurol Scand 97:279-286

Scheffel U, Dannals RF, Wong DF, Yokoi F, Carroll FI, Kuhar MJ (1992) Dopamine transporter imaging with novel, selective cocaine analogs. Neuroreport 3:969-972

Scheffel U, Horti AG, Koren AO, Ravert HT, Banta JP, Finley PA et al(2000) 6-[^{18}F]Fluoro-A-85380: an in vivo tracer for the nicotinic acetylcholine receptor. Nucl Med Biol 27:51-56

Schwarz J, Antonini A, Tatsch K, Kirsch CM, Oertel WH, Leenders KL (1994) Comparison of ^{123}I-IBZM SPECT and ^{11}C-raclopride PET findings in patients with parkinsonism. Nucl Med Commun 15:806-813

Seibyl J, Wallace, Smith E et al (1994) Whole body biodistribution, radiation absorbed dose, and brain SPECT imaging with [^{123}I]β-CIT in healthy human subjects. J Nucl Med 35:764-770

Serrati C, Marchal G, Rioux P, Viader F, Petit Taboue MC, Lochon P, Luet D, Derlon JM, Baron JC (1994) Contralateral cerebellar hypometabolism: a predictor for stroke outcome? J Neurol Neurosurg Psychiatry 57:174-179

Shinotoh H, Yamasaki T, Inoue O, Itoh T, Suzuki K, Hashimoto K, Tateno Y, Ikehira H (1986) Visualization of specific binding sites of benzodiazepine in human brain. J Nucl Med 27:1593-1599

Shoghi-Jadid K, Small GW, Agdeppa ED, Kepe V, Ercoli LM, Siddarth P, Read S, Satyamurthy N, Petric A, Huang SC, Barrio JR (2002) Localization of neurofibrillary tangles and beta-amyloid plaques in the brains of living patients with Alzheimer disease. Am J Geriatr Psychiatry 10:24-35

Shulkin BL (1997) PET applications in pediatrics (review) (20 refs). Q J Nucl Med 41:281-291

Siegel GJ, Agranoff BW, Wayne Albers R, Fisher SK, Uhler MD (1999) Basic Neurochemistry. Molecular, cellular and medical aspects, 6th edn. Lippincott-Raven, Philadelphia

Sokoloff L (1960) The metabolism of the central nervous system in vivo. In: Field J, Magoun HW, Hall VE (eds) Handbook of physiology-neurophysiology, vol 3. American Physiological Society, Washington DC, pp 1843-1864

Soler C, Beauchesne P, Maatougui K, Schmitt T, Barral FG, Michel D, Dubois F, Brunon J (1998) Technetium-99m sestamibi brain single-photon emission tomography for detection of recurrent gliomas after radiation therapy. Eur J Nucl Med 25:1649-1657

Soucy JP, McNamara D, Mohr G, Lamoureux F, Lamoureux J, Danais S (1990) Evaluation of vasospasm secondary to subarachnoid hemorrhage with technetium-99m-hexamethylpropyleneamine oxime (HM-PAO) tomoscintigraphy. J Nucl Med 31:972-977

Stefan H, Kuhnen C, Biersack HJ, Reichmann K (1987) Initial experience with ^{99m}Tc hexamethyl-propylene amine oxime (HM-PAO) single photon emission computed tomography (SPECT) in patients with focal epilepsy. Epilepsy Res 1:134-138

Stefan H, Pawlik G, Böcher-Schwarz HG, Biersack HJ, Burr W, Penin H, Heiss W-D (1987) Functional and morphological abnormalities in temporal lobe epilepsy: a comparison of interictal and ictal EEG, CT, MRI, SPECT and PET. J Neurol 234:377-384

Swartz BE, Halgren E, Delgado-Escueta AV, Mandelkern M, Gee M, Quinones N, Blahd WH, Repchan J (1989) Neuroimaging in patients with seizures of probable frontal lobe origin. Epilepsia 30:547-558

Swartz BE, Theodore WH, Sanabria E, Fisher RS (1992a) Positron emission and single photon emission computed tomographic studies in the frontal lobe with emphasis on the relationship to seizure foci. In: Chauvel P, Delgado-Escueta A, Holgren E, Bancaud J (eds) Advances in neurology, vol 57. Raven, New York, pp 487-497

Theodore WH, Newmark ME, Sato S, de LaPaz R, DiChiro G, Brooks R, Patronas N, Kessler RM, Manning R, Margolin R, Channing M, Porter RJ (1984) ^{18}F-fluorodoxyglucose positron emission tomography in refractory complex partial seizures. Ann Neurol 14:429-437

Theodore WH, Fishbein D, Dubinsky R (1988) Patterns of cerebral glucose metabolism in patients with partial seizures. Neurology 38:1201-1206

Thomas P, Migneco O, Darcourt J, Chatel M (1992) Single photon emission computed tomography study of subclinical rhythmic electrographic discharge in adults. Electroencephalogr Clin Neurophysiol 83:223-227

Uhl GR, Hedreen JC, Price DL (1985) Parkinson's disease: loss of neurons from the ventral tegmental area contralateral to therapeutic surgical lesions. Neurology 35:1215-1218

Van Royen E, Verhoeff NF, Speelman JD, Wolters EC, Kuiper MA, Janssen AG (1993) Multiple system atrophy and progressive supranuclear palsy. Diminished striatal D2 dopamine receptor activity demonstrated by ^{123}I-IBZM single photon emission computed tomography. Arch Neurol 50:513-516

Vorstrup S, Brun B, Lassen NA (1986) Evaluation of the cerebral vasodilatory capacity by the acetazolamide test before EC-IC bypass surgery in patients with occlusions of the internal carotid artery. Stroke 17:1291-1298

Wagner HNJ, Burns HD, Dannals RF, Wong DF, Langstrom B, Duelfer T, Frost JJ, Ravert HT, Links JM, Rosenbloom SB, Lukas SE, Kramer AV, Kuhar MJ (1983) Imaging dopamine receptors in the human brain by positron emission tomography. Science 221:1264-1266

Wise RJS, Bernardi S, Frackowiak RSJ, Legg NJ, Jones T (1983) Serial observations on the pathophysiology of acute stroke: the transition from ischemia to infarction as reflected in regional oxygen extraction. Brain 106:197-222

Wolfson LI, Leenders KL, Brown LL, Jones T (1985) Alterations of regional cerebral blood flow and oxygen metabolism in Parkinson's disease. Neurology 35:1399-1405

Yamamoto YL, Ochs R, Gloor P, Ammann W, Meyer E, Evans AC, Cooke B, Sako K, Gotman J, Feindel WH, Diksic M, Thompson CJ, Robitaille Y (1983) Patterns of rCBF and focal energy metabolic changes in relation to electroencephalographic abnormality in the interictal phase of partial epilepsy. In: Baldy-Moulinier M, Ingvar D-H, Meldrum BS (eds) Current problems in epilepsy, vol 1. Cerebral blood flow, metabolism and epilepsy. Libbey, London, pp 51-62

Zubieta JK, Frey KA, Koeppe RA, Kilbourn MR, Mulholland GK, Foster NL et al (1994) Muscarinic receptor binding in aging and Alzheimer's disease determined with [^{11}C]n-methyl-4-piperidyl benzilate and PE. J Nucl Med 35 [Suppl 5]:20P

3 Assessment of Myocardial Viability by Radionuclide Techniques

Roxana Campisi, Felix Y. J. Keng, and Heinrich R. Schelbert

CONTENTS

R. Campisi, MD
F. Y. J. Keng, MD
H. R. Schelbert, MD
Department of Molecular and Medical Pharmacology, David Greffen School of Medicine at UCLA, 10833 Le Conte Avenue, AR-144 CHS, Los Angeles, CA 90095-1735, USA

3.1 Introduction

Ischemic cardiomyopathy associated with poor left ventricular (LV) function often presents a clinical management problem. There is overwhelming evidence that such patients have a poor prognosis when treated medically. Heart transplantation has now become a therapeutic alternative. However, the limited number of donor hearts makes this approach available to only the most qualified patients. On the other hand, it has been well documented that the long-term benefit of myocardial revascularization in this patient population is significantly better than medical treatment (Alderman et al. 1993). Because operative mortality remains high in these patients, the main concern is in the selection of those patients who will really benefit from revascularization.

Dysfunctional myocardium in patients with poor LV function can be due to one or a combination of the following: (a) necrosis followed by scar tissue formation (fibrosis); (b) chronic ischemia without necrosis; or (c) transient ischemia despite reperfusion. The last two mechanisms are usually referred to as "hibernation" and "stunning," respectively, which represent viable myocardium in these patients. Identifying "viable myocardium" from non-viable scar tissue is crucial because it is well known that revascularization in patients with substantial "viable myocardium" can improve LV function, symptoms, and survival.

3.2 Definition of Myocardial Viability

3.2.1 Myocardial Stunning

It has been documented in animal models as well as in humans that reversible abnormal wall motion in segments with normal or nearly normal resting

blood flow represents myocardial stunning (Heyndrickx et al. 1975; Bolli 1992, 1998). Stunning has been demonstrated in patients with coronary artery disease in situations such as unstable angina, exercise-induced ischemia, acute myocardial infarction with early reperfusion, post-coronary artery bypass surgery, and heart transplantation (Kloner et al. 1998). Previously, myocardial stunning was considered as a regional contractile dysfunction that occurred after a brief episode of myocardial ischemia (Braunwald and Cloner 1982). There is now evidence that recurrent episodes of ischemia in the same coronary territory may occur in patients with coronary artery disease (Kloner et al. 1998), resulting in chronic contractile dysfunction which is known as "repetitive stunning" (Bolli 1998). This mechanism is probably the most common form of myocardial stunning in patients with depressed ventricular function.

3.2.2 Myocardial Hibernation

Rahimtoola (1987) first described "hibernating" myocardium as a persistently impaired myocardial function in the setting of reduced coronary blood flow. This concept entails a perfusion-contraction match derived from clinical observations and, in contrast to stunned myocardium, still lacks definitive animal or human clinical models. Its original concept, however, has been questioned since measurements of blood flow with positron emission tomography (PET) have shown normal or near-normal flow at rest and a reduced coronary flow reserve in "hibernating segments" (Vanoverschelde et al. 1993; Marinho et al. 1996; Conversano et al. 1996). Vanoverschelde et al. (1993) reported that in patients with completely occluded left anterior descending coronary arteries but without prior myocardial infarction, collateral-dependent myocardium showed either severely reduced or normal wall motion. Both types of myocardium exhibited normal blood flow at rest. However, collateral-dependent myocardium with wall motion abnormalities showed an impaired coronary flow reserve, whereas collateral-dependent myocardium with normal wall motion exhibited normal flow reserve. Thus, recurrent episodes of transient ischemia (i.e., "repetitive stunning"), rather than a true existence of hibernating myocardium, might account for chronically impaired myocardial contractile function. It is important to note that PET only quantifies transmural myocardial blood flow, and that chronic subendocardial hypoperfusion might be enough to explain dysfunctional contraction. It would be seen as a mild transmural perfusion reduction and therefore might escape detection by PET imaging (Edwards et al. 1992). Another argument in favor of the existence of true hypoperfusion are studies in humans showing increased regional myocardial blood flow after coronary revascularization of reversibly dysfunctional myocardium (Maes et al. 1995; Wolpers et al. 1997).

Nevertheless, from a clinical standpoint, the "true mechanisms" of chronic poor LV dysfunction (i.e., hibernation or stunning) are not that relevant. Bolli (1992) described that a wide overlap of hibernation and stunning may occur. It is therefore very likely that in the majority of the clinical cases both mechanisms are present. Regardless of the mechanism(s) involved, the identification of dysfunctional myocardium in patients with chronic poor LV function that will improve after coronary revascularization is important.

3.3 Identification of Viable Myocardium

Different imaging modalities are available to assess myocardial viability such as SPECT, PET, MRI, and echocardiography. This chapter reviews the usefulness of radionuclide techniques in detecting viable myocardium, to select those patients with ischemic cardiomyopathy and poor LV function who will benefit most from revascularization. Critical for preserving viable myocardium is the amount of residual blood flow and preserved cell membrane function, which in turn is predicated upon some degree of sustained metabolic activity. Radionuclide techniques probe each of these critical components. Some approaches evaluate only a single aspect, whereas others explore several components of cell function in concert. Rather than reviewing how each of these components critical to cell survival can be assessed with radionuclide studies, for logistical reasons the various radionuclide approaches currently employed are discussed. For each radionuclide or imaging approach we describe the technical concepts and then implications for patient management. Throughout the chapter we refer at times to the metabolic evaluation of viability with ^{18}F-deoxyglucose (FDG), because this approach is often used for comparison by other techniques and

is considered by many to be the gold standard of viability assessment.

3.3.1 Thallium-201 Imaging of Blood Flow and Cell Membrane Integrity

Thallium-201 (^{201}Tl) was the most widely used radionuclide for the assessment of myocardial viability by planar or SPECT imaging techniques. ^{201}Tl is a potassium analogue and its final distribution after intravenous administration is primarily intracellular. Its early myocardial uptake is proportional to regional blood flow and the flow-dependent extraction fraction of ^{201}Tl as was confirmed by the microsphere technique (Weich et al. 1977). Following its initial distribution in the myocardium, ^{201}Tl concentration in the normal and ischemic regions changes as a function of time, known as the redistribution process (Pohost et al. 1977). Clinically, redistribution implies the partial or total resolution of initial perfusion defects at repeat imaging 2.5–4 h after ^{201}Tl administration (Fig. 3.1). The process of redistribution can be seen after transient underperfusion distal to a stenotic vessel with exercise, pharmacologic stress, or even in the resting state (Gimple et al. 1994). It is important to note that although the initial ^{201}Tl uptake represents myocardial blood flow, redistribution 3–4 h later reflects myocardial cellular membrane integrity and the intracellular potassium transport, which is indirect evidence of myocardial viability (Pohost et al. 1977).

Several imaging protocols have been employed for the evaluation of myocardial viability using ^{201}Tl: (a) stress/4-h redistribution; (b) stress/4-h redistribution/24-h redistribution; (c) stress/4-h redistribution/reinjection; and (d) rest/4-h redistribution. The most commonly employed are stress/4-h redistribution/reinjection, and rest/4-h redistribution.

3.3.1.1 Study Protocols

3.3.1.1.1 Stress 4-Hour Redistribution

Evaluation of stress-induced ischemia is usually a frequent and important question in patients with coronary artery disease. Inducible ischemia can be demonstrated when a perfusion defect improves from stress to rest images, whereas viability is determined by the change in tracer uptake between the resting and delayed images. When a perfusion defect demonstrates total resolution on the delayed images, it obviously implies stress induced ischemia and viability (Gibson et al. 1983). When ^{201}Tl is administered during exercise or pharmacologic stress, it is not possible to differentiate to what extent a reversible defect represents hibernating/stunned myocardium vs ischemia. Thus, reversible and irreversible stress/redistribution perfusion defects have a highly variable predictive value for recovery of regional LV dysfunction (Maddahi et al. 1994).

One technical aspect to enhance the detection of redistribution is the quantitative analysis of regional ^{201}Tl uptake (Beller 1996). Some perfusion defects that appear irreversible on visual analysis demonstrate redistribution when quantitative analysis is performed on initial and delayed images. The majority of studies have shown that a relative threshold of 50% of maximal count density can distinguish regions with ^{201}Tl perfusion defects that will have a high probability of improved function after revascularization (Gibson et al. 1983; Yamamoto et al. 1993). Persistent defects that are mild to moderate (25–50% relative reduction in ^{201}Tl activity) are also indicative of viability. In fact, these levels of activity have been shown to reflect a high prevalence of myocardial viability by FDG criteria

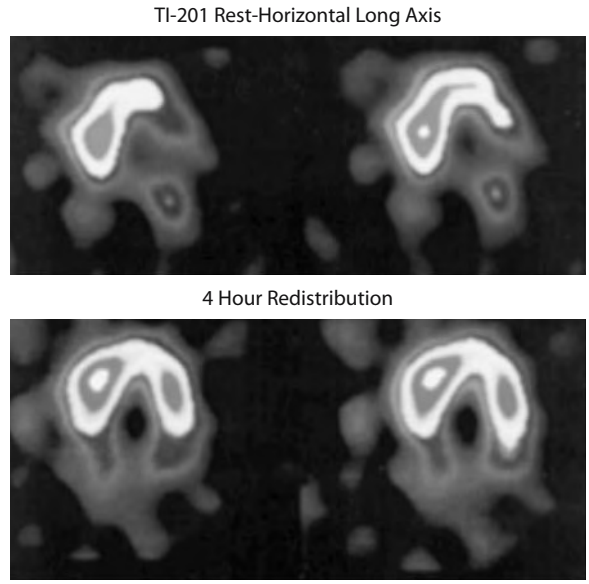

Fig. 3.1. Thallium-201 rest *(top)* and 4-h redistribution *(bottom)* images. Note the severe reduction in tracer uptake in the posterolateral wall on the initial images with almost complete defect resolution on the delayed images. (Courtesy of M. Hernandez Pampaloni)

(Bonow et al. 1991) and exhibit significant improvement in regional function following revascularization. In contrast, very few segments with persistent perfusion defects of more than 50% reduction in ^{201}Tl counts on post-stress and delayed images will improve function after revascularization (Gibson et al. 1983; Beller 1996). Kitsiou et al. (1998) using quantitative analysis, indicated that the identification of a reversible ^{201}Tl perfusion defects on stress images in an asynergic region more accurately predicted recovery of function after revascularization than mild to moderate irreversible thallium defects. The authors concluded that even at a similar mass of viable myocardium (as reflected by the final thallium content) the presence of inducible ischemia was associated with a significantly increased likelihood of functional recovery.

3.3.1.1.2 Stress, 4-Hour Redistribution, 24-Hour Redistribution

Redistribution imaging at 24 h after ^{201}Tl injection has been utilized to enhance detection of viability in persistent perfusion defects noted at 4 h (Gutman et al. 1983; Kiat et al. 1988). Kiat et al. (1988) reported that the presence of late redistribution at 18–24 h predicted enhanced regional perfusion after revascularization. They showed that 95% of myocardial segments with late redistribution showed such improvement as compared with only 37% of segments with persistent defects at 18–24 h.

This protocol, however, has limitations. A major problem is the suboptimal count statistics at 24 h following a standard 3-mCi dose, with poor target-to-background ratio making interpretation difficult. This could be overcome by a higher initial ^{201}Tl dose and longer acquisition times. Interestingly, Watson et al. (1990) have shown that by employing quantitative scintigraphy, most of the perfusion defects exhibiting late redistribution do already demonstrate some evidence of redistribution on the early images (2.5- to 4-h images). Perrone-Filardi et al. (1996) showed that 24-h ^{201}Tl redistribution images changed the interpretation of viable myocardium in only 2% of the 219 persistent perfusion defects analyzed by quantitative analysis. Also, Dilsizian et al. (1991) reported that late redistribution images after a resting injection of ^{201}Tl changed viability interpretation in only 4 of 127 segments that were interpreted as irreversible perfusion defects at 4 h. Thus, delayed 24-h redistribution imaging affects image interpretation and hence accuracy of detection of viability only minimally in a minimal amount of segments.

3.3.1.1.3 Stress 4-Hour Redistribution – Reinjection

Another approach to assess viable myocardium with ^{201}Tl is the injection of a second dose, 1–1.5 mCi of ^{201}Tl, which is administered following acquisition of the 2.5- to 4-h redistribution images. The purpose of the reinjection is to enhance the count statistics, and it provides better visual assessment of perfusion defect reversibility at rest.

Dilsizian et al. (1990) showed that, in 100 patients with coronary artery disease, 33% of abnormal segments demonstrated persistent defects on the 3- to 4-h images. Approximately half of these patients revealed improved or normal ^{201}Tl uptake after reinjection of a second dose of ^{201}Tl. Taking these observations together with other studies, ^{201}Tl reinjection immediately after 4-h SPECT imaging has been shown to improve the detection of viable myocardium in 30–50% of regions with fixed perfusion defects observed on 4-h redistribution images (Dilsizian et al. 1990; Tamaki et al. 1990; Ohtani et al. 1990).

Bonow et al. (1991) compared the reinjection protocol with myocardial uptake of FDG PET imaging in 16 patients with coronary artery disease and poor LV function and irreversible defects on the standard stress 4-h redistribution protocol. The FDG uptake was observed in 94% of perfusion defects on postexercise images that had partial or complete redistribution. Fifty-one percent of the persistent perfusion defects exhibited enhanced ^{201}Tl uptake after reinjection. The same percentage of such defects showed preserved FDG uptake. The investigators reported that detection of viability by enhanced ^{201}Tl uptake with the reinjection protocol and PET imaging of FDG uptake was concordant in 88% of defects. The authors concluded that the reinjection protocol was as sensitive as PET using FDG for detection of myocardial viability. However, post-revascularization results were not reported in this study.

The reinjection protocol was also compared with a reinjection-late 24-h redistribution approach (Dilsizian et al. 1990; Bobba et al. 1998). Dilsizian et al. (1990) showed that late 24-h imaging after reinjection did not seem to detect more viable segments compared with images acquired 10 min after reinjection. Bobba et al. (1998) reported the use of an imaging protocol without a delayed 4-h SPECT study prior to reinjection. Although the

increased incidence of delayed 24-h reversibility compared with post-reinjection at 4 h was not frequent, it was most often seen in the absence of reversibility in the immediate post-reinjection images, and in the context of unstable angina or acute coronary syndromes, rather than in chronic ischemic heart disease.

3.3.1.1.4
Rest 4-Hour Redistribution

In the rest 4-h redistribution protocol, ^{201}Tl is injected with the patient at rest, the first set of images being obtained 10–20 min later and redistribution imaging 4 h later. This has been the preferred protocol for evaluation of myocardial viability in many centers. With this protocol, hibernating myocardium exhibits a reduced ^{201}Tl uptake on the initial images, but this initial perfusion defect is expected to improve on the redistribution images.

3.3.1.2
Clinical Implications

3.3.1.2.1
Predicting Improvement In Regional and Global LV Function

Various studies have shown that ^{201}Tl reversibility after reinjection predicts improvement in regional wall motion with an overall positive predictive accuracy of 69% and a negative predictive accuracy of 89% (Dilsizian et al. 1990; Tamaki et al. 1990; Ohtani et al. 1990; Haque et al. 1995; Vanoverschelde et al. 1996; Bax et al. 1996a,b). Dilsizian et al. (1990) reported that 87% of regions with enhanced ^{201}Tl uptake on reinjection images showed normal ^{201}Tl uptake and improved wall motion after angioplasty. In contrast, all regions without enhanced ^{201}Tl uptake after reinjection demonstrated abnormal ^{201}Tl uptake as well as abnormal wall motion both before and after PTCA. Similarly, Ohtani et al. (1990) reported that 47% of persistent perfusion defects observed at 3-h redistribution showed further increase in ^{201}Tl uptake after reinjection and the majority of these segments exhibited enhanced resting wall motion after coronary artery bypass surgery. Bax et al. (1996a) also assessed improvement of global LV function after revascularization in 17 patients with ^{201}Tl reinjection imaging. This protocol identified 5 of 6 patients who showed improvement in LVEF of at least 5% and identified non-viability in 6 of 11 patients without such improvement. It has also been reported that ^{201}Tl reinjection imaging has a sensitivity of 72% and specificity of 73% in predicting improvement in global LV function (Vanoverschelde et al. 1996).

Several reports have shown that ^{201}Tl rest-redistribution imaging (planar and tomographic studies) predicts improvement in regional wall motion after revascularization with an overall sensitivity and specificity of 90 and 54%, respectively (Perrone-Filardi et al. 1996; Mori et al. 1991; Ragosta et al. 1993; Alfieri et al. 1993; Marzullo et al. 1993; Udelson et al. 1994; Charney et al. 1994; Qureshi et al. 1997). Sub-analysis of rest-redistribution SPECT studies (four reports with 83 patients) have shown cumulative positive and negative predictive values of 69 and 92%, respectively, for an improvement in regional function after revascularization (Perrone-Filardi et al. 1996; Bax et al. 1996a; Udelson et al. 1994; Charney et al. 1994). Three studies have reported on the prediction of functional recovery after revascularization with this protocol (Fig. 3.2; Mori et al. 1991; Ragosta et al. 1993; Iskandrian et al. 1983). The average positive and negative predictive accuracies of ^{201}Tl rest-redistribution scintigraphy for predicting improvement in global LVEF after revascularization (by at least 5%) was 70 and 77%, respectively.

It is of clinical relevance to consider how much viable myocardium is required to improve LV function after revascularization. Ragosta et al. (1993) using the rest-redistribution protocol have shown that in patients with depressed LV function the ejection fraction significantly increased (27±7 vs 41±11%; $p<0.01$) at 8 weeks after revascularization in patients with 7 of 14 myocardial segments being viable by ^{201}Tl (i.e., 50% of the left ventricle). In contrast, LVEF remained unchanged (27±5 vs 30±8%; not significant) in those with fewer than seven viable segments.

3.3.1.2.2
Assessment of Cardiac Risk and Prediction of Cardiac Events

The link between residual viability evaluated with ^{201}Tl imaging and improved clinical outcome after coronary bypass surgery in patients with ischemic cardiomyopathy remains largely unexplored. Gioia et al. (1995) assessed the prognostic value of ^{201}Tl rest-redistribution SPECT imaging in patients with coronary artery disease and depressed LV function. In that study, groups with viable and non-viable

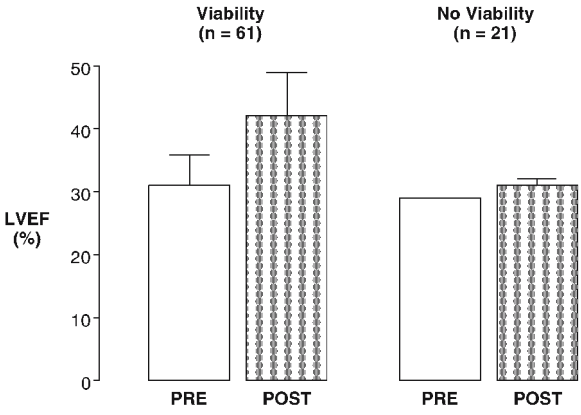

Fig. 3.2. Changes in left ventricular ejection fraction from baseline (*PRE*) to following interventional revascularization (*POST*). The data summarize the findings reported from three clinical investigations using ^{201}Tl redistribution imaging in a total of 82 patients: Ragosta et al. 1993, Iskandrian et al. 1983, and Gioia et al. 1995. The *left set of bars* indicate the patients with and the *right set of bars* the patients without evidence of viability

myocardium were comparable with respect to extent of coronary artery disease, LVEF, and extent of reversible and fixed perfusion defects. The authors reported a 13% annual mortality in those patients with myocardial viability treated medically vs 6% for those with comparable viability but undergoing revascularization. Pagley et al. (1997) reviewed the outcomes in 70 patients with multi-vessel coronary artery disease and an LVEF <40% who underwent planar quantitative rest ^{201}Tl imaging before coronary artery bypass surgery. Segmental viability scores were summed and divided by the number of segments visualized to determine a viability index. This viability index was significantly related to the 3-year survival free of cardiac events (cardiac death or heart transplantation) after bypass surgery (p=0.011) and was independent of age, ejection fraction, and number of diseased coronary vessels. There were six cardiac deaths and no transplants in patients with a higher viability index (>0.67) compared with 15 cardiac deaths and two transplants in patients with a lower viability index (0.67). Survival free of cardiac deaths or transplantation was significantly better in patients with greater viability by Kaplan-Meier analysis (Fig. 3.3). Thus, resting ^{201}Tl scintigraphy may be useful in the preoperative risk stratification for identification of patients most likely to benefit from revascularization.

3.3.2 Technetium-99m Sestamibi and Relative Myocardial Blood Flow

^{99m}Tc-sestamibi is a synthetic lipophilic cationic myocardial perfusion agent that is initially distributed in the myocardium according to blood flow. It actively and passively exchanges across sarcolemmal and mitochondrial membranes, and 90% of ^{99m}Tc-sestamibi activity is found in the mitochondria as the original free cationic complex, showing negligible redistribution over time (Carvalho et al. 1992). A negative mitochondrial charge gradient is essential for sestamibi accumulation and retention in the myocyte, which can only be maintained if the myocyte is viable (Beanlands et al. 1990). Therefore, delivery of ^{99m}Tc-sestamibi is dependent upon myocardial perfusion and its retention upon membrane integrity, and thus, upon myocardial viability (Rocco et al. 1989).

The role of ^{99m}Tc-sestamibi as an agent to evaluate myocardial viability remains controversial. The major concern is that since distribution of ^{99m}Tc-sestamibi after resting injection is proportional to resting flow in low-flow regions, resting uptake of the tracer in these areas will be diminished and therefore will underestimate the extent of viability. In addition, its lack of significant redistribution could result in overestimation of non-reversibility (Caner et al. 1998).

Many studies have compared ^{99m}Tc-sestamibi imaging with other scintigraphic protocols, such

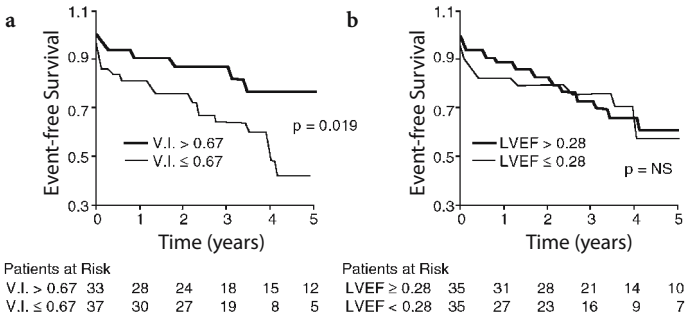

Fig. 3.3. Survival free from cardiac events such as, for example, cardiovascular death or cardiac transplantation by Kaplan-Meier Survival Analysis. **a** The event-free survival among patients with a viability index (*V.I.*) of greater than 0.67 and a survival index of less than 0.67. **b** In this group of patients with poor left ventricular ejection fraction, the event-free survival was largely independent of the ejection fraction (*LVEF*). (From Pagley et al. 1997)

as ^{201}Tl stress redistribution-reinjection (Cuocolo et al. 1992; Dilsizian et al. 1995), ^{201}Tl rest (Marzullo et al. 1993; Udelson et al. 1994; Dondi et al. 1993), ^{201}Tl rest redistribution (Dondi et al. 1993; Cuocolo et al. 1993; Kauffman et al. 1996), and FDG-PET imaging techniques (Altehoefer et al. 1992, 1994; Sawada et al. 1994; Soufer et al. 1995; Maes et al. 1997). These studies were consistent in showing that ^{99m}Tc-sestamibi was less accurate in detection of myocardial viability compared with the other modalities (Bax et al. 1997a).

In order to maximize the ability of ^{99m}Tc-sestamibi to detect viable myocardium, several approaches have been suggested. As with ^{201}Tl, quantitation of ^{99m}Tc-sestamibi imaging can be performed. It has been shown that relative ^{99m}Tc-sestamibi activity of more than 50–60% of maximal activity is usually indicative of myocardial viability (Fig. 3.4; Udelson et al. 1994; Kauffman et al. 1996; Maes et al. 1997). Due to the high count density of technetium, ^{99m}Tc-sestamibi imaging allows evaluation of regional and global LV function by first-pass radionuclide ventriculography or by gated acquisition of the SPECT perfusion images (Palmas et al. 1995; Chua et al. 1994). Wall motion data obtained from gated images can aid in the detection of viable myocardium because preserved function assessed by wall motion and thickening suggests preserved viability in the presence of diminished perfusion. Maunoury et al. (1997) have shown that indices of systolic LV function can also be derived also from gated ^{201}Tl perfusion images, which seems to offer similar prognostic information as obtained with ^{99m}Tc-sestamibi-gated SPECT. Finally, investigations have described the use of nitrate infusion during ^{99m}Tc-sestamibi injection or acquisition of delayed redistribution ^{99m}Tc-sestamibi images in order to obtain information comparable to that of ^{201}Tl for evaluation of viable myocardium (Dilsizian et al. 1994; Bisi et al. 1994; Sciagraa et al. 1996).

Most studies with ^{99m}Tc-sestamibi report a high sensitivity for predicting improvement in regional LV function (range 73–100%), whereas specificity was variable ranging from 35 to 86% (Marzullo et al. 1993; Udelson et al. 1994; Maes et al. 1997; Marzullo et al. 1992; Dakik et al. 1997). The accuracy of ^{99m}Tc-sestamibi can be enhanced by nitrate administration which improves mostly the specificity (Bisi et al. 1994; Sciagraa et al. 1997). Data have also suggested that myocardial "counts" can predict improvement in LVEF. Schneider et al. (1998) used a rest ^{99m}Tc-sestamibi protocol with nitrate augmentation and showed that by using an infarct-location adjusted optimal threshold, the protocol had a positive predictive value of 90% and a negative predictive value of 91% for prediction of improvement of LVEF. Fujiwara et al. (1998) showed that a reverse redistribution of ^{99m}Tc-sestamibi reflected recovery of LV function. Despite the promising results, further investigations are needed to validate the usefulness of ^{99m}Tc-sestamibi in evaluating myocardial viability as well as predicting outcome in patients with coronary artery disease and depressed ventricular function.

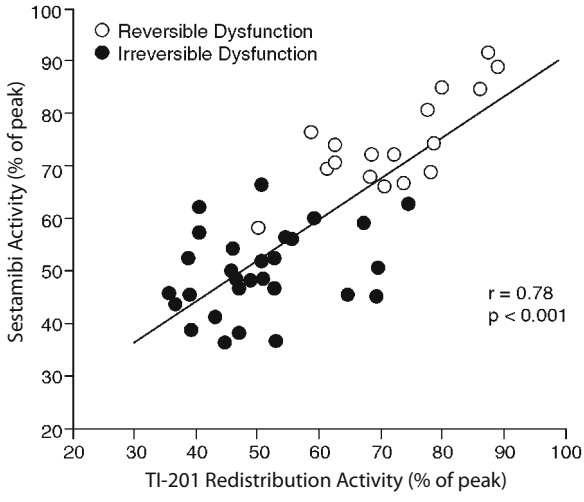

Fig. 3.4. Comparison between the relative ^{201}Tl redistribution and the ^{99m}Tc-sestamibi activity (both in percent of the peak myocardial activity) in segments with reversible and irreversible contractile dysfunction. (From Udelson et al. 1994)

3.3.3 Technetium-99m Tetrofosmin and Relative Myocardial Blood Flow

Technetium-99m tetrofosmin is a cationic lipophilic myocardial perfusion agent with electrochemical properties similar to those of ^{99m}Tc-sestamibi. ^{99m}Tc-tetrofosmin has good diagnostic accuracy for detection of coronary artery disease when compared with ^{201}Tl (Zaret et al. 1995). Its uptake and retention depends on cellular metabolism, suggesting that cellular viability might be essential for the tracer uptake and its retention (Platts et al. 1995). Like ^{99m}Tc-sestamibi, it shows little redistribution over time and it has been suggested that this may have limitations for viability assessment. For example, in a low-flow ischemia animal model with profound systolic dysfunction, tetrofosmin uptake was quantitatively comparable to initial ^{201}Tl

uptake. Delayed ^{201}Tl redistribution was slightly but significantly higher than ^{99m}Tc-tetrofosmin uptake (Koplan et al. 1996). In contrast, Takahashi et al. (1996) reported that ^{99m}Tc-tetrofosmin uptake was a good indicator of myocardial viability.

Clinical studies that examined myocardial viability with this agent are lacking. It has been reported that ^{99m}Tc-tetrofosmin closely correlates with regional reinjection ^{201}Tl activity and that defect size on resting ^{99m}Tc-tetrofosmin images is similar to that obtained with reinjection ^{201}Tl images (Matsunari et al. 1995). Galassi et al. (1998) reported a 90% concordance between ^{201}Tl redistribution and ^{99m}Tc-tetrofosmin uptake for the evaluation of myocardial viability by quantitative analysis of defect severity. The role of ^{99m}Tc-tetrofosmin in viability assessment, however, remains uncertain.

Prediction of regional and global wall motion improvement with ^{99m}Tc-tetrofosmin has been evaluated in only one study. Matsunari et al. (1997) showed that with a quantitative approach and SPECT imaging, rest ^{99m}Tc-tetrofosmin and rest redistribution of ^{201}Tl imaging were comparable in predicting functional recovery after revascularization.

3.3.4 Myocardial Metabolism with Radio-Iodinated Fatty Acid Analogs

Most of the clinical interest focused on two types of fatty acid tracers, 15-(*p*-[^{123}I]-iodophenyl)-pentadecanoic acid (IPPA), an aromatic fatty acid analog, and 15-(*p*-[^{123}I]-iodophenyl)-3-methylpentadecanoic acid (BMIPP), a branched-chain fatty acid analog. These two agents can be employed in SPECT imaging for the assessment of myocardial viability (Machulla et al. 1978; Goodman et al. 1984). BMIPP has become more popular probably because of its longer retention in the myocardium leading to superior image quality (Knapp et al. 1986). Image acquisition protocols differ between the two agents. For IPPA, the protocol involves serial SPECT image acquisition at 4, 12, 20, 28, and 36 min after injection, whereas for BMIPP, a static image is usually acquired 20–30 min after injection (Hansen et al. 1988; Nishimura et al. 1998).

Studies with fatty acid imaging in patients with prior myocardial infarcts have reported discrepancies between relative myocardial blood flow and BMIPP uptake (Takahashi et al. 1996; Tamaki et al. 1996; Franken et al. 1994). This "mismatch" between regional myocardial blood flow and fatty acid uptake (i.e., fatty acid uptake reduced more severely than blood flow) has been taken to suggest the presence of myocardial viability (Fig. 3.5). Furthermore, it appears that the reduction in BMIPP uptake relative to perfusion correlates with the blood flow – FDG mismatch pattern by PET imaging (Kawamoto et al. 1994). These studies suggest an uncoupling of fatty acid uptake from blood flow in acutely injured but potentially viable myocardium. The significance of these findings needs to be explored further.

Some studies have examined the outcome of regional LV contractile function after revascularization. Most of these studies were performed in patients after acute myocardial infarction. They demonstrated that both IPPA (Iskandrian et al. 1995) and BMIPP (Nishimura et al. 1998; Franken et al. 1996) were of value in predicting recovery of ventricular function following revascularization. Furthermore, Tamaki et al. (1996) reported that the probability of cardiac events including cardiac death, non-fatal MI, unstable angina, and the need for revascularization was increased in patients with chronic coronary artery disease as a function of the extent of mismatches of BMIPP to ^{201}Tl. Finally, Nishimura et al. (1998) reported from a retrospective multicenter trial the potential usefulness of BMIPP and ^{201}Tl imaging in predicting recurrent ischemia in the chronic phase of myocardial infarction. The extent of BMIPP defect was correlated stronger with ejection fraction at the time of discharge and at 90 days after MI than the extent of ^{201}Tl defect, although this study did not report any significant prognostic value of fatty acid imaging.

3.3.5 Myocardial Oxidative Metabolism with ^{11}C-Acetate

^{11}C-acetate allows the evaluation of flux through the tricarboxylic acid (TCA) cycle and because of its link to oxidative phosphorylation, it is an indicator of myocardial oxidative metabolism. After intravenous administration, the tracer becomes rapidly incorporated into the TCA cycle and is finally released from the cycle as $^{11}CO_2$. The rate of release from the myocardium parallels the rate of TCA cycle activity and by inference, estimates the rate of oxidative phosphorylation (for a detailed review of this tracer see Schelbert 1996). The net myocardial uptake, which reflects primarily delivery and extraction of tracer, also yields information on the distribution

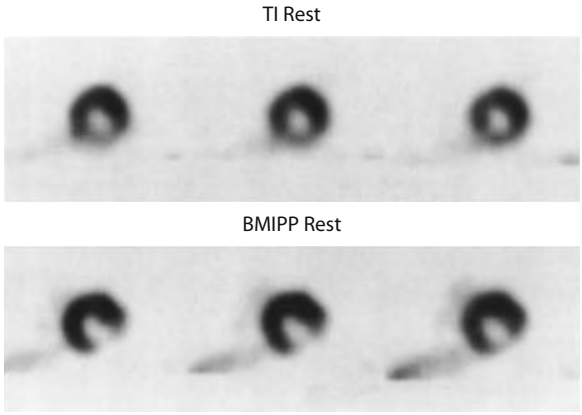

Fig. 3.5. Comparison of regional myocardial blood flow as assessed at rest with ^{201}Tl (TL REST) and fatty acid uptake (BMIPP REST). Note the more severely reduced BMIPP uptake in the inferolateral wall on the short-axis SPECT images in a patient with coronary artery disease. (From Tamaki et al. 1996)

of regional myocardial blood flow. Both Gropler et al. (1993) and Rubin et al. (1996) have shown that the threshold criteria applied to ^{11}C-acetate images exhibited better predictive values for functional recovery than did the criteria with ^{18}F-deoxyglucose. These investigators therefore favor the use of ^{11}C-acetate for the identification of viable myocardium.

In reversibly dysfunctional myocardium, blood flow was initially thought to have a linear correlation with oxygen consumption. However, a non-linear biphasic correlation has been described between both variables (Wolpers et al. 1997; Feigl et al. 1990) which in fact might account for the above described observations with ^{11}C-acetate. Thus, measurements of oxygen consumption are more accurate than blood flow measurements alone in detecting viable tissue. However, the utility of ^{11}C-acetate for identifying viable tissue still remains uncertain. It has been reported that there is a considerable overlap in ^{11}C-acetate clearance rates between reversibly and irreversibly dysfunctional myocardium, whereas relative blood flow discriminated better between both types of myocardium in these studies (Wolpers et al. 1997). Moreover, Hata et al. (1996) have shown that responses in ^{11}C-acetate clearance rates to low-dose dobutamine stimulation could differentiate both types of tissue. Further studies are needed to clarify the advantage of ^{11}C-acetate over estimates of blood flow for detecting viable myocardium.

3.3.6 Perfusion and Metabolism by PET

3.3.6.1 Evaluation of Myocardial Blood Flow

For the evaluation and quantitation of regional myocardial blood flow with PET, several tracers are available. Foremost are ^{13}N-ammonia, ^{82}Rb and ^{15}O-water (Schelbert 1996; Schelbert et al. 1996). The initial distribution of these flow tracers in myocardium parallels the distribution of myocardial blood flow. Quantitation of regional flows is possible with ^{13}N-ammonia employing dynamic image acquisition and two or three compartment tracer kinetic models, all validated in animal experiments. ^{15}O-water offers similarly accurate and extensively validated estimates of regional myocardial blood flow but requires subtraction of blood pool activity with ^{15}O-carbon-monoxide labeled red blood cells. Studies suggest that measurements can also be obtained by employing factor analysis of the serially acquired ^{15}O-water images, thus eliminating the need for additional blood pool imaging (Hermansen et al. 1998). Lastly, semiquantitative approaches have been used in the past with ^{82}Rb for obtaining estimates of regional flows, whereas later studies suggest the possibility of obtaining true estimates of blood flow with ^{82}Rb and an appropriate tracer kinetic model.

Assessment of regional blood flow in either relative or absolute terms may identify the presence of viable myocardium within dysfunctional regions. While normal blood flow in a dysfunctional region represents stunning, a severe blood flow deficit most likely represents non-viable tissue that is unlikely to improve function after revascularization (Gewirtz et al. 1994; Beanlands et al. 1997; Kitsiou et al. 1999). Absolute blood flow measurements have shown that viability will rarely be present in myocardium with flows below 0.25 ml/g/min (Gewirtz et al. 1994). Regional flow reductions of intermediate severity are more difficult to interpret. They may represent an admixture of subendocardial scar tissue with normal myocardial tissue, a condition unlikely to show improvement in function following revascularization. Conversely, such intermediate flow reduction could represent the coexistence of ischemic myocardium with either normal or scar tissue, which will likely improve function with revascularization. Some reports have shown that absolute measurements of blood flow alone are an unreliable measure of viability because of the

considerable overlap in the values between reversibly and irreversibly damaged dysfunctional myocardium (Wolpers et al. 1997; Hata et al. 1996; Kitsiou et al. 1999; Vanoverschelde et al. 1992). Another study suggested that the late ^{13}N-ammonia retention, rather than estimates of regional flow, provided more useful information regarding functional recovery after revascularization (Kitsiou et al. 1999). However, it seems that this study pointed more to the limitation of absolute as compared with relative estimates of regional flows. In any event, evaluation of regional myocardial blood flow either in absolute or in relative terms appears to be of limited value for the accurate identification of viable myocardium especially when regional flow is only mildly to moderately reduced.

3.3.6.2 Evaluation of Glucose Utilization

Numerous studies have pointed out the incremental value of glucose metabolism assessments in addition to the evaluation of regional myocardial blood flow for identifying myocardial viability.

3.3.6.2.1 General Considerations

^{18}F-deoxyglucose (FDG) is an analog of glucose and is considered a marker of external glucose utilization. This tracer is transported into the myocyte by the same carrier as glucose and is phosphorylated to FDG-6-phosphate by the enzyme hexokinase (Schelbert 1996). This product is a poor substrate for glycogen synthesis, glycolysis and the fructose-pentose shunt. FDG-6-phosphate undergoes little dephosphorylation in the myocardium and therefore ^{18}F activity represents exogenous glucose uptake.

Rates of regional myocardial glucose utilization can be obtained from serially acquired FDG images using a two-compartment tracer kinetic model (Ratib et al. 1982; Krivokapich et al. 1982). This model assumes a mostly uni-directional tracer transport from blood into myocardium and, further, a fixed relationship between the transmembranous exchange and phosphorylation rate of glucose and of FDG as defined by the so-called lumped constant (Ratib et al. 1982; Krivokapich et al. 1982). However, studies in isolated heart preparations and in vivo experimental systems have suggested that this "lumped constant" may not be constant but varies depending on study conditions (Hariharan et al. 1995; Rhodes et al. 1999).

For the assessment of myocardial viability the finding of increased exogenous glucose utilization during mild acute myocardial ischemia served as the initial mechanistic underpinning. Yet, questions remain as to whether mechanisms accounting for the enhanced glucose utilization during acute ischemia can indeed be extrapolated to more chronic conditions such as hibernation and repetitive stunning. Translocation of glucose transporters GLUT 4 and GLUT 1 and increased expression of the mostly insulin-independent GLUT 1 as demonstrated in human dysfunctional myocardium may represent a flux generating step (Young et al. 1997; Brosius et al. 1997). As reviewed by Lopaschuk (1997), oxidation of glucose appears to be limited in "chronically" ischemic myocardium so that glycolysis and glucose oxidation are uncoupled. There is an excess in glycolysis with increased release of pyruvate in the form of lactate from the myocardium.

3.3.6.2.2 Flow-Metabolism Patterns in Dysfunctional Myocardium

For the detection of viable myocardium the most widespread approach is the evaluation of myocardial blood flow in conjunction with myocardial glucose uptake. With this protocol, three patterns are observed (Fig. 3.6): normal blood flow with normal FDG uptake, reduced blood flow with normal or increased FDG uptake (flow metabolism mismatch) and reduced blood flow with reduced FDG uptake (flow metabolism match). The pattern of *mismatch* between flow and metabolism detects reversibly dysfunctional myocardium (viable tissue), whereas the *match* pattern represents irreversibly dysfunctional myocardium (non-viable tissue).

It is important to consider some technical aspects of FDG studies. The plasma glucose level of the patient can influence myocardial glucose utilization. In the fasting state, normal myocardium preferentially consumes the fatty acid. In contrast, with increasing plasma glucose and insulin levels as, for example, after oral glucose loading, glucose becomes a major source of energy (Choi et al. 1993). Of note, ischemic myocardium preferentially utilizes glucose as energy substrate. Thus, FDG imaging can be performed either after glucose administration or in the fasting state. However, studies performed in the fasting state often result in inadequate tracer accumulation in the myocardium and poor target-

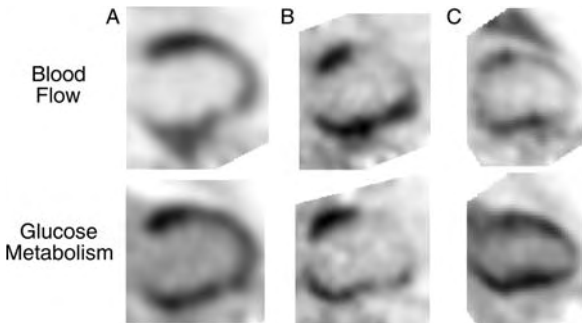

Fig. 3.6. Patterns of myocardial blood flow and glucose metabolism (as obtained with ^{13}N-ammonia and ^{18}F-deoxyglucose PET) in 3 patients with ischemic cardiomyopathy and poor left ventricular function. Only vertical long axis cuts through the mid-left ventricle are shown. Patient A demonstrates an enlarged left ventricular cavity with a mild decrease in perfusion in the anterior wall, apex, and the distal inferior wall. Glucose metabolism is homogeneous and exceeds perfusion in the anterior wall. In patient B there is a severe perfusion defect in the akinetic anterior wall that is matched to the glucose metabolic images by showing a decreased uptake of FDG referred to as "match" pattern. In contrast, in patient C, there is an extensive perfusion defect involving the anterior wall and the apex. However, the glucose metabolic images demonstrate preserved FDG uptake in the anterior and distal anterior wall. This pattern is referred to as a "blood flow / metabolism mismatch"

to-background ratio (Choi et al. 1993; Berry et al. 1991). Therefore, the glucose loaded state is preferable for identifying viable myocardium. This can be achieved by oral glucose administration approximately 1 h prior to the tracer injection.

Patients with diabetes mellitus, many of whom have coronary artery disease, may also be challenging. Poorly controlled diabetics with high resting plasma glucose result in inadequate studies of limited diagnostic quality. The need for blood glucose standardization could thus be seen as a limitation for FDG imaging. Two alternatives can be considered in these patients to obtain high diagnostic quality images: the hyperinsulinemic-euglycemic glucose clamp technique (Hicks et al. 1991; Knuuti et al. 1992) or supplemental intravenous small doses of regular insulin (Schöder et al. 1999). Because the former is a very demanding procedure in the clinical setting, the latter is usually preferred. Schöder et al. (1999) have reported that this protocol preserves the diagnostic accuracy of blood flow metabolism imaging in patients with type-II diabetes.

There has been concern that the quantitation of glucose uptake by FDG may underestimate regional glucose metabolism in vivo. Hariharan et al. (1995) showed in rat hearts that the uptake and retention of FDG in the myocardium was linearly related to glucose utilization only under steady-state conditions. The experimentally derived correction factor, the lumped constant that equates FDG uptake to glucose uptake was inaccurate when the physiological milieu of the heart was altered. These authors cautioned that estimates of regional rates of myocardial glucose utilization might be unreliable for the evaluation of myocardial viability. Whether these observations, to some extent obtained under extreme supra-physiologic conditions in isolated hearts, apply to human myocardium remains uncertain. If true, they may at least partially explain the limited value of absolute measurements of regional glucose metabolic rates for identifying dysfunctional myocardium. It is also possible that the variability of regional glucose metabolic rates as a function of variable circulating substrate in hormonal levels may similarly account for the limited value of absolute measurements. This variability further emphasizes the importance of relative regional FDG uptake values and the frequent need for simultaneous assessment of and comparison with regional myocardial blood flow.

3.3.6.3 Myocardial FDG Imaging with SPECT-like Devices

As an important technical aspect, FDG imaging was originally performed with dedicated PET only. However, studies have reported the feasibility of myocardial FDG imaging with modified or specifically designed SPECT systems (Fig. 3.7; Bax et al. 1996c; Sandler et al. 1998). SPECT with high-energy collimator devices appears to yield diagnostic findings with an accuracy approaching that of PET (Bax et al. 1996c). Initial studies have demonstrated the feasibility of identifying blood flow-metabolism patterns with SPECT-like devices alone, with predictive accuracies approaching those previously reported by dedicated PET systems. Bax et al. (1996c) reported the agreement between ^{13}N-ammonia and FDG-PET and ^{201}Tl and FDG to detect viability in dyssynergic myocardium to be 76% with both techniques, yielding comparable results in 17 of 20 patients. Chen et al. also reported an excellent statistical agreement (kappa=0.736) between the FDG-SPECT studies using a high-energy collimator and PET (Bax et al. 1996c; Chen et al. 1997). One study in 17 patients with ^{201}Tl and FDG-SPECT imaging using high-energy photon collimators reported predictive accuracies similar to those for PET and exceeded those for low-dose dobutamine echocardiography (Bax et

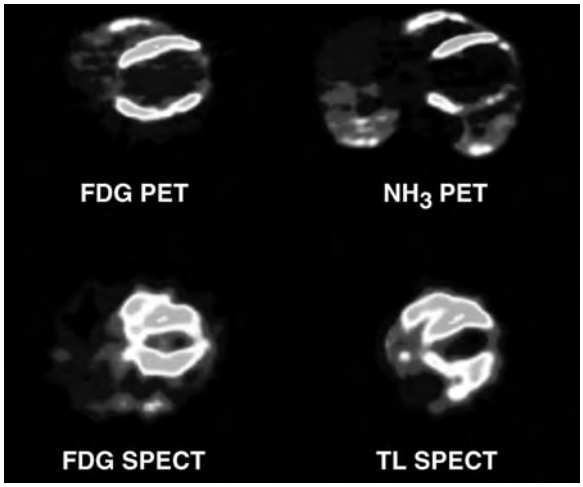

Fig. 3.7. Comparison of blood flow and metabolism imaging by PET and by SPECT. For the PET study, myocardial blood flow was evaluated with ^{13}N- ammonia (NH_3), whereas for the SPECT study myocardial perfusion was assessed with ^{201}Tl (TL). (From Bax et al. 1996c)

al. 1996a). The FDG-SPECT approach also appears to outperform the conventional ^{201}Tl-SPECT approach (Bax et al. 1997a). Image artifacts with apparent reductions in flow tracer uptake especially in the inferior wall of the left ventricle complicate the correlative interpretation of SPECT perfusion and FDG images (Sawada et al. 1994). Correction for photon attenuation and scatter in SPECT imaging is now possible and is likely to overcome this limitation (Matsunari et al. 1998). With the anticipated widespread availability of FDG through regional distribution centers, flow-metabolism imaging for the identification of viable myocardium is likely to become clinically more widely accessible and at a lower cost.

3.3.6.4 Predicting Improvement in Regional and Global LV Function

The predictive accuracy of blood flow and glucose metabolism for detecting viable tissue has been evaluated in 13 studies totaling 422 patients using PET, the PET-SPECT hybrid technique (SPECT perfusion with PET-FDG imaging) or FDG-SPECT imaging (Gropler et al. 1993; Schöder et al. 1999; Tillisch et al. 1986; Tamaki et al. 1992; Lucignani et al. 1992; Carrel et al. 1992; Marwick et al. 1992; Knuuti et al. 1994; Paolini et al. 1994; vom Dahl et al. 1996a; Baer et al. 1996; Bax et al. 1997b). Wall motion abnormalities at rest were predicted to be reversible after revascularization in regions with normal flow and metabolism having a mismatched pattern, and irreversible in those having matched pattern. Based on these criteria, positive predictive accuracies ranged from 72 to 95% and negative predictive accuracies from 74 to 100%. The variability in predictive accuracies between studies might depend on patient selection, coronary anatomy, success of revascularization, criteria for image analysis and the time from revascularization to re-evaluation of regional myocardial wall motion.

Several investigators have reported the beneficial effect of revascularization of viable myocardium detected by blood flow-metabolism imaging on the global LV function. Average increases in ejection fraction ranged from 8% to 51% when PET had shown substantial amounts of viable dysfunctional myocardium (Maes et al. 1995; Schöder et al. 1999; Tillisch et al. 1986; Lucignani et al. 1992; Carrel et al. 1992; Marwick et al. 1992; Paolini et al. 1994; vom Dahl et al. 1996a; Depre et al. 1995; Schwarz et al. 1996; Haas et al. 1997; Flameng et al. 1997; Fath-Ordoubadi et al. 1998; Pagano et al. 1998; Beanlands et al. 1998) As shown in Fig. 3.8, when data were separately analyzed based on the LVEF prior to surgery, these studies showed a greater benefit in patients with ischemic cardio-

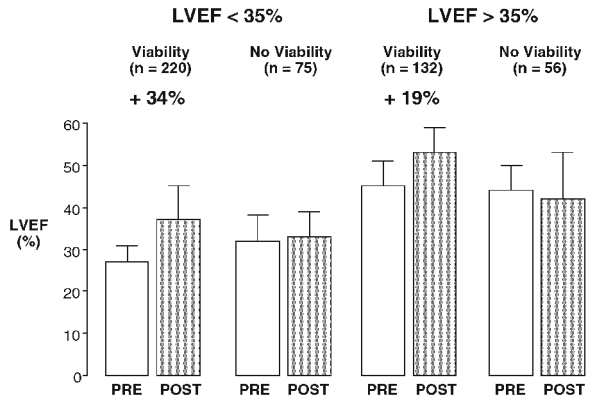

Fig. 3.8. Changes in left ventricular ejection fraction from baseline (*PRE*) to following revascularization (*POST*). The data represent the summary of 18 clinical studies in a total of 483 patients: Maes et al. 1995, Schöder et al. 1999, Tillisch et al. 1986, Lucignani et al. 1992, Carrel et al. 1992, Marwick et al. 1992, Paolini et al. 1994, Schwarz et al. 1996, Haas et al. 1997, Flameng et al. 1997, Fath-Ordoubadi et al. 1998, Pagano et al. 1998, Beanlands et al. 1998, vom Dahl et al. 1996b, Maes et al. 1994, vom Dahl et al. 1994, Depre et al. 1995, and Bax et al. 1997. Viability in these studies was determined with markers of metabolism using ^{11}C-acetate in two studies and ^{18}F-deoxyglucose in the remaining 16 studies

myopathy and LVEF below 35% than those with EF greater than 35% (42% increase in EF vs 19%, respectively).

The magnitude of a post-revascularization improvement in global LV function depends on the relative amounts of normal and remodeled LV myocardium, scar tissue and fibrosis and, in particular, viable, i.e., reversibly dysfunctional, myocardium. Such dependence had already been demonstrated by previous studies on blood flow metabolism imaging where the LV ejection improved significantly only in patients with "mismatches" in at least two or more of a total of seven myocardial regions. Later investigations provided additional support for such relationship and described a linear correlation between the extent of a mismatch (as the fraction of the LV myocardium) and the percent improvement in LVEF following revascularization (Fig. 3.9; Pagano et al. 1998).

3.3.6.5 Improvement in Congestive Heart Failure Symptoms and Exercise Capacity

With the exception of a few studies with single-photon-emitting tracers, mostly PET-based assessments of blood flow and metabolism have explored these important clinical endpoints. Several studies report significant post-revascularization changes in heart failure symptoms in patients with reversibly dysfunctional myocardium (Marwick et al. 1992; Haas et al. 1997; Eitzman et al. 1992; Di Carli et al. 1994). In one of these studies the percentage of patients with congestive heart failure classes III and IV declined significantly in only those patients with extensive blood flow metabolism mismatches who had been successfully revascularized (Di Carli et al. 1994). Revascularization of patients with mismatches were associated with substantial gains in LVEF during exercise (Carrel et al. 1992; Marwick et al. 1992, 1999). Peak rate-pressure product, maximal heart rate, and exercise capacity increased in those patients with multiple viable regions on preoperative PET imaging. There were no significant changes in exercise capacity and symptoms in patients with matched patterns only. The same investigators further showed that the improvement in exercise capacity correlated (r=0.63) with the extent of viable myocardium (Marwick et al. 1999). Other data have shown that by measuring physical activity with a specific activity scale, the post-revascularization gain in physical activity was found to correlate directly with the extent of the blood flow metabolism mismatch in 36 patients with ischemic cardiomyopathy (LVEF 28±6%; Fig. 3.10; Di Carli et al. 1995). Large flow metabolism mismatches were associated with substantial gains in physical activity, whereas only small gains were achieved when no or only small amounts of flow metabolism mismatches were present. A flow metabolism mismatch involving 18% or more of the left ventricle was associated with a sensitivity and specificity of 76 and 78%, respectively, for predicting a significant improvement in heart failure class after bypass surgery.

Of interest is that one laboratory failed to observe significant differences in congestive heart failure symptoms following revascularization between patients with and without mismatches (Marwick et al. 1992, 1999). Similarly, the LVEF at rest failed to increase significantly although there were significant gains in exercise performance and in LV function during exercise. As an important point, these investigations defined viability as disparities between regional myocardial uptake of FDG at rest and regional blood flow during pharmacologic stress. It is therefore likely that a substantial number of patients had only stress – rest mismatches. Revascularization in these patients would therefore not lead to an improvement in resting LV function, but rather during exercise, and augment the capacity for exercise.

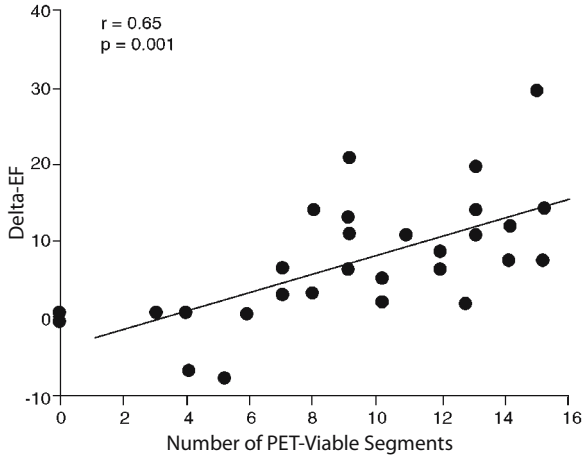

Fig. 3.9. Post-revascularization improvement in left ventricular ejection fraction (LVEF) as a function of the number of viable myocardial segments as determined by PET. (From Pagano et al. 1998)

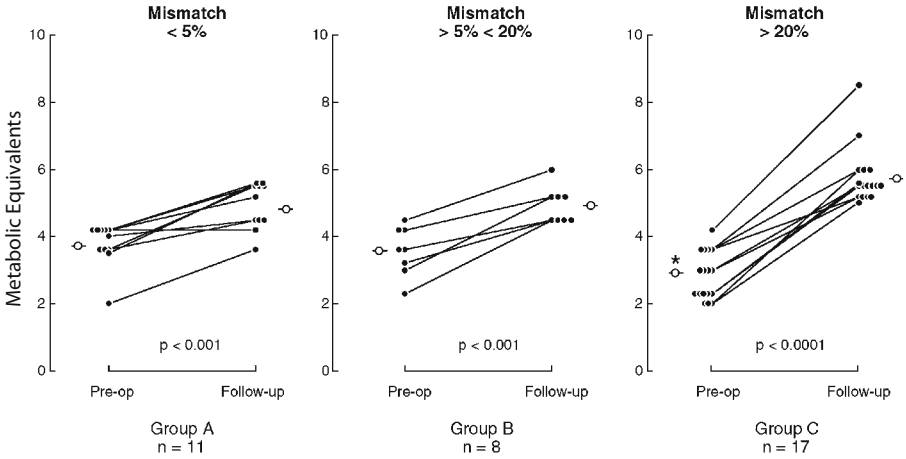

Fig. 3.10. Improvement in physical activity (measured in metabolic equivalents) as a function of the pre-operative extent of a blood flow metabolism mismatch (in percent of the entire left ventricular myocardium). Note that the increase in physical activity was most striking in group-C patients with a blood flow metabolism mismatch occupying more than 20% of the left ventricular myocardium. (From Di Carli et al. 1995)

3.3.6.6 Assessment of Cardiac Risk and Prediction of Cardiac Events

Lastly, evaluation of myocardial blood flow and glucose utilization in patients with coronary artery disease offers important clinical information about future cardiac events (Eitzman et al. 1992; Di Carli et al. 1994; 1998; Tamaki et al. 1993; Lee et al. 1994; vom Dahl et al. 1996b). Generally, follow-up after PET imaging indicates a higher incidence of cardiac events in patients with than in patients without blood flow metabolism mismatches. Three studies have examined the efficacy of revascularization over medical therapy in patients with moderate to severe LV dysfunction with and without evidence of viable myocardium (Eitzman et al. 1992; Di Carli et al. 1994; Lee et al. 1994). Despite not being randomized, these studies are the main source of understanding how to optimize treatment decisions in this patient population. The study population included patients with coronary artery disease and LVEF of less than 40%. Twenty to 68% of them had severe heart failure and approximately one third presented with angina. Survival and recurrent ischemic events (myocardial infarction, unstable angina and ventricular arrhythmia) were assessed for an average of 12–17 months. The patients were grouped based on the presence or absence of PET mismatch patterns. In patients with PET mismatch, 1-year event-free survival was poor with medical therapy. In contrast, 1-year event-free survival in these patients was significantly improved by revascularization. In patients without PET mismatch, 1-year event-free survival was similar with either medical therapy or revascularization. Thus, these studies show a clear benefit of revascularization over medical therapy for patients exhibiting a PET mismatch. Furthermore, the presence of blood flow metabolism mismatch and lack of revascularization were found to be the strongest predictors of cardiac death (Eitzman et al. 1992; Di Carli et al. 1994).

Di Carli et al. (1998) described the survival benefits of revascularization in patients with viable myocardium irrespective of symptoms (Fig. 3.11). In contrast, in patients without PET mismatch, coronary revascularization appeared to improve survival and symptoms only in patients with angina. Furthermore, long-term survival in patients with ischemic cardiomyopathy undergoing surgical revascularization appears to be similar to that achieved with cardiac transplantation. In 112 patients with ejection fractions below 35%, 5-year survival of patients with viable myocardium undergoing coronary artery bypass surgery was not different from that in patients who underwent transplantation (Duong et al. 1995).

3.3.6.7 Myocardial Revascularization and Impact of PET, Timing of Surgery

Observations have suggested that myocardial hibernation does not represent a steady state but rather an incomplete adaptation to ischemia (Elsässer et al. 1997). The precarious balance between perfusion and myocardial viability cannot be sustained

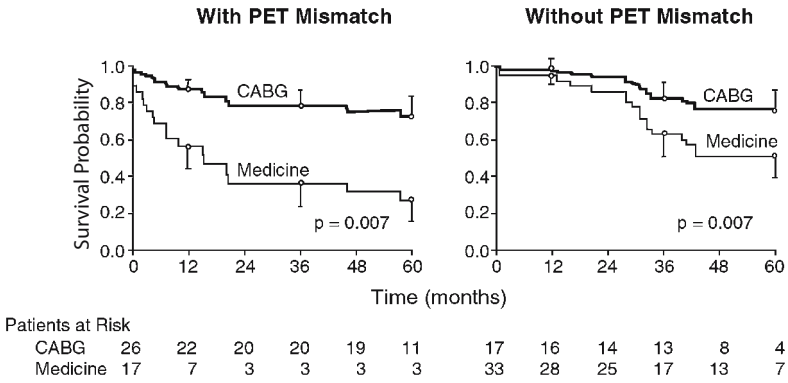

Fig. 3.11. Estimated survival probabilities by Kaplan-Meier analysis for patients with left ventricular function treated medically and with surgical revascularization based on the absence or presence of viability as determined by PET blood flow metabolism imaging. (From Di Carli et al. 1998)

indefinitely and necrosis, apoptosis, or both might occur if flow is not restored (Schwarz et al. 1996; Elsässer et al. 1997).

Dysfunctional myocardium characteristically exhibits "abnormal myocytes" (Flameng et al. 1981). Such myocytes reveal peri-nuclear loss of contractile protein and replacement by glycogen deposits. The structure of the cell nucleus is usually preserved; there are numerous small mitochondria of normal morphologic appearance (Borgers et al. 1995). Structural changes were correlated with the patterns of blood flow and metabolism which demonstrated a disproportionately greater fraction of abnormal myocytes in myocardium with flow metabolism mismatches (Vanoverschelde et al. 1993; Depre et al. 1995; Maes et al. 1994). In contrast, segments with normal flow and metabolism contained mostly normal myocytes with some abnormal cells and fibrosis, whereas myocardial segments with concordant reductions in flow and metabolism, considered as irreversibly dysfunctional, contained large amounts of fibrosis and scar tissue.

Some studies demonstrated a direct and statistically significant correlation between the fraction of abnormal myocytes and the relative FDG uptake (Depre et al. 1995), implicating such cells as the structural correlate of enhanced glucose uptake. However, the lack of such correlation between the severity of structural changes and FDG in another study (Schwarz et al. 1996) points to additional mechanisms of the enhanced glucose utilization.

The severity of morphological degeneration appears to correlate with the timing and the degree of functional recovery after revascularization (Schwarz et al. 1996; Elsässer et al. 1997). In fact, patients with mild morphological alterations showed faster and more complete recovery of LV function than those with more severe changes (Elsässer et al. 1997). In support of this notion, the role of PET imaging for identification of high-risk patients with depressed ventricular function (ejection fraction less than 35%) was investigated (Beanlands et al. 1998). PET identified viable myocardium in 35 of 46 patients who were scheduled for revascularization. Preoperative mortality was significantly lower in patients undergoing early revascularization (<35 days) compared with those receiving late revascularization (>35 days; 0 vs 24%). Furthermore, LVEF improved significantly among patients in the early revascularization group (24±7 vs 31±11%) and not in those that underwent late revascularization (27±5 vs 28±6%).

3.4 Conclusion

This chapter emphasizes the considerable clinical evidence of the benefits of assessing myocardial viability prior to coronary revascularization. The various techniques highlighted and accompanying clinical data all point to the fact that viability assessment will lead to the correct use of resources for patients who would benefit the most from intervention, thus saving health care costs tremendously.

Each of the techniques mentioned has its strong points and its limitations. In selecting the type of test and tracer, one has to consider the temporal factors, availability of equipment, patient comfort and convenience, image quality, and costs involved. The authors consider perfusion-metabolic imaging with PET as the ideal choice. This is because assessment of myocardial viability is especially important in

patients with ischemic cardiomyopathy when conventional SPECT-based imaging may be of limited diagnostic value because of the poor signal-to-noise ratios. Several studies have confirmed the higher diagnostic yield of FDG compared with conventional ^{201}Tl imaging in patients with markedly diminished LV function. However, if PET is unavailable, FDG-SPECT would come in a close second and we still consider ^{201}Tl imaging protocols an excellent choice for daily viability assessment. It is envisioned that with technological advancement, the costs for such tests and equipment will decrease and with widespread availability all modalities will approach each other in the degree of diagnostic accuracy.

Acknowledgements

The authors thank D. Martin for assistance in preparing the figures and E. Rosenfeld for assistance in preparing the text. The Laboratory of Structural Biology and Molecular Medicine is operated for the U.S. Department of Energy by the University of California under contract no. DE-AC03-76-SF00012. This work was supported in part by the Director of the Office of Energy Research, Office of Health and Environmental Research, Washington D.C., by grant no. HL 33177, National Institutes of Health, Bethesda, Maryland, and by an Investigative Group Award by the Greater Los Angeles Affiliate of the American Heart Association, Los Angeles. R. Campisi is the recipient of the 1998 Society of Nuclear Medicine-DuPont Pharma Fellowship Grant.

References

Alderman EL, Corley SD, Fisher LD, Chaitman BR, Faxon DP, Foster ED, Killip T, Sosa JA, Bourassa MG. Five-year angiographic follow-up of factors associated with progression of coronary artery disease in the Coronary Artery Surgery Study (CASS). CASS Participating Investigators and Staff. J Am Coll Cardiol 1993;22:1141–1154

Alfieri O, La Canna G, Giubbini R, Pardini A, Zogno M, Fucci C. Recovery of myocardial function. The ultimate target of coronary revascularization. Eur J Cardiothorac Surg 1993;7:325–330

Altehoefer C, Kaiser HJ, Deorr R, Feinendegen C, Beilin I, Uebis R, Buell U. Fluorine-18 deoxyglucose PET for assessment of viable myocardium in perfusion defects in 99mTc-MIBI SPET: a comparative study in patients with coronary artery disease. Eur J Nucl Med 1992;19:334–342

Altehoefer C, Dahl J vom, Biedermann M, Uebis R, Beilin I, Sheehan F, Hanrath P, Buell U. Significance of defect severity in technetium-99m-MIBI SPECT at rest to assess myocardial viability: comparison with fluorine-18-FDG PET. J Nucl Med 1994;35:569–574

Baer FM, Voth E, Deutsch HJ, Schneider CA, Horst M, Vivie ER de, Schicha H, Erdmann E, Sechtem U. Predictive value of low dose dobutamine transesophageal echocardiography and fluorine-18 fluorodeoxyglucose positron emission tomography for recovery of regional left ventricular function after successful revascularization. J Am Coll Cardiol 1996;28:60–69

Bax JJ, Cornel JH, Visser FC, Fioretti PM, van Lingen A, Reijs AE, Boersma E, Teule GJ, Visser CA. Prediction of recovery of myocardial dysfunction after revascularization. Comparison of fluorine-18 fluorodeoxyglucose/thallium-201 SPECT, thallium-201 stress-reinjection SPECT and dobutamine echocardiography. J Am Coll Cardiol 1996a;28:558–564

Bax JJ, Cornel JH, Visser FC, Huybregts MA, Van Lingen A. Prediction of reversibility of wall motion abnormalities after revascularization using F18-fluorodeoxyglucose single photon emission computed tomography [letter]. Eur Heart J 1996b;17:480–481

Bax JJ, Visser FC, Blanksma PK, Veening MA, Tan ES, Willemsen TM, van Lingen A, Teule GJ, Vaalburg W, Lie KI, Visser CA. Comparison of myocardial uptake of fluorine-18-fluorodeoxyglucose imaged with PET and SPECT in dyssynergic myocardium. J Nucl Med 1996c;37:1631–1636

Bax JJ, Visser FC, Cornel JH, van Lingen A, Fioretti PM, Visser CA. Improved detection of viable myocardium with fluorodeoxyglucose-labeled single-photon emission computed tomography in a patient with hibernating myocardium: comparison with rest-redistribution thallium 201-labeled single-photon emission computed tomography. J Nucl Cardiol 1997a;4:178–179

Bax JJ, Cornel JH, Visser FC, Fioretti PM, van Lingen A, Huitink JM, Kamp O, Nijland F, Roelandt JR, Visser CA. Prediction of improvement of contractile function in patients with ischemic ventricular dysfunction after revascularization by fluorine-18 fluorodeoxyglucose single-photon emission computed tomography. J Am Coll Cardiol 1997b;30:377–383

Beanlands RS, Dawood F, Wen WH, McLaughlin PR, Butany J, D'Amati G, Liu PP. Are the kinetics of technetium-99 m methoxyisobutyl isonitrile affected by cell metabolism and viability? Circulation 1990;82:1802–1814

Beanlands RS, deKemp R, Scheffel A, Nahmias C, Garnett ES, Coates G, Johansen HL, Fallen E. Can nitrogen-13 ammonia kinetic modeling define myocardial viability independent of fluorine-18 fluorodeoxyglucose? J Am Coll Cardiol 1997;29:537–543

Beanlands RS, Hendry PJ, Masters RG, de Kemp RA, Woodend K, Ruddy TD. Delay in revascularization is associated with increased mortality rate in patients with severe left ventricular dysfunction and viable myocardium on fluorine 18-fluorodeoxyglucose positron emission tomography imaging. Circulation 1998;98:II51–II56

Beller GA. Comparison of 201Tl scintigraphy and low-dose dobutamine echocardiography for the noninvasive assessment of myocardial viability [editorial; comment]. Circulation 1996;94:2681–2684

Berry J, Baker J, Pieper K, Hanson M, Hoffman J, Coleman R. The effect of metabolic milieu on cardiac PET imaging using fluorine-18-deoxyglucose and nitrogen-13- ammonia in normal volunteers. J Nucl Med. 1991;32:1518–1525

Bisi G, Sciagraa R, Santoro GM, Fazzini PF. Rest technetium-99 m sestamibi tomography in combination with short-

term administration of nitrates: feasibility and reliability for prediction of postrevascularization outcome of asynergic territories. J Am Coll Cardiol 1994;24:1282–1289

Bobba K, Botvinick EH, Sciammarella MG, Starsken NF, Zhu YY, Lapidus A, Dae MW. Is there any advantage to the acquisition of 24-hour thallium images, in the presence of persistent perfusion defects at 4 h after reinjection? Eur J Nucl Med 1998;25:509–514

Bolli R. Myocardial‚stunning' in man. Circulation 1992;86:1671–1691

Bolli R. Basic and clinical aspects of myocardial stunning. Prog Cardiovasc Dis 1998;40:477–516

Bonow RO, Dilsizian V, Cuocolo A, Bacharach SL. Identification of viable myocardium in patients with chronic coronary artery disease and left ventricular dysfunction. Comparison of thallium scintigraphy with reinjection and PET imaging with 18F-fluorodeoxyglucose [see comments]. Circulation 1991;83:26–37

Borgers M, Ausma J. Structural aspects of the chronic hibernating myocardium in man. Basic Res Cardiol 1995;90:44–46

Braunwald E, Kloner RA. The stunned myocardium: prolonged, postischemic ventricular dysfunction. Circulation 1982;66:1146–1149

Brosius FC, Nguyen N, Egert S, Lin Z, Deeb GM, Haas F, Schwaiger M, Sun D. Increased sarcolemmal glucose transporter abundance in myocardial ischemia. Am J Cardiol 1997;80:77A–84A

Caner B, Beller GA. Are technetium-99m-labeled myocardial perfusion agents adequate for detection of myocardial viability? Clin Cardiol 1998;21:235–242

Carli M di, Schelbert HR, Asgarzadie F, Rokshar S, Mody F, Czernin J, Brunken R, Laks H, Phelphs ME, Maddahi J. Is there a relationship between myocardial viability and change in heart failure post revascularization in patients with poor LV function? J Nucl Med 1994;35

Carli MF di, Asgarzadie F, Schelbert HR, Brunken RC, Laks H, Phelps ME, Maddahi J. Quantitative relation between myocardial viability and improvement in heart failure symptoms after revascularization in patients with ischemic cardiomyopathy. Circulation 1995;92:3436–3444

Carli MF di, Maddahi J, Rokhsar S, Schelbert HR, Bianco-Batlles D, Brunken RC, Fromm B. Long-term survival of patients with coronary artery disease and left ventricular dysfunction: implications for the role of myocardial viability assessment in management decisions. J Thorac Cardiovasc Surg 1998;116:997–1004

Carrel T, Jenni R, Haubold-Reuter S, Schulthess G von, Pasic M, Turina M. Improvement of severely reduced left ventricular function after surgical revascularization in patients with preoperative myocardial infarction. Eur J Cardiothorac Surg. 1992;6:479–484

Carvalho PA, Chiu ML, Kronauge JF, Kawamura M, Jones AG, Holman BL, Piwnica-Worms D. Subcellular distribution and analysis of technetium-99m-MIBI in isolated perfused rat hearts. J Nucl Med 1992;33:1516–1522

Charney R, Schwinger ME, Chun J, Cohen MV, Nanna M, Menegus MA, Wexler J, Franco HS, Greenberg MA. Dobutamine echocardiography and resting-redistribution thallium-201 scintigraphy predicts recovery of hibernating myocardium after coronary revascularization. Am Heart J 1994;128:864–869

Chen E, MacIntyre J, Go R, Brunken R, Saha G, Wong C, Neumann D, Cook S, Khandekar S. Myocardial viability studies using fluorine-18-FDG SPECT: a comparison with fluorine-18-FDG PET. J Nucl Med. 1997;38:582–586

Choi Y, Brunken RC, Hawkins RA, Huang S-C, Buxton DB, Hoh CK, Phelps ME, Schelbert HR. Factors affecting myocardial 2-[F-18]fluoro-2-deoxy-D-glucose uptake in positron emission tomography studies of normal humans. Eur J Nucl Med. 1993;20:308–318

Chua T, Kiat H, Germano G, Maurer G, van Train K, Friedman J, Berman D. Gated technetium-99 m sestamibi for simultaneous assessment of stress myocardial perfusion, postexercise regional ventricular function and myocardial viability. Correlation with echocardiography and rest thallium-201 scintigraphy. J Am Coll Cardiol 1994;23:1107–1114

Conversano A, Walsh JF, Geltman EM, Perez JE, Bergmann SR, Gropler RJ. Delineation of myocardial stunning and hibernation by positron emission tomography in advanced coronary artery disease. Am Heart J 1996;131:440–450

Cuocolo A, Maurea S, Pace L, Nicolai E, Nappi A, Imbriaco M, Trimarco B, Salvatore M. Resting technetium-99 m methoxyisobutylisonitrile cardiac imaging in chronic coronary artery disease: comparison with rest-redistribution thallium-201 scintigraphy. Eur J Nucl Med 1993;20:1186–1192

Cuocolo A, Pace L, Ricciardelli B, Chiariello M, Trimarco B, Salvatore M. Identification of viable myocardium in patients with chronic coronary artery disease: comparison of thallium-201 scintigraphy with reinjection and technetium-99m-methoxyisobutyl isonitrile [see comments]. J Nucl Med 1992;33:505–511

Dahl J vom, Eitzman D, Al-Aouar A, Kanter H, Hicks R, Deeb G, Kirsh M, Schwaiger M. Relation of regional function, perfusion, and metabolism in patients with advanced coronary artery disease undergoing surgical revascularization. Circulation 1994;90:2356–2366

Dahl J vom, Altehoefer C, Sheehan F, Buechin P, Uebis R, Messmer B, Buell U, Hanrath P. Recovery of regional left ventricular dysfunction after coronary revascularization: impact of myocardial viability assessed by nuclear imaging and vessel patency at follow-up angiography. J Am Coll Cardiol 1996a;28:948–958

Dahl J vom, Altehoefer C, Büchin P, Sheehan F, Schwarz E, Koch K, Schulz G, Uebis R, Schöndube F, Messmer B, Büll U, Hanrath P. Effect of myocardial viability and coronary revascularization on clinical outcome and prognosis: a follow-up study of 161 patients with coronary heart disease. Z Kardiol 1996b;85:868–881

Dakik HA, Howell JF, Lawrie GM, Espada R, Weilbaecher DG, He ZX, Mahmarian JJ, Verani MS. Assessment of myocardial viability with 99mTc-sestamibi tomography before coronary bypass graft surgery: correlation with histopathology and postoperative improvement in cardiac function. Circulation 1997;96:2892–2898

Depré C, Vanoverschelde J-LJ, Melin J, Borgers M, Bol A, Ausma J, Dion R, Wijns W. Structural and metabolic correlates of the reversibility of chronic left ventricular ischemic dysfunction in humans. Am J Physiol 1995;268:H1265–H1275

Dilsizian V, Rocco TP, Freedman NM, Leon MB, Bonow RO. Enhanced detection of ischemic but viable myocardium by the reinjection of thallium after stress-redistribution imaging [see comments]. N Engl J Med 1990;323:141–146

Dilsizian V, Smeltzer WR, Freedman NM, Dextras R, Bonow RO. Thallium reinjection after stress-redistribution imaging. Does 24-hour delayed imaging after reinjection

enhance detection of viable myocardium? Circulation 1991;83:1247–1255

Dilsizian V, Arrighi JA, Diodati JG, Quyyumi AA, Alavi K, Bacharach SL, Marin-Neto JA, Katsiyiannis PT, Bonow RO. Myocardial viability in patients with chronic coronary artery disease. Comparison of 99mTc-sestamibi with thallium reinjection and [18F]fluorodeoxyglucose [published errata appears in Circulation 91:3026]. Circulation 1994;89:578–587

Dondi M, Tartagni F, Fallani F, Fanti S, Marengo M, DiTommaso I, Zheng QF, Monetti N. A comparison of rest sestamibi and rest-redistribution thallium single photon emission tomography: possible implications for myocardial viability detection in infarcted patients. Eur J Nucl Med 1993;20:26–31

Duong T, Hendi P, Fonarow G, Asgarzadie F, Stevenson L, Carli M di, Hage A, Moriguchi J, Kobashigawa J, Brunken R, Czernin J, Blitz A, Laks H, Phelps M, Schelbert H, Maddahi J. Role of positron emission tomographic assessment of myocardial viability in the management of patients who are referred for cardiac transplantation. Circulation 1995;92:1–123

Edwards NC, Sinusas AJ, Bergin JD, Watson DD, Ruiz M, Beller GA. Influence of subendocardial ischemia on transmural myocardial function. Am J Physiol 1992;262:H568–H576

Eitzman D, Al-Aouar Z, Dahl J vom, Kirsh M, Schwaiger M. Clinical outcome of patients with advanced coronary artery disease after viability studies with positron emission tomography. J Am Coll Cardiol 1992;20:559–565

Elsässer A, Schlepper M, Kleovekorn WP, Cai WJ, Zimmermann R, Meuller KD, Strasser R, Kostin S, Gagel C, Meunkel B, Schaper W, Schaper J. Hibernating myocardium: an incomplete adaptation to ischemia. Circulation 1997;96:2920–2931

Fath-Ordoubadi F, Pagano D, Marinho NV, Keogh BE, Bonser RS, Camici PG. Coronary revascularization in the treatment of moderate and severe postischemic left ventricular dysfunction. Am J Cardiol 1998;82:26–31

Feigl E, Neat G, Huang A. Interrelations between coronary artery pressure, myocardial metabolism and coronary blood flow. J Mol Cell Cardiol 1990;22:375–390

Flameng W, Suy R, Schwarz F, Borgers M, Piessens J, Thone F, Van Ermen H, De Geest H. Ultrastructural correlates of left ventricular contraction abnormalities in patients with chronic ischemic heart disease: determinants of reversible segmental asynergy post-revascularization surgery. Am Heart J 1981;102:846–857

Flameng WJ, Shivalkar B, Spiessens B, Maes A, Nuyts J, VanHaecke J, Mortelmans L. PET scan predicts recovery of left ventricular function after coronary artery bypass operation. Ann Thorac Surg 1997;64:1694–1701

Franken P, DeGeeter F, Dendale P, Demoor D, Block P, Bossuyt A. Abnormal free fatty acid uptake in subacute myocardial infarction after coronary thrombolysis: correlation with wall motion and inotropic reserve. J Nucl Med 1994;35:1758–1765

Franken P, Dendale P, DeGeeter F, Demoor D, Bossuyt A, Block P. Prediction of functional outcome after myocardial infarction using BMIPP and sestamibi scintigraphy. J Nucl Med 1996;37:718–722

Fujiwara S, Takeishi Y, Atsumi H, Chiba J, Takahashi K, Tomoike H. Quantitative assessment of myocardial 99mTc-sestamibi uptake during exercise: usefulness of response rate for assessing severity of coronary artery disease. Jpn Circ J 1998;62:592–598

Galassi AR, Tamburino C, Grassi R, Foti R, Mammana C, Virgilio A, Licciardello G, Musumeci S, Giuffrida G. Comparison of technetium 99m-tetrofosmin and thallium-201 single photon emission computed tomographic imaging for the assessment of viable myocardium in patients with left ventricular dysfunction. J Nucl Cardiol 1998;5:56–63

Gewirtz H, Fischman A, Abraham S, Gilson M, Strauss H, Alpert N. Positron emission tomographic measurements of absolute regional myocardial blood flow permits identification of nonviable myocardium in patients with chronic myocardial infarction. J Am Coll Cardiol 1994;23:851–859

Gibson RS, Watson DD, Taylor GJ, Crosby IK, Wellons HL, Holt ND, Beller GA. Prospective assessment of regional myocardial perfusion before and after coronary revascularization surgery by quantitative thallium-201 scintigraphy. J Am Coll Cardiol 1983;1:804–815

Gimple LW, Beller GA. Myocardial viability. Assessment by cardiac scintigraphy. Cardiol Clin 1994;12:317–332

Gioia G, Powers J, Heo J, Iskandrian AS. Prognostic value of rest-redistribution tomographic thallium-201 imaging in ischemic cardiomyopathy. Am J Cardiol 1995;75:759–762

Goodman M, Knapp F, Elmaleh D, Strauss H. Synthesis and evaluation of radioiodinated terminal p-iodophenyl-substituted alpha- and beta-methyl-branched fatty acids. J Med Chem 1984;25:390

Gropler RJ, Geltman EM, Sampathkumaran K, Perez JE, Schechtman KB, Conversano A, Sobel BE, Bergmann SR, Siegel BA. Comparison of carbon-11-acetate with fluorine-18-fluorodeoxyglucose for delineating viable myocardium by positron emission tomography. J Am Coll Cardiol 1993;22:1587–1597

Gutman J, Berman DS, Freeman M, Rozanski A, Maddahi J, Waxman A, Swan HJ. Time to completed redistribution of thallium-201 in exercise myocardial scintigraphy: relationship to the degree of coronary artery stenosis. Am H J 1983;106:989–995

Haas F, Haehnel CJ, Picker W, Nekolla S, Martinoff S, Meisner H, Schwaiger M. Preoperative positron emission tomographic viability assessment and perioperative and postoperative risk in patients with advanced ischemic heart disease [see comments]. J Am Coll Cardiol 1997;30:1693–1700

Hansen C, Corbett J, Pippin J. Iodine-123 phenylpentadecanoic acid and single photon emission computed tomography in identifying heart disease: comparison with thallium-201 myocardial tomography. J Am Coll Cardiol 1988;12:78

Haque T, Furukawa T, Takahashi M, Kinoshita M. Identification of hibernating myocardium by dobutamine stress echocardiography: comparison with thallium-201 reinjection imaging. Am Heart J 1995;130:553–563

Hariharan R, Bray M, Ganim R, Doenst T, Goodwin G, Taegtmeyer H. Fundamental limitations of [^{18}F]2-deoxy-2-fluoro-D-glucose for assessing myocardial glucose uptake. Circulation 1995;91:2435–2444

Hata T, Nohara R, Fujita M, Hosokawa R, Lee L, Kudo T, Tadamura E, Tamaki N, Konishi J, Sasayama S. Noninvasive assessment of myocardial viability by positron emission tomography with ^{11}C acetate in patients with old myocardial infarction: usefulness of low-dose dobutamine infusion. Circulation 1996;94:1834–1841

Hermansen F, Ashburner J, Spinks TJ, Kooner JS, Camici PG, Lammertsma AA. Generation of myocardial factor images

directly from the dynamic oxygen-15-water scan without use of an oxygen-15-carbon monoxide blood-pool scan. J Nucl Med 1998;39:1696–1702

Heyndrickx G, Millard R, McRitchie R et al. Regional myocardial functional and electrophysiological alterations after brief coronary occlusion in conscious dogs. J Clin Invest 1975;56:978–985

Hicks R, Herman W, Kalff V, Molina E, Wolfe E, Hutchins G, Schwaiger M. Quantitative evaluation of regional substrate metabolism in the human heart by positron emission tomography. J Am Coll Cardiol 1991;18:101–111

Iskandrian A, Powers J, Cave V, Wasserleben V, Cassell D, Heo J. Assessment of myocardial viability by dynamic tomographic iodine 123 iodophenylpentadecanoic acid imaging: comparison with rest-redistribution thallium 201 imaging. J Nucl Cardiol. 1995;2:101–109

Iskandrian AS, Hakki AH, Kane SA, Goel IP, Mundth ED, Segal BL. Rest and redistribution thallium-201 myocardial scintigraphy to predict improvement in left ventricular function after coronary arterial bypass grafting. Am J Cardiol 1983;51:1312–1316

Kauffman GJ, Boyne TS, Watson DD, Smith WH, Beller GA. Comparison of rest thallium-201 imaging and rest technetium-99 m sestamibi imaging for assessment of myocardial viability in patients with coronary artery disease and severe left ventricular dysfunction [see comments]. J Am Coll Cardiol 1996;27:1592–1597

Kawamoto M, Tamaki N, Yonekura Y, Tadamura E, Fujibayashi Y, Magata Y, Nohara R, Sasayama s, Ikekubo K, Kato H et al. Combined study with I-123 fatty acid and thallium-201 to assess ischemic myocardium: comparison with thallium redistribution and glucose metabolism. Ann Nucl Med 1994;8:47–54

Kiat H, Berman DS, Maddahi J, De Yang L, Van Train K, Rozanski A, Friedman J. Late reversibility of tomographic myocardial thallium-201 defects: an accurate marker of myocardial viability. J Am Coll Cardiol 1988;12:1456–1463

Kitsiou AN, Srinivasan G, Quyyumi AA, Summers RM, Bacharach SL, Dilsizian V. Stress-induced reversible and mild-to-moderate irreversible thallium defects: are they equally accurate for predicting recovery of regional left ventricular function after revascularization? Circulation 1998;98:501–508

Kitsiou AN, Bacharach SL, Bartlett ML, Srinivasan G, Summers RM, Quyyumi AA, Dilsizian V. 13N-ammonia myocardial blood flow and uptake: relation to functional outcome of asynergic regions after revascularization. J Am Coll Cardiol 1999;33:678–686

Kloner RA, Bolli R, Marban E, Reinlib L, Braunwald E. Medical and cellular implications of stunning, hibernation, and preconditioning: an NHLBI workshop. Circulation 1998;97:1848–1867

Knapp F, Ambrose K, Goodman M. New radioiodinated methyl-branched fatty acids for cardiac studies. Eur J Nucl Med 1986;12:S39

Knuuti M, Nuutila P, Ruotsalainen U, Saraste M, Härkönen R, Ahonen A, Teräs M, Haaparanta M, Wegelius U, Haapanen A, Hartiala J, Voipio-Pulkki L-M. Euglycemic hyperinsulinemic clamp and oral glucose load in stimulating myocardial glucose utilization during positron emission tomography. J Nucl Med 1992;33:1255–1262

Knuuti M, Saraste M, Nuutila P, Härkönen R, Wegelius U, Haapanen A. Myocardial viability: fluorine-18-deoxyglucose positron emission tomography in prediction of wall motion recovery after revascularization. Am Heart J 1994;127:785–796

Koplan BA, Beller GA, Ruiz M, Yang JY, Watson DD, Glover DK. Comparison between thallium-201 and technetium-99m-tetrofosmin uptake with sustained low flow and profound systolic dysfunction. J Nucl Med 1996;37:1398–1402

Krivokapich J, Huang SC, Phelps ME, Barrio JR, Watanabe CR, Selin CE, Shine KI. Estimation of rabbit myocardial metabolic rate for glucose using fluorodeoxyglucose. Am J Physiol 1982;243:H884–H895

Lee K, Marwick T, Cook S, Go R, Fix J, James K, Sapp S, MacIntyre W, Thomas J. Prognosis of patients with left ventricular dysfunction, with and without viable myocardium after myocardial infarction. Circulation 1994;90:2687–2694

Lopaschuk G, Stanley W. Glucose metabolism in the ischemic heart. Circulation 1997;95:313–315

Lucignani G, Paolini G, Landoni C, Zuccari M, Paganelli G, Galli L, Credico G di, Vanoli G, Rossetti C, Mariani MA, Gilardi MC, Colombo F, Grossi A, Fazio F. Presurgical identification of hibernating myocardium by combined use of technetium-99 m hexakis 2-methoxyisobutylisonitrile single photon emission tomography and fluorine-18 fluoro-2-deoxy-D-glucose positron emission tomography in patients with coronary artery disease. Eur J Nucl Med 1992;19:874–881

Machulla HJ, Stocklin G, Kupfernagel CH, Freundlieb CH, Hock A, Vyska K, Feinendegen LE. Comparative evaluation of fatty acids with C-11, C1–34 m, Br-77, I-23, for metabolic studies of the myocardium: concise communication. J Nucl Med 1978;19:298–302

Maddahi J, Schelbert H, Brunken R, Di Carli M. Role of thallium-201 and PET imaging in evaluation of myocardial viability and management of patients with coronary artery disease and left ventricular dysfunction. J Nucl Med 1994;35:707–715

Maes A, Flameng W, Nuyts J, Borgers M, Shivalkar B, Ausma J, Bormans G, Schiepers C, De Roo M, Mortelmans L. Histological alterations in chronically hypoperfused myocardium. Correlation with PET findings. Circulation 1994;90:735–745

Maes A, Flameng W, Borgers M, Nuyts J, Ausma J, Bormans G, Van de Werf F, De Roo M, Mortelmans L. Regional myocardial blood flow, glucose utilization and contractile function before and after revascularization and ultrastructural findings in patients with chronic coronary artery disease. Eur J Nucl Med 1995;22:1299–1305

Maes AF, Borgers M, Flameng W, Nuyts JL, van de Werf F, Ausma JJ, Sergeant P, Mortelmans LA. Assessment of myocardial viability in chronic coronary artery disease using technetium-99 m sestamibi SPECT. Correlation with histologic and positron emission tomographic studies and functional follow-up. J Am Coll Cardiol 1997;29:62–68

Marinho NV, Keogh BE, Costa DC, Lammerstma AA, Ell PJ, Camici PG. Pathophysiology of chronic left ventricular dysfunction. New insights from the measurement of absolute myocardial blood flow and glucose utilization. Circulation 1996;93:737–744

Marwick T, Nemec J, Lafont A, Salcedo E, MacIntyre W. Prediction by postexercise fluoro-18 deoxyglucose positron emission tomography of improvement in exercise capacity after revascularization. Am J Cardiol 1992;69:854–859

Marwick T, Zuchowski C, Lauer M, Secknus M-A, Williams

M, Lytle B. Functional status and quality of life in patients with heart failure undergoing coronary bypass surgery after assessment of myocardial viability. J Am Coll Cardiol 1999;33:750–758

Marzullo P, Sambuceti G, Parodi O. The role of sestamibi scintigraphy in the radioisotopic assessment of myocardial viability [see comments]. J Nucl Med 1992;33:1925–1930

Marzullo P, Parodi O, Reisenhofer B, Sambuceti G, Picano E, Distante A, Gimelli A, L'Abbate A. Value of rest thallium-201/technetium-99 m sestamibi scans and dobutamine echocardiography for detecting myocardial viability. Am J Cardiol 1993;71:166–172

Matsunari I, Fujino S, Taki J, Senma J, Aoyama T, Wakasugi T, Hirai J, Saga T, Ichiyanagi K, Hisada K. Myocardial viability assessment with technetium-99m-tetrofosmin and thallium-201 reinjection in coronary artery disease. J Nucl Med 1995;36:1961–1967

Matsunari I, Fujino S, Taki J, Senma J, Aoyama T, Wakasugi T, Hirai J, Saga T, Yamamoto S, Tonami N. Quantitative rest technetium-99 m tetrofosmin imaging in predicting functional recovery after revascularization: comparison with rest-redistribution thallium-201. J Am Coll Cardiol 1997;29:1226–1233

Matsunari I, Boening G, Ziegler S, Nekolla S, Stollfuss J, Kosa I, Ficaro E, Schwaiger M. Attenuation-corrected ^{99m}Tc-tetrofosmin single-photon emission computed tomography in the detection of viable myocardium: comparison with positron emission tomography using ^{18}F-fluorodeoxyglucose. J Am Coll Cardiol 1998;32:927–935

Maunoury C, Chen CC, Chua KB, Thompson CJ. Quantification of left ventricular function with thallium-201 and technetium-99m-sestamibi myocardial gated SPECT [published errata appears in J Nucl Med 38:1834]. J Nucl Med 1997;38:958–961

Mori T, Minamiji K, Kurogane H, Ogawa K, Yoshida Y. Rest-injected thallium-201 imaging for assessing viability of severe asynergic regions. J Nucl Med 1991;32:1718–1724

Nishimura T, Nishimura S, Kajiya T, Sugihara H, Kitahara K, Iamai K, Muramatsu T, Takahashi N, Yoshida H, Osada T, Terada K, Ito T, Narusa H, Iwabuchi M. Prediction of functional recovery and prognosis in patients with acute myocardial infarction by 123I-BMIPP and 201Tl myocardial single photon emission computed tomography: a multicenter trial. Ann Nucl Med 1998;12:237–248

Ohtani H, Tamaki N, Yonekura Y, Mohiuddin IH, Hirata K, Ban T, Konishi J. Value of thallium-201 reinjection after delayed SPECT imaging for predicting reversible ischemia after coronary artery bypass grafting. Am J Cardiol 1990;66:394–399

Pagano D, Townend JN, Littler WA, Horton R, Camici PG, Bonser RS. Coronary artery bypass surgery as treatment for ischemic heart failure: the predictive value of viability assessment with quantitative positron emission tomography for symptomatic and functional outcome. J Thorac Cardiovasc Surg 1998;115:791–799

Pagley PR, Beller GA, Watson DD, Gimple LW, Ragosta M. Improved outcome after coronary bypass surgery in patients with ischemic cardiomyopathy and residual myocardial viability. Circulation 1997;96:793–800

Palmas W, Friedman JD, Diamond GA, Silber H, Kiat H, Berman DS. Incremental value of simultaneous assessment of myocardial function and perfusion with technetium-99 m sestamibi for prediction of extent of coronary artery disease. J Am Coll Cardiol 1995;25:1024–1031

Paolini G, Lucignani G, Zuccari M, Landoni C, Vanoli G, Credico G di, Rossetti C, Mariani MA, Fazio F, Grossi A. Identification and revascularization of hibernating myocardium in angina-free patients with left ventricular dysfunction. Eur J Cardiothorac Surg 1994;8:139–144

Perrone-Filardi P, Pace L, Prastaro M, Squame F, Betocchi S, Soricelli A, Piscione F, Indolfi C, Crisci T, Salvatore M, Chiariello M. Assessment of myocardial viability in patients with chronic coronary artery disease. Rest-4-hour-24-hour 201Tl tomography versus dobutamine echocardiography [see comments]. Circulation 1996;94:2712–2719

Platts EA, North TL, Pickett RD, Kelly JD. Mechanism of uptake of technetium-tetrofosmin. I. Uptake into isolated adult rat ventricular myocytes and subcellular localization [published errata appears in J Nucl Cardiol 2:560]. J Nucl Cardiol 1995;2:317–326

Pohost G, Zir L, Moor R. Differentiation of transiently ischemic from infarcted myocardium by serial imaging after single dose of Tl-201. Circulation 1977;55:294

Qureshi U, Nagueh SF, Afridi I, Vaduganathan P, Blaustein A, Verani MS, Winters WL Jr, Zoghbi WA. Dobutamine echocardiography and quantitative rest-redistribution 201Tl tomography in myocardial hibernation. Relation of contractile reserve to 201Tl uptake and comparative prediction of recovery of function. Circulation 1997;95:626–635

Ragosta M, Beller GA, Watson DD, Kaul S, Gimple LW. Quantitative planar rest-redistribution ^{201}Tl imaging in detection of myocardial viability and prediction of improvement in left ventricular function after coronary bypass surgery in patients with severely depressed left ventricular function. Circulation 1993;87:1630–1641

Rahimtoola SH. A perspective on the three large multicenter randomized clinical trials of coronary bypass surgery for chronic stable angina. Circulation 1987;72:V123–V135

Ratib O, Phelps ME, Huang SC, Henze E, Selin CE, Schelbert HR. Positron tomography with deoxyglucose for estimating local myocardial glucose metabolism. J Nucl Med 1982;23:577–586

Rhodes CG, Camici PG, Taegtmeyer H, Doenst T. Variability of the lumped constant for [18F]2-deoxy-2-fluoroglucose and the experimental isolated rat heart model: clinical perspectives for the measurement of myocardial tissue viability in humans [letter]. Circulation 1999;99:1275–1276

Rocco TP, Dilsizian V, Strauss HW, Boucher CA. Technetium-99 m isonitrile myocardial uptake at rest. II. Relation to clinical markers of potential viability [see comments]. J Am Coll Cardiol 1989;14:1678–1684

Rubin P, Lee D, Davila-Roman V, Geltman E, Schechtman K, Bergmann S, Gropler R. Superiority of C-11 acetate compared with F-18 fluorodeoxyglucose in predicting myocardial functional recovery by positron emission tomography in patients with acute myocardial infarction. Am J Cardiol 1996;78:1230–1236

Sandler MP, Bax JJ, Patton JA, Visser FC, Martin WH, Wijns W. Fluorine-18-fluorodeoxyglucose cardiac imaging using a modified scintillation camera. J Nucl Med 1998;39:2035–2043

Sawada SG, Allman KC, Muzik O, Beanlands RS, Wolfe ER Jr, Gross M, Fig L, Schwaiger M. Positron emission tomography detects evidence of viability in rest technetium-99 m sestamibi defects. J Am Coll Cardiol 1994;23:92–98

Schelbert H. Principles of positron emission tomography. In: Skorton D, Schelbert H, Wolf G, Brundage B (eds) Marcus' cardiac imaging, 2nd edn. Saunders, Philadelphia, 1996, pp 1063–1092

Schelbert H, Demer L. Evaluation of myocardial blood flow in cardiac disease. In: Skorton D, Schelbert H, Wolf G, Brundage B (eds) Marcus' cardiac imaging, 2nd edn. Saunders, Philadelphia, 1996, pp 1093–1112

Schneider CA, Voth E, Gawlich S, Baer FM, Horst M, Schicha H, Erdmann E, Sechtem U. Significance of rest technetium-99 m sestamibi imaging for the prediction of improvement of left ventricular dysfunction after Q wave myocardial infarction: importance of infarct location adjusted thresholds. J Am Coll Cardiol 1998;32:648–654

Schöder H, Campisi R, Ohtake T, Hoh CK, Moon DH, Czernin J, Schelbert HR. Blood flow-metabolism imaging with positron emission tomography in patients with diabetes mellitus for the assessment of reversible left ventricular contractile dysfunction. J Am Coll Cardiol 1999;33:1328–1337

Schwarz ER, Schaper J, Dahl J vom, Altehoefer C, Grohmann B, Schoendube F, Sheehan FH, Uebis R, Buell U, Messmer BJ, Schaper W, Hanrath P. Myocyte degeneration and cell death in hibernating human myocardium. J Am Coll Cardiol 1996;27:1577–1585

Sciagraa R, Bisi G, Santoro GM, Agnolucci M, Zoccarato O, Fazzini PF. Influence of the assessment of defect severity and intravenous nitrate administration during tracer injection on the detection of viable hibernating myocardium with data-based quantitative technetium 99m-labeled sestamibi single-photon emission computed tomography. J Nucl Cardiol 1996;3:221–230

Sciagraa R, Bisi G, Santoro GM, Zerauschek F, Sestini S, Pedenovi P, Pappagallo R, Fazzini PF. Comparison of baseline-nitrate technetium-99 m sestamibi with rest-redistribution thallium-201 tomography in detecting viable hibernating myocardium and predicting postrevascularization recovery. J Am Coll Cardiol 1997;30:384–391

Soufer R, Dey HM, Ng CK, Zaret BL. Comparison of sestamibi single-photon emission computed tomography with positron emission tomography for estimating left ventricular myocardial viability. Am J Cardiol 1995;75:1214–1219

Takahashi N, Reinhardt CP, Marcel R, Leppo JA. Myocardial uptake of 99mTc-tetrofosmin, sestamibi, and 201Tl in a model of acute coronary reperfusion. Circulation 1996;94:2605–2613

Tamaki N, Ohtani H, Yonekura Y, Nohara R, Kambara H, Kawai C, Hirata K, Ban T, Konishi J. Significance of fill-in after thallium-201 reinjection following delayed imaging: comparison with regional wall motion and angiographic findings [see comments]. J Nucl Med 1990;31:1617–1623

Tamaki N, Ohtani H, Yonekura Y, Shindo M, Nohara R, Kambara H, Kawai C, Hirata K, Ban T, Konishi J. Viable myocardium identified by reinjection thallium-201 imaging: comparison with regional wall motion and metabolic activity on FDG-PET. J Cardiol 1992;22:283–293

Tamaki N, Kawamoto M, Takahashi N, Yonekura Y, Magata Y, Nohara R, Kambara H, Sasayama S, Hirata K, Ban T, Konishi J. Prognostic value of an increase in fluorine-18 deoxyglucose uptake in patients with myocardial infarction: comparison with stress thallium imaging. J Am Coll Cardiol 1993;22:1621–1627

Tamaki N, Tadamura E, Kudoh T, Hattori N, Yonekura Y, Nohara R, Sasayama S, Ikekubo K, Kato H, Konishi J. Prognostic value of iodine-123 labelled BMIPP fatty acid analogue imaging in patients with myocardial infarction. Eur J Nucl Med 1996;23:272–279

Tillisch J, Brunken R, Marshall R, Schwaiger M, Mandelkern M, Phelps M, Schelbert HR. Reversibility of cardiac wall motion abnormalities predicted by positron tomography. N Engl J Med 1986;314:884–888

Udelson JE, Coleman PS, Metherall J, Pandian NG, Gomez AR, Griffith JL, Shea NL, Oates E, Konstam MA. Predicting recovery of severe regional ventricular dysfunction. Comparison of resting scintigraphy with 201Tl and 99mTc-sestamibi. Circulation 1994;89:2552–2561

Vanoverschelde JL, Melin JA, Bol A, Vanbutsele R, Cogneau M, Labar D, Robert A, Michel C, Wijns W. Regional oxidative metabolism in patients after recovery from reperfused anterior myocardial infarction. Relation to regional blood flow and glucose uptake. Circulation 1992;85:9–21

Vanoverschelde JL, Wijns W, Deprae C, Essamri B, Heyndrickx GR, Borgers M, Bol A, Melin JA. Mechanisms of chronic regional postischemic dysfunction in humans. New insights from the study of noninfarcted collateral-dependent myocardium [see comments]. Circulation 1993;87:1513–1523

Vanoverschelde JL, D'Hondt AM, Marwick T, Gerber BL, De Kock M, Dion R, Wijns W, Melin JA. Head-to-head comparison of exercise-redistribution-reinjection thallium single-photon emission computed tomography and low dose dobutamine echocardiography for prediction of reversibility of chronic left ventricular ischemic dysfunction [see comments]. J Am Coll Cardiol 1996;28:432–442

Watson D. Quantitative analysis of Tl-201 redistribution at 24 hours compared to 2 and 4 hours post-injection (Abstract). J Nucl Med 1990;31:763

Weich HF, Strauss HW, Pitt B. The extraction of thallium-201 by the myocardium. Circulation 1977;56:188–191

Wolpers H, Burchert W, van den Hoff J, Weinhardt R, Meyer G, Lichtlen P. Assessment of myocardial viability by use of ^{11}C-acetate and positron emission tomography. Circulation 1997;95:1417–1424

Yamamoto K, Asada S, Masuyama T, Nanto S, Matsumura Y, Naito J, Hirayama A, Mishima M, Naka M, Sasaki J et al. Myocardial hibernation in the infarcted region cannot be assessed from the presence of stress-induced ischemia: usefulness of delayed image of exercise thallium-201 scintigraphy. Am Heart J 1993;125:33–40

Young L, Renfu Y, Russell R, Hu X, Caplan M, Ren J, Shulman G, Sinusas A. Low-flow ischemia leads to translocation of canine heart GLUT-4 and GLUT-1 glucose transporters to the sarcolemma in vivo. Circulation 1997;95:415–422

Zaret BL, Rigo P, Wackers FJ, Hendel RC, Braat SH, Iskandrian AS, Sridhara BS, Jain D, Itti R, Serafini AN et al. Myocardial perfusion imaging with 99mTc tetrofosmin. Comparison to 201Tl imaging and coronary angiography in a phase III multicenter trial. Tetrofosmin International Trial Study Group [see comments]. Circulation 1995;91:313–319

4 Thromboembolism Imaging

Henry D. Royal and David A. Hillier

CONTENTS

4.1 Introduction

Dramatic developments regarding the diagnosis and treatment of pulmonary embolism occurred in the 1960s. Anticoagulants were introduced into clinical practice (Barritt and Jordan 1960) and techniques for pulmonary arteriography were refined (Wiener et al. 1966; Dalen et al. 1971; Stein 1971). With the advent of Anger cameras and the availability of appropriate radiopharmaceuticals, ventilation-perfusion imaging for the diagnosis of pulmonary embolism became widely available in the 1970s. Shortly thereafter, the foundations of the current criteria used to interpret ventilation-perfusion studies were laid (McNeil 1976; Biello et al. 1979). From the very beginning, the diagnosis and treatment of pulmonary embolism was surrounded by controversy. One of the more controversial papers from these early days claimed that pulmonary embolism was overdiagnosed and overtreated, particularly in young, otherwise healthy adults. The unreliability of ventilation-perfusion imaging was partly to blame for this problem (Robin 1977).

Twenty-five years after the widespread introduction of ventilation-perfusion imaging, little seems to have changed. A few technical advances have occurred and minor refinements in the criteria used to interpret ventilation-perfusion studies have been made. Conventional dogma continues to be that pulmonary embolism kills and these fatalities can be readily prevented if the diagnosis of pulmonary embolism is made and the patient is treated (Dalen and Alpert 1975). Given the apparent stagnant state of affairs, why read yet another chapter on the diagnosis and treatment of this common, familiar disease?

With current emphasis on evidence-based medicine (Anonymous 1992; Oxman et al. 1993) and patient outcomes (Eddy 1990a,b), pressure is building for significant changes in how we think about the diagnosis and treatment of pulmonary embolism. Heretical questions such as "Does all pulmonary embolism need to be treated?" are being asked (Kelley et al. 1991; Stein et al. 1995). As more and more diagnostic tests are developed to detect pulmonary embolism, the concept of diagnostic "truth" becomes more complicated. Emphasis on patient outcomes have transformed diagnostic truth from the simple "If the pulmonary arteriogram was positive, the patient had pulmonary embolism" to the more complicated "How do we identify patient's in whom the risk of treatment is less than the risk of no treatment?"

In this chapter the conventional, comfortable, and sometimes mythological views of pulmonary embolism are, whenever possible, contrasted with alternative views. Only new thinking will allow us to finally make needed progress in how we diagnose

H. D. Royal, MD; D. A. Hillier, MD, PhD
Division of Nuclear Medicine, Mallinckrodt Institute of Radiology, 510 S. Kingshighway Blvd., Saint Louis, MO 63110, USA

and manage patients suspected of pulmonary embolism.

This chapter consists of four sections. The first section, on clinical issues, reviews basic medical decision-making principles that are used in order to understand the complicated problems involved with the diagnosis and management of patients suspected of having pulmonary embolism. The importance of estimating the pre-test probability of pulmonary embolism and of risk stratification is emphasized. The next section discusses ventilation-perfusion imaging, the strengths and weaknesses of the PIOPED study, and the current state of the criteria used to interpret ventilation-perfusion studies. The third section delineates the role of other diagnostic tests in the diagnosis of pulmonary embolism with particular emphasis on the role of spiral CT and pulmonary arteriography. The final section summarizes the current state of affairs and proposes future advances.

4.2 Clinical Issues

In the 1960s and 1970s, when tools became available for the diagnosis (ventilation-perfusion imaging and pulmonary arteriography) and treatment (heparin and warfarin) of pulmonary embolism, efforts were made to make clinicians aware of this potentially lethal disease that now could be identified and treated. One of the most often quoted articles estimated that 200,000 deaths were caused in the US every year from pulmonary embolism and implied that 88,000 of these deaths could be prevented if pulmonary embolism were diagnosed and treated (Dalen and Alpert 1975). In addition, autopsy studies then and since have demonstrated that the prevalence of undiagnosed pulmonary embolism is high in this very select population (Morpurgo and Schmid 1995; Cohen et al. 1996; Goldhaber et al. 1982). These factors have led to the conventional view that pulmonary embolism is a relatively common cause of preventable death. Even today, an often quoted statistic is that untreated pulmonary embolism has a mortality rate of 30% that could be reduced to 8% if the patient were treated.

What is the scientific basis for these seminal ideas, i.e., pulmonary embolism is a relatively common, treatable, often undiagnosed cause of death, which have so greatly influenced our thinking about pulmonary embolism over the past 30 years? As with many other diseases, early reports on the importance and effectiveness of treatment of pulmonary embolism are probably inflated. The 88,000 preventable deaths cited above are based on several very speculative estimates. Firstly, accurately determining the prevalence of pulmonary embolism is a very difficult task. Factors that will have major effects on the measured prevalence include the intensity of the diagnostic work-up, the diagnostic criteria used, and the population studied. Secondly, the natural history of treated and untreated pulmonary embolism has been poorly studied. There is reasonably good scientific evidence that the prognosis of untreated (Stein et al. 1995) and treated pulmonary embolism (Carson et al. 1992; Douketis et al. 1998) is better than the 30% and 8% mortality figures given by Dalen and Alpert (1975).

The results of autopsy studies are often cited as evidence that clinically important pulmonary embolism is frequently undiagnosed (Morpurgo and Schmid 1995; Rubinstein et al. 1988). Unfortunately, extrapolating the results of autopsy studies to living patients is fraught with errors. Not only are the deceased subjects a very select group of patients, it is also difficult to reliably determine if the emboli were simply agonal events or whether they significantly shortened patient life expectancy. It is likely that the incidence of undiagnosed pulmonary embolism is decreasing (Cohen et al. 1996; Dismuke and Wagner 1986).

Even the effectiveness of anticoagulation has only been studied in one small, quite old, randomized controlled study (Barritt and Jordan 1960). In this study, the diagnosis of pulmonary embolism was made based solely on clinical grounds. No pulmonary arteriography or ventilation-perfusion imaging was available at the time of this study. Presumably, these patients had massive pulmonary embolism, and in patients with massive pulmonary embolism mortality rates of 30% untreated and 8% treated may be reasonable. Dalen and Alpert (1975) used these mortality rates derived from patients with presumed massive pulmonary embolism to estimate the annual mortality due to pulmonary embolism in the US.

4.2.1 Importance of Risk Stratification

Fortunately, the simple monolithic view of pulmonary embolism is crumbling. Increasingly it is being recognized as a complex, multifaceted disease, often

the complication of other diseases, which ultimately are major determinants in the patient's survival. The patients at greatest risk for sudden preventable death due to pulmonary embolism are post-operative patients. Given the current emphasis on prophylaxis, it is not surprising that decreases in deaths due to post-operative pulmonary embolism have been well documented. Pulmonary embolism in healthy ambulatory patients rarely occurs.

The next quantum advance that we must make in our thinking about pulmonary embolism is that the diagnosis is not simply a binary (present or not present) task. Our level of sophistication when making the diagnosis of coronary artery disease is much greater than our level of sophistication when making the diagnosis of pulmonary embolism. The importance of risk stratification with coronary artery disease is universally recognized. Risk stratification for pulmonary embolism will have to account for: (a) the physiological impact of pulmonary emboli that have already occurred, (b) the potential for future emboli, and (c) the overall medical condition of the patient. Ventilation-perfusion imaging cannot be used to assess the last two factors. Patients who have extensive, documented deep venous thrombosis are at higher risk than patients who have limited or no documented deep venous thrombosis. Patients with underlying cardiopulmonary disease are likely not to be able to tolerate pulmonary embolism as well as otherwise healthy patients.

4.2.2 Medical Decision Making

At a time when interest in the diagnosis and treatment of pulmonary embolism was growing, interest in medical decision making was also growing. In 1975 the *New England Journal of Medicine* devoted an entire issue to the topic of medical decision making (McNeil and Adelstein 1975; McNeil et al. 1975). The editors for this unique issue were two nuclear medicine physicians from the Brigham and Women's Hospital in Boston. Not surprisingly, medical decision making was quickly applied to the use of diagnostic tests in diseases such as pulmonary embolism.

Few disciplines in medicine have provoked as strong a reaction from the medical community as medical decision making. Individuals in the medical community appear to either love or hate the concepts, which provide the foundation for medical decision making. Some individuals shun medical decision making as an oversimplified impractical construct that has no clinical relevance; others believe that medical decision making provides some basic tools that can help further our understanding of the complexities of making decisions in medicine (Jaeschke et al. 1994a,b). For a summary of concepts, definitions, and applications, see the Appendix.

4.2.3 Pre-test Probability

It should be clear that it is not possible to determine the post-test probability of disease solely based on the test result (see Appendix). The pre-test probability plays an equally important role in this assessment. For pulmonary embolism some experts argue that it is not possible to determine the pre-test probability for particular patients. This pessimism is not supported by the literature. In the PIOPED study, patients were stratified not only by the result of ventilation-perfusion imaging, but also by the clinician's pre-test assessment of the probability for pulmonary embolism (PIOPED Investigators 1990). Pre-test probability was broadly categorized as low (0%–19%), intermediate (20%–79%), or high (80%–100%). Examination of the results of the PIOPED study clearly show that for the same test results the post-test probability of disease varied depending on the clinician's assessment of the pre-test probability (Fig. 4.1).

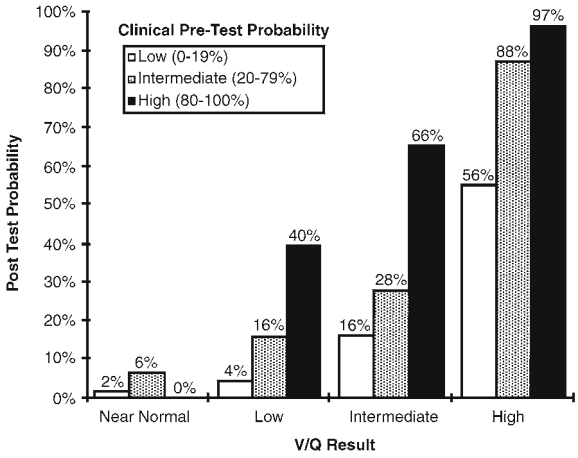

Fig. 4.1. The effect of the clinicians' estimate of pre-test probability on the post-test probability for each category of test results in the PIOPED study. The pre-test probability clearly had an effect on the post-test probability of disease (PIOPED Investigators 1990)

The difficulty with assessing the pre-test probability of pulmonary embolism is that there is no simple clinical rule that has been widely accepted to produce a valid result. Most recently, Wells et al. (1998) demonstrated that the risk for thromboembolic disease could be accurately assessed by using the clinical history, the results of ventilation-perfusion imaging, and the results of serial compression ultrasound of the lower extremities. Using a simple scheme, these authors proposed a method for accurately assessing pre-test probability (Fig. 4.2).

4.2.4 Utility Analysis

Once the post-test probability of disease is known, the clinician must decide what to do next. Management of patients with pulmonary embolism can be simply modeled using utility analysis, which provides some useful insight into why we do the things that we do.

Utility analysis considers the expected outcome for patients based on different patient management decisions. There are six major outcomes in patients suspected of pulmonary embolism. These outcomes and their utility are listed in Table 4.1. These six outcomes can be divided into two groups of three. The first group is the outcome from patients who do not have pulmonary embolism, and the second group is the outcome from patients who do have pulmonary embolism. For patients without pulmonary embolism, the best outcome is that they are not treated with anticoagulation; therefore, they are not unnecessarily exposed to the risk of anticoagulation. The next best outcome is that they are exposed to the morbidity of having a pulmonary arteriogram to prove that they do not have pulmonary embolism

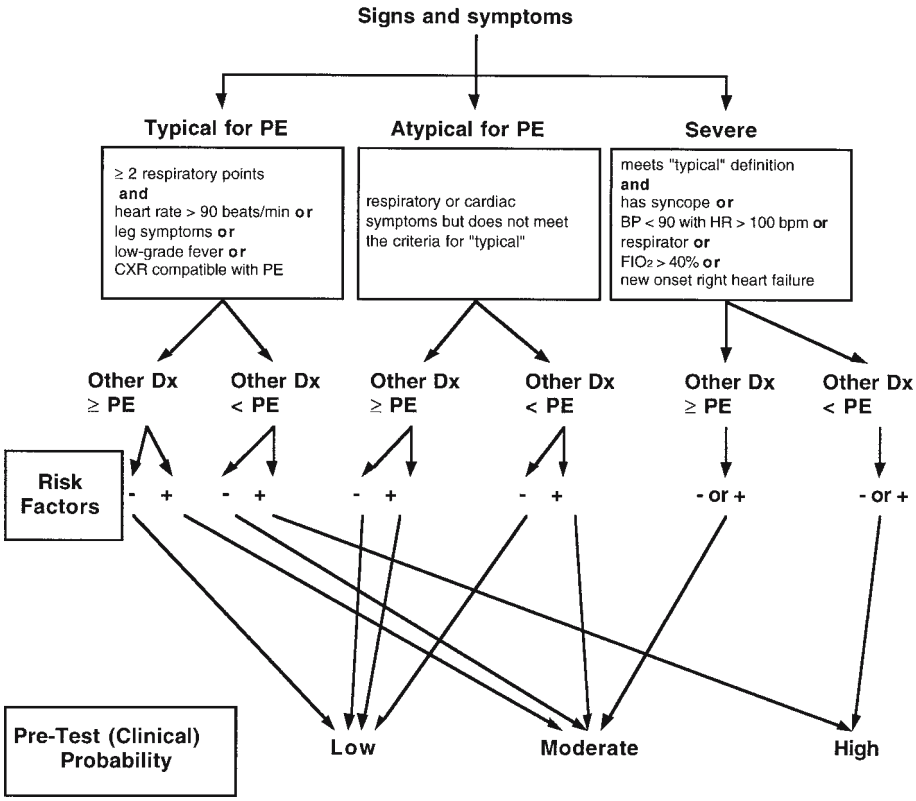

Fig. 4.2. An algorithm for the assessment of the pre-test probability of disease. Respiratory points consist of dyspnea or worsening of chronic dyspnea, pleuritic chest pain, chest pain that is non-retrosternal and non-pleuritic, and arterial oxygen saturation less than 92% while breathing room air that corrects with oxygen supplementation less than 40%, hemoptysis, and pleural rub. Risk factors are surgery within 12 weeks, immobilization (complete bedrest) for 3 or more days in the 4 weeks before presentation, previous deep venous thrombosis or objectively diagnosed pulmonary embolism, fracture of a lower extremity and immobilization of the fracture within 12 weeks, strong family history of deep venous thrombosis or pulmonary embolism (two or more family members with objectively proven events or a first-degree relative with hereditary thrombophilia), cancer (treatment ongoing, within the past 6 months, or in the palliative stages), the postpartum period, and lower-extremity paralysis. (Modified from Wells et al. 1998)

Table 4.1. Expected utilities (outcomes)

Patients without pulmonary embolism		Patients with pulmonary embolism	
Management strategy	Expected utility	Management strategy	Expected utility
No therapy; no pulmonary angiogram	1.00	Therapy	0.84
Pulmonary angiogram; no therapy	0.98	Pulmonary angiogram, therapy	0.82
Therapy	0.92	No therapy	0.70

and they thus avoid the risk of anticoagulation. The worst outcome for patients without pulmonary embolism is that they are needlessly anticoagulated. Typically, the best outcome is given a value of 1. Less good outcomes are given values less than 1, and these values should be directly related to the loss of health. Although exact quantification is difficult, it is easy to agree about the hierarchy of outcomes. Clearly, not receiving anticoagulation if it is unnecessary is the best outcome. Traditionally, the risk of pulmonary arteriography is viewed as being less than the risk of anticoagulation; therefore, pulmonary arteriography is often done in order to prove that the patient does not have pulmonary embolism.

For patients who have pulmonary embolism, there are also three major outcomes. The outcome with the highest utility would be patients who are treated with anticoagulants but who do not get subjected to the morbidity of pulmonary arteriography. The second best outcome is to require a pulmonary arteriography in order to accurately make the diagnosis of pulmonary embolism, and thus, be anticoagulated. The worst outcome is to have untreated pulmonary embolism. Again, these three outcomes have a natural hierarchy even though their exact values may be questioned. Another important thing to note is that the best outcome for patients with pulmonary embolism has to be worse than the worst outcome for patients without pulmonary embolism, because patients with pulmonary embolism are not only subjected to the risk of anticoagulation, but they have the additional risk of treated thromboembolic disease.

If these six outcomes in patients with pulmonary embolism are plotted on a graph of utilities and prevalence of pulmonary embolism (Fig. 4.3), the three utilities in patients without the pulmonary embolism are plotted on the y-axis where the prevalence is 0% and the three utilities for patients with pulmonary embolism can be plotted on the y-axis where the prevalence of pulmonary embolism equals 100%. Mathematically, it can be shown that the expected utility for the three major patient management options (treatment, no treatment, and pulmonary arteriography) fall on a line connecting the points that represent each of these management strategies.

When the traditional values for the six outcomes discussed previously are used, it is apparent that the expected utility from performing a pulmonary arteriogram is higher than the expected utility for the other two management strategies when the prevalence of pulmonary embolism in the population ranges from approximately 15%–75% (shaded area under the curve in Fig. 4.3). Hence, the often quoted statement that if the result of a pulmonary ventilation-perfusion study is intermediate, the patient management option with the greatest utility is to perform pulmonary arteriography; if the prevalence of pulmonary embolism is greater than approximately 75%, the best strategy is to treat the patient, and if the prevalence is less than approximately 15%, the best strategy is to not treat the patient.

In clinical practice there is an apparent discordance between what the foregoing utility analysis would indicate (obtain a pulmonary arteriogram

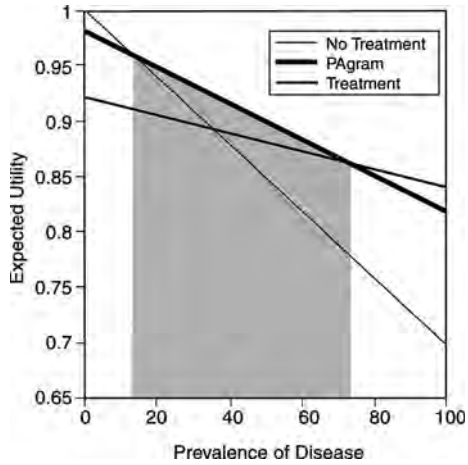

Fig. 4.3. The traditional expected utilities of three different management strategies for patients suspected of pulmonary embolism are plotted as a function of the prevalence of disease. The *shaded area* shows that the greatest expected utility can be obtained by performing a pulmonary arteriogram in patients who have a prevalence of disease ranging between 15% and 75%. Note that at the extremes of this range, there is very little difference in the expected utility of the alternative management strategy

when the prevalence of disease is between 15% and 75%) and what actually happens. In our institution, only approximately 14% of patients with an intermediate likelihood ratio result on their ventilation-perfusion study are referred for pulmonary arteriography. There are two explanations for this discordance. The first explanation is that the prevalence of pulmonary embolism (or the post-test probability of disease) is not determined from the results of the ventilation-perfusion study alone. In fact, the likelihood ratio for an intermediate probability ventilation-perfusion study is close to 1; therefore, as shown in Figure 4.3, the post-test probability will be very similar to the pre-test probability. The average prevalence of pulmonary embolism in patients referred for pulmonary embolism in our hospital is approximately 15%, so not treating the patient and not obtaining a pulmonary arteriogram in patients with an intermediate likelihood ratio result is not inconsistent with optimizing the expected utility as shown in Figure 4.3. With a prevalence of 15%, the expected utility of not treating the patient and of obtaining a pulmonary arteriogram is similar. Maybe this helps explain why it often seems that the decision to obtain a pulmonary arteriogram in patients with intermediate likelihood ratio results on their ventilation-perfusion study is based on the flip of a coin.

Unfortunately, current interpretation criteria for ventilation-perfusion imaging blur the distinction between the test result and post-test probability of disease (which necessarily includes an assessment of the pre-test probability). To make a management recommendation based solely on the test results without accounting for pre-test probability is wrong. At our institution, we have tried to emphasize the importance of incorporating the pre-test probability with the test results in order to calculate the post-test probability by reporting the ventilation-perfusion imaging results as likelihood ratios rather than probabilities which are easily confused with post-test probabilities.

A second, and equally important, reason why only a few patients with an intermediate probability for pulmonary embolism are referred to pulmonary arteriography is that the expected utilities for different management strategies may vary greatly with individual patients. For example, it is likely that an otherwise healthy patient who has a removable risk factor for thromboembolic disease (surgery) who is now ambulating and has a negative lower-extremity compression ultrasound is at low risk for recurrent thromboembolic disease, even if they are untreated. The expected utilities for such a patient are shown in Figure 4.4. Note that no treatment and no pulmonary arteriogram would be indicated for any prevalence of pulmonary embolism. The only assumption that has changed is that the expected utility for treated and untreated pulmonary embolism is now 0.98 and 0.9, respectively. Expected utilities of 0.92 and 0.7 were used in Figure 4.3. When the morbidity from recurrent thromboembolic disease is lower than the risk from anticoagulation, the preferred option is no treatment.

The most important point in the preceding decision is that the management of patients suspected of pulmonary embolism cannot be rationally determined based on the results of the ventilation-perfusion study alone. The risks of pulmonary arteriography, anticoagulation, and untreated pulmonary embolism for each patient must also be considered.

4.2.5 Patient Outcome

Patient outcome has become increasingly recognized as the most important factor in determining the best diagnostic and management strategy (Eddy 1990a,b). Utility analysis, as described previously, provides a mathematical model that can be used to predict patient outcome. An alternative approach is to directly measure patient outcome. One possible design for a patient outcome study for a diagnostic test is shown in Figure 4.5. This study design is simi-

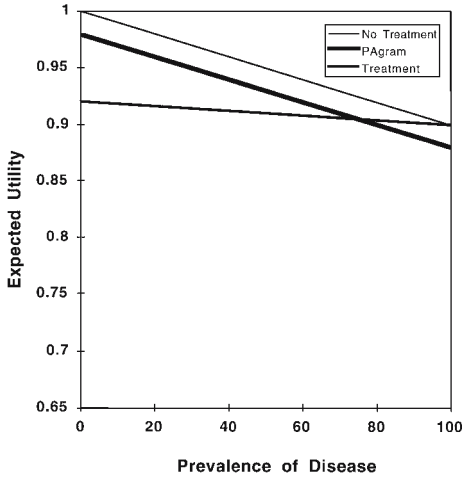

Fig. 4.4. Expected utilities of three different management strategies in patients suspected of pulmonary embolism who are at low risk for recurrent disease if untreated. If the risk of recurrent thromboembolic disease is less than the risk from treatment, the expected utility of no treatment is always greater than the expected utility of treatment

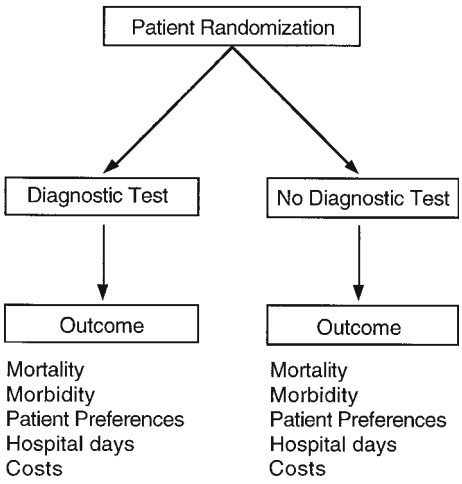

Fig. 4.5. Study design to determine the impact of a diagnostic test on patient outcome. The most reliable way to determine if a diagnostic test uniquely contributes to improved patient outcome is to randomize eligible patients to have or not have the diagnostic test. Justifying the use of diagnostic tests that have no measurable effects on patient outcomes will become increasing difficult as health care resources become more limited

lar to the study design typically used to measure the effects of a therapeutic intervention. Key elements are that patients are randomized to have or not have the diagnostic test that is being evaluated and the study endpoints are outcomes that are important to patients and society rather than diagnostic accuracy (e.g., sensitivity, specificity). Outcomes of interest would include mortality, morbidity, and costs. Using this paradigm, diagnostic tests would only be recommended if they have some measurable effect on patient or societal outcomes. Patient outcome studies are more difficult to perform than simple diagnostic accuracy studies, but they provide far more valuable information.

Diagnostic strategies that do not include pulmonary arteriography have been shown to accurately identify patients who are at low risk for recurrent thromboembolic disease when they are not treated (Wells et al. 1998; Perrier et al. 1999). In a well-designed study, Wells et al. (1998) showed that the occurrence of recurrent thromboembolic disease in a large portion of patients who were evaluated using only clinical history and non-invasive studies was as low as the recurrent thromboembolic rate in populations who had negative pulmonary arteriograms. Several older studies have also shown that ventilation-perfusion studies can be used to identify groups of patients with low incidence of recurrent thromboembolic disease, even when anticoagulation is not given (Lee et al. 1985; Smith et al. 1987; Kahn et al. 1989; Hull et al. 1990; Jacobson et al. 1997). In the future, it will be difficult to justify recommendations for more invasive, more costly diagnostic and managing strategies if a change in patient outcomes cannot be documented.

4.3 Ventilation-Perfusion Imaging

4.3.1 Technical Issues

Several radiopharmaceuticals are available to study regional ventilation. In the US, ^{99m}Tc-aerosols and ^{133} Xenon ventilation studies are most common because of the unavailability of pertechnegas and the cost of ^{81m}Krypton. Despite their differences, all of these agents are suitable for studying regional ventilation.

Currently, it is common practice to perform both a ventilation and perfusion study on patients suspected of pulmonary embolism. The motivation for performing a dual study is partly due to the fact that the technical quality of a ventilation study performed with the xenon or a technetium-labeled agent ventilation study is better when performed prior to the injection of ^{99m}Tc-macro-aggregated-albumen (MAA).

When the ventilation study is performed first, it has to be performed in all patients since patients cannot be selected based on the results of their perfusion study. If the ventilation study were performed after the perfusion study, the ventilation study could probably be avoided in one half to two thirds of patients who do not have any significant discrete perfusion abnormalities. Avoiding unnecessary ventilation studies may have a higher priority in managed care system than in a fee-for-service system. Performing the ventilation study after the perfusion study in selected patients has several advantages including: (a) avoiding unnecessary ventilation studies; and (b) being able to perform the ventilation study in the view in which the perfusion abnormality is best seen. The disadvantages of performing the ventilation study after the perfusion study include: (a) a technically less satisfactory study due to downscatter (or crosstalk) from ^{99m}Tc; and (b) each perfusion study takes longer because a smaller dose of ^{99m}Tc-MAA should be used. Whatever technique is used, our technical ability to detect perfusion abnormalities is better than our ability to

detect ventilatory abnormalities; therefore, technical mismatches (perfusion defects with no apparent ventilation defects) can occur.

Imaging technology has improved significantly since the mid-1970s. SPECT imaging of perfusion and ventilation is now possible. These technical advances, however, do not solve inherent problems of ventilation-perfusion imaging. Firstly, diseases other than pulmonary embolism sometimes present with ventilation-perfusion mismatches and pulmonary embolism can sometimes cause ventilation-perfusion matches. Secondly, ventilation-perfusion imaging can only reliably detect acute pulmonary embolism. Emboli may resolve quickly, especially in younger patients without pre-existing cardiopulmonary disease. Older, partially lysed emboli that are adherent to the vessel wall may not decrease regional pulmonary perfusion and therefore may not be detectable with perfusion imaging. In contrast, these older, partially lysed emboli may still cause intraluminal filling defects demonstrable with pulmonary arteriography or spiral CT. Given the apparently good outcome in a patient with a low likelihood ratio result on a ventilation-perfusion study, the clinical significance of partially lysed emboli that do not cause a perfusion abnormality can be questioned. Thirdly, ventilation-perfusion imaging can only provide information about what has already happened in the lungs. The patient's ultimate prognosis will depend on the occurrence of future emboli. Evaluating venous structures that are likely sources of emboli can only accurately assess the risk for future emboli.

4.3.2 Interpretation Criteria

The interpretation criteria for ventilation-perfusion scintigraphy have been codified by numerous groups (Table 4.2; Kwok et al. 1996). These interpretation criteria provide a useful framework for inexperienced physicians to use and to learn how to interpret ventilation-perfusion studies. By necessity, the interpretation criteria are overly simplistic and cannot replace the judgment of an experienced physician. Experience is important because of the ambiguity and simplicity of the interpretation criteria. For example, the interpretation criteria only allow for a binary (matched or mismatched) classification of ventilation and perfusion defects. In practice, degree to which a perfusion defect has an associated ventilatory abnormality varies on a continuum. Deciding when to consider a perfusion defect as matched or mismatched requires some judgment. The significance of a perfusion abnormality is also affected by additional characteristics such as how well the abnormality conforms to the segmental anatomy of the lung, how distinct the borders of the abnormality are, and the severity of the perfusion abnormality. The patient's presentation and the time that has elapsed since the event that raised the suspicion of pulmonary embolism need to be considered. If a ventilation-perfusion study is obtained within hours of a patient having syncope, it is unlikely that one or two moderate-size perfusion defects could account for the patient's presentation. On the other hand, if the syncopal episode was days ago, these same findings would need to be interpreted more cautiously since considerable lysis of the patient's emboli may have occurred. None of these nuances are incorporated into the simple interpretation criteria as shown in Table 4.2.

4.3.2.1 PIOPED

Ventilation-perfusion imaging was the subject of a rigorous prospective multicenter study known as the PIOPED (Prospective Investigation of Pulmonary Embolic Disease) study (PIOPED Investigators 1990). The motivation for this study came from concerns that prior retrospective single institution studies comparing the results of ventilation-perfusion imaging with pulmonary arteriography were biased because only a small subset of patients who had ventilation-perfusion imaging were referred for pulmonary arteriography. In the major arm of the PIOPED study, all patients with any perfusion abnormality on ventilation-perfusion imaging were required to have a pulmonary arteriogram. This requirement for pulmonary arteriography undoubtedly resulted in some selection bias since clinicians presumably would only allow their patients to enroll in a study in which a high percentage would have a mandatory pulmonary arteriogram if they had a relatively high suspicion for pulmonary embolism. This supposition is supported by the fact that the prevalence of pulmonary embolism in the PIOPED study is high (33%).

This study had a few strengths and several major weaknesses. One of its greatest strengths was that it clearly showed that clinicians can assess pre-test probability. For the same ventilation-perfusion imaging result, the post-test probability of pulmo-

Table 4.2. V/Q criteria for categorizing probability of pulmonary embolism. (From Kwok 1996)

Probability	Sullivan (based on McNeil 1976)	Biello et al. (1979)	PIOPED (1990)	Revised PIOPED
Normal	No Q defects	No Q defects	No Q defects Q outlines exactly the shape of the lungs on CXR	Same as PIOPED
Very low			<3 small Q defects with normal CXR	
Low	Multiple V/Q matches Single subsegmental V/Q mismatch	Small V/Q mismatches V/Q matches without corresponding CXR changes Q defect<<CXR density	Nonsegmental Q defect 1 moderate V/Q mismatch, with normal CXR Q defect<<CXR density Large or moderate V/Q matches, involving <4 segments in 1 lung and <3 segments in l lung region with normal CXR or CXR findings<<Q defects >3 small Q defects with normal CXR	Non-segmental Q defect Any Q defect<<CXR abnormality V/Q matches provided that the CXR is normal and perfusion in some areas of the lungs is normal[a] Any number of small Q defects with a normal CXR
Intermediate	Q defect with matched density on CXR Mixed V/Q mismatches and matches Single segment, lobe or lung V/Q mismatch Multiple subsegmental V/Q mismatches	Severe diffuse OPD with Q defects Single medium or large V/Q mismatch Q defect same size as CXR change	Anything not falling into normal, very low, low, or high-probability categories Borderline high or borderline low Difficult to categorize as low or high	1 moderate to 2 large V/Q mismatches or the arithmetic equivalent in moderate or large and moderate defects[b] Single V/Q match and normal CXR Difficult to categorize as low or high, or not described as low or high
High	Multiple segmental or larger V/Q mismatches	≥2 medium or large V/Q mismatches Q defect>>CXR density	≥2 large V/Q mismatches, with normal CXR or findings<<Q defects ≥2 moderate V/Q mismatches and 1 large V/Q mismatch without CXR findings ≥4 moderate V/Q mismatches without CXR findings	≥2 large V/Q mismatches or the arithmetic equivalent in moderate or large and moderate defects[b]

V, ventilation; *Q*, perfusion; *CXR*, chest radiograph; *OPD*, obstructive pulmonary disease; <<, substantially smaller than; >>, substantially larger than; *non-segmental Q defect* means very small effusion, cardiomegaly, enlarged aorta, hila, or mediastinum, elevated diaphragm.
Biello criteria: *small*, <25% of a segment; *medium*, 25%–90% of a segment; *large*, >90% of a segment.
PIOPED criteria: *small*, <25% of a segment; *moderate*, 25%–75% of a segment; *large*, >75% of a segment.
[a]Very extensive defects can be categorized as low probability. Single V/Q matches are borderline for low probability and thus should be categorized as intermediate in most circumstances by most readers, although individual readers may correctly interpret individual scans with this pattern as showing low probability.
[b]Two large V/Q mismatches are borderline for high probability. Individual readers may correctly interpret individual scans with this pattern as showing high probability for pulmonary embolism. In general, it is recommended that more than this degree of mismatch be present for inclusion in the high-probability category.

nary embolism changed as expected when the clinician's assessment of pre-test probability was considered (Fig. 4.1). Another strength of the PIOPED study is that information about observer variability for both ventilation-perfusion imaging and pulmonary arteriography was obtained (Table 4.3). Ordinarily, we think of the results of pulmonary arteriography as being positive or negative. In the PIOPED study, the interpretation of the pulmonary arteriogram was read as positive, negative, or uncertain in 33%, 64%, and 3% of patients, respectively. Technically unsatisfactory pulmonary arteriograms that were uninterpretable occurred in 5% of patients. Blinded independent observers agreed that the pulmonary arteriogram was positive, negative, or uncertain 92%, 83%, and 89% of the time, respectively. The fact that there is considerable observer variability in the reading of pulmonary arteriograms is often

Table 4.3. Observer agreement: PIOPED Investigators (1990)

Ventilation-perfusion study		Pulmonary arteriogram	
High	95%	Present	92%
Intermediate	75%	Absent	83%
Low	70%	Uncertain	89%
Very low	92%		
Normal	94%		

overlooked. It is unrealistic to expect that a completely independent test for pulmonary embolism (ventilation-perfusion imaging) would agree with the reading of the pulmonary arteriogram better than two blinded readings of the same pulmonary arteriogram would agree. Given that 17% of negative pulmonary arteriograms will be read as positive by one of two blinded readers, it is remarkable that low likelihood ratio results on ventilation-perfusion imaging agree with negative pulmonary arteriography 85%–90% of the time.

There are several major flaws with PIOPED. Firstly, the endpoint was diagnostic accuracy (How often does ventilation-perfusion imaging agree with the pulmonary arteriogram?) rather than patient outcome. A much more valuable study would have been to randomize patients with low and/or intermediate likelihood ratio results on their ventilation-perfusion study to have or not have a pulmonary arteriogram. Would there have been any measurable difference in outcome between the patients with and without a pulmonary arteriogram? The costs and patient discomfort would be more in the pulmonary arteriogram group. What would have been the offsetting benefits? Would fewer or more patients be anticoagulated? Would there be a change in mortality or morbidity?

Secondly, PIOPED perpetuated the use of discrete categories for the interpretation of ventilation-perfusion studies, when in fact the results of any complex imaging test are better represented as a continuum and should be reported as likelihood ratios (Jaeschke et al. 1994a,b). Use of discrete categorizations also distorts any analysis of observer variability. For example, as shown in Figure 4.6, the results of any complex imaging test naturally falls on a continuum from definitely normal to definitely abnormal. When this continuum is broken up into discrete segments such as normal, low, intermediate, and high likelihood ratio results, this artificially creates some apparent observer disagreement. As shown in Figure 4.6, using a continuous scale, readers A and B disagree more on the interpretation of the study, but since both readers A and B's interpretations fall within the category of low they are said to agree. In contrast, readers B and C are closer together on the continuous scale, yet when forced to put their results into these discrete categories, they appear to disagree. The creation of discrete category introduces the problem of exactly how to identify the line dividing each of the categories on the continuous scale. For example, the dividing line between normal and low is difficult to define unambiguously. Discrete categories can also frustrate readers since they may have to agonize about which side of the artificial line they must choose to categorize the result. Allowing readers to give an approximate likelihood ratio for the results of ventilation imaging studies would: (a) help identify true observer variability, (b) decrease the artificial mental anguish induced by an arbitrary discrete scale, and (c) more clearly convey the results of the test.

A third major problem with PIOPED is that it has continued to confuse the test result with the post-test probability of disease. As previously shown in Figure 4.1, the clinical history and other information must be combined with the test result in order to come up with a true post-test probability. Failure to distinguish the test result from post-test probability has resulted in enormous confusion in the literature where management recommendations are based on test results that are mistakenly interpreted as post-test probabilities. For example, in Figure 4.1, note that the post-test probability for pulmonary embolism was less for a patient with a high result and a low pre-test probability (56%) than it was for a patient with an intermediate result and a high pre-test probability (66%). Likewise, the post-test probability for a patient with an intermediate result and a low pre-test probability (16%) was the same as for a patient with a low result and an intermediate pre-test probability (16%).

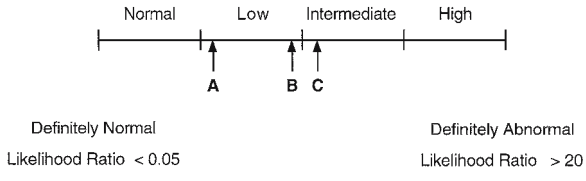

Fig. 4.6. Continuous vs discrete results. Forcing readers to use a discrete scale, rather than a continuous scale, often distorts studies of observer agreement. The results of observers B and C would be classified as disagreements when a discrete scale is used, even though they are more in agreement than are observers A and B

Another major shortcoming of the current interpretation criteria is that no distinction is made between intermediate likelihood ratio results for mild, moderate, or massive pulmonary embolism. More risk stratification information is available from ventilation-perfusion imaging than is conveyed by the simple categories of normal, low, intermediate, and high.

Finally, the PIOPED Investigators (1990) reported the results of their study using sensitivity and specificity (Table 4.4). These measures are only appropriate if the simple binary test results are obtained. It is virtually impossible to interpret the results of complex imaging results that have multiple outcomes when they are presented in this way. A much better way to present the results is as likelihood ratios (Table 4.5). As explained in the Appendix, the likelihood ratio is calculated by dividing the P(T–|D+) by P(T–|D–). The likelihood ratios listed in Table 4.5 provide much more useful information (Jaeschke et al. 1994a,b) than the sensitivities and specificities that were provided by the PIOPED Investigators and that are listed in Table 4.4. A high likelihood ratio result increases the pre-test odds of disease by a factor of almost 14. An intermediate likelihood ratio result does not change the pre-test odds of disease; therefore, if the pre-test odds were low before performing ventilation-perfusion imaging, they remain low after imaging. Low likelihood ratio results and near-normal/normal results decrease the pre-test odds by a factor of 0.37 and 0.19, respectively. These last two likelihood ratios are not as low as desirable, but it must be remembered that the observer agreement for a negative pulmonary arteriogram was only 83% (Table 4.3). That means that 17% of the time, the second observer reads the pulmonary arteriogram as (falsely) positive. This observer variability with negative pulmonary arteriograms partly explains the less than desirable likelihood ratios for low and near-normal/normal results. When clinical follow-up is used to classify the disease status of patients, the values for the likelihood ratios for low and near-normal/normal results are much lower.

Table 4.4. PIOPED results

Scan category	Sensitivity (%)	Specificity (%)
High	41	97
High or intermediate	82	52
High, intermediate, or low	98	10

Table 4.5. PIOPED results

Scan category	PE+	PE–	$P(T_n\|D+)$	$P(T_n\|D-)$	LR_n
High	102	14	0.4064	0.0292	13.93
Intermediate	105	217	0.4183	0.4521	0.93
Low	39	199	0.1554	0.4146	0.37
Near normal/normal	5	50	0.0199	0.1042	0.19
Total	251	480			

PE pulmonary embolism; $P(T_n|D+)$ probability of the n^{th} test result with presence of disease; LR_n likelihood ratio of the n^{th} test result.

4.4 Other Diagnostic Tests

The diagnosis and management of patients suspected of pulmonary embolism requires information from several sources. The clinical evaluation of the patient and the role of ventilation-perfusion imaging have already been discussed. This section describes the other diagnostic tests. The chest radiograph has long been used in conjunction with ventilation-perfusion imaging. Likewise, pulmonary arteriography has long been regarded as the reference standard for diagnosis of pulmonary embolism. Three newer diagnostic tests that are available to evaluate patients include serum D-dimer levels, compression ultrasound of the lower extremities, and CT of the pulmonary arteries.

4.4.1 Chest Radiograph

The chest radiograph is routinely obtained in all patients suspected of pulmonary embolism. Because the findings on the chest radiograph are non-specific for pulmonary embolism (Worsley et al. 1993; Stein et al. 1991), the chest radiograph is useful mainly for discovering other causes for the patient's signs and symptoms such as pneumonia, pneumothorax, congestive heart failure, and pleural effusions.

The non-specificity of radiographic abnormalities is illustrated in Table 4.6 (Elgazzar 1997). The likelihood ratio for most findings is close to 1; therefore, the chest radiograph findings do not increase or decrease the pre-test odds for pulmonary embolism, except for the presence of Westermark's sign (likelihood ratio: 4) and pulmonary edema (likelihood ratio: 0.3).

There is almost universal agreement that a chest radiograph is needed to interpret ventilation-per-

Table 4.6. Chest radiograph findings in suspected pulmonary embolism

Finding	$P(T_n\|D+)$	$P(T_n\|D-)$	LR_n
Atelectasis	0.71	0.46	1.54
Pleural effusion	0.54	0.37	1.46
Pleural-based opacity	0.35	0.21	1.67
Elevated hemidiaphragm	0.30	0.23	1.30
Oligemia	0.21	0.12	1.75
Prominent pulmonary artery	0.26	0.23	1.13
Cardiomegaly	0.14	0.13	1.08
Pulmonary edema	0.04	0.13	0.31
Westermark's sign[a]	0.13	0.03	4.33

[a]Prominent pulmonary artery and decreased pulmonary vascularity

fusion studies, although one group of investigators recently reported that the availability of the chest radiograph did not affect their interpretations of ventilation-perfusion studies (Denton et al. 1998). These investigators acknowledged that their inability to demonstrate the need for a chest radiograph was likely due to the fact that few of their patients had abnormalities on their chest radiograph. Occasionally, with a low or near-normal ventilation-perfusion study, one is tempted not to obtain a chest radiograph since the chest radiograph is very unlikely to change the interpretation of the ventilation-perfusion study. Not obtaining a chest radiograph under these circumstances is a mistake, because alternative explanations for the patient's symptoms may be apparent on the chest radiograph.

Another issue that always arises is how close in time the chest radiograph needs to be to the ventilation-perfusion studies. There is a common, simple, less accurate answer and an uncommon, complicated, longer, more accurate answer. The simple answer is the chest radiograph should be obtained within 24 h of the ventilation-perfusion study. The complicated answer is that it depends on the clinical circumstances. If a patient has acute onset of shortness of breath 1 h prior and the most recent chest radiograph was 2 h prior, a repeat chest radiograph should be obtained. The rationale for this recommendation is that there are acute processes such as small pneumothoraces that can be seen on a chest radiograph that may not be detected by ventilation-perfusion imaging. On the other hand, if a patient with no intervening pulmonary symptoms has a near-normal chest radiograph that is 48–72 h old, and if the results of the ventilation-perfusion imaging are normal or low likelihood ratio, no repeat chest radiograph is needed. If there are unexpected findings on the ventilation-perfusion study, the chest radiograph should be repeated.

Our current interpretation criteria are vague about how to use the results of chest radiographs. All chest radiograph abnormalities are lumped together in the generic term "chest radiograph abnormality." There are conflicting reports about how to interpret ventilation-perfusion studies in patients with pleural effusions (Bedont and Datz 1985; Goldberg et al. 1996). In truth, different radiographic abnormalities should likely affect our interpretation of ventilation-perfusion imaging differently. Chronic radiographic abnormalities must have a different meaning than acute abnormalities since chronic abnormalities cannot explain a patients acute symptoms. Finally, should chest radiographic abnormalities that are clearly caused by a disease process other than pulmonary embolism (e.g., pneumonia, cancer) be interpreted as an intermediate likelihood ratio for pulmonary embolism simply because they cause a triple match?

4.4.2 D-Dimer

A rapid assay for testing of whole-blood D-dimer is now available. D-dimer is a fibrin degradation product that is highly sensitive for the detection of thromboembolic disease; however, it is non-specific since it also can be elevated in patients with a variety of other diseases including myocardial infarction, pneumonia, heart failure, cancer, and recent surgery (Goldhaber 1998). An elevated D-dimer level is not helpful in making the diagnosis of pulmonary embolism; however, a normal D-dimer level is helpful in excluding the diagnosis.

In one large study (Ginsberg et al. 1998), the combination of a non-diagnostic lung scan (low or intermediate likelihood ratio) and a normal D-dimer test result had a negative predictive value of 97.2%. In total, 62% of all patients with non-diagnostic lung scan results (i.e., intermediate probability for pulmonary embolism) had normal D-dimer test results; therefore, pulmonary embolism could be excluded in a large percentage of patients with the addition of this simple test. When the authors also included the pre-test probability of the disease, the negative predictive value of a non-diagnostic lung scan and a normal D-dimer test were 98.7%, 94.6%, and 77.8% in patients with low, moderate, and high pre-test probabilities, respectively (Fig. 4.7). The authors concluded that in low and intermediate pre-test probability patients with a non-diagnostic lung scan and normal D-dimer test results had a high

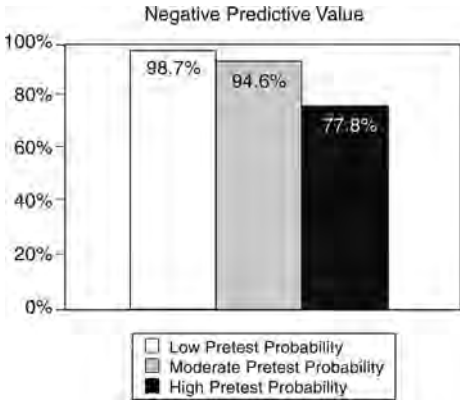

Fig. 4.7. Negative predictive value for patients with a low or intermediate result on the ventilation-perfusion study and a negative serum D-dimer test. The negative predictive value is acceptably high with a low or intermediate probability for recurrent thromboembolic disease, a negative serum D-dimer, and a low or moderate pre-test probability (Ginsberg et al. 1998)

enough negative predictive value to exclude clinically significant pulmonary embolism.

Larger studies have been performed that confirm the results of these earlier series, and corroborate the utility of a negative D-dimer test. Algorithms for the work-up of suspected pulmonary embolism start with this blood test. A negative D-dimer result (serum level <1 ìg/ml) is associated with a very low likelihood of pulmonary embolism (Michiels et al. 2003; Abcarian et al. 2004). For patients with a low pre-test probability, the work-up is stopped in most institutions. If the clinical suspicion remains high, imaging procedures are the next step.

4.4.3 Detection of Deep Venous Thrombosis

Several non-invasive tests have been recommended for detecting deep venous thrombosis. Impedance plethysmography, a test that measures reserve venous capacity in the rapidity of outflow from the deep venous system of the lower extremities, has largely been replaced by the use of compression ultrasound. Compression ultrasound involves a meticulous examination of the major deep venous structures of the lower extremities. Thrombosis is identified by the inability to compress the vein. Compression ultrasound has numerous limitations including the fact that it is very operator dependent, it can only reliably detect thrombosis in the thigh and knee, and there is considerable difficulty in differentiating new from old thrombi. Because of the difficulty in assessing thrombosis below the knee, serial compression ultrasound has been recommended in order to improve the sensitivity of this technique in detecting clinically significant disease (Kearon et al. 1998a,b). When serial ultrasound is negative the risk for recurrent thromboembolic disease in patients with a low or intermediate result on the ventilation-perfusion study was <2% during a 6-month follow-up period. Doppler ultrasound that looks at venous flow patterns in the vein is less reliable in detecting deep venous thrombosis.

4.4.4 Pulmonary Arteriogram

Pulmonary arteriography is regarded as the reference standard for the diagnosis of pulmonary embolism. Its limitations are rarely emphasized. In the PIOPED study (Stein et al. 1992), there were five deaths among the 1111 patients who had had a pulmonary arteriogram. In addition, there were nine major non-fatal complications that included respiratory distress, renal failure, and bleeding requiring transfusions. There were minor complications in an additional 60 patients.

As discussed previously, observer agreement for a complex imaging test, such as pulmonary arteriography, is less than perfect. Observer agreement depends on the quality of the pulmonary arteriogram. In the PIOPED study, 691 of the 1099 pulmonary arteriograms were rated as good quality, 355 were rated as fair quality, and 46 were rated as poor quality. Observer agreements on positivity were 93%, 90%, and 98% for good-, fair-, and poor-quality arteriograms, respectively. Agreement on negativity was less good. There was 88% agreement for good-quality arteriograms, 77% agreement for fair quality, and 54% for poor-quality arteriograms.

It is important to recognize that the phenomenon demonstrated by pulmonary arteriography is very different from the pathology that is detected by regional perfusion studies. The detection task for pulmonary arteriography is to identify an intraluminal filling defect. The detection task becomes more and more difficult as the vessel size gets smaller and there are more and more vessels. Observer agreement clearly decreases as vessel size gets smaller.

The ability of pulmonary arteriography to distinguish acute from chronic emboli is not well documented since there is no independent reference standard. It is likely that acute emboli cause com-

plete occlusion of a vessel since a soft, freely mobile embolus is likely to completely obstruct the vessel. Once the embolus becomes adherent to the vessel wall and once some thrombolysis has occurred, tracking of contrast can be seen around the embolus. This finding is regarded as being the most reliable finding for acute pulmonary embolism. It remains to be seen whether or not the presence of intraluminal filling defects on pulmonary arteriography or the presence of regional perfusion abnormalities on a perfusion study have greater prognostic significance. Interestingly, the best validation for pulmonary arteriography has been follow-up of patients who have had negative pulmonary arteriograms and who have not been anticoagulated (Novelline et al. 1978). In this retrospective analysis, 180 patients with suspected pulmonary embolus and negative arteriograms were followed for a minimum of 6 months. Of the 167 patients who did not undergo therapy, none died as a result of thromboembolic disease. A total of 20 patients died of other causes. None of the 147 remaining patients suffered a recurrent embolus. This suggests that, indeed, the pulmonary emboli that are missed with pulmonary angiography are not of great health risk, and that a negative pulmonary arteriogram can be regarded as adequate information to not introduce therapy. It is somewhat surprising that such good prognostic information can be obtained solely from examining the pulmonary arteries.

4.4.5 CT-Pulmonary Angiography (CTPA)

Early reports revealed that pulmonary emboli could be seen with contrast-enhanced computed tomography (CT) (Breatnach and Stanley 1984; Chintapalli et al. 1988; Goodman et al. 1997). However, motion artifacts due to respiratory motion and sampling error of older single slice CT systems, prevented its use as a first-line diagnostic tool for detecting pulmonary embolism. Technological advances manifested by helical CT and electron beam CT enabled acquisitions during one single breath hold. The introduction of multidetector and multi-slice systems, and later retrospective gating, provide fast and high resolution CT. Subsegmental pulmonary emboli can be detected with these advanced technologies (Geraghty et al. 1992; Schoepf and Costello 2004). Magnetic resonance angiography protocols utilizing gadolinium enhancement also have been developed to acquire images of the pulmonary vasculature in a single breath-hold, which can detect subsegmental pulmonary emboli (Meaney et al. 1997). However, MR angiography lacks sufficient spatial resolution for reliable evaluation of the peripheral pulmonary arteries (Schoepf and Costello 2004)

CT pulmonary angiography (CTPA) is minimally invasive, an advantage over conventional pulmonary angiography. CT has the additional benefit of imaging the thorax, potentially facilitating a diagnosis to explain the patient's symptoms other than pulmonary embolism. A number of studies have suggested that CT is more "accurate" than ventilation-perfusion scintigraphy in diagnosing pulmonary embolism. These early studies should be interpreted with caution since they involved a small number of selected patients, and commonly excluded technically inadequate studies and patients in whom the exam could not be performed.

An early prospective study (Mayo et al. 1997) evaluated CTPA and ventilation-perfusion scintigraphy in 139 patients. Final diagnosis was established by concordant interpretation of CT and scintigraphic studies. If the ventilation-perfusion scintigraphy was interpreted as low or very low probability for PE and the CT was negative and the clinical suspicion was high, a pulmonary arteriogram was performed. If the ventilation-perfusion scintigraphy or CTPA results were intermediate or if they were discordant, a pulmonary arteriogram was performed. In negative cases, a 3-month follow-up was undertaken via a phone call to the patient's physician. The results showed that CTPA yielded a true positive reading in 40 cases, false positive in two cases, true negative in 88 cases, false negative in five cases and was indeterminate in four cases. Positive predictive value was therefore 95% and negative predictive value also 95%. By comparison, pulmonary embolism was present in 30 of 36 high probability results on their ventilation-perfusion studies, 6 of 20 intermediate probability exams, 8 of 58 low probability exams and 2 of 25 very low probability or normal exams. The positive predictive value of a high probability exam was therefore 83% and the negative predictive value of a normal, low or very low probability exam was 88%.

CT angiography has several limitations. Relative contraindications include marginal renal function, history of contrast reaction, hemodynamic instability and severe dyspnea. In one study (Garg et al. 1998), 4.9% of patients were excluded from contrast administration for such reasons. An additional 13% had suboptimal studies and were excluded from cal-

culations of sensitivity, specificity and predictive values. It is estimated that approximately 5%–10% of CT studies with contrast will be technically inadequate (Kuzo and Goodman 1997; Goodman et al. 1997). Some vessels are not well seen and others cannot be visualized on CTPA (Remy-Jardin et al. 1992). These are predominantly vessels oriented obliquely in the right middle lobe and lingula. However, given the nature of pulmonary emboli, which tend to be multiple, this was not felt to be a major limitation. Criteria for interpretation of pulmonary embolism on CTPA and potential pitfalls in the evaluation of CT exams have been described (Beigelman et al. 1998). A good understanding of the vascular anatomy of the lung (e.g., arteries run with bronchi while veins run independently) is necessary. Pitfalls include the external compression of arteries by lymph nodes, which may mimic a mural thrombus. Volume averaging may be confusing when vessels run obliquely. Perivascular edema may produce a collar of low attenuation simulating an embolus. Motion artifacts were frequently a problem, which is negligible in the new generation multi-slice systems with fine collimation and high resolution. Streak artifacts originating from the SVC due to high rate of injection into the SVC can mimic PE. Insufficient enhancement may occur due to delayed injection, SVC obstruction, shunts, increased pulmonary vascular resistance from consolidation or large pleural effusion. Self-evidently, the display window setting can adversely affect interpretation.

In 2002, a meta-analysis was performed on the detection of pulmonary emboli with CTPA (Safriel and Zinn 2002). The rationale for this study emphasized that scintigraphy alone is insufficient to establish pulmonary embolism in the majority of patients suspected of having it (about 75% of V/Q scans). Between 1990 and 2000, they found 12 studies that fulfilled their criteria, and the pooled group comprised 1250 patients. They found an overall sensitivity of 74.1% and specificity of 89.5% and concluded that CTPA was a sensitive and specific primary imaging tool for detecting pulmonary emboli. It was also effective in patients with an abnormal chest radiograph, underlying lung disease or other pathology that caused the respiratory symptoms.

A recent state-of-the-art paper (Schoepf and Costello 2004) claims that CTPA has become the first-line imaging modality for the work-up of pulmonary embolism. However, CTPA cannot be considered as the standard of reference, because the inter-observer agreement for subsegmental pulmonary emboli is low (45%–66%). The inter-observer agreement of CTPA is still better than for scintigraphy (van Rossum et al. 1998; Blachere et al. 2000). The high negative predictive value of a normal CTPA was again emphasized. A similar performance can be quoted for a normal lung perfusion scan. The additional advantage of CT is for patients with pulmonary abnormalities, for whom ventilation-perfusion scintigraphy usually is not diagnostic.

The experience of the interpreters in reading CTPA is important, as reported in the meta-analysis paper for two European trials. These revealed a discrepancy in performance between academic and community hospitals: sensitivity 91% vs 60% and specificity 91% vs 86%, respectively (Safriel and Zinn 2002). This difference may be attributed to experience and training. Given the additional variability in interpretation of subsegmental filling defects, and the lack of an "imaging reference standard" for pulmonary embolism, it will take time before CTPA will be considered as the routine first-line test for evaluating patients suspected of suffering from pulmonary embolism. In our own institution, the number of ventilation-perfusion scans dropped in the mid 1990s, but regained much of its loss around the turn of the century. Currently, it is again the first-line test for patients referred from the emergency room for work-up of pulmonary embolism.

4.5 Conclusion

The prevailing view is that pulmonary embolism is a monolithic disease. Diagnostic strategies are based on studies that have imperfect binary diagnostic endpoints. Since the dogma has been that all patients with pulmonary embolism need to be treated, there have been few attempts to overtly risk-stratify patients.

A great deal of the shortcomings of how we currently diagnose and manage patients with suspected pulmonary embolism are due to how we have evaluated diagnostic tests in the past. Diagnostic accuracy tests which compare the results of one imperfect diagnostic test (e.g., ventilation-perfusion imaging) to another imperfect test (e.g., pulmonary arteriography) are inevitably misleading. What we need is outcome studies establishing which diagnostic strategies result in the best patient outcomes. One reason for accepting a negative pulmonary arteriogram as a strong indicator of good prognosis is

that the risk of recurrent thromboembolism is low in these patients, even when they are not anticoagulated. Likewise, other diagnostic strategies that use readily available noninvasive diagnostic tests have been shown to identify low risk patients.

In order to be optimized, diagnostic and management strategies must account for information from a variety of sources. Management strategies based on the result of one single test, e.g., all patients with an intermediate likelihood ratio result on their ventilation/perfusion scan should have a pulmonary arteriogram, are naive and doomed to failure. Rational decisions can only be made based on patient's post-test probability of disease, the risk of invasive diagnostic tests and the risk of treatment or no treatment. The post-test probability of disease is determined by combining the pre-test probability and the test result. The risk of no treatment depends on the clot burden in the lung, the potential for future emboli and the overall medical condition of the patient. It is unclear whether the clot burden in the lung is best assessed by the number of regional perfusion abnormalities detected by scintigraphy, or intraluminal filling defects detected by pulmonary arteriography or CTPA. One could argue that the presence of regional perfusion abnormalities has more prognostic significance than the presence of intraluminal filling defects that have no effect on regional perfusion. In the former instance, the lung is being overwhelmed by the embolic burden whereas in the latter case, the lungs own potent thrombolytic mechanisms are able to keep up with the embolic burden. The risk of future emboli cannot be assessed by any test that looks solely at the lungs.

The advent of high resolution, multi-slice helical CT will have an impact on the work-up of pulmonary embolism. The acquisition duration is short, allowing for high quality scans in a single breath hold in the vast majority of patients. Many institutions favor CTPA as first-line work-up for in-patients. The likelihood that an explanation will be found for the symptoms is much higher with CT with and without contrast, than with ventilation-perfusion scintigraphy. For out-patients, it is a different matter and the issues have not been sorted out. For patients with a low pre-test probability for pulmonary embolism, it is probably more cost effective to confirm this impression with a completely normal perfusion scan or low-probability ventilation-perfusion scintigraphy. Moreover, the radiation exposure is lower for standard ventilation-perfusion imaging than for CTPA.

Appendix: Medical Decision Making

A very basic need in medical decision making is a way to quantify the accuracy of diagnostic tests. The most common and simplest approach assumes that test outcomes and disease states are binary (positive or negative). A 2+2 table, in which the columns usually represent the disease states and the rows represent the test results (Table A4.1), is usually used to calculate several ratios (accuracy, sensitivity, specificity, predictive value of a positive test, predictive value of a negative test, likelihood of a positive test, and the likelihood ratio of a negative test) related to

Table A4.1. 2+2 Decision matrix

		Disease State D+	Disease State D–
Test Results	T+	TP	FP
	T–	FN	TN

T+ = Test Positive
T– = Test Negative
D+ = Diagnosis Positive
D– = Diagnosis Negative

TP = True Positive
FP = False Positive
TP = False Negative
TP = True Negative

Derived Ratios

$$\text{Accuracy} = \frac{TP + TN}{TP + TN + FP + FN}$$

$$\text{Sensitivity} = \frac{TP}{TP + FN}$$

$$\text{Specificity} = \frac{TN}{TN + FP}$$

$$\text{Predictive Value of a Positive Test} = \frac{TP}{TP + FP}$$

$$\text{Predictive Value of a Negative Test} = \frac{TN}{TN + FN}$$

$$\text{Likelihood Ratio of a Positive Test} = \frac{\text{Sensitivity}}{\text{1-Specificity}}$$

$$\text{Likelihood Ratio of a Negative Test} = \frac{\text{1-Sensitivity}}{\text{Specificity}}$$

Probability Notation

$\text{Sensitivity} = P(T+|D+)$
$\text{Specificity} = P(T-|D-)$
$\text{Predictive Value of a Positive Test} = P(D+|T+)$
$\text{Predictive Value of a Negative Test} = P(D-|T-)$

$$\text{Likelihood Ratio for the n}^{\text{th}}\text{ Test Result} = \frac{P(T_n|D+)}{P(T_n|D-)}$$

the accuracy of diagnostic tests (Table A4.1). These ratios can also be written more concisely in probability notation. When using probability notation, the vertical bar "|" is read as "given the condition that" so the notation P(T+|D+) is read as "the probability of having a positive test result given the condition that the patient has the disease."

In this simplified binary world, sensitivity and specificity are regarded as the best measures of test performance since, unlike accuracy and the predictive value of the test, these values are not affected by the prevalence of disease. Unfortunately, sensitivity and specificity have many other shortcomings including the fact that disease states and test outcomes are not binary and sensitivity or specificity can be artificially inflated or deflated depending on the threshold which is used to divide positive and negative disease states (Royal 1994).

The effects of the choice of the threshold on sensitivity and specificity is illustrated in Fig. A4.1. The results of complex imaging tests do not naturally fit into the binary world of sensitivity and specificity. These results are more realistically viewed as a continuum that ranges from very normal results to very abnormal results. In order to capture the range of possible test results, they are typically categorized as definitely normal, probably normal, possibly abnormal, probably abnormal, and definitely abnormal, rather than simply as positive or negative. When test results are tabulated in this way, a family of sensitivity and specificity pairs can be generated depending on the threshold that is used to distinguish "positive" from "negative" test results. If a very strict threshold is used (Point 1 in Figs. A4.1 and A4.2), the test will have a low sensitivity (because the test result needs to be "definitely abnormal" in order to consider it a positive result) but a high specificity (since few non-diseased patients will have that test result). The family of sensitivity and specificity pairs can be plotted on a graph where the y-axis is sensitivity and the x-axis is 1-specificity (Fig. A4.2). This graph is called a receiver-operating-characteristics (ROC) curve.

More recently, likelihood ratios have gained in popularity. Likelihood ratios have several major advantages over sensitivity and specificity. Once their meaning is understood, this one value provides more meaningful information about the meaning of a particular test result than does sensitivity or specificity. In addition, their use is more appropriate with complex non-binary test outcomes such as the results of imaging tests. The general formula for the likelihood ratio is:

$$LR_n = \frac{P(T_n|D+)}{P(T_n|D-)}$$

where LR_n is the likelihood ratio of the n^{th} test result, $P(T_n|D+)$ is the probability of getting the n^{th} test

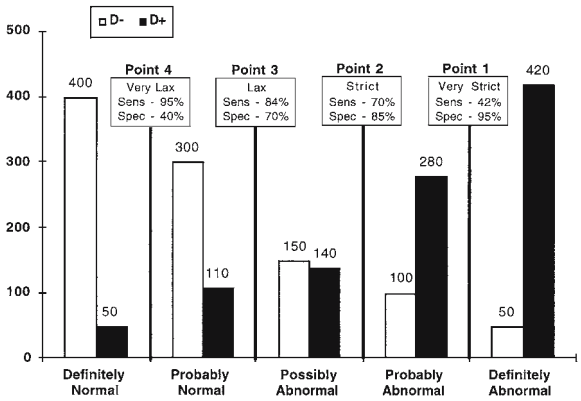

Fig. A4.1. A frequency histogram showing the distribution of test results that might be obtained in a diseased (*filled bar*) and a non-diseased (*open bar*) population. The number of subjects having each of the test results is shown *above the bars*. As would be expected, test results from the diseased population are more likely to be abnormal. In order to construct an ROC curve (see Fig. A4.2), a family of sensitivity and specificity pairs is generated by calculating the sensitivity and specificity for four possible thresholds (Points 1–4). For each threshold, all results to the left of the threshold are considered normal and all of the results to the right are considered abnormal

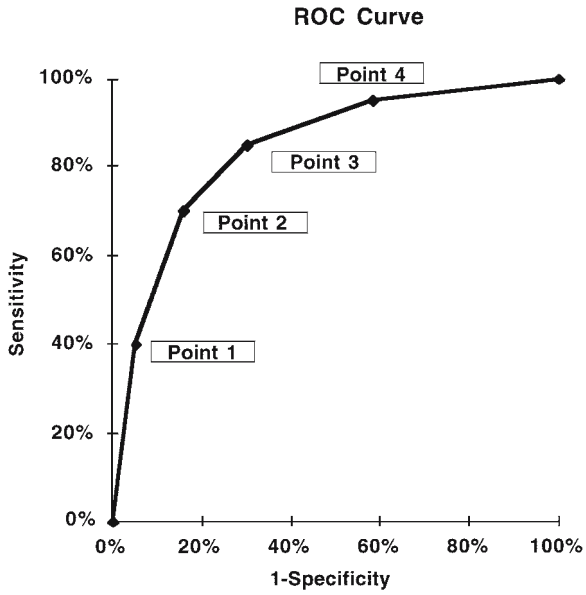

Fig. A4.2. The sensitivity/specificity pairs generated from Fig. A4.1 are plotted. Note that any sensitivity or specificity can be achieved by varying the threshold (Points 1–4); however, there is a trade-off between sensitivity and specificity

result in patients with the disease, and $P(T_n|D-)$ is the probability of getting the n^{th} test result in patients without the disease.

If the n^{th} test result is more common in patients with the disease, the likelihood ratio will be greater than 1; if the n^{th} test result is more common in patients without the disease, the likelihood ratio will be less than 1; if the n^{th} test result occurs with the same frequency in patients with and without the disease, the likelihood ratio will be close to 1. Test results that are useful for ruling in a disease typically have likelihood ratios greater than 10; test results that are useful for ruling out the disease typically have likelihood ratios of less than 0.1. The likelihood ratio for the test results shown in Fig. A4.1 are listed in Table A4.2. Note how likelihood ratios better capture the meaning of each individual test result. When a family of sensitivity and specificity pairs is generated as was done to construct the ROC curve, the test results in different categories are summed, so important information about the meaning of each test result is lost. As is shown below, another important advantage of likelihood ratios is that they simplify the calculation of the post-test probability of disease.

Measures of test performance, such as sensitivity and specificity, tell us how often a patient with the disease (or without the disease) will have positive (or negative) test results [P(T+|D+), P(T-|D-), respectively]. This is not the clinically relevant question. The clinician wants to know how often a patient with a positive test result will have the disease, P(D+|T+), and how often the patient with a negative test result will not have the disease, P(D-|T-). In order to determine the predictive value of a positive or negative test, information about the prevalence of disease or pre-test probability, P(D+), in the population studied is needed. If the test result, the performance characteristics of the test, and the pre-test probability are known, the post-test probability can be calculated. There are three ways in which to make this calculation. These three ways are illustrated in the following example: the effects of pre-test probability on post-test probability for a range of likelihood ratios is shown in Table A4.3. Assume that the prevalence of disease is 10% and that the sensitivity of the test is 87% and the specificity 75%. The first way to calculate the post-test probability is to use an intuitive method (Table A4.3). Based on the prevalence of disease, the sums of the columns in a 2+2 matrix can be calculated (Table A4.3, Step 1). An arbitrary but large number is used to minimize round-off error. If the prevalence of disease is 10%, and if the arbitrary large number of studied patients is 1000, the sum of the disease-positive results would be 100 and the sum of the disease-negative results would be 900. Once the sums of the disease-positive and disease-negative columns are known, the values of the 2+2 matrix can be calculated. If the sensitivity of the test is 87%, 87 of the 100 patients with the disease will have a positive test result and 13 will have a negative test result (Table A4.3, Step 2). If the specificity is 75%, 730 of the 900 patients without disease will have a negative test result and 170 will have a positive test result (Step 3). Once the squares of the 2+2 matrix have been filled in, then the predictive value of a positive and negative test result can be calculated. If the test results are positive, 87 of the 210 patients who had positive test results will actually have the disease (Step 4). Likewise, 730 of the 750 patients with negative test results will not have the disease (Step 5).

Table A4.2. Likelihood ratios

Test result	D+	D–	$P(T_n\|D+)$	$P(T_n\|D-)$	LR_n
Definitely normal	50	400	0.05	0.40	0.125
Probably normal	110	300	0.11	0.30	0.367
Possibly abnormal	140	150	0.14	0.15	0.933
Probably abnormal	280	100	0.28	0.10	2.80
Definitely abnormal	420	50	0.42	0.05	8.40

Table A4.3. Post-test probability: intuitive method

Assumptions
P(D+) = 0.1
P(T+|D+) = 0.87
P(T–|D–) = 0.75

Test Results	Disease State D+	Disease State D–	
T+	Step 2 **87** (0.87 100)	Step 3 **225** (900–675)	Step 4 $P(D+\|T+) = \frac{87}{87+225} = 27.9\%$
T–	**13** (100–87)	**675** (0.75 900)	Step 5 $P(D-\|T-) = \frac{675}{13+675} = 98.1\%$
Step 5 **Column Totals**	**100**	**900**	

A second method (Table A4.4) used to calculate the predictive value of a positive test and the predictive value of a negative test is to use Bayes' theorem. Bayes' theorem uses the same simple formula (true positives divided by true positives plus false positives) as the intuitive method described previously but the formula is rewritten using probability notation. The formula for Bayes' theorem appears to be more complicated than it really is. The advantage of Bayes' theorem is that the post-test probability of disease can be determined in one step.

Finally, the simplest way to calculate post-test probability is to use odds rather than probabilities and to use the likelihood ratios (Table A4.5). The mathematical manipulations, which are necessary, are considerably simpler than those required for Bayes' theorem. Once familiar with likelihood ratios and odds, post-test probabilities can easily be calculated in one's head. The first step in this method is to convert the pre-test probability to pre-test odds. A 10% chance of having the disease is the same as one chance of having the disease and nine chances of not having the disease. Using odds notation this is written as 1:9. Using the likelihood ratio, the post-test odds of disease can be calculated simply by multiplying the chances of having disease by the likelihood ratio (Table A4.5, Step 3). If desired, odds can then be converted back to probabilities (Table A4.5, Step 4). The effect of pre-test probability on post-test probability for a range of likelihood ratios is shown in Figure A4.3.

Table A4.4. Post-test probability: Bayes theorem

Assumptions
P(D+) = 0.1
P(T+|D+) = 0.87
P(T–|D–) = 0.75

Predictive value of a positive test:

$$P(D+|T+) = \frac{TP}{TP + FP} = \frac{P(T+|D+)\ \ P(D+)}{P(T+|D+)\ \ P(D+) + P(T+|D-\ \ (1-P(D+))}$$

$$P(D+|T+) = \frac{87}{87 + 225} = \frac{0.87\ \ 0.1}{0.87\ \ 0.1 + 0.25\ \ 0.9} = 27.9\%$$

Predictive value of a negative test:

$$P(D-|T-) = \frac{TN}{TN + FN} = \frac{P(T-|D-)\ \ P(D-)}{P(T-|D-)\ \ P(D-) + P(T-|D-\ \ (1-P(D-))}$$

$$P(D-|T-) = \frac{675}{675 + 13} = \frac{0.75\ \ 0.9}{0.75\ \ 0.9 + 0.13\ \ 0.1} = 98.1\%$$

Table A4.5. Post-test probability: likelihood ratio

Assumptions

P(D+) = 0.1
P(T+|D+) = 0.87
P(T–|D–) = 0.75

Step 1: Convert probabilities to odds
If P(D+) = 0.1 then Odds = 1-: 9

Step 2: Calculate the likelihood ratios
For a test with binary outcomes:
Likelihood Ratio of a Positive Test =

$$\frac{\text{Sensitivity}}{\text{1-Specificity}} = \frac{0.87}{1-0.75} = 3.48$$

Step 3: Calculate the post-test odds
Post-test odds = pre-test odds likelihood ratio

For a positive test:
Post-test odds = 1-: 9 3.48 = 3.48 : 9

For a negative test:
Post-test odds = 1-: 9 0.17333 = 0.17333 : 9

Step 4: Convert post-test odds to post-test probability
For a positive test

$$P(D+|T+) = \frac{\text{Odds}(D+)}{\text{Odds}(D+) + \text{Odds}(D-)} = \frac{3.48}{3.48+9} = 27.9\%$$

For a negative test

$$P(D-|T-) = \frac{\text{Odds}(D-)}{\text{Odds}(D-) + \text{Odds}(D+)} = \frac{9}{0.17333+9} = 98.1\%$$

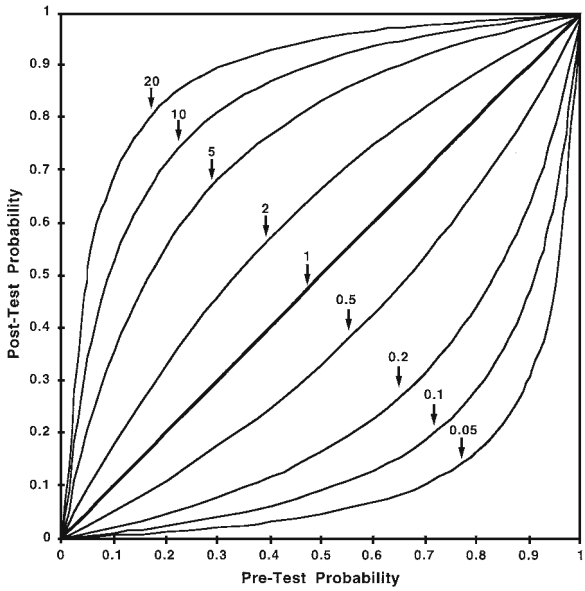

Fig. A4.3. Effects of likelihood ratios and pre-test probability on the post-test probability of disease. Each line on this graph shows the effects of a test result with a particular likelihood ratio on post-test probability for a given pre-test probability

References

Abcarian PW, Sweet JD, Watabe JT et al (2004) Role of a quantitative D-dimer assay in determining the need for CT angiography of acute pulmonary embolism. AJR Am J Roentgenol 182:1377–1381

Anonymous (1992) Evidence-based medicine. A new approach to teaching the practice of medicine. Evidence-Based Medicine Working Group (see comments). J Am Med Assoc 268:2420–2425

Barritt DW, Jordan SC (1960) Anticoagulant drugs in the treatment of pulmonary embolism: a controlled trial. Lancet 1:1309–1312

Bedont RA, Datz FL (1985) Lung scan perfusion defects limited to matching pleural effusions: low probability of pulmonary embolism. Am J Roentgenol 145:1155–1157

Beigelman C, Chartrand-Lefebvre C, Howarth N, Grenier P (1998) Pitfalls in diagnosis of pulmonary embolism with helical CT angiography. Am J Roentgenol 171:579–585

Biello DR, Mattar AG, McKnight RC, Siegel BA (1979) Ventilation-perfusion studies in suspected pulmonary embolism. Am J Roentgenol 133:1033–1037

Blachere H, Latrabe V, Montaudon M et al (2000) Pulmonary embolism revealed on helical CT angiography: comparison with ventilation-perfusion radionuclide lung scanning. AJR Am J Roentgenol 174:1041–1047

Breatnach E, Stanley RJ (1984) CT diagnosis of segmental pulmonary artery embolus. J Comput Assist Tomogr 8:762–764

Carson JL, Kelley MA, Duff A, Weg JG, Fulkerson WJ, Palevsky HI, Schwartz JS, Thompson BT, Popovich J Jr, Hobbins TE et al (1992) The clinical course of pulmonary embolism (see comments). N Engl J Med 326:1240–1245

Chintapalli K, Thorsen MK, Olson DL, Goodman LR, Gurney J (1988) Computed tomography of pulmonary thromboembolism and infarction. J Comput Assist Tomogr 12:553–559

Cohen AT, Edmondson RA, Phillips MJ, Ward VP, Kakkar VV (1996) The changing pattern of venous thromboembolic disease. Haemostasis 26:65–71

Dalen JE, Alpert JS (1975) Natural history of pulmonary embolism. Prog Cardiovasc Dis 17:257–270

Dalen JE, Brooks HL, Johnson LW, Meister SG, Szucs MM Jr, Dexter L (1971) Pulmonary angiography in acute pulmonary embolism: indications, techniques, and results in 367 patients. Am Heart J 81:175–185

Denton ER, Barrington SF, Kettle AG, Morrison ID, O'Doherty MJ (1998) The value of the chest radiograph in reporting aerosol ventilation-perfusion scans. Nucl Med Commun 19:71–76

Dismuke SE, Wagner EH (1986) Pulmonary embolism as a cause of death. The changing mortality in hospitalized patients. J Am Med Assoc 255:2039–2042

Douketis JD, Kearon CK, Bates S, Duku EK, Ginsberg JS (1998) Risk of fatal embolism in patients with treated venous thromboembolism. J Am Med Assoc 279:458–462

Eddy DM (1990a) Clinical decision making: from theory to practice. Anatomy of a decision. J Am Med Assoc 263: 441–443

Eddy DM (1990b) Clinical decision making: from theory to practice. Practice policies – what are they? (See comments.) J Am Med Assoc 263:877–878, 880

Elgazzar AH (1997) Scintigraphic diagnosis of pulmonary embolism: unraveling the confusion seven years after PIOPED. Nucl Med Annu 1997:69–101

Garg K, Welsh CH, Feyerabend AJ, Subber SW, Russ PD, Johnston RJ, Durham JD, Lynch DA (1998) Pulmonary embolism: diagnosis with spiral CT and ventilation-perfusion scanning: correlation with pulmonary angiographic results or clinical outcome. Radiology 208:201–208

Geraghty JJ, Stanford W, Landas SK, Galvin JR (1992) Ultrafast computed tomography in experimental pulmonary embolism. Invest Radiol 27:60–63

Ginsberg JS, Wells PS, Kearon C, Anderson D, Crowther M, Weitz JI, Bormanis J, Brill-Edwards P, Turpie AG, MacKinnon B, Gent M, Hirsh J (1998) Sensitivity and specificity of a rapid whole-blood assay for D-dimer in the diagnosis of pulmonary embolism. Ann Intern Med 129:1006–1011

Goldberg SN, Richardson DD, Palmer EL, Scott JA (1996) Pleural effusion and ventilation/perfusion scan interpretation for acute pulmonary embolus. J Nucl Med 37:1310–1313

Goldhaber SZ (1998) Pulmonary embolism. N Engl J Med 339:93–104

Goldhaber SZ, Hennekens CH, Evans DA, Newton EC, Godleski JJ (1982) Factors associated with correct antemortem diagnosis of major pulmonary embolism. Am J Med 73:822–826

Goodman LR, Lipchik RJ, Kuzo RS (1997) Acute pulmonary embolism: the role of computed tomographic imaging. J Thorac Imaging 12:83–102

Hull RD, Raskob GE, Coates G, Panju AA (1990) Clinical validity of a normal perfusion lung scan in patients with suspected pulmonary embolism. Chest 97:23–26

Jacobson AF, Patel N, Lewis DH (1997) Clinical outcome of patients with intermediate probability lung scans during six-month follow-up. J Nucl Med 38:1593–1596

Jaeschke R, Guyatt G, Sackett DL (1994a) Users' guides to the medical literature. III. How to use an article about a diagnostic test. A. Are the results of the study valid? Evidence-Based Medicine Working Group. J Am Med Assoc 271:389–391

Jaeschke R, Guyatt GH, Sackett DL (1994b) Users' guides to the medical literature. III. How to use an article about a diagnostic test. B. What are the results and will they help me in caring for my patients? The Evidence-Based Medicine Working Group. J Am Med Assoc 271:703–707

Kahn D, Bushnell DL, Dean R, Perlman SB (1989) Clinical outcome of patients with a "low probability" of pulmonary embolism on ventilation-perfusion lung scan. Arch Intern Med 149:377–379

Kearon C, Ginsberg JS, Hirsh J (1998a) The role of venous ultrasonography in the diagnosis of suspected deep venous thrombosis and pulmonary embolism. Ann Intern Med 129:1044–1049

Kearon C, Julian JA, Newman TE, Ginsberg JS (1998b) Noninvasive diagnosis of deep venous thrombosis. Ann Intern Med 129:425

Kelley MA, Carson JL, Palevsky HI, Schwartz JS (1991) Diagnosing pulmonary embolism: new facts and strategies (see comments). Ann Intern Med 114:300–306

Kuzo RS, Goodman LR (1997) CT evaluation of pulmonary embolism: technique and interpretation. Am J Roentgenol 169:959–965

Kwok CG, Skibo LK, Segall GM (1996) Low probability lung scan in a patient at high risk for pulmonary embolism (clinical conference). J Nucl Med 37:165–170

Lee ME, Biello DR, Kumar B, Siegel BA (1985) "Low-probability" ventilation-perfusion scintigrams: clinical outcomes in 99 patients. Radiology 156:497–500

Mayo JR, Remy-Jardin M, Muller NL, Remy J, Worsley DF, Hossein-Foucher C, Kwong JS, Brown MJ (1997) Pulmonary embolism: prospective comparison of spiral CT with ventilation-perfusion scintigraphy. Radiology 205:447–452

McNeil BJ (1976) A diagnostic strategy using ventilation-perfusion studies in patients suspect for pulmonary embolism. J Nucl Med 17:613–619

McNeil BJ, Adelstein SJ (1975) Measures of clinical efficacy. The value of case finding in hypertensive renovascular disease. N Engl J Med 293:221–226

McNeil BJ, Keller E, Adelstein SJ (1975) Primer on certain elements of medical decision making. N Engl J Med 293:211–215

Meaney JF, Weg JG, Chenevert TL, Stafford-Johnson D, Hamilton BH, Prince MR (1997) Diagnosis of pulmonary embolism with magnetic resonance angiography (see comments). N Engl J Med 336:1422–1427

Michiels JJ, Schroyens W, De Backer W et al (2003) Non-invasive exclusion and diagnosis of pulmonary embolism by sequential use of the rapid ELISA D-dimer assay, clinical score and spiral CT. Int Angiol 22:1–14

Morpurgo M, Schmid C (1995) The spectrum of pulmonary embolism. Clinicopathologic correlations. Chest 107:18S–20S

Novelline RA, Baltarowich OH, Athanasoulis CA, Waltman AC, Greenfield AJ, McKusick KA (1978) The clinical course of patients with suspected pulmonary embolism and a negative pulmonary arteriogram. Radiology 126:561–567

Oxman AD, Sackett DL, Guyatt GH (1993) Users' guides to the medical literature. I. How to get started. The Evidence-Based Medicine Working Group. J Am Med Assoc 270:2093–2095

Perrier A, Desmarais S, Miron MJ, Moerloose P de, Lepage R, Slosman D, Didier D, Unger PF, Patenaude JV, Bounameaux H (1999) Non-invasive diagnosis of venous thromboembolism in outpatients. Lancet 353:190–195

PIOPED Investigators (1990) Value of the ventilation/perfusion scan in acute pulmonary embolism. Results of the prospective investigation of pulmonary embolism diagnosis (PIOPED) (see comments). J Am Med Assoc 263:2753–2759

Remy-Jardin M, Remy J, Wattinne L, Giraud F (1992) Central pulmonary thromboembolism: diagnosis with spiral volumetric CT with the single-breath-hold technique: comparison with pulmonary angiography. Radiology 185:381–387

Robin ED (1977) Overdiagnosis and overtreatment of pulmonary embolism: the emperor may have no clothes. Ann Intern Med 87:775–781

Royal HD (1994) Technology assessment: scientific challenges. Am J Roentgenol 163:503–507

Rubinstein I, Murray D, Hoffstein V (1988) Fatal pulmonary emboli in hospitalized patients. An autopsy study. Arch Intern Med 148:1425–1426

Safriel Y, Zinn H (2002) CT pulmonary angiography in the detection of pulmonary emboli: a meta-analysis of sensitivities and specificities. Clin Imaging 26:101–105

Schoepf UJ, Costello P (2004) CT angiography for diagnosis of pulmonary embolism: state of the art. Radiology 230:329–337

Smith R, Maher JM, Miller RI, Alderson PO (1987) Clinical outcomes of patients with suspected pulmonary embolism and low-probability aerosol-perfusion scintigrams. Radiology 164:731–733

Stein PD (1971) Wedge arteriography for the identification of pulmonary emboli in small vessels. Am Heart J 82:618–623

Stein PD, Terrin ML, Hales CA, Palevsky HI, Saltzman HA, Thompson BT, Weg JG (1991) Clinical, laboratory, roentgenographic, and electrocardiographic findings in patients with acute pulmonary embolism and no pre-existing cardiac or pulmonary disease (see comments). Chest 100:598–603

Stein PD, Athanasoulis C, Alavi A, Greenspan RH, Hales CA, Saltzman HA, Vreim CE, Terrin ML, Weg JG (1992) Complications and validity of pulmonary angiography in acute pulmonary embolism. Circulation 85:462–468

Stein PD, Henry JW, Relyea B (1995) Untreated patients with pulmonary embolism. Outcome, clinical, and laboratory assessment (see comments). Chest 107:931–935

Van Rossum AB, van Erkel AR et al (1998) Accuracy of helical CT for acute pulmonary embolism: ROC analysis of observer performance related to clinical experience. Eur Radiol 8:1160–1164

Wells PS, Ginsberg JS, Anderson DR, Kearon C, Gent M, Turpie AG, Bormanis J, Weitz J, Chamberlain M, Bowie D, Barnes D, Hirsh J (1998) Use of a clinical model for safe management of patients with suspected pulmonary embolism. Ann Intern Med 129:997–1005

Wiener SN, Edelstein J, Charms BL (1966) Observations on pulmonary embolism and the pulmonary angiogram. Am J Roentgenol Radium Ther Nucl Med 98:859–873

Worsley DF, Alavi A, Aronchick JM, Chen JT, Greenspan RH, Ravin CE (1993) Chest radiographic findings in patients with acute pulmonary embolism: observations from the PIOPED Study. Radiology 189:133–136

5 Renal Imaging

François Jamar and Raffaella Barone

CONTENTS

The use of radioisotopes in studies of the urinary system is dedicated to three major goals: quantification of renal function, dynamic imaging (i.e. renography) and parenchymal scintigraphy. This chapter deals with the current status and recent achievements in these fields with particular emphasis on pharmacological interventions.

5.1 Renal Tracers

Two types of radioactive tracers are used for renal studies: tracers cleared from plasma by glomerular filtration and those cleared by tubular secretion. The first class comprises ^{99m}Tc-DTPA, ^{125}I-iothalamate and ^{51}Cr-DTPA. Glomerular filtration is a passive mechanism through which plasma is cleared from water and solutes. The glomerular filtration (GFR) rate represents 20% of renal plasma flow and is ideally reflected by the clearance of (non-radioactive) inulin. Renal clearance of the listed radioactive tracers approaches the clearance of inulin indicating almost complete glomerular filtration without significant tubular reabsorption and extrarenal clearance. ^{99m}Tc-DTPA is commonly used for both imaging studies and clearance measurements while ^{125}I-iothalamate and ^{51}Cr-EDTA do not produce adequate photons for imaging and are therefore less widely used. Furthermore, although it is recognised as the tracer of choice for GFR measurements because its clearance is virtually identical to that of inulin, ^{51}Cr-EDTA is not available in the US (Blaufox 1991). ^{99m}Tc-DTPA is minimally bound to plasma proteins resulting in a small error (<5%) in the measurement of the GFR (Russell et al. 1986). ^{99m}Tc-DTPA is widely used because it not only allows the measurement of absolute renal function but also imaging in a variety of renal disorders. Furthermore, it is inexpensive, fairly stable and has a low radiation dose.

Tubular tracers include those cleared in urine after tubular uptake and ^{99m}Tc-DMSA, which is retained in the renal cortex and minimally excreted in urine, hence providing an ideal way to perform parenchymal scanning (Fig. 5.1). Up to 40% of the injected dose is retained in tubular cells (proximal tubule and loop of Henle), which enables imaging of the cortex with fine resolution (Moretti et al. 1984). ^{99m}Tc-DMSA uptake also reflects effective renal plasma flow (ERPF) and can be used as a marker of tubular dysfunction in rare disorders such as congenital tubular acidosis and in more common applications such as chemotherapy-induced renal toxicity (Anninga et al. 1994).

The other tubular agents are excreted in urine. Their prototype is radioiodinated orthoiodohippurate (^{123}I- or ^{131}I-hippuran, OIH), which is cleared from plasma by tubular secretion (Nordyke et al. 1960). Its clearance is 81%–96% of the clearance of the reference agent para-aminohippuric acid (PAH) and makes it suitable for the estimation of ERPF. Labelled with either ^{123}I or ^{131}I, OIH can be used for renographic studies. However, ^{131}I is far from optimal with regard to physical properties and hence to image quality and radiation burden. ^{123}I has there-

F. Jamar, MD, PhD
Centre of Nuclear Medicine, University of Louvain Medical School, UCL 54.30, Avenue Hippocrate, 54, 1200 Brussels, Belgium
R. Barone, MD
Centre of Nuclear Medicine, University of Louvain Medical School, UCL 54.30, Avenue Hippocrate, 54, 1200 Brussels, Belgium

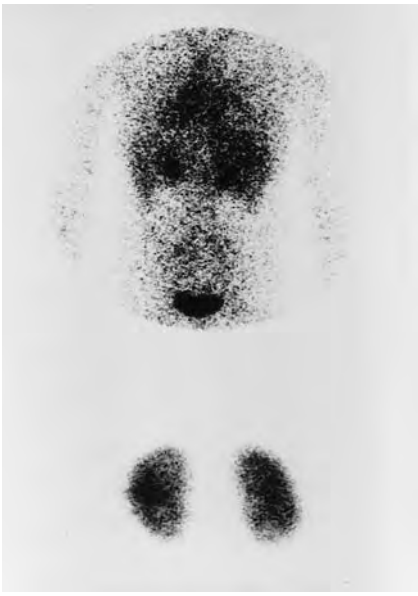

Fig. 5.1. ^{99m}Tc-DMSA scan in a patient with acute pyelonephritis showing globally homogeneous cortical uptake with little background activity and a small defect in the lower pole of the right kidney (*bottom*). The *top image* was obtained in a patient with congenital tubular acidosis and shows almost no cortical retention of the tracer

fore been introduced: it provides nice renograms but is not readily available and more expensive. Due to these limitations efforts were directed from the early 1980s towards designing a ^{99m}Tc-labelled tracer that would have a higher extraction fraction than ^{99m}Tc-DTPA and would overcome the practical drawbacks of OIH as listed above. This search has mainly focused on two families of donor ligand systems: the diamine dithiolate (N_2S_2) and triamide mercaptide (N_3S) (Eshima et al. 1990). The availability of one of the latter, ^{99m}Tc-mercaptoacetyltriglycine (MAG_3), in a kit formulation, is one of the major achievements of the last decade in renal nuclear medicine. It provides high quality imaging with an extraction efficiency two- to threefold that of ^{99m}Tc-DTPA and has become the most widely used agent for renography. The dosimetry is more favourable than with hippuran and the tracer is readily available (Taylor et al. 1987). Its extraction by the tubular cells is only 50%–60% that of PAH because of a high protein binding (Müller-Suur et al. 1990; Jafri et al. 1988). Owing to that, it is almost a perfect tubular agent since there is hardly any glomerular filtration (Müller-Suur and Müller-Suur 1989). Some limitations include the need to boil for labelling, the presence of several potential species depending on the kit formulation and some liver activity and hepatobiliary clearance, especially with low renal function (Shattuck et al. 1994).

Further developments were made by Verbruggen et al. (1992) who synthesised L,L-ethylenedicysteine (^{99m}Tc-L,L-EC) and labelled it with ^{99m}Tc. This compound is the more polar metabolite of the brain agent ^{99m}Tc-L,L-ethylenedicysteine diethylester (^{99m}Tc-ECD). In alkaline conditions, it has the advantage over MAG_3 to be labelled efficiently and with high stability at room temperature. Several validation studies were undertaken in animals and humans and the physiological properties of ^{99m}Tc-L,L-EC are now well characterised (Table 5.1) (van Nerom et al. 1993; Stoffel et al. 1994). Major differences with MAG_3 are the higher extraction fraction, lower protein binding and lack of hepatobiliary clearance. Clearance of L,L-EC totals 70% of the clearance of OIH as compared to 51% for MAG_3 (Stoffel et al. 1994). Initial clinical studies indicated that L,L-EC is a valid alternative to MAG_3 for the coming years (Kabasakal et al. 1995; Gupta et al. 1995). Taylor et al. (1997) showed that the clearance of the stereoisomer ^{99m}Tc-D,D-EC might be even closer to that of OIH.

5.2 Measurement of Absolute Renal Function

Two major parameters of renal function are currently used as clinical indicators: renal blood flow

Table 5.1. Pharmacokinetic properties of OIH, ^{99m}Tc-MAG_3 and ^{99m}Tc-L,L-EC

	OIH	^{99m}Tc-MAG_3	^{99m}Tc-L,L-EC
Molecular weight (Da)	303	374	379
Extraction efficiency (%)	66-87	50	53
Glomerular filtered fraction (%)	<20	<5	17
Protein binding (%)	53-70	79-90	24
RBC binding (%)	15–29	5	<5
Distribution volume (ml/kg)	190	125	192
Clearance (% of OIH)	100	49-67	70

RBC, red blood cells

(RBF) and glomerular filtration. Glomerular filtration is related to RBF and the integrity of the glomeruli (expressed as the filtration fraction) and in routine applications, the GFR is reflected by serum creatinine. However, the relationship between endogenous creatinine clearance and GFR is affected by several factors, including low renal function. Indeed when the renal function decreases, there seems to be a compensatory increase in tubular reabsorption of creatinine. It is thus inaccurate and relatively insensitive to detect subtle to moderate changes of renal function (Walser et al. 1988; Levey et al. 1988). The reference method for measuring GFR is the clearance of continuously infused – steady state – inulin, which is exclusively excreted by glomerular filtration without reabsorption at the tubular level. However, the technique is time-consuming, cumbersome and expensive and therefore, no longer in use. Many methods using radioactive tracers such as ^{99m}Tc-DTPA or ^{51}Cr-EDTA have been proposed. The continuous infusion method is probably the most accurate but again is time-consuming and only used for research purposes (Donker et al. 1977). For all agents the most popular way for measuring GFR is the single-injection method followed by a small number of blood samples, typically two to four usually obtained between 2 and 4 h after injection (Chantler et al. 1969; Bröchner-Mortensen and Rödbro 1976). In this system, the plasma clearance is assumed to be mono-exponential from 90–120 min onwards following injection although compartmental analysis describes plasma clearance as bi-exponential (Sapirstein et al. 1955) (Fig. 5.2). This simplification makes it possible to abandon the Sapirstein equation, which necessitates multiple blood samples. As a result of this simplified equation, there is systematic overestimation by neglecting the first exponential which is corrected for empirically. GFR can be estimated according to the general formula:

$$GFR = k \times V_d \times \alpha$$

where V_d is the volume of distribution, calculated from the injected dose and intercept of plasma activity at t_0, α the slope of the exponential function and k a correction factor varying according to the method used.

More simplified methods, using only one sample were proposed especially for paediatric purposes, even using capillary blood (Fjeldborg and Bröchner-Mortensen 1986). For example, Ham and Piepsz (1991) using a single sample at 120 min, and applying a method based on the distribution volume were able to derive a formula to calculate ^{51}Cr-EDTA clearance in children regardless of age and to determine reference values (Piepsz et al. 1994). A multitude of other methods for calculating the ^{99m}Tc-DTPA clearance were introduced over the last two decades. Following the approach by Gates (1982), some of these techniques are based on gamma camera imaging and may necessitate the calibration of the camera response by external standards, heart activity or one blood sampling. Critical analysis of all these methods is not the purpose of this chapter. Just as an example, Fawdry et al. (1985), comparing five simplified methods including three with camera uptake measurements, found that a patient with a GFR of 80 ml/min as measured by the single-injection multiple-sample technique, would have a predicted GFR at the 95% confidence interval in the range of 30–136 ml/min. In this study the most accurate method gave a predicted GFR of 67–81 ml/min. In general the simplified methods have proven relatively inaccurate especially for GFR below 30 ml/min (Li et al. 1997). Gamma camera based methods, however, offer the advantage to be a complement to renographic studies and to allow the determination of relative – split – renal function. In view of the difficulty to analyse the relative merits and drawbacks of the multiple methods published, a consensus report was published by the Radionuclides in Nephrourology Committee on Renal Clearance (Blaufox et al. 1996a). They recommend the Groth 4-h methodology (single-sample) for patients with GFR >30 ml/min and urinary clearances for GFR <30 ml/min; two-sample methods should be used for investigational purposes. Finally, an elegant technique was devised by Rabito et al. (1993) for continuous monitoring of renal function. Using a Cd-Te detector they made up a battery-operated arm probe (Ambulatory Renal Monitor, "ARM") that could be used to identify real-time changes in renal function. The use of this relatively simple equipment may lead to an improved management of patients in whom critical changes of the renal function require a rapid measurement, such as patients in intensive care unit or following major surgery.

Although indirect measurements have been performed (Peters et al. 1990), direct measurement of RBF requires complicated methods such as the indicator-dilution or inert gas washout techniques (Schillig 1964; Ladegofed 1966). Smith et al. (1938) introduced the concept of effective renal plasma flow (ERPF) which only describes the fraction of the plasma flow that goes to the nephrons (i.e.

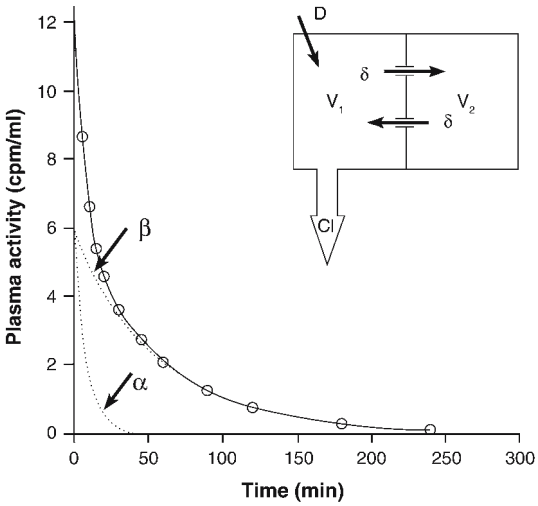

Fig. 5.2. Schematic representation of the open bi-compartmental model of Sapirstein. V_1 and V_2 represent the plasma and interstitial fluid volumes, respectively; *D* and *Cl* stand for dose and renal clearance. The continuous line shows the bi-exponential curve fitted to the original data (*open circles*). The *dotted lines* are the two components of this bi-exponential curve. In the simplified mono-exponential model, only curve β is considered with samples between 2 and 4 h

for urine formation) since about 10% of the RBF is used for the renal capsule, perirenal fat and interstitial tissue. ERPF can be measured by the clearance method and the reference method uses PAH, the extraction coefficient of which is close to 100% (Smith et al. 1945). As for GFR, many methods have been devised to substitute PAH clearance. Most used radioiodinated OIH and again two-sample or single-sample simplified techniques were proposed. One of the most popular was devised by Tauxe et al. (1982) and is based on a single sample obtained at 44 min: this method was recommended in the consensus report of the Radionuclides in Nephrourology Committee on Renal Clearance (Blaufox et al. 1996a). Methods based on fractional uptake can also be used to estimate the relative renal function (Chachati et al. 1987). Since the early 1990s, substitution of ^{99m}Tc-MAG_3 to OIH has called for methods and algorithms for estimating ERPF using MAG_3 clearance (Russell et al. 1988, 1996; Müller-Suur et al. 1991). Simplified methods, based either on plasma samples or on gamma camera images did not appear entirely satisfactory in part due to the variable extraction fraction of the tracer. Nonetheless, some were implemented in clinical settings, especially in paediatrics, using the gamma camera (Gordon et al. 1991) or single-sample approach (Piepsz et al. 1993). The latter method, applied in a multicentric study, made it possible to determine reference values in *children with minimal renal disease* (Meyer et al. 1998). A completely different concept was applied by Bubeck (1993). This principle is based on a theoretical volume of distribution determined by normalising the plasma concentration in one sample with respect to individual body dimensions. Importantly, this principle can be applied to both adults and children and does not require imaging. Rather than ERPF, this methodology measures a "tubular extraction rate" (TER) and does not take into account the variability between OIH and MAG_3 clearances. A significant concern that has been raised for MAG_3 clearance is the relatively high day-to-day variation in measurements (Piepsz et al. 1996). Finally, simplified methods were proposed to derive ERPF from plasma clearance of ^{99m}Tc-L,L-EC (Stoffel et al. 1996).

5.3 Renography and Pharmacological Intervention

5.3.1 Standard Renography

The dynamic study of renal function using the gamma camera makes it possible to evaluate three distinct phases: perfusion, concentration and excretion. This can be achieved with Glomerular (^{99m}Tc-DTPA) or tubular (OIH and ^{99m}Tc-MAG_3) tracers. There are relatively few indications in nephrology and baseline scans have been progressively replaced by renographic studies augmented by pharmacological interventions, especially furosemide-induced diuresis in the study of dilated excretion systems, angiotensin-converting enzyme inhibitors (ACEI) for the diagnosis of renovascular hypertension and stress renography in assessing essential hypertension (Clorius and Schmidlin 1983).

There are two exceptions to this move. First, standard renography remains a very useful tool in acute renal failure (Blaufox 1991). Ultrasonography remains indisputable but beyond that, radiological studies with contrast media are not advisable since they can precipitate azotaemia in these patients, particularly in diabetic patients. It was shown years ago that non-visualisation of one or both kidneys had a negative prognostic value, provided acute obstruction could be ruled out (Sherman and Blaufox 1980). Other indications in acute renal diseases include acute tubular necrosis, renal emboli or renal vein thrombosis.

The other widely accepted exception is the evaluation of renal transplants. Renal transplantation has now more than 30 years experience and has become the treatment of choice of end-stage renal failure (Eggers 1988). The high success of the technique is not only due to improvements in the surgical management but also to a better selection of donors (including HLA-matched living-related donors and living non-related donors). Immunosuppressive therapy is the major contributor to the long-term success of transplantation (Carpenter 1990). Nevertheless, acute and chronic complications of renal grafts still frequently occur and nuclear medicine procedures are frequently considered because they are non-invasive and do not bear the risk of jeopardising the function as would be the case with contrast media. The most common indications for renograms are acute tubular necrosis (ATN), acute rejection, arterial thrombosis and chronic rejection. Differential diagnosis of transplant dysfunction now includes drug-induced nephrotoxicity (e.g. cyclosporine) (Myers et al. 1984; Andoh et al. 1996). Transplant infarcts can be studied with ^{99m}Tc-DMSA. For renographic studies, ^{99m}Tc-MAG_3 is the agent of choice, although the typical back-diffusion pattern observed in ATN with ^{99m}Tc-DTPA is a major advantage for this tracer. Interpretation of the renograms is usually made on visual criteria and renographic curves following the three classical phases described by Taplin (1971) (Fig. 5.3). Semiquantitative indices have been derived such as the perfusion index proposed by Hilson et al. (1978). Interested readers should refer to an interesting review on the topic describing the interpretation criteria in some details (Dubovsky et al. 1999). To summarise, MAG_3 (or OIH) renograms are particularly useful in kidney transplants to identify: (a) absence of perfusion in acute rejection and arterial thrombosis (Fig. 5.4), (b) good function and parenchymal retention in ATN (Fig. 5.5) and (c) progressive degradation of uptake parameters in chronic rejection (Fig. 5.6). It must finally be stressed that there is no definition of the normal renal transplant's function: in evaluating chronic rejection, the patient is his/her own control and changes are more important than any parameter taken individually (Hilson 1991).

5.3.2 ACE Inhibition and Renovascular Hypertension

Renovascular hypertension (RVH) due to renal artery stenosis (RAS) accounts for approximately 1% of all cases of hypertension. However, since it

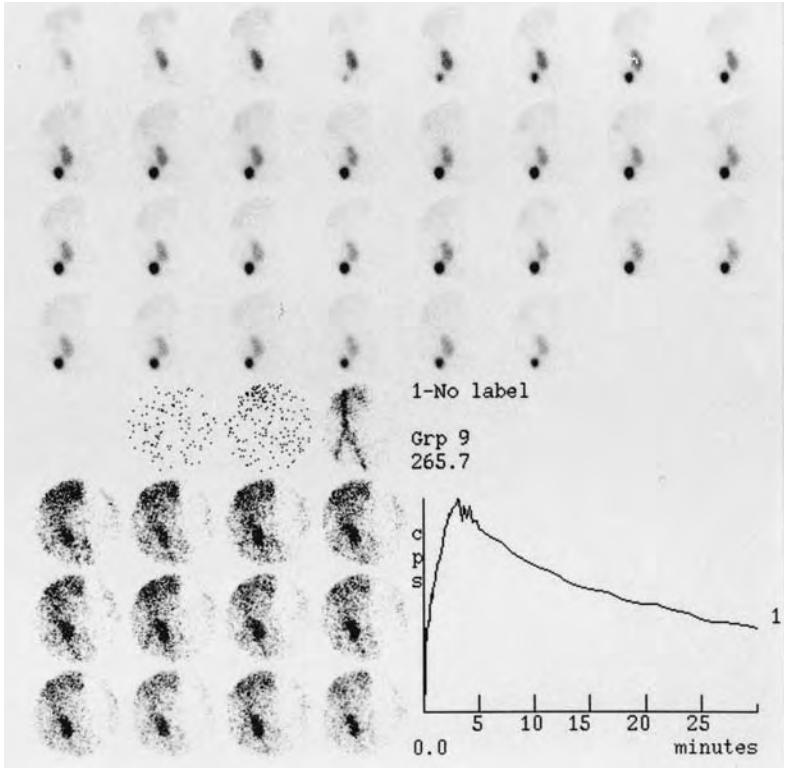

Fig. 5.3. Normal transplant study with ^{99m}Tc-MAG_3. The first-pass study (*left lower panel*) shows excellent perfusion and the renographic study (*upper panel*) good tracer uptake with short parenchymal transit time (3-4 min). The transplant curve is normal (*right lower panel*)

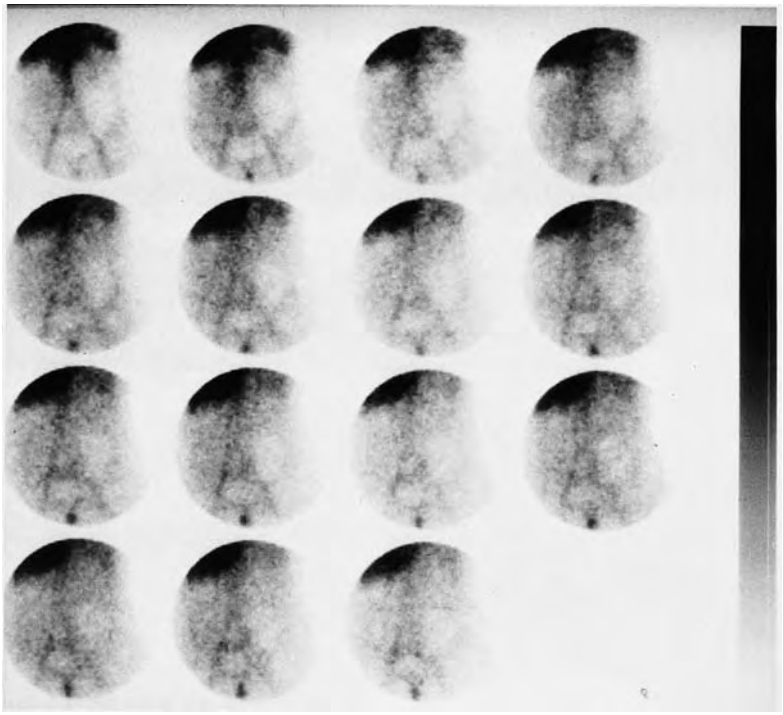

Fig. 5.4. Vascular phase study with ^{99m}Tc-MAG$_3$ showing no perfusion at all in the left-sided transplant, indicating acute arterial thrombosis. The transplant appears as a "background defect"

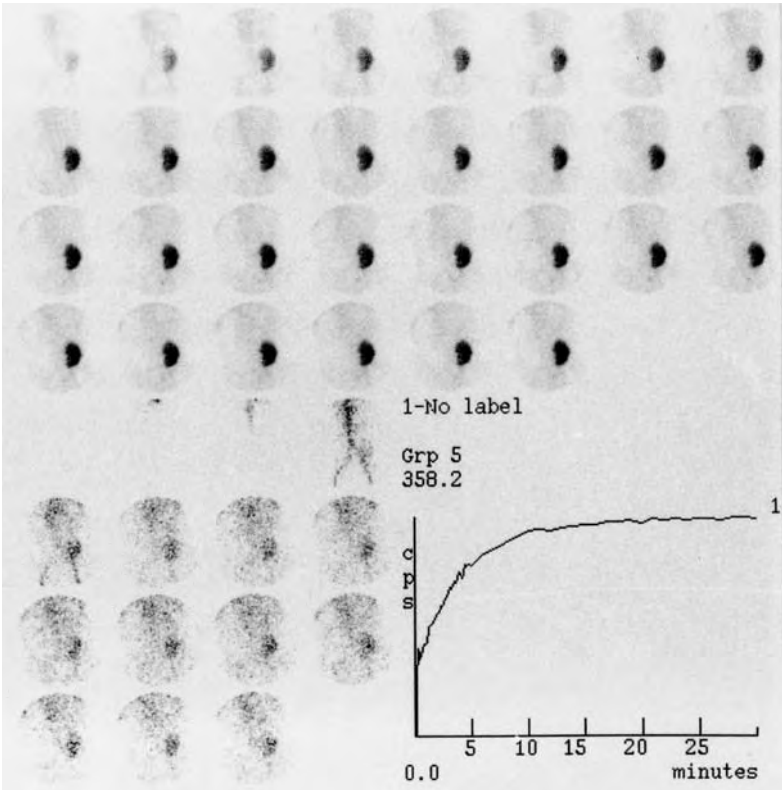

Fig. 5.5. Typical study with ^{99m}Tc-MAG$_3$ in acute tubular necrosis showing good perfusion (*left lower panel*), good tubular uptake and parenchymal retention (*upper panel*). The renographic curve shows good uptake and a plateau from 10 min post-injection

often offers a case for cure (angioplasty), it must be recognised early, as part of primary management of hypertensive disease. There is thus a need for a screening method that is highly sensitive but also specific enough in view of the low prevalence of the disease. Given the high prevalence of hypertension in a general population, screening must be non-invasive and inexpensive.

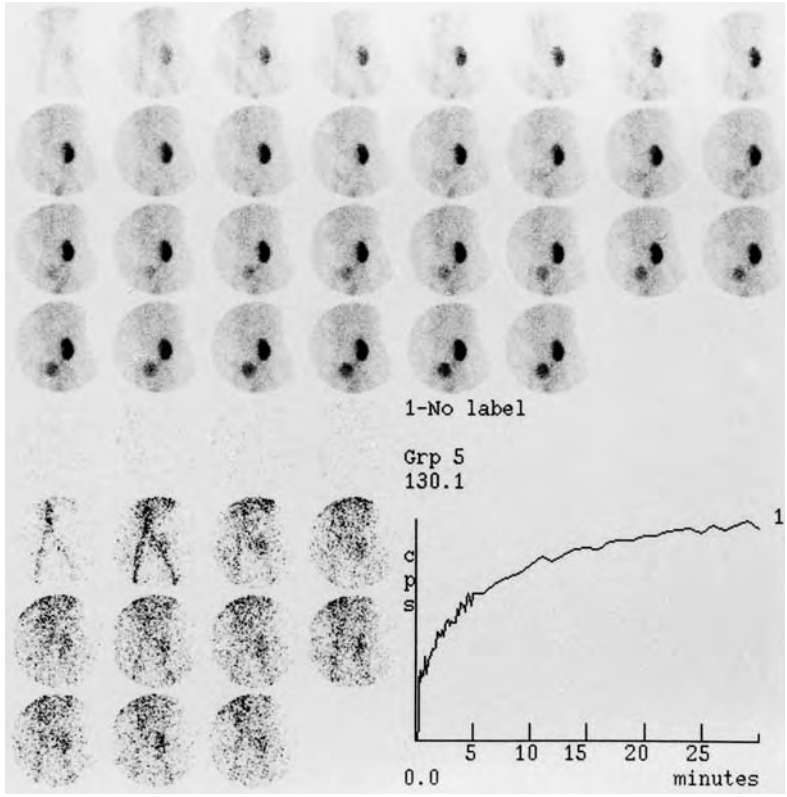

Fig. 5.6. ^{99m}Tc-MAG$_3$ study in chronic rejection showing impaired flow phase (*left lower panel*), delayed uptake and altered washout of the tracer (*upper panel*). The curve shows delayed concentration and impaired excretion

First of all, clinical clues suggesting RVH must be considered. They include abrupt onset of hypertension at any age, severe or malignant hypertension, cases that are difficult to control with medical treatment (three-drug regimen), unexplained impairment of renal function and inconstant physical signs such as an abdominal bruit, evidence of vascular occlusive disease and retinopathy (Vidt 1991); evidence for a small unilateral kidney is also suggestive. Beyond these suggestive features, most tests developed for diagnosing RVH are rather invasive (e.g. arteriography or renal vein renin sampling) or insufficiently sensitive and/or specific (e.g. peripheral renin assay and "captopril test"). RAS is demonstrated by direct arteriography or less invasively by intravenous digital subtraction angiography; these tests, however, do not provide functional information and do not establish whether hypertension in a particular individual is related to RAS: only successful revascularisation followed by cure of hypertension is the proof.

Another clinical feature of RVH, which was deliberately omitted in the above list of clues, is impairment of renal function as a consequence of angiotensin-converting enzyme inhibitors and, to a lesser extent, poor antihypertensive effect. This clinical fact, along with the serendipitous finding by Majd et al. (1983) led several groups to develop protocols for studying the effect of ACEI (essentially captopril) on nephroscintigraphy in RVH. The effects and mechanisms involved can be summarised as follows: RAS leads to a decrease in periglomerular arterial gradient: transglomerular filtration pressure, hence GFR, is maintained by vasoconstriction of the efferent arteriole, secondary to increased intrarenal angiotensin II. When angiotensin II production is blocked in the presence of captopril, this compensative mechanism is abolished: glomerular pressure falls, leading to decreased GFR and urine formation. These pathophysiological consequences can explain the findings on renography. With a filtered agent such as ^{99m}Tc-DTPA, the drop in GFR results in moderate to severe reduction of tracer uptake by the affected kidney which in extreme cases can be complete with only background activity and no appearance of tracer in the collecting system. ^{99m}Tc-MAG$_3$ and OIH typically disclose progressive accumulation of the tracer in tubular cells with relatively modest or no decrease in uptake: retention of the tracer in the renal parenchyma and prolonged renal transit time can be explained by decreased urine formation following GFR reduction.

Since the description of captopril renography, a number of different protocols were proposed and the time had come for standardisation. This was achieved by the Consensus Report on ACE Inhibitor Renography, published after the Ninth Symposium on Radionuclides in Nephrourology and later endorsed as guidelines of the Society of Nuclear Medicine (Taylor et al. 1996; Taylor 2002). The recommendations are summarised in Table 5.2.

^{99m}Tc-MAG$_3$ is preferred in cases of reduced renal function (Prigent 1993). ACEI and diuretic treatment should ideally be stopped before scanning. Both concurrent therapies are known to slightly alter the diagnostic value of the test (Visscher et al. 1995; Setaro et al. 1991; Kopecky et al. 1987). In addition, ACEI renography with chronic diuretic treatment may result in hypotension, especially in dehydrated patients (Svetkey et al. 1989; Dondi et al. 1989; Elliot et al. 1993). The recently introduced angiotensin II antagonists, such as sartans may have an effect on the renogram comparable to ACEI and should probably be discontinued (Taylor 2002). In a retrospective study, Picciotto et al. (2003) reported, however, that performing ACEI renography in patients under chronic monotherapy with sartans with the acute administration of captopril, has the same diagnostic performance than captopril renography in off-drugs patients. A last practical issue is whether scanning with and without ACEI should or could be performed on the same day. It seems that both 1-day (baseline study followed by ACEI study) and 2-day protocols are acceptable. If a 1-day protocol is chosen, care must be taken to increase the tracer dose for the second study (e.g. 1 mCi followed by 5–10 mCi). Such a protocol is appropriate for patients with a relatively high likelihood of RVH, whereas in our opinion, in patients with a relatively low likelihood of the disease, renography can be started with ACEI since a normal study will avoid the need for a baseline study.

Table 5.2. Recommended protocol for ACEI renography. [Adapted from Taylor et al. (1996) and Taylor (2002)]

- If possible discontinue ACEI (4 days) and diuretics (3 days)
- 4 h Fasting before captopril; no fasting if enalaprilat iv
- Good oral hydration (500 ml 30–60 min before test)
- Intravenous line if hypotension anticipated (high-risk patients, enalaprilat)
- ^{99m}Tc-DTPA or -MAG$_3$, or OIH are adequate
- Captopril 25 mg (or 50 mg) orally 60 min before tracer injection

or enalaprilat 40 μg/kg slow iv, 15 min before tracer injection

- Usually 30-min renogram (1- to 3-s images for flow study – optional)

A more important issue is to determine which patients do need an ACEI renogram. To be cost-effective, the test should not be used as a general screening test in a hypertensive population, but rather concentrate on moderate- to high-risk patients (Blaufox et al. 1996b). These groups are defined by clinical features as listed previously and include patients with "typical presentation" of RVH (abrupt onset, abdominal bruits, small kidney, malignant course and unexplained azotaemia) or patients with a milder course who are unresponsive to well conducted antihypertensive treatment or who display worsening of renal function when started on ACEI therapy. Diabetic patients, in whom contrast media injection should ideally be avoided are also candidates to ACEI renography.

Interpretation of the test relies on the comparison of renographic images but mainly on the comparison of curves, looking for worsening [flattening, delayed peak (increased of >2 min or 40% of baseline value), reduced uptake] of the pattern under ACEI as compared with the baseline study (Fig. 5.7a,b). Typical curves were proposed by Fommei et al. (1993). Changes in relative renal function are also important to consider. Evaluation of the flow phase (first-pass angiography) is not reliable (Schreij et al. 1996). Diagnostic criteria have been well defined and should be used to classify patients with high, intermediate and low probability of RVH (Nally et al. 1991). Pitfalls include bilateral RVH, poor global renal function, long-term ACEI therapy and dehydration (Setaro et al. 1991; Mann et al. 1991; Blaufox et al. 1998).

The sensitivity and specificity of ACEI renography have been highly variable with data ranging between 45% and 100% for sensitivity and between 62% and 100% for specificity. Large studies, however, reported performances in the 90% range (Roccatello et al. 1992; Elliot et al. 1993; Fommei et al. 1993). More pessimistic results were recently published on a large series of high-risk hypertensive patients with a sensitivity of 68% and a specificity of 90% (van Jaarsveld et al. 1997). Nevertheless, whatever the sensitivity and specificity, the prevalence of the disease should be taken into consideration. If we look critically at the diagnostic performances collected by Taylor et al. (1996) in 1720 patients, the overall sensitivity and specificity were 88.2% and 92.2%, respectively. With a prevalence of RVH among the compiled studies of 30%, this leads to a positive predictive value (PPV) of 82.8% (range in individual studies: 46%–100%) and a negative predictive value (NPV) of 94.8% (range in indi-

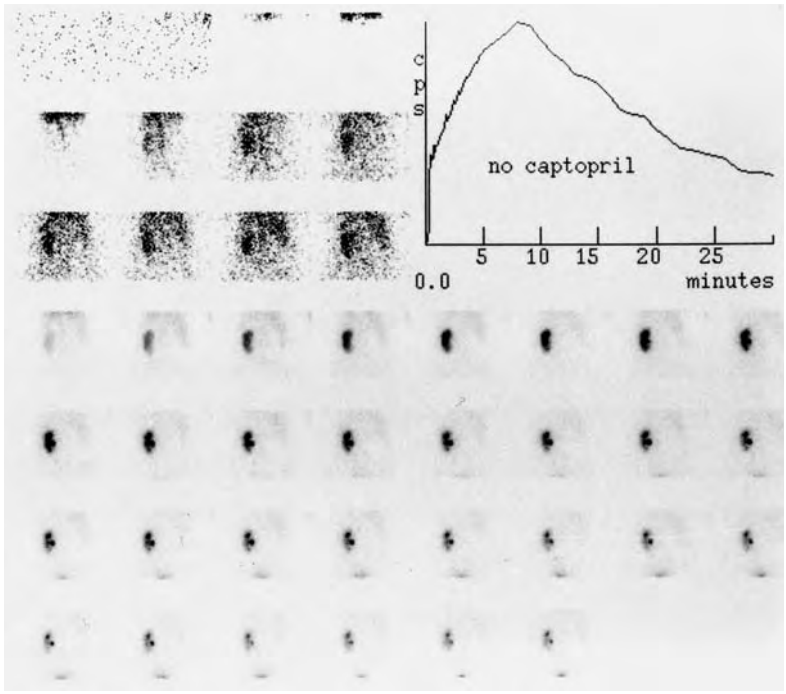

a

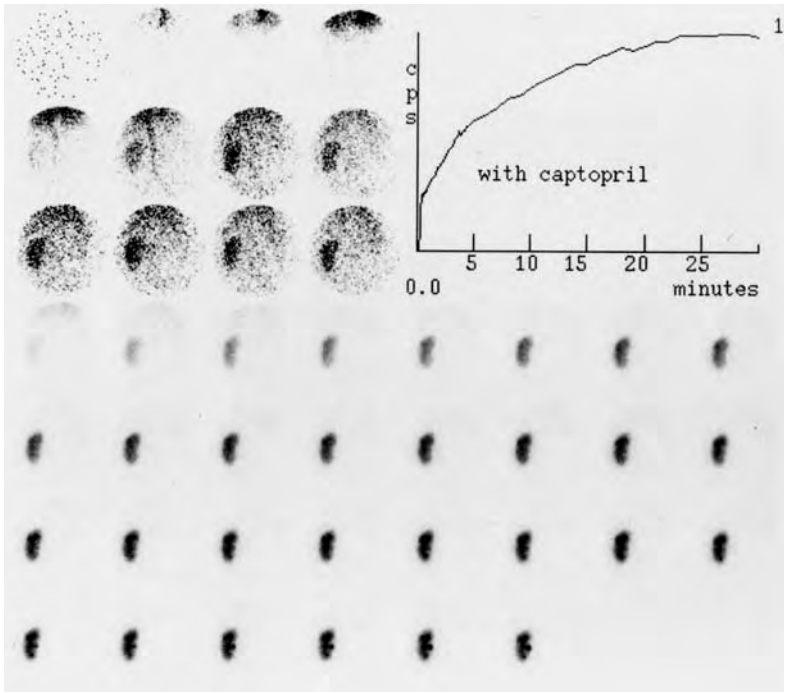

b

Fig. 5.7a,b. Evaluation of a patient with severe, abrupt-onset, hypertension and a single kidney. The baseline ^{99m}Tc-MAG$_3$ study (no captopril; **a**) shows slightly delayed parenchymal transit but is otherwise normal. The captopril study (25 mg orally; **b**) discloses severely reduced excretion with worsening of the renographic curve. Note that tracer uptake is not affected by captopril

vidual studies: 81%–99%): these results are quite acceptable. However, if we used these diagnostic performances as a rationale to apply ACEI renography in a general population (prevalence of RVH: 1%) and in a more selected hospital-referral population (prevalence of RVH: 10%), the corresponding PPVs would be as low as 10.3% and 55.7%, respectively, with highly confident NPVs of 99.9% and 98.6%, respectively. Although these figures were only generated for illustrative purposes, they indicate that, in a non-selected population, the method is likely to perform adequately as an exclusion test but would be of little value in the positive diagnosis of functionally significant RAS. This further emphasises the need for optimal selection of the patients as outlined by Blaufox et al. (1996b). It must be kept in

mind that interobserver variability is not small and may be an explanation for differences in diagnostic performances of ACEI renography, besides differences in patient selection (Krijnen et al. 2002). Beside its role in diagnosing RVH, ACEI renography has proven accurate in predicting blood pressure response to revascularisation (Dondi et al. 1992; Geyskes and de Bruyn 1991). Finally, the effect on patient management following ACEI renography has been rather poorly assessed: Ramsay et al. (1997) concluded from a retrospective study in 95 patients that changes in individual patient management were observed in only 34% of the cases. Outcome studies that more clearly define the place of ACEI renography in the armamentarium of hypertension workup, with particular insight into decision making, are therefore needed in order to optimally meet the clinicians' expectations (Huot et al. 2002).

In conclusion, ACEI renography has been used successfully over the last 15 years. The methodology is more cost-effective than arteriography (Blaufox et al. 1996b). Although most authors have provided evidence that the test was accurate in selected populations, some rather negative studies indicate the need for both optimal standardisation of the practice, including consensus on interpretation criteria and improved patient selection for clinical applications. Combination of ACEI renography with duplex Doppler sonography may be an appropriate approach before submitting patients to arteriography, as suggested by Miralles et al. (1997) and Kaplan-Pavlovic and Nadja (1998).

5.3.3 Diuretic Renography and Obstructive Uropathy

Diuresis-augmented renography was first described by Radó et al. (1967). In the subsequent years, the method was developed as a simple technique to differentiate between obstructive and non-obstructive dilated upper urinary tracts (O'Reilly et al. 1978; Britton et al. 1979). Upper urinary tract obstruction may be due to a variety of causes that can be categorised as intraluminal (e.g. calculi), intramural (e.g. stricture and idiopathic hydronephrosis) and extrinsic (e.g. retroperitoneal fibrosis); in addition, dilation may be due to lower urinary tract abnormalities such as posterior urethral valves or primary megaureter. Dilation of the renal pelvis is usually detected by ultrasonography and can be confirmed by intravenous pyelography. These techniques give very little functional information and may not be able to identify obstruction, which is characterised by an increased pressure. In acute obstruction, pelvic pressures, which normally range between 4 and 10 cm H_2O may increase up to 60 cm H_2O (Brown 1994). This in turn raises tubular pressure which is followed by a decrease in renal blood flow and reduction in GFR. There is some adaptive elasticity of the pelvis which in some cases reduces the pressure and hence the insult to the tubuli. This protective mechanism is however not the rule and at this stage intervention should be questioned. The decision depends on the balance between resistance and compliance to flow, urine output and GFR. The first two parameters can be assessed using urodynamic studies as described by Whitaker (1973), but these methods are invasive and not widely performed. This is particularly true in children and neonates: in the latter group, idiopathic hydronephrosis is recognised five times more frequently than in the past due to the development of foetal ultrasonography (Brown et al. 1987). Since the phenomenon may be transient, all neonates need not be operated provided a simple test can assess the degree of obstruction and split renal function.

Many protocols to perform diuretic renography are found in the literature and are reviewed on a regular basis (O'Reilly 2003). The standard conditions are summarised in Table 5.3. In general, the choice of the radiopharmaceutical is not of critical importance and will generally be made between ^{99m}Tc-DTPA, ^{123}I-OIH and ^{99m}Tc-MAG_3. Currently, ^{99m}Tc-MAG_3 is preferred and probably the most widely used. Due to its high extraction fraction, it gives high quality images of both the cortex and collecting system resulting in sharp curves that are easier to interpret than with ^{99m}Tc-DTPA. MAG_3 and to a lesser extent OIH are advisable in case of decreased renal function, either in adults or, more generally in neonates.

Three items deserve further comments. First, the degree of hydration should be optimal: this can be achieved by oral hydration in most patients (500 ml water or juice). In young children and when sedation is felt necessary, hydration through an iv line is more adequate. Typical flow rates are in the range of 15 ml/kg isotonic saline during the first 30 min, starting 15 min before tracer injection, followed by 200 ml/kg/24 h over the next few hours. The use of hypotonic fluids was proposed by Howman-Giles et al. (1987) as a way to increase the effect of furosemide and to overcome the importance of hydration in avoiding false positive tests: this technique is known as the *volume expansion diuretic renal scan*.

Secondly, the time of administration of furosemide varies between groups. It is usually given at the dose of 40 mg in adults 0.5 mg/kg in children and 1 mg/kg in infants (Conway 1992). Most publications indicate a time of administration between 20 (known as F+20) and 30 min following tracer injection (O'Reilly 1992). However, since this may lead to a substantial number of equivocal responses, an alternative was proposed in which furosemide is injected 15 min (F-15) before injection of the radiopharmaceutical (English et al. 1987). The rationale for that has been well outlined by Brown et al. (1992). They showed that after injection of 40 mg furosemide, the increase in urinary flow rates was perceptible after 2 min but maximal at 15 min post-injection. Thus, if maximal diuresis is required throughout the scan, injection of furosemide should take place before administration of the radiopharmaceutical. This method reduces the rate of equivocal results from 15%–17% to 3% (O'Reilly 1992; Upsdell et al. 1988). Nevertheless, the standard F+20 seems appropriate in most cases and should be complemented in selected cases by a F-15 study (O'Reilly et al. 1996). Injection of furosemide at the time of tracer injection (F0) has also shown a valid alternative to discriminate normal collecting systems from those with impairment of output efficiency (Wong et al. 1999; Donoso et al. 2003). This method is particularly adapted to children by reducing the acquisition time. It is also noteworthy that using sophisticated quantitative indexes, furosemide injection could be avoided in up to 21% of children (Kuyvenhoven et al. 2003). Third, the role of the bladder in kidney washout should be considered. In all cases, the bladder should be emptied before initiation of the study and a procedure should never be terminated (unless normal) without assessing a potential *bladder effect*. This has been well studied by Jones et al. (1990) who noted increased pelvic pressure during bladder filling resulting in a reduced drainage of the pelvicaliceal system, which can cause false positive results. In children, bladder catheterisation is advised (Conway 1992) although it is unclear whether only children with a high pre-test probability should have a continuous bladder drainage (O'Reilly et al. 1996). This is particularly true in the case of associated lower urinary tract dilation. An alternative is to perform the test without catheterisation and to perform a post-micturition scan, a procedure that may convert an obstructive to a non-obstructive pattern (Gordon et al. 1988).

Interpretation of a diuretic scan relies both on visual examination of the dynamic scan and on inspection of time-activity curves derived for each kidney using the regions of interest (ROIs) method (Fig. 5.8). Typical curves were described by O'Reilly (1992). *Type I* curve corresponds to a normal drainage before diuresis: this pattern is most unlikely to be associated with obstruction following diuresis and should be considered as a normal study. *Type II* curves represent obstruction with a continuous rise or plateau following diuresis. Although this type of curve is usually related to definite obstruction, unrecognised dehydration, massive dilation and bladder effect must be excluded. Poor renal function may also be associated with such a pattern and it is well accepted that a single-kidney GFR below 16 ml/min would induce an inadequate diuretic response. In such cases, the test should be considered inconclusive (O'Reilly et al. 1996). *Type IIIa* response is characterised by a sharp response to diuretic injection. In this case, dilation represents stasis and not obstruction (Fig. 5.9). *Type IIIb* is called the equivocal response: in this case, there is some response to furosemide although it is not as marked as in type IIIa. In cases with low renal function, it is unlikely that F-15 will improve the accuracy of the test. When the renal function is good and hydration has been well controlled, F-15 is useful to confirm the presence of subtotal obstruction. Some authors have proposed evaluating the washout phase using quantitative indices such as $T_{1/2}$ (Kass and Fink-Bennett 1990; Conway 1992). There is some consensus that a $T_{1/2}$ >20 min represents obstruction and that with a $T_{1/2}$ <15 min there is no obstruction. Between 15 and 20 min, the test is considered inconclusive. Alternatively, Kletter and Nurnberger (1989) have proposed the E_{max} or maximal elimination rate. Neither this approach nor the half-time method have proven entirely satisfactory in terms of reproducibility, operator-independence and definition of normal and

Table 5.3. Recommended protocol for diuresis renography

- Good hydration (usually oral; in some cases iv fluids)
- Complete bladder emptying before starting (indwelling catheter in children)
- ^{99m}Tc-MAG_3 (or OIH) preferred (^{99m}Tc-DTPA adequate if good renal function)
- Patient usually in supine position (erect position may be useful in selected cases)
- Furosemide (40 mg in adults; 0.5–1.0 mg/kg in children) iv injection 20 min after tracer (F+20) in selected cases furosemide injected 15 min before tracer (F-15) or at the time of tracer injection (F0)
- Bladder voiding after standard scan (per- or post-micturition views)
- Abundant fluids after procedure are advised

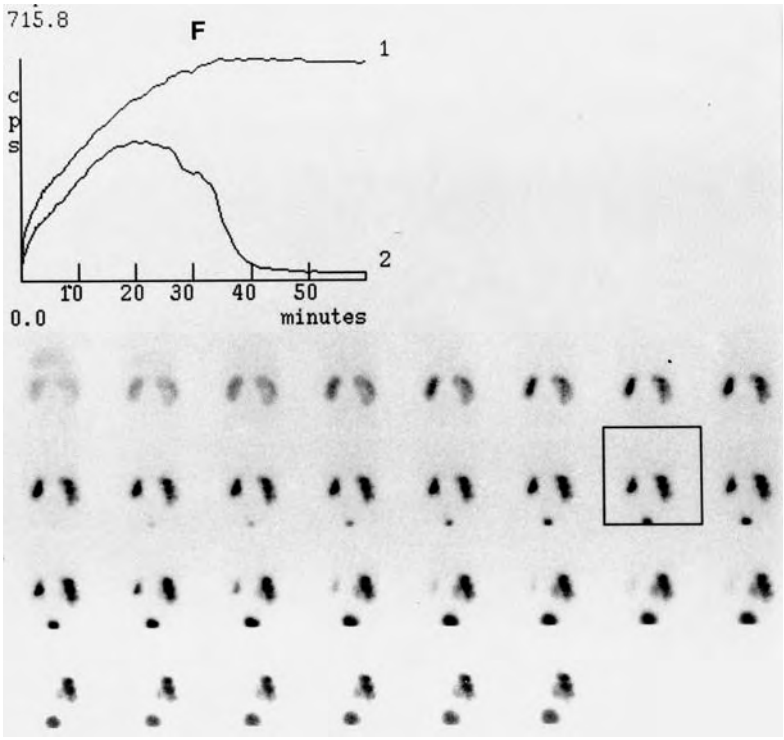

Fig. 5.8. Diuretic renogram with ^{99m}Tc-MAG_3 in an infant with suspected right pelviureteric junction obstruction. There is progressive accumulation in the collecting system which is unaffected by furosemide (*F*) injection (*box*). The type II curve (*1*) confirms obstruction. The left kidney curve (*2*) shows discrete stasis with good response to furosemide and is considered normal

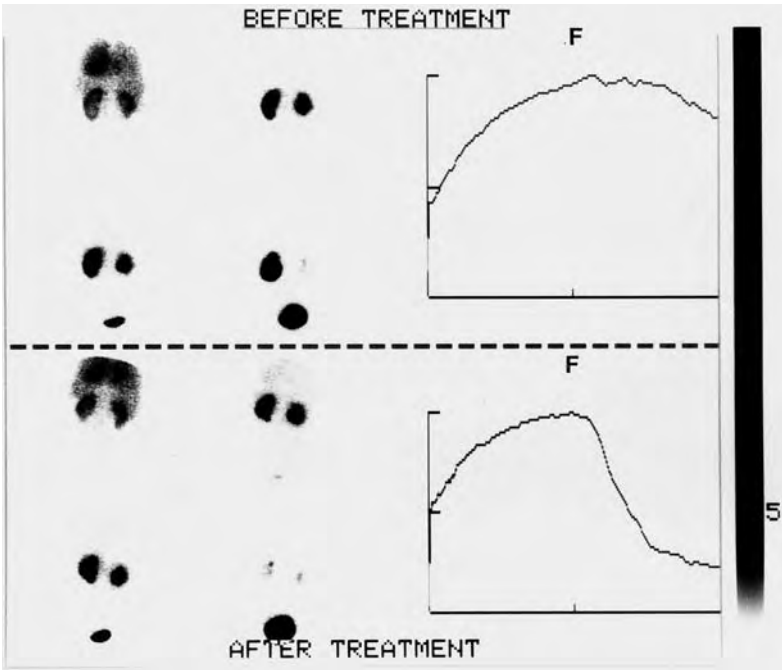

Fig. 5.9. Diuretic renogram with ^{99m}Tc-DTPA in a child with left pelviureteric junction obstruction, before (*top*) and after (*bottom*) percutaneous pyeloplasty. Note the conversion from a type IIIb (almost type II) curve before intervention to a type IIIa curve thereafter, indicating residual hypotonia of the pelvis. *F*, furosemide injection

abnormal ranges and hence they have relatively little clinical impact as stated by the Consensus Committee on Diuresis Renography (O'Reilly et al. 1996). A fourth pattern was subsequently described and is referred to as *delayed decompensation* or Homsy's sign (Homsy et al. 1988). In this case, diuretic injection is followed by a transient response, which seems decompensated at higher urinary flow rates, that is within 15 min of furosemide administration. It is most likely to represent obstruction – *intermittent*

hydronephrosis – which can be confirmed by a F-15 study (O'Reilly 1992).

In addition to the excretion pattern, it is important to properly assess the function of the dilated kidney, especially for prenatally detected hydronephrosis. A substantial proportion of babies suspected of pelviureteric junction obstruction improve spontaneously without treatment (Homsy et al. 1986); Piepsz et al. (1989) therefore proposed selecting those children with an altered single-kidney GFR for immediate surgery and to sequentially follow the others by a repeat study at 6 months. This attitude is more conservative and takes into consideration the maturation potential of renal function.

Finally, relatively little has been published about obstruction of the lower urinary tract. It is however of importance to assess the effect of chronic retention on dilation of the upper urinary tract (George et al. 1983, 1984). The effect of dilated ureters on pelvic washout was also studied and typical ureteral curves, obtained with continuous bladder drainage were proposed for interpretation of ureter dynamics (Jamar et al. 1992) (Fig. 5.10). Diuretic renography has also been proposed as a substitute to intravenous pyelogram in the follow-up of posterior urethral valves (Gordon et al. 1987).

To conclude, the methodology and interpretation of diuresis renography are now well established. Interestingly, although it has gained wide acceptance, the validity of the technique to diagnose obstruction cannot be directly assessed by comparison with a gold standard method. Several outcome studies, in adults and infants showed that the function of kidneys with an obstructive pattern was improved after surgery whereas it remained stable in non-obstructed entities without any intervention (O'Reilly 1989; Upsdell et al. 1992; Piepsz et al. 1989; King et al. 1984). Nonetheless, it is a fact that diuretic renography has almost completely replaced the invasive and sophisticated urodynamic studies and has significantly narrowed the spectrum of indications for intravenous pyelogram.

5.4 Renal Cortical Imaging

Renal cortical scintigraphy was initially used as a morphological tool. The development of ultrasonography and CT scanner along with refinements of intravenous pyelography provided clinicians with excellent anatomical information so that renal scintigraphy, especially with ^{99m}Tc-DMSA, has evolved to a more functional assessment of the renal parenchyma. Although ^{99m}Tc-DMSA scanning can occasionally be useful in assessing congenital abnormalities (e.g. evaluation of horseshoe kidney) or space-occupying lesions, the major indications now include the diagnosis of urinary tract infection

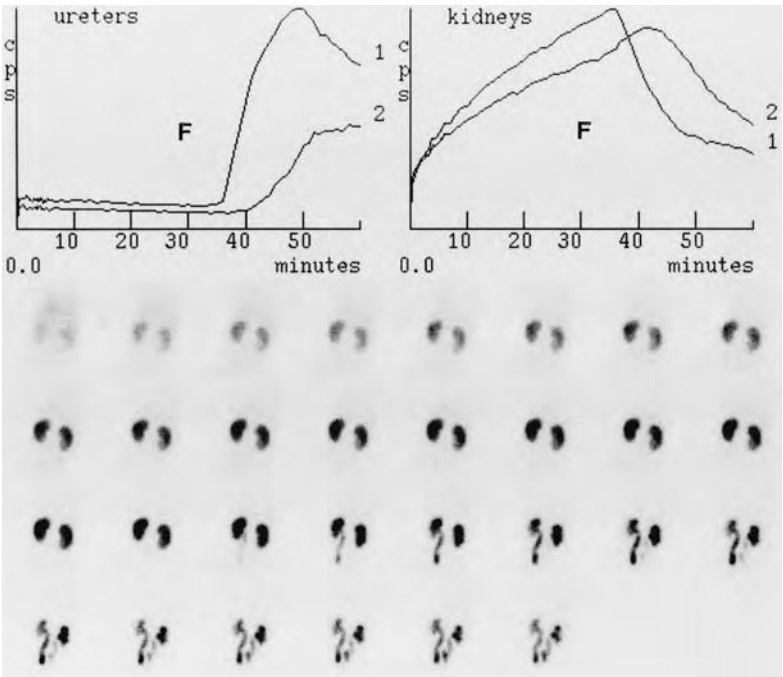

Fig. 5.10. ^{99m}Tc-MAG$_3$ study in a child with primary megaureter, performed with continuous bladder drainage. There is progressive accumulation of the tracer in both ureters after furosemide injection (*F*) and delayed renal washout (*curves*, *right upper panel*). The ureteric curves (*left upper panel*) are obstructive: type IIa (curve *2*) and IIc (curve *1*) according to Jamar et al. (1992)

(UTI), renal scarring especially in vesicoureteric reflux (VUR), as an alternative to nephrographic agents, and measurement of split renal function (Piepsz et al. 1999).

The diagnosis of upper UTI is usually easy in adults, based on clinical signs, elevated erythrocyte sedimentation rate and C-reactive protein, urine analysis and culture. It remains, however, a challenge in children sometimes due to the paucity of the clinical picture. Furthermore, when present, symptoms are rather non-specific and fever may be the only sign. Prompt diagnosis is necessary because of the potentially significant long-term sequelae. Adequate management of UTI can prevent scarring which can lead to hypertension, loss of functional cortex and, in extreme cases, chronic renal failure (Smellie et al. 1985). A large prospective study showed that a normal DMSA scan in acute UTI was predictive of a normal follow-up course whereas an abnormal scan was related to VUR in one third of the cases and suggestive of a less indolent course (Camacho et al. 2004). Although the clinical presentation of UTI and VUR may be different, it is impossible not to establish links between UTI, VUR and scarring. In children, scarring is almost always associated with VUR and was found in 12% of children with UTI and 25% of those with recurrent episodes (Smellie et al. 1981).

The role of ^{99m}Tc-DMSA scintigraphy has been well established in identifying potentially reversible defects in acute pyelonephritis and permanent functional damage in scarring (Bingham and Maisey 1978; Merrick et al. 1980; Gordon 1987; Jakobsson et al. 1992). It must however not be considered a necessary method for establishing the diagnosis of acute pyelonephritis which is usually based on clinical and biological data. Although it has been a common procedure for almost 20 years, interpretation of ^{99m}Tc-DMSA scintigraphy is far from easy. Gacinovic et al. (1996) reported a lack of inter-observer consistency though this was not confirmed by two subsequent studies using more definite evaluation criteria (Patel et al. 1993; de Sadeleer et al. 1998). The key question is to define whether a DMSA scan is normal or abnormal. In a study by Clarke et al. (1996), images were considered equivocal in 68/496 children. Of interest is the fact that the sensitivity – or more precisely the prevalence of abnormalities – of ^{99m}Tc-DMSA scanning is relatively low in UTI. This is not due to an intrinsic weakness of the method but to the fact that abnormalities can only be detected when significant damage to the renal cortex has occurred. This was nicely shown in animal experimental studies in which correlation with histopathology was obtained (Majd and Rushton 1992; Parkhouse et al. 1989). Thus, the role of DMSA scintigraphy is not only to help in the diagnosis of UTI but mainly to assess the functional consequences of UTI on the integrity of the parenchyma.

Normal images demonstrate fairly uniform distribution in the cortex with centrally located relatively photopenic defects, corresponding to the calices and papillary pyramids (Eggli and Tulchinsky 1993). Activity is not visible in the collecting system except in obstruction (Piepsz et al. 1986). In acute pyelonephritis, three patterns are observed: a focal defect without loss of organ contour, multiple focal defects and diffuse involvement of an entire kidney, characterised by reduced uptake and often enlargement due to oedema (Figs. 5.11 and 5.12). In chronic pyelonephritis and scarring, focal retraction(s) of the cortex with loss of organ contour are the most common abnormalities whereas atrophy of either one or both kidneys is found in 10%–20% of cases (Clarke et al. 1996). Better delineation of the lesions can be obtained using pinhole scintigraphy; some authors have proposed the use of high-resolution SPECT (Joseph et al. 1990; Tarkington et al. 1990; Yen et al. 1996). Despite experimental evidence that SPECT is more accurate than planar imaging in the diagnosis of acute pyelonephritis (Giblin et al. 1993), its benefit in patients looks rather marginal and it seems mainly useful in assessing scarring (Williams 1992). Furthermore, a study in normal

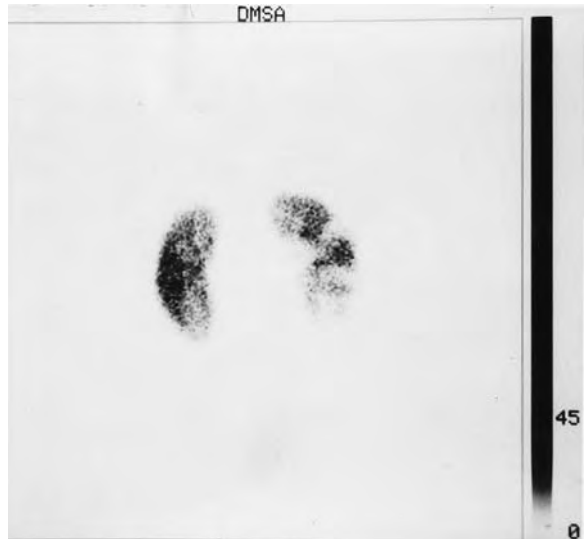

Fig. 5.11. ^{99m}Tc-DMSA scan in acute pyelonephritis in a child showing normal distribution in the left kidney and severe cortical defects without loss of renal contour on the right side

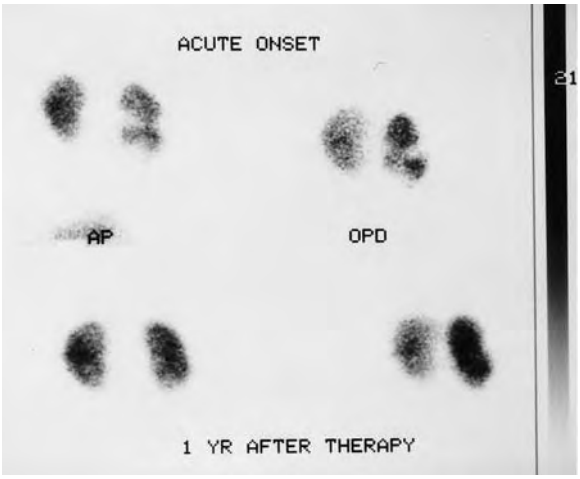

Fig. 5.12. ^{99m}Tc-DMSA study in acute pyelonephritis (*top*) with almost complete resolution of the cortical defects following treatment (*lower panel*)

volunteers demonstrated abnormalities on SPECT images with entirely normal planar images (de Sadeleer et al. 1996): systematic use of SPECT carries the risk of over-diagnosing either acute cortical defects or scars.

In clinical practice, in children younger than 5 years, ^{99m}Tc-DMSA scanning should be performed following UTI, regardless of the result of ultrasound, to exclude scarring. The decision to proceed to direct or indirect isotopic cystogram or to micturating – X-ray – cystogram will depend on the age and gender (Gordon 1990). Finally, it must be stated that an abnormal scan at the time of acute infection is not predictive of scarring and some defects may take time to resolve. Therefore, repeat scanning is required in the follow-up (2 to 6 months after infection) to identify scarring. DMSA scan is a better predictor of VUR if performed within 2 months of infection (Jakobsson 1997).

References

Andoh TF, Burdmann EA, Fransechini N et al (1996) Comparison of acute rapamycin nephrotoxicity with cyclosporine and FK506. Kidney Int 50:1110-1117

Anninga JK, Valdès Olmos RA, de Kraker J et al (1994) Technetium-99m dimercaptosuccinic acid and ifosfamide tubular dysfunction in children with cancer. Eur J Nucl Med 21:658-662

Bingham JB, Maisey MN (1978) An evaluation of the use of ^{99m}Tc-DMSA as a static renal imaging agent. Br J Radiol 51:599-607

Blaufox MD (1991) Procedures of choice in renal nuclear medicine. J Nucl Med 32:1301-1309

Blaufox MD, Aurell M, Bubeck B et al (1996a) Report of the radionuclides in nephrourology committee on renal clearance. J Nucl Med 37:1883-1888

Blaufox MD, Middleton ML, Bongiovanni J et al (1996b) Cost efficacy of the diagnosis and therapy of renovascular hypertension. J Nucl Med 37:171-177

Blaufox MD, Fine EJ, Heller S et al (1998) Prospective study of simultaneous orthoiodohippurate and diethylenetriaminepentaacetic acid captopril renography. The Einstein/Cornell Collaborative Hypertension Group. J Nucl Med 39:522-528

Britton KE, Nimmon CC, Whitfield HN et al (1979) Obstructive uropathy: successful evaluation with radionuclides. Lancet I:905-907

Bröchner-Mortensen J, Rödbro P (1976) Comparison between total and renal plasma clearance of (51Cr)EDTA. Scand J Clin Lab Invest 36:247-249

Brown SCW, Upsdell SM, O'Reilly PH (1992) The importance of renal function in the interpretation of diuresis renography. Br J Urol 69:121-125

Brown SCW (1994) Nuclear medicine in the clinical diagnosis and treatment of obstructive uropathy. In: Murray IPC, Ell PJ (eds) Nuclear medicine in clinical diagnosis and treatment, vol 1. Churchill Livingstone, Edinburgh, pp 271-293

Brown T, Mandell J, Lebowitz RL (1987) Neonatal hydronephrosis in the era of sonography. Am J Roentgenol 148:959-963

Bubeck B (1993) Renal clearance determination with one blood sample: improved accuracy and universal applicability by a new calculation principle. Semin Nucl Med 23:73-86

Camacho V, Estorch M, Fraga G et al (2004) DMSA study performed during febrile urinary tract infection: a predictor of patient outcome? Eur J Nucl Med published online (DOI: 10.1007/s00259-003-1410-z)

Carpenter CB (1990) Immunosuppression in organ transplantation. N Engl J Med 322:1224-1226

Chachati A, Meyers A, Godon JP et al (1987) Rapid method for the measurement of differential renal function validation. J Nucl Med 28:829-836

Chantler C, Garnett ES, Parsons V et al (1969) Glomerular filtration rate measurement in man by the single injection method using ^{51}Cr-EDTA. Clin Sci 37:169-180

Clarke SEM, Smellie JM, Prescod N et al (1996) Technetium-99m-DMSA studies in pediatric urinary tract infection. J Nucl Med 37:823-828

Clorius JH, Schmidlin P (1983) The exercise renogram. A new approach documents renal involvement in systemic hypertension. J Nucl Med 24:104-109

Conway JJ (1992) The "well tempered" diuretic renogram: a standard method to examine the asymptomatic neonate with hydronephrosis or hydroureteronephrosis. J Nucl Med 33:2047-2051

De Sadeleer C, Bossuyt A, Goes E et al (1996) Renal technetium-99m-DMSA SPECT in normal volunteers. J Nucl Med 37:1346-1349

De Sadeleer C, Tondeur M, Melis K et al (1998) A Belgian study on the reproducibility in reporting Tc-99m DMSA planar scintigraphy. Eur J Nucl Med 25:855 (abstract)

Dondi M, Franchi R, Levorato M et al (1989) Evaluation of hypertensive patients by means of captopril enhanced renal scintigraphy with technetium-99m DTPA. J Nucl Med 30:615-621

Dondi M, Fanti S, de Fabritiis A et al (1992) Prognostic value of

captopril renal scintigraphy in renovascular hypertension. J Nucl Med 33:2040-2044
Donker AJM, van der Hem GK, Sluiter WJ et al (1977) A radioisotope method for simultaneous determination of the glomerular filtration rate and the effective renal plasma flow. Nether J Med 20:97-103
Donoso G, Kuyvenhoven JD, Ham H et al (2003) ^{99m}Tc-MAG3 diuretic renography in children: a comparison between F0 and F+20. Nucl Med Commun 24:1189-1193
Dubovsky EV, Russell CD, Bischof-Delaloye A et al (1999) Report of the radionuclides in nephrology committee for evaluation of transplanted kidney (review of techniques). Semin Nucl Med 29:175-188
Eggers PW (1988) Effect of transplantation on the Medicare end-stage renal disease program. N Engl J Med 318:223-229
Eggli DF, Tulchinsky M (1993) Scintigraphic evaluation of pediatric urinary tract infection. Semin Nucl Med 23:199-218
Elliot WJ, Martin WB, Murphy MB (1993) comparison of two non-invasive screening tests for renovascular hypertension. Arch Intern Med 153:755-764
English PJ, Testa HJ, Lawson RS et al (1987) Modified method of diuresis renography for the assessment of equivocal pelviureteric obstruction. Br J Urol 59:10-14
Eshima D, Fritzberg AR, Taylor A (1990) 99m-Tc renal tubular function agents: current status. Semin Nucl Med 20:28-40
Fawdry RM, Gruenewald SM, Collins LT et al (1985) Comparative assessment of techniques for estimation of glomerular filtration rate with 99m-Tc-DTPA. Eur J Nucl Med 11:7-12
Fjeldborg P, Bröchner-Mortensen J (1986) Determination of 51-Cr-EDTA clearance in infants by a single capillary blood sample. Scand J Clin Lab Invest 46:335-340
Fommei E, Ghione S, Hilson AJW et al (1993) Captopril radionuclide test in renovascular hypertension: a European multicentre study. Eur J Nucl Med 20:617-623
Gacinovic S, Buscombe J, Costa DC et al (1996) Inter-observer agreement in the reporting of ^{99m}Tc-DMSA renal studies. Nucl Med Commun 17:596-602
Gates GF (1982) Glomerular filtration rate: estimation from fractional renal accumulation of 99m-Tc-DTPA (Stannous). AJR 138:565-570
George NJR, O'Reilly PH, Barnard RJ et al (1983) High pressure chronic retention. Br Med J 286:1780-1783
George NJR, O'Reilly PH, Barnard RJ et al (1984) Practical management of patients with dilated upper tracts and chronic retention of urine. Br J Urol 56:9-12
Geyskes GG, de Bruyn AJG. (1991) Captopril renography and the effect of percutaneous transluminal angioplasty on blood pressure in 94 patients with renal artery stenosis. Am J Hypertens 4:685S-689S
Giblin JG, O'Connor KP, Fildes RD et al (1993) The diagnosis of acute pyelonephritis in the piglet using single-photon emission computerized tomography dimercaptosuccinic acid scintigraphy: a pathological correlation. J Urol 1150:759-762
Gordon I (1987) Indications for ^{99m}Tc-dimercaptosuccinic acid scan in children. J Urol 137:464-467
Gordon I (1990) Urinary tract infection in paediatrics: the role of diagnostic imaging. Br J Radiol 63:507-511
Gordon I, Ransley PG, Hubbard CS (1987) 99m-Tc DTPA scintigraphy compared with intravenous urography in the follow-up of posterior urethral valves. Br J Urol 60:447-449
Gordon I, Mialdea-Fernandez RM, Peters AM (1988) Pelviureteric junction obstruction. The value of a post-micturition view in 99m-Tc DTPA diuretic renography. Br J Urol 61:409-412
Gordon I, Anderson PJ, Orton M et al (1991) Estimation of technetium-99m-MAG3 renal clearance in children: two gamma camera techniques compared with multiple plasma samples. J Nucl Med 32:1704-1708
Gupta NK, Bomanji JB, Waddington W et al (1995) Technetium-99m-L,L-ethylenedicysteine scintigraphy in patients with renal disorders. Eur J Nucl Med 22:617-624
Ham HR, Piepsz A (1991) Estimation of glomerular filtration rate in infants and in children using a single-plasma sample method. J Nucl Med 32:1294-1297
Hilson AJW (1991) The renal transplant perfusion index: where are we now? Eur J Nucl Med 18:227-228
Hilson AJW, Maisey MN, Brown CB et al (1978) Dynamic renal transplant imaging with Tc-99m DTPA (Sn) supplemented by a transplant perfusion index in the management of renal transplants. J Nucl Med 19:994-1000
Homsy YL, Williot P, Danais S (1986) Transitional neonatal hydronephrosis: fact or fantasy? J Urol 136:336-340
Homsy YL, Mehta PH, Huot D et al (1988) Intermittent hydronephrosis: a diagnostic challenge. J Urol 140:1222-12226
Howman-Giles R, Uren R, Roy LP et al (1987) Volume expansion diuretic renal scan in urinary tract obstruction. J Nucl Med 28:824-828
Huot SJ, Hansson JH, Dey H et al (2002) Utility of captopril renal scan for detecting renal artery stenosis. Arch Intern Med 162:1981-1984
Jafri RA, Britton KE, Nimmon CC et al (1988) Technetium-99m MAG3, a comparison with iodine-123 and iodine-131 orthoiodohippurate, in patients with renal disorders. J Nucl Med 29:147-158
Jakobsson B (1997) Importance of timing when using technetium-99m-dimecaptosuccinic acid scan in urinary tract infection. In: Taylor A, Nally JV, Thomsen H (eds) Radionuclides in nephrourology. Society of Nuclear Medicine, Reston, VA, pp 185-189
Jakobsson B, Nolstedt L, Svensson L et al (1992) Technetium-99m-DMSA scan in the diagnosis of acute pyelonephritis: relation to clinical and radiological findings. Pediatr Nephrol 6:328-334
Jamar F, Piret L, Wese FX et al (1992) Influence of ureteral status on kidney washout during 99m-Tc DTPA diuresis renography in children. J Nucl Med 33:73-78
Jones DA, Lupton EW, George NJR (1990) Effect of bladder filling on upper urodynamics in man. Br J Urol 65:492-496
Joseph DB, Young DW, Jordon SP (1990) Renal cortical scintigraphy and single photon emission computerized tomography (SPECT) in the assessment of renal defects in children. J Urol 144:595-597
Kabasakal L, Atay S, Vural AV et al (1995) Evaluation of ^{99m}Tc-ethylenedicysteine in renal disorders and determination of extraction ratio. J Nucl Med 36:1398-1403
Kaplan-Pavlovic S, Nadja C (1998) Captopril renography and duplex Doppler sonography in the diagnosis of renovascular hypertension. Nephrol Dial Transplant 13:313-317
Kass EJ, Fink-Bennett D (1990) Contemporary techniques for the radioisotopic evaluation of the dilated urinary tract. Urol Clin North Am 17:273-289
King LR, Coughlin PWF, Bloch EC et al (1984) The case for immediate pyeloplasty in the neonate with ureteropelvic junction obstruction. J Urol 132:725-728

Kletter K, Nurnberger N (1989) Diagnostic potential of diuresis renography: limitations by the severity of hydronephrosis and by impairment of renal function. Nucl Med Commun 10:51-61

Kopecky RT, Deaver TF, McAfee JG (1987) Furosemide augments the effects of captopril on nuclear studies in renovascular stenosis. Hypertension 10:181-188

Krijnen P, Oei HY, Claessens RAMJ et al (2002) Interobserver agreement on captopril renography for assessing renal vascular disease. J Nucl Med 43:330-337

Kuyvenhoven J, Piepsz A, Ham H (2003) When could the administration of furosemide be avoided? Clin Nucl Med 28:732-737

Ladegofed J (1966) Measurements of the renal blood flow in man with the ^{133}Xe washout technique. Scand J Clin Lab Invest 18:299-315

Levey AS, Perrone RD, Madias NE (1988) Serum creatinine and renal function. Ann Rev Med 39:465-490

Levitt BGS, Kogan S, Reda E et al (1988) The dilated urinary tract in children. Br J Urol 61:413-419

Li Y, Lee HB, Blaufox MD (1997) Single-sample methods to measure GFR with technetium-99m-DTPA. J Nucl Med 38:1290-1295

Majd M, Rushton HG (1992) Renal cortical scintigraphy in the diagnosis of acute pyelonephritis. Semin Nucl Med 22:98-111

Majd M, Potter BM, Guzzetta PC et al (1983) Effect of captopril on efficacy of renal scintigraphy in detection of renal artery stenosis. J Nucl Med 24:23 (abstract)

Mann SJ, Pickering TG, Sos TA et al (1991) Captopril renography in the diagnosis of renal artery stenosis; accuracy and limitations. Am J Med 90:30-40

Merrick MV, Uttley WS, Wild SR (1980) The detection of pyelonephritic scarring in children by radioisotopic imaging. Br J Radiol 53:544-556

Meyer G, Piepsz A, Kolinska J et al (1998) Technetium-99m mercaptoacetyltriglycine clearance values in children with minimal renal disease: can a normal range be determined? Eur J Nucl Med 25:760-765

Miralles M, Covas MI, Martinez-Miralles E et al (1997) Captopril test and renal duplex scanning for the primary screening of renovascular disease. Am J Hypertens 10:1290-1296

Moretti JL, Rapin JR, Saccavini JC et al (1984) 2,3-dimercaptosuccinic-acid chelates. 2. Renal localization. Int J Nucl Med Biol 11:275-279

Müller-Suur R, Müller-Suur C (1989) Glomerular filtration and tubular secretion of MAG-3 in the rat kidney. J Nucl Med 30:1986-1991

Müller-Suur R, Bois-Svensson I, Mesko L (1990) A comparative study of renal scintigraphy and clearance with technetium-99m-MAG3 and iodine-123-hippurate in patients with renal disorders. J Nucl Med 31:1811-1817

Müller-Suur R, Magnusson G, Bois-Svensson I et al (1991) Estimation of technetium 99m mercaptoacetyltriglycine plasma clearance by use of one single plasma sample. Eur J Nucl Med 18:28-31

Myers BD, Ross J, Newton L et al (1984) Cyclosporine-associated chronic nephropathy. N Engl J Med 311:699-705

Nally JW Jr, Chen C, Fine EJ et al (1991) Diagnostic criteria of renovascular hypertension with captopril renography. Am J Hypertens 4:749S-752S

Nordyke RA, Tubis M, Blahd WH (1960) Use of radioiodinated hippuran for individual kidney function tests. J Lab Clin Med 56:438-445

O'Reilly PH (1989) Functional outcome of pyeloplasty for ureteropelvic junction obstruction: a prospective study in 50 consecutive cases. J Urol 142:273-276

O'Reilly PH (1992) Diuresis renography. Recent advances and recommended protocols. Br J Urol 69:113-120

O'Reilly PH (2003) Standardization of the renogram technique for investigating the dilated upper urinary tract and assessing the results of surgery. BJU Int 91:239-243

O'Reilly PH, Testa HJ, Lawson RS et al (1978) Diuresis renography in equivocal urinary tract obstruction. Br J Urol 50:76-80

O'Reilly P, Aurell M, Britton K et al (1996) Consensus on diuresis renography for investigating the dilated upper urinary tract. J Nucl Med 37:1872-1876

Parkhouse HF, Godley ML, Cooper J et al (1989) Renal imaging with ^{99}Tc^{m}-labelled DMSA in the detection of acute pyelonephritis: an experimental study in the pig. Nucl Med Commun 10:63-70

Patel K, Charron M, Hoberman A et al (1993) Intra- end interobserver variability in interpretation of DMSA scans using a set of standardized criteria. Pediatr Radiol 23:506-509

Peters AM, Brown J, Crossman D et al (1990) Noninvasive measurement of renal blood flow with technetium-99m-DTPA in the evaluation of patients with suspected renovascular hypertension. J Nucl Med 31:1980-1985

Picciotto G, Sargiotto A, Petrarulo M et al (2003) Reliability of captopril renography in patients under chronic therapy with angiotensin II (AT1) receptor antagonists. J Nucl Med 44:1574-1581

Piepsz A, Ham HR, Roland JH et al (1986) Technetium-99m DMSA imaging and the obstructed kidney. Clin Nucl Med 11:389-391

Piepsz A, Hall M, Ham R et al (1989) Prospective management of neonates with pelviureteric junction stenosis. Scand J Urol Nephrol 23:31-36

Piepsz A, Gordon I, Hahn K et al (1993) Determination of the technetium-99m mercaptoacetyltriglycine plasma clearance in children by means of a single blood sample: a multicentre study. Eur J Nucl Med 20:244-248

Piepsz A, Pintelon H, Ham HR (1994) Estimation of normal chromium-51 ethylene diamine tetra-acetic acid clearance in children. Eur J Nucl Med 21:12-16

Piepsz A, Tondeur M, Kinthaert J et al (1996) Reproducibility of technetium-99m mercaptoacetyltriglycine clearance. Eur J Nucl Med 23:195-198

Piepsz A, Blaufox MD, Gordon I et al (1999) Consensus of renal cortical scintigraphy in children with urinary tract infection. Semin Nucl Med 29:160-174

Prigent A (1993) Diagnosis of renovascular hypertension: the role of captopril renal scintigraphy and related issues. Eur J Nucl Med 20:625-644

Rabito CA, Moore RH, Bougas C et al (1993) Noninvasive, real-time monitoring of renal function: the ambulatory renal monitor. J Nucl Med 34:199-207

Radó JP, Bános C, Takó J (1967) Frusemide renography. Lancet ii:1419-1420

Ramsay D, Belton I, Finlay D (1997) A review of captopril renal scintigraphy and its effect on patient management. Nucl Med Commun 18:631-633

Roccatello D, Picciotto G, Rabbia C et al (1992) Prospective study of captopril renography in hypertensive patients. Am J Nephrol 12:406-411

Russell CD, Rowell K, Scott JW (1986) Quality control of technetium-99m DTPA: correlation of analytic tests with in vivo protein binding in man. J Nucl Med 27:560-562

Russell CD, Thorstad BL, Yester MV et al (1988) Quantitation of renal function with technetium-99m MAG3. J Nucl Med 29:1931-1933

Russell CD, Taylor AT, Dubovsky EV (1996) Measurement of renal function with technetium-99m-MAG3 in children and adults. J Nucl Med 37:588-593

Sapirstein LA, Vidt DG, Mandel MJ et al (1955) Volumes of distribution and clearances of intravenously injected creatinine in the dog. Am J Physiol 181:330-336

Schillig S (1964) Indicator-dilution techniques in the estimation of renal blood flow. Am Heart J 68:675-681

Schreij G, van Es PN, van Kroonenburgh MJPG et al (1996) Baseline and postcaptopril renal blood flow measurements in hypertensives suspected of renal artery stenosis. J Nucl Med 37:1652-1655

Setaro JF, Chen CC, Hoffer PB et al (1991) Captopril renography in the diagnosis of renal artery stenosis and prediction of improvement after revascularization. Am J Hypertens 4:698S-705S

Shattuck LA, Eshima D, Taylor AT et al (1994). Evaluation of the hepatobiliary excretion of ^{99m}Tc-MAG3 and reconstitution factors affecting the radiochemical purity. J Nucl Med 35:349-355

Sherman RA, Blaufox MD (1980) Clinical significance of nonvisualization with ^{131}I-hippuran renal scan. In: Hollenberg NK, Lange S (eds) Radionuclides in nephrology. Thieme, Stuttgart, pp 235-239

Smellie JM, Normand ICS, Katz G (1981) Children with urinary tract infection: a comparison of those with and those without vesicoureteric reflux. Kidney Int 20:717-722

Smellie JM, Ransley PG, Normand ICS et al (1985), Development of new renal scars. A collaborative study. Br Med J 290:1957-1960

Smith HW, Goldring W, Chassis H (1938) The measurement of tubular excretory mass, effective blood flow and filtration rate in the normal human kidney. J Clin Invest 17:263-278

Smith HW, Finkelstein N, Aliminosa L et al (1945) The renal clearances of substituted hippuric acid derivatives and other aromatic acids in dog and man. JCI 24:388-404

Stoffel M, Jamar F, van Nerom C et al (1994) Evaluation of technetium-99m-L,L-ethylenedicysteine in renal transplant recipients: a comparative study with technetium-99m-mercaptoacetyltriglycine and iodine-125-orthoiodohippurate. J Nucl Med 35:1951-1958

Stoffel M, Jamar F, van Nerom C et al (1996) Estimation of technetium-99m L,L-ethylenedicysteine clearance by simplified methods: correlation with effective renal plasma flow. Eur J Nucl Med 23:365-370

Svetkey LP, Himmelstein SI, Dunnick NR et al (1989) Prospective analysis of strategies for diagnosing renovascular hypertension. Hypertension 14:247-257

Taplin GV (1971) Kidney function and disease. In: Blahd WH (ed) Nuclear medicine, 2nd edn. McGraw-Hill, New York, pp 382-386

Tarkington MA, Fildes RD, Levin K et al (1990) High resolution single photon emission computerized tomography (SPECT) ^{99m}Technetium-dimercaptosuccinic acid scintigraphy: a state of the art technique. J Urol 144:598-600

Tauxe WH, Dubovsky EV, Kidd TJ et al (1982) New formulas for the calculation of effective renal plasma flow. Eur J Nucl Med 7:51-54

Taylor A (2002) Renovascular hypertension: nuclear medicine techniques. Q J Nucl Med 46:268-282

Taylor A, Eshima D, Christian PE et al (1987) Evaluation of Tc-99m mercaptoacetyltriglycine in patients with impaired renal function. Radiology 162:365-370

Taylor A, Nally J, Aurell M et al (1996) Consensus report on ACE inhibitor renography for detecting renovascular hypertension. J Nucl Med 37:1876-1882

Taylor A, Hansen L, Eshima D et al (1997) Comparison of technetium-99m-LL-Ec isomers in rats and humans. J Nucl Med 38:821-826

Upsdell SM, Leeson SM, Brooman PJC et al (1988) Diuretic-induced urinary flow rates at varying clearances and their relevance to the performance and interpretation of diuresis renography. Br J Urol 61:14-18

Upsdell SM, Testa HJ, Lawson RS (1992) The F-15 diuresis renogram in suspected obstruction of the upper urinary tract. Br J Urol 69:126-131

Van Jaarsveld BC, Krijnen P, Derkx FH et al (1997) The place of renal scintigraphy in the diagnosis of renal artery stenosis. Fifteen years of clinical experience. Arch Intern Med 157:1226-1234

Van Nerom CG, Bormans GM, de Roo MJ et al (1993) First experience in healthy volunteers with ^{99m}Tc-L,L-ethylenedicysteine: a new renal imaging agent. Eur J Nucl Med 20:738-746

Verbruggen AM, Nosco DL, van Nerom CG et al (1992) Technetium-99m-L,L-ethylenedicysteine: a renal imaging agent. I. Labeling and evaluation in animals. J Nucl Med 33:551-557

Vidt DG (1991) The diagnosis of renovascular hypertension: a clinician's viewpoint. Am J Hypertens 4:663S-668S

Visscher CA, de Zeeuw D, Huisman RM (1995) Effect of chronic ACE inhibition on the diagnostic value of renography for renovascular hypertension: a preliminary report. Nephrol Dial Transplant 10:263-265

Walser M, Drew HH, LaFrance ND. (1988) Creatinine measurements often yield false estimates of progression in chronic renal failure. Kidney Int 34:412-418.

Whitaker RH (1973) Methods of assessing obstruction in dilated ureters. Br J Urol 45:15-22

Williams ED (1992) Renal single photon computed tomography: should we do it? Semin Nucl Med 22:112-121

Wong DC, Rossleigh MA, Farnsworth RA (1999) F+0 diuresis renography in infants and children. J Nucl Med 40:1805-1811

Yen T-C, Chang W-P, Chang S-L et al (1996) Technetium-99m-DMSA renal SPECT in diagnosing and monitoring pediatric acute pyelonephritis. J Nucl Med 37:1349-1353

6 Skeletal Scintigraphy

Christiaan Schiepers

CONTENTS

6.1 Introduction

Bone scintigraphy is one of the common procedures in routine nuclear medicine. The study is relatively simple, no patient preparation is required, and the imaging procedure is well standardized throughout diagnostic imaging departments. Modern equipment has greatly enhanced the ease of operation and permits imaging in planar, tomographic and whole body mode.

Bone scintigraphy is an extremely sensitive procedure for evaluating a variety of skeletal disorders, and can also be applied for certain soft tissue abnormalities such as calcifications, hematoma, and contusion. The main indications for referral are screening of patients with malignancy, trauma, orthopedic problems, sports injuries, endocrine and rheumatologic disorders.

Bone is a specialized form of connective tissue, with hardness as its characterizing feature. Bone is a dynamic tissue, a metabolically active structure where osteogenesis and resorption occur continuously, and which processes can be followed with radioactive tracers. Metabolic rates are affected by disease processes and can be greatly enhanced as in M. Paget or decreased as in involutional osteoporosis.

Bone scanning has been around for some time. In 1962 Blau and collaborators introduced ^{18}F-fluoride as a bone imaging agent. The annihilation radiation of this positron emitter is relatively high and suited for rectilinear scanners. Van Dyke et al. (1965) reported in 1965 the use of ^{18}F with a gamma camera. Since the advent of PET, this radio-pharmaceutical has been revived and allows for true regional quantification of bone blood flow and fluoride influx rate (Schiepers et al. 1990).

A historic breakthrough was the development of ^{99m}Tc labeled polyphosphate complexes by Subramanian and McAfee in 1971. This made bone scanning possible on routine gamma cameras and thus for daily application in the clinic. Gamma cameras have been optimized for ^{99m}Tc, and a high dose activity can be administered. These developments have led to the present important place of bone scintigraphy in clinical practice.

6.2 Radiopharmaceuticals

6.2.1 Fluoride

Radioactive fluoride, $^{18}F^-$ labeled sodium fluoride (NaF), is again being used in clinical practice after PET systems became available. The skeletal uptake is quite high, approximately 70%, and 25% is excreted in the urine by 6 h. The half-life of 109.8 min of ^{18}F is relatively short but permits transportation from a central radiopharmacy to the nuclear medicine clinic. Imaging times are reasonable, and a fluoride scan can be completed within 2 h after NaF administration. Thus, ^{18}F-fluoride forms an excellent tracer to study

C. Schiepers, MD, PhD
Department of Molecular and Medical Pharmacology, David Geffen School of Medicine at UCLA, 10833 Le Conte Avenue, AR-144 CHS, Los Angeles, CA 90095-6942, USA

the fluoride kinetics in the skeleton, and provides a method for absolute quantification of regional blood flow. The small solutes leave the capillaries in bone by passive free diffusion, and traverse through the fluid spaces to reach the osseous tissues. The uptake mechanism of fluoride is adsorption in the water shell around newly formed bone crystals, a process of minutes to hours. The exchange with hydroxyl ions of the hydroxy-apatite in the bone matrix, i.e. the actual incorporation, takes days and, therefore, cannot be measured accurately with this tracer.

6.2.2 Technetium Complexes

Presently, labeled diphosphonates are the radiopharmaceuticals of choice for skeletal scintigraphy. In order to obtain stable chelated complexes, reducing agents ($SnCl_2$) are needed, which keep technetium in a low valence state so that binding occurs. Generally, the clearance from the vascular compartment is fast, with half times of 2–4 min. Peak uptake varies for the different agents, but is usually around 1 h. The bone to background ratio also varies due to the different clearance and uptake rates of other tissues and, therefore, the maximum ratio occurs much later at 4–6 h. Patient convenience is also an important factor. The combination of contrast, peak uptake, radionuclide decay and practical issues, results in optimal imaging 2–4 h after tracer administration. At this time about one third of the administered dose is bound to bone, one third is excreted in the urine and the remainder is associated with other tissues, about 10% of which is bound to blood proteins.

Adverse reactions to the injection of the radiopharmaceutical are virtually non-existent. The reported incidents are usually related to other agents in the kits that are necessary for stabilization, e.g. pH buffers, reducing agents to keep technetium in a low valence state, and/or metabolites.

6.3 Methods

The image acquisition is based on scintillation detection (see Chap. 16). Several geometric configurations have been designed for nuclear imaging equipment. The standard gamma camera has one head, which can be tilted, angled and moved to image patients in the supine, sitting or standing position. In addition, whole body scanning and tomographic imaging is possible. Due to the significantly lower photon flux in nuclear imaging compared to conventional radiography, acquisition duration is prolonged. Presently, gantries with two or three heads are available to shorten the acquisition duration. Varying angles between the camera heads are possible to execute specific protocols and accelerate the acquisition. Systems with detectors over the full 360° are the standard in PET, but not in conventional single photon imaging. A feature of all tomographic systems in nuclear medicine is the simultaneous acquisition of multiple image planes.

6.3.1 Positron Imaging

The annihilation radiation of ^{18}F is readily detected with a positron camera. PET systems are optimized for 511 keV and allow correction for attenuation effects. For a more detailed description of this methodology the reader is referred to Chaps. 16 and 17. PET is a tomographic technique, which is truly quantitative, i.e. physiologic parameters as bone blood flow and tracer uptake rate can be determined. A detailed description of the various blood flow determination methods with $^{18}F^-$ can be found in the literature: quantitative with a gamma camera (Charkes 1980), based on whole body clearance (Wootton et al. 1976, 1981), and with PET (Hawkins et al. 1992).

In general, a transmission scan is necessary to correct for attenuation effects, and a dynamic emission scan of 1 h to measure fluoride uptake as a function of time. The initial framing or sampling rate needs to be high, in the order of 5–15 s/frame, to measure bone blood flow accurately. Arterial blood sampling is recommended to measure the clearance of fluoride from the vascular compartment. However, a large vascular structure in the field of view, e.g. heart, aorta, or major vessel, offers the possibility to measure the vascular clearance with the PET scanner and sophisticated processing techniques such as factor analysis (Schiepers et al. 1997b, 1998b).

6.3.2 Single Photon Imaging

The photopeak of 140 keV of ^{99m}Tc is ideal for the sodium iodide detector of a gamma camera, and allows for administration of high doses, e.g. 700–900 MBq of ^{99m}Tc. There is no special patient prepa-

ration for a bone scan. After the tracer administration, the patient is advised to drink plenty of fluids and to void frequently. Thus, excretion of tracer is enhanced and the radiation dose to the bladder minimized. Before scanning, the patient is asked to empty the bladder. Self-evidently, the patients need to be instructed about possible contamination because of tracer in the urine. Various protocols are available and imaging can be accomplished in several modes: static, dynamic or whole body. In addition, tomography can be performed with a dedicated system.

The movement of tracer immediately after the injection can be followed with flow imaging, or radionuclide angiography. Hereafter the tracer disperses in the extra-cellular space, the so-called second phase or blood pool phase. After an interval of 2–3 h the delayed phase of bone scintigraphy is performed. Therefore, this protocol has been named 'three-phase bone imaging'. For the flow phase, images of 2–4 s duration are acquired for a total time of 60–90 s. According to Fogelman et al. (1993; Ryan and Fogelman 1995) the blood pool phase needs to be completed within 10 min in order to limit the contribution of bony uptake. The delayed images are usually recorded with high resolution, i.e. pixel size of 3–4 mm.

In the static mode, images are acquired during a 'steady state' of the tracer distribution throughout the body. The standard available options of zooming and acquisition of spot views under specific angles, e.g. anterior or posterior oblique, can be attempted if a certain area needs to be inspected in detail. The bladder remains a problem, since urine is being produced continuously during scanning. Most institutions will mount low energy, high-resolution collimators, and preferably ultra-high resolution for tomography, since physicians like high-resolution images. Currently, cameras have a wide field of view, allowing for whole body scans and spot views that comprise the entire width of the body. This has the advantage that uptake between body parts can be compared directly, in addition to the standard left/right comparison.

Previously, pinhole images were recommended in case high magnification was needed, e.g. evaluation of the caput femoris in osteo-necrosis. With the currently available equipment, this is no longer necessary. Camera sensitivity and resolution have been improved and a zoomed image (1.5–4 times) of the area of interest, with a corresponding increase in acquisition time, will suffice. It is important to note that the information density is the relevant parameter here. In other words, if the zoom is 2, the imaged area of the object is only a quarter of the original matrix (both x and y dimensions are cut half). Therefore, the acquisition duration needs to be increased by a factor 4 in order to maintain the information density, i.e. acquire the same number of counts per pixel.

Whole body imaging is the routine in most nuclear medicine clinics. The patient is scanned in posterior and anterior views. This can be accomplished by passing the patient through the camera gantry or by moving the detector over the patient on a stationary bed. Special dual headed camera systems have been developed to image both sides in a single pass. This protocol is ideal for screening purposes, e.g. in oncology, and additional spot views of suspicious areas may be acquired later.

Tomographic sections of a certain body part can be reconstructed with SPECT imaging. This is only available for the delayed phase, since emission tomography assumes an equilibrium distribution of the radioactivity in the body. Tomography greatly enhances contrast and eliminates superimposed activity by providing three-dimensional images, i.e. in axial, coronal and sagittal planes. An additional requirement is patient immobility compliance. Whereas PET traditionally has full 360° acquisition, SPECT utilizes a rotating gantry. Currently, single, dual and triple headed systems are available. With more camera heads the acquisition can be shortened, greatly enhancing patient convenience and throughput. Best results are obtained with a 360° acquisition, 128×128 matrix for high resolution, 3–6° angular steps and 20–30 s per view. This results in a 30–45 min total acquisition time for a single head camera, which is tolerable for most patients, but a multi-headed system is preferable for a clinically acceptable time.

6.3.3 Radiation Dosimetry

According to ICRP-53 (International Commission on Radiological Protection 1987), the effective dose equivalent (EDE) for a routine whole-body bone scan with ^{99m}Tc-MDP is 0.008 mSv/MBq, amounting to 5.9 mSv for a standard dose of 740 MBq (20 mCi). The EDE for an ^{18}F-NaF whole body survey is more than three times higher with 0.027 mSv/MBq or 10.0 mSv for a standard dose of 370 MBq (10 mCi). Therefore, 6 mCi (222 MBq) of ^{18}F-NaF deliver the same EDE to the adult body as 20 mCi (740 MBq)

of ^{99m}Tc-MDP. Overall, the radiation dosimetry is less favorable for ^{18}F-Fluoride than ^{99m}Tc-labeled diphosphonates.

The red marrow dose is almost five times higher, i.e. 0.04 vs 0.0096 mSv/MBq, and the bone surface dose eight times higher, i.e. 0.04 vs 0.0063 mSv/MBq. The higher dose to bone and bone marrow is related to the higher uptake of fluoride compared to the diphosphonates. The only exception is the bladder, where the radiation dose from ^{99m}Tc is 0.05 mSv/MBq compared to 0.022 mSv/MBq from ^{18}F, related to the longer half-life of ^{99m}Tc. In addition, the ICRP calculations assume an average voiding frequency of every 4 h (1), increasing the radiation dose. As mentioned earlier, the radiation burden can be decreased significantly by drinking ample fluids and voiding frequently, increasing the elimination of tracer from the body.

6.4 Image Interpretation

Knowledge of normal uptake in the skeleton is mandatory. This experience is usually gained through training and interpreting sessions with experts. Fortunately, skeletal scintigraphy is a routine procedure, so that each practicing specialist can easily get acquainted and become proficient. Normal variants, however, can be tricky and many an atlas is devoted to these.

The first step is to check for focal or diffuse abnormalities, i.e. areas of increased and/or decreased uptake, the next step is to compare left vs. right. In pediatric patients, the growth plates are active, which translates into increased uptake. Additional information may be retrieved from the different phases, e.g. increased uptake during the flow phase, indicating hyperemia. Multi-phase imaging is important to differentiate increased uptake in the soft tissues from truly increased bone uptake.

A distinctive feature of bone scintigraphy is its high sensitivity to detect abnormalities such as fractures, infection, degenerative changes, metabolic bone disorders, metastases, but the test is notoriously non-specific. Many disease entities present with abnormal uptake on the bone scan. However, certain patterns may favor one diagnosis over another. For instance, a linear array of hot spots in the rib cage suggests fractures. Multiple scattered areas of focally increased uptake are highly suspicious for metastatic disease. Slight to moderately increased uptake in a diffuse pattern in joints suggests degenerative changes, especially when it is also seen in neighboring joints. Common pitfalls are: patient rotation obscuring the symmetry; genitourinary contamination; dental implants or disease, radiopharmaceutical problems.

Self-evidently, the clinical context is important to focus the possibilities and limit the number of differential diagnoses. Image interpretation was purposely described first, since it is our policy to read the films 'blind or blank' to gather all available information. Secondly, the clinical history, signs and symptoms are added and a final report dictated. This sequence prevents omissions and increases the likelihood that the majority of differential diagnoses is included.

Last but not least, correlative imaging has to be performed (Pomeranz et al. 1994; Ryan and Fogelman 1995). It is impossible to provide the referring physician with adequate information if the bone scan is not interpreted in conjunction with other image modalities, i.e. conventional radiography, CT, MR or US. Specialized procedures are usually done after the bone scan, guided by the detected abnormalities. In most cases, correlative interpretation of the results of all imaging modalities provides the diagnosis.

6.5 Selected Clinical Applications

6.5.1 Positron Imaging with ^{18}F-Fluoride

PET systems became available in most nuclear medicine clinics in the 1990s, making high resolution imaging possible. Several studies have compared conventional bone scintigraphy to ^{18}F-fluroride PET imaging of the skeletal system and have confirmed this notion (Hoh 1993 and Blake 2001). In a prospective comparison between planar, SPECT and ^{18}F-fluoride PET bone scintigraphy in 53 patients with newly diagnosed lung cancer ^{18}F-fluoride had the highest accuracy for detection of bone metastases (Schirrmeister 2001). Importantly, the accuracy of ^{18}F-fluoride imaging was significantly higher than planar bone imaging. Hetzel et al. (2003) studied 103 patients with lung cancer using planar bone scintigraphy, SPECT and ^{18}F-Fluoride PET. PET had the lowest number of false negative findings and a higher diagnostic accuracy than both conventional bone-imaging techniques.

Using the lesion-to-normal uptake ratio, it was not possible to differentiate benign from malignant lesions (Hoh et al. 1993). This is not too surprising given the non-specific nature of NaF as tracer.

In breast cancer, PET using FDG (fluoro-deoxy-glucose) as tumor tracer, was not more sensitive than conventional bone scintigraphy to detect skeletal metastases (Moon et al. 1998). It has been observed that sclerotic lesions, in general, have lower uptake (lower standardized uptake value, SUV) than lytic lesions. Moreover, PET using FDG detected fewer sclerotic lesions than conventional bone scintigraphy with MDP (Moon et al. 1998; Cook et al. 1998).

With ^{18}F-NaF and dynamic PET imaging, certain physiologic and biochemical bone parameters can be measured in-vivo. These quantitative indices are the measurement of local bone blood flow and fluoride influx rate. ^{18}F-Fluoride kinetics of vertebrae have been studied in the healthy human male (Schiepers et al. 1990; Hawkins et al. 1992), as well as in metabolic bone disease such as osteoporosis and Paget's disease (Schiepers et al. 1991, 1997a; Ryan and Fogelman 1995). Cook et al. (2002) studied vertebral bodies involved with Paget's disease and found that fluoride was more tightly bound to the bone matrix in this metabolic bone disease compared to normal vertebrae. Bone remodeling is closely related to bone blood flow as shown by tetracycline labeling (Reeve et al. 1988). Thus, metabolic parameters of bone may be measured non-invasively with PET. Another application is the evaluation of bone graft viability (Berding et al. 1995). The potential of ^{18}F-fluoride PET in clinical practice has been dealt with elsewhere (Schiepers 1993).

An example of an ^{18}F-Fluoride PET scan is given in Fig. 6.1. A sagittal image of the torso is shown with a set of corresponding transverse slices at the levels indicated. Note the exquisite detail and high resolution obtained.

The latest advent is PET-CT, combining two standard imaging systems into one gantry. Image fusion is easily achieved because the patient is imaged with both modalities in the same position on the scanner bed, within a short period of time. In clinical practice, the CT provides images of diagnostic quality that greatly enhance the localization of lesions. In Fig. 6.2 PET/CT images are displayed of an older male with benign facet joint disease. By combining anatomical and functional imaging, specificity is added to the imaging procedures and the diagnosis of benign disease can be made (Fig. 6.2), which saves time and greatly benefits the patient. A PET/CT study (Even-Sapir et al. 2004) in a population with a variety of cancers, demonstrated a sensitivity close to 100% and specificity of 88% for skeletal metastasis detection with ^{18}F-fluoride. Compared to PET alone, there was a significant difference in sensitivity but not in specificity (Even-Sapir et al. 2004). In Fig. 6.3 an example of a PET-CT scan is shown with multiple metastases from prostate cancer.

6.5.2 Oncology

Skeletal scintigraphy with technetium complexes is indicated for screening purposes in various cancers, such as prostate and breast. The intent here is to detect occurrence and extent of malignant disease, presenting as hot or sometimes as cold spots. The whole body mode is ideal for surveying the skeleton, and is superior to conventional radiography. Since the study is not very specific and in some malignancies the number of false positives exceeds that of true-positives, a combination of scintigraphy and radiography is necessary. For the spine, especially vertebrae, MR imaging is recommended to confirm presence of absence of bone metastases. A logical decision tree of imaging modalities may be devel-

Fig. 6.1. Fluoride PET scan of a 28-year-old male with juvenile osteoporosis. Sagittal plane of the torso of a volumetric dataset acquired with a 2D PET system 1 h after administration of 300 MBq of ^{18}F-fluoride. Corresponding axial slices of the head, jaw, neck, thoracic and lumbar spine, and pelvis are given on the right. Note the increased uptake in the superior and inferior aspects of thoracic and lumbar vertebrae

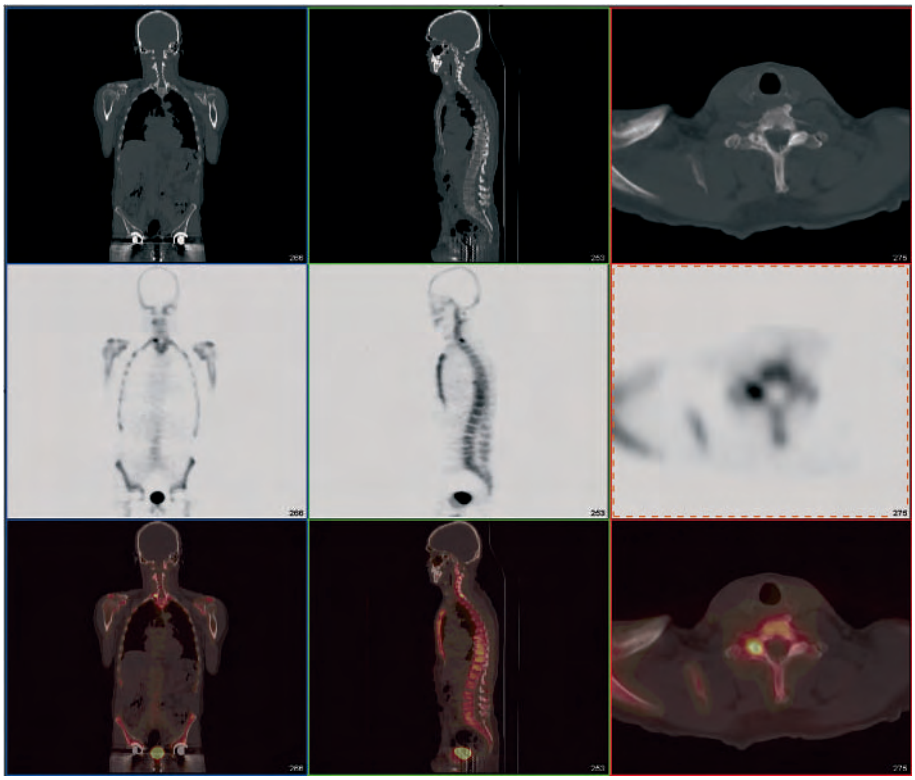

Fig. 6.2. PET/CT scan using ^{18}F-fluoride and no contrast in a 67-year-old man with treated prostate cancer and a normal serum PSA level. *Left panel*, coronal cuts; *middle panel*, sagittal; and *right panel*, axial images. *Top row*, CT in bone window; *middle row*, PET; and *bottom row*, the fused image with CT in gray scale and PET in color. Note the increased uptake in the right C3 facet joint. The CT shows only degenerative changes, where the hot spot is localized (fused image)

oped as fits the individual laboratory and/or health system (Pomeranz et al. 1994). In the last decade, referrals for metastasis screening have dropped, since the yield of bone scanning in the early stages of cancer has been shown to be low.

In general, bone metastases reveal increased uptake (Brown et al. 1993). Since the metastases are usually located in the bone marrow, it is not the metastasis itself that is seen on the bone scan, but the reaction of the bone to the expanding malignant bone marrow. In highly aggressive and fast expanding tumors, therefore, the lesions are cold, since there is not enough time for the bone to respond and the regional bone blood flow may be jeopardized to such extent that the tracer cannot be delivered. Cold lesions have been reported for leiomyosarcoma, ductal breast cancer, and multiple myeloma. The feasibility of whole body imaging with ^{18}F-fluoride in oncological disorders was reported by Hoh and colleagues in 1993 (Hoh et al. 1993). Just as in single photon bone imaging, there was considerable overlap between uptake in benign and malignant lesions. Given the difference in costs, single photon imaging with technetium complexes will remain the test of choice for screening of bone metastases.

Of considerable clinical interest is the probability of a solitary lesion on the bone scan to be benign. Widely varying frequencies have been reported: 15%–35% in the patient without malignancy, between 40%–80% in patients with known malignancy (Brown et al. 1993). Lesion distribution is sometimes important. In breast cancer, distant metastasis is rare in the absence of lesions in the thorax, i.e. ribs, sternum, and thoracic spine (Goldfarb et al. 1998).

Primary bone tumors generally show a very high uptake. Bone scintigraphy is indicated to evaluate the extent of disease and screening for metastases. Monitoring of therapy response is no indication since the bone scan remains positive for a long time. ^{201}Tl-chloride or ^{18}F-FDG are better radiopharmaceuticals for this purpose. Skeletal scintigraphy is useful in diagnosis and screening of osteogenic sarcoma, Ewing's sarcoma, and chondrosarcoma.

An interesting finding is the so-called flare phenomenon, an increasing uptake in lesions and skel-

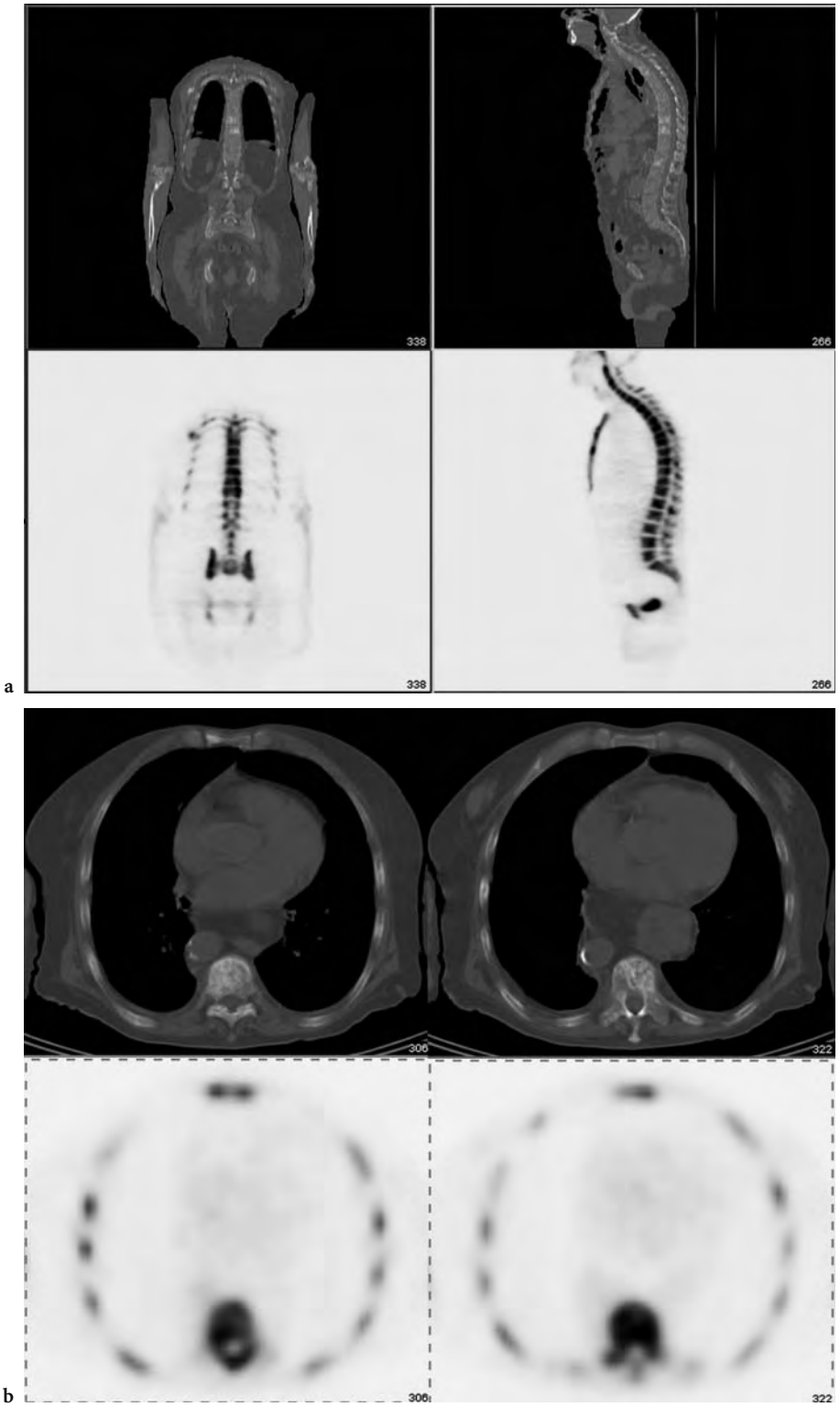

Fig. 6.3. ^{18}F-Fluoride PET/CT images of an 82-year-old man with hormone refractory prostate cancer. **a** Coronal (*left*) and sagittal (*right*) planes of the CT (*top row*) and PET (*bottom row*). **b** Axial cuts of the chest at two different levels, T8 (*left panel*) and T9 (*right panel*). Note the difference between CT abnormality and the corresponding PET abnormality. T8 has minor uptake whereas T9 uptake involves a much larger part of the vertebral body. These findings suggest a more sclerotic lesion in T8 and active disease involvement in T9

eton after initiation of chemotherapy, hemi-body radiation or high dose radionuclide therapy. In general, this is related to the response of affected bone to the therapeutic agents and is usually associated with a therapeutic effect.

6.5.3 Infection and Inflammation

In case of osteomyelitis, a three-phase bone scan is performed with increased flow to the affected area in the acute stage. The blood pool is also increased and the delayed images (third phase) show abnormal uptake in the bone, which further increases at 24 h imaging (fourth phase). In case the initial increased uptake decreases in time and appears not to affect the bones, a diagnosis of soft tissue disease such as cellulitis may be established. The indication of the bone scan is to demonstrate involvement of the bone. If the test is negative, osteomyelitis is unlikely, if it is positive, further work up is indicated with an infection survey, i.e., gallium, labeled immunoglobulins or WBC (white blood cells), which are dealt with in Chap. 7. Alternatively, an MR of the affected area may be performed to check for bone marrow edema.

6.5.4 Orthopedics

The bone scan is very sensitive in detecting trauma and, in general, will be positive 1–2 days after a traumatic bone event. Fractures will show increased uptake up to 1 year in about two-thirds of cases (Collier et al. 1993). Therefore, monitoring of therapy is of less value.

Nuclear medicine in sports injuries is an emerging field, a trend that can be expected to continue. Stress fractures in athletes are not infrequent, and routine radiographic evaluation often provides negative or questionable results, especially in the early stages. Stress fractures are most common in the lower extremities, with running the reported cause in most cases. Ultrasound is a possible adjunct to physical examination. Stress fractures occur more frequently in female athletes than males. A stress fracture is a fatigue fracture, related to repetitive stresses to normal bone (Anderson and Greenspan 1996). Accurate and timely diagnosis is required to prevent possible costly and disabling complications (Reeder et al. 1996). Bone scintigraphy is indicated to differentiate stress fractures from shin splints or periostitis. In shin splints there is micro-trauma to the bone, which still has a sufficient reparative ability and healing response, whereas in a stress fracture there is a "critical mass" of injured bone leading to mechanical failure. Since the therapy is so different for these entities, i.e., decreasing but continuing exercise at a lower level in shin splints and "active-rest" plus immobilization in stress fractures, it is important to make the correct diagnosis. In Fig. 6.4 a three-phase bone scan of a young female athlete is shown, having both a shin splint and stress fracture.

A frequent referral for a bone scan is the loosening vs. infection of an orthopedic prosthesis. Bone uptake is increased during the first year after prosthesis (hip, knee, shoulder or elbow implant). The time that the delayed scan is positive is somewhat longer for non-cemented than cemented prostheses, limiting the usefulness of skeletal scintigraphy during the first months after surgery (Rahmy et al. 1994). Increased uptake around the stem and tip usually heralds loosening. The differential diagnosis with infection has to be made by performing an infection survey with ^{67}Ga-citrate or labeled WBC and plain films. If the imaging findings are still inconclusive, addition of a colloid scan may be indicated to assess the presence and location of normal but displaced bone marrow (see Chap. 7).

SPECT has provided new indications for bone scintigraphy. A routine referral is low back pain with normal radiographs. In case of negative planar scintigraphy, tomography needs to be performed to exclude facet syndrome of the spine, occult fracture, spondylolysis or spondylolisthesis. Tomographic imaging is a real adjunct, because of the increased contrast and resolution, and ability to view the skeleton in 3-D (Fig. 6.5). In patients with poorly localized or persistent bone pain, not satisfactorily explained with radiographic imaging, skeletal scintigraphy is helpful. In these situations, planar imaging of the whole body may reveal unsuspected traumatic pathology, and tomographic imaging may disclose small lesions. SPECT is very helpful to delineate the lesion, e.g. in avascular necrosis, Legg-Calve-Perthes disease.

A role for PET in orthopedic nuclear medicine has yet to be identified. Osteonecrosis has been studied (Schiepers et al. 1998c). In this preliminary study, the healing response of a unilaterally injured femoral head could be predicted. Skeletal flow and fluoride influx rate in the abnormal and normal hips were compared directly, and the relation to final outcome evaluated, i.e. surgical replacement or conservative treatment. A flow ratio of at least 2 between the abnormal and normal femoral head was necessary

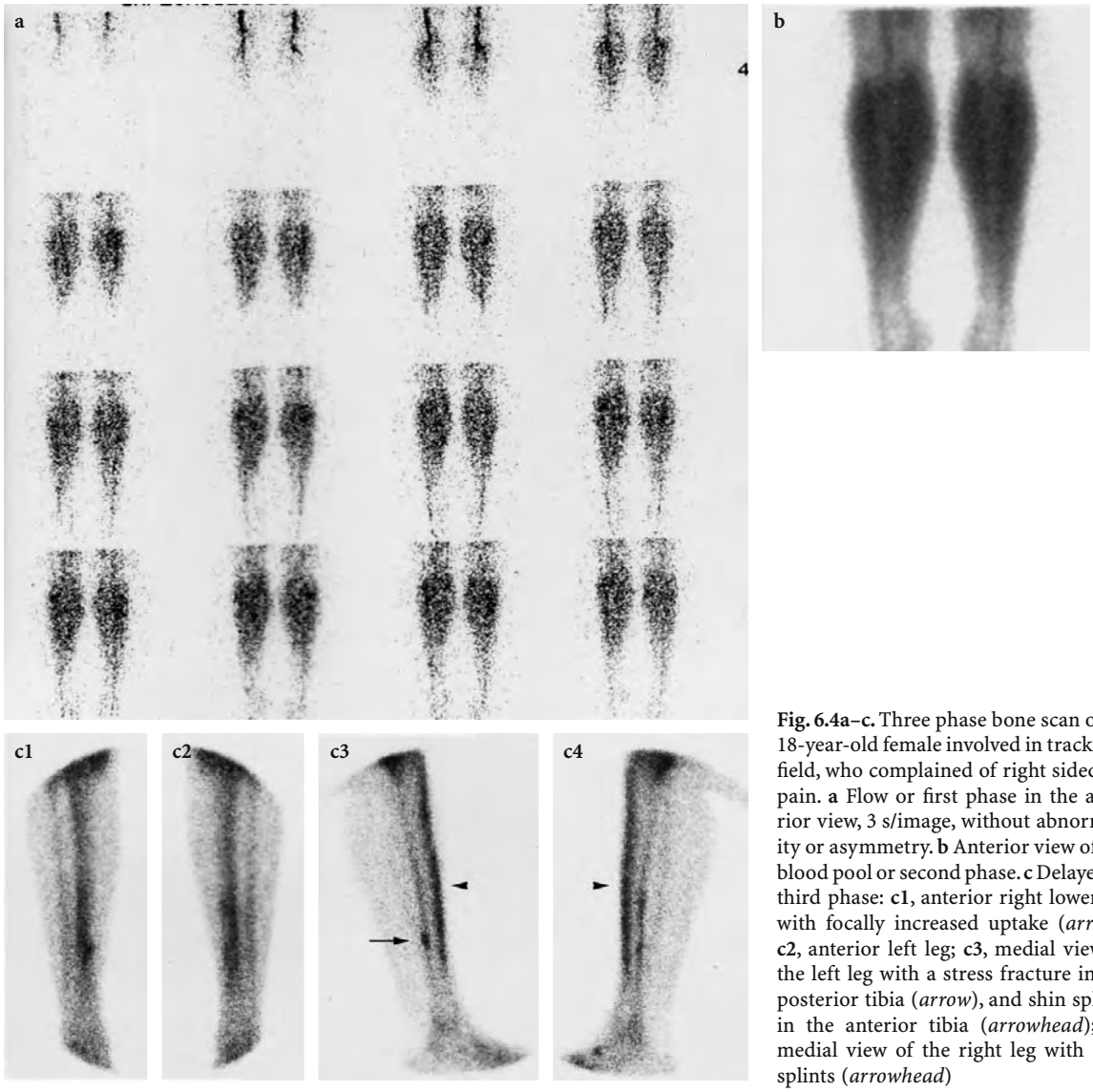

Fig. 6.4a–c. Three phase bone scan of an 18-year-old female involved in track and field, who complained of right sided leg pain. **a** Flow or first phase in the anterior view, 3 s/image, without abnormality or asymmetry. **b** Anterior view of the blood pool or second phase. **c** Delayed or third phase: **c1**, anterior right lower leg with focally increased uptake (*arrow*); **c2**, anterior left leg; **c3**, medial view of the left leg with a stress fracture in the posterior tibia (*arrow*), and shin splints in the anterior tibia (*arrowhead*); **c4**, medial view of the right leg with shin splints (*arrowhead*)

to predict a successful outcome with a conservative regimen. A minimum flow of 0.04 ml/min/ml was measured in a patient, whose affected femoral head healed conservatively. It was concluded that a highly technical procedure like PET appeared feasible in clinical practice, and permitted prediction of outcome depending on regional skeletal flow measurements in vivo.

6.5.5 Vascular Bone Disorders

Reflex sympathetic dystrophy (RSD) is a disorder with a widely variable clinical presentation. The pathophysiology is not completely understood. The syndrome is best described as an exaggerated response to injury due to an abnormal sympathetic reflex. Early and effectively treatment is important, otherwise the prognosis is guarded, leading to significant disability with lasting socioeconomic consequences.

RSD is a complex entity, which is characterized by increased flow in stage I (3–6 months), and the typical increased peri-articular uptake on the delayed scan. In stage II the flow is decreased. The contribution of scintigraphy in the diagnosis and therapy of upper extremity RSD has been reported previously (Schiepers 1997; Schiepers et al. 1998a), where the utility of dynamic scintigraphy was evaluated. Both the three phase bone scan and vascular scan were used for diagnosis and staging. Bone scintigraphy was highly accurate to diagnose RSD, and vascular

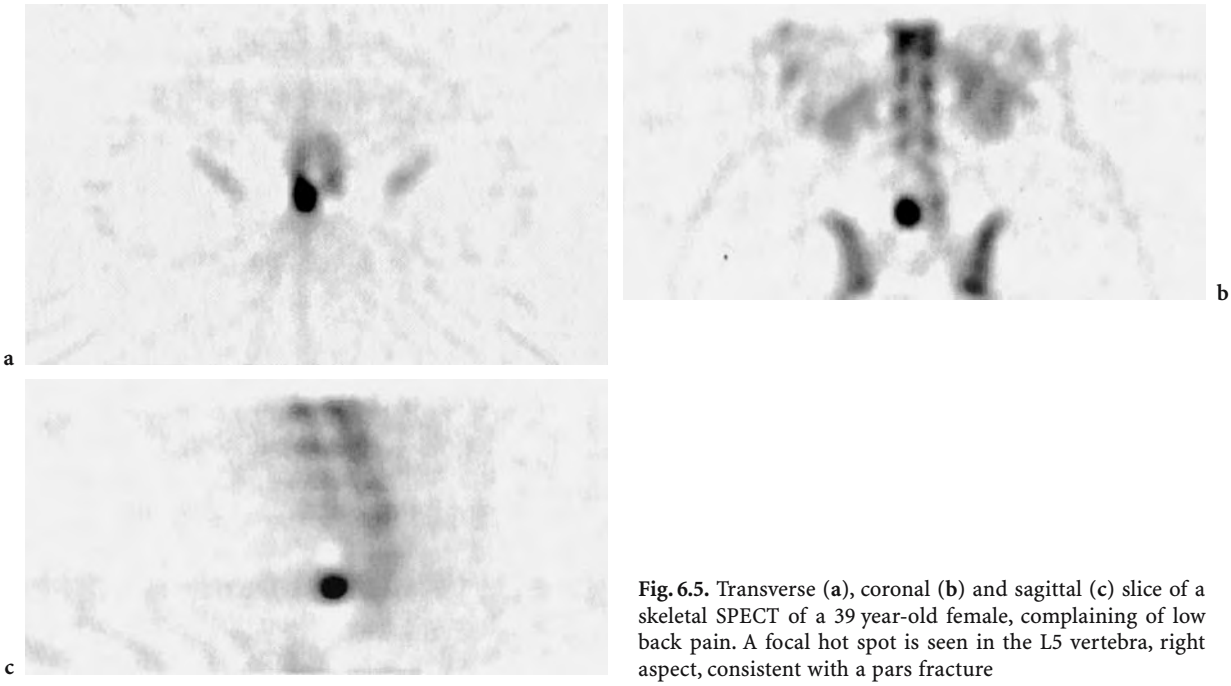

Fig. 6.5. Transverse (**a**), coronal (**b**) and sagittal (**c**) slice of a skeletal SPECT of a 39 year-old female, complaining of low back pain. A focal hot spot is seen in the L5 vertebra, right aspect, consistent with a pars fracture

scintigraphy was best for staging of RSD. Staging by bone and vascular scintigraphy was discordant in a quarter of patients. Since the RSD stage determines the type of therapy, a combination of both studies is indicated in the work-up and monitoring of upper extremity RSD.

6.6 Conclusion

Skeletal scintigraphy, both as positron and single photon imaging, is an extremely sensitive test to evaluate a large spectrum of abnormalities related to the skeleton. The study is notoriously non-specific and other imaging modalities, i.e. plain radiography, CT, MR, US are usually necessary to reduce the number of diagnostic possibilities. The addition of sophisticated imaging modalities provides the opportunity of correlative imaging, which will yield the final diagnosis in the vast majority of patients.

For the foreseeable future the place of skeletal scintigraphy will remain the same. Clinical indications for quantitative imaging need to be further investigated. In single photon imaging, new tracers will be developed with faster uptake and/or clearance from the vascular compartment. Thus, the delay of hours between tracer administration and imaging may be shortened, enhancing patient convenience. New equipment may further increase spatial resolution, so that even smaller abnormalities can be detected (see Chap. 16). Development of specialized image reconstruction and processing techniques will produce higher contrast in tomograms and improve image quality (see Chap. 17).

The combination of anatomic and functional imaging, e.g. PET/CT, is the newest addition to our diagnostic armamentarium, providing ease of localization and enhanced specificity to lesion characterization.

References

Anderson MW, Greenspan A (1996) Stress fractures. Radiology 199:1–12

Berding G, Burchert W, van den Hoff J et al (1995) Evaluation of the incorporation of bone grafts used in maxillofacial surgery with [^{18}F]fluoride ion and dynamic positron emission tomography. Eur J Nucl Med 22:1133–1140

Blake GM, Park-Holohan SJ, Cook GJ, Fogelman I (2001) Quantitative studies of bone with the use of 18F-fluoride and 99mTc-methylene diphosphonate. Semin Nucl Med 31:28–49

Blau M, Nagler W, Bender MA (1962) Fluorine-18: A new isotope for bone scanning J Nucl Med 3:332–334

Brown ML, Collier BD, Fogelman I (1993) Bone scintigraphy: part 1. oncology and infection, J Nucl Med 34:2236–2240

Charkes ND (1980) Skeletal blood flow: implications for bone scan interpretation. J Nucl Med 21:91–98

Collier BD, Fogelman I, Brown ML (1993) Bone scintigraphy: part 2. orthopedic bone scanning, J Nucl Med 34:2241–2246

Cook GJ, Houston S, Rubens R, Maisey MN, Fogelman I (1998)

Detection of bone metastases in breast cancer by 18FDG PET: differing metabolic activity in osteoblastic and osteolytic lesions. J Clin Oncol 16:3375–3379

Cook GJ, Blake GM, Marsden PK, Cronin B, Fogelman I (2002) Quantification of skeletal kinetic indices in Paget's disease using dynamic 18F-fluoride positron emission tomography. J Bone Miner Res 17:854–859

Even-Sapir E, Metser U, Flusser G, Zuriel L, Kollender Y, Lerman H et al (2004) Assessment of malignant skeletal disease: initial experience with 18F-fluoride PET/CT and comparison between 18F-fluoride PET and 18F-fluoride PET/CT. J Nucl Med 45:272–278

Fogelman I, Collier BD, Brown ML (1993) Bone scintigraphy, part 3. bone scanning in metabolic bone disease. J Nucl Med 34:2247–2252

Goldfarb CR, Ongseng FO, Finestone H, Szakacs GM, Guelfguat M, Jonas D (1998) Distribution of skeletal metastases in patients with breast carcinoma. J Nucl Med 39:114P

Hawkins RA, Choi Y, Huang SC et al (1992) Evaluation of the skeletal kinetics of ^{18}F-fluoride ion with PET. J Nucl Med 33:633–642

Hoh CK et al (1993b) Whole body skeletal imaging with [F-18] fluoride ion and pet. J Comput Assist Tomogr 17:34–41

International Commission on Radiological Protection (1987) Radiation dose to patients from radiopharmaceuticals, 1st edn. Pergamon, Oxford

Moon DH, Maddahi J, Silverman DH, Glaspy JA, Phelps ME, Hoh CK (1998) Accuracy of whole-body fluorine-18-FDG PET for the detection of recurrent or metastatic breast carcinoma. J Nucl Med 39:431–435

Pomeranz SR, Pretorius HT, Ramsingh PS (1994) Bone scintigraphy and multi-modality imaging in bone neoplasia: strategies for imaging in the new health care climate. Semin Nucl Med 24:188–207

Rahmy AI; Tonino AJ; Tan WD (1994) Quantitative analysis of technetium-99m-methylene diphosphonate uptake in unilateral hydroxy-apatite-coated total hip prostheses: first year of follow-up. J Nucl Med 35:1788–1791

Reeder MT, Dick BH, Atkins JK, Pribis AB, Martinez JM (1996) Stress fractures. Current concepts of diagnosis and treatment. Sports Med 22:198–212

Reeve J, Arlot M, Wootton R et al (1988) Skeletal blood flow, iliac histomorphometry, and strontium kinetics in osteoporosis: a relationship between blood flow and corrected apposition rate. J Clin Endocrinol Metab 66:1124-1131

Ryan PJ, Fogelman I (1995) The bone scan: where are we now? Semin Nucl Med 25:76–91

Schiepers C (1993) Skeletal fluoride kinetics of $^{18}F^-$ and positron emission tomography(PET): in vivo estimation of regional bone blood flow and influx rate in humans. In: Schoutens et al (eds) Bone circulation and vascularization in normal and pathological conditions. Plenum, New York, pp 95–101

Schiepers C (1997) Clinical value of dynamic bone and vascular scintigraphy in diagnosing reflex sympathetic dystrophy of the upper limb. In: Cooney WP, Schuind F (eds) Hand clinics, post-traumatic upper extremity RSD. Saunders, Philadelphia, pp 423–429

Schiepers CWJ, Hawkins RA, Choi Y et al (1990) Kinetics of bone metabolism assessed with $^{18}F^-$ and PET. Eur J Nucl Med 16:450

Schiepers C, Geusens P, Vleugels S et al (1991) Positron emission tomography (PET) with ^{18}F- to evaluate metabolic rate in bone disorders. J Miner Bone Res 6:S243

Schiepers C, Nuyts J, Bormans G, Dequeker J, Bouillon R, Mortelmans L, Verbruggen A, de Roo M (1997a) Fluoride kinetics of the axial skeleton measured in-vivo with positron emission tomography ($^{18}F^-$ - PET): initial experience in metabolic bone disease. J Nucl Med 38:1970–1976

Schiepers C., Wu H.M., Nuyts, J. Dahlbom M., Hoh CK, Huang SC, Phelps ME (1997b) Fluoride PET: is non-invasive quantitation feasible with factor analysis? J Nucl Med 38:93P

Schiepers C, Bormans I, de Roo M (1998a) Three phase bone scan and dynamic vascular scintigraphy in algo-neurodystrophy of the upper extremity. Acta Orthop Belg 64:322–327

Schiepers C, Hoh CK, Wu HM, Dahlbom M, Phelps ME (1998b) Factor analysis for generation of input functions replaces blood sampling in tracer kinetic modeling. J Nucl Med 39:206P

Schiepers C, Broos P, Miserez M, Bormans G, de Roo M (1998c) Measurement of skeletal flow with Positron Emission Tomography and F-18 fluoride in femoral head osteonecrosis. Arch Orthop Trauma Surg 118:131–135

Subramanian G, McAfee JF (1971) A new complex of ^{99m}Tc for skeletal imaging, Radiology 99:192–198

Van Dyke D, Anger HO, Yano Y, Bozzini C (1965) Bone blood flow shown with ^{18}F and the positron camera. Am J Physiol 209:65–70

Wootton R, Reeve J, Veall N (1976) The clinical measurement of skeletal blood flow. Clin Sci Mol Med 50:261–268

Wootton R, Tellez M, Green JR, Reeve J (1981) Skeletal blood flow in Paget's disease of bone. Metab Bone Dis Relat Res 4/5:263–270

7 Imaging Infection and Inflammation

Huub J. J. M. Rennen, Chantal P. Bleeker-Rovers, and Wim J. G. Oyen

CONTENTS

H. J. J. M. Rennen, PhD
Department of Nuclear Medicine, Radboud University Nijmegen Medical Centre, PO Box 9101, 6500 HB Nijmegen, The Netherlands
C. P. Bleeker-Rovers, MD
Department of Nuclear Medicine and Department of Internal Medicine, Radboud University Nijmegen Medical Centre, PO Box 9101, 6500 HB Nijmegen, The Netherlands
W. J. G. Oyen, MD
Professor, Department of Nuclear Medicine (565), Radboud University Nijmegen Medical Centre, PO Box 9101, 6500 HB Nijmegen, The Netherlands

7.1 Introduction

Scintigraphic visualization of the localization of infection and inflammation is a challenging problem in clinical practice because it may have important implications for the management of patients with infectious or inflammatory disorders. In order to enable clinicians to rapidly administer the most appropriate treatment, adequate delineation and diagnosis of inflammatory foci is of critical importance. If the clinical history and physical examination are indecisive, the clinician can choose from several diagnostic modalities to determine the localization, extent and severity of the disease. Sensitive radiological investigations like magnetic resonance imaging (MRI) and helical computerized tomography (CT) are able to locate relatively small focal abnormalities. However, these radiological methods rely on morphological changes, and as a result they are less accurate in early stages of infection or inflammation and are unable to discriminate active processes from anatomical changes due to a cured infection or after surgery (scar tissue).

In contrast, radiopharmaceuticals used for imaging infection and inflammation accumulate in the infectious/inflammatory lesion due to the locally changed physiological condition, such as enhanced blood flow, enhanced vascular permeability, or influx of white blood cells. Thus, scintigraphic imaging does not depend on morphological changes, but is based on physiochemical processes in tissues. Therefore, scintigraphic techniques can visualize infectious foci in their early phases, when morphological changes are not yet apparent. In addition, scintigraphic imaging is an excellent noninvasive method of whole-body scanning that can determine the extent of the infectious or inflammatory disease throughout the body.

This chapter will focus on well-established and widely available radiopharmaceuticals and on the potential of positron emission tomography (PET) using ^{18}F-fluorodeoxyglucose (FDG) in the diagnosis

of infectious and inflammatory processes. Before discussing the various scintigraphic methods, the pathophysiology of inflammation and infection is briefly described.

7.1.1 The Pathophysiology of Inflammation and Infection

Inflammation is defined as the response of tissues to any kind of injury in order to bring serum molecules and cells of the immune system to the site of damage. Such injury can be caused by trauma, ischemia, a neoplasm or an infection. Infection simply means "contamination with micro-organisms" (Roitt 1997). Infection is not always accompanied by inflammation, for example in the case of a severely immunocompromised patient. In general, the inflammatory response is characterized by locally increased blood supply, increased vascular permeability in the affected area, enhanced transudation of plasma proteins and enhanced influx of white blood cells. In response to tissue damage, powerful defense mechanisms are activated, consisting of white blood cells and plasma proteins (opsonins, antibodies, complement). Furthermore, a complex variety of chemical mediators are involved. These are molecules that are generated during the inflammatory response and that modulate the inflammatory process. The migration of white blood cells from the blood stream is facilitated by chemical mediators which upregulate the expression of adhesion molecules on both endothelial cells and white blood cells. First, the white blood cells adhere to the vascular endothelium due to locally enhanced expression of these adhesion molecules. Subsequently, they pass through the endothelium and the basal membrane (diapedesis) and migrate into the inflammatory focus (chemotaxis). This process starts within minutes of the injury and usually resolves within hours or days (Roitt 1997). It causes the classical symptoms of acute inflammation: rubor (redness), calor (warmth), tumor (swelling), dolor (pain) and functio laesa (impaired function).

White blood cells are differentiated into various subclasses. Granulocytes are white blood cells with conspicuous cytoplasmic granules and are subdivided according to the staining properties of the granules into polymorphonuclear neutrophils (PMNs), eosinophils and basophils. Lymphocytes, monocytes and macrophages are other members of the family of white blood cells. In acute infection or inflammation, infiltrating cells are predominantly polymorphonuclear neutrophils. In chronic infection or inflammation, persisting for weeks or months, the cellular infiltrate mainly consists of mononuclear cells, such as lymphocytes, monocytes, and macrophages.

7.2 Currently Available Radiopharmaceuticals for Infection/Inflammation Imaging

To date there are at least four agents that are most commonly used for imaging infection or inflammation: (1) ^{67}Ga citrate, (2) radiolabeled white blood cells, (3) radiolabeled anti-granulocyte antibody preparations, and (4) FDG PET (Fig. 7.1).

7.2.1 ^{67}Ga Citrate

After injection, ^{67}Ga citrate accumulates as an iron analogue via binding to circulating transferrin. This complex extravasates at the site of inflammation due to locally enhanced vascular permeability. In the inflamed tissue, ^{67}Ga is transferred to lactoferrin that is locally excreted by white blood cells or to siderophores produced by micro-organisms (Weiner 1990). Physiologically, 10%–25% of the radionuclide is excreted via the kidneys during the first 24 h. After 24 h the principal route of excretion is hepatobiliary.

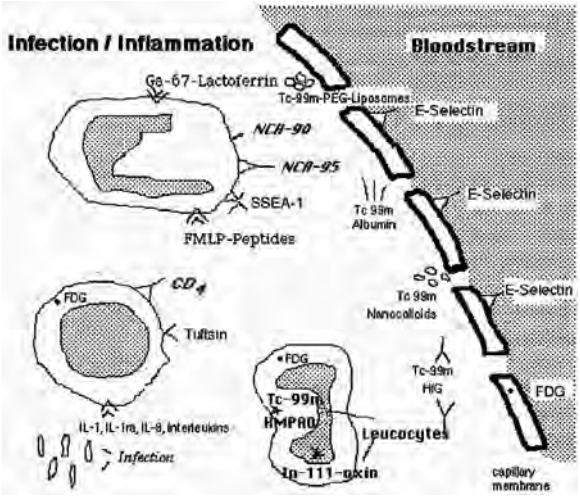

Fig. 7.1. Different radiopharmaceuticals for the detection of inflammation and infection and the pathophysiology of their uptake mechanism

After 48 h about 75% of the injected dose remains in the body and is equally distributed among the liver, bone, bone marrow, and soft tissues (Hoffer 1980). ^{67}Ga citrate has been used extensively in clinical practice in several pathological conditions demonstrating high sensitivity for both acute and chronic infection and noninfectious inflammation (Palestro 1994). However, there are several shortcomings that limit its clinical application. Specificity is poor owing to the physiological bowel excretion and accumulation in malignant tissues and areas of bone modeling (Perkins 1981; Bekerman et al. 1984). In addition, the radiopharmaceutical has unfavorable imaging characteristics such as a long physical half-life (78 h) and high-energy gamma radiation (93–889 keV), causing high radiation absorbed doses. These unfavorable characteristics and the development of newer radiopharmaceuticals have resulted in the replacement of gallium imaging by scintigraphy with labeled white blood cells, with a few exceptions. White blood cell scanning is of limited value in patients with suspected vertebral osteomyelitis and sequential gallium imaging appears to be a better way to diagnose this condition (Palestro 1994). Also, in immunocompromised patients, ^{67}Ga citrate imaging is the procedure of choice for detecting opportunistic respiratory tract infections (Palestro 1994). Finally, ^{67}Ga citrate scintigraphy is still the gold standard for radionuclide imaging in patients with fever of unknown origin (FUO), where it is able to detect both acute and chronic inflammatory conditions and neoplasms (Palestro 1994; Knockaert et al. 1994).

However, its limited specificity and the generally unfavorable characteristics when compared to FDG PET may result in replacement of this technique by FDG PET in patients with FUO in the near future.

Fig. 7.2. A 49-year-old female with leukocytosis and fever after renal transplantation. ^{111}In-oxine white blood cell scan at 3.5 h post injection shows a homogeneous infiltration in the transplanted kidney (*arrowhead*) with a white blood cell uptake index of 2 (normal <0.2) as a sign of transplant infection (proven with biopsy)

7.2.2 Radiolabeled White Blood Cells

Imaging using in-vitro labeled autologous white blood cells was developed in the 1970s. A blood sample of approximately 50 ml is collected and white blood cells are separated in vitro from red blood cells. These white blood cells are then labeled with radioactive isotopes (^{111}In or ^{99m}Tc) and reinjected. Using standard labeling procedures, only a few granulocytes are damaged by labeling, whereas most lymphocytes are damaged. The damaged cells are rapidly cleared from the circulation after reinjection (Thakur and McAfee 1984). After intravenous administration, the radiolabeled white blood cells initially sequestrate in the lungs with subsequent rapid clearance from the lungs. The radiolabel rapidly clears from the blood and in most cases uptake in granulocytic infiltrates is high while a substantial portion of the white blood cells accumulate in the spleen and the liver. Autologous white blood cells can be labeled with ^{111}In using oxine (McAfee and Thakur 1976). The use of HMPAO, a lipophilic chelator, allows for efficient labeling of white blood cells with ^{99m}Tc (Peters et al. 1986). In contrast to ^{111}In-oxine, some of the ^{99m}Tc-HMPAO is released from the white blood cells after injection and subsequently is excreted via the kidneys (within minutes) and the hepatobiliary system (after several hours) (Peters 1994). ^{99m}Tc-labeled white blood cells have replaced ^{111}In-labeled white blood cells for most indications, because of the more optimal radiation characteristics. As a result of the biodistribution of ^{99m}Tc-HMPAO-labeled white blood cells, the use of ^{111}In-labeled white blood cells is preferred for evaluation of the kidneys, bladder and gall bladder (see Fig. 7.2). ^{111}In-labeled white blood cells are also preferred if late images are needed as in chronic infection (Peters 1994). With regard to diagnostic accuracy, there is no need for a better imaging agent than radiolabeled white blood cells. The preparation of this radiopharmaceutical, however, is laborious: isolating and labeling a patient's white blood cells takes a trained technician approximately 3 h. In

addition, the need to handle potentially contaminated blood can result in transmission of bloodborne pathogens such as the hepatitis virus or the human immunodeficiency virus to technicians or patients (Lange et al. 1990; Fleury et al. 2003).

The principal clinical indications for radiolabeled white blood cells include inflammatory bowel disease, osteomyelitis, the follow-up of patients with infections of vascular or orthopedic prostheses and soft tissue infections (Peters 1994; Liberatore et al. 1998; Larikka et al. 2001). There has always been concern that chronic infections could be missed by labeled white blood cell scans, because these infections generate a smaller granulocyte response than acute infections. However, a study in 155 patients demonstrated that sensitivity of labeled white blood cells for detection of acute infections (90%) was not significantly different from sensitivity for detection of chronic infections (86%) (Datz and Thorne 1986).

7.2.3 Anti-granulocyte Antibodies and Antibody Fragments

Ever since it became clear that infectious and inflammatory foci could be visualized by radiolabeled autologous white blood cells, investigators have tried to develop a method aiming to label white blood cells in vivo. The use of radiolabeled monoclonal antibodies (Mab) against surface antigens present on granulocytes has the advantage that labeling procedures are easier and do not require handling of potentially contaminated blood. Disadvantages of the use of Mab, however, are the high molecular weight, resulting in slow diffusion into sites of inflammation, a long plasma half-life, uptake in the liver due to clearance by the reticulo-endothelial system. A long interval is often required between administration of radiolabeled antibodies and acquisition of images in order to improve target-to-background ratios. Use of Mab of murine origin sometimes induces production of human anti-mouse antibodies (HAMA), which can lead to allergic reactions and altered pharmacokinetics when repeated injections are given (Becker et al. 1994b). This is, of course, a major limitation for follow-up studies. The use of antibody fragments (Fab' or $F(ab')_2$) or humanization of the antibodies could overcome most of these limitations: theoretically, immunogenicity is lower, blood clearance is faster and accumulation in inflammatory foci is higher. Moreover, since Fab' antibody fragments have an intrinsic lower affinity for the epitope, bone marrow uptake is lower, which is an advantage for imaging of infections of the central skeleton. Although radiolabeled anti-granulocyte antibodies and antibody fragments are included among radiolabeled compounds for specific targeting of infiltrating granulocytes, recent studies have demonstrated that they localize in infectious processes to a large extent by nonspecific extravasation due to locally enhanced vascular permeability (Skehan et al. 2003; Lipp et al. 1996). Binding of the antibodies to infiltrating white blood cells may contribute to the retention of the radiolabel in the inflammatory focus.

7.2.3.1 Anti-nonspecific-cross-reacting Antigen-95

One of the most widely used anti-granulocyte antibodies is the commercially available murine anti-nonspecific-cross-reacting antigen-95 (anti-NCA-95) IgG (BW 250/183), labeled with ^{99m}Tc, which recognizes the nonspecific cross-reacting antigen 95 (NCA-95) expressed on human granulocytes and (pro)myelocytes. This Mab has been used successfully for imaging various infectious and inflammatory processes (Joseph et al. 1988; Lind et al. 1990; Steinstrasser and Oberhausen et al. 1996), including subacute infectious endocarditis (Morguet et al. 1994), lung abscesses (Peltier et al. 1993), septic loosening of hip and knee prostheses (Boubaker et al. 1995; Klett et al. 2003), and diabetic foot infections (Dominguez-Gadea et al. 1993). Peripheral bone infections were also adequately visualized (Peltier et al. 1993; Scheidler et al. 1994), but sensitivity decreased in cases where the focus was located closer to the spine because of physiological bone marrow uptake, so imaging with ^{99m}Tc-anti-NCA-95 is less suitable for diagnosing vertebral osteomyelitis (Gratz et al. 1997). The worst results were obtained in spondylodiscitis (Fig. 7.3). In 40 patients with spondylodiscitis all lesions showed photopenic effects (Gratz et al. 1997). A proposed explanation is increased pressure in the vertebral bodies, which prevents labeled white blood cells or antibodies from penetrating. Pulmonary infections other than abscesses were not visualized (Peltier et al. 1993; Prvulovich et al. 1995). ^{99m}Tc-anti-NCA-95 scanning appeared to be a safe and reliable method for detecting infectious foci in neonates and infants with fever of unknown origin (Gratz et al. 1998). The preparation was also used in the evaluation of patients with inflamma-

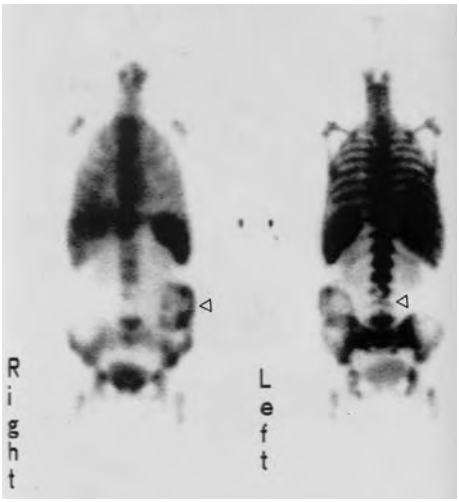

Fig. 7.3. A 63-year-old male with fever of unknown origin with a cold lesion in lumbar spine (*right panel*) as a sign of spondylodiscitis and a hot lesion in the left abdomen (*left panel*) as a sign of soft tissue abscess in the transplant kidney. Whole-body scan with antibody BW 250/183 4 h post injection

tory bowel disease, but it appeared to be less accurate than radiolabeled white blood cells partly due to nonspecific bowel uptake (Segarra et al. 1991; Papos et al. 1996; Gyorke et al. 2000). Due to the relatively slow blood clearance, imaging 24 h after injection is generally necessary for correct localization of the inflammatory process. The major drawback of radiolabeled anti-NCA-95, however, is the production of HAMA after the first injection.

7.2.3.2 Anti-stage-specific Embryonic Antigen-1

Anti-stage-specific embryonic antigen-1 (anti-SSEA-1, NeutroSpec, Mallinckrodt Inc., MO) is a monoclonal antibody of the IgM subclass, that recognizes CD15 antigens on granulocytes with high affinity ($K_d=10^{-11}$ M). The in vivo binding exceeds 50%, suggesting involvement of more specific accumulation in inflammatory sites, such as in vivo migration of white blood cells from the circulation to the focus. ^{99m}Tc-anti-SSEA-1 IgM was successfully used in patients with various inflammatory and infectious diseases, such as osteomyelitis, diabetic foot ulcers, and post-surgical infection (Thakur et al. 1996, 2001) with similar diagnostic accuracy when compared to radiolabeled white blood cells. Imaging with ^{99m}Tc-anti-SSEA-1 IgM also proved to be a highly sensitive test for detection of appendicitis in equivocal cases (Kipper et al. 2000; Rypins and Kipper 2000). ^{99m}Tc-anti-SSEA-1 IgM is a convenient radiolabeled compound (imaging after 1 h, easy preparation) and no HAMA formation has been observed. Disadvantages are high liver uptake and transient mild neutropenia that has been observed after ^{99m}Tc-anti-SSEA-1 injection in several patients. In most cases, however, this does not represent a clinical problem and does not impair image quality (Signore et al. 2002).

7.2.3.3 Anti-nonspecific-cross-reacting Antigen-90 Fab'

^{99m}Tc-labeled anti-NCA-90 Fab' (sulesomab, LeukoScan, Immunomedics GmbH, Darmstadt, Germany), which binds to NCA-90 surface antigen on granulocytes, is a commercially available infection imaging agent. Promising results have been obtained in the scintigraphic detection of endocarditis (Gratz et al. 2000) and nonclassic appendicitis (Barron et al. 1999). Scintigraphy using ^{99m}Tc-anti-NCA-90 Fab' also helped reach a final diagnosis in eight out of 20 patients with FUO (Maugeri et al. 2001). ^{99m}Tc-anti-NCA-90 Fab' proved to be no alternative for radiolabeled white blood cells in patients with inflammatory bowel disease due to limited sensitivity (Stokkel et al. 2002; Charron et al. 2001). Also, nonspecific bowel activity is often present, especially in the delayed images (Ivancevic et al. 2001). At first, scintigraphy using ^{99m}Tc-anti-NCA-90 Fab' appeared to provide rapid localization of bone and soft tissue infections with a negligible HAMA response rate and accuracy comparable to that of white blood cell scanning (Becker et al. 1994a, 1996; Harwood et al. 1999; Hakki et al. 1997). In other studies, however, ^{99m}Tc-anti-NCA-90 Fab' scintigraphy was found to be less specific for the diagnosis of musculoskeletal infections than white blood cell scanning (Devillers et al. 2000; Ivancevic et al. 2002; Ryan 2002; Gratz et al. 2003). In addition, false-negative results were found in several patients with chronic infections (Gratz et al. 2003). These studies suggest that ^{99m}Tc-anti-NCA-90 Fab' scintigraphy could be used for imaging of acute orthopedic infections, with its greatest strength being a high negative predictive value. Positive studies may require further correlative imaging.

7.2.4 FDG PET

^{18}F-Fluorodeoxyglucose (FDG) accumulates in tissues with a high rate of glycolysis, which not exclu-

sively occurs in neoplastic cells. FDG uptake is present in all activated white blood cells (granulocytes, monocytes as well as lymphocytes) enabling imaging of acute and chronic inflammatory processes. The mechanism of FDG uptake in activated white blood cells is related to the fact that these cells use excess glucose as an energy source only after activation during the metabolic burst. FDG, like glucose, passes the cell membrane. Phosphorylated FDG is not further metabolized and remains trapped inside the cell in contrast to phosphorylated glucose that enters the glycolytic pathway.

Increased uptake and retention of FDG has been shown in lesions with a high concentration of inflammatory cells, such as granulocytes and activated macrophages. Since the first report on high FDG uptake in a human abdominal abscess (Tahara et al. 1989), there have been many reports of FDG accumulation in different infections and inflammatory lesions (de Winter et al. 2002; Zhuang and Alavi 2002).

PET using FDG has been studied in a wide variety of bone and soft-tissue infections of bacterial, tuberculous, and fungal origin. Sensitivity generally exceeds 90%. FDG PET has been especially successful in cases of acute osteomyelitis (Guhlmann et al. 1998; Zhuang et al. 2000; Kalicke et al. 2000; Stumpe et al. 2000). The high spatial resolution allows differentiation between osteomyelitis or inflammatory spondylitis and infection of the soft tissue surrounding the bone (Kalicke et al. 2000). High spatial resolution and rapid accumulation into infectious foci are significant advantages over conventional imaging techniques such as labeled white blood cells. However, in a direct comparison of the diagnostic value of white blood cell scintigraphy and FDG PET, the former showed superior diagnostic performance compared to FDG PET in cases of FUO (Kjaer et al. 2004). The poorer performance of FDG PET is in particular attributable to a high percentage of false positive scans, leading to low specificity.

Moreover, low specificity due to indiscriminate uptake in any cell type with high glycolytic activity is a general limitation. For example, FDG PET cannot discriminate between tumor and inflammatory lesions. Moreover, FDG uptake in infectious foci is affected by serum glucose levels. Though FDG PET is still rather expensive, with the growing availability of PET scanners, it is expected that infection imaging with FDG PET will have a place in clinical practice of infection imaging in the near future. However, indications of FDG PET as compared to conventional techniques have not yet been defined unequivocally.

7.3 Infection Imaging in Patients with Infectious or Inflammatory Disorders

7.3.1 Infected Joint Prosthesis

An important group referred to nuclear medicine for infection imaging is patients with suspected infection of a joint prosthesis. In most patients the complications of prosthetic joint surgery are readily diagnosed. A significant number of patients with joint prosthesis present with aseptic loosening of the prosthesis as can be determined radiographically (Harris and Seldge 1990). However, 1%–3% of the patients with joint prostheses present with infected implants (Hanssen and Rand 1998) and the differentiation of aseptic loosening from infection can be difficult. In case of suspicion of any type of postoperative complication, a negative bone scintigraphy effectively rules out any complication (Love et al. 2001). However, the majority of the infections occur within 1 year after implantation, and at that time enhanced periprosthetic uptake is observed on the bone scan in most patients (Palestro and Torres 1997). Therefore, an abnormal bone scan will require additional studies to determine the cause of the abnormality. Although not the ideal agent in these patients ^{67}Ga citrate can be used to delineate infected prostheses, with a moderate overall accuracy of 70%–80% (Palestro and Torres 1997). Radiolabeled white blood cells can accurately delineate infections in this patient population. However, in many cases the physiological uptake of the labeled white blood cells in the bone marrow complicates the interpretation of the images. In combination with sulfur colloid, which accumulates in active marrow but not in infection, the diagnostic accuracy for diagnosing painful prosthesis exceeds 90% (Palestro et al. 1991). Furthermore, infected prostheses can be diagnosed very accurately using radiolabeled anti-granulocyte antibody preparations. In a study of 53 patients with infected joint prostheses Leukoscan (^{99m}Tc-labeled anti-CD66 Fab') had a diagnostic accuracy of 88%, as compared to 81% for radiolabeled white blood cells (Becker et al. 1996). FDG is sensitive for delineating infected prostheses. It appears that FDG PET does not allow differentiation between aseptic loosening of prostheses and infected prostheses, resulting in low specificity (Zhuang et al. 2001; Love et al. 2000).

7.3.2 Osteomyelitis

A three phase bone scan in otherwise normal bone is able to diagnose osteomyelitis with high sensitivity and specificity. Obviously, in patients with osseous abnormalities, the specificity of the bone scan is much lower. In those patients ^{67}Ga citrate or radiolabeled white blood cells can be applied to increase the specificity. Radiolabeled white blood cells are less suitable for diagnosing chronic low-grade osteomyelitis, however. In patients suspected of vertebral osteomyelitis radiolabeled white blood cells are not the first choice because these images will often show a photopenic defect in the spine. The preferred technique for patients with disease localized in the vertebrae is a ^{99m}Tc-MDP scan and ^{67}Ga citrate scanning. In case of spinal osteomyelitis, the ^{99m}Tc-MDP scan will show intense uptake in the affected vertebrae with a reduction of the space between the discs.

In several studies, FDG PET enabled correct visualization of spondylodiscitis (Schmitz et al. 2001; Gratz et al. 2002; Stumpe et al. 2002). FDG PET proved to be superior to MRI, ^{67}Ga citrate scintigraphy and three phase bone scan in these patients (Gratz et al. 2002; Stumpe et al. 2002). FDG PET was also able to differentiate between mild infection and degenerative changes (Stumpe et al. 2002). PET images are not disturbed by the presence of metallic implants, which is a major advantage when compared to CT and MRI. In addition, FDG PET is a very sensitive tool even for chronic and low-grade infections (Guhlmann et al. 1998; Chacko et al. 2003; de Winter et al. 2002).

7.3.3 Pulmonary Infections

^{67}Ga citrate can be used for imaging of suspected pulmonary infections. In these patients the physiological uptake of ^{67}Ga in the gastrointestinal tract will not deteriorate the images. The sensitivity of ^{67}Ga citrate for imaging infections in the chest region is good, but the specificity is relatively low. Furthermore, due to the relatively high radiation burden and the 1- to 3-day delay between injection and imaging time, ^{67}Ga citrate scanning is replaced nowadays by high-resolution chest-CT. Radiolabeled white blood cells can effectively visualize sarcoidosis, interstitial pneumonia, tuberculosis and other pulmonary infections. In many cases radiolabeled white blood cells or ^{67}Ga citrate can also be used to assess the location and extent of disease, differentiating active disease from scar tissue, guiding potential biopsy, and determining recurrence and response to therapy. More recent studies indicate that pulmonary infections can be imaged effectively with FDG PET. Although the differentiation between neoplasm and infection with FDG PET may be difficult, FDG PET has a high sensitivity for imaging a variety of benign pulmonary disorders (Alavi et al. 2002).

7.3.4 Abdominal Infections

Early treatment following rapid and accurate diagnosis of intra-abdominal infections has been shown to improve outcome (Fry et al. 1980; Bohnen et al. 1983; McLauchlan et al. 1995). For this purpose, ultrasonography, computed tomography and magnetic resonance imaging are currently considered the modalities of choice (Montgomery and Wilson 1996). However, in early stages of infections without anatomical changes, or in postoperative patients with equivocal anatomical changes, scintigraphic imaging can be very useful (Gagliardi et al. 1988; Lantto 1994). Although ^{67}Ga citrate has a reasonable diagnostic accuracy for diagnosing abdominal infection, the physiological gastrointestinal uptake of ^{67}Ga citrate limits the interpretation of the images (Staab and McCartney 1978). Therefore ^{67}Ga citrate is not the agent of choice for diagnosing abdominal infections. Radiolabeled white blood cells are the most suitable radiopharmaceutical in these patients. Because ^{111}In-labeled white blood cells normally do not localize in the gastrointestinal tract, they have an advantage over ^{99m}Tc-labeled white blood cells. In a study in 170 patients suspected of abdominal infections who were studied with ultrasound, CT and ^{111}In-white blood cells, white blood cell scanning had a sensitivity of 86% for detecting abdominal abscesses (Knochel et al. 1980). Based on these data the authors recommended that patients who are not critically ill and who have no localizing signs should be studied first with ^{111}In-labeled white blood cells.

7.3.5 Fever of Unknown Origin

In patients with FUO the imaging with radiolabeled white blood cells is not very helpful, because in this patient population only 25%–35% of the

patients actually have an infection (Knockaert et al. 2003). Patients with FUO can be classified into four categories; infections, tumors, noninfectious inflammatory diseases and miscellaneous, and in this subgroup of patients an imaging agent that also gives diagnostic information in the patients without infection is more valuable. Because of the FDG accumulation in inflammatory foci and in a wide range of neoplastic lesions FDG PET appears to be a suitable agent in patients with FUO. The percentage of FDG PET scans helpful in the diagnostic process in patients with FUO varied from 37% to 69% (Bleeker-Rovers et al. 2004; Blockmans et al. 2001; Meller et al. 2000; Lorenzen et al. 2001). In a retrospective study of 16 patients with FUO in whom conventional diagnostics had not been conclusive, Lorenzen et al. (2001) found that FDG PET was helpful in 69%. Meller et al. (2000) prospectively studied the utility of FDG coincidence imaging in 20 patients with FUO. In 55% of these patients FDG PET was helpful in establishing a final diagnosis. Positive predictive value was 90% and negative predictive value was 75% compared to a positive predictive value of ^{67}Ga scintigraphy in the same patients of 75% and a negative predictive value of 70% (Meller et al. 2000). In a prospective study of 58 patients with FUO, Blockmans et al. (2001) demonstrated that FDG PET was helpful in 41% of the patients. ^{67}Ga scintigraphy was only helpful in 25% of a subgroup of 40 patients in the same study (Blockmans et al. 2001). In 35 patients with FUO, we found that FDG PET was helpful in the diagnostic process of 13 patients (37%), while the probability of a diagnosis was 54% (Bleeker-Rovers et al. 2004).

7.3.6 Vascular Graft Infections

In general, to visualize infectious vascular lesions one should preferably use a radiopharmaceutical with a relatively short residence time in the circulation. The background activity of the images obtained with ^{67}Ga and radiolabeled IgGs in many cases is too high for accurate visualization of vascular lesions. Vascular infections can be very accurately detected with radiolabeled white blood cells. In a study in 162 patients with vascular graft infection, the overall sensitivity, specificity, and accuracy of ^{111}In-labeled white blood cells was 100%, 92.5% and 97.5%, respectively (Liberatore et al. 1998). Figure 7.4 shows the extent of a graft infection after clinical diagnosis.

Fig. 7.4. A 61-year-old man with aortobifemoral bypass graft, redness, and swelling of the right inner thigh. The antigranulocyte antibody scan showed a 24-h intensive uptake in the right iliac part of the prosthesis (*top arrowhead*) and a soft tissue uptake (*arrowhead* at lower border of image)

Although so far there is only limited clinical experience FDG PET also appears to be a useful tool to detect vascular infections. Stumpe et al. (2000) studied ten patients with suspected blood vessel graft infection with FDG PET. In five patients with infection, the lesions were successfully identified while the scans in the patients without infection were negative (Stumpe et al. 2000). Similarly, Chacko et al. reported the correct identification of vascular graft infection in three patients with FDG PET (Chacko et al. 2003).

7.3.7 Vasculitis

Vasculitis is a collective noun for a wide range of inflammatory vascular diseases, such as giant cell arteritis, polymyalgia rheumatica, polyarteritis nodosa, Takayasu, Churg-Strauss, Wegener's granulomatosis, vasculitis of the skin, among others. The detection of vascular inflammation and monitoring of the activity of the disease is still a challenging clinical problem. Various radiopharmaceuticals have been tested for the diagnosis of vasculitis. Gallium-67-citrate scintigraphy had a 94% specificity and a 90% positive predictive value in patients with temporal arteritis (Genereau et al. 1999). Reuter et al. (1995) showed that radiolabeled white blood cell scintigraphy was superior to conventional angiography and CT for detecting and monitoring vasculitis of the respiratory tract. In contrast, ^{111}In-white blood cell scintigraphy had a low sensitivity in

patients with Takayasu arteritis (Chen et al. 1995). More recent reports suggest that FDG PET is a useful imaging technique for diagnosing and determining the extent of various forms of vasculitis (Fig. 7.5). In 25 patients with biopsy-proven temporal arteritis or polymyalgia rheumatica Blockmans et al. (2000) found a sensitivity of FDG PET of 56%, a specificity of 98%, a positive predictive value of 93% and a negative predictive value of 80%. Bleeker-Rovers et al. (2003) studied the use of FDG PET in 27 patients suspected of vasculitis. FDG PET results were true positive in ten patients, true negative in 14 patients and false negative in three patients resulting in a positive predictive value of 100% and a negative predictive value of 82%. These recent studies also suggest that FDG PET may become a useful tool for evaluating the effect of treatment of vasculitis.

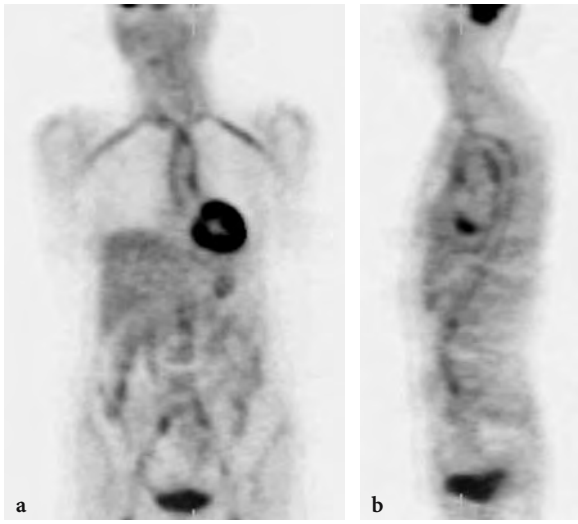

Fig. 7.5. A 64-year-old woman with unexplained weight loss and elevated erythrocyte sedimentation rate. FDG PET showed increased vascular FDG uptake in the thoracic and abdominal aorta, both subclavian, carotid, iliac, and femoral arteries suggesting vasculitis. She was eventually diagnosed with vasculitis and responded well to corticosteroids

7.4 New Radiopharmaceuticals to Image Infection and Inflammation

Each of the radiopharmaceuticals that are currently available for infection imaging has its limitations. The applicability of ^{67}Ga citrate is limited due to the physiological bowel uptake and the high radiation dose. Despite the high diagnostic accuracy of radiolabeled white blood cells, the cumbersome and time-consuming preparation is an important limitation of this radiopharmaceutical. Furthermore, the diagnostic accuracy of radiolabeled anti-granulocyte antibody preparations in various patient populations is insufficient, and FDG PET is not available in the majority of institutions. Therefore, there is still a need for a better agent to image infection or inflammation. Currently this search focuses on agents that avidly bind to cells or receptors expressed on cells involved in inflammatory processes.

During the past two decades various analogues of receptor-binding ligands for receptors expressed on white blood cell subsets have been tested for imaging infection and inflammation. Apart from the defensive proteins in plasma, a large variety of chemical mediators (e.g. interleukins, chemotactic factors, vascular mediators) appear in the affected region that regulate the activity of the immune cells in the region. The immune cells involved (granulocytes, monocytes, and lymphocytes) have specific receptors on their cell surface for these chemical mediators. In general, these chemical mediators have a high affinity for the receptors on the white blood cell plasma membrane. Their high affinity makes these mediators suitable vehicles for the scintigraphic visualization of the homing of white blood cells in infectious and inflammatory foci. Examples of receptor binding peptides under investigation are interleukin-8, platelet-factor 4 and interleukin-2.

Interleukin-8 (IL-8) is a small chemotactic protein, binding with high affinity to receptors on neutrophils (Patel et al. 2001). The potential of radiolabeled IL-8 to image inflammation was reported for the first time by Hay and colleagues (1997). In a pilot study in eight diabetic patients these investigators showed that ^{123}I-IL-8 could visualize active foot infections (Gross et al. 2001). Recently, a ^{99m}Tc-labeled IL-8 preparation using HYNIC as a chelator was developed (Rennen et al. 2001, 2002, 2003). Studies with ^{99m}Tc-IL-8 in patients with infectious and inflammatory disorders are ongoing.

Platelet factor 4 (PF4) is a chemotactic cytokine like IL-8. ^{99m}Tc-labeled P483H, a PF-4 analogue, has been studied in 30 patients to test its applicability as an imaging agent for scintigraphic detection of infection and inflammation with good results (86% sensitivity, 81% specificity, 83% accuracy; Palestro et al. 1999). Due to the high physiological uptake in the lungs, the agent is not suited for detection of pulmonary infections. In addition, in some patients excessive thyroid uptake was observed, which correlated with the peptide:heparin ratio.

Chronic inflammation is characterized by infiltration of monocytes and lymphocytes. Thus to visualize chronic inflammatory processes, ligands of receptors on these mononuclear cells should be applied. Radiolabeled interleukin-2 (IL-2) targets IL-2 receptors expressed on activated T-lymphocytes. ^{123}I-IL-2 has been used successfully in patients with type 1 diabetes (Signore et al. 1996). Studies in patients with autoimmune disorders such as Hashimoto thyroiditis, Graves' disease, Crohn's disease and celiac disease demonstrated localization of ^{123}I- or ^{99m}Tc-labeled IL-2 at the site of lymphocytic infiltration (Signore 1999; Signore et al. 2003). In patients with active Crohn's disease, the focal uptake of ^{123}I-IL-2 in the intestinal wall decreased after corticosteroid therapy, and potentially this technique can be used to monitor the effect of therapy (Signore et al. 2000a). Scintigraphic results using ^{123}I-IL-2 in patients with celiac disease was consistent with the histologically determined number of infiltrating IL-2 receptor-positive cells in the jejunal mucosa (Signore et al. 2000b). ^{99m}Tc-IL-2 also accumulated in the thyroid glands of patients with Hashimoto's thyroiditis and Graves' disease (Signore et al. 2003).

The agents described above have a specific affinity for receptors expressed on cells involved in the inflammatory response, and these agents target the cells infiltrating the inflamed tissue. As these agents accumulate in the focus due to a common feature of infection and inflammation, they can not be used to differentiate between infection and inflammation. Agents that specifically target the infectious organism (e.g. bacteria or fungi) have the potential to distinguish microbial from nonmicrobial inflammation. During the last decade a few agents have been presented that aim to specifically visualize infectious foci by targeting the infectious organism, the most intensively studied agent being Infecton. Infecton is ciprofloxacin labeled with ^{99m}Tc. Ciprofloxacin is a fluoroquinolone antimicrobial agent that binds to prokaryotic topoisomerase IV and DNA gyrase as expressed in proliferating bacteria (Anderson and Osheroff 2001; Pan et al. 2001). It has been hypothesized that ^{99m}Tc-labeled ciprofloxacin could specifically target living bacteria in vivo and thus that Infecton is able to specifically visualize bacterial infection. The first results obtained with Infecton in 56 patients with known or suspected sites of infection suggested that Infecton had a high sensitivity (84%) to visualize infection (Vinjamuri et al. 1996). The efficacy of Infecton for imaging infections was evaluated in 879 patients in a large multicenter study. The overall sensitivity and specificity for infection were 85.5% and 81.6%, respectively (Britton et al. 2002). Despite these impressive figures from this large multinational study, several reports dispute the claim that Infecton only visualizes bacterial infection. Firstly, the specific interaction of Infecton with living bacteria as opposed to dead bacteria, fungi, or white blood cells could not be demonstrated in vitro (Welling et al. 2000). Secondly, in rabbits with infected and uninfected knee prostheses, increased ^{99m}Tc-ciprofloxacin uptake was also observed in rabbits with noninfected knee implants (Sarda et al. 2002). Lastly, in 71 patients suspected of osteomyelitis (n=30) or septic arthritis (n=41), the specificity of the Infecton scan was very low (50% and 57%, respectively) (Dumarey et al. 2002). The clinical usefulness of Infecton as an imaging agent to discriminate bacterial infection from other disease is currently under investigation in a large clinical trial, using an improved formulation of ^{99m}Tc-ciprofloxacin.

7.5 Conclusions

Scintigraphy using autologous white blood cells, labeled with ^{111}In or ^{99m}Tc, is still considered the "gold standard" nuclear medicine technique for the imaging of infection and inflammation for its excellent diagnostic accuracy. However, ^{67}Ga citrate is still the agent of choice for several indications, while antigranulocyte antibodies may provide an alternative for in-vitro labeled white blood cells. New developments show a gradual shift from basic, nonspecific, cumbersome, and even hazardous techniques to more intelligent approaches, based on small agents binding to their targets with high affinity. In general, the lower molecular weight should also lead to enhanced blood clearance reducing blood pool activity. New agents should also obviate the need to handle blood as this presents potential hazards of transmission of hepatitis virus or human immunodeficiency virus to both patients and medical personnel. Radiolabeled compounds are being designed enabling specific distinction between infection and noninfectious inflammatory disease and between acute and chronic processes. The ideal agent will thus be determined by the clinical situation. The advantages of ^{99m}Tc as a radionuclide will be fully explored. FDG PET may become as useful in the rapid detection and management of infectious and inflammatory diseases as it is in the management of malignant diseases.

References

Alavi A, Gupta N, Alberini JL, Hickeson M, Adam LE, Bhargava P, Zhuang H (2002) Positron emission tomography imaging in nonmalignant thoracic disorders. Semin Nucl Med 32:293–321

Anderson VE, Osheroff N (2001) Type II topoisomerases as targets for quinolone antibacterials: turning Dr. Jekyll into Mr. Hyde. Curr Pharm Des 7:337–353

Barron B, Hanna C, Passalaqua AM, Lamki L, Wegener WA, Goldenberg DM (1999) Rapid diagnostic imaging of acute, nonclassic appendicitis by leukoscintigraphy with sulesomab, a technetium 99m labeled antigranulocyte antibody Fab' fragment. Surgery 125:288–296

Becker W, Bair J, Behr T et al (1994a) Detection of soft-tissue infections and osteomyelitis using a technetium-99m-labeled anti-granulocyte monoclonal antibody fragment. J Nucl Med 35:1436–1443

Becker W, Goldenberg DM, Wolf F (1994b) The use of monoclonal antibodies and antibody fragments in the imaging of infectious lesions. Semin Nucl Med 24:142–153

Becker W, Palestro CJ, Winship J, Feld T, Pinsky CM, Wolf F, Goldenberg DM (1996) Rapid imaging of infections with a monoclonal antibody fragment (Leukoscan). Clin Orthop 329:263–272

Bekerman C, Hoffer PB, Bitran JD (1984) The role of gallium-67 in the clinical evaluation of cancer. Semin Nucl Med 14:296–323

Bleeker-Rovers CP, Bredie SJH, van der Meer JWM, Corstens FHM, Oyen WJG (2003) F-18-fluorodeoxyglucose positron emission tomography in diagnosis and follow-up of patients with different types of vasculitis. Nether J Med 61:323–329

Bleeker-Rovers CP, de Kleijn EM, Corstens FH, van der Meer JW, Oyen WJ (2004) Clinical value of FDG PET in patients with fever of unknown origin and patients suspected of focal infection or inflammation. Eur J Nucl Med Mol Imaging 31:29–37

Blockmans D, Stroobants S, Maes A, Mortelmans L (2000) Positron emission tomography in giant cell arteritis and polymyalgia rheumatica: evidence for inflammation of the aortic arch. Am J Med 108:246–249

Blockmans D, Knockaert D, Maes A, de Caestecker J, Stroobants S, Bobbaers H, Mortelmans L (2001) Clinical value of [18F]fluoro-deoxyglucose positron emission tomography for patients with fever of unknown origin. Clin Infect Dis 32:191–196

Bohnen J, Boulanger M, Meakins JL, McLean AP (1983) Prognosis in generalized peritonitis: relation to cause and risk factors. Arch Surg 118:285–290

Boubaker A, Delaloye AB, Blanc CH et al (1995) Immunoscintigraphy with antigranulocyte monoclonal antibodies for the diagnosis of septic loosening of hip prostheses. Eur J Nucl Med 22:139–147

Britton KE, Wareham DW, Das SS, Solanki KK, Amaral H, Bhatnagar A, Katamihardja AH, Malamitsi J, Moustafa HM, Soroa VE, Sundram FX, Padhy AK (2002) Imaging bacterial infection with (99m)Tc-ciprofloxacin (Infecton). J Clin Pathol 55:817–823

Chacko TK, Zhuang H, Nakhoda KZ, Moussavian B, Alavi A (2003) Applications of fluorodeoxyglucose positron emission tomography in the diagnosis of infection. Nucl Med Commun 24:615–624

Charron M, di Lorenzo C, Kocoshis SA et al (2001) (99m)Tc antigranulocyte monoclonal antibody imaging for the detection and assessment of inflammatory bowel disease newly diagnosed by colonoscopy in children. Pediatr Radiol 31:796–800

Chen CC, Kerr GS, Carter CS et al (1995) Lack of sensitivity of indium-111 mixed white blood cell scans for active disease in Takayasu's arteritis. J Rheumatol 22:478–481

Datz FL, Thorne DA (1986) Effect of chronicity of infection on the sensitivity of the In-111-labeled white blood cell scan. AJR Am J Roentgenol 147:809–812

De Winter F, Vogelaers D, Gemmel F, Dierckx RA (2002) Promising role of 18-F-fluoro-D-deoxyglucose positron emission tomography in clinical infectious diseases. Eur J Clin Microbiol Infect Dis 21:247–257

Devillers A, Garin E, Polard JL et al (2000) Comparison of Tc-99m-labelled antiwhite blood cell fragment Fab' and Tc-99m- HMPAO white blood cell scintigraphy in the diagnosis of bone and joint infections: a prospective study. Nucl Med Commun 21:747–753

Dominguez-Gadea L, Martin-Curto LM, de la CH, Crespo A (1993) Diabetic foot infections: scintigraphic evaluation with 99Tcm-labelled anti-granulocyte antibodies. Nucl Med Commun 14:212–218

Dumarey N, Blocklet D, Appelboom T, Tant L, Schoutens A (2002) Infecton is not specific for bacterial osteo-articular infective pathology. Eur J Nucl Med Mol Imaging 2:530–535

Fleury HJ, Pinson P, Faure M et al (2003) HIV-1 transmission during scintigraphy. Lancet 362:210

Fry DE, Garrison RN, Heitsch RD, Calhoun K, Polk HC Jr (1980) Determinants of death in patients with intra-abdominal abscess. Surgery 88:517–523

Gagliardi PD, Hoffer PB, Rosenfield AT (1988) Correlative imaging in abdominal infection: an algorithmic approach using nuclear medicine, ultrasound, and computed tomography. Semin Nucl Med 18:320–334

Genereau T, Lortholary O, Guillevin L, Cacoub P, Galezowski N, Cherin P, Babinet P, Herreman G, Wechsler B, Cohen P, Herson S, Caillat-Vigneron N (1999) Temporal 67gallium uptake is increased in temporal arteritis. Rheumatology (Oxf) 38:709–713

Gratz S, Braun HG, Behr TM et al (1997) Photopenia in chronic vertebral osteomyelitis with technetium-99m-antigranulocyte antibody (BW 250/183). J Nucl Med 38:211–216

Gratz S, Behr TM, Herrmann A et al (1998) Immunoscintigraphy (BW 250/183) in neonates and infants with fever of unknown origin. Nucl Med Commun 19:1037–1045

Gratz S, Raddatz D, Hagenah G et al (2000) 99mTC-labelled antigranulocyte monoclonal antibody FAB' fragments versus echocardiography in the diagnosis of subacute infective endocarditis. Int J Cardiol 75:75–84

Gratz S, Dorner J, Fischer U, Behr TM, Behe M, Altenvoerde G, Meller J, Grabbe E, Becker W (2002) 18F-FDG hybrid PET in patients with suspected spondylitis. Eur J Nucl Med Mol Imaging 29:516–524

Gratz S, Schipper ML, Dorner J et al (2003) LeukoScan for imaging infection in different clinical settings: a retrospective evaluation and extended review of the literature. Clin Nucl Med 28:267–276

Gross MD, Shapiro B, Fig LM, Steventon R, Skinner RW, Hay

RV (2001) Imaging of human infection with 131I-labeled recombinant human interleukin-8. J Nucl Med 42:1656–1659

Guhlmann A, Brecht-Krauss D, Suger G, Glatting G, Kotzerke J, Kinzl L, Reske SN (1998) Fluorine-18-FDG PET and technetium-99m antigranulocyte antibody scintigraphy in chronic osteomyelitis. J Nucl Med 39:2145–2152

Gyorke T, Duffek L, Bartfai K et al (2000) The role of nuclear medicine in inflammatory bowel disease. A review with experiences of aspecific bowel activity using immunoscintigraphy with 99mTc anti-granulocyte antibodies. Eur J Radiol 35:183–192

Hakki S, Harwood SJ, Morrissey MA et al (1997) Comparative study of monoclonal antibody scan in diagnosing orthopaedic infection. Clin Orthop Feb(335):275–285

Hanssen AD, Rand JA (1998) Evaluation and treatment of infection at the site of a total hip or knee arthroplasty. J Bone Joint Surg Am 80:910–922

Harris WH, Sledge CB (1990) Total hip and total knee replacement (2). N Engl J Med 323:801–807

Harwood SJ, Valdivia S, Hung GL, Quenzer RW (1999) Use of Sulesomab, a radiolabeled antibody fragment, to detect osteomyelitis in diabetic patients with foot ulcers by leukoscintigraphy. Clin Infect Dis 28:1200–1205

Hay RV, Skinner RS, Newman OC, Kunkel SL, Lyle LR, Shapiro B, Gross MD (1997) Scintigraphy of acute inflammatory lesions in rats with radiolabelled recombinant human interleukin-8. Nucl Med Commun 18:367–378

Hoffer P (1980) Gallium: mechanisms. J Nucl Med 21:282–285

Ivancevic V, Wolter A, Munz DL (2001) Nonspecific bowel activity in imaging inflammation with Tc-99m labelled monoclonal anti-NCA-90 Fab' fragment MN3. Nuklearmedizin 40:71–74

Ivancevic V, Perka C, Hasart O et al (2002) Imaging of low-grade bone infection with a technetium-99m labelled monoclonal anti-NCA-90 Fab' fragment in patients with previous joint surgery. Eur J Nucl Med Mol Imaging 29:547–551

Joseph K, Hoffken H, Bosslet K, Schorlemmer HU (1988) In vivo labelling of granulocytes with 99mTc anti-NCA monoclonal antibodies for imaging inflammation. Eur J Nucl Med 14:367–373

Kalicke T, Schmitz A, Risse JH, Arens S, Keller E, Hansis M, Schmitt O, Biersack HJ, Grunwald F (2000) Fluorine-18 fluorodeoxyglucose PET in infectious bone diseases: results of histologically confirmed cases. Eur J Nucl Med 27:524–528

Kipper SL, Rypins EB, Evans DG, Thakur ML, Smith TD, Rhodes B (2000) Neutrophil-specific 99mTc-labeled anti-CD15 monoclonal antibody imaging for diagnosis of equivocal appendicitis. J Nucl Med 41:449–455

Kjaer A, Lebech A, Eigtved A, Højgaard L (2004) Fever of unknown origin: prospective comparison of diagnostic value of 18F-FDG PET and 111In-granulocyte scintigraphy. Eur J Nucl Med Mol Imaging 31:622–626

Klett R, Kordelle J, Stahl U et al (2003) Immunoscintigraphy of septic loosening of knee endoprosthesis: a retrospective evaluation of the antigranulocyte antibody BW 250/183. Eur J Nucl Med Mol Imaging 30:1463–1466

Knochel JQ, Koehler PR, Lee TG, Welch DM (1980) Diagnosis of abdominal abscesses with computed tomography, ultrasound, and 111In white blood cell scans. Radiology 137:425-432

Knockaert DC, Mortelmans LA, de Roo MC, Bobbaers HJ (1994) Clinical value of gallium-67 scintigraphy in evaluation of fever of unknown origin. Clin Infect Dis 18:601–605

Knockaert DC, Vanderschueren S, Blockmans D (2003;Fever of unknown origin in adults: 40 years on. J Intern Med 253:263–275

Lange JM, Boucher CA, Hollak CE et al (1990) Failure of zidovudine prophylaxis after accidental exposure to HIV-1. N Engl J Med 322:1375–1377

Lantto E (1994) Investigation of suspected intra-abdominal sepsis: the contribution of nuclear medicine. Scand J Gastroenterol 29 [Suppl 203]:11–14

Larikka MJ, Ahonen AK, Junila JA et al (2001) Extended combined 99mTc-white blood cell and bone imaging improves the diagnostic accuracy in the detection of hip replacement infections. Eur J Nucl Med 28:288–293

Liberatore M, Iurilli AP, Ponzo F, Prosperi D, Santini C, Baiocchi P, Rizzo L, Speziale F, Fiorani P, Colella AC (1998) Clinical usefulness of technetium-99m-HMPAO-labeled white blood cell scan in prosthetic vascular graft infection. J Nucl Med 39:875–879

Lind P, Langsteger W, Koltringer P et al (1990) Immunoscintigraphy of inflammatory processes with a technetium-99m-labeled monoclonal antigranulocyte antibody (MAb BW 250/183). J Nucl Med 31:417–423

Lipp RW, Wirnsberger GH, Ratschek M et al (1996) The influence of vascular diathesis on the localization of inflammatory foci in renal allografts with a specific antigranulocyte antibody. Eur J Nucl Med 23:395–400

Lorenzen J, Buchert R, Bohuslavizki KH (2001) Value of FDG PET in patients with fever of unknown origin. Nucl Med Commun 22:779–783

Love C, Pugliese PV, Afriyie MO, Tomas MB, Marwin SE, Palestro CJ (2000) Utility of F-18 FDG imaging for diagnosing the infected joint replacement. Clin Positron Imaging 3:159

Love C, Tomas MB, Marwin SE, Pugliese PV, Palestro CJ (2001) Role of nuclear medicine in diagnosis of the infected joint replacement. Radiographics 21:1229–1238

Maugeri D, Santangelo A, Abbate S et al (2001) A new method for diagnosing fever of unknown origin (FUO) due to infection of muscular-skeletal system in elderly people: leukoscan Tc-99m labelled scintigraphy. Eur Rev Med Pharmacol Sci 5:123–126

McAfee JG, Thakur ML (1976) Survey of radioactive agents for the in vitro labeling of phagocytic leucocytes. I. Soluble agents. II. Particles. J Nucl Med17:480–492

McLauchlan GJ, Anderson ID, Grant IS, Fearon KCH (1995) Outcome of patients with abdominal sepsis treated in an intensive care unit. Br J Surg 82:524–529

Meller J, Altenvoerde G, Munzel U, Jauho A, Behe M, Gratz S, Luig H, Becker W (2000) Fever of unknown origin: prospective comparison of [18F]FDG imaging with a double-head coincidence camera and gallium-67 citrate SPET. Eur J Nucl Med 27:1617–1625

Montgomery RS, Wilson SE (1996) Intraabdominal abscesses: image-guided diagnosis and therapy. Clin Infect Dis 23:28–36

Morguet AJ, Munz DL, Ivancevic V et al (1994) Immunoscintigraphy using technetium-99m-labeled anti-NCA-95 antigranulocyte antibodies as an adjunct to echocardiography in subacute infective endocarditis. J Am Coll Cardiol 23:1171–1178

Palestro CJ (1994) The current role of gallium imaging in infection. Semin Nucl Med 24:128–141
Palestro CJ, Torres MA (1997) Radionuclide imaging in orthopedic infections. Semin Nucl Med 27:334–345
Palestro CJ, Swyer AJ, Kim CK, Goldsmith SJ (1991) Infected knee prostheses: diagnosis with In-111 white blood cell, Tc-99m sulfur colloid, and Tc-99m MDP imaging. Radiology 179:645–648
Palestro CJ, Tomas MB, Bhargava KK, Afriyie MO, Nicodemus CF, Lister-James J, Dean RT (1999) Tc-99m P483H for imaging infection: phase 2 multicenter trial results. J Nucl Med 40:15P
Pan XS, Yague G, Fisher LM (2001) Quinolone resistance mutations in Streptococcus pneumoniae GyrA and ParC proteins: mechanistic insights into quinolone action from enzymatic analysis, intracellular levels, and phenotypes of wild-type and mutant proteins. Antimicrob Agents Chemother 45:3140–3147
Papos M, Nagy F, Narai G et al (1996) Anti-granulocyte immunoscintigraphy and [99mTc]hexamethylpropyleneamineoxime-labeled white blood cell scintigraphy in inflammatory bowel disease. Dig Dis Sci 41:412–420
Patel L, Charlton SJ, Chambers JK, Macphee CH (2001) Expression and functional analysis of chemokine receptors in human peripheral blood white blood cell populations. Cytokine 14:27–36
Peltier P, Potel G, Lovat E et al (1993) Detection of lung and bone infection with anti-granulocyte monoclonal antibody BW 250/183 radiolabelled with 99Tcm. Nucl Med Commun 14:766–774
Perkins PJ (1981) Early gallium-67 abdominal imaging: pitfalls due to bowel activity. AJR Am J Roentgenol 136:1016–1017
Peters AM (1994) The utility of [99mTc]HMPAO-white blood cells for imaging infection. Semin Nucl Med 24:110–127
Peters AM, Danpure HJ, Osman S et al (1986) Clinical experience with 99mTc-hexamethylpropylene-amineoxime for labelling leucocytes and imaging inflammation. Lancet 2:946–949
Prvulovich EM, Miller RF, Costa DC et al (1995) Immunoscintigraphy with a 99Tcm-labelled anti-granulocyte monoclonal antibody in patients with human immunodeficiency virus infection and AIDS. Nucl Med Commun 16:838–845
Rennen HJ, Boerman OC, Oyen WJG, van der Laken CJ, Corstens FHM (2001) Specific and rapid scintigraphic detection of infection with Tc-99m-labeled interleukin-8. J Nucl Med 42:117–123
Rennen HJ, van Eerd JE, Oyen WJ, Corstens FH, Edwards DS, Boerman OC (2002) Effects of coligand variation on the in vivo characteristics of Tc-99m-labeled interleukin-8 in detection of infection. Bioconjug Chem 13:370–377
Rennen HJ, Boerman OC, Oyen WJ, Corstens FH (2003) Kinetics of 99mTc-labeled interleukin-8 in experimental inflammation and infection. J Nucl Med 44:1502–1509
Reuter H, Wraight EP, Qasim FJ, Lockwood CM (1995) Management of systemic vasculitis: contribution of scintigraphic imaging to evaluation of disease activity and classification. QJM 88:509–516
Roitt IM (1997) Essential immunology, 9th edn. Blackwell Scientific, Oxford
Ryan PJ (2002) Leukoscan for orthopaedic imaging in clinical practice. Nucl Med Commun 23:707–714
Rypins EB, Kipper SL (2000) Scintigraphic determination of equivocal appendicitis. Am Surg 66:891–895
Sarda L, Saleh-Mghir A, Peker C, Meulemans A, Cremieux AC, Le Guludec D (2002) Evaluation of (99m)Tc-ciprofloxacin scintigraphy in a rabbit model of Staphylococcus aureus prosthetic joint infection. J Nucl Med 43:239–245
Scheidler J, Leinsinger G, Pfahler M, Kirsch CM (1994) Diagnosis of osteomyelitis. Accuracy and limitations of antigranulocyte antibody imaging compared to three-phase bone scan. Clin Nucl Med 19:731–737
Schmitz A, Risse JH, Grunwald F, Gassel F, Biersack HJ, Schmitt O (2001) Fluorine-18 fluorodeoxyglucose positron emission tomography findings in spondylodiscitis: preliminary results. Eur Spine J 10:534–539
Segarra I, Roca M, Baliellas C et al (1991) Granulocyte-specific monoclonal antibody technetium-99m-BW 250/183 and indium-111 oxine-labelled leucocyte scintigraphy in inflammatory bowel disease. Eur J Nucl Med 18:715–719
Signore A (1999) Interleukin-2 scintigraphy: an overview. Nucl Med Commun 20:938
Signore A, Picarelli A, Chianelli M, Biancone L, Annovazzi A, Tiberti C, Anastasi E, Multari G, Negri M, Pallone F, Pozzilli P (1996) I-interleukin-2 scintigraphy: a new approach to assess disease activity in autoimmunity. J Pediatr Endocrinol Metab 9 [Suppl 1]:139–144
Signore A, Chianelli M, Annovazzi A et al (2000a) 123I-interleukin-2 scintigraphy for in vivo assessment of intestinal mononuclear cell infiltration in Crohn's disease. J Nucl Med 41:242–249
Signore A, Chianelli M, Annovazzi A, Rossi M, Maiuri L, Greco M, Ronga G, Britton KE, Picarelli A (2000b) Imaging active lymphocytic infiltration in coeliac disease with iodine- 123-interleukin-2 and the response to diet. Eur J Nucl Med 27:18–24
Signore A, Annovazzi A, Corsetti F et al (2002) Biological imaging for the diagnosis of inflammatory conditions. BioDrugs 16:241–259
Signore A, Picarelli A, Annovazzi A, Britton KE, Grossman AB, Bonanno E, Maras B, Barra D, Pozzilli P (2003) 123I-Interleukin-2: biochemical characterization and in vivo use for imaging autoimmune diseases. Nucl Med Commun 24:305–316
Skehan SJ, White JF, Evans JW, Parry-Jones DR, Solanki CK, Ballinger JR, Chilvers ER, Peters AM (2003) Mechanism of accumulation of 99mTc-sulesomab in inflammation. J Nucl Med 44:11–18
Staab EV, McCartney WH (1978) Role of 67Ga in inflammatory disease. Semin Nucl Med 8:219–234
Steinstrasser A, Oberhausen E (1996) Granulocyte labelling kit BW 250/183 – results of the European multicenter trial. Nuklearmedizin 35:1–11
Stokkel MP, Reigman HE, Pauwels EK (2002) Scintigraphic head-to-head comparison between 99mTc-WBCs and 99mTc-LeukoScan in the evaluation of inflammatory bowel disease: a pilot study. Eur J Nucl Med Mol Imaging 29:251–254
Stumpe KD, Dazzi H, Schaffner A, von Schulthess GK (2000) Infection imaging using whole-body FDG-PET. Eur J Nucl Med 27:822–832
Stumpe KD, Zanetti M, Weishaupt D, Hodler J, Boos N, von Schulthess GK (2002) FDG positron emission tomography for differentiation of degenerative and infectious endplate abnormalities in the lumbar spine detected on MR imaging. AJR Am J Roentgenol 179:1151–1157

Tahara T, Ichiya Y, Kuwabara Y et al (1989) High [18F]-fluorodeoxyglucose uptake in abdominal abscesses: a PET study. J Comput Assist Tomogr 13:829–831

Thakur ML, McAfee JG (1984) The significance of chromosomal aberrations in indium-111-labeled lymphocytes. J Nucl Med 25:922–927

Thakur ML, Marcus CS, Henneman P, Butler J, Sinow R, Diggles L, Minami C, Mason G, Klein S, Rhodes B (1996) Imaging inflammatory diseases with neutrophil-specific technetium-99m-labeled monoclonal antibody anti-SSEA-1. J Nucl Med 37:1789–1795

Thakur ML, Marcus CS, Kipper SL et al (2001) Imaging infection with LeuTech. Nucl Med Commun 22:513–519

Vinjamuri S, Hall AV, Solanki KK, Bomanji J, Siraj Q, O'Shaughnessy E, Das SS, Britton KE (1996) Comparison of 99mTc Infecton imaging with radiolabelled white-cell imaging in the evaluation of bacterial infection. Lancet 347:233–235

Weiner R (1990) The role of transferrin and other receptors in the mechanism of 67Ga localization. Int J Rad Appl Instrum B 17:141–149

Welling MM, Nibbering PH, Paulusma-Annema A, Hiemstra PS, Pauwels EKJ, Calame W (2000) Reply to letter to the editor. J Nucl Med 41:2099–2102

Zhuang H, Alavi A (2002) 18-fluorodeoxyglucose positron emission tomographic imaging in the detection and monitoring of infection and inflammation. Semin Nucl Med 32:47–59

Zhuang H, Duarte PS, Pourdehand M, Shnier D, Alavi A (2000) Exclusion of chronic osteomyelitis with F-18 fluorodeoxyglucose positron emission tomographic imaging. Clin Nucl Med 25:281–284

Zhuang H, Duarte PS, Pourdehnad M, Maes A, van Acker F, Shnier D, Garino JP, Fitzgerald RH, Alavi A (2001) The promising role of 18F-FDG PET in detecting infected lower limb prosthesis implants. J Nucl Med 42:44–48

8 Gastrointestinal Nuclear Medicine

Jean-Luc C. P. Urbain

CONTENTS

8.1 Esophageal Transit Scintigraphy

8.1.1 Introduction

Esophageal transit scintigraphy is typically performed after a 4- to 6-h fasting period. Medications affecting esophageal motility should be discontinued for at least 24 h. Water is the preferred bolus material because it is homogeneous and does not disperse along the esophagus. Technetium-99m sulfur colloid is the radiotracer of choice. It is inexpensive, easily prepared, optimally detected by the Anger camera and neither secreted nor absorbed by the esophageal mucosa. However, in multiple swallow studies, its use is limited by scattered radiation from the stomach.

Typically, a water bolus of 10–20 ml, labeled with 7.5 Mbq (200 μCi) of ^{99m}Tc-sulfur colloid is given to the patient. Practice swallows with normal water are recommended to educate the patient to swallow the labeled bolus in a single gulp.

8.1.2 Acquisition Procedure

The patient is positioned supine under the camera in order to eliminate the effect of gravity. The upright position is used only to evaluate the effectiveness of medications or surgical procedures. In both instances, the mouth, esophagus and proximal stomach are visualized in a single field of view.

Anterior imaging is usually performed. The bolus material is administered to the patient with a syringe or a straw, and swallowed in one gulp. In a multiple swallow test, 4–6 bolus swallows are recommended to decrease the intraindividual variations in esophageal transit time.

In order to adequately assess motility, we acquire a total of 140 dynamic 64×64 pixel images in two steps: first, 120 images of 0.25 s followed by 20 images of 30 s each. After the initial bolus swallow, the patient takes "dry swallows" every 30 s to assess the residual activity in the esophagus. In patients with significant stasis, delayed images are taken at 15 and 30 min.

8.1.3 Analysis and Quantification

Time-activity curves are generated by drawing regions of interest around the upper, mid and lower segments of the esophagus (Fig. 8.1). Global esophageal transit is calculated using the following formula:

J.-L. C. P. Urbain, MD, PhD
Department of Nuclear Medicine, St. Joseph's Health Centre, The University of Western Ontario, 268 Grosvenor St., London, Ontario N6A 4V2, Canada

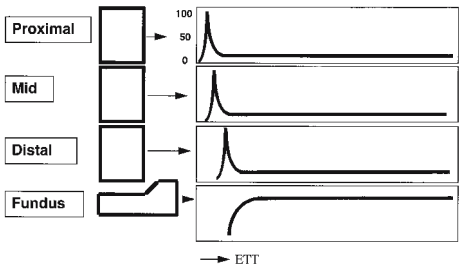

Fig. 8.1. Processing of esophageal transit scintigraphy. Regions of interest are drawn around the upper, middle, and lower third of the esophagus and a time activity curve is generated for each segment. A curve of fundal activity can also be generated. Esophageal transit line represents the time required for the bolus to transit from the upper esophageal sphincter to the fundus

$$C(t) = 100 \times (Emax - E(t)) / Emax \quad (1)$$

In Eq. 1, C(t) is the percent esophageal emptying at time (t), Emax is the maximal count rate in the esophagus, E(t) is the esophageal count rate at time (t) (Tolin et al. 1979). Both global or segmental esophageal transits can be assessed using different parameters, such as the esophageal transit time (ETT), segmental emptying time, global esophageal emptying time, esophagogastric transit time (Taillefer and Beauchamp 1984).

Different methods have been introduced to integrate data obtained from multiple swallows, facilitate the qualitative assessment of radionuclide esophageal transit and improve the diagnostic ability of esophageal motor disorders. The technique of "condensed images" displays in one single image, the spatial distribution of the radioactive bolus along the esophagus path (Klein 1986). Another method integrates the dynamic sequences into a single condensed image to represent average esophageal transit of multiple boluses (Tatsch 1992).

8.1.4 Visualization and Interpretation

Completeness of bolus ingestion, progression through the esophagus, retention in the esophagus or gastroesophageal reflux are first assessed by cine display of the images.

In normal individuals, the esophageal transit time for a liquid bolus is less than 10 s. The condensed picture shows a smooth progression of the bolus along the esophagus, with a physiologic deceleration in its mid portion due to the aortic arch.

8.1.5 Clinical Applications

The role of scintigraphy is to provide a physiological, quantitative and non invasive evaluation of suspected esophageal motor disorders, before and after medical or surgical treatment.

Achalasia: This disorder is characterized by a marked, prolonged and chaotic retention of the tracer in the distal segment of the esophagus with very little passage into the stomach.

Diffuse esophageal spasm: There is a prolonged transit time associated with decreased segmental esophageal emptying, periods of esophageal retrograde motion and fragmentation of the tracer. Time-activity curves show multiple peaks of activity in all esophageal segments.

Nutcracker esophagus: This disorder is characterized by high amplitude esophageal contractions and shows a prolonged retention of activity in the distal esophagus and a mild distal to mid esophagus esophageal reflux. However, since the esophageal contractions are peristaltic, scintigraphy can be entirely normal.

Non specific motor disorders: The most common finding is a prolonged esophageal transit time with an uncoordinated pattern.

Neuromuscular and connective tissue disorders: Radionuclide esophageal transit is the only test to assess early involvement of the esophagus by progressive systemic sclerosis and is typically characterized by stagnation of the tracer in the lower two-thirds of the esophagus. This retention can be cleared by increasing the pressure in the esophagus either by the upright position or a glass of water.

Miscellaneous: Radionuclide esophageal transit is the only test which allows for the physiologic quantitative evaluation of esophageal motility before and after surgical treatment for hiatal hernia and reflux and for the assessment of the transposed stomach or colon after esophagectomy.

8.2 Gastric Emptying Scintigraphy

8.2.1 Introduction

Introduced more than 30 years ago, gastric emptying scintigraphy has been significantly refined and optimized over the years. The simultaneous mea-

surement of solid and liquid emptying by scintigraphy is now well established as the "gold standard" method to evaluate gastric emptying.

Conventional gastric emptying is a simple procedure which measures the transit of a standardized radiolabeled test meal through the stomach; it requires static imaging at defined time intervals, minimal processing and analysis. Hereafter, we present the technique employed at our institution. Conventional gastric emptying provides little information on gastric physiology and pathophysiology. Over the past 10 years, mathematical modeling of the gastric emptying curves, compartmental analysis of the stomach and later, dynamic antral scintigraphy (DAS) have provided new tools to evaluate the pathophysiology of gastric motors disorders.

8.2.2 Standard Gastric Emptying Procedure

Gastric emptying is performed after a 12-h overnight fast and discontinuation of any medication likely to interfere with gastric motility. Patients should refrain from smoking since it may delay gastric evacuation. Diabetic patients should be studied early in the morning, after receiving two thirds of their usual insulin dose. There is currently no consensus on the optimal test meal to study gastric emptying. However, radiolabeled eggs, which are readily available, easy to prepare and stably labeled are used in most nuclear medicine laboratories. The eggs are mixed with 20–40 Mbq (0.5–1.0 mCi) ^{99m}Tc sulfur colloid, cooked till firm in a Teflon-coated pan, and given to the patient as an egg sandwich. To evaluate liquid emptying, water is labeled with 3 Mbq (75 μCi) of ^{111}In-DTPA. Ingestion of the test meal should be completed within 10 min.

Imaging is preferably performed with the subject sitting or standing. A ^{57}Co marker placed on the xiphoid process or iliac crest facilitates repositioning of the patient and automated processing.

8.2.2.1 Acquisition

Immediately after the completion of the meal, the patient is positioned in front of the camera fitted with a medium-energy parallel-hole collimator. An initial 1-min image of the stomach is acquired in the 140 keV±20% technetium window. The patient then ingests the water and a second 1-min image is taken in the technetium window to calculate the downscatter percentage of indium into the technetium window. Simultaneous anterior and posterior static images (dual head system), or an anterior, immediately followed by a posterior view (single head system) of the stomach are taken in a 64×64 or 128×128 matrix in the technetium and indium windows at regular time intervals up to 50% emptying.

Depth attenuation must be corrected for by calculation of the geometric mean (i.e., the square root of the anterior activity multiplied by the posterior activity) of gastric counts. Counts are then decay and downscatter corrected, and normalized to 100% based on total gastric counts obtained immediately following ingestion of the meal (time t = 0). Solid and liquid data are then plotted as percentage retention of food in the stomach over time.

8.2.2.2 Visual Assessment and Quantification

In normal subjects, immediately after meal ingestion, both solid and liquid phases are retained in the proximal stomach. Water distributes then uniformly throughout the stomach and is rapidly emptied into the duodenum. In contrast, solids move progressively from the proximal to the distal stomach where they are ground and slowly emptied into the duodenum (Fig. 8.2).

Measurement of the half emptying time ($T_{1/2}$), or time required by the stomach to empty 50% of the ingested meal, is the simplest way to assess gastric transit. It is routinely and commonly used for clinical evaluation.

8.2.2.3 Modeling of Gastric Emptying Curves

Liquid emptying curves are usually adequately described by the single exponential function:

$$y(t) = e^{-kt} \quad (2)$$

In Eq. 2, y(t) is the fractional meal retention at time t, and k the emptying rate in min^{-1}. T1/2 is equal to 0.693 k.

Gastric emptying of solids is sigmoid in shape and characterized by an initial shoulder with little emptying ("lag phase" or Tlag), followed by a pro-

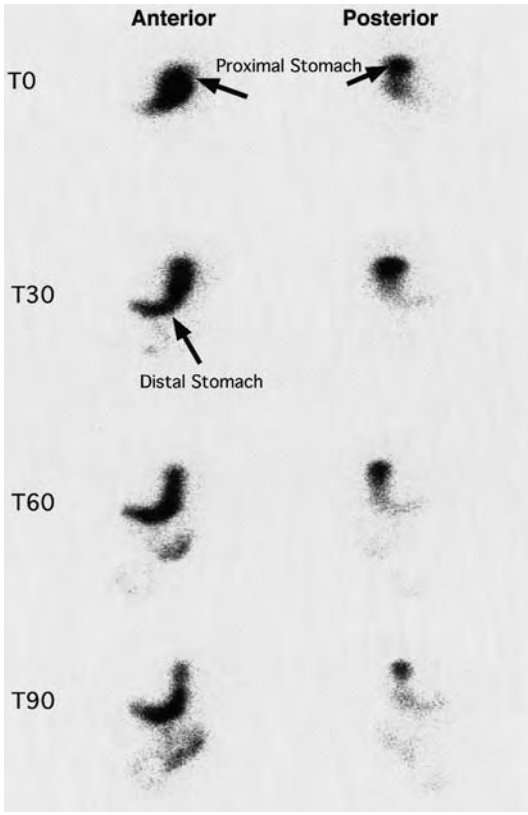

Fig. 8.2. Gastric emptying of solids. Anterior and posterior projections of the stomach are displayed immediately (T_0), 30 min (T_{30}), 60 min (T_{60}), and 90 min (T_{90}) after meal completion. Initially, solid food is stored in the proximal portion of the stomach. Over time, the solid particles move to the distal portion of the stomach for grinding and emptying into the duodenum through the pylorus

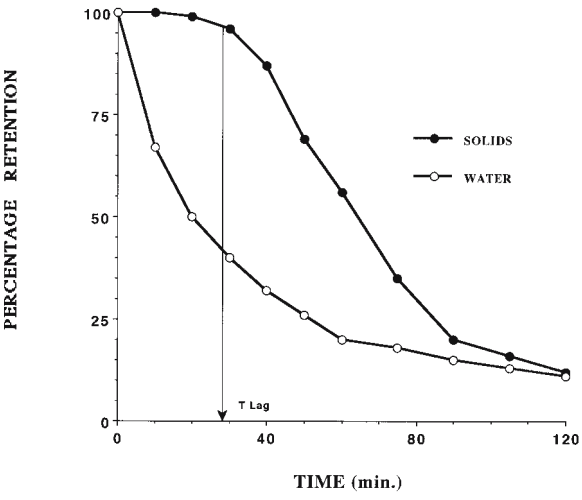

Fig. 8.3. Gastric emptying curves for solids and liquids. A liquid emptying curve follows a mono-exponential pattern. A solid emptying curve is sigmoidal in shape with an initial plateau (lag phase) followed by a linear emptying phase and a late slower portion

longed linear phase and finally a much slower phase (Fig. 8.3). The lag phase corresponds qualitatively and quantitatively to the redistribution of solid food particles from the fundus to the distal stomach and more specifically to the time to peak activity in the distal stomach (Urbain et al. 1989).

The modified power exponential function adequately fits biphasic solid emptying data:

$$y(t) = (1 - (1-e^{-kt})^{ß}) \quad (3)$$

In Eq. 3, y(t) is the fractional meal retention at time t, k is the gastric emptying rate in min^{-1} and ß is the extrapolated y-intercept from the terminal portion of the curve. The parameters k and ß are determined by a non-linear least squares algorithm using the measured fractional retention y(t) and time t as input. Four parameters can be derived from the gastric emptying curve: Tlag in minutes, the emptying rate in percent of emptying per minute, and the half emptying time ($T_{1/2}$) in minutes.

8.2.2.4 Clinical Applications

Diabetes mellitus: Rapid gastric emptying can be observed in the early stages of diabetic autonomic neuropathy (Kong et al. 1996). Delay in solid gastric emptying is very common in symptomatic and asymptomatic long-standing diabetes. This delay is essentially due to a prolonged lag phase while the emptying rate is preserved. Advanced gastroparesis is characterized by a markedly prolonged gastric emptying, with a linear solid emptying curve. A prolonged lag period with a normal $T_{1/2}$ has also been described in patients with longstanding disease (Urbain et al. 1993).

Liquid emptying is only abnormal when solid food emptying is severely impaired (Urbain et al. 1990a).

Idiopathic dyspepsia: In functional dyspepsia associated with gastroparesis, there is a prolonged lag phase and slow emptying rate that reflects the retention of food in the distal stomach (Malagelada 1991).

Gastric surgery: In patients with partial gastrectomy such as the Roux-en-Y procedure, there is an initial precipitous emptying followed by a slow evacuation phase resulting in a delay in both solid and liquid emptying. There is no lag phase, and both liquids and solids empty in a similar fashion (Urbain et al. 1990b).

8.2.3 Compartmental Analysis of the Stomach

Scintigraphy, like electrophysiologic and manometric studies, enables characterization of the respective role of the proximal and distal stomach in the gastric emptying process. Distinct regions of interest are drawn over the proximal and distal stomach. Food retention in each compartment is normalized to the total maximum gastric activity at time zero and displayed on time activity curves. Mathematical compartmental analysis of food distribution in the stomach has been investigated (Jadali et al. 1994).

In normal subjects, total and proximal liquid gastric curves are almost identical because there is no retention of liquid in the distal stomach. In contrast, solids are retained in the stomach by the pylorus and the distal stomach emptying curve for solids takes an asymmetric bell shape pattern.

In diabetic gastroparesis, there is significant retention of food in the proximal stomach which might correspond to a decrease in fundic motor activity (Urbain et al. 1993).

In contrast, patients with functional dyspepsia with or without gastroparesis display a normal proximal stomach emptying corroborating the normal electromechanical findings (Urbain et al. 1995).

8.2.4 Dynamic Antral Scintigraphy (DAS)

The most significant development in gastric emptying over the past decade has been the introduction of dynamic gastric scintigraphy; this procedure enables characterization of the frequency and amplitude of antral contractions, and correlation between gastric motility and gastric emptying.

8.2.4.1 Procedure

The subject is given a standard solid food test meal labeled with 75 Mbq (2 mCi) of ^{99m}Tc sulfur colloid. Static images of the stomach are acquired at regular time intervals; in addition, 1-s anterior dynamic images are acquired for 4 min after each set of static images.

Time-activity curves are generated from proximal, middle and distal regions of interest in the antrum and then analyzed using the autocorrelation function and a Fourier transform to determine the mean frequency and amplitude of the antral contraction.

8.2.4.2 Interpretation and Clinical Significance

In normal subjects, antral contraction frequency and amplitude correlate inversely with the lag phase, emptying rate and total gastric emptying course, i.e. the greater the antral motility, the faster the gastric emptying (Urbain et al. 1990c, 1993, 1995).

In diabetic gastroparesis, delayed gastric emptying is due to a retention of food in the proximal stomach and a decrease in the amplitude of antral contractions despite a higher frequency (Urbain et al. 1993).

Patients with functional dyspepsia seem to have a paradoxical increase in the amplitude of antral contractions and gastric emptying delay may be caused by a preponderance of non expulsive antral contractions and pyloric dysmotility (Urbain et al. 1995).

8.3 Colon Transit Scintigraphy

8.3.1 Introduction

Patients are asked to discontinue any medications likely to affect colon transit, for at least 3 days before the test. No dietary change is needed. The study should not be performed within a 4-week period following a colonoscopy.

Oral administration of ^{111}In-DTPA is the most commonly used radionuclide to assess colon transit. It is administered either in encapsulated nondigestible capsules (Stubbs et al. 1991), plastic particles (Madsen and Jensen 1989) or methylacrylate-coated resin particles that dissolve in the ileocecal region (Camilleri et al. 1989). The easiest method consists of the oral administration of 4 Mbq (100 μCi) ^{111}In-DTPA in water (Smart et al. 1991).

8.3.2 Acquisition, Analysis, and Quantification

Imaging is typically performed at 6, 24, 48, 72 and 96 h following the oral administration of ^{111}In-DTPA. Anterior and posterior images of the abdo-

men are obtained for 10 min, using a LFOV camera with medium-energy collimator.

Different methods exist to analyze colon transit images. The simplest method consists of determining the percentage of retention in each segment over time and to calculate the time required to clear 50% of the initial radioactivity (Madsen and Jensen 1989). Quantitation of residual activity in the different colonic regions at 4 and 24 h provides accurate colon transit information (Camilleri and Zinsmeister 1992). Colon transit time can also been assessed by the "condensed images" technique (Notghi et al. 1993).

The "geometric mean center" (GMC) technique is now widely used to determine the segmental emptying of the anatomic regions of the colon (Fig. 8.4) (Krevsky et al. 1986).

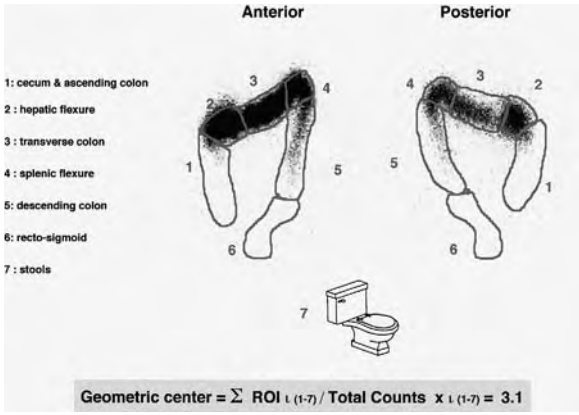

Fig. 8.4. Colon transit geometric center technique. Regions of interest (ROI) are generated around the six segments of the colon on the anterior and posterior images to determine the geometric mean of counts in each segment. The counts in ROI 7 are equal to the difference between input activity in the colon and the counts in the entire colon. The geometric center is calculated according to the formula Σ ROI $\iota_{(1-7)}$ / total counts x $\iota_{(1-7)}$. This weighted numerical value represents the center of the activity as it travels though the colon

8.3.3 Findings and Interpretation

In normal subjects, the ascending colon empties in a linear manner after an initial lag phase suggesting its storage role (Proano et al. 1990). Periods of no emptying alternating with periods of emptying can be observed. A linear progression through the colon is also demonstrated when using the GMC analysis (Stubbs et al. 1991). Solid or liquid tracers produce similar patterns of colon transit (Smart et al. 1991). Significant interstudy variability in transit can be observed. Colon transit is slower and more variable in females than males, but there is no effect of aging (McLean et al. 1992).

In patients with idiopathic constipation, the GMC analysis makes it possible to differentiate colonic inertia from pelvic obstruction of defecation. Colonic inertia is a pancolonic disorder characterized by a very slow transit throughout the entire length of the colon, in patients with significant stasis of radioactivity in the esophagus. In contrast, obstructed defecation is associated with an abnormal retention in the rectosigmoid (Krevsky et al. 1989a).

8.3.4 Clinical Applications

The most common clinical application of colon transit scintigraphy is the evaluation of patients with idiopathic constipation. It has also been used to demonstrate the prokinetic effect on the colon of drugs such as cisapride or naloxone (Kaufman et al. 1988; Krevsky et al. 1989b).

8.3.5 Whole Gut Transit

Several methods have been proposed to investigate the entire gastrointestinal tract in a single test. In our institution, ^{111}In-DTPA in water is given with a solid meal. The egg sandwich (see above) is labeled with ^{99m}Tc to simultaneously study gastric emptying of solids. In normal subjects, water empties from the stomach rapidly (90% within 2 h) and a geometric mean of abdominal counts is obtained at 2–3 h to determine 100% of the administered ^{111}In-DTPA activity. This determination enables us to generate terminal ileum filling rates as well as the input bolus into the colon to measure the GMC. Whole gut transit techniques may be limited in patients with severe gastroparesis, particularly when liquid emptying is markedly delayed.

8.4 Gastrointestinal Bleeding Scintigraphy

8.4.1 Introduction

Over the past 20 years, the management of patients with a GI bleed has changed dramatically. The widespread availability of upper and lower GI endoscopy

and the progress in interventional radiology and embolization techniques have given nuclear medicine a new role in the diagnostic and therapeutic algorithms of gastrointestinal bleeding.

In our institution, a bleeding scan is performed in patients with a lower GI bleed to evaluate the importance of the bleed and, more importantly to localize the site of bleeding before selective catheterization and embolization or surgery.

Both in vivo and in vitro red cell labeling methods are available for performing GI bleeding studies. In vivo labeling using the injection of stannous ion followed 20–30 min later by ^{99m}Tc-pertechnetate is convenient and easy to perform. However, labeling efficiency is variable and inconsistent varying from 60% to 90%. When present in significant amount, free pertechnetate is secreted by the gastric mucosa and the kidneys. This may interfere significantly with the ability to detect a bleed in the stomach, proximal small bowel, and/or colon. The in vivo/vitro technique consists in the intravenous administration of the stannous ion, the ^{99m}Tc pertechnetate labeling of a blood sample collected in a syringe containing an anticoagulant and ^{99m}Tc pertechnetate and the reinjection of the labeled sample. The labeling efficiency approaches 95%. The absence of blood manipulation and risk of contamination is a significant advantage of these two techniques. In the in-vitro technique, a sample of blood is withdrawn from the patient and an anticoagulant and stannous solution are added. Sodium hypochlorite and ACD solution are then added to oxidize the extracellular stannous ion. ^{99m}Tc pertechnetate is added to the blood sample and diffuses into the red blood cells, where it is reduced and trapped. Labeling efficiency is high and image quality appears superior (Maurer et al. 1998).

8.4.2 Acquisition Protocol

In our institution, we acquire sequential sets of 15-min continuous dynamic study with 15-s framing for a total of 60 images in a 128×128 byte matrix. Each 15 min the acquisition is saved at completion. The study is stopped when the bleeding site is identified. If the patient is not bleeding during the initial hour following the administration of the labeled red cells, the study is terminated.

Patients are often brought back to the department within the next 24 h for additional imaging if an acute onset of bleeding occurs.

8.4.3 Findings and Interpretation

Bleeding rate detection varies from 0.05 to 0.1 ml/min depending on the efficiency of the labeling procedure and other technical factors (Brown 1995). The cine display of the continuous dynamic set of images permits, in most cases, visualization and precise localization of the bleeding site by tracking down the progression of blood within the bowel (Fig. 8.5). If the patient is bleeding profusely, a quick transfer is organized, either to interventional radiology for selective catheterization and embolization, or to the operating room for surgery.

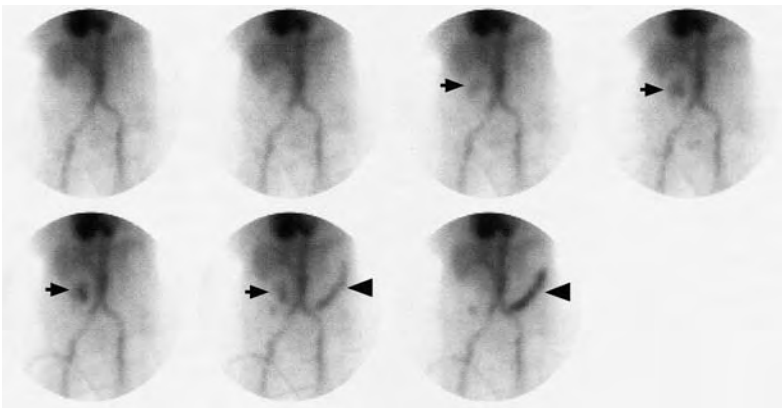

Fig. 8.5. Gastrointestinal bleeding scan. The images are cine displayed on the computer monitor and examined for the site of bleeding and motion of blood within the intestine. Images of this sequence have been reframed for illustration. In this case there is a site of bleeding in the right upper quadrant seen on the third image (*arrow on the left*). Images 6 and 7 show that the blood travels from the right towards the splenic flexure (*arrowhead on the right*) indicating that the bleeding occurs in the region of the hepatic flexure. Colonoscopy demonstrated that this patient had an angiodysplastic lesion at that level

References

Brown M (1995) Gastrointestinal bleeding scan. In: Principles of nuclear medicine, 2nd edn. Sauders, Philadelphia, pp 929-934

Camilleri M, Zinsmeister AR (1992) Towards a relatively inexpensive, non-invasive, accurate test for colonic motility disorders. Gastroenterology 103:36-42

Camilleri M, Colemont MJ, Phillips SF, Brown ML, Thomforde GM, Chapman N, Zinsmeister AR (1989) Human gastric emptying and colonic filling of solids characterized by a new method. Am J Physiol 257:G284-G290

Jadali F, Charkes ND, Urbain JL, Maurer AH (1994) A mathematical model of gastric emptying with a physiological basis. J Nucl Med 35:A684, p 170

Kaufman PN, Krevsky B, Malmud LS, Maurer AH, Somers MB, Siegel JA, Fischer RS (1988) Role of opiate receptors in the regulation of colonic transit. Gastroenterology 94:1351-1356

Kong MF, Macdonald IA, Tattersall RB (1996) Gastric emptying in diabetes. Diabetic Med 13:112-119

Krevsky B, Malmud LS, D'Ercole F, Maurer AH, Fisher RS (1986) Colonic transit scintigraphy: a physiologic approach to the quantitative measurements of colonic transit in humans. Gastroenterology 91:1102-1112

Krevsky B, Maurer AH, Fisher RS (1989a) Patterns of colonic transit in chronic idiopathic constipation. Am J Gastroenterol 84:127-132

Krevsky B, Maurer AH, Malmud LS, Fischer RS (1989b) Cisapride accelerates colonic transit in constipated patients with colonic inertia. Am J Gastroenterol 84:882-887

Madsen JL, Jensen M (1989) Gastrointestinal transit of technietium-99m-labeled cellulose fibre and indium-111-labeled plastic particles. JNM 30:402-406

Malagelada JR (1991) Where do we stand on gastric motility? Scand J Gastroenterol 175P [Suppl]:42-51

Malmud LS, Fisher RS (1978) Quantitation of gastroesophageal reflux before and after therapy using the gastroesophageal scintiscan. South Med J 71 [Suppl 1]:10-15

Maurer AH, Urbain JL, Krevsky B, Knight LC, Revesz G, Brown K (1998) Effects of in vitro versus in vivo red cell labeling on image quality in gastrointestinal bleeding studies. J Nucl Med Technol 26:87-90

McLean RG, Smart RC, Lubowski DZ, King DW, Barbagallo S, Talley NA (1992) Oral colon transit scintigraphy using indium-111-DTPA: variability in healthy subjects. Int J Colorect Dis 7:173-176

Notghi A, Kumar D, Panagamuwa B, Tulley NJ, Hesslewood SR, Harding LK (1993) Measurement of colonic transit time using radionuclide imaging: analysis by condensed images. Nucl Med Commun 14:204-218

O'Connor MK, Byrne PJ, Keeling P, Hennessy TP (1988) Esophageal scintigraphy: applications and limitations in the study of esophageal disorders. Eur J Nucl Med 14:131-136

Proano M, Camilleri M, Phillips SF, Brown ML, Thomforde GM (1990) Transit of solids through the human colon: regional quantification in the unprepared bowel. Am J Physiol 258: G856-G862

Rosenthal L (1988) Hepatobiliary imaging. In: Diagnostic nuclear medicine, 2nd edn. Williams and Wilkins, Baltimore, pp 582-609

Smart RC, McLean RG, Gaston-Parry D et al (1991) Comparison of oral iodine-131 cellulose and indium-111-DTPA as tracers for colon transit scintigraphy: analysis by colon activity profiles. J Nucl Med 32:1668-1674

Stubbs JB, Valenzuala GA, Stubbs CC, Croft BC, Teates CD, Plankey MW, McCallum RW (1991) A noninvasive scintigraphic assessment of the colonic transit of non-digestible solids in man. J Nucl Med 32:1375-1381

Taillefer R, Beauchamp G (1984) Radionuclide esophagogram. Clin Nucl Med 9:465-483

Tatsch K, Schroettle W, Kirsch CM (1991) Multiple swallow test for the quantitative and qualitative evaluation of esophageal motility disorders. J Nucl Med 32:1365-1370

Tolin RD, Malmud LS, Reillely J, Fisher RS (1979) Esophageal scintigraphy to quantitate esophageal transit (Quantitation of esophageal transit). Gastroenterology 76:1402-1408

Urbain J-LC, Siegel JA, Charkes ND, Maurer AH, Fisher RS, Malmud LS (1989) The two-component stomach: effects of meal particle size on fundal and antral emptying. Eur J Nucl Med 15:254-259

Urbain JLC, Vantrappen G, Janssens J, van Cutsem E, Peeters T, DeRoo M (1990a) Intravenous erythromycin dramatically accelerates gastric emptying in gastroparesis diabeticorum and normals and abolishes the emptying discrimination between solids and liquids. J Nucl Med 31:1490-1493

Urbain JLC, Penninckx F, Siegel JA, Vandenborre PH, VanCutsem E, VanDenMaegdenberg V, DeRoo M (1990b) Effect of proximal vagotomy and Roux-en-Y diversion on gastric emptying kinetics in asymptomatic patients. Clin Nucl Med 15:688-691

Urbain JLC, Van Cutsem E, Siegel JA et al (1990c) Visualization and characterization of gastric contractions using a radionuclide technique. Am J Physiol 259:G1062-G1067

Urbain JLC, Vekemans MC, Bouillon R et al (1993) Characterization of gastric antral motility disturbances in diabetes using the scintigraphic technique. J Nucl Med 34:576-581

Urbain JL, Vekemans MC, Parkman H et al (1995) Characterization of gastric antral motility in functional dyspepsia using digital antral scintigraphy. J Nucl Med 36:1579-1586

9 Hepatobiliary Scintigraphy

Mark Tulchinsky

CONTENTS

9.1 General Principles of Hepatobiliary Scintigraphy

9.1.1 Radiopharmaceuticals

Development of ^{99m}Tc-labeled iminodiacetic acid (IDA) derivatives provided us with an elegant way of studying key elements of hepatobiliary physiology and pathophysiology (Loberg et al. 1976). This area of diagnostic scintigraphy allows for depiction of liver blood flow, hepatocellular function, bile formation and excretion, as well as biliary tract integrity and dynamics. It further sheds light on gastrointestinal tract motility and patency as bile travels along, or in some less fortunate instances, outside its lumen.

Hepatobiliary radiopharmaceuticals witnessed one of the most prolific and fruitful developments, detailed elsewhere (Krishnamurthy and Turner 1990; Hladic and Norenberg 1996). To reiterate, the focus was ultimately placed on perfection of IDA derivatives, which are actively taken up and transported intracellularly by hepatocytes' organic anion-transporting polypeptide (similar to non-conjugated bilirubin). They are later excreted into canaliculi unchanged via the apical ATP-dependent export pump. Modern IDA analogues are probably the closest we have come to the concept of an ideal radiopharmaceutical (Karesh 1996).

The two in common clinical use today are ^{99m}Tc-disofenin, 2,6-diisopropylacetanilide iminodiacetic acid (DISIDA), and ^{99m}Tc-mebrofenin, bromo-2,4,6-trimethylacetanilide iminodiacetic acid (BromIDA). Considering a patient's total bilirubin level, a clinical question addressed by the test, availability and the cost, one makes a specific choice. If the latter two are of no concern, ^{99m}Tc-mebrofenin is the ideal choice, for it has the best hepatic uptake and washout, while displaying the least activity outside hepatobiliary system (Krishnamurthy and Turner 1990).

A typical adult dose is 200 MBq (5 mCi) of either compound injected as an intravenous bolus. BromIDA should be used in jaundiced patients, escalating the dose to 7.5 mCi and 10 mCi at total bilirubin levels of 4 mg/dl and 8 mg/dl, respectively. Pediatric patients should receive 7 MBq/kg (0.2 mCi/kg), but no less than 37 MBq (1 mCi). The gallbladder wall is the target radiation exposure organ, receiving 0.11 mGy/MBq dose (Gilbert et al. 1987).

9.1.2 Hepatobiliary Scintigraphy Technique

Ensuring an optimal scintigraphic result starts with proper patient preparation. It is well recognized that biliary flow and GB motility is a complex process that can be dramatically altered by a multitude of variables. Ideally, the patient is instructed to avoid opiates and opioid drugs and to fast for 4–24 h prior

M. Tulchinsky, MD, FACP, FACNP
Associate Professor and Associate Chief of Nuclear Medicine Section, Department of Radiology, Penn State University, Milton S. Hershey Medical Center, 500 University Drive, M.C. H066, P.O. Box 850, Hershey, PA 17033-0850, USA

to the test. It is preferred that the last pre-test meal (a bedtime snack) contains a significant fatty component if it can be tolerated by the patient. This would empty the GB, rendering it in the state of refilling at the start of scintigraphy the following morning.

Our institutional routine hepatobiliary scintigraphy (HBS) includes an optional rapid blood flow (scintiangiography) phase, and a slower dynamic (hepatobiliary) phase. Optimal resolution and counting statistics can be obtained by acquiring images in a 128×128 matrix size. The framing rate for the scintiangiography phase is one frame per second for a total of 60 s, while the subsequent images are acquired at one frame per 15 s for 1 h. The flow is best viewed by re-framing the rapid phase into 3–5 s per displayed frame, while the slower dynamic phase is re-framed into 2–4 min per displayed frame. If further dynamic imaging is required, it is typically acquired and displayed similar to the hepatobiliary phase for as long as the intervention is planned to last. When the gallbladder is the focus of attention, such as in the case of a gallbladder ejection fraction (GBEF) study, a 25°–35° left anterior obliquity renders the best separation of GB from duodenal activity (Fig. 9.1). Individualization on the basis of initial imaging may be needed in those who may have unusual GB position (intrahepatic, vertical-posterior, etc.). Some indications (such as bile leak) call for even longer static acquisitions and will be addressed later.

While the activity is continuously changing during HBS, and thus violates the pre-requisite of the steady state distribution, single photon emission computed tomography (SPECT) could be acquired with special modifications to provide improved visualization of regional liver function and the biliary tree (Oppenheim and Krepshaw 1988). SPECT imaging of the parenchymal phase is rarely useful in clinical practice, but may be helpful in delineating hepatocellular function of a small and deeply located liver lesion that cannot be appreciated on planar HBS (Steiner et al. 2003).

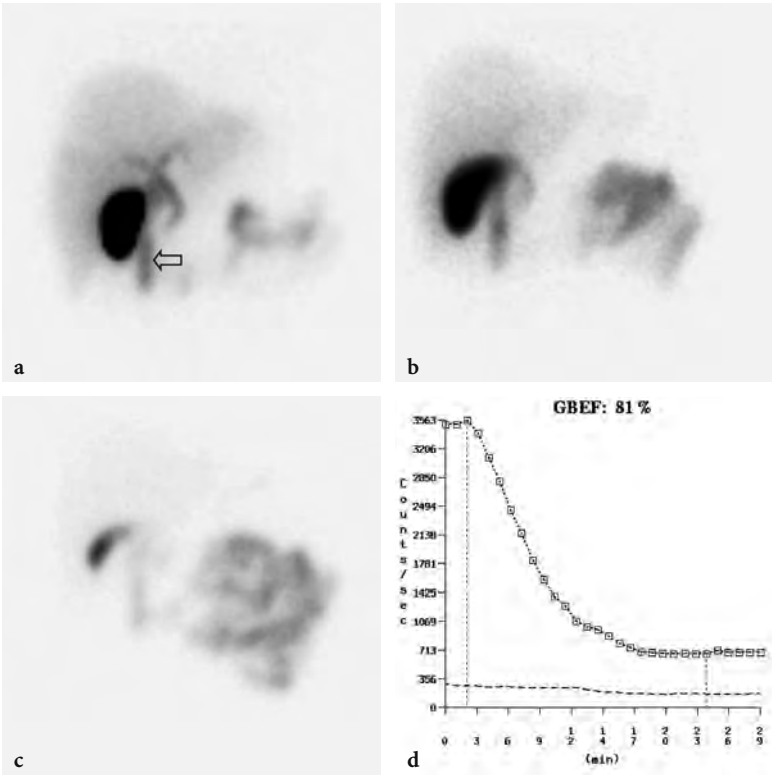

Fig. 9.1a–d. Normal gallbladder ejection fraction (*GBEF*) following the 15-min infusion protocol. **a** Normal 60-min anterior image demonstrates a filled GB abutting the duodenal activity (*arrow*). **b** The first frame prior to cholecystokinin infusion is acquired in the left anterior oblique projection to achieve an optimal separation of the GB and the duodenum, which allows for less interference of duodenal activity with that obtained from the stationary GB region used for the curve and GBEF generation. The rest of post-cholecystokinin dynamic images (not shown here) are obtained in the same projection. **c** The image corresponding to the trough GB activity at minute 24 from the start of CCK injection. **d** A normal curve following cholecystokinin infusion with calculated GBEF of 81%

9.1.3 Qualitative Assessment of Hepatobiliary Scintigraphy

The scintiangiography phase may reveal gross abnormalities of the heart and the aorta, such as cardiomegaly or aneurisms (Stryker and Siegel 1997). Liver blood flow via the hepatic artery is typically faint, as it represents only 25% of overall blood circulation through the organ. Activity in the liver begins to accumulate more rapidly upon recirculation, as blood returns via the portal vein 3–5 s later. It is just before the portal phase that a focal blush signals a lesion with arterial hypervascularization, such as hepatocellular carcinoma, adenoma, or focal nodular hyperplasia. Conversely, decreased flow can be seen in hypovascular lesions exemplified by an abscess and a cyst (Yeh et al. 1973).

Next is the hepatocellular or parenchymal imaging phase. The first 8-10 min of imaging offers a window into the functional hepatocellular integrity. Normally, the blood pool activity in the heart clears completely by the eighth minute (it may be faintly seen on the first 4-min image), with the tracer concentrated densely in the liver. In cases of severe hepatocellular disease (hepatitis, cirrhosis, etc.) the cardiac blood pool activity can persist for hours following the injection. Avid tracer uptake allows one to examine the liver for a hepatocyte-replacing, space-occupying lesions (such as metastatic disease, hemangioma, liver abscess, liver cyst, etc.) (Fig. 9.2). An appearance of the tracer in the ductal system signals the beginning of the biliary dynamic phase. While the left and right hepatic ducts are typically seen, visualization of the segmental hepatic ducts is rare in the normal individual and may indicate pathology. Biliary tree dilation can range anywhere from a slight residual prominence in a previously obstructed system to a more pronounced appearance in a partial obstruction, such as sphincter of Oddi stricture or dysfunction.

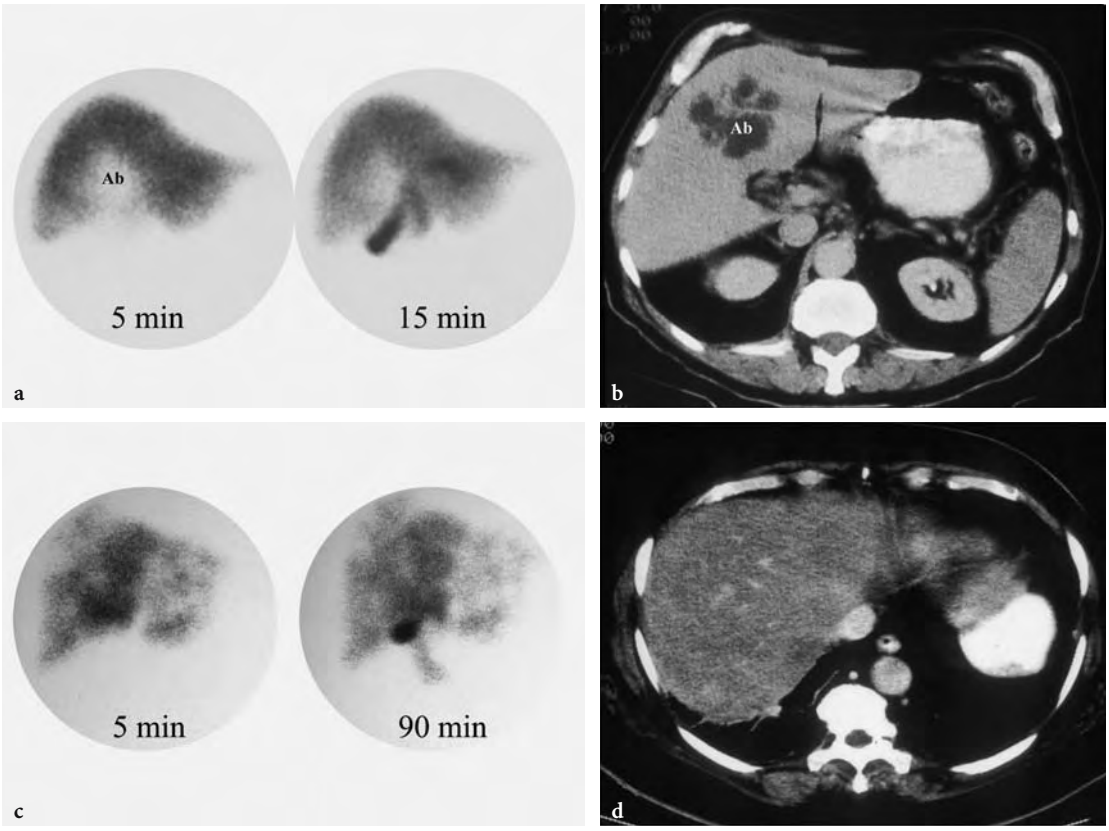

Fig 9.2a–d. Two hepatocyte-replacing lesion patterns on hepatobiliary scintigraphy. **a** Anaerobic liver abscess exhibited as a solitary photopenic defect (*Ab*) on a representative hepatobiliary image at 5 and 15 min. Subsequent views (not shown here) also showed the defect, but with progressively decreasing clarity as the hepatic activity diminished. **b** A CT scan showed characteristic appearance of an abscess (*Ab*) corresponding to the photopenic defect. **c** A multifocal photopenic pattern is depicted on 5- and 90-min hepatobiliary images. **d** While the most common cause of such a finding is metastatic disease, in this unusual case the CT was most consistent with multifocal fatty replacement, which was subsequently confirmed by liver biopsy

When the bile enters the duodenum it signals the intestinal phase of the study. The time from the radiotracer injection to this phase is commonly called a "biliary-to-bowel transit time." Depending on the bile production rate and driving pressure gradients in the hepatobiliary system, it may be as short as 10–15 min or as long as 1–2 h. A recent meal, stimulating a lasting GB contraction with increasing bile flow, represents an example of the former (Qvist et al. 1989). Exemplifying the latter is cholecystokinin (CCK) pre-treatment, which causes preferential bile flow into the relaxing GB and away from CBD and duodenum (Kim et al. 1990). Another major factor determining this time is the patency (anatomical or functional) of the hepatobiliary system, starting at the beginning of the common hepatic duct and ending at the level of sphincter of Oddi. Finally, the bile production rate plays an important role, explaining severe transit time delays in intrahepatic cholestasis.

As the tracer fills the bowel there is a concomitant parenchymal washout, expressed numerically as T1/2 (see Sect. 9.1.4). Under normal conditions it is homogeneous throughout the liver. However, focal nodular hyperplasia (FNH) is the most typical example of focal delayed ("hot spot") washout. It can also be seen in hepatic adenoma and, rarely, in hepatocellular carcinoma. These three entities cannot be definitively differentiated scintigraphically, but some general rules do apply. A typical triad for FNH consists of increased flow on scintiangiography phase (76% of all FNH cases), increased or normal uptake of ^{99m}Tc-sulfur colloid and IDA compound, with frequent (92%) delayed focal washout on HBS (Tanasescu et al. 1984; Boulahdour et al. 1993). Adenoma typically has unremarkable flow and reduced ^{99m}Tc-sulfur colloid uptake. Hepatocellular carcinoma usually has reduced ^{99m}Tc-sulfur colloid and IDA uptake, with very rare instances of delayed "hot spot" on HBS, but commonly very ^{67}Ga-citrate avid. However, the clinical value of these observations is limited, as there are no reliable data on sensitivity and specificity of those patterns in differentiating among the hepatic lesions.

It is useful to pay attention to the pattern of bowel activity and its relationship to the liver. A displaced bowel loop or an unusual liver shape may signal a displacement by a pathological structure, such as a markedly enlarged and radioactivity lacking hydrops gallbladder (Fig. 9.3). An abdominal mass can similarly display persistent non-filling of a bowel loop in the corresponding area (Lee et al. 2001). An unusually dilated small bowel loop that fills only to a point may signal the intestinal obstruction (Tobin et al. 1987). A markedly dilated stomach filled with refluxed radioactive bile can be a secondary finding of a small bowel obstruction (Lantz et al. 1994).

9.1.4 Quantitative Analysis in Hepatobiliary Scintigraphy

By far the most common analytical application to HBS is quantitation of GBEF (Figs. 9.1 and 9.4). It is the difference in GB counts, corrected by the background activity, between its maximal and minimal intensity, as a percent of the former. While a simple calculation, care should be taken to confirm that the GB region of interest (ROI) contains the GB throughout this imaging segment. It is common for the GB to change orientation, typically with the fundus moving in the cranial direction, assuming a more horizontal position. Such motion may cause a partial escape of GB outside the ROI, which is commonly drawn on the early image and applied to the entire image set, leading to an erroneously higher GBEF. Patient motion can have a similar effect by moving the GB outside a stationary ROI. An inappropriately positioned background ROI that includes bowel activity may occasionally lead to an erroneous result. Another common problem with a stationary GB ROI is an unintentional inclusion of nearby bowel activity that moves into the ROI towards the end of the study. It is sometimes necessary to apply individual GB and background ROIs to the pre-CCK and the image with least GB activity.

All contemporary gamma camera systems offer quantitative GBEF as part of a standard package. Yet, some practitioners advocate visual (qualitative) assessment of images for characterization of gallbladder emptying (O'Neill and McCreath 2000). In nuclear medicine practice today, however, it is difficult to find justification for omitting computer processing for GBEF in favor of visual inspection alone.

A recent investigation advanced a mean GBEF (mGBEF) as a more reproducible measure of the organ's motility (Toftdahl et al. 1996). It is defined as 100% minus the area under the time-activity curve, normalized to 100% and divided by the time interval from maximum to minimum counts per minute. While this parameter appears promising, testing it as a predictor of post-surgical success in patients with acalculous gallbladder disease is imperative prior to wide clinical acceptance.

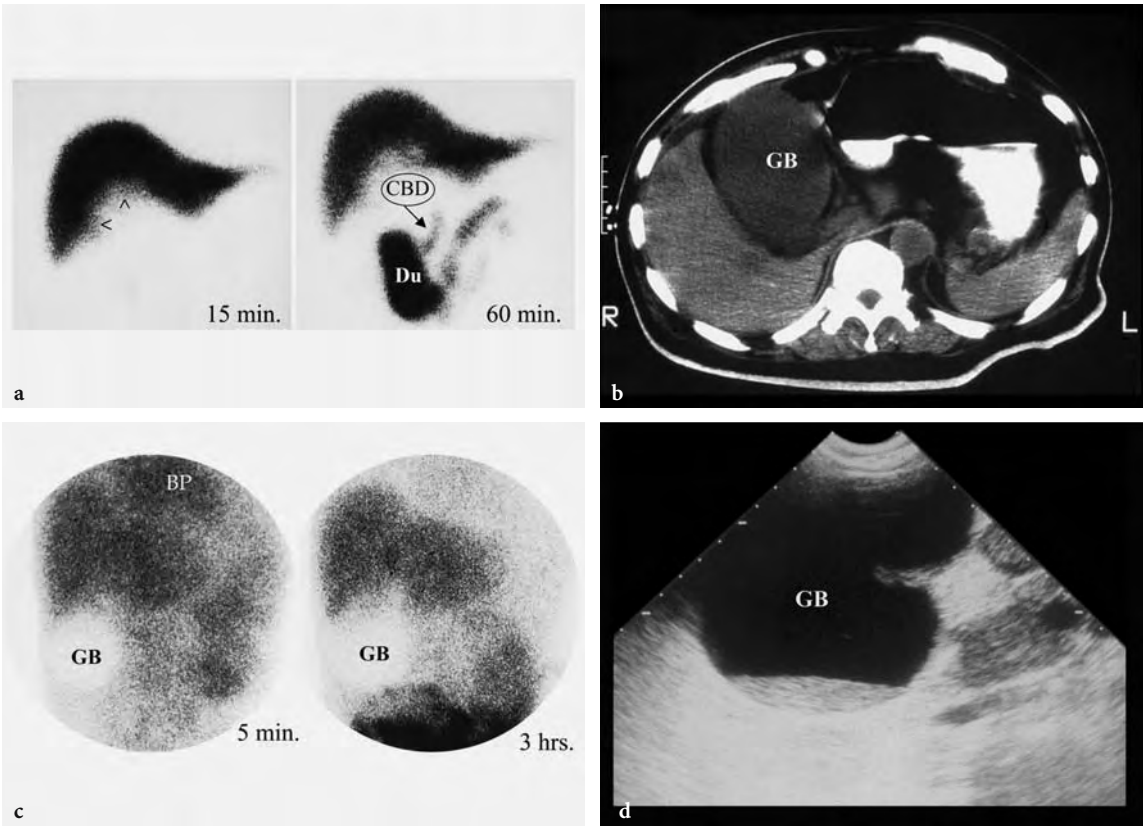

Fig. 9.3a–d. Two examples of bowel activity displacement caused by hydrops gallbladder (*GB*). **a** The first case shows an unusually deep rounded indentation at the inferior margin of the liver (*arrowheads*) on the 15-min image. There is an inferomedial displacement of the common bile duct (*CBD*) and inferior displacement of the duodenal activity (*Du*) on the 60-min image. **b** CT scan showing a hydrops gallbladder occupying an unusually large area under the liver edge. **c** A second example depicts hydrops in a form of a photopenic "light-bulb" finding. It did not fill in with radioactive bile at 4- or 24-h images (not shown here). This case also demonstrates poor hepatocellular function in this patient with a cirrhotic liver, reflected in increased cardiac blood pool (*BP*) and general body background activity. **d** The ultrasound image demonstrated sludge at the fundus of the hydrops gallbladder

A number of parameters are calculated from the time activity curves generated from the ROIs placed over the heart (activity in the circulation), liver, hepatic hilum, CBD, and duodenum. The whole liver activity curve analysis initially involved determination of time to the maximal activity (T_{max}) and half-time of clearance ($T_{1/2}$) from T_{max} (Gilbert et al. 1987), which is a measure of bile formation and/or impedance to its flow. The normal T_{max} is reached within 10 min of imaging, while the normal $T_{1/2}$ for DISIDA and BromIDA are 18.8±2.5 min (Gilbert et al. 1987; Brown et al. 1988) and 16.8±1.3 min (Gilbert et al. 1987; Krishnamurthy and Krishnamurthy 1988), respectively. The hepatic activity washout, also called percent of radiotracer excreted, can be expressed by a percent clearance from T_{max} to a specific time (typically at 30, 45, 60, and 90 min). This method is especially useful if an intervention is applied during the study to challenge the biliary dynamics (Shaffer et al. 1986; Thomas et al. 2000). Another clinically useful parameter of bile transit is the hepatic hilum to duodenum transit time. It was found to be the most reproducible and the best discriminator between symptomatic and asymptomatic patients with sphincter of Oddi dysfunction (Cicala et al. 1991).

Adding some complexity of deconvolutional analysis, the hepatic uptake of IDA compounds can be quantitatively expressed as extraction fraction (Brown et al. 1988). This parameter reflects functional hepatocellular integrity (100% in normal cases). In spite of usefulness in distinguishing hepatocellular disease from biliary problems, it is uncommonly used in contemporary practice.

The gallbladder bile concentration function is amenable to scintigraphic analysis (Krishnamur-

thy and Krishnamurthy 2002). Interestingly, it was shown to remain normal in chronic acalculous cholecystitis. Another sophisticated method, where ultrasound data is incorporated with scintigraphy, was developed to study GB's biliary turnover rate (Radberg et al. 1993; Prandini 2003). While advancing our knowledge of GB physiology and pathophysiology, these methods are yet to find clinical utility.

9.2 Clinical Applications of Hepatobiliary Scintigraphy

9.2.1 Acute Cholecystitis

HBS can demonstrate an obstructed cystic duct, a typical finding in acute cholecystitis (ACC), by the lack of activity in the GB. While newly formed radiolabeled bile in a normal fasting individual appears in the GB within the first hour, a variety of factors and disease states can delay it. However, very few circumstances (mentioned in the later discussion of false positive results) other then ACC totally preclude it. Some evidence suggests that non-visualization of GB in ACC may have more to do with very high GB pressures rather than the classically cited cystic duct obstruction (Borly et al. 1995).

ACC was the most common clinical application as HBS started to enter diagnostic practice. The initial useful criterion for a positive test was non-visualization of radioactivity in the GB within 4 h of imaging. It was soon recognized that most false positive results were secondary to chronic cholecystitis (Freitas and Gulati 1980; Freitas et al. 1983). Several augmentations were developed to enhance specificity, including waiting for up to 24 h (Drane et al. 1984), pre-treating patients with CCK (CCK pre-HBS), administering CCK after the first hour (CCKpost-HBS), and morphine augmented HBS (Choy et al. 1984). Morphine augmentation captured an overwhelming popularity in the contemporary practice. While similar in sensitivity to the 4-h HBS (96% versus 97%), it has significantly better specificity (84% versus 68%) for ACC (Cabana et al. 1995). It also has better specificity than CCK pre-HBS (Chen et al. 1997).

In a traditional approach the patient is imaged first for 1 h. If no GB activity is observed during that time, and other causes (recent meal, prolonged fasting, etc.) of non-visualization are excluded, the diagnoses to consider are either acute or chronic cholecystitis. Continued non-visualization during the 30 min following morphine injection establishes the former diagnosis, while appearance of the GB confirms the latter one. Another variation of the technique is to inject morphine as soon as one observes activity in the small bowel (Achong and Tenorio 2003). It may shorten the study considerably, but could limit the study's diagnostic ability for chronic cholecystitis.

A possibility of a false negative study is important to keep in mind. In general, if the GB is visualized within the first 30 min, the chance of false negative is much lower than in cases of later appearance (Hicks et al. 1990). Activity in the duodenal diverticulum (Brown et al. 1981; Gupta et al. 2000), focal accumulation during enterogastric reflux (Subramanian et al. 1985) or via an enterobiliary fistulae (Ripley and Fink-Bennett 1985) can simulate the GB. On rare occasion it is difficult to differentiate activity in the duodenum from that in the gallbladder. A simple maneuver that consists of 225 ml of water ingestion can settle the question. Since it has no cholecystokinetic effect, the decreasing intensity would indicate its duodenal origin (Keller et al. 1984; Wahl 1984). However, an image in the left anterior obliquity (LAO) and the right lateral view would typically accomplish the same goal. Best seen in the right lateral projection, the GB activity would appear anterior while the duodenum is found in posterior location. The LAO view unwraps overlying GB and duodenum by moving GB towards the patient's right while duodenum shifts left.

Sometimes there is enough activity entering the portion of cystic duct just proximal to obstruction that it can be mistaken for the GB, especially if it is dilated (Massie et al. 1983; Coleman et al. 1984; Achong and Oates 1991). One should not be misguided away from the diagnosis by the appearance of the GB in the presence of percutaneous gallbladder drainage, as it happens frequently in patients with ACC treated in such a way (Borly et al. 1995). Similarly, GB perforation secondary to ACC may result in its visualization (Achong et al. 1992; Shih et al. 1993). Intense pericholecystic liver uptake ("rim sign") may resemble the GB and lead to a false negative interpretation (Arose et al. 1987).

Acute acalculous cholecystitis is a life threatening disease, usually found in patients with severe intercurrent illness, which deserves special discussion. There is evidence that it is triggered by endotoxin injury to the GB in critically ill patients (Cullen et al.

2000). The injury causes hemorrhagic changes and loss of contractility, while the cystic duct obstruction is not as common as in acute calculous cholecystitis. It would be logical to expect that under such circumstances sensitivity of HBS may suffer. Surprisingly, the literature shows that morphine augmented HBS is very useful in this condition with sensitivity (greater than 90%) not significantly different from calculous ACC, but with somewhat reduced specificity (Weissmann et al. 1983; Ramanna et al. 1984; Mirvis et al. 1986; Swayne 1986; Flancbaum et al. 1989; Prevot et al. 1999; Jamart 2000). It is likely that the more frequent false positive studies are because of multiple factors (endotoxin, medications, prolonged fasting, etc.) that render GB atonic and congested in this very ill patient population. Some authors advocate white blood cell imaging for those with doubtful HBS results (Ziessman 2001).

False positive examinations should be infrequent if the patient is prepared properly. One of the most common preventable reasons is a recent meal that keeps the GB contracted (Klingensmith et al. 1981a; Qvist et al. 1989). Therefore, a 4-h fasting prior to the study initiation is important. The opposite extreme, prolonged fasting (more than 24 h) can also cause non-visualization of the GB (Larsen et al. 1982; Warner et al. 1987). This latter situation can be helped by CCK pre-treatment (Patterson and Kam 1985). Some authors suggested that acute pancreatitis may prevent or delay GB visualization (Edlund et al. 1982), while later evidence (Neoptolemos et al. 1983) does not support this claim. For reasons unknown, Ceftriaxone therapy may cause a false positive examination and should be discontinued prior to the test (Lorberboym et al. 1996). It used to be that chronic cholecystitis was the most common cause of a false positive (Freitas and Gulati 1980; Freitas et al. 1983). This assertion is doubtful in the era of morphine augmented HBS. Similarly, it is unclear if the commonly cited intercurrent severe illness (Kalff et al. 1983; Fig et al. 1990) and hyperalimentation (Shuman et al. 1982) continues to cause false positives in the current practice (Drane et al. 1984; Sippo et al. 1987; Flancbaum et al. 1989; Flancbaum and Choban 1995).

It was reported that GB non-visualization after morphine has a higher predictive value in diagnosis of ACC when it is accompanied by an increased activity in the common hepatic duct (Kim et al. 2000). The authors postulate that increasing activity in the common hepatic duct results from competent contraction of the sphincter of Oddi. Conversely, lack of increasing activity suggests a failed attempt of morphine to contract the sphincter, hence, a failed attempt at driving the bile into the GB.

"Rim sign" (hepatic activity abutting the GB fossa) is a specific (specificity of 100%), but insensitive (sensitivity of 45%) indicator of ACC (Meekin et al. 1987). More importantly, it alerts one to an increased likelihood of complication, such as GB gangrene (Brachman et al. 1984) or perforation (Smith et al. 1986). The etiology is linked to the presence of local capsular edema and sinusoidal congestion (Meekin et al. 1987). While some advocate calling ACC on the basis of the "rim sign" alone as soon as it is observed (Bushnell et al. 1986; Meekin et al. 1987), others warn that the "rim sign" is not specific enough (Lowry and Tran 1991; Shih et al. 1992; Jacobson 1995) and advocate proceeding with complete (including morphine augmentation) HBS (Oates et al. 1996). One of the most common false positive "rim sign" calls by a less experienced observer is made in female patients with a band of increased activity from the scatter at the inferior edge of the right breast (Fig. 9.4).

9.2.2 Gallbladder Hypokinesia Syndrome

There is a heterogeneous group of conditions that presents as a chronic, periodic abdominal pain, often biliary-like ("colicky") in character, and united by a common finding of gallbladder hypokinesia. First described and detailed utilizing cholecystokinin cholecystography (Cozzolino et al. 1963; Nathan et al. 1969; Valberg et al. 1971; Dunn et al. 1974), it remains a highly debated and evolving entity (Corazziari et al. 1999). Because of complex mechanisms involved in GB contractile regulation (Krishnamurthy and Krishnamurthy 1996; Corazziari et al. 1999; Johnson 2003), its hypokinesia in response to CCK can be a reflection of a great variety of etiologies. Some of them originate in the GB itself, such as chronic calculous cholecystitis, chronic acalculous cholecystitis, and the cystic duct syndrome. Others are at various remote locations that can be as near as sphincter of Oddi dysfunction, or as remote as inflammatory bowel disease. While the former group is likely to benefit from cholecystectomy, the latter one is not. It is a daunting task for a clinician to identify patients in the latter group to avoid unnecessary cholecystectomy. The ability to exclude these patients, and the

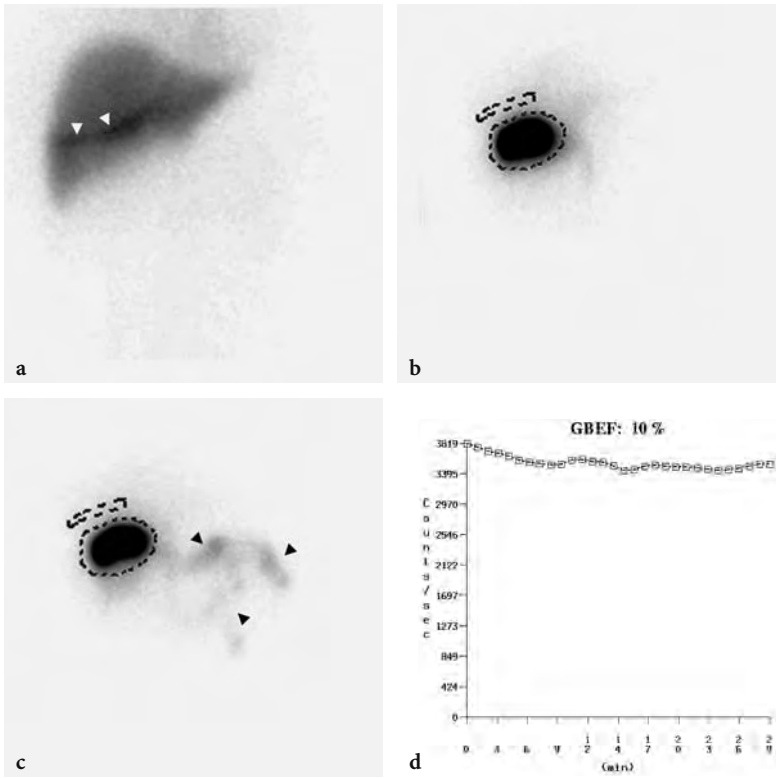

Fig. 9.4a–d. Gallbladder ejection fraction (*GBEF*) after 15-min cholecystokinin (CCK) infusion protocol for a dyskinesia case. **a** The parenchymal image acquired for 4 min following the tracer injection showing normal extraction. There is breast attenuation with higher activity due to scatter along its edge (*white arrowheads*). This pattern can be mistaken for the "rim sign" when located close to the gallbladder fossa, as observed here. This woman filled the GB in 12 min following the tracer injection (images not shown here). **b** The pre-CCK challenge image shows no significant bile activity in the intestine. The gallbladder is outlined by the stationary region, which will be applied to the rest of the dynamic post CCK acquisition. The background stationary region is placed superior to it. **c** There is minimal activity in the small bowel (*black arrowheads*) on the post-CCK image. **d** The curve generated from the stationary GB region, corrected by the background activity, reflects the minimal evacuation of bile in response to CCK. The calculated *GBEF* is 10%

subsequent ratio of the two groups within a study population, is what probably explains variability in the reported power of CCK-GBEF to predict the relief of symptoms following cholecystectomy. A majority of studies report high predictive value of the test (Pickleman et al. 1985; Yap et al. 1991; Zech et al. 1991; Middleton and Williams 1992; Sorenson et al. 1993; Khosla et al. 1997; Canfield et al. 1998; Goncalves et al. 1998; Klieger and O'Mara 1998; Dumont and Caniano 1999) while a minority offers an opposing view (Mishkind et al. 1997; Adams et al. 1998; Gani 1998).

Diagnostic stimulation of GB contraction is presently a focus of some controversy in respect to the choice between the fatty meal and intravenous CCK. Standardization does not exist in either the composition of the former or the dosage of the latter. While the fatty meal would seem to be the most physiological approach, it is not studied specifically in the gallbladder dyskinesia population to determine its predictive value for relief of symptoms after surgery. However, there are well established normal values for some standardized fatty meals (Shafer et al. 1983; Bobba et al. 1984; Fisher et al. 1987b; Mackie et al. 1987; Xynos et al. 1994; Buchpiguel et al. 1996; Patankar et al. 1996; Hadigan et al. 2003; Ziessman et al. 2003). The debate about CCK infusion rate is also unsettled and best exemplified in published argument exchanges (Middleton and Williams 1995; Krishnamurthy and Krishnamurthy 2003). The only clinically validated slow infusion technique in adults involved administration over 45 min (Yap et al. 1991). It was observed that maximal GB contraction was achieved by 15 min into the infusion. Hence, an infusion over 15 min with image acquisition for 30 min seems to be most practical. There is a well established normal range for a total CCK dose of 0.02 μg per kilogram administered over

15 min (Raymond et al. 1988). This dosage was later used successfully to predict response to cholecystectomy in children and adolescents with gallbladder hypokinesia syndrome (Dumont and Caniano 1999). While GBEF of less than 35% is considered abnormal (Raymond et al. 1988), some authors advocate a more liberal threshold of 50% (Dumont and Caniano 1999). It is optimal to acquire images in 25°–35° left anterior oblique projection to prevent contribution of duodenal activity to the GB ROI.

Application of GBEF in hospitalized patients who are typically unstable, undergoing some treatment, and often suffering from nausea, abdominal pain and other gastrointestinal symptoms, warrants a word of caution. It is likely that in such cases GBEF may be abnormal as a result of pharmacological, hormonal, or neural influences, causing significant reduction in specificity of the test (Moody et al. 1990; Raduns et al. 1990). Only a normal result under such circumstances would be clinically helpful. Therefore, experts recommend using this test in clinically stable outpatients only (Ziessman 2001). For example, increased GB contractility is observed with cholinergic agonists (Llamas-Elvira et al. 1990; Garrigues et al. 1992), hypercalcemia (Malagelada et al. 1976), erythromycin (Catnach et al. 1992), nonsteroidal anti-inflammatory drugs (O'Donnell et al. 1992), and those with vagotomy (Masclee et al. 1990). These circumstances may promote false negative results, while false positive studies are more common and can result from reduced GB contractility secondary to narcotics, endotoxins associated with severe intercurrent illness (Cullen et al. 2000), hyperglycemia (de Boer et al. 1994), somatostatin (Fisher et al. 1987a; Ewins et al. 1992; Hopman et al. 1992; Grimaldi et al. 1993; Stolk et al. 1993), diabetic neuropathy (Mitsukawa et al. 1990), spinal cord injury (Fong et al. 2003), achalasia (Annese et al. 1991), inflammatory bowel syndrome (Sood et al. 1993), liver cirrhosis (Kao et al. 2000), and progesterone (Tierney et al. 1999).

9.2.3 Post-Operative Applications

The most useful post-operative application of HBS is in patients with a suspected bile leak. Laparoscopic cholecystectomy is a common procedure with 1%–3% of early symptomatic bile leak. Interestingly, the incidence of asymptomatic self-resolving leak is about 7% (Hasl et al. 2001). The diagnosis is based on extraluminal appearance of the bile. It can be seen in the gallbladder fossa (a "phantom gallbladder"), track along or around the liver, make its way to the paracolic gutter, or appear as a typical diffuse peritoneal distribution pattern (Fig. 9.5). It is useful to keep in mind the typical normal pattern of tracer transit through the biliary and the bowel tracts in distinguishing the instances of extraluminal appearance. One can appreciate the rate of leakage, which would convey the clinical gravity. In our experience the voluminous leaks are unlikely to cease spontaneously. Chronic leaks may misleadingly appear as a minimal activity and much later in the study, as the receiving biloma fills to its capacity. It is imperative in those instances to obtain up to 4-h delay images. In a sizable series from Case Western Reserve University the test's sensitivity and specificity was an impressive 100% (Sandoval et al. 1997), consistent with our institutional experience. While anatomic modalities can visualize intra-abdominal fluid collections, only HBS is able to definitively and noninvasively differentiate the bile leak from postoperative seroma, lymphocele, and hematoma. HBS is similarly diagnostic in other abdominal surgeries with potential for biliary leak or biliary fistula formation (Marshall et al. 1984; Lineaweaver et al. 1985; Nagle et al. 1985; Salam et al. 1987; Balsam and Wasserstein 1990; Velchik et al. 1991; Bhatnagar et al. 1995; Herrlin 1995; Sharma et al. 1997; Outomuro et al. 2000; Benson et al. 2001; Lee 2001).

HBS is helpful in the diagnostic evaluation of patients with postcholecystectomy abdominal pain, which is observed in 5%–60% of those patients (Zeman et al. 1985). This heterogeneous group includes sphincter of Oddi dysfunction, cystic duct or GB remnants, and biliary tree obstruction or injury. It was initially suggested that sphincter of Oddi dysfunction may be diagnosed before cholecystectomy on CCK-HBS by observing a prominent CBD post-CCK (DeRidder and Fink-Bennett 1984). However, later reports showed that CCK-HBS is not useful for this indication (Kalloo et al. 1994; Ruffolo et al. 1994). The accuracy of CCK augmented HBS for sphincter of Oddi dysfunction detection in postcholecystectomy patients was near perfect in some of the early reports (Sostre et al. 1992). In a larger prospective series (Rosenblatt et al. 2001) the test was found to correlate poorly with manometry (the reference standard). Encouragingly, the authors discovered that abnormal HBS in this population predicted those who gained sustained symptomatic relief after sphincterotomy. This observation was later confirmed in a larger series at another institution (Cicala et al. 2002).

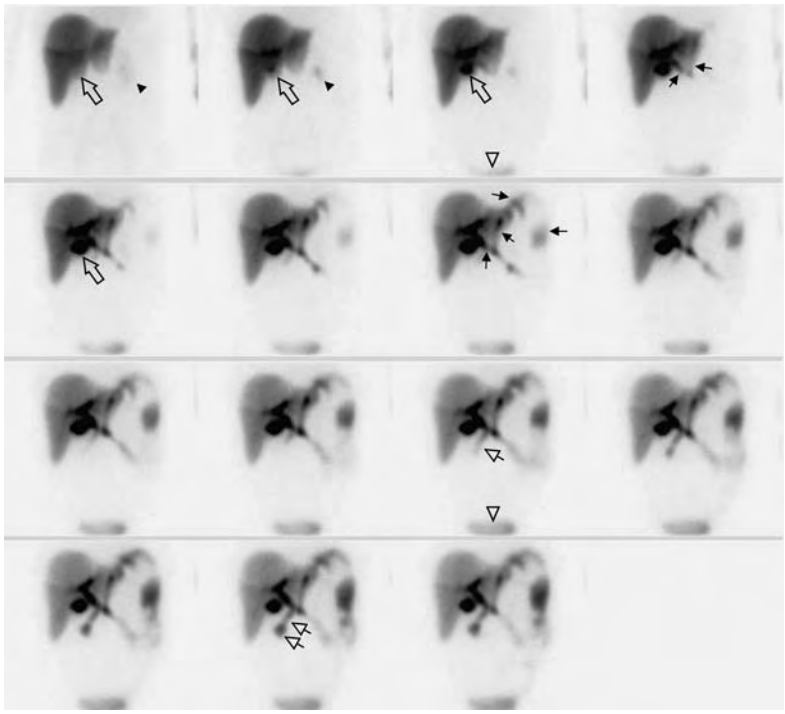

Fig. 9.5. Post-laparoscopic cholecystectomy biliary leak. This is a typical display of the first hour of dynamic imaging, formatted into 15 frames that were acquired for 4 min each. The first frame showed normal liver uptake with a photopenic area consistent with a gallbladder fossa (*hollow arrow*). Subtle renal uptake of ^{99m}Tc-disofenin is normal (*filled arrowheads* on frames 1 and 2) and later seen excreted into the urinary bladder (indicated by *hollow arrowhead* on frames 3 and 11). The gallbladder fossa fills in progressively, with more intense activity starting from the second frame onward (indicated by the *hollow arrow* on frames 2, 3, and 5), resembling a gallbladder appearance in this recently cholecystectomized female ("phantom gallbladder"). A cranial extension of extraluminal activity is subtly appreciated on the fourth frame, which extends in a linear fashion along the left liver lobe (*black arrows*). This pattern becomes progressively more intense as it continues to make its way under the left hemidiaphragm and down the left pericolic gutter (outlined by the *black arrows* on the seventh frame). There appears to be some activity slowly getting into the small intestine (outlined by *arrows with hollow arrowheads* on the eleventh and fourteenth frames)

The latter investigators used a practical measure of the hepatic hilum to the duodenum transit time. It becomes unimportant that incoming literature points out that this parameter correlates poorly with manometry (Craig et al. 2003), for it is able to predict which patient is likely to benefit from sphincterotomy and can do that better than manometry (Cicala et al. 2002). Another useful approach to this group of patients is to augment HBS with morphine injection (Thomas et al. 2000). An abnormally slow DISIDA clearance from the liver had about 80% sensitivity and specificity. On the other hand, acceleration of biliary tracer clearance from the liver by administering glyceryl trinitrate is a useful approach to demonstrating sphincter of Oddi dysfunction and differentiating it from organic obstruction (Bertalan et al. 2004). Supposedly, the nitrate relaxes the tight sphincter of Oddi and allows for faster flow through the CBD. This recently introduced methodology is awaiting the ultimate evaluation by testing it for prediction of symptomatic relief or improvement after sphincterotomy. Other less frequent symptomatic complications after cholecystectomy where HBS is useful include the cystic duct or gallbladder remnants (D'Alonzo and Velchik 1984), biliary tree obstruction (Falco et al. 1993; Negrin et al. 1995), and increased incidence of symptomatic biliary reflux into the stomach and esophagus (Mekhtikhanov et al. 1991; Obradovic et al. 2000).

HBS plays an important role in the evaluation of liver transplant patients. The bile leak detection can be definitively diagnosed and localized in those without severe intrahepatic cholestasis (Lantsberg et al. 1990; Mochizuki et al. 1991; Gelfand et al. 1992; Banzo et al. 1998). Vascular occlusion can be detected early on HBS by visualizing reduced or absent tracer uptake in an anatomically normal (on CT or US) region (Brown et al. 1986). While reduced hepatocellular function and cholestasis are nonspecific findings in rejection (Engeler et al. 1992),

sequential HBS is helpful in assessing its response to therapy (Loken et al. 1986). Transplant infarct is the final stage of rejection and would be scintigraphically indistinguishable from primary vascular occlusion, resulting in ominous "phantom liver" sign (Williams et al. 1985).

9.2.4 Common Bile Duct Obstruction

Acute common bile duct (CBD) obstruction evolves through three main stages. During the initial 24 h the GB provides an overflow reservoir for the bile that cannot normally empty via the CBD. There is no dilatation of the biliary ducts, thus it commonly escapes detection on anatomic imaging. HBS is done rarely at this stage, but would typically show good liver uptake, visualization of the GB, and no activity in the bowel (Fig. 9.6) (Klingensmith et al. 1981b). After about 24 h, the GB compensation is overwhelmed and the biliary tree begins to distend. The back pressure shuts down the bile production, causing the "liver scan appearance" on HBS (Noel et al. 1985). This is the most typical finding in complete CBD obstruction, consisting of reasonably good hepatic extraction with no tracer transit into the GB, CBD or the bowel within 24 h of observation (Verdegaal et al. 1978). Anatomic modalities would reveal CBD dilation. If the obstruction is not relieved in 96 h, the hepatocellular damage progresses with corresponding decrease in hepatic tracer uptake. Structural evaluation would often show progression of CBD dilation that extends to involve intrahepatic ducts. A common cause of false positive HBS for obstruction is severe cholestasis with or without hepatocellular dysfunction (Lieberman and Krishnamurthy 1986; Donohoe et al. 1987).

Unlike the thus far discussed complete CBD obstruction, diagnosing partial obstruction is much more complicated. Early studies established some basic principles (Verdegaal et al. 1978). Usually, the intestinal activity is delayed, but observed within 24 h. One of the proposed criteria is a higher

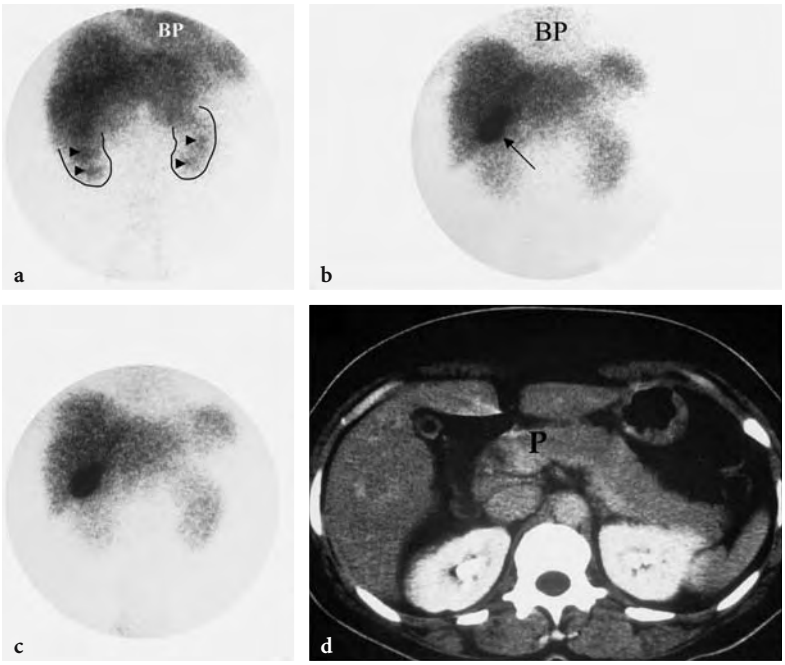

Fig. 9.6a–d. An example of an acute common bile duct obstruction (probably within 24 h of study initiation) by an inflamed pancreas is depicted. **a** The static view obtained at 5 min after injection shows increased cardiac blood pool (*BP*) activity in this alcoholic patient with liver cirrhosis. Vicarious renal excretion (the renal shine through from under the liver is *outlined in black*) is prominent with some focal concentration in the calices (*arrowheads*). **b** The image at 50 min revealed an unequivocal gallbladder filling with radioactive bile (*arrow*), but no activity in the bowel. There is a hint of *BP* activity, which in conjunction with parenchymal tracer retention points to significant hepatocellular disease and intrahepatic cholestasis. **c** At 2 h, the patient was given a cholecystokinin challenge. The image at 30 min after the initiation of CCK showed no GB contraction or bowel activity. This pattern persisted on the 24-h image (not shown here). **d** A CT scan showed an enlarged pancreas (*P*) that was later confirmed to have caused the common bile duct obstruction

concentration of activity in the hepatic ducts or the common bile duct after 2 h, compared to liver activity (regardless of the gallbladder visualization). This pattern is not specific and may be seen in other hepatobiliary pathologies. Caution should be exercised in calling partial obstruction on the basis of scintigraphically apparent biliary duct dilation, as an increasing concentration of radiotracer even in a normal size duct creates a "blooming" artifact (Floyd and Collins 1983). False positive studies can result after opioid administration (Taylor et al. 1982; Barlas et al. 2002), which can be clarified by reversing this effect with Naloxone (Patch et al. 1991). Further discussion on partial obstruction in postcholecystectomy sphincter of Oddi dysfunction can be found in Sect. 9.2.3.

9.2.5 Biliary Atresia

When the point of study is demonstration of biliary tree patency, increasing the bile flow (commonly achieved with phenobarbital or cholecystokinin) may become critical. It is especially important in differentiating biliary atresia from the neonatal hepatitis syndrome (severe intrahepatic cholestasis). For an optimal diagnostic result, these patients must be pretreated with a minimum of 3 (preferably 5–7) days of phenobarbital (Majd et al. 1981). The dosage is typically 5 mg/kg/day in divided doses, but it may need adjustment if the blood levels are subtherapeutic (below 15 mg/dl). Oral feeding is withheld for several hours before and up to 4 h after (duration of fasting depends on the clinical situation) the tracer injection to prevent dilution of biliary activity in the bowel. Delayed static views are obtained hourly for at least the first 6–8 h with an additional view acquired for 10 min at 24 h (Fig. 9.7). A clear bowel activity excludes biliary atresia and the imaging can be stopped at that time. If bowel activity is not seen by 24 h, atresia is highly likely, but the child should be further evaluated with cholangiogram, since some cases of severe cholestasis may cause a false positive study. Vicarious renal excretion can cause a false negative study – an avoidable situation when

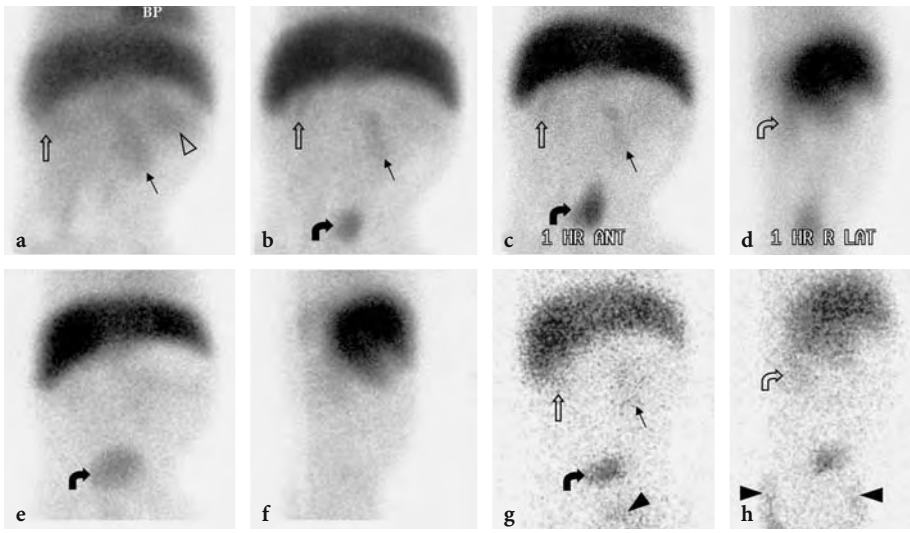

Fig. 9.7a–h. A 72-day-old infant boy with persistent jaundice demonstrates no biliary excretion on this ^{99m}Tc-mebrofenin study. **a** The first 4-min anterior image shows somewhat reduced liver uptake, signaled by significant cardiac blood pool (*BP*) activity. Subtle blood pool activity is appreciated in the spleen (*hollow arrowhead*), left kidney (*black arrow*), and inferior pole of the right kidney (*hollow arrow*). **b** Cardiac blood pool decreased during the study, leaving only a hint of activity on the 40-min anterior image. Renal activity is now in the collecting system, including the urinary bladder accumulation (*curved black arrow*). **c** The 1-h image showed no activity attributable to bowel excretion. Urinary activity persists. **d** The right lateral and left anterior oblique (not shown) views are routinely obtained at this time to confirm the origin of abdominal activity. Only a hint of radioactivity is seen in the right kidney (*hollow curved arrow*) with inferior pole descending below the inferior liver edge. **e** No radioactivity is seen in the abdomen below the liver except for the urinary bladder on this 8-h anterior view. An ovoid photopenia below the left liver lobe reflects the attenuation of recent feeding in the stomach. **f** The right lateral view at 8 h confirms lack of extrahepatic abdominal activity. **g** The 24-h anterior image is usually grainy secondary to very low radioactivity remaining in the patient. There is barely visible radioactivity in the kidneys and urinary bladder, as well as urine in the diaper (*black arrowhead*). **h** The right lateral view is a grainy twin to the image obtained at 1 h [image (**d**)], except for diaper activity (*black arrowhead*). Surgery the following day confirmed biliary atresia

multiple views (anterior, posterior and left anterior oblique) are obtained to help sorting out the location of activity focus. Routine use of BromIDA is strongly recommended to reduce renal activity. The overall accuracy, sensitivity, and specificity of this technique for the diagnosis of biliary atresia are 91%, 97%, and 82%, respectively (Nadel 1996).

9.3 Conclusion

HBS continues to enjoy frequent application in a variety of hepatobiliary conditions, but most widely in gallbladder hypokinesia syndrome (acalculous biliary disease). While its application is supported by several convincing studies, well-designed controlled investigations are too few. Indeed, it is mostly the preponderance of strongly suggestive evidences and sound physiologic rationale that supports its current use. Yet another major challenge to even broader acceptance is significant variability in methodology among the practitioner. In this age of evidence based medicine and standardization in disease management pathways it is our challenge to fill those voids such that patients in need would continue benefiting from this elegant physiologically based modality.

References

Achong DM, Oates E (1991) The cystic duct sign during morphine-augmented cholescintigraphy. Clin Nucl Med 16:627-629

Achong DM, Tenorio LE (2003) Early morphine administration to expedite gallbladder visualization during cholescintigraphy for acute cholecystitis. Clin Nucl Med 28:723-724

Achong DM, Newman JS, Oates E (1992) False-negative morphine-augmented cholescintigraphy: a case of subacute gallbladder perforation. J Nucl Med 33:256-257

Adams DB, Tarnasky PR, Hawes RH, Cunningham JT, Brooker C, Brothers TE, Cotton PB (1998) Outcome after laparoscopic cholecystectomy for chronic acalculous cholecystitis. Am Surg 64:1-5; discussion 5-6

Annese V, Caruso N, Accadia L, Gabbrielli A, Modoni S, Frusciante V, Federici T (1991) Gallbladder function and gastric liquid emptying in achalasia. Dig Dis Sci 36:1116-1120

Arose B, Shreeve WW, Baim RS, Atkins HL (1987) Phantom gallbladder. A variant of the rim sign. Clin Nucl Med 12:457-460

Balsam D, Wasserstein GJ (1990) Spontaneous perforation of the common bile duct in children. Radiology 174:578

Banzo I, Blanco I, Gutierrez-Mendiguchia C, Gomez-Barquin R, Quirce R, Carril JM (1998) Hepatobiliary scintigraphy for the diagnosis of bile leaks produced after T-tube removal in orthotopic liver transplantation. Nucl Med Commun 19:229-236

Barlas D, Margouleff D, Vignogna-Barlas L, Lesser ML (2002) Opioids prolong nuclear hepatobiliary imaging when given prior to scanning. J Emerg Med 23:231-236

Benson AJ, Reinschmidt J, Billingsley JL, Timmons JH, Parish GH (2001) Biliary-colonic fistula diagnosed via hepatobiliary scintigraphy. Clin Nucl Med 26:150-151

Bertalan V, Madacsy L, Pavics L, Lonovics J (2004) Scintigraphic sign of functional biliary obstruction is pathognomic for sphincter of Oddi dysfunction. Hepatogastroenterology 51:76-81

Bhatnagar A, Mondal A, Pathania OP, Dhawan RT, Chopra MK, Khanna CM (1995) Efficacy of hepatobiliary scintigraphy in demonstrating cholangio-colic fistulae. Is formation of internal biliary fistula related to external leak closure? Clin Nucl Med 20:318-321

Bobba VR, Krishnamurthy GT, Kingston E, Turner FE, Brown PH, Langrell K (1984) Gallbladder dynamics induced by a fatty meal in normal subjects and patients with gallstones: concise communication. J Nucl Med 25:21-24

Borly L, Stage JG, Gronvall S, Hojgaard L (1995) Cholescintigraphy in patients with acute cholecystitis before and after percutaneous gallbladder drainage. Eur J Gastroenterol Hepatol 7:1093-1097

Boulahdour H, Cherqui D, Charlotte F, Rahmouni A, Dhumeaux D, Zafrani ES, Meignan M (1993) The hot spot hepatobiliary scan in focal nodular hyperplasia. J Nucl Med 34:2105-2110

Brachman MB, Tanasescu DE, Ramanna L, Waxman AD (1984) Acute gangrenous cholecystitis: radionuclide diagnosis. Radiology 151:209-211

Brown JF, Buchanan JW, Wagner HN Jr (1981) Pitfalls in technetium-99m HIDA biliary imaging: duodenal diverticulum simulating the gallbladder. J Nucl Med 22:747-748

Brown PH, Juni JE, Lieberman DA, Krishnamurthy GT (1988) Hepatocyte versus biliary disease: a distinction by deconvolutional analysis of technetium-99m IDA time-activity curves. J Nucl Med 29:623-630

Brown RK, Memsic LD, Busuttil RW, Pusey E, Ray RA, Kangarloo H, Hawkins RA (1986) Accurate demonstration of hepatic infarction in liver transplant recipients. J Nucl Med 27:1428-1431

Buchpiguel CA, Sapienza MT, Vezzozzo DP, Rockman R, Cerri GG, Magalhaes AE (1996) Gallbladder emptying in normal volunteers. Comparative study between cholescintigraphy and ultrasonography. Clin Nucl Med 21:208-212

Bushnell DL, Perlman SB, Wilson MA, Polcyn RE (1986) The rim sign: association with acute cholecystitis. J Nucl Med 27:353-356

Cabana MD, Alavi A, Berlin JA, Shea JA, Kim CK, Williams SV (1995) Morphine-augmented hepatobiliary scintigraphy: a meta-analysis. Nucl Med Commun 16:1068-1071

Canfield AJ, Hetz SP, Schriver JP, Servis HT, Hovenga TL, Cirangle PT, Burlingame BS (1998) Biliary dyskinesia: a study of more than 200 patients and review of the literature. J Gastrointest Surg 2:443-448

Catnach SM, Fairclough PD, Trembath RC, O'Donnell LJ, McLean AM, Law PA, Wickham JE (1992) Effect of oral erythromycin on gallbladder motility in normal subjects and subjects with gallstones. Gastroenterology 102:2071-2076

Chen CC, Holder LE, Maunoury C, Drachenberg CI (1997) Morphine augmentation increases gallbladder visualiza-

tion in patients pretreated with cholecystokinin. J Nucl Med 38:644-647
Choy D, Shi EC, McLean RG, Hoschl R, Murray IP, Ham JM (1984) Cholescintigraphy in acute cholecystitis: use of intravenous morphine. Radiology 151:203-207
Cicala M, Scopinaro F, Corazziari E, Vignoni A, Viscardi A, Habib FI, Torsoli A (1991) Quantitative cholescintigraphy in the assessment of choledochoduodenal bile flow. Gastroenterology 100:1106-1113
Cicala M, Habib FI, Vavassori P, Pallotta N, Schillaci O, Costamagna G, Guarino MP, Scopinaro F, Fiocca F, Torsoli A, Corazziari E (2002) Outcome of endoscopic sphincterotomy in post cholecystectomy patients with sphincter of Oddi dysfunction as predicted by manometry and quantitative choledochoscintigraphy. Gut 50:665-668
Coleman RE, Freitas JE, Fink-Bennett DM, Bree RL (1984) The dilated cystic duct sign. A potential cause of false-negative cholescintigraphy. Clin Nucl Med 9:134-136
Corazziari E, Shaffer EA, Hogan WJ, Sherman S, Toouli J (1999) Functional disorders of the biliary tract and pancreas. Gut 45 [Suppl 2]:II48-II54
Cozzolino HJ, Goldstein F, Greening RR, Wirts CW (1963) The cystic duct syndrome. JAMA 185:920-924
Craig AG, Peter D, Saccone GT, Ziesing P, Wycherley A, Toouli J (2003) Scintigraphy versus manometry in patients with suspected biliary sphincter of Oddi dysfunction. Gut 52:352-357
Cullen JJ, Maes EB, Aggrawal S, Conklin JL, Ephgrave KS, Mitros FA (2000) Effect of endotoxin on opossum gallbladder motility: a model of acalculous cholecystitis. Ann Surg 232:202-207
D'Alonzo W, Velchik MG (1984) Post cholecystectomy syndrome due to a cystic duct remnant diagnosed by hepatobiliary scintigraphy. Clin Nucl Med 9:719-720
De Boer SY, Masclee AA, Lam WF, Lemkes HH, Schipper J, Frohlich M, Jansen JB, Lamers CB (1994) Effect of hyperglycaemia on gallbladder motility in type 1 (insulin-dependent) diabetes mellitus. Diabetologia 37:75-81
DeRidder P, Fink-Bennett D (1984) The dilated common duct sign. A potential indicator of a sphincter of Oddi dyskinesia. Clin Nucl Med 9:262-263
Donohoe KJ, Woolfenden JM, Stemmer JL (1987) Biliary imaging suggesting common duct obstruction in acute viral hepatitis. Case report. Clin Nucl Med 12:711-712
Drane WE, Nelp WB, Rudd TG (1984) The need for routine delayed radionuclide hepatobiliary imaging in patients with intercurrent disease. Radiology 151:763-769
Dumont RC, Caniano DA (1999) Hypokinetic gallbladder disease: a cause of chronic abdominal pain in children and adolescents. J Pediatr Surg 34:858-861; discussion 861-852
Dunn FH, Christensen ED, Reynolds J, Jones V, Fordtran JS (1974) Cholecystokinin cholecystography. Controlled evaluation in the diagnosis and management of patients with possible acalculous gallbladder disease. Jama 228:997-1003
Edlund G, Kempi V, van der Linden W (1982) Transient nonvisualization of the gallbladder by Tc-99m HIDA cholescintigraphy in acute pancreatitis: concise communication. J Nucl Med 23:117-120
Engeler CM, Kuni CC, Nakhleh R, Engeler CE, duCret RP, Boudreau RJ (1992) Liver transplant rejection and cholestasis: comparison of technetium 99m-diisopropyl iminodiacetic acid hepatobiliary imaging with liver biopsy. Eur J Nucl Med 19:865-870
Ewins DL, Javaid A, Coskeran PB, Shah S, Butler J, Deprez PH, Miell J, Calam J, Barrett JJ, Dawson JM, et al. (1992) Assessment of gall bladder dynamics, cholecystokinin release and the development of gallstones during octreotide therapy for acromegaly. Q J Med 83:295-306
Falco E, Magliani L, Biassoni P, Barbera F, Costa R, Schenone F, Conzi GF (1993) Biliary surgery and cholescintigraphy with iminodiacetic acid (IDA) analogs. An evaluation of the results and the complications. Minerva Chir 48:387-392
Fig LM, Wahl RL, Stewart RE, Shapiro B (1990) Morphine-augmented hepatobiliary scintigraphy in the severely ill: caution is in order. Radiology 175:467-473
Fisher RS, Rock E, Levin G, Malmud L (1987a) Effects of somatostatin on gallbladder emptying. Gastroenterology 92:885-890
Fisher RS, Rock E, Malmud LS (1987b) Effects of meal composition on gallbladder and gastric emptying in man. Dig Dis Sci 32:1337-1344
Flancbaum L, Choban PS (1995) Use of morphine cholescintigraphy in the diagnosis of acute cholecystitis in critically ill patients. Intensive Care Med 21:120-124
Flancbaum L, Alden SM, Trooskin SZ (1989) Use of cholescintigraphy with morphine in critically ill patients with suspected cholecystitis. Surgery 106:668-673; discussion 673-664
Floyd JL, Collins TL (1983) Discordance of sonography and cholescintigraphy in acute biliary obstruction. AJR Am J Roentgenol 140:501-502
Fong YC, Hsu HC, Sun SS, Kao A, Lin CC, Lee CC (2003) Impaired gallbladder function in spinal cord injury on quantitative Tc-99m DISIDA cholescintigraphy. Abdom Imaging 28:87-91
Freitas JE, Gulati RM (1980) Rapid evaluation of acute abdominal pain by hepatobiliary scanning. JAMA 244:1585-1587
Freitas JE, Coleman RE, Nagle CE, Bree RL, Krewer KD, Gross MD (1983) Influence of scan and pathologic criteria on the specificity of cholescintigraphy: concise communication. J Nucl Med 24:876-879
Gani JS (1998) Can sincalide cholescintigraphy fulfil the role of a gall-bladder stress test for patients with gall-bladder stones? Aust NZ J Surg 68:514-519
Garrigues V, Ponce J, Cano C, Sopena R, Hoyos M, del Val A, Berenguer J (1992) Effect of selective and nonselective muscarinic blockade on cholecystokinin-induced gallbladder emptying in man. Dig Dis Sci 37:101-104
Gelfand MJ, Smith HS, Ryckman FC, Balistreri WF, Specker B, Caron KH, Pedersen SH (1992) Hepatobiliary scintigraphy in pediatric liver transplant recipients. Clin Nucl Med 17:542-549
Gilbert SA, Brown PH, Krishnamurthy GT (1987) Quantitative nuclear hepatology. J Nucl Med Technol 15:38-43
Goncalves RM, Harris JA, Rivera DE (1998) Biliary dyskinesia: natural history and surgical results. Am Surg 64:493-497; discussion 497-498
Grimaldi C, Darcourt J, Harris AG, Lebot E, Lapalus F, Delmont J (1993) Cholescintigraphic study of effect of somatostatin analog, octreotide, on bile secretion and gallbladder emptying in normal subjects. Dig Dis Sci 38:1718-1721
Gupta S, Rajagopal S, Chander R, Sawroop K, Bhatnagar A (2000) Giant duodenal diverticulum: a cause of false-positive findings of magnetic resonance imaging, cholangiopancreatography, and hepatobiliary scintigraphy. Clin Nucl Med 25:1037-1038

Hadigan C, Fishman SJ, Connolly LP, Treves ST, Nurko S (2003) Stimulation with fatty meal (Lipomul) to assess gallbladder emptying in children with chronic acalculous cholecystitis. J Pediatr Gastroenterol Nutr 37:178-182

Hasl DM, Ruiz OR, Baumert J, Gerace C, Matyas JA, Taylor PH, Kennedy GM (2001) A prospective study of bile leaks after laparoscopic cholecystectomy. Surg Endosc 15:1299-1300

Herrlin K (1995) The diagnosis of anastomotic leak after gastroesophagostomy with biliary scintigraphy. Clin Nucl Med 20:709-711

Hicks RJ, Kelly MJ, Kalff V (1990) Association between false negative hepatobiliary scans and initial gallbladder visualization after 30 min. Eur J Nucl Med 16:747-753

Hladic WB III, Norenberg JP (1996) Radiopharmaceuticals for hepatobiliary imaging. In: Robert E Henkin MD, FACNP (ed) Nuclear medicine, vol II. Mosby, St Louis, pp 986-996

Hopman WP, van Liessum PA, Pieters GF, Jansen JB, Lamers CB, Smals AG, Rosenbusch G, Kloppenborg PW (1992) Postprandial gallbladder motility and plasma cholecystokinin at regular time intervals after injection of octreotide in acromegalics on long-term treatment. Dig Dis Sci 37:1685-1690

Jacobson AF (1995) False-negative morphine-augmented hepatobiliary scintigraphy with a rim sign. Clin Nucl Med 20:579-582

Jamart J (2000) Cholescintigraphy in the diagnosis of acute acalculous cholecystitis. Eur J Nucl Med 27:459-461

Johnson CD (2003) Arris & Gale lecture. Regulation and responses of gallbladder muscle activity in health and disease. Ann R Coll Surg Engl 85:297-305

Kalff V, Froelich JW, Lloyd R, Thrall JH (1983) Predictive value of an abnormal hepatobiliary scan in patients with severe intercurrent illness. Radiology 146:191-194

Kalloo AN, Sostre S, Meyerrose GE, Pasricha PJ, Szabo Z (1994) Gallbladder ejection fraction. Nondiagnostic for sphincter of Oddi dysfunction in patients with intact gallbladders. Clin Nucl Med 19:713-719

Kao CH, Hsieh JF, Tsai SC, Ho YJ, Chen SD (2000) Evidence of impaired gallbladder function in patients with liver cirrhosis by quantitative radionuclide cholescintigraphy. Am J Gastroenterol 95:1301-1304

Karesh SM (1996) Principles of radiopharmacy. In: Robert E, Henkin MD, FACNP (ed) Nuclear medicine, vol I. Mosby, St Louis, pp 334-349

Keller IA, Weissmann HS, Kaplun LL, Freeman LM (1984) The use of water ingestion to distinguish the gallbladder and duodenum on cholescintigrams. Radiology 152:811-813

Khosla R, Singh A, Miedema BW, Marshall JB (1997) Cholecystectomy alleviates acalculous biliary pain in patients with a reduced gallbladder ejection fraction. South Med J 90:1087-1090

Kim CK, Palestro CJ, Solomon RW, Molinari DS, Lee SO, Goldsmith SJ (1990) Delayed biliary-to-bowel transit in cholescintigraphy after cholecystokinin treatment. Radiology 176:553-556

Kim CK, Yun M, Lim JK, Lin X, Krynyckyi BR, Machac J (2000) Refinement of the positive predictive value of gallbladder nonvisualization after morphine administration for acute cholecystitis based on the temporal pattern of common bile duct activity. Clin Nucl Med 25:603-607

Klieger PS, O'Mara RE (1998) The clinical utility of quantitative cholescintigraphy: the significance of gallbladder dysfunction. Clin Nucl Med 23:278-282

Klingensmith WC 3rd, Spitzer VM, Fritzberg AR, Kuni CC (1981a) The normal fasting and postprandial diisopropyl-IDA Tc 99m hepatobiliary study. Radiology 141:771-776

Klingensmith WC 3rd, Whitney WP, Spitzer VM, Klintmalm GB, Koep LM, Kuni CC (1981b) Effect of complete biliary-tract obstruction on serial hepatobiliary imaging in an experimental model: concise communication. J Nucl Med 22:866-868

Krishnamurthy GT, Krishnamurthy S (2002) Hepatic bile entry into and transit pattern within the gallbladder lumen: a new quantitative cholescintigraphic technique for measurement of its concentration function. J Nucl Med 43:901-908

Krishnamurthy GT, Krishnamurthy S (2003) What value is normal for gallbladder ejection fraction, and how is it established? Radiology 226:593-594; author reply 594-595

Krishnamurthy GT, Turner FE (1990) Pharmacokinetics and clinical application of technetium 99m-labeled hepatobiliary agents. Semin Nucl Med 20:130-149

Krishnamurthy S, Krishnamurthy GT (1988) Nuclear hepatology: where is it heading now? J Nucl Med 29:1144-1149

Krishnamurthy S, Krishnamurthy GT (1996) Cholecystokinin and morphine pharmacological intervention during 99mTc-HIDA cholescintigraphy: a rational approach. Semin Nucl Med 26:16-24

Lantsberg S, Lanchbury EE, Drolc ZA (1990) Evaluation of bile duct complications after orthotopic liver transplantation by hepatobiliary scanning. Nucl Med Commun 11:761-769

Lantz MM, Sziklas JJ, Spencer RP (1994) Massive gastric dilatation secondary to small bowel obstruction. Demonstration by hepatobiliary images. Clin Nucl Med 19:464

Larsen MJ, Klingensmith WC 3rd, Kuni CC (1982) Radionuclide hepatobiliary imaging: nonvisualization of the gallbladder secondary to prolonged fasting. J Nucl Med 23:1003-1005

Lee JK (2001) Tc-99m DISIDA hepatobiliary scintigraphy showing bile leakage into the thoracic cavity. Clin Nucl Med 26:861-862

Lee MJ, Zuckier LS, Zalta B, Fine E (2001) The persistently absent bowel loop: a sign of mass effect on the bowel detected by cholescintigraphy. Clin Nucl Med 26:939-940

Lieberman DA, Krishnamurthy GT (1986) Intrahepatic versus extrahepatic cholestasis. Discrimination with biliary scintigraphy combined with ultrasound. Gastroenterology 90:734-743

Lineaweaver W, Robertson J, Rumley T (1985) PIPIDA scan diagnosis of traumatic rupture of the gallbladder. Injury 16:238-240

Llamas-Elvira JM, Sopena R, Martinez-Paredes M, Jimenez-Heffernan A, Gonzalez FM, Torres M, Latre JM, Mateo A (1990) Muscarinic control of gallbladder dynamics. A study using 99Tcm-HIDA and cholinergic agonists and antagonists. Nucl Med Commun 11:813-817

Loberg MD, Cooper M, Harvey E, Callery P, Faith W (1976) Development of new radiopharmaceuticals based on N-substitution of iminodiacetic acid. J Nucl Med 17:633-638

Loken MK, Ascher NL, Boudreau RJ, Najarian JS (1986) Scintigraphic evaluation of liver transplant function. J Nucl Med 27:451-459

Lorberboym M, Machado M, Glajchen N, Pertsemlidis D (1996) Transient false-positive hepatobiliary scan associated with ceftriaxone therapy. Clin Nucl Med 21:4-7

Lowry PA, Tran HD (1991) Delayed visualization of the gallbladder with a rim sign. An unusual finding in chronic cholecystitis. Clin Nucl Med 16:1-3

Mackie CR, Baxter JN, Grime JS, Hulks G, Cuschieri A (1987) Gall bladder emptying in normal subjects – a data base for clinical cholescintigraphy. Gut 28:137-141

Majd M, Reba RC, Altman RP (1981) Hepatobiliary scintigraphy with 99mTc-PIPIDA in the evaluation of neonatal jaundice. Pediatrics 67:140-145

Malagelada JR, Holtermuller KH, Sizemore GW, Go VL (1976) The influence of hypercalcemia on basal and cholecystokinin-stimulated pancreatic, gallbladder, and gastric functions in man. Gastroenterology 71:405-408

Marshall DG, Brabyn DG, Vezina WC (1984) Spontaneous perforation of the common bile duct in infancy detected by 99mTc HIDA scanning. Can J Surg 27:590-591

Masclee AA, Jansen JB, Driessen WM, Geuskens LM, Lamers CB (1990) Effect of truncal vagotomy on cholecystokinin release, gallbladder contraction, and gallbladder sensitivity to cholecystokinin in humans. Gastroenterology 98:1338-1344

Massie JD, Moinuddin M, Phillips JC (1983) Acute calculous cholecystitis with patent cystic duct. AJR Am J Roentgenol 141:39-42

Meekin GK, Ziessman HA, Klappenbach RS (1987) Prognostic value and pathophysiologic significance of the rim sign in cholescintigraphy. J Nucl Med 28:1679-1682

Mekhtikhanov ZS, Nesterov VG, Astap'eva ON (1991) Quantitative hepato-biliary scintigraphy in the diagnosis of duodenogastric reflux and dysfunction of the Oddi's sphincter in post-cholecystectomy syndrome. Vestn Khir Im I I Grek 146:25-28

Middleton GW, Williams JH (1992) Is gall bladder ejection fraction a reliable predictor of acalculous gall bladder disease? Nucl Med Commun 13:894-896

Middleton GW, Williams JH (1995) Fast or slow cholecystokinin infusion in 99mTc HIDA imaging? Australas Radiol 39:100

Mirvis SE, Vainright JR, Nelson AW, Johnston GS, Shorr R, Rodriguez A, Whitley NO (1986) The diagnosis of acute acalculous cholecystitis: a comparison of sonography, scintigraphy, and CT. AJR Am J Roentgenol 147:1171-1175

Mishkind MT, Pruitt RF, Bambini DA, Hakenewerth AM, Thomason MH, Zuger JH, Novick T (1997) Effectiveness of cholecystokinin-stimulated cholescintigraphy in the diagnosis and treatment of acalculous gallbladder disease. Am Surg 63:769-774

Mitsukawa T, Takemura J, Ohgo S, Mizuta M, Ii T, Kuribayashi T, Matsukura S (1990) Gallbladder function and plasma cholecystokinin levels in diabetes mellitus. Am J Gastroenterol 85:981-985

Mochizuki T, Tauxe WN, Dobkin J, Shah AN, Shanker R, Todo S, Starzl TE (1991) Detection of complications after liver transplantation by technetium-99m mebrofenin hepatobiliary scintigraphy. Ann Nucl Med 5:103-107

Moody FG, Calabuig R, Li YF, Harari Y, Rodriguez LF, Weisbrodt NW (1990) Biliary and gut function following shock. J Trauma 30:S179-S184

Nadel HR (1996) Hepatobiliary scintigraphy in children. Semin Nucl Med 26:25-42

Nagle CE, Fink-Bennett D, Freitas JE (1985) Bile ascites in adults. Diagnosis using hepatobiliary scintigraphy and paracentesis. Clin Nucl Med 10:403-405

Nathan MH, Newman A, McFarland J, Murray DJ (1969) Cholecystokinin cholecystography. Radiology 93:1-8

Negrin JA, Zanzi I, Margouleff D (1995) Hepatobiliary scintigraphy after biliary tract surgery. Semin Nucl Med 25:28-35

Neoptolemos JP, Fossard DP, Berry JM (1983) A prospective study of radionuclide biliary scanning in acute pancreatitis. Ann R Coll Surg Engl 65:180-182

Noel AW, Velchik MG, Alavi A (1985) The "liver scan" appearance in cholescintigraphy. A sign of complete common bile duct obstruction. Clin Nucl Med 10:264-269

Oates E, Selland DL, Chin CT, Achong DM (1996) Gallbladder nonvisualization with pericholecystic rim sign: morphine-augmentation optimizes diagnosis of acute cholecystitis. J Nucl Med 37:267-269

Obradovic VB, Artiko V, Chebib HY, Petrovic MN, Vlajkovic M, Petrovic NM (2000) Estimation of the enterogastric reflux by modified scintigraphic method. Hepatogastroenterology 47:738-741

O'Donnell LJ, Wilson P, Guest P, Catnach SM, McLean A, Wickham JE, Fairclough PD (1992) Indomethacin and postprandial gallbladder emptying. Lancet 339:269-271

O'Neill GT, McCreath G (2000) An audit of biliary scintigraphy in a district general hospital (1993-1998) with special reference to the investigation of acalculous gallbladder disease. Nucl Med Commun 21:829-834

Oppenheim BE, Krepshaw JD (1988) Dynamic hepatobiliary SPECT: a method for tomography of a changing radioactivity distribution. J Nucl Med 29:98-102

Outomuro J, Serena A, Campos L, Pineda JR, Montes J (2000) Nonvisualization of the common bile duct and normal biliary to bowel transit: an indirect sign of bilioenteric fistula. Clin Nucl Med 25:309-311

Patankar R, Ozmen MM, Aldous A, Khader Z, Fleming JS, Johnson CD (1996) Standardization of a technique for BrIDA cholescintigraphy. Nucl Med Commun 17:724-728

Patch GG, Morton KA, Arias JM, Datz FL (1991) Naloxone reverses pattern of obstruction of the distal common bile duct induced by analgesic narcotics in hepatobiliary imaging. J Nucl Med 32:1270-1272

Patterson FK, Kam JW (1985) Practical hepatobiliary imaging using pretreatment with sincalide in 139 hepatobiliary studies. Clin Nucl Med 10:333-335

Pickleman J, Peiss RL, Henkin R, Salo B, Nagel P (1985) The role of sincalide cholescintigraphy in the evaluation of patients with acalculus gallbladder disease. Arch Surg 120:693-697

Prandini N (2003) Methods of measuring gallbladder motor functions – the need for standardization: scintigraphy. Dig Liver Dis 35 [Suppl 3]:S62-S66

Prevot N, Mariat G, Mahul P, Granjon D, Cuilleron M, Tiffet O, De Filipis JP, Jospe R, Auboyer C, Dubois F (1999) Contribution of cholescintigraphy to the early diagnosis of acute acalculous cholecystitis in intensive-care-unit patients. Eur J Nucl Med 26:1317-1325

Qvist N, Oster-Jorgensen E, Rasmussen L, Hovendal C, Pedersen SA (1989) Postprandial gallbladder filling: relation to gastrointestinal motility. Scand J Gastroenterol 24:969-974

Radberg G, Asztely M, Moonen M, Svanvik J (1993) Contraction and evacuation of the gallbladder studied simultaneously by ultrasonography and 99mTc-labeled diethyl-iminodiacetic acid scintigraphy. Scand J Gastroenterol 28:709-713

Raduns K, McGahan JP, Beal S (1990) Cholecystokinin sonography: lack of utility in diagnosis of acute acalculous cholecystitis. Radiology 175:463-466

Ramanna L, Brachman MB, Tanasescu DE, Berman DS, Waxman AD (1984) Cholescintigraphy in acute acalculous cholecystitis. Am J Gastroenterol 79:650-653

Raymond F, Lepanto L, Rosenthall L, Fried GM (1988) Tc-99m-

IDA gallbladder kinetics and response to CCK in chronic cholecystitis. Eur J Nucl Med 14:378-381
Ripley SD, Fink-Bennett D (1985) Enterobiliary fistulae: a potential cause of a false-negative hepatobiliary study in the diagnosis of acute cholecystitis. Eur J Nucl Med 10:167-168
Rosenblatt ML, Catalano MF, Alcocer E, Geenen JE (2001) Comparison of sphincter of Oddi manometry, fatty meal sonography, and hepatobiliary scintigraphy in the diagnosis of sphincter of Oddi dysfunction. Gastrointest Endosc 54:697-704
Ruffolo TA, Sherman S, Lehman GA, Hawes RH (1994) Gallbladder ejection fraction and its relationship to sphincter of Oddi dysfunction. Dig Dis Sci 39:289-292
Salam M, Glowniak JV, Vetto RM, Jarboe JE, Haines JE, Krishnamurthy GT (1987) Detection of bile leakage from traumatic right hepatic duct laceration with technetium-99m DISIDA cholescintigraphy. Clin Nucl Med 12:589-591
Sandoval BA, Goettler CE, Robinson AV, O'Donnell JK, Adler LP, Stellato TA (1997) Cholescintigraphy in the diagnosis of bile leak after laparoscopic cholecystectomy. Am Surg 63:611-616
Shafer RB, Marlette JM, Morley JE (1983) The effects of Lipomul, CCK, and TRH on gallbladder emptying. Clin Nucl Med 8:66-69
Shaffer EA, Hershfield NB, Logan K, Kloiber R (1986) Cholescintigraphic detection of functional obstruction of the sphincter of Oddi. Effect of papillotomy. Gastroenterology 90:728-733
Sharma R, Mondal A, Sen IB, Sawroop K, Ravishanker L, Kashyap R (1997) Spontaneous perforation of the gallbladder during infancy diagnosed on hepatobiliary imaging. Clin Nucl Med 22:759-761
Shih WJ, Mills BJ, Pulmano C (1992) A prominent porta hepatitis resulting in a rim sign appearance on cholescintigraphy. Clin Nucl Med 17:400-401
Shih WJ, Magoun S, Mills BJ, Pulmano C (1993) Bile leak from gallbladder perforation mimicking bowel activity and a false-negative result in a morphine-augmented cholescintigraphy. J Nucl Med 34:131-133
Shuman WP, Gibbs P, Rudd TG, Mack LA (1982) PIPIDA scintigraphy for cholecystitis: false positives in alcoholism and total parenteral nutrition. AJR Am J Roentgenol 138:1-5
Sippo WC, Moreno AJ, Cabellon S, Turnbull GL (1987) The effect of prolonged fasting and total parenteral nutrition on hepatobiliary imaging with technetium-99m DISIDA. Clin Nucl Med 12:169-172
Smith R, Rosen JM, Alderson PO (1986) Gallbladder perforation: diagnostic utility of cholescintigraphy in suggested subacute or chronic cases. Radiology 158:63-66
Sood GK, Baijal SS, Lahoti D, Broor SL (1993) Abnormal gallbladder function in patients with irritable bowel syndrome. Am J Gastroenterol 88:1387-1390
Sorenson MK, Fancher S, Lang NP, Eidt JF, Broadwater JR (1993) Abnormal gallbladder nuclear ejection fraction predicts success of cholecystectomy in patients with biliary dyskinesia. Am J Surg 166:672-674; discussion 674-675
Sostre S, Kalloo AN, Spiegler EJ, Camargo EE, Wagner HN Jr (1992) A noninvasive test of sphincter of Oddi dysfunction in postcholecystectomy patients: the scintigraphic score. J Nucl Med 33:1216-1222
Steiner D, Klett R, Puille M, Doppl W, Bauer R (2003) Diagnosis of focal nodular hyperplasia with hepatobiliary scintigraphy using a modified SPECT technique. Clin Nucl Med 28:136-137
Stolk MF, van Erpecum KJ, Koppeschaar HP, de Bruin WI, Jansen JB, Lamers CB, van Berge Henegouwen GP (1993) Postprandial gall bladder motility and hormone release during intermittent and continuous subcutaneous octreotide treatment in acromegaly. Gut 34:808-813
Stryker J, Siegel A (1997) Abdominal aortic aneurysm visualized with hepatobiliary scintigraphy. Clin Nucl Med 22:645-646
Subramanian KS, Freeman ML, Reznikov I, Van Drunen M, Bushnell D, Shirazi P, Kaplan E (1985) Enterogastric reflux mimicking gallbladder visualization in acute cholecystitis. J Nucl Med 26:961-962
Swayne LC (1986) Acute acalculous cholecystitis: sensitivity in detection using technetium-99m iminodiacetic acid cholescintigraphy. Radiology 160:33-38
Tanasescu D, Brachman M, Rigby J, Yadegar J, Ramanna L, Waxman A (1984) Scintigraphic triad in focal nodular hyperplasia. Am J Gastroenterol 79:61-64
Taylor A Jr, Kipper MS, Witztum K, Greenspan G, Kan M (1982) Abnormal 99mTc-PIPIDA scans mistaken for common duct obstruction. Radiology 144:373-375
Thomas PD, Turner JG, Dobbs BR, Burt MJ, Chapman BA (2000) Use of (99m)Tc-DISIDA biliary scanning with morphine provocation for the detection of elevated sphincter of Oddi basal pressure. Gut 46:838-841
Tierney S, Nakeeb A, Wong O, Lipsett PA, Sostre S, Pitt HA, Lillemoe KD (1999) Progesterone alters biliary flow dynamics. Ann Surg 229:205-209
Tobin M, Velchik MG, Powe J, Hibbard C, Alavi A (1987) The cholescintigraphic pattern of small bowel obstruction. Clin Nucl Med 12:223-225
Toftdahl DB, Hojgaard L, Winkler K (1996) Dynamic cholescintigraphy: induction and description of gallbladder emptying. J Nucl Med 37:261-266
Valberg LS, Jabbari M, Kerr JW, Curtis AC, Ramchand S, Prentice RS (1971) Biliary pain in young women in the absence of gallstones. Gastroenterology 60:1020-1026
Velchik MG, Roth GM, Wegener W, Alavi A (1991) Bronchobiliary fistula detected by cholescintigraphy. J Nucl Med 32:136-138
Verdegaal W, Esseveld M, Frensdorff E, Kruyswijk H, Warners P, Winter W, King YT (1978) Hepatobiliary scanning with 99mTc-pyridoxylidene glutamate. A retrospective study investigating the criteria for differentiation between intrahepatic and extrahepatic obstruction. Radiol Clin (Basel) 47:442-455
Wahl RL (1984) The "water-ida": a simple means to separate duodenal from gallbladder activity on cholescintigraphic studies. Eur J Nucl Med 9:335-336
Warner BW, Hamilton FN, Silberstein EB, Gaskill M, Teague D, Bower RH, Fischer JE (1987) The value of hepatobiliary scans in fasted patients receiving total parenteral nutrition. Surgery 102:595-601
Weissmann HS, Berkowitz D, Fox MS, Gliedman ML, Rosenblatt R, Sugarman LA, Freeman LM (1983) The role of technetium-99m iminodiacetic acid (IDA) cholescintigraphy in acute acalculous cholecystitis. Radiology 146:177-180
Williams HC, Pope CF, Siskind BN, Lange RC, Flye MW (1985) Vascular thrombosis in acute hepatic allograft rejection: scintigraphic appearance. J Nucl Med 26:478-481
Xynos E, Pechlivanides G, Zoras OJ, Chrysos E, Tzovaras G,

Fountos A, Vassilakis JS (1994) Reproducibility of gallbladder emptying scintigraphic studies. J Nucl Med 35:835-839

Yap L, Wycherley AG, Morphett AD, Toouli J (1991) Acalculous biliary pain: cholecystectomy alleviates symptoms in patients with abnormal cholescintigraphy. Gastroenterology 101:786-793

Yeh SH, Shih WJ, Liang JC (1973) Intravenous radionuclide hepatography in the differential diagnosis of intrahepatic mass lesions. J Nucl Med 14:565-567

Zech ER, Simmons LB, Kendrick RR, Soballe PW, Olcese JA, Goff WB 2nd, Lawrence DP, DeWeese RA (1991) Cholecystokinin enhanced hepatobiliary scanning with ejection fraction calculation as an indicator of disease of the gallbladder. Surg Gynecol Obstet 172:21-24

Zeman RK, Burrell MI, Dobbins J, Jaffe MH, Choyke PL (1985) Postcholecystectomy syndrome: evaluation using biliary scintigraphy and endoscopic retrograde cholangiopancreatography. Radiology 156:787-792

Ziessman HA (2001) Cholecystokinin cholescintigraphy: clinical indications and proper methodology. Radiol Clin North Am 39:997-1006, ix

Ziessman HA, Jones DA, Muenz LR, Agarval AK (2003) Cholecystokinin cholescintigraphy: methodology and normal values using a lactose-free fatty-meal food supplement. J Nucl Med 44:1263-1266

10 Peptide Imaging

Irene Virgolini and T. Traub-Weidinger

CONTENTS

I. Virgolini, MD
Professor, Medical University of Innsbruck, Clinic of Nuclear Medicine, Anichstraße 35, 6020 Innsbruck, Austria
T. Traub-Weidinger, MD
Medical University of Innsbruck, Clinic of Nuclear Medicine, Anichstraße 35, 6020 Innsbruck, Austria

10.1 Introduction

Receptors are high-affinity binding proteins that respond to specific ligands with a defined physiological event. Changes in the interaction of a ligand with its receptor have been implemented in a variety of human diseases such as diabetes and hyperlipoproteinemia. Over the past decade, substantial documentation with receptor-mediated imaging agents has been presented. Radiotracers and nuclear medicine technology are used to detect many types of cancers in their early stages by recognition of tumor-specific properties. However, among thousands of possible candidates, only a few radioligands have entered the clinic and are useful in daily routine. Over the past three decades, such radioligands have evolved from monoclonal antibodies, which are large proteins, through $F(ab')_2$ and Fab fragments to the smaller "molecular recognition units," and finally to small biologically active (synthetic) peptides. The molecular weight of such peptides is extremely diverse, ranging from small peptides which can be produced by solid phase or solution synthesis to larger polypeptides (>50 residues) which are more efficiently prepared by molecular cloning.

One of the characteristics that can be exploited for imaging is the high-affinity binding of a radiopeptide tracer to receptors expressed on the surface of specific cells. The high level expression of pep-

tide receptors on various tumor cells, as compared with normal tissues or normal peripheral blood cells (Virgolini et al. 1994a; Reubi 1995), has provided the molecular basis for the clinical use of radiolabeled peptides as tumor tracers in nuclear medicine. In fact, receptor scintigraphy using radiolabeled peptide ligands has proven its effectiveness in clinical practice. In particular, somatostatin (SST) and vasoactive intestinal peptide (VIP) analogs have successfully been used for imaging purposes.

Molecular cloning of human SST and VIP receptors (hSSTR, hVIPR) has recently provided new insight into the biology and interaction of SST and VIP. These receptors are widely distributed throughout the human body and seem to be responsible for the divergent effects observed for SST, VIP, and their analogs. Somatostatin is a 14-amino-acid peptide acting as a neurotransmitter or as a hormone, depending on the site of action and target cell type. Hormonal effects of SST include the suppression of release of growth hormone (GHRF) from the anterior pituitary gland (Brazeau et al. 1973) as well as inhibition of release of other pituitary, pancreatic, and gastrointestinal hormones or secretary proteins (Brazeau et al. 1973; Plewe et al. 1984). In addition, SST inhibits growth and proliferation of various tumor cells (Reichlin 1983). Vasoactive intestinal peptide is a 28-amino-acid neuroendocrine mediator with a broad range of biological activities in various cells and tissues. Initially, VIP was characterized as a vasodilatory substance (Said and Mutt 1970) responsible for the watery diarrhea syndrome in patients with VIP-secreting tumors (Verner and Morrison 1958; Bloom et al. 1973; Said and Faloona 1975). VIP and its analogs promote growth and proliferation of both normal and malignant cells (Pincus et al. 1990; Haegerstrand et al. 1989; Virgolini et al. 1994a).

Five different hSSTR (Yamada et al. 1992a,b, 1993; Yasuda et al. 1992; Demchyschyn et al. 1993; Corness et al. 1993; Rohrer et al. 1993; Bell et al. 1995) have been characterized in detail and have been cloned. In several species, VIPR subtypes have been characterized and/or cloned (Laburthe and Couvineau 1988; Couvineau and Laburthe 1985; Couvineau et al. 1986, 1990, 1994; Ishihara et al. 1992; Lutz et al. 1993; Sreedharan et al. 1991; Usdin et al. 1994; Ullrich et al. 1998). The human VIPR cloned from the small intestinal epithelium (hVIPR; Couvineau et al. 1994) presents a human common VIP/PACAP receptor, similar to the VIPR cloned from human colonic cancer cells (Sreedharan et al. 1991). This receptor has been termed VIPR1, whereas another VIPR (termed VIPR2) has been cloned from animal (Lutz et al. 1993; Inagaki et al. 1994) and human species (Svoboda et al. 1994). VIPR2 is characterized by substantial affinity for helodermin (Robberecht et al. 1989). Also secretin appears to distinguish between these receptors (Adamou et al. 1996). They are members of a distinct subfamily of GTP-binding protein-coupled seven-helix transmembrane spanning receptors, being similar in their amino acid sequences but differing in extracellular amino terminal and intracellular carboxy-terminal domains. There is at least one PACAP receptor, termed PAC1, which is characterized by high affinity for PACAP and low affinity for VIP (Robberecht et al. 1994; Harmar et al. 1998; Vaudry et al. 1997).

Several efforts have been undertaken to identify hSSTR subtypes expressed by primary human tumors; however, the expression patterns have not been established in detail (Fig. 10.1). We have reviewed (Virgolini et al. 1997) the results of several attempts to identify hSSTR subtypes in primary human tumors. The patterns of expression of mRNA for hSSTR subtypes and their distributions are different, but often overlapping in various tumors. Using the RT-PCR (reverse transcription polymerase chain reaction) technique, in situ hybridization or Northern blotting, numerous observations suggest that hSSTR are expressed in various human tumors. However, the expression of hSSTR seems to be very individual and varies from tumor entity to tumor entity. In initial studies only the hSSTR2 was identified frequently in primary human tumors (Reubi et al. 1994). With the years, other hSSTR have been frequently described (Greenman and Melmed 1994a,b; Kubota et al. 1994; Panetta and Patel 1994; Vikic-Topic et al. 1995; Miller et al. 1995; John et al. 1996; Buscail et al. 1996; Janson et al. 1996; Schaer et al. 1997; Laws et al. 1997; Jais et al. 1997; O'Nilsson et al. 1998; Fisher et al. 1998). The data published vary from research group to research group, most probably due to the different techniques applied and also to the different tumor entities investigated. Others and ourselves have identified the hSSTR3 as another peptide receptor expressed on or in human tumor cells (Pangerl et al. 1997; Schaer et al. 1997). Human-SSTR3 may be responsible for binding both VIP and SST/octreotide (common binding site), and for the observed cross-competition between these peptides in primary human tumors as well as a variety of human tumor cell lines (Virgolini et al. 1994a, 1996b, 1998a; Peck-Radosavljevic et al. 1998). Contrary

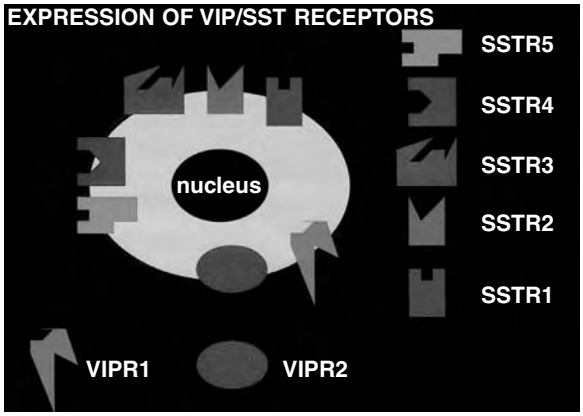

Fig. 10.1. Presentation of somatostatin (*SST*) and vasoactive intestinal peptide (VIP) receptor expression in human tumor cells. Five different SST and two different VIP receptors were characterized and cloned

to other SSTR subtypes, only the hSSTR3 appears to be over-expressed at a very high level in or on all tumors (Pangerl et al. 1997; Raderer et al. 1998a). In terms of the VIP receptors, Reubi et al. (2000a,b) showed VIPR subtype expression on tumors using receptor subtype-selective analogs: VIPR1 expression was found more frequently in malignant epithelial neoplasms, such as carcinomas of the lung, stomach, colon, rectum, breast, prostate, pancreatic ducts, liver, or urinary bladder. In contrast, the VIPR2 was only expressed in leiomyosarcomas. Predominant expression of PAC1 was observed in tumors originating from the neuronal and endocrine system including glial tumors (astrocytoma, glioblastoma, oligodendroglioma), neuroblastomas, as well as pituitary adenomas (Oka et al. 1998; Robberecht et al. 1994, 1993; Vertongen et al. 1996). Therefore, catecholamine-secreting tumors (pheochromocytoma, paraganglioma) and many endometrial carcinomas express PAC1 receptors (Reubi et al. 2000a,b).

10.2 Radiolabeled Peptides as Imaging Agents

The SSTR/VIPR imaging agents used for clinical studies are listed in Table 10.1. Some of these radiolabeled agents were also tested for their in vitro binding to hSSTR/hVIPR subtypes expressed on COS7 or CHO cells. Surprisingly, for several of the peptides differences were described in the binding behavior of the parent substance, the labeled and/or unlabeled ligand (Smith-Jones et al. 1998). All these tracers were found to bind to tumor cell lines known to express SSTR as well as to primary human tumors. For most SSTR/VIPR tracers, significantly increased binding to tumor cells as opposed to normal cells was documented.

Native SST exists in two forms (14 or 28 amino acids), but it is readily attacked by aminopeptidases and endopeptidases, and has a short in vivo half-life. Consequently, synthetic SST analogs, which incorporate a Phe-(D)Trp-Lys-Thr (or similar sequence) and which are metabolically stabilized, at both the

Table 10.1. Overview of selected imaging agents (as of June 2004)

Radioligand	Availability	Receptor binding data
^{123}I-octreotide	No longer in use	Not studied
^{123}I-Tyr^3-octreotide	No longer in use	hSSTR2, 5 (3)
^{111}In-DTPA-D-Phe^1-octreotide	Commercially available	hSSTR2, 5 (3)
^{111}In-DOTA-Tyr^3-octreotide	May be prepared in house	hSST2, 5 (3)
^{111}In-DOTA-lanreotide (MAURITIUS)	In house	hSST2–5 (1)
^{99m}Tc-HYNIC-octreotide	In house	Not studied
^{99m}Tc-depreotide (P829)	Commercially available	hSST2, 3, 5
^{99m}Tc-Demotate1 (Tyr^3-Octreotate analog)	May be prepared in house	Not studied
^{123}I-VIP	In house	hSSTR3, VIPR1, 2
^{99m}Tc-TP 3654 (VIP analog)	In house	not studied
^{99m}Tc-Neurotensin-XI	First clinical data	NTR1
^{111}In-DTPA-D-Glu^1-minigastrin	Phase I/II	CCK2
^{99m}Tc-RP527 (Bombesin/GRP analog)	First clinical experiences	GRP (BB2)
^{99m}Tc-Bombesin (BN)	First clinical experiences	Not studied
^{111}In-DTPA-Pro1, Tyr4-BN	In house	Not studied
PET-TRACER		
^{64}Cu-DOTA-Aoc-BN(7-14)	In house	Not studied
^{64}Cu-TETA-octreotide	In house	Not studied
^{68}Ga-DOTA-Tyr^3-octreotide	In house	hSSTR 2 (3,4,5)
^{68}Ga-DOTA-Tyr^3-octreotate	In house	
^{18}F-FP-Gluc-TOCT (octreotate analog)	In house	hSSTR2 (3,4)

N- and C-terminals, were developed for clinical applications. In the past, three commercially available SST analogs, i.e., octreotide (Rosenberg and Brown 1991), lanreotide (Giusti et al. 1997), and vapreotide (Stiefel and Morant 1993), have been shown to be effective in controlling the growth of some human tumors. These SST analogs all have similar binding profiles for four of the five hSSTR subtypes (i.e., a high affinity for hSSTR2 and hSSTR5, moderate affinity for hSSTR3, and very low affinity for hSSTR1), but lanreotide and vapreotide have a moderate affinity for hSSTR4, whereas octreotide has little or no affinity for this hSSTR (Lamberts et al. 1996).

10.2.1 Octreotide-Based Agents

In initial studies ^{123}I-Tyr^3-octreotide was used to demonstrate the feasibility to detect and localize human neuroendocrine tumors (Lamberts et al. 1990; Krenning et al. 1989, 1993; Kvols 1994). However, the labeling with ^{123}I-sodium iodide of high specific activity is expensive and is hardly available worldwide. Furthermore, iodination of peptides requires technology and skills, which are usually restricted to larger nuclear medicine institutions. Due to substantial accumulation of ^{123}I-Tyr^3-octreotide in the gut as a result of hepatobiliary clearance of the agent, interpretation of the abdominal images can sometimes be very difficult. Similar high abdominal accumulation was also found with ^{123}I-octreotide (Virgolini et al. 1996a). Some of the aforementioned problems have successfully been overcome by the introduction of ^{111}In-DTPA-D-Phe^1-octreotide which is the first receptor radiopharmaceutical available on the market (OctreoScan, Mallinckrodt Medical, St. Louis, Mo.). In this molecule a DTPA group is coupled to the NH_2 group of the N-terminal D-Phe residue (Bakker et al. 1991). As opposed to ^{123}I-Tyr^3-octreotide, ^{111}In-DTPA-D-Phe^1-octreotide shows minor accumulation in the liver and is predominantly excreted via the kidneys (Krenning et al. 1992). Therefore, the interpretation of scintigrams of the abdominal region is less affected by intestinal background radioactivity.

Clinical studies with ^{111}In-DTPA-D-Phe^1-octreotide have clearly shown that this receptor radiopharmaceutical is effective in diagnosing and staging tumors and their metastases, due to binding to hSSTR2 (Lamberts et al. 1996; Smith-Jones et al. 1998a,b).

Another analog of octreotide, ^{111}In-DOTA-D-Phe^1-Tyr^3-octreotide, has been prepared showing similar in vivo accumulation as compared with ^{111}In-DTPA-D-Phe^1-octreotide (Krenning et al. 1996, 1997). The purpose of this development was to create a ligand, which can be stably labeled with ^{90}Y for receptor-mediated radiotherapy (Otte et al. 1997, 1998). In this molecule the Phe^3 was replaced with Tyr to increase the hydrophilicity of the radiolabeled peptide.

Several efforts have been made to label octreotide with ^{99m}Tc. At our institution, ^{99m}Tc-labeled N-α-(6-hydrazinonicotinoyl)-octreotide (HYNIC-octreotide) did not display sufficiently high binding affinity for hSSTR compared with other octreotide analogs (Krois et al. 1996). However, scintigraphic data have demonstrated excellent image quality for similar HYNIC-octreotide analogs in human studies (Bangard et al. 1998; Decristoforo et al. 2000; Gabriel et al. 2003).

One of the drawbacks of ^{111}In-DTPA-octreotide is the limited spatial resolution of the radiopeptide. The development of a suitable chelator for radiometal labeling, such as DOTA, a universal ligand for labeling with trivalent metal ions, resulted in synthesis of the PET tracer ^{68}Ga-DOTA-Tyr^3-octreotide (^{68}Ga-DOTA-TOC; Hofmann et al. 2001).

The first data of ^{64}Cu-TETA-octreotide showed a high rate of lesion detection, sensitivity, favorable dosimetry and pharmacokinetic in a small cohort of neuroendocrine tumor patients (Anderson et al. 2001).

Improvements on octreotide itself included the replacement by octreotate, thereby increasing the internalization rate and subsequently the in vivo uptake by hSSTR2 expressing tumor cells (de Jong et al. 1998a). The change from octreotide to octreotate analogs increased not only the binding affinity, internalization rate and selectivity of hSSTR2 but clinical studies with Tyr^3-octreotate derivatives have shown considerable improvement of SSTR scintigraphy (de Jong et al. 1998b). A new octreotate derived with the tetramine chelator has been introduced for clinical studies (Maina et al. 2002). In the same way, the ^{18}F-labeled carbohydrated analog of octreotide, i.e., ^{18}F-fluoropropionyl-Lys0-Tyr3-octreotate (^{18}F-FP-Gluc-octreotate), which shows very high binding affinity to hSSTR2, moderate affinity to hSSTR4 and 5, and no affinity to hSSTR1 and 2 is under clinical evaluation for PET applications (Wester et al. 2003).

In general, it has to be mentioned that the different chemical structures, different charges and

hydrophilicity of the SST analogs showed marked changes in the subtype receptor affinity profiles (Reubi et al. 2000a).

10.2.2 ^{111}In-DOTA-Lanreotide

^{111}In-DOTA-lanreotide or MAURITIUS (*m*ulticenter *a*nalysis of a *u*niversal *r*eceptor *i*maging and *t*reatment *i*nitiative: a E*u*ropean *s*tudy) is an SST analog which is a conjugate of DOTA coupled directly to the N-terminus of lanreotide (Smith-Jones et al. 1998a,b). The substance can be stably labeled with a variety of radionuclides. ^{111}In-/^{90}Y-DOTA-lanreotide binds with high affinity (dissociation constant K_d 1-12 nM) to numerous primary human tumors such as intestinal adenocarcinomas and breast cancer. ^{111}In-/^{90}Y-DOTA-lanreotide exhibits a similar high binding affinity (K_d 2-11 nM) for the human breast cancer cell lines T47D and ZR75-1, the prostate cancer cell lines PC3 and DU145, the colonic adenocarcinoma cell line HT29, the pancreatic adenocarcinoma cell line PANC1, and the melanoma cell line 518A2. When expressed in COS7 cells, ^{111}In-/^{90}Y-DOTA-lanreotide binds with high affinity to hSSTR2 (K_d≈5 nM), hSSTR3 (K_d 5 nM), hSSTR4 (K_d 3.8 nM), and hSSTR5 (K_d 10 nM), and with lower affinity to hSSTR1 (K_d≈200 nM).

^{111}In-/^{90}Y-DOTA-lanreotide has been applied at several centers in Europe to prove the concept of receptor-mediated radiotherapy controlled by dosimetry using the same ligand showing stable disease in 41% of 154 patients and regressive tumor disease in 14% of patients with different tumor entities expressing hSSTR. A direct comparison of ^{111}In-DOTA-lanreotide with ^{111}In-DTPA-D-Phe^1-octreotide and ^{111}In-DOTA-Tyr3-octreotide has resulted in discrepancies in the scintigraphic imaging pattern in one third of tumor patients concerning both the tumor uptake as well as the detection of tumor lesions (Virgolini et al. 2002).

10.2.3 ^{99m}Tc-Depreotide (P829)

Although clinical results with ^{111}In- and ^{123}I-labeled peptides have been excellent, extensive efforts have been made in preparing and evaluating peptides labeled with ^{99m}Tc. The SST/VIP peptide analogs are small molecules that target their receptor and clear rapidly from the circulation. Accordingly, radionuclides with short half-lives are the labels of choice. These permit the administration of larger amounts of radioactivity and reduce the radiation dose to the patient. Provided that the energy of the gamma photon emitted is appropriate, this results in a high count rate and high image quality, which translates into a high diagnostic efficacy.

In contrast to ^{111}In and ^{123}I, ^{99m}Tc is considered the optimal radionuclide in nuclear medicine, freely available from in-house ^{99}Mo/^{99m}Tc generators, and attempts have been made to label SST/VIP with ^{99m}Tc. Several chelate systems have been used for labeling SST analogs with ^{99m}Tc such as N^4-aromatic and N^4 aliphatic ligands, N^3S ligands, or HYNIC chelators (Maina et al. 1994; Mather and Ellison 1994; Krois et al. 1996; Thakur et al. 1997). None of these methods have proven optimal for in vivo trials with the exception of the N^3S system used in the agent P829 (Vallabhajosula et al. 1996). P829 carries a sequence, which mimics the binding domain for SST. P829 is synthesized using solid phase peptide synthesis and N-(9-fluorenyl)methoxycarbonyl chemistry. ^{99m}Tc-P829 has been identified as a suitable hSSTR ligand, which binds to hSSTR2, 3, and 5 with high affinity (Virgolini et al. 1998a). The cyclic hexapeptide domain of the peptide component of ^{99m}Tc-P829 contains the pharmacophore L-tyrosine-D-tryptophan-L-lysine-L-valine that binds to the SSTR of tumor cells. In fact, ^{99m}Tc-P829 has indicated clinical potential for imaging lung tumors, melanomas, or breast cancers (Virgolini et al. 1998a; Blum et al. 1999; Hustinx et al. 1997; Lastoria et al. 1996). The product was meanwhile (as one of the first receptor imaging agents) registered for imaging non small cell lung cancer in combination with - planar radiography or CT.

10.2.4 ^{99m}Tc-Vapreotide (RC-160)

Vapreotide (RC-160, Octastatin) is a SST analog being developed for gastroenterologic, neuroendocrine, and oncologic applications. The peptide binds to hSSTR2 and hSSTR5 with high affinity, and moderately also to hSSTR3 and hSSTR4.

Using CTPA (1,4,8,11-tetraazacyclotetradecane) as a bifunctional agent, RC-160 was labeled with ^{99m}Tc and was evaluated in mice bearing experimental human prostate cancers. In these studies, tumor uptake was estimated to be significantly higher compared with other compounds (Thakur et al. 1997). Studies by Guhlke et al. (1997) and Bogatzky et al.

(1997) have shown that RC-160 can also be labeled with either ^{131}I, ^{99m}Tc, or ^{188}Re using other chelating systems. However, no clinical data have become available in humans in recent years.

10.2.5 ^{123}I-VIP and Analogs

Vasoactive intestinal peptide (VIP) is a 28-amino-acid neuropeptide with a broad range of biological activities. Vasoactive intestinal peptide receptor scintigraphy uses naturally occurring VIP labeled with ^{123}I in positions 10 and 22 of the amino acids (Virgolini et al. 1994b, 1995).

Although the results obtained thus far suggest ^{123}I-VIP to be a promising tumor tracer with the potential to provide additional information to conventional imaging, there are still some shortcomings which hamper widespread clinical use of the compound. Attempts have been made to label VIP with ^{99m}Tc since ^{123}I-VIP is difficult and costly to produce.

In developing such a radiopharmaceutical, we have identified P1666 among VIP peptide candidates to be a promising ^{99m}Tc-labeled VIP analog for administration to tumor patients (Shirzad et al. 1998; Lister-James et al. 1998). Other VIP analogs have also been implemented including an ^{18}F-labeled VIP analog (Jagoda et al. 1997) as well as several ^{99m}Tc-VIP analogs (Pallela et al. 1998a–c). First in vivo results for the ^{99m}Tc-labeled VIP analog TP3654 showed promising results for imaging VIP-receptor positive cancer (Thakur et al. 2000).

10.2.6 Radiolabeled Neurotensin Analogs

Native neurotensin (NT) is a tridecapeptide localized both in the central nervous system and in peripheral tissues, mainly in the gastrointestinal tract. In the central nervous system, NT plays the role of neurotransmitter or neuromodulator of dopamine transmission, and of anterior pituitary hormone secretion. Therefore, it shows potent hypothermic and analgetic effects in the brain. In the periphery, NT acts as a local hormone exerting a paracrine and endocrine modulation of the digestive tract (Vincent et al. 1999). The pharmacological effect of NT results from the specific interaction of the peptide with the cell surface. Until now there are known three NT receptors (NTR). NTR1 is a well documented receptor, including Ca2+ release after inositol 1,4,5-triphosphate stimulation (Chabry et al. 1994), activation of MAPKs (Poinot-Chazel et al. 1996) via protein kinase C, leading to its role in cell proliferation, whereas the levocobastine sensitive NTR2 is still a matter of controversy (Yamada et al. 1998). NTR3 is non-G protein coupled capable of binding the peptide with high affinity (Mazella et al. 1998). The prevalence of NT receptors (NTR) in several human tumors makes it an attractive target for the delivery of cytotoxic drugs and imaging agents (Wang et al. 2000; Reubi et al. 1998, 1999; Maoret et al. 1994), which binds to NTR and induces tumor growth (Moody et al. 2001; Seethalakshim et al. 1997). The short plasma half-life hinders the biochemical application, and some effort has been undertaken to develop neurotensin derivatives for possible clinical application (Achilefu et al. 2003; Garcia-Garayoa et al. 2001; Hillairet de Boisferon et al. 2002).

10.2.7 Radiolabeled Bombesin/Gastrin Releasing Peptides

Bombesin and gastrin releasing peptide (GRP) are members of a family of brain-gut peptides (Walsh 1994a). The 14-amino-acid peptide bombesin (BN) has a high affinity for gastrin-releasing peptide (GRP) receptors expressed in a variety of tumors. Stimulation of proliferation by BN was reported for lung, breast and pancreatic cancer (Alexander et al. 1988; Nelson et al. 1991; Wang et al. 1996). BN and GRP mediate their action through membrane-bound, G protein-coupled receptors, which include at least four different subtypes, namely the neuromedin B receptor subtype (BB1), the GRP receptor subtype (BB2), the BB3 and BB4 subtypes (Spindel et al. 1990; Wada et al. 1991; Fathi et al. 1993; Nagalla et al. 1995). With the exception of the GRP receptor (Ferris et al. 1997; Rettenbacher and Reubi 2001), these subtypes have been poorly investigated with regard to their subtypes and function in human tissue. High density of GRP receptors were identified by in vitro receptor autoradiography in human prostate, breast and gastrointestinal cancer (Sun et al. 2000; Markwalder and Reubi 1999; Fleischmann et al. 2000; Gugger and Reubi 1999; Caroll et al. 1999; Saurin et al. 1999). Accordingly, interest in developing radiometal labeled BN derivatives has been shown (Nock et al. 2003; Hoffmann et al. 2003; la Bella et al. 2002). First data show

promising results for possible tumor imaging: ^{99m}Tc-BN (Scopinaro et al. 2002, 2003a,b), ^{99m}Tc-RP527 (van der Wiele et al. 2000), ^{111}In-DTPA-Pro^{1},Tyr^{4}-BN (Breeman et al. 2002), and ^{64}Cu-DOTA-Aoc-BN(7-14) (Rogers et al. 2003).

10.2.8 Radiolabeled Cholecystokinin/Gastrin Analogs

The gastrointestinal peptides cholecystokinin (CCK) and gastrin exist in different molecular forms. Pro-CCK and pro-gastrin can be processed to peptides of variable length but, as biological active peptides they have the same five terminal amino acids at their carboxy terminus. Both act as neurotransmitter in the brain, as regulator of various functions of the gastrointestinal tract, (i.e., stomach, pancreas, and gallbladder; Walsh 1994). Besides their physiological role of growth factor in the gastrointestinal tract, they can also act as growth factors in same tumor entities, such as colonic, gastric, and brain carcinoma (Dockray 2000; Rehfeld and van Solinge 1996; Camby et al. 1996). Until now, three CCK receptor subtypes are known. CCK1 (former CCK-A) and CCK2 (former CCK-B) subtypes are well described (Wank et al. 1992), distinguishable pharmacologically by their low CCK1- versus high CCK2-affinity for gastrin. CCK2 receptors were described in small cell lung carcinomas, medullary thyroid carcinoma, astrocytomas, in sex cord stromal ovarian carcinomas, in some neuroendocrine gastroenteropancreatic tumors, especially insulinomas, in breast and endometrial adenocarcinomas and in soft tissue tumors, in particular leiomyosarcomas (Reubi et al. 1997; Blaker et al. 2002; Reubi and Waser 2003; Schaer et al. 1999). CCK1 were expressed in neuroendocrine lung and gastroenteropancreatic tumors, and meningiomas (Reubi et al. 1997; Reubi and Waser 2003; Mailleux and Vanderhaeghen 1990). For CCK2 receptor imaging ^{111}In-DTPA-D-Glu1-minigastrin has been developed and clinically investigated (Behr et al. 1999; Behr and Behe 2002).

10.2.9 Other Radiolabeled Peptides

Substance P, a neuropeptide involved in a variety of functions of the central and peripheral nervous systems, is able to stimulate proliferation of malignant tumor cells (Hökfelt et al. 2001). One of the substance P receptor subtypes is the NK1 receptor frequently expressed in glial tumors, medullary thyroid cancer, small cell lung cancer, pancreatic as well as breast cancer (Henning et al. 1995; Friess et al. 2003). However, until now there is only one report of visualization of the thymus in autoimmune disease using an ^{111}In-labeled DTPA derivative of substance P (van Hagen et al. 1996).

More than 10 years ago, linear α-melanocyte-stimulating hormone (α-MSH) analogs were labeled with ^{111}In and examined for their biodistribution and malignant melanoma-targeting properties in vivo compromising their in vivo imaging potential and preventing their therapeutic applications (Wraight et al. 1992). More recently, a novel class of cyclic α-MSH analogs that coordinate their ^{99m}Tc and ^{188}Re into their three-dimensional structures were developed, no in vivo visualization of cancer expressing α-MSH receptors was performed in humans (Chen et al. 2000; Giblin et al. 1998).

Not only tumor receptor imaging, but also tumor angiogenesis imaging is a new and interesting tool for peptide development. Recently, RDG (Arg-Gly-Asp) peptides, which are described to antagonize tumor angiogenesis, are in the preclinical phase of in vitro and in vivo experiments (Haubner et al. 1999, 2000; Capello et al. 2003).

10.3 Scintigraphy with Radiolabeled Peptides

10.3.1 Scintigraphy with ^{111}In-DTPA-D-Phe1-Octreotide

Abundant information exists on the best scanning procedures for OctreoScan (Krenning et al. 1993). In principle, early planar images should be acquired at approximately 4–6 h post-injection of 10 μg peptide labeled with approximately 150 MBq (4 mCi) ^{111}In chloride. Late planar images should be acquired at 24 h. Depending on the clinical indication for SSTR scintigraphy, whole-body imaging should be performed in those patients in whom the extent of the disease has to be evaluated. It is very important to use a slow scanning procedure of 6 cm, or less, per minute (Krenning et al. 1993). Single photon emission computed tomography (SPECT) should be performed in all patients, preferably at 24 h. In some patients a 48-h acquisition may be necessary to evaluate unclear accumulation in the abdomen. All images should be obtained with a large-field-of-view gamma camera, equipped with a

medium-energy parallel-hole collimator. Data from both ^{111}In photon peaks (172 and 245 keV; window width 20%) should be used. For planar imaging a matrix of 128×128 (500 kcounts preset), and for SPECT a 64×64 matrix, should be used (60 projections, 45–60 s per projection). In our institution tomographic reconstruction is performed with a Wiener and ramp filter.

Technical progress with SPECT/CT hybrid imaging has affected the diagnostic interpretation of SSTR scintigraphy in 32% and induced changes in patient management in 14% of the studied 72 patients (Krausz et al. 2003). In 104 patients with neuroendocrine tumors image fusion of CT and SPECT provided additional information and changed patient management (Kienast et al. 2003).

10.3.2 Scintigraphy with 99mTc-Depreotide

In analyzing early and delayed imaging with ^{99m}Tc-depreotide, no appreciable diagnostic difference was reported (Lastoria et al. 1996; Virgolini et al. 1998a; Blum et al. 1998). In general, the image quality was better for the delayed images (i.e., 90 min post injection). We recommend imaging at 15 and 90 min after injection of approximately 50 μg peptide labeled with 740 MBq (20 mCi) ^{99m}Tc-depreotide. Standard planar and SPECT acquisitions should be obtained with a LEAP collimator.

10.3.3 Scintigraphy with 123I-VIP

Iodine-123 VIP scintigraphy was performed in more than 500 patients at the University of Vienna during the years 1993–1998. In general, the application of ^{123}I-VIP is safe; however, blood pressure may drop during the initial minutes after bolus injection. Patients may experience a feeling of "heat" if the tracer is injected too quickly. We recommend early (15–60 min after injection) and delayed (3–6 h after injection) planar images of the abdomen in anterior, posterior, and lateral views. In all patients SPECT imaging should be performed at 2–4 h.

The preferred dose of ^{123}I-VIP is 150–200 MBq (2–3 mCi), with 1 μg (300 pmol). The VIP standard planar and SPECT acquisitions should be obtained with a large-field-of-view gamma camera equipped with a low-energy, general-purpose collimator. In clinical routine sequential imaging is not required. Planar images should be acquired in a 128×128 matrix for 500 kcounts. For SPECT imaging, a 64×64 matrix, 60 projections, 30–60 s per projection, are recommended. All patients should receive sodium perchlorate and potassium iodide prior to injection of ^{123}I-VIP for thyroid blockade. More recently, we have modified native VIP to produce a stable VIP labeled with technetium (^{99m}Tc-P1666). First imaging studies in 16 patients have shown the potential to visualize primary/recurrent intestinal adenocarcinoma and/or metastatic spread. However, because of the clinical side effects (heat, sweating headache and facial flushing) observed after administration, ^{99m}Tc-P1666 does not seem to be helpful in the clinical work-up (Virgolini et al. 1999).

10.3.4 Scintigraphy with Other Radiolabeled Peptides

The new tetramine-functionalized Tyr^3-octreotate derivative (Demotate 1), easily labeled with ^{99m}Tc at high specific activities showed promising data for visualization of SSTR positive lesions (Decristoforo et al. 2000, 2003).

The ^{99m}Tc labeled octreotide derivate HYNIC-TOC was described for scintigraphic evaluation compared to ^{111}In-DTPA-octreotide with improved target-to-background ratios (Gabriel et al. 2003).

PET tracers such as ^{68}Ga-DOTA-TOC (Hofmann et al. 2001, 2003; Henze et al. 2003a,b) or ^{64}Cu-TETA-octreotide (Aderson et al. 2001), are also under clinical evaluation. The first clinical results were reported for ^{18}F-FP-Gluc-TOCT by Wester et al. (2003).

Other peptides such as the ^{99m}Tc-labeled neurotensin (8-13): i.e. amino acids 8-13) and the GRP derivate ^{99m}TC-BN are currently under evaluation (Buchegger et al. 2003; Scopinaro et al. 2002, 2003a,b).

10.4 Oncologic Applications

10.4.1 Colorectal Cancer

10.4.1.1 The Clinical Problem

Colorectal cancer is among the leading causes of cancer death worldwide and accounts for approxi-

mately 10% of all cancer deaths. It is second to lung cancer in men and to breast cancer in women, and it is estimated that one in 20 persons is affected in Western countries (de Cosse et al. 1994; Boring et al. 1994; Seidman et al. 1985). The only curative therapy is surgical resection, whereas oncologic intervention in patients with advanced, inoperable cancer remains palliative at best (Scheithauer et al. 1993). Because of the strong association between early detection of primary and recurrent tumors or metastases and prognosis, exact determination of the tumor burden is important for the clinical management. Imaging methods available include endoscopy, ultrasound, barium enema, as well as CT and MRI. Although these methods have specific roles in the evaluation of patients with colorectal cancer, none are "optimal," since peritoneal metastasis or small extrahepatic lesions mimicking postoperative scars (Schlag et al. 1989) might escape detection.

Various groups have shown that gastrointestinal adenocarcinomas express high-affinity binding sites for VIP as well as hSSTR3 and other subtypes (Reubi 1995; Virgolini et al. 1994a; Pangerl et al. 1997).

10.4.1.2 123I-VIP Receptor Scintigraphy

In an initial series with ^{123}I-labeled VIP (Virgolini et al. 1994b, 1995) we demonstrated the ability of the tracer to localize even small-sized adenocarcinomas of the gastrointestinal tract along with the safety of the agent. In addition, a higher sensitivity for the peptide tracer was found when compared with an ^{111}In-labeled, commercially available anti-TAG-72.3-antibody (Raderer et al. 1996).

Based on these findings, we have followed 80 consecutive patients in order to determine the diagnostic capability of ^{123}I-VIP for visualization of adenocarcinomas of the colon and rectum (Raderer et al. 1998c). Thirteen patients were free of tumor after complete resection of a Dukes' stage C cancer, 8 patients presented with primary and 14 with locally recurrent tumors, but were free of metastases. Ten patients had locally recurrent disease and liver, lung, or lymph node metastases, respectively. Organ metastases (i.e., liver, lung, or lymph nodes) were present in 35 patients. The size of the primary or recurrent tumors varied between 3 and 16 cm, and the size of metastases between 1 and 13 cm. Scan results were evaluated independently by two nuclear medicine physicians in a blinded way, and results were then compared with CT results not older than 4 weeks. Seven of eight primary (87%) and 21 of 24 (82%) locally relapsing cancers were imaged with ^{123}I-VIP (Fig. 10.2). Negative VIP scans were obtained in all 13 patients in whom the cancers had been curatively resected. All patients with lymph node metastases showed positive VIP scans (4 of 4), and positive scans were obtained in 25 of 28 (89%) patients with liver metastases and in two of three cases with lung metastases. In four patients with relapsing cancer, the VIP scan indicated the presence of disease before CT, and in two patients the diagnosis of scar tissue instead of a local recurrence of rectal cancer as suggested by CT could be established.

Furthermore, our data support in vitro results demonstrating a high expression of VIP receptors in a large percentage of colorectal adenocarcinomas (Reubi 1995; Virgolini et al. 1994a). However, it has to be emphasized that the majority of patients undergoing VIP receptor scanning had not received chemotherapy before injection of the tracer. Virtually nothing is known about the influence of chemotherapeutic agents on receptor expression. Despite the limited number of patients (four patients with

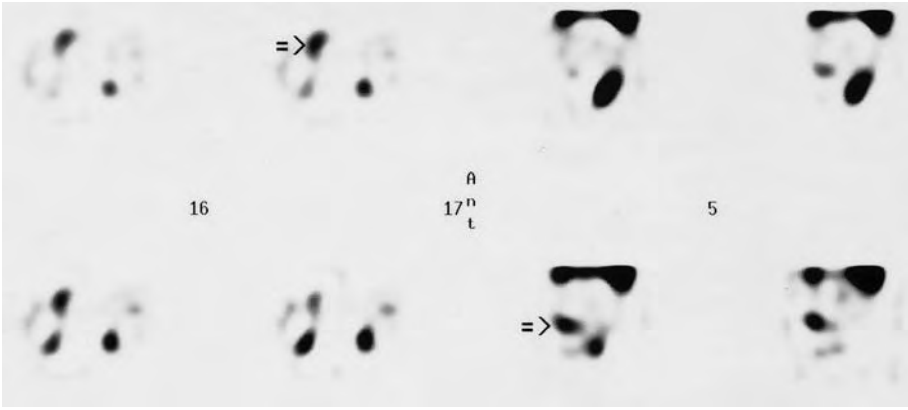

Fig. 10.2. ^{123}I-VIP receptor scintigraphy indicates the primary colorectal tumor (*arrow*) 2 h after injection of 1 μg (150 MBq) radioligand with single photon emission computed tomography (SPECT); four images in *left panel* (*16*, *17*): transverse reconstruction; four images in *right panel* (*5*): sagittal reconstruction

adjuvant treatment and 12 patients with palliative, 5-FU based therapy), a negative impact of cytotoxic agents on scintigraphy cannot be excluded. All patients undergoing adjuvant treatment had negative scans, but also did not develop signs of malignancy in a 3-month follow-up period after scintigraphy. In contrast, two patients with locally relapsing cancers and three patients with liver lesions had negative scans, whereas the remaining seven patients with palliative treatment had positive scans. Further investigations to evaluate the influence of treatment on receptor expression are necessary.

Our results add to the accumulating body of evidence that ^{123}I-VIP receptor scintigraphy is a highly promising method for imaging and staging of gastrointestinal adenocarcinomas. Apart from the clinical application of peptide-imaging, the over-expression of peptide binding sites offers the potential to apply radiolabeled peptides for targeted tumor therapy. However, despite the capabilities of VIP as an imaging agent, the high lung uptake does not permit the use of the compound labeled with isotopes suitable for therapy.

We conclude that ^{123}I-VIP offers valuable additional information to conventional radiological imaging in a broad cohort of patients, including subjects with small cancers or suspected recurrent cancers in scar tissue in the pelvis resulting from initial surgery.

10.4.1.3 Scintigraphy with Radiolabeled Somatostatin Analogs

In several studies we (Virgolini et al. 1994b) and others (Krenning et al. 1993) have found that OctreoScan (Mallinckrodt, Medical, St. Louis, Mo.) is not useful in imaging colorectal adenocarcinomas. This may be explained by the lack of sufficient binding to hSSTR3 or hSSTR4 which both seem to be the major receptors expressed in colonic cancer tissues (Virgolini 1997; Virgolini et al. 1997). In contrast, we found significant uptake of ^{99m}Tc-P829 by primary tumors as well as lung metastases from intestinal adenocarcinomas (Leimer et al. 1998a), underlining our in vitro observations of binding of ^{99m}Tc-P829 to hSSTR3 as well as to a variety of adenocarcinoma cell lines (Virgolini et al. 1998a). In addition, ^{111}In-DOTA-lanreotide, which is supposed to also bind to the subtype receptors hSSTR3 and hSSTR4, produced positive images in patients with colon cancer (Fig. 10.3; Virgolini et al. 1998c,d).

10.4.2 Pancreatic Cancer

10.4.2.1 The Clinical Problem

Adenocarcinoma of the pancreas is a common cause of cancer death (National Cancer Institute 1991). To date, the only therapeutic measure with curative potential is surgical intervention with total removal of clinically apparent malignant tissue. Despite improvement in terms of perioperative morbidity and mortality, the overall prognosis for patients diagnosed with pancreatic cancer remains poor, since even those individuals undergoing surgical resection have a very high risk of relapse (Warshaw and Fernandez-del Castillo 1992; American Cancer Society 1991). More than 80% of all patients die within the first year of diagnosis, and only approximately 3% of patients are still alive after 5 years (American Cancer Society 1991). One of the major obstacles in the treatment of this disease is the fact that pancreatic adenocarcinoma is almost always diagnosed at an advanced stage (Kalser et al. 1985). This is due to the lack of spe-

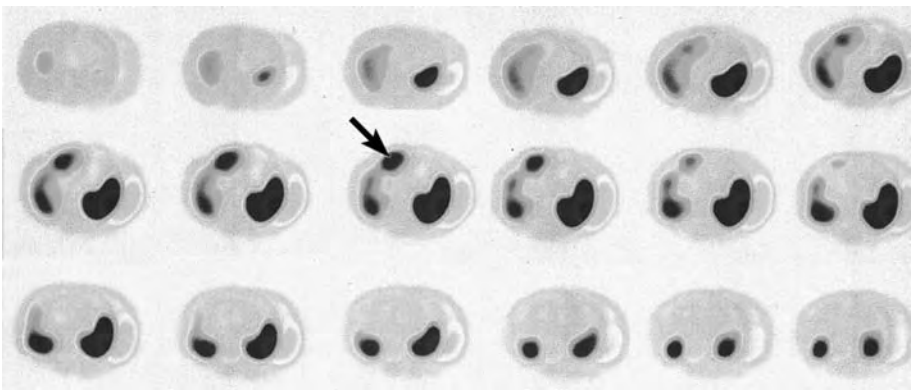

Fig. 10.3. ^{111}In-DOTA-lanreotide scintigraphy in a patient with colon cancer and a single liver metastasis (*arrow*) at 3 h post injection of 150 MBq radioligand. SPECT: transverse reconstruction

cific symptoms or signs, and lesions smaller than 2 cm may escape detection by conventional radiological imaging (Kelly and Benjamin 1995).

Sonography, endosonography, and CT are the most widely applied methods for diagnosis and staging of pancreatic cancer (van Dyke et al. 1985; Balthazar and Chako 1990). The most reliable, and thus most widely applied modality for detection and imaging of pancreatic cancer, remains CT (van Dyke et al. 1985), whereas MRI still has to prove its advantage over conventional CT (Freeny et al. 1988). Scintigraphic methods, for the time being, continue to be experimental approaches.

10.4.2.2 ^{123}I-VIP Receptor Scintigraphy

Pancreatic adenocarcinomas of the gastrointestinal tract have been shown to express abundant numbers of VIP receptors (Virgolini et al. 1994a; Reubi 1995; Jiang et al. 1997). The feasibility and safety of this peptide receptor scan has been demonstrated (Virgolini et al. 1994b, 1995) showing the localization of most gastrointestinal adenocarcinomas and liver metastases, including patients suffering from pancreatic adenocarcinoma. As this tumor entity poses a diagnostic challenge, VIP receptor scanning results obtained in a total of 60 consecutive patients with pancreatic adenocarcinomas were evaluated and compared with conventional radiological imaging methods and surgical exploration results (Fig. 10.4; Raderer et al. 1998a,b). In this series 22 patients presented with organ-confined malignancy (19 at study entry, and two developed tumor recurrence during follow-up after initial surgery), whereas 25 patients had distant metastases along with the local malignancy, and seven patients had liver metastases after resection of the primary lesion (six upon study entry, one case of tumor development during follow-up). In five of these patients, abdominal lymph node metastases were present at the time of scanning. Of 10 patients who had undergone potentially curative surgery, seven remained free of disease during follow-up until death or for at least 6 months. All patients were administered ^{123}I-VIP (150–200 MBq, 4–5 mCi); ~1 μg VIP). Primary pancreatic tumors were visualized by ^{123}I-VIP in 19 of 21 patients (90%) with disease confined to the pancreas and in eight of 25 patients (32%) suffering both from locoregional and disease metastatic to the liver. The overall ^{123}I-VIP scan sensitivity for primary pancreatic adenocarcinomas was 58% (27 of 46 scans). Liver metastases were detected in 29 of 32 patients (sensitivity 90%) and abdominal lymph node metastases in four of five patients. In five patients the VIP receptor scan indicated the malignant lesion prior to CT. In vitro results confirmed specific binding of ^{123}I-VIP to primary pancreatic tumor cells as well as to PANC1 adenocarcinoma cells. We conclude that ^{123}I-VIP receptor scanning has additional information to standard diagnostic methods and could influence the decision making process in the treatment of pancreatic cancer. Especially noteworthy are the results obtained in five of 60 patients (8.3%) in whom VIP receptor scanning indicated recurrence of disease and/or metastatic liver spread prior to conventional methods. Possible changes in the choice of treatment modalities for pancreatic cancer following VIP receptor scanning suggest a profound impact in terms of quality of life and cost-effectiveness. The diverging results in the two subgroups deserve special emphasis, because our data imply that ^{123}I-VIP receptor scintigraphy has the highest diagnostic accuracy in a cohort of patients who usually present a diagnostic problem with conventional radiological imaging. Thus, ^{123}I-VIP receptor scanning may be applied as an additional and complementary method in the evaluation of presurgical patients with suspected cancer of the pancreas.

The diagnostic sensitivity for liver metastases achieved in our study was similar to that reported for conventional radiological imaging, i.e., sonography or CT (van Dyke et al. 1985; Freeny et al. 1988). Iodine-123 VIP is preferentially excreted via the kidneys;

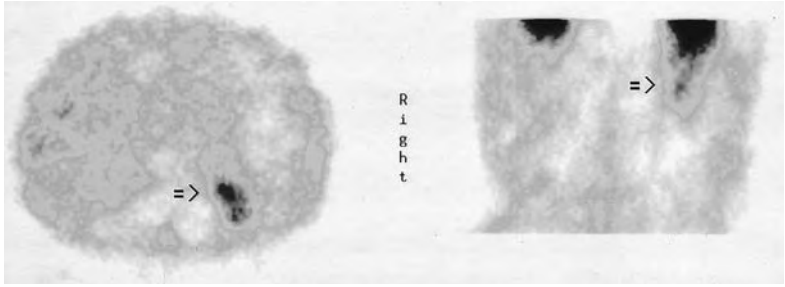

Fig. 10.4. ^{123}I-VIP receptor scintigraphy indicates the recurrent pancreatic tumor (*arrow*) 2 h after injection of 1 μg (150 MBq) radioligand (SPECT; *left panel:* transverse reconstruction; *right panel:* coronal reconstruction)

thus, it does not concentrate in physiologic liver and biliary tissues, offering the opportunity of visualizing hepatic metastases. The smallest liver lesions imaged in our patients were approximately 1.5 cm with the median size of liver metastases being 3 cm (range 1.5–10 cm). Although the early detection of metastatic disease to the liver may not directly translate into a prolongation of survival, this information nevertheless is important for physicians involved in the management of such patients. There is international consensus that patients with metastatic disease are best spared an operation (Warshaw and Fernandez-del Castillo 1992), since extensive surgery does not affect overall survival and bears the risk of increased perioperative mortality and morbidity. The same holds true for the early detection of lymph node metastases, and in this study VIP visualized abdominal lymph node metastases in four of five patients.

In conclusion, ^{123}I-VIP receptor scanning has promising potential for the clinical use in diagnosing and/or staging of pancreatic cancer. As demonstrated in our study, ^{123}I-VIP receptor scintigraphy could possibly influence the decision making process in patients with verified or suspected cancer of the pancreas, due to its ability to visualize malignancy even in the absence of conventional radiological abnormalities. We conclude that scintigraphy with ^{123}I-VIP could provide valuable additional information to the available conventional radiological imaging modalities for staging and early diagnosis of pancreatic cancer. In fact, the high sensitivity especially for small lesions and metastatic deposits might have a profound impact on clinical management of such patients.

10.4.2.3 Scintigraphy with Radiolabeled Somatostatin Analogs

Previously, ^{111}In-DTPA-D-Phe^{1}-octreotide was used for imaging gastrointestinal tumors (Krenning et al. 1993; Virgolini et al. 1994b). However, whereas VIP scans were positive in a small cohort of patients with pancreatic exocrine tumors, negative imaging results were obtained by labeled octreotide. The most likely explanation for these negative in vivo results is a lack of high-affinity receptors specific for octreotide on pancreatic adenocarcinomas. The VIP receptor scan was also superior to immunoscintigraphy in a study in which a direct comparison of the monoclonal antibody ^{111}In-CYT-103 (OncoScint) with ^{123}I-VIP was performed (Raderer et al. 1996). Promising results with the administration of fluorodeoxyglucose (FDG) for positron emission tomography (PET) have been reported (Inokuma et al. 1995). Forthcoming investigations will have to be performed in order to evaluate the diagnostic value of VIP SPECT and FDG PET in a direct comparison.

Initial imaging results with ^{99m}Tc-P829 (Fig. 10.5; Leimer et al. 1998a) as well as with ^{111}In-DOTA-lanreotide (Virgolini et al. 1998c,d) have indicated the potential of these tracers to image gastrointestinal adenocarcinomas including pancreatic cancer. This is most probably based on the recognition of different hSSTR subtypes expressed on or in pancreatic tumors (Raderer et al. 1998a,b). For both these SSTR ligands, however, only limited clinical data are available.

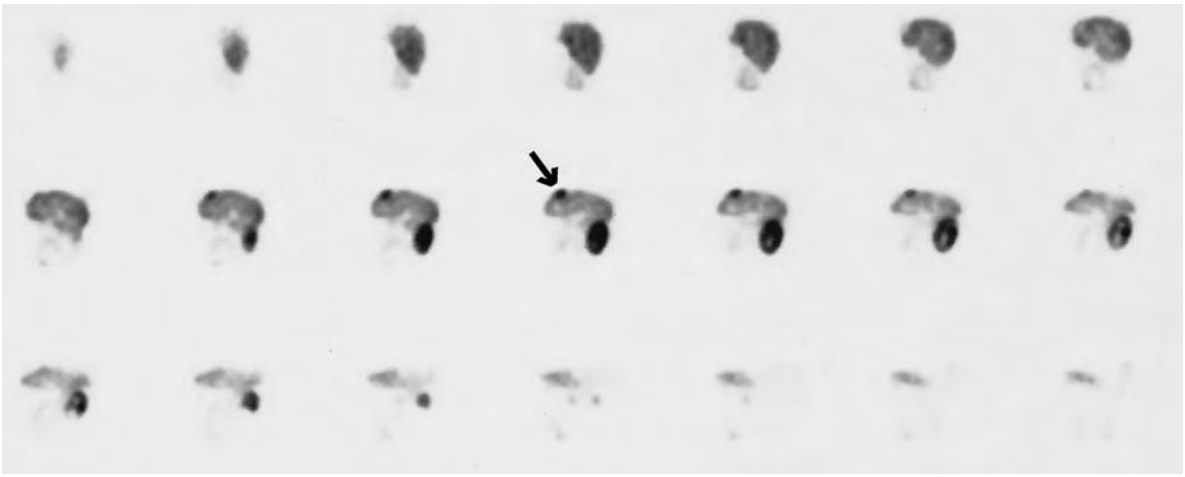

Fig. 10.5. ^{99m}Tc-Depreotide (P829) scintigraphy indicates in a patient with pancreatic adenocarcinoma and a larger liver metastasis (*arrow*) at 90 min post injection of 150 MBq radioligand (SPECT: sagittal reconstruction)

10.4.2.4 Scintigraphy with Other Peptides

By autoradiography, neurotensin receptors (NTR) are specifically detectable in pancreatic carcinomas (Wang et al. 2000; Reubi et al. 1999). A first clinical study of ^{99m}Tc-labeled neurotensin analog NT-XI in four patients with ductal pancreatic adenocarcinoma showed promising data (Buchegger et al. 2003).

Bombesin and gastrin releasing peptides play a physiological and pathophysiological role in pancreatic tissue. The presence of GRP/BN receptors was reported in three distinct tissue compartments of the pancreas, namely GRP receptors in the exocrine parenchyma in chronic pancreatitis, in peritumoral vessels around ductal pancreatic carcinomas, and BB3 receptors in residual pancreatic islets. Imaging of these receptors may have implications for the differentiation of chronic pancreatitis from ductal pancreas carcinoma (Fleischmann et al. 2000).

10.4.3 Lung Cancer

10.4.3.1 The Clinical Problem

Lung cancer was the most frequent malignancy in the European Union in 1990 (Black et al. 1997). Also in the United States, lung cancer is the leading cancer site with the highest mortality rate in both men and women, and had a projected mortality of >150,000 deaths in 1997 (Parker et al. 1997). Early detection and treatment may lead to improved survival for some types of lung cancer (Naruke et al. 1997). The best opportunity for cure of lung cancer is surgical excision of the primary tumor and of metastases to regional lymph nodes. If the cancer has spread, then surgery is not an option and other treatment regimes are applied including chemotherapy and external beam radiation, but these measures are rarely curative (Ginsberg et al. 1993). Therefore, an accurate diagnosis with confirmatory cytology or histology and an estimate of the stage of the disease are extremely important.

The major histologic types of lung cancer are squamous cell carcinoma, adenocarcinoma, large cell lung carcinoma (referred to as NSCLC, non-small cell lung cancer) and small cell lung carcinoma (SCLC). In addition, there are other, less common, lung tumors such as carcinoid tumors.

Diagnosis based on histopathology requires bronchoscopy, or open-lung biopsy in order to differentiate benign from malignant lesions before and often after surgical resection or radiation therapy of the primary tumor lesions. Bronchoscopy, including bronchial washings and brushing, has a sensitivity of 65% for malignancy, and transbronchial biopsy increases the sensitivity to 79% for lesions that are accessible (Wang et al. 1988). These invasive procedures have a relatively high incidence of pneumothorax. Beyond the clinical diagnosis conventional imaging techniques are used including chest radiograph, CT, or MRI. These diagnostic methods provide anatomical information and can neither accurately stage the disease when metastases occur without anatomical change nor differentiate between malignant and non-malignant tumors.

Approximately 130,000 new solitary pulmonary nodules (SPNs) are detected each year on chest radiographs performed as part of preoperative evaluations for unrelated surgery or as part of annual physical examinations. In various studies 28–39% of resected SPNs were malignant, accounting for approximately 20% of newly diagnosed lung cancer (Siegelman et al. 1986). Significant progress has been made by the introduction of PET showing overall the highest sensitivity (96%) and specificity (88%) in detecting lung cancer in patients with SPN (Kahn et al. 1991; see Chaps. 11 and 12).

10.4.3.2 ^{123}I-VIP Receptor Scintigraphy

Due to the high physiologic uptake of VIP in the lungs (Virgolini et al. 1995), the visualization of VIPR-positive lung tumors is difficult. Therefore, VIPR scintigraphy does not have application for detecting lung tumors or lung metastases.

10.4.3.3 Scintigraphy with Radiolabeled Somatostatin Analogs

In vitro studies have demonstrated that 50%–75% of SCLC have specific high-affinity binding sites for SSTR. Furthermore, SCLC sites have been localized through scintigraphic imaging with the radiolabeled SST analogs ^{123}I-octreotide and ^{111}In-DTPA-D-Phe^{1}-octreotide which bind to tissue expressing hSSTR2 and hSSTR5 (O'Bryne et al. 1994; Kwekkeboom et al. 1991). Controversial reports exist concern-

ing SSTR expression in NSCLC tumors. Whereas some in vitro studies have failed to demonstrate the presence of SSTR in NSCLC (Reubi et al. 1990), SST analog imaging in patients with NSCLC have been successful. Since a tumor may contain numerous different cell types, including neoplastic cells, stroma, inflammatory cells and necrotic tissue, it has been hypothesized that there may be uptake of the radiolabeled SSTR ligand by other cells within the tumor mass, such as lymphocytes, which are known to express SSTR (Sreedharan et al. 1989). O'Bryne et al. (1994) have shown for the first time that NSCLC samples express a single class of specific high-affinity SSTR binding sites. Moreover, we (Virgolini et al. 1998a) identified two classes of specific high-affinity binding sites for ^{99m}Tc-P829 in NSCLC, and the presence of hSSTR was confirmed by mRNA analysis using Northern blot analysis. Thomas et al. (1994) using limiting dilution-PCR (LiD-PCR) found high levels of transcription of SSTR1 in lung tumors, especially in NSCLC. Fujita et al. (1994) showed the expression of SSTR subtype genes at high level in two squamous cell carcinoma cell lines, in which the representative neuroendocrine markers were low. We have shown high-affinity binding sites for ^{111}In-DOTA-lanreotide in NSCLC samples with predominant expression of hSSTR4. Furthermore, ^{111}In-DOTA-lanreotide scintigraphy indicated the primary tumor in all 16 patients with NSCLC, lymph node metastases in 6/6 patients and bone lesions in 3/3 patients (Traub et al. 2001).

The FDG PET technique has been shown to accurately detect SPN with a sensitivity of 98% and a specificity of 69% in a prospective blinded study (Lowe et al. 1998). However, FDG PET is not routinely available and is expensive. ^{99m}Tc-P829 scintigraphy was included into the diagnostic work-up following identification of a suspicious lesion on the chest radiograph or after the CT (Blum et al. 1998). The potential for wider availability and cost-effectiveness of ^{99m}Tc-P829 scintigraphy compared with FDG PET is suggested by kit production and ^{99m}Tc compatibility with existing conventional nuclear medicine detector systems.

The position of ^{99m}Tc-P829 (Fig. 10.6) in the clinical management of patients suspected of having lung cancer might not only be limited to the primary evaluation of the SPN but could be extended to assess post-treatment pulmonary changes. Post-treatment pulmonary changes, such as persistent tumor, scarring, or necrosis, are not adequately characterized by CT or MRI. A tissue biopsy negative for tumor cannot be accepted as definitive because of limitations in accurately sampling regions of viable tumor in the middle of a scar. Suspicious local and distant tumor recurrence can be accurately characterized using whole-body FDG PET (Patz et al. 1994). Whether ^{99m}Tc-P829 would be clinically useful in the secondary management of lung cancer remains to be established against FDG. Similar to ^{99m}Tc-P829 ^{111}In-DOTA-lanreotide concentrates in NSCLC.

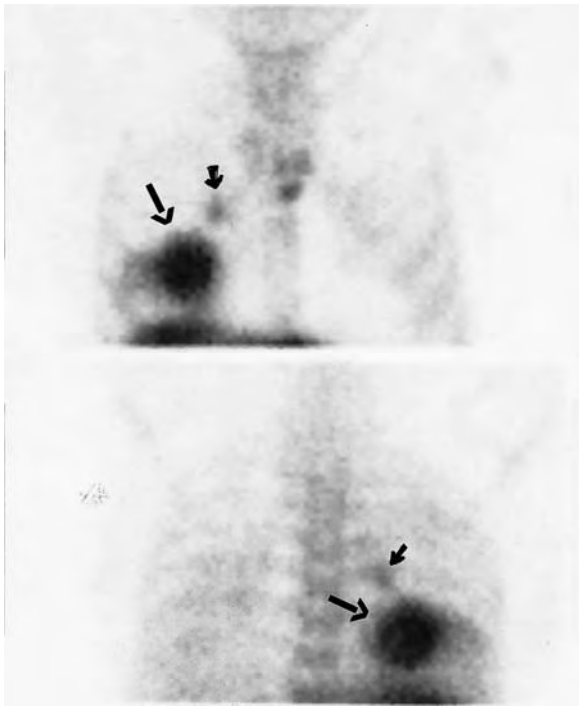

Fig. 10.6. ^{99m}Tc-P829 scintigraphy indicates in a patient with non-small-cell lung carcinoma (NSCLC) the tumor sites at 90 min after injection of 50 µg (600 MBq) radioligand. Planar imaging: anterior (*top panel*) and posterior (*bottom panel*) views. In addition to the large tumor mass (*long arrow*) a small lymph node metastasis was identified above the tumor lesion (*short arrow*) which was not identified on CT but was verified by surgery

10.4.4 Breast Cancer

10.4.4.1 The Clinical Problem

In women the most commonly diagnosed cancer was breast cancer (Parker et al. 1997). The problem with breast cancer is to determine the characteristics and extent of the disease as an aid in planning and

monitoring treatment. Which nodes are involved is of importance for prognosis. Several radiopharmaceuticals have been applied in patients with breast cancer, including FDG, sestamibi, tetrofosmin, and receptor tracers (Bombardieri et al. 1997).

The study of breast cancer is complicated by the heterogeneity of the disease. One way of simplifying is to subdivide these tumors into clinically relevant subgroups. There are indications that breast cancer, of which some express the SSTR, can be subdivided this way. It is well recognized that estrogen (ER) and progesterone receptor (PR) expression is associated with prolonged survival time. A retrospective study in 110 patients suggested that the presence of SSTR predict a longer disease-free survival (Foekens et al. 1989). In fact, human breast cancers have been shown to express SSTR with high incidence. During the past 10 years this has been demonstrated by several in vitro studies using autoradiography, radioligand binding studies, or Northern blotting. Furthermore, it was documented that the expression of SSTR in breast cancer tissue is significantly higher than in normal breast tissue (Vikic-Topic et al. 1995; Schaer et al. 1997; Virgolini et al. 1996c; Zia et al. 1996).

10.4.4.2 ^{123}Iodine VIP Receptor Scintigraphy

Whereas ^{123}I-VIP has poor sensitivity for localizing ER/PR-positive breast cancer (11%), the sensitivity of VIP in ER/PR-negative breast cancer is approximately 85% (Taucher et al. 1996). At several sites (Thakur et al. 1997; Pallela et al. 1998a-c) ^{123}I-VIP-agonist receptor scintigraphy was used for imaging breast cancer based on the very high expression of VIPR reported in patients with breast cancer (Reubi 1995; Virgolini et al. 1996c; Moody et al. 1998). No clinical data have been published yet.

10.4.4.3 Scintigraphy with Radiolabeled Somatostatin Analogs

Van Eijck et al. (1994) administered ^{111}In-DTPA-D-Phe^1-octreotide to 52 patients with breast cancer and was able to demonstrate the presence of SSTR in 85% of ductal and in 56% of lobular carcinomas. When subdividing the primary tumors according to size, 86% of T2 tumors and 61% of T1 tumors were visualized. Examination of the axillary lymph node status revealed only four of 14 histopathologically confirmed metastatic localizations. Higher density in vivo correlated mostly with homogeneous and dense distribution of SSTR at autoradiography, whereas lower dense distribution corresponded with a non-homogeneous and sparse distribution of these receptors in vitro. Moreover, the low density of these receptors seemed to be due to a non-invasive component (mainly ductal carcinoma in situ). Furthermore, a higher sensitivity of SSTR was observed compared with tumor markers such as CA 15-3 and CEA in detecting recurrence in patients with SSTR-positive primary tumors., Vural et al. (1997) have shown that ^{111}In-DTPA-D-Phe^1-octreotide was able to detect 16 of 17 histopathologically confirmed breast cancers (15 invasive ductal carcinoma, one mucinous adenocarcinoma, one intraductal carcinoma) compared with 13 detected by ^{201}Tl. In our series more than 90% of primary human breast tumors were detected using ^{111}In-DTPA-D-Phe^1-octreotide (Fig. 10.7; Taucher et al. 1996). In a study by Schulz et al. (2002), an excellent correlation between the outcome of SSTR scintigraphy and the expression of hSSTR 2a (p=0.025) and hsst 5 (p<0.001), but no expression of either hSSTR 1(p=0.343) or hSSTR3 (p=0.400) has been found.

We (Virgolini et al. 1998a) have demonstrated the in vivo binding capacity of ^{99m}Tc-P829 in breast cancer patients (Fig. 10.8). This ligand seems to bind

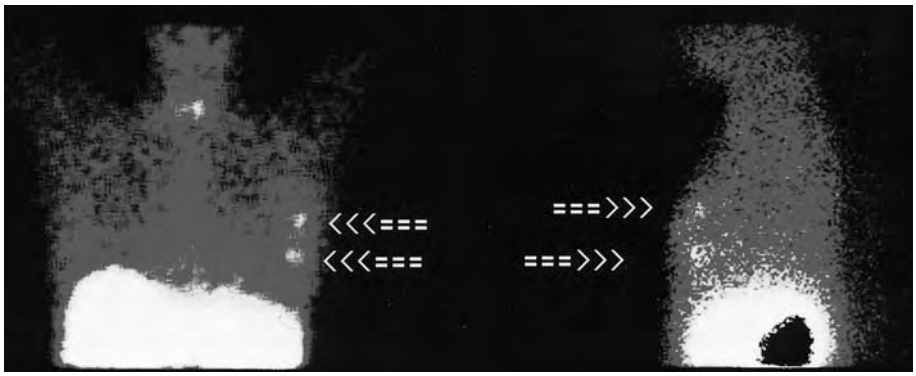

Fig. 10.7. ^{111}In-DTPA-D-Phe^1-octreotide scintigraphy in a patient with breast cancer. The *arrows* indicate two tumor masses in the left breast. Planar images in anterior (*left panel*) and left lateral view (*right panel*)

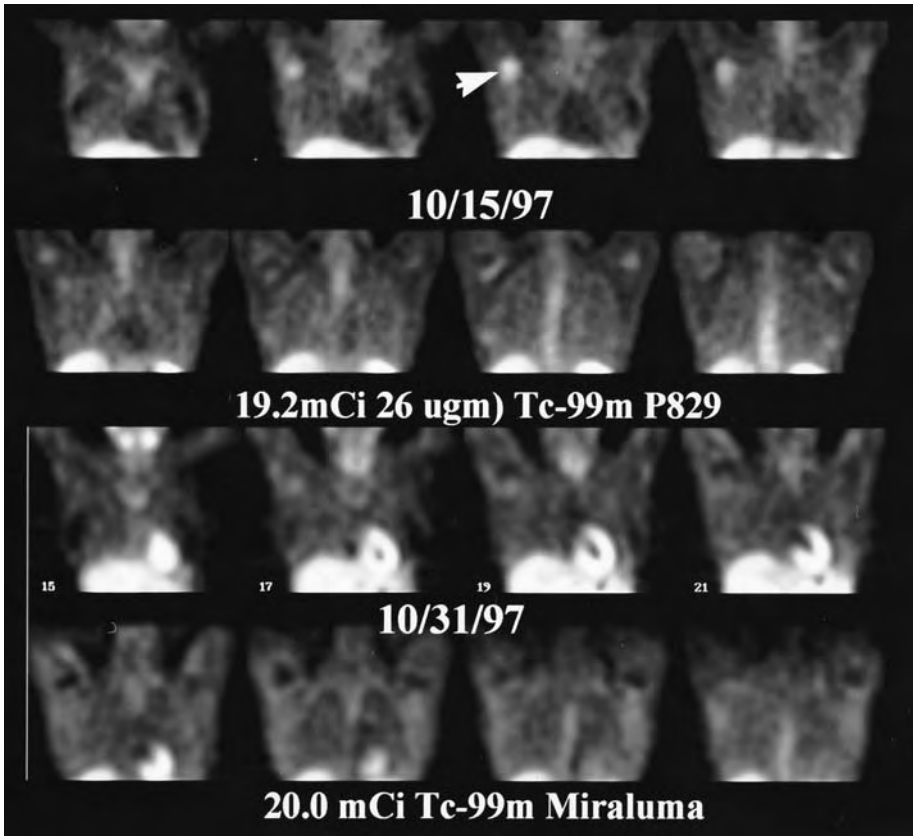

Fig. 10.8. ^{99m}Tc-P829 scintigraphy indicates in a patient with breast cancer (primary tumor resected) axillary lymph node recurrence (*arrow, upper two rows*) 1.5 h after injection of 50 μg (700 MBq) radioligand (SPECT; coronal reconstruction). Scintigraphy with Sestamibi (Miraluma, Dupont Pharma, Billerica, Mass.) showed only faint uptake (*lower two rows*). (Courtesy of H. Handmaker)

with high affinity to hSSTR2 and also to hSSTR 3 and 5. In these studies ^{99m}Tc-P829 performed better than MIBI

10.4.5 Neuroendocrine Tumors

10.4.5.1 The Clinical Problem

Neuroendocrine tumors are rare disease entities, often presenting as bizarre diagnostic puzzles (Moertel 1987). The fact that these malignancies arise from hormonally active cells explains the wide variety of symptoms encountered in patients with neuroendocrine cancers of various origin. The different manifestations are related to the release of hormones or other biologically active substances produced in excessive amounts, such as insulin, gastrin, VIP, glucagon, or serotonin (Kvols 1994). Such cancers constitute a group of relatively slow-growing malignancies, which are sometimes diagnosed after years of symptoms in affected patients. This is related to the fact that the amount of hormones secreted does not necessarily correlate with tumor size, whereas small cancers tend to escape clinical detection by conventional radiological imaging. Thus, the start of successful therapy or symptomatic palliation is often delayed.

10.4.5.2 Carcinoid Tumors

Carcinoid tumors constitute the group with the highest incidence among all cases of neuroendocrine malignancies, predominantly arising in the gastrointestinal tract but also at various other sites (Vinik et al. 1989). According to epidemiological data, gastrointestinal tract carcinoids occur in 1.5 cases per 100,000 people per year (Godwin 1975). The onset of symptoms related to excessive serotonin production summarized under the term "carcinoid syndrome" may precede the correct diagnosis and localization of the tumor by years. While long-term symptomatic control of tumor-related symptoms can be achieved in some patients by non-invasive means, the treatment of choice in localized disease remains surgical resection, since it is the only measure with potential

cure. On the other hand, the removal of the primary cancer in the absence of symptoms, such as bowel obstruction, does not significantly alter the prognosis in disseminated disease.

In vitro data have demonstrated a high amount of receptors for various hormones and peptides on malignant cells of neuroendocrine origin, including carcinoid tumors (Reubi 1995; Reubi et al. 1989). Among the latter, binding sites for members of the SST family (hSSTR1–5) are frequently found, and their expression has led to therapeutic and diagnostic attempts to specifically target these receptors. The use of OctreoScan (Mallinckrodt-Medical, St. Louis, Mo.) for imaging purposes has been incorporated into the clinical work-up of patients suspected of suffering from neuroendocrine tumors (Krenning et al. 1993). In our series, which is in line with results reported by Krenning et al. (1993), primary or recurrent carcinoid tumors could be visualized by means of ^{111}In-DTPA-D-Phe^{1}-octreotide in 95 of 104 patients (91%), whereas metastatic sites were identified in 110 of 116 patients (95%) (Fig. 10.9.). In 11 of 21 patients (51%) with suggestive symptoms but without identified lesions by conventional imaging, focal tracer uptake identified the location of the carcinoid tumor. In addition, the presence of metastatic disease was demonstrated in three patients after resection. In a direct comparison of 131 patients evaluated with both imaging modalities, ^{111}In-DTPA-D-Phe^{1}-octreotide was found to be superior to ^{123}I-VIP, with 35 of 38 (93%) vs 32 of 38 (84%) scans being positive in primary or recurrent tumors, and 58 of 65 (90%) vs 53 of 92 (82%) being positive in patients with metastatic sites, and seven of 16 (44%) vs four of 16 (25%) in patients with symptoms but otherwise negative work-up. Overall, additional lesions not seen by conventional imaging were found in 43 of 158 (41%) vs 25 of 103 (25%) with ^{111}In-DTPA-D-Phe^{1}-octreotide and ^{123}I-VIP, respectively. These results indicate a high sensitivity of both peptide tracers for localizing tumor sites in patients with known or suspected carcinoid tumors, with ^{111}In-DTPA-D-Phe^{1}-octreotide scintigraphy being more sensitive than ^{123}I-VIP receptor scanning. Both ^{123}I-VIP and ^{111}In-DTPA-D-Phe^{1}-octreotide had a higher diagnostic yield than conventional imaging, as verified by surgical intervention or long term follow-up. As expected from pharmacokinetic data (Battari et al. 1988; Gespach et al. 1988), one of the shortcomings of ^{123}I-VIP is its inability to visualize small pulmonary lesions. In fact, approximately 40% of the tracer is trapped in the lungs a few minutes after administration, supplying a high rate of physiologic background. Thus, small lesions with a low receptor density cannot be distinguished from normal lung uptake. ^{111}In-DTPA-D-Phe^{1}-octreotide, which is not trapped in the lungs, demonstrated a striking superiority for imaging of lung lesions, whereas less than 50% of pulmonary deposits could be seen on VIP receptor scintigraphy. We conclude that ^{111}In-DTPA-D-Phe^{1}-octreotide represents the more sensitive method for diagnosis and staging of patients suffering from carcinoid tumors, whereas the combination of both peptide receptor scans does not appear to further enhance diagnostic information.

In asymptomatic patients for hormone overexpression of gastroenteropancreatic (non-functioning GEP) tumors, SSTR scintigraphy, particularly SPECT, seems to be a useful tool in the detection of lesions contributing to correct patient classification and appropriate selection of therapeutic strategy. Liver SPECT showed higher sensitivity than conventional imaging techniques (CIT; sensitivity of SSTR scintigraphy: 92%, sensitivity of CIT: 80%; Schillaci et al. 2003a,b).

Our data also indicate that ^{111}In-DOTA-lanreotide, similarly to ^{111}In-DTPA-D-Phe^{1}-octreotide, accumulates in neuroendocrine tumors including carcinoid tumors (Virgolini et al. 1998c,d). Comparison with conventional imaging techniques, SSTR scintigraphy and PET with the PET tracer ^{18}F-DOPA supplemented diagnostic information of the primary as well as in the metastatic location of gas-

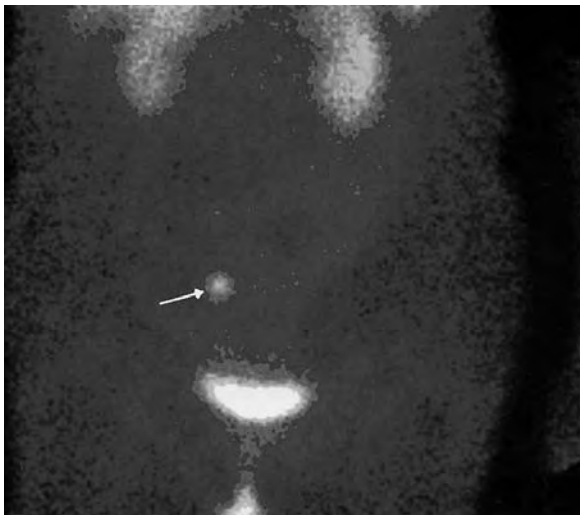

Fig. 10.9. ^{111}In-DTPA-D-Phe^{1}-octreotide scintigraphy in a patient with recurrent carcinoid tumor. Planar anterior view: the *arrow* indicates a single metastatic tumor site in the right ovary at 6 h post injection

trointestinal carcinoid tumors with an overall sensitivity of 65% for ^{18}F-DOPA PET, 57% for SSTR scintigraphy, 29% for ^{18}F-PET and 73% for conventional imaging techniques (Hoegerle et al. 2001a).

10.4.5.3 Insulinomas

In reviewing 28 patients with histologically verified insulinomas undergoing ^{123}I-VIP as well as ^{111}In-DTPA-D-Phe^{1}-octreotide scintigraphy, ^{123}I-VIP visualized tumor lesions in 15 of 21 patients, whereas ^{111}In-DTPA-D-Phe^{1}-octreotide visualized tumor lesions in 12 of 28 patients. In 15 patients the two tracers were compared directly: ^{123}I-VIP scintigraphy was positive in 12 of 15 patients (80%), whereas ^{111}In-DTPA-D-Phe^{1}-octreotide scintigraphy was positive in 8 of 15 (60%). In these patients radiological imaging disclosed primary tumor lesions in 55% only. Bertherat et al. (2003) reported that insulinomas displaying hSSTR2 binding, were also hSSTR5 sensitive. But one third of insulinomas did not express hSSTR2/hSSTR5 subtypes, which may be involved in a beta-cell dysfunction. Therefore, in vitro experiments at our institution indicated predominant expression of hSSTR3 in all insulinoma specimens investigated (Hejna et al. 1998). These results indicate a superior imaging capability for ^{123}I-VIP acting as a ligand for hSSTR3, which is probably not sufficiently targeted by ^{111}In-DTPA-D-Phe^{1}-octreotide (Lamberts et al. 1996).

10.4.5.4 Other Neuroendocrine Tumors

The SSTR scintigraphy using ^{111}In-DTPA-D-Phe^{1}-octreotide has a high positive predictive value for the vast majority of neuroendocrine tumors (Krenning et al. 1993). ^{111}Indium-DTPA-D-Phe^{1}-octreotide has earned its place in the diagnostic work-up as well as follow-up of patients with neuroendocrine tumors. These tumors seem to express the hSSTR2 predominantly (Reubi et al. 1994). First clinical use of ^{99m}Tc-P829 scintigraphy in neuroendocrine tumors compared to ^{111}In-DTPA-D-Phe^{1}-octreotide scintigraphy showed poorer results for ^{99m}Tc-P829 imaging (Lebtahi et al. 2002). ^{68}Ga-DOTA-TOC has been described as a PET tracer for neuroendocrine tumors with a higher receptor affinity, a higher spatial resolution and the ability of quantification (Hoffmann et al. 2001). First clinical data have shown a superiority of this tracer for detecting small tumor lesions or tumors bearing a low density of hSSTR (Kowalski et al. 2003; Hoffmann et al. 2003). ^{64}Cu-TETA-octreotide has been described as suitable for scintigraphic imaging of SSTR positive tumors (Aderson et al. 2001). In an intra-patient comparison of a cohort of 41 patients with endocrine tumors ^{99m}Tc-HYNIC-octreotide exhibited a higher sensitivity than ^{111}In-DTPA-D-Phe^{1}-octreotide, especially for the tumor-to-normal tissue ratio (Gabriel et al. 2003).

In paragangliomas, which express quite intensively SST receptors, imaging is useful for the diagnosis and management of the disease (Duet et al. 2003) and has a sensitivity of more than 90% (Kwekkeboom et al. 1993). Despite positive results in patients with VIPomas (Virgolini et al. 1998b), ^{123}I-VIP receptor scintigraphy has no further place in the work-up of most other neuroendocrine tumors (Virgolini et al. 1996c). The majority of these tumors have been shown to express hSSTR2 which is not targeted by ^{123}I-VIP.

10.4.6 Thyroid Cancer

A relatively large number of patients with differentiated metastatic thyroid cancer may present with an ^{131}I-negative whole-body scan. The discovery of neoplastic foci in these patients, even if no ^{131}I-uptake is present, may lead to further treatment, such as surgery or external radiotherapy.

It has been shown that SST and its analogs affect the cell growth of neoplastic thyroid cancer cells through cell surface binding (Ain and Taylor 1994). The profile of hSSTR subtype receptor expression has already been identified for thyroid cancer cells indicating the existence of SSTR2, 3 and 5 (Ain et al. 1997). Initial results have indicated the ability of ^{111}In-DTPA-D-Phe^{1}-octreotide to localize non-medullary thyroid cancer (Tenenbaum et al. 1995; Postema et al. 1996). These results provided the basis for using ^{111}In-DTPA-D-Phe^{1}-octreotide in thyroid cancer patients with a negative ^{131}I-scan: ^{111}In-DTPA-D-Phe^{1}-octreotide scintigraphy was positive in 12 of 16 ^{131}I-scan-negative patients and was positive in eight of nine patients with a positive ^{131}I scan (Baudin et al. 1996). A high rate of "false positive" ^{111}In-DTPA-D-Phe^{1}-octreotide imaging was reported for recurrent thyroid carcinoma with negative ^{131}I scans (Garin et al. 1998). Nevertheless, in metastatic thyroid cancer patients SSTR scintigraphy may be helpful in the detection of lesions,

and may expand the therapeutic options in these patients. In particular, initial dosimetry with the SST analog ^{111}In-DOTA-lanreotide has indicated a very high tumor dose (up to 50 mGy/MBq) for this type of cancer (Fig. 10.10; Virgolini et al. 1998d). Preliminary results of comparison of ^{111}In-DOTA-lanreotide scintigraphy with ^{111}In-DOTA-TOCT have shown a higher sensitivity for the lanreotide compound (Virgolini et al. 2002). Furthermore, binding studies with various cancer cells have demonstrated high SSTR binding for both ligands, but a higher maximal binding capacity for ^{111}In-DOTA-lanreotide (Leimer et al. 2000).

10.4.6.1 Medullary Thyroid Cancer

This cancer type originates from parafollicular C-cells in the thyroid gland secrets calcitonin, which produces rarely clinical symptoms by its hormonal activity. It can occur due to genetic aberrations (MEN-syndrome) associated to other endocrine lesions including tumors of the adrenal medulla, of the islet cells and the parathyroid glands (Donovan and Gagal 1997). The staging of metastatic medullary thyroid cancer (MTC) with the conventional imaging procedures is sometimes difficult. Scintigraphy can be performed with ^{99m}Tc-DMSA, with ^{123}I-MIBG and with labeled SST analogs (Clark 1998). Preliminary data of ^{99m}Tc-HYNIC-EDDA-TOC shows a possible scintigraphic imaging possibility. But further results are needed (Muehllechner et al. 2003).

A new and possible promising tracer in the diagnostic management of MTC is ^{18}F-DOPA (fluorine-18-dihydroxyphenylalanine). Hoegerle et al. (2001) described in 11 MTC patients with 27 tumor lesions of primary and metastatic disease an overall sensitivity of 81% for morphological imaging techniques, 63% for ^{18}F-DOPA, 52% for SSTR scintigraphy, and 44% for ^{18}F-PET. However, with respect to lymph node staging the best results were obtained with ^{18}F-DOPA PET.

The high sensitivity of the pentagastrin stimulation test in detecting primary or metastatic MTC indicates the presence of tumor (Pacini et al. 1994). This tumor cell reaction to the pentagastrin stimulation test suggests a widespread expression of the corresponding receptor type on the human MTC.

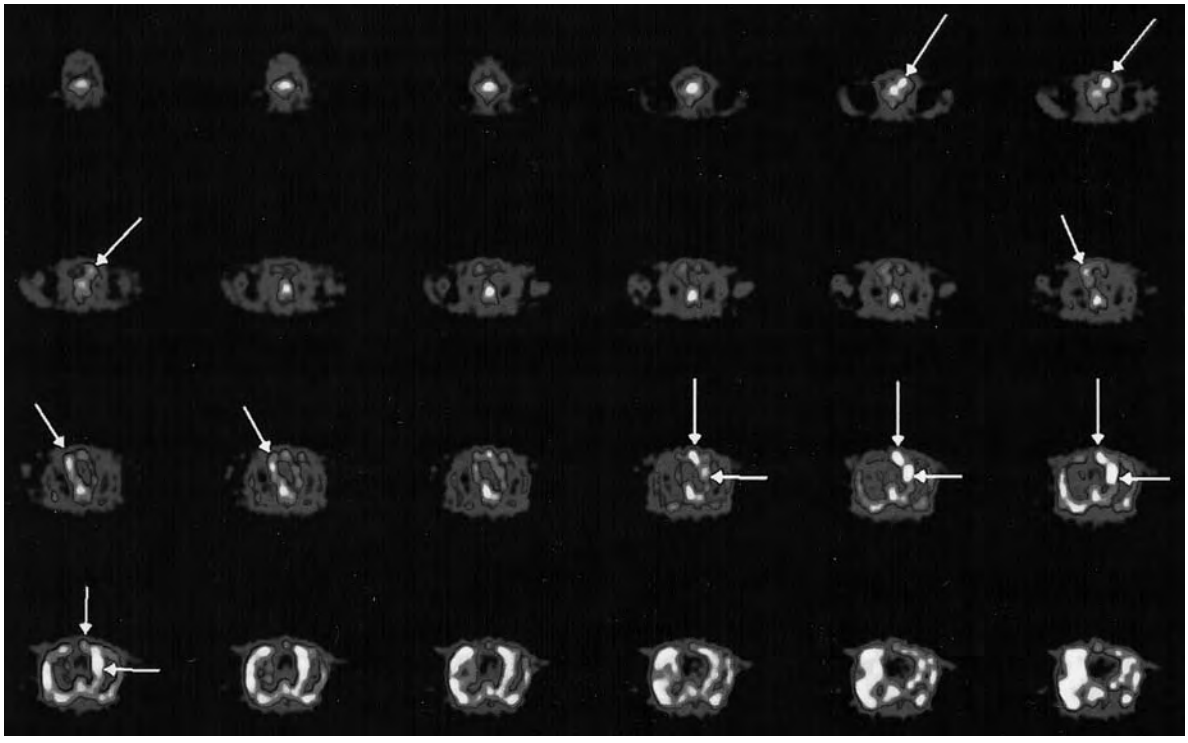

Fig. 10.10. ^{111}In-DOTA-lanreotide scintigraphy in a patient with Hürthle cell carcinoma and an ^{131}I-negative whole-body scan visualizes several tumor sites (*arrows*). Transverse images indicate major tumor lesions in the left neck, mediastinum, and right basal lungs

Autoradiographic studies showed cholecystokinin (CCK)-B/gastrin receptors in 90% of MTCs. ^{111}In-DTPA-D-Glu^{1}-minigastrin scintigraphy was successfully introduced in the clinical management of MTC for the diagnosis and the follow-up with a sensitivity of more than 90% (Behe and Behr 2003). Scintigraphy can also be performed with ^{99m}Tc(V)DMSA (diagnostic sensitivity: 60%–90%, with ^{123}I-MIBG (diagnostic sensitivity: 50%–70%) and with radiolabeled SST analogs (diagnostic sensitivity: 60%–85%, Clarke 1998). Therefore, comparison with ^{18}F-PET and CT showed a higher sensitivity for the combination of ^{111}In-DTPA-D-Glu^{1}-minigastrin and CT of approximately 93% compared to ^{18}F-PET (sensitivity: 61%; Gotthart et al. 2003).

10.4.7 Merkel Cell Carcinoma

This rare, highly malignant and aggressive cutaneous tumor shows characteristics of neuroendocrine tumors by electron microscopy and immunohistochemistry. The SSTR scintigraphy may be of interest for staging as reported by Kwekkeboom et al. (1992) and by Guitera-Rovel et al. (2001).

10.4.8 Melanoma

The sensitivity of the ^{123}I-VIP scintigraphy for the detection of melanomas is 70% and is comparable with the sensitivity of ^{111}In-DTPA-D-Phe^{1}-octreotide scintigraphy (Krenning et al. 1993; Virgolini et al. 1996c). ^{99m}Tc-P829 was proposed to be a suitable tracer for imaging melanoma sites; however, the results of larger clinical studies remain to be seen (Lastoria et al. 1996).

10.4.9 Lymphoma

The overall sensitivity of the ^{123}I-VIP scintigraphy for imaging of lymphomas (Hodgkin's and non-Hodgkin's lymphomas) is reported to be approximately 75% (Virgolini et al. 1996c), whereas the ^{111}In-DTPA-D-Phe^{1}-octreotide scan sensitivity is somewhat higher (Lugtenburg et al. 1998). The latter authors concluded that in patients with stage I and stage IIa supra-diaphragmatic Hodgkin's disease SSTR scintigraphy is clearly indicated. A prospective study of 126 patients with HD showed that in 15 out of 83 patients (18%) with HD stage I and II SSTR scintigraphy effected an upstaging to stage III and IV (Lugtenburg et al. 2001). We have found that tumors in patients with intestinal MALTomas lack the hSSTR3 subtype receptor which may explain why intestinal MALTomas are usually detected with ^{111}In-DOTA-lanreotide but not with ^{111}In-DTPA-D-Phe^{1}-octreotide (Raderer et al. 1999).

The majority of lymphomas of the mucosa-associated lymphoid tissue (MALT)-type arise in the stomach, but extragastric locations are also frequently encountered. Based on previous results, indicating that SSTR expression distinguishes between gastric and extragastric MALT-type lymphoma, we have reported excellent ^{111}In-octreotide scintigraphic results in the initial staging as well as in non-invasive monitoring of extragastric MALT-type lymphomas irrespective of the site of presentation (Raderer et al. 2001).

We have used ^{111}In-DOTA-lanreotide in some patients with Hodgkin's lymphomas showing a high sensitivity (Virgolini et al. 1998c, 2001). Furthermore, we also found a high sensitivity of ^{99m}Tc-P829 in patients with Hodgkin's and non-Hodgkin's lymphomas.

10.4.10 Prostate Cancer

GRP receptors were identified by in vitro studies in primary tumor as well as in bone metastases with a higher receptor density in well-differentiated than in poorly differentiated prostate carcinomas (Markwalder and Reubi 1999). First clinical results of ^{99m}Tc-BN showed that true positive scans were obtained in eight of ten patients with subsequently histologically proven prostate carcinoma. Additionally, hot spots were observed in the prostatic fossa in two carcinoma patients with prostate specific-antigen level higher than 20 ng/ml as early as 1 min post injection. Invasion of the obturator nodes was detected by SPECT in three patients, and this was confirmed by surgery (Scopinaro et al. 2003).

10.5 Other Tumors

A variety of other human tumors may express hSSTR or hVIPR, and several peptide tracers have

been used to demonstrate these tumors. In over 100 primary human tumors samples as well as over 20 tumor cell lines investigated for hSSTR and hVIPR subtype expression, one of the hSSTR or hVIPR subtypes was found to be expressed (Pangerl et al. 1997). These observations support the notion that the neuroendocrine peptide hormones VIP and SST are important growth regulators. Ideally, the in vivo study should be compared directly with in vitro receptor expression (Fig. 10.11) in order to gain further insights into the complex peptide hormone-receptor interactions.

10.6 Future Prospects

Some peptide tracers have been shown to be effective in both diagnosis and staging of tumors and their metastases. Initial efforts have implemented these peptides to prove the concept of receptor-mediated radiotherapy by using large amounts of the diagnostic compound. Such a therapy has been performed in patients with SSTR2-expressing tumors (Krenning et al. 1994) using large amounts of ^{111}In-DTPA-D-Phe^{1}-octreotide. However, ^{111}In is not an optimal radionuclide for therapy. We have developed a novel radioligand, termed MAURITIUS (i.e., ^{111}In-/^{90}Y-DOTA-lanreotide). In contrast to ^{111}In-DTPA-D-Phe^{1}-octreotide, which binds only to hSSTR2 and 5 with high affinity, MAURITIUS is capable of binding to hSSTR2–5 with high affinity and to hSSTR1 with low affinity, both on primary tumor cells as well as a variety of immortalized tumor cells (Smith-Jones et al. 1998a,b; Virgolini et al. 1998a; Leimer et al. 1998b). This makes the peptide a "universal" SSTR subtype recognizing ligand. Especially the high-affinity binding to the SSTR3 is very important since this hSSTR subtype is expressed most often in human tumors. Also, hSSTR3 acts as an acceptor for VIP (Peck-Radosavljevic et al. 1998). With this concept MAURITIUS is labeled with ^{111}In for diagnostic dosimetry (Virgolini et al. 1998d) and is then used in the ^{90}Y-MAURITIUS version for therapy (Leimer et al. 1998b). Treatment options for patients refractory to standard-dose cytotoxic treatment are limited, and the mostly poor performance status of patients with advanced disease precludes the application of aggressive treatment modalities (e.g., high-dose chemotherapy), which would further impair the quality of life in these patients.

Treatment with "^{90}Y-MAURITIUS" could lead to a significant reduction in analgetic medication, probably sparing patients side effects of higher doses of opiates (constipation, nausea) or non-steroidal anti-inflammatory drugs (gastrointestinal complications). This new therapy could offer palliation and disease control at a reduced cost due to the limited number of administrations. The final peptide therapy strategy in a variety of cancers is most probably cheaper than conventional radiotherapy or prolonged chemotherapy. Overall, receptor-medi-

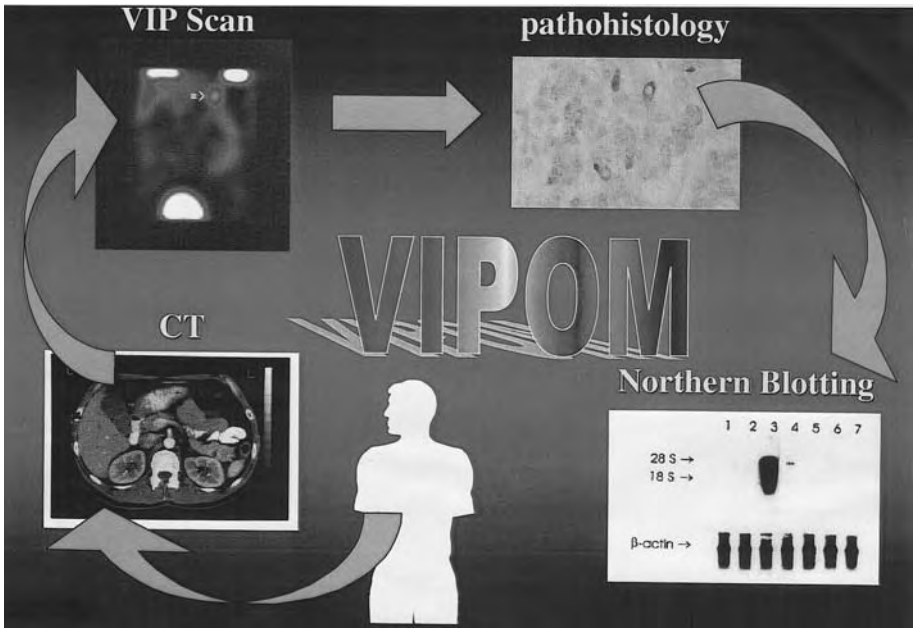

Fig. 10.11. Work-up example. We propose the optimal work-up to gain further insights into the biology and pathophysiology of receptor-ligand interactions on the basis of excellent interactions between a variety of different medical fields, ranging from molecular biology to nuclear medicine and surgery

ated radiotherapy with "^{90}Y-MAURITIUS" might be effective in patients refractory to conventional strategies.

Over the years, other peptides have followed our concept of receptor-mediated therapy based on dosimetry. Analogs of DOTA-octreotide or -octreotate labeled with yttrium-90 or lutitium-77 have entered a clinical phase 3 status with very promising results in a variety of tumor entities.

In the past years, fundamental and clinical research on ^{123}I-VIP receptor scintigraphy has been extensively pursued. This peptide represents an efficient imaging agent for receptor-positive tumors.

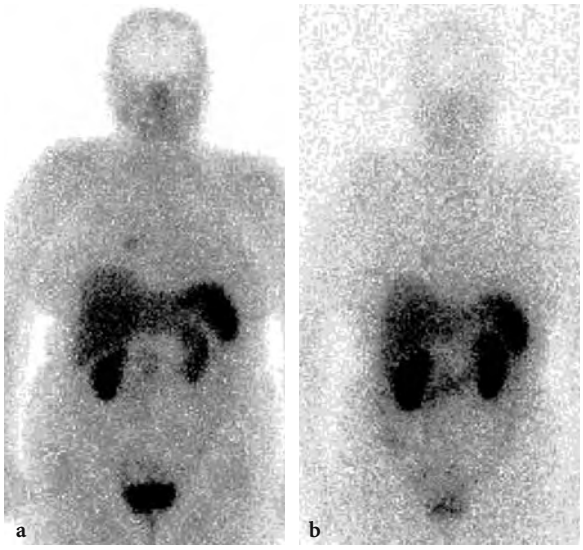

Fig. 10.12. ^{99m}Tc-HYNIC-octreotide images a solitary metastasis in the right lung (**a**), whereas ^{111}In-DTPA-D-Phe1-octreotide (**b**) was negative in the same patient with papillary thyroid cancer

Since ^{123}I is not the ideal radionuclide for diagnostic applications, attempts have been made to label VIP and its analogs with ^{99m}Tc, which is available and more cost-effective. ^{99m}Tc-VIP may be superior due to the better imaging quality. Therefore, the labeling of more stable VIP analogs with ß-emitting nuclides may open new therapeutic opportunities to treat receptor-positive tumors. To answer these questions, additional work needs to be done. The labeling of peptides with technetium-99m has also brought very promising results in the somatostatin receptor area as shown in Figs. 10.12 and 10.13. Other receptor and subtype receptor areas are under preclinical and first clinical investigations with similar promising results, such as those obtained recently with the neurotensin analog ^{99m}Tc-Demotensin (Fig. 10.14.)

PET tracers, such as ^{68}Ga-DOTA-octreotide (Fig. 10.15), ^{64}Cu-TETA-octreotide, and ^{18}F-FP-Gluc-octreotide with higher affinity to SSTR positive lesions and with better spatial resolution will show in the near future their clinical potential.

Finally, the technical progress with the development of SPECT/CT hybrid, PET/CT or PET/MRI cameras, or fusion techniques, will enhance the field of peptide receptor scintigraphy.

Acknowledgments

The authors appreciate the excellent team work of our former Experimental Nuclear Medicine Group at the Dept. of Nuclear Medicine, University of Vienna (Drs. A. Kurtaran, M. Leimer, S. Li, T. Pangerl, M. Raderer, C. Novotny, and Q. Yang), the continuous help of Dr. P. Angelberger (Department of Radiochemistry, Research Center Seibersdorf), as well as the cooperation of Drs. C. Decristoforo and M. Gabriel from the Dept. of Nuclear Medicine, University of Innsbruck.

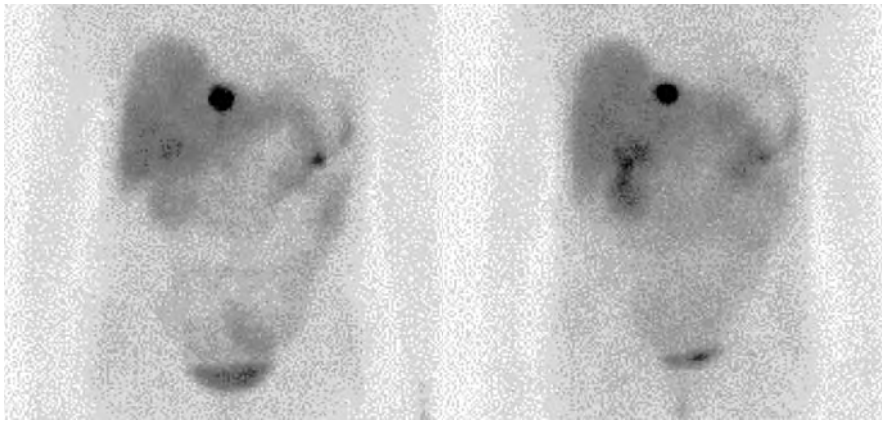

Fig. 10.13. Comparative scintigraphy in a carcinoid tumor patient with a solitary liver lesion using two different technetium-99m somatostatin analogs. (Courtesy of Dr. Gabriel, Innsbruck)

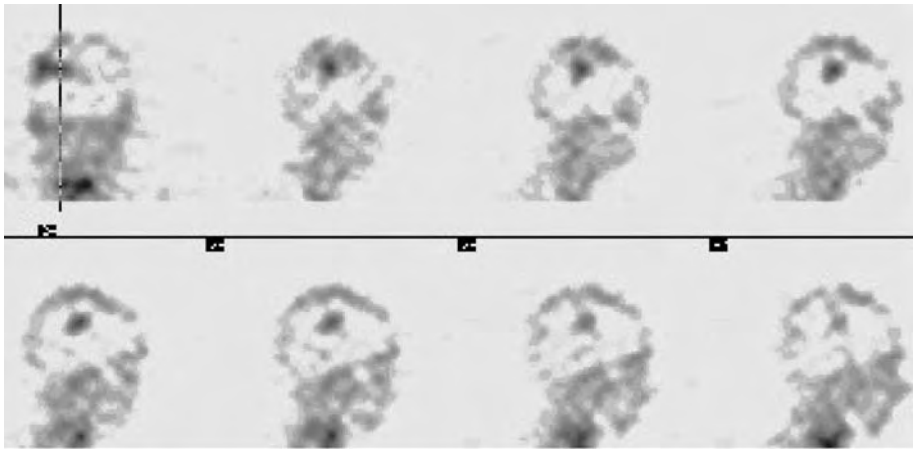

Fig. 10.14. ^{99m}Tc-Demotensin scintigraphy in a patient with NSCLC. The SPECT study shows a single metastasis in the brain at 2 h post injection. (Courtesy of Dr. Gabriel, Innsbruck)

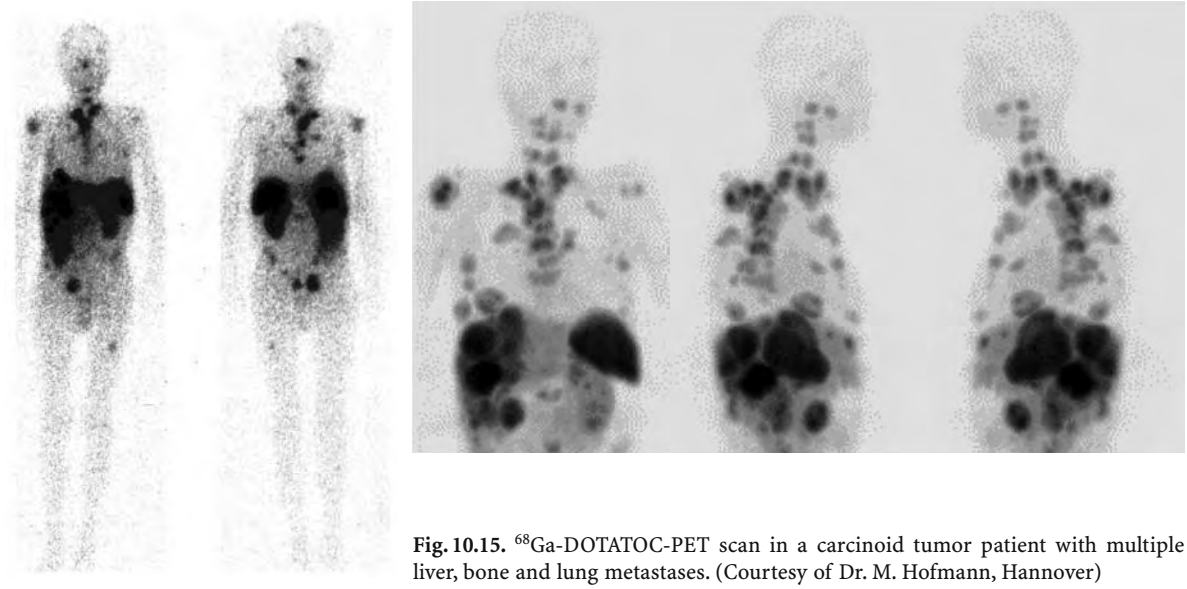

Fig. 10.15. ^{68}Ga-DOTATOC-PET scan in a carcinoid tumor patient with multiple liver, bone and lung metastases. (Courtesy of Dr. M. Hofmann, Hannover)

References

Adamou A, Aiyar N, van Horn S, Elshourhagy NA (1996) Cloning and functional characterization of human vasoactive intestinal peptide (VIP)-2 receptor. Biochem Biophys Res Commun 209:383-392

Ain KB, Taylor KD (1994) Somatostatin analogs affect proliferation of human thyroid carcinoma cell lines in vitro. J Clin Endocrinol Metab 78:1097-1102

Ain KB, Taylor KD, Tofiq S, Venkataraman G (1997) Somatostatin receptor subtype expression in human thyroid and thyroid carcinoma cell lines. J Clin Endocrinol Metab 82:1857-1862

Achilefu S, Srinivasan A, Schmidt MA, Jimenez HN, Bugaj JE, Erion JL (2003) Novel bioactive and stable neurotensin peptide analogue capable of delivering radiopharmaceuticals and molecular beacons to tumor. J Med Chem 46:3403-3411

Alexander RW, Upp JrJR, Poston GJ, Gupta V, Townsend Jr CM, Thompson JC (1988) Effects of bombesin on human small cell carcinoma in vivo. Cancer Res 48:1439-1441

American Cancer Society (1991) Cancer facts and figures 1991. American Cancer Society, Atlanta

Anderson CJ, Dehdeshti F, Cutler PD et al (2001) 64Cu-TETA-octreotide as a PET imaging agent for patients with neuroendocrine tumors. J Nucl Med 42:213-221

Bakker Wh, Alberts R, Bruns C, Breeman WAP, Hofland LJ, Marbach P, Pless J, Pralet D, Stolz B, Koper JW, Lamberts SWJ, Visser TJ, Krenning EP (1991) [^{111}In-DTPA-D-PHE^1]-octreotide, a potential radiopharmaceutical for imaging of somatostatin receptor-positive tumours: synthesis, radiolabelling and in vitro validation. Life Sci 49:1583-1591

Balthazar EJ, Chako AC (1990) Computed tomography of pancreatic masses. Am J Gastroenterol 85:343-349

Bangard M, Behe M, Bender H, Guhlke S, Risse J, Grünwald F, Mäcke H, Biersack HJ (1998) Technetium-99m-octreotide for the detection of somatostatin receptor positive (SSTR+) tumors: preliminary results. Eur J Nucl Med 25:837

Battari A, Martin JM, Luis J, Pouzol O, Secchi J, Marvaldi J,

Pichon J (1988) Solubilization of the vasoactive intestinal peptide receptor from human colonic adenocarcinoma cells. J Biol Chem 263:17685-17689

Baudin E, Schlumberger M, Lumbroso J, Travagli JP, Caillou B, Parmentier C (1996) Octreotide scintigraphy in patients with differentiated thyroid carcinoma: contribution for patients with negative radioiodine scan. J Clin Endocrinol Metab 81:2541-2545

Behr TM, Behe MP (2002) Cholecystokinin-B/Gastrin receptor-targeting peptides for staging and therapy of medullary thyroid cancer and other cholecystokinin-B receptor-expressing malignancies. Semin Nucl Med 32:97-109

Behr TM, Behe M, Angerstein C et al (1999) Cholecystokinin-B/gastrin receptor binding peptides: preclinical development and evaluation of their diagnostic and therapeutic potential. Clin Cancer Res 5:3124s-3138s

Behe M, Behr TM (2003) Cholecystokinin-B (CCK.B) / gastrin receptor targeting for staging and therapy of medullary thyroid cancer and other CCK-B receptor expressing malignancies. Biopolymers 66:399-418

Bell GI, Yasada K, Kong H (1995) Molecular biology of somatostatin receptors. Ciba Found Symp 190:65–88

Bertherat J, Tenenbaum F, Perlemoine K, Videau C, Alberini JL, Richard B, Dousset B, Bertagna X, Epelbaum J (2003) Somatostatin receptor 2 and 5 are the major somatostatin receptors in insulinomas; an in vivo and in vitro study. J Clin Endocrinol 88:5353-5360

Black RJ, Bray F, Ferlay J, Parkin DM (1997) Cancer incidence and mortality in the European Union: cancer registry data and estimates of national incidence for 1990. Eur J Cancer 33:1075-1107

Blaker M, de Weerth A, Tomettem M, Schulz M, Hoppner W, Arlt D, Hoang-Vu C, Dralle H, Terpe H, Jonas L, von Schrenck T (2002) Expression of cholecytochinin-2 receptor in normal human thyroid gland and medullary thyroid carcinoma. Eur J Endocrinol 146:89-96

Bloom SR, Polak JM, Pearse AGE (1973) Vasoactive intestinal peptide and watery diarrhea syndrome. Lancet ii:14–16

Blum J, Handmaker H, Rinne N (1999) The utility of a somatostatin-type receptor binding peptide radiopharmaceutical (P829) in the evaluation of solitary pulmonary nodules. Chest. 115:224-232

Bogatzky J, Guhlke S, Bender H, Sartor J, Knapp FF, Biersack HJ (1997) Receptor binding studies with rhenium-RC160, a directly-labeled somatostatin analog, with membranes of the colon cancer cell line HT 29, CHO cells and ovary carcinoma cell line EFO-21. Eur J Nucl Med 24:1059A

Bombardieri E, Crippa F, Maffioli L, Greco M (1997) Nuclear medicine techniques for the study of breast cancer. Eur J Nucl Med 24:809-824

Boring CC, Squires TS, Tong T, Montgomery S (1994) Cancer statistics 1994. CA Cancer J Clin 44:7-26

Brazeau P, Vale W, Burgus R, Ling N, Butcher M, Livier J, Guellemin R (1973) Hypothalamic polypeptide that inhibits the secretion of immunoreactive pituitary growth hormone. Science 119:77-79

Breeman WA, Hofland LJ, de Jong M, Bernard BF, Srinivasan A, Kweekeboom DJ, Visser TJ, Krenning EP (1999) Evaluation of radiolabelled bombesin analogues for receptor-targeted scintigraphy and radiotherapy. Int J Cancer 81:658-665

Breeman WA, de Jong M, Erion JL, Bugaj JE, Srinivasan A, Bernard BF, Kweekeboom DJ, Visser TJ, Krenning EP (2002) Preclinical comparison of (111)In-labeled DTPA-or DOTA-bombesin analogs for receptor-targeted scintigraphy and radionuclide therapy. J Nucl Med 43:1650-1656

Buchegger F, Bonvin F, Kosinski M, Schaffland AO, Prior J, Reubi JC, Blauenstein P, Tourwe D, Garcia Garayoa E, Bischof Delaloye A (2003) Radiolabeled neurotensin analog, 99Tc-NT-XI, evaluated in ductal pancreatic adenocarcinoma patients. J Nucl Med 44:1649-1654

Buscail L, Saint-Laurent N, Chastre E, Vaillant JC, Gespach C, Capella G, Kalthoff H, Luis F, Vaysse N, Susini C (1996) Loss of SSTR2 somatostatin receptor gene expression in human pancreatic and colorectal cancer. Cancer Res 54:1823-1827

Caroll RE, Caroll R, Benya RV (1999) Charcterization of gastrin-releasing peptide receptors aberrantly expressed by non-abtral gastric adenocarcinomas. Peptides 20:229-237

Camby I, Salmon I, Oiry C, Galleyrand JC, Nagy N, Danguy A, Brotchi J, Pateels JL, Martinez J, Kiss R (1996) The influence of gastrin and/or cholecytokinin antagonists on the proliferation of three human astrocytic tumor cell lines. Neuropeptides 30:433-437

Capello A, Breeman WAP, van Hagen PM, Krenning EP, de Jong M (2003) Increased apoptosis induction with a RDG linked somatostatin analogue. Eur J Nucl Med Mol Imaging 30 [Suppl 2]:396

Chabry J, Labbe-Jullie C, Glly D, Kitabgi P, Vincent JP, Mazella J (1994) Stable expression od the cloned rat brain neurotensin receptor into fibroblasts: binding properties, photoaffinity labeling, transduction mechanisms, and internalization. J Neurochem 63:19-27

Chen J, Cheng Z, Hoffman TJ et al (2000) Melanoma-targeting properties of ^{99m}technetium-labeled cyclic alpha-melanocyte-stimulating hormone peptide analogues. Cancer Res 60:5649-5658

Christian JA, Cook GJ, Harmer C (2003) Indium-111-labelled octreotide scintigraphy in the diagnosis and management of non-iodine avid metastatic carcinoma of the thyroid. Br L Cancer 89:258-261

Clarke SEM (1998) Medullary thyroid carcinoma. In: Murray IPC, Ell PJ (eds) Nuclear medicine in clinical diagnosis and treatment, vol 2. Churchill-Livingstone, Edinburgh, pp 959-968

Corness JD, Demchyschyn LL, Seeman P (1993) A human somatostatin receptor (SSTR3), located on chromosome 22, displays preferential affinity for somatostatin-14 like peptides. FEBS 321:279-284

Couvineau A, Laburthe M (1985) The human vasoactive intestinal peptide receptor: molecular identification by covalent cross-linking in colonic epithelium. J Clin Endocrinol Metab 61:50-55

Couvineau A, Amiranoff B,Laburthe M (1986) Solubilization of the liver vasoactive intestinal peptide receptors. J Biol Chem 261:14482-14489

Couvineau A, Voisin T, Guijarro L, Laburthe M (1990) Purification of vasoactive intestinal peptide receptor from porcine liver by a newly designed one-step affinity chromatography. J Biol Chem 265:13386-13390

Couvineau A, Rouyer-Fessard C, Darmoul D, Maoret JJ, Carrero I, Ogier-Denis E Laburthe M (1994) Human intestinal VIP receptor: cloning and functional expression of two cDNA encoding proteins with different N-terminal domains. Biochem Biophys Res Commun 200:769-776

DeCosse JJ, Tsoulias GJ, Jacobson JS (1994) Colorectal cancer: detection, treatment and rehabilitation. CA Cancer J Clin 44:27-42

De Jong M, Bernard BF, de Bruin E et al (1998a) Internalization of radiolabelled [DTPA0]octreotide and [DOTA0,Tyr3]octreotide: peptides for somatostatin receptor-targeted scintigraphy and radionuclide therapy. Nucl Med Commun 19:283-288

De Jong M, Breeman WA, Bakker WH et al (1998b) Comparison of ^{111}In-labeled somatostatin analogues for tumor scintigraphy and radionuclide therapy. Cancer Res 58:437-441

Decristoforo C, Mather SJ, Cholewinski W et al (2000) ^{99m}Tc-EDDA/HYNIC-TOC: a new ^{99m}Tc-labelled radiopharmaceutical for imaging somatostatin receptor-positive tumours: first clinical results and intra-patient comparison with ^{111}In-labelled octreotide derivates. Eur J Nucl Med 27:1318-1325

Decristoforo C, Maina T, Nock B, Gabriel M, Cordopatis P, Moncayo R (2003) 99mTc-Demotate 1: first data in tumour patients-results of a pilot/phase I study. Eur J Nucl Med Mol Imaging 30:1211-1219

Demchyschyn LL, Srikant CB, Sunahara RK, Kent G, Seeman P, van Tol HH, Panetta R, Patel YC, Niznik HB (1993) Cloning and expression of a human somatostatin-14-selective receptor variant (somatostatin receptor 4) located on chromosome 20. Mol Pharmacol 43:894-901

Dockray GJ (2000) Gastrin, growth, and colonic neoplasia. Gut 47:747-748

Donovan DT, Gagel RF (1997) Medullary thyroid carcinoma and the Multiple Endocrine Neoplasia Syndromes. In: Falk A (ed) Thyroid diseases: endocrinology, surgery, nuclear medicine and radiotherapy. Lippincott-Raven, Philadelphia, pp 619-644

Duet M, Sauvaget E, Petelle B, Rizzo N, Guichard JP, Wassef M, Le Cloirec J, Herman P, Tran Ba Huy P (2003) Clinical impact of somatostatin receptor scintigraphy in the management of paragangliomas of the head and neck. J Nucl Med 44:1767-1774

Ehlers RA, Kim Sh, Zhang Y, Ethridge RT, Murrilo C, Hellmich C, Evans DB, Townsend CM Jr, Mark Evers B (2000) Gut peptide receptor expression inhuman pancreatic cancer. Ann Surg 231:838-848

Egli A, Alberto R, Tannahill L et al. Organometallic ^{99m}Tc-aquaion labels peptide to an unprecedented high specific activity. J Nucl Med 1999; 40: 1913-1917.

Fathi Z, Corjay MH, Shapira H, Wada E, Benya R, Jensen R, Viallet J, Sausville EA, Battey JF (1993) BRS-3: novel bombesin receptor subtype selectivity expressed in testis and lund carcinoma cells. J Biol Chem 268:5979-5984

Ferrari S, Dondi M, Fanti S, Giacomini S, Mercuri M, Bacci G 2003 Somatostatin receptor (SSTR) scintigraphy in patients with osteosarcoma. Cancer Biother Radiopharm 18:8847-8851

Ferris HA, Carroll RE, Creswick KC, Banya RV (1997) Location and characterization of the human GRP receptor expressed by gastrointestinal epithelial cells. Peptides 18:663-672

Fisher WE, Doran TA, Muscarella II P, Boros LG, Ellison EC, Schirmer WJ (1998) Expression of somatostatin receptor subtype 1–5 genes in human pancreatic cancer. J Natl Cancer Inst 90:322-324

Fleischmann A, Laderach U, Friess H, Buechler MW, Reubi JC (2000) Bombesin receptors in distinct tissue compartments of human pancreatic diseases. Lab Invest 80:1807-1817

Florio T, Montella L, Corsaro A, De Chiara A, Apice G, Fazioli F, Lastoria S, Schettini G, Palmieri G (2003) In vitro and in vivo expression of somatostatin receptors in intermediate and malignant soft tissue tumors. Anticancer Res 23:2465-2471

Foekens JA, Portengen H, Putten WLJ (1989) Prognostic value of receptors for insulin-like growth factor 1, somatostatin and epidermal growth factor in human breast cancer. Cancer Res 49:7002-7009

Freeny PC, Marks WM, Ryan JA, Traverso LW (1988) Pancreatic ductal adenocarcinoma: 2 diagnosis and staging with dynamic CT. Radiology 166:125-133

Friess H, Zhu Z, Shi X, Shrikhande SV, Wang L, Lieb K, Korc M, Palma C, Zimmermann A, Reubi JC, Büchler MW (2003) Neurokinin-1 receptor (NK-1R) expression and potential effects on tumor growth in human pancreatic cancer. Lab Invest 83:731-742

Fujita T, Yamaji Y, Sato M, Murao K, Takhara J (1994) Gene expression of somatostain receptor subtypes, SSTR1 and SSTR2, in human lung cancer cell lines. Life Sci 55:1797-1806

Gabriel M, Decristoforo C, Donnemiller E, Ulmer H, Watfah Rychhhlinski C, Mather SJ, Moncayo R (2003) An intrapatient comparison of 99mTc-EDDA/HYNIC-TOC with 111In-DTPA-octreotide for diagnosis of somatostatin receptor-expressing tumors. J Nucl Med 44:708-716

Garcia-Garayoa E, Allemann-Tannahill L, Blauenstein P et al (2001) In vitro and in vivo evaluation of new radiolabeled neurotensin(8-13) analogues with high affinity for NT1 receptors. Nucl Med Biol 28:75-84

Garcia-Garayoa E, Blauenstein P, Bruehlmeier M et al (2002) Preclinical evaluation of a new, stabilized neurotensin(8-13) pseudopeptide radiolabeled with ^{99m}Tc. J Nucl Med 43:374-383

Garin E, Devillers A, Le Cloirec J, Bernard AM, Lescouarché J, Herry JY, Reubi JC, Bourguet P (1998) Use of In-111-penetreotide somatostatin receptor scintigraphy to detect recurrent thyroid carcinoma in patients without detectable iodine uptake. Eur J Nucl Med 25:687-694

Gespach C, Bawab W, de Cremoux P, Calvo F (1988) Pharmacology, molecular identification and functional characteristics of vasoactive intestinal peptide receptors in human breast cancer. Cancer Res 48:5079-5083

Giblin MF, Wang N, Hoffmann TJ, Jurisson SS, Quinn TP (1998) Design and characterization of á melanotropin peptide analogs cyclized through rhenium and technetium metal coordination. Proc Natl Aad Sci USA 95:12814-12818

Ginsberg RJ, Kris MG, Armstrong JG (1993) Cancer of the lung. In: De Vita V, Hellman S, Rosenberg SA (eds) Cancer principles and practice of oncology, 4th edn. Lippincott, Philadelphia, pp 673-723

Giusti M, Ciccarelli, Dallabonzana D, Delitala G, Faglia G, Liuzzi A, Gussoni G, Disem GG (1997) Clinical results of long term slow release lanreotide treatment of acromegaly. Eur J Clin Invest 27:277-284

Guitera-Rovel P, Lumbroso J, Gautier-Gouis MS, Spatz A, Mercier S, Margulis A, Mamelle G, Kolb F, Lartigau E, Avril MF (2001) Indium-111-octreotide scintigraphy of Merkel call carcinomas and their metastases. Ann Oncol 12:807-811

Godwin JD (1975) Carcinoid tumors: an analysis of 2837 cases. Cancer 36:560-569

Gotthart M, Battmann A, Beuter D, Bauhofer A, Schipper ML, Béhé P, Klose KJ, Behr TM (2003) In-111-DTPA-D-Glu1-Minigastrin is superior to F-18-FDG PET and CT in the diagnosis of metastatic medullary thyroid cancer. Eur J Nucl Med Mol Imaging 30:S158

Greenman Y, Melmed S (1994a) Heterogeneous expression of two somatostatin receptor subtypes in pituitary tumors. J Clin Endocrinol Metab 78:398-403

Greenman Y, Melmed S (1994b) Expression of three somatostatin receptor subtypes in pituitary adenomas: evidence for preferential SSTR5 expression in the mammosomatotroph lineage. J Clin Endocrinol Metab 79:724-729

Gugger M, Reubi JC (1999) Gastrin-releasing peptide receptors in non-neoplastic and neoplastic human breast. Am J Pathol 155: 2067-2076

Guhlke S, Zamora PO, Sartor J, Knapp FF, Rhodes BA, Biersack HJ (1997) Stabilization of rhenium-188 and iodine-131 labeled peptides for radiotherapy. Eur J Nucl Med 24:1059A

Haegerstrand A, Jonzon B, Daalsgard CJ, Dalsgaard CJ, Nilsson J (1989) Vasoactive intestinal polypeptide stimulates cell proliferation and adenylate cyclase activity of cultured human keratinocytes. Proc Natl Acad Sci USA 86:5993-5996

Harmar AJ, Arimura A, Gozes I, Journot L, Laburthe M, Pisegna JR, Robberecht P, Said SI, Sreedharan SP, Wank SA, Waschek JA (1998) International union of pharmacology. XVIII. Nomenclature of receptors for vasoactive intestinal peptide and piutiary adenylate cyclase-activating polypeptide. Pharmacol Rev 50:265-270

Haubner R, Wester HJ, Reuning U, Senekowitsch-Schmidtke R, Diefenbach B, Kessler H, Stöckin G and Schwaiger M (1999) Radiolabeled a_vb_3 integrin antagonists: a new class of tracer for tumor targeting. J Nucl Med 40:1061-1971

Haubner R, Wester HJ, Mang C, Senekowitsch-Schmidtke R, Kessler H and Schwaiger M (2000) Synthesis and first evaluation of a [18F]SAA-labeled RDG-peptide for monitoring the avb3 integrin expression. J Nucl Med 41:42P

Hejna M, Kurtaran A, Raderer M, Pangerl T, Niederle B, Vorbeck F, Vierhapper H, Angelberger P, Virgolini I (1998) ^{123}I-vasoactive intestinal peptide (VIP) receptor and ^{111}In-DTPA-Phe^1-octreotide scanning in patients with insulinoma. Eur J Nucl Med 25:977A

Henning IM, Laissue JA, Horisberger U, Reubi JC (1995) Sbstance P receptors in human primary neoplasms: tumoural and vascular localisation. Int J Cancer 61:786-792

Henze J, Schuhmacher P, Hipp A, Dimitrakopoulou-Strauss H, Maecke R, Strauss LG, Haberkorn U (2003a) ^{68}GA-DOTA°-D Phe^1-Tyr^3-Octreotide (DOTATOC) kinetics in the follow-up of irradiated meningeomas. Annual meeting of the Society of Nuclear Medicine, abstract 381

Henze J, Schuhmacher P, Hipp A, Dimitrakopoulou-Strauss H, Maecke R, Strauss LG, Haberkorn U (2003b) Kinetic analyis of ^{68}GA-DOTA°-*D* Phe^1-Tyr^3-Octreotide (DOTATOC) in untreated meningeomas. Annual meeting Society of Nuclear Medicine, New Orleans 2003, abstract 880

Hofmann M, Maecke H, Borner R, Weckesser E, Schoffski P, Oei L, Schumacher J, Henze M, Heppeler A, Meyer J, Knapp H (2001) Biokinetics and imaging with the somatostatin receptor PET radioligand (68)Ga-DOTATOC: preliminary data. Eur J Nucl Med 28(12):1751-1757

Hofmann M, Boerner A, Meyer G, Maecke H, Berding G, Oei M, Clauss R, Knapp WH (2003) Use of SUV in Ga-68-DOTATOC PET- Influence of varying peptide amout. Eur J Nucl Med Mol Imaging 30:S204

Hoffmann TJ, Gali H, Smith CJ, Sieckman GL, Hayes DL, Owen NK, Volkert WA (2003) Novel series of 111In-labeled bombesin analogs as potential radiopharmaceuticals for specific targeting of gastrin-releasing peptide reeptors expressed on human pancreate cancer cells. J Nucl Med 44:823-831

Hillairet de Boiferon M, Raguin O, Thiercelin C, Dussaillant M, Rostene W, Barbet J, Pelegrin A, Gruaz-Guyon A (2002) Improved tumor selectivity of radiolabeled peptides by receptor and antigen dual targeting in the neurotensin receptor model. Bioconjug 13:654-662

Hoegerle S, Altenhofer C, Ghanem N, Koehler N, Waller CF, Sheruebl, Moser E, Nitzsche E (2001) Whole-body 18F-Dopa PET for detection of gastrointestinal carcinoid tumor. Radiology 220:373-380

Hoegerl S, Altenhoefer C, Ghanem N, Brink I, Moser E, Nitze E (2003b) 18F-DOPA positron emission tomography for tumor detection in patients with medullary thyroid carcinoma and elevated calcitonin levels. Eur J Nucl Med Mol Imaging 28:64-71

Hökfelt T, Pernow B, Wahren J (2001) Substance P: a pioneer among neuropeptides. J Intern Med 249:27-40

Hustinx R, Paulus P, Foidart J, Bury T, Cataldo D, Rigo P (1997) Efficacy of Tc 99 m P829, a radiolabeled somatostatin analog, in visualising mediastinal spread of non-small cell lung cancer. Eur J Nucl Med 24:959A

Inagaki N, Yoshida H, Mizuta M, Mizuno N, Fujii Y, Gonoi T, Miyazaki JI, Seino S (1994) Cloning and functional characterization of a third pituitary adenylate cyclase-activating polypeptide subtype receptor-expressed in insulin-secreting cells. Proc Natl Acad Sci USA 91:2679-2683

Inokuma T, Tamaki N, Torizuka T, Fujita T, Magata Y, Yonekura Y, Ohshio G, Imamura M, Konishi J (1995) Value of fluorine-18-fluorodeoxyglucose and thallium 201 in the detection of pancreatic cancer. J Nucl Med 36:229-235

Ishihara T, Shigemoto R, Mori K, Takahashi K, Nagata S (1992) Functional expression and tissue distribution of a novel receptor for vasoactive intestinal polypeptide. Neuron 8:811-819

Jagoda E, Aloi L, Seidel J, Lang L, Moody T, Green S, Caraco C, Daube Witherspoon M, Green MV, Eckelman WC (1997) The biodistribution of a F-18 labeled derivate of vasoactive intestinal peptide (dVIP) in a xenograft mouse model of breast cancer. J Nucl Med 38:239A

Jais P, Terris B, Ruszniewski, LeRomancer M, Reyl-Desmars F, Vissuzaine C, Cadiot G, Mignon M, Lewin MGM (1997) Somatostatin receptor subtype gene expression in human endocrine gastroenteropancreatic tumors. Eur J Clin Invest 27:639-644

Janson ET, Gobl A, Kälkner KM, Ölber K (1996) A comparison between the efficacy of somatostatin receptor scintigraphy and that of in situ hybridization of somatostatin receptor subtype 2 messenger RNA to predict therapeutic outcome in carcinoid patients. Cancer Res 56:2561-2565

Jiang S, Kopras E, McMichael M, Bell RH Jr, Ulrich CD (1997) Vasoactive intestinal peptide (VIP) stimulates in vitro growth of VIP-1 receptor bearing human pancreatic adenocarcinoma derived cells. Cancer Res 57:1475-1480

John M, Meyerhof W, Richter D, Waser B, Schaer JC, Scherübl H, Boese-Landgraf J, Neuhaus P, Ziske C, Mölling K, Riecken EO, Reubi JC, Wiedenmann B (1996) Positive somatostatin receptor scintigraphy correlates with the presence of somatostatin receptor subtype 2. Gut 38:33-39

Kahn A, Herman P, Vorwecki P (1991) Solitary pulmonary nodules: comparison and classification with standard, thin section, and reference phantom CT. Radiology 179:477-481

Kalser MH, Barkin J, MacIntyre JM (1985) Pancreatic cancer: assessment of prognosis by clinical presentation. Cancer 56:397-402

Kelly DM, Benjamin IS (1995) Pancreatic carcinoma. Ann Oncol 6:19-28

Kienast O, Dobrozemsky G, Özer S, Traub T, Novotny C, Niederle B, Raderer M, Kainberger F, Dudczak R, Kurtaran A (2003) Clinical impact of image fusion by means of XCT/SPECT: Vienna experience with 111In-labeled somatostatin analogues, 123I-MIBG and 131I-WBS. Eur J Nucl Med 30:S182

Kowalski J, Henze M, Schuhmacher J, Macke HR, Hofmann M, Haberkorn U (2003) Evaluation of positron emission tomography imaging using [68Ga]-Dota-DPhe(1)-Tyr(3)-ocreotide in comparison to [111In]-DTPAOC SPECT. First results in patients with neuroendocrine tumors. Mol Imaging Biol 5:42-48

Krausz Y, Keidar Z, Kogan I, Even-Sapir E, Bar-Schalom R, Engel A, Rubinstein R, Sachs J, Bocher M, Agranovicz S, Chisin R, Israel O (2003) SPECT/CT hybrid imaging with 111In-pentreotide in assessment of neuroendocrine tumours. Clin Endocrinol 59:565-573

Krenning EP, Bakker WH, Breeman WA, Koper JW, Kooij PP, Ausem L, Lamberts JS, Reubi JC, Lamberts SW et al (1989) Localization of endocrine-related tumors with radioiodinated analogue of somatostatin. Lancet 1:242-244

Krenning EP, Bakker WH, Kooij PPM, Breeman WAP, OEI HY, de Jong M, Reubi JC, Visser TJ, Bruns C, Kwekkeboom DJ, Reijs AEM, van Hagen PM, Koper JW, Lamberts SWJ (1992) Somatostatin receptor scintigraphy with [^{111}In-DTPA-D-Phe^{1}]-octreotide in man: metabolism, dosimetry and comparison with [123I-Tyr-3-]-octreotide. J Nucl Med 33:652-658

Krenning EP, Kwekkeboom DJ, Bakker WH, Breeman WA, Kooij PP, Oei Hy, van Hagen M, Postema PT, de Jong M, Reubi JC et al (1993) Somatostatin receptor scintigraphy with (^{111}In-DOTA-d-Phe^{1})- and (^{123}I-Thyt^{3})-octreotide: the Rotterdam experience with more than 1000 patients. Eur J Nucl Med 18:1-16

Krenning EP, Kooij PP, Bakker WH, Breeman WH, Postema PT, Kwekkeboom DJ, Oei HY, Jong M, Visser TJ, Reijs AE (1994) Radiotherapy with a radiolabeled somatostatin analogue, ^{111}In-DTPA-D-Phe^{1}-octreotide. A case history. Ann NY Acad Sci 733:496-504

Krenning EP, Kooij PP, Pauwels S, Breeman WA, Postema PT, Herder de WW, Valkema R, Kwekkeboom DJ (1996) Somatostatin receptor: scintigraphy and radionuclide therapy. Digestion 57:57-61

Krenning EP, Bakker WH, Kwekkeboom DJ, Kooij PPM, van der Pluijm ME, Behe M, Mäcke H (1997) Biodistribution of a new chelated somatostatin analogue, [In-111-DOTA-D-Phe^{1}-Tyr^{3}]-octreotide; comparison with [In-111-DTPA-D-Phe-1]-octreotide in humans. J Nucl Med 38:103A

Krois D, Riedel C, Angelberger P, Kalchberger P, Virgolini I, Lehner H (1996) Synthesis of N-a-(6-hydrazinonicotinoyl)-octreotide: a precursor of a ^{99m}Tc-complex. Liebigs Ann 1463-1469

Kubota A, Yamada Y, Kagimoto S, Kagimoto S, Shimatsu A, Imamura M, Suda K, Imura H, Seino S, Seino Y (1994) Identification of somatostatin receptor subtypes and an implication for the efficacy of somatostatin analogue SMS 201–995 in treatment of human endocrine tumors. J Clin Invest 93:1321-1325

Kurtaran A, Pangerl T, Scheuba C, Schima W, Schober E, Kaserer K, Teleky B, Virgolini I (1997) Vasualization of intestinal splenosis by somatostatin receptor scintigraphy. Am J Gastroenterol 93:1375-1376

Kurtaran A, Scheuba C, Kaserer K, Angelberger P, Niederle B, Virgolini I (1998) Comparison of ^{111}In-DTPA-D-Phe^{1}-octreotide and ^{99m}Tc-(V)-dimercapto-succinic acid scanning in the preoperative localisation of medullary thyroid carcinoma. J Nucl Med 39:1907-1909

Kvols L (1994) Medical oncology considerations in patients with metastatic neuroendocrine tumors. Semin Oncol 21:56-60

Kwekkeboom D, Krenning E, Bakker W (1991) Radioiodinated somatostatin analog scintigraphy in small-cell lung cancer. J Nucl Med 32:1845-1848

Kwekkeboom DJ, Hoff AM, Lamberts SWJ et al (1992) Somatostatin analogue scintigraphy: a simple and sensitive method for the in visualisation of Merkel-cell tumors and their metastases. Arch Dermatol 128: 818-821

Kwekkeboom DJ, van Urk H, Pauw KH et al (1993) Octreotide scintigraphy for detection of paragangliomas. J Nucl Med 34:873-878

La Bella R, Garcia-Garayoa E, Bahler M, Blauenstein P, Schibili R, Conrath P, Tourwe D, Schubiger PA (2002) A 99mTc (I)-postlabeled high affinity bombesin analogue as a potential tumor imaging agent. Bioconjug 13:599-604

Laburthe M, Couvineau A (1988) Molecular analysis of vasoactive intestinal peptid receptors. A comparison with receptors for VIP-related peptides. In: Said S, Mutt V (eds) Vasoactive intestinal peptide and related peptides. NY Acad Sci 527:296-313

Lamberts SWJ, Bakker WH, Reubi JC, Krenning EP (1990) Somatostatin receptor imaging in the localization of endocrine tumors. N Engl J Med 323:1246-1249

Lamberts SWJ, van der Lely AJ, de Herder WW, Hofland LJ (1996) Drug therapy: octreotide. N Engl J Med 334:246-254

Lastoria S, Muto P, Caracò C, Vergara P, Varrella L, Pezullo F, Ionna F, Mozillo N, Lister-James J, Salvatore M (1996) Somatostatin receptor scintigraphy (SRS) with technetium -99 m labeled synthetic peptides in melanoma. J Nucl Med 37:138A

Laws SAM, Gough AC, Evans AA, Bains MA, Primrose JN (1997) Somatostatin receptor subtype mRNA expression in human colorectal cancer and normal colonic mucosae. Br J Cancer 75:360-366

Lebtahi R, LeCloirec J, Houzard JC et al (2002) Detection of neuroendocrine tumors: ^{99m}Tc-P829-scintigraphy compared with ^{111} In-pentreotide scintigraphy. J Nucl Med 43:889-895

Leimer M, Kurtaran A, Raderer M, Smith-Jones P, Bischof C, Valencak J, Scima W, Lister-James J, Virgolini I (1998a) In vitro and in vivo binding of ^{99m}Tc-P829 to gastrointestinal adenocarcinomas. Eur J Nucl Med 39:923A

Leimer M, Kurtaran A, Smith-Jones P, Raderer M, Havlik E, Angelberger P, Vorbeck F, Niederele B, Virgolini I (1998b) Response to treatment with 90Y-DOTA-lanreotide of a patient with metastatic gastrinoma. J Nucl Med 39:2090-2094

Leimer M, Traub T, Andreae F, Angelberger P, Ofluoglu S, Stelzer O, Zettnig G, Kurtaran A, Flores J, Dudczak R, Virgolini I (2000) Binding of 111In-DOTA-lanreotide and 111In-DOTA-Tyr3-DPHE1-octreotide to thyroid. Eur J Nucl Med 27:A7010

Li S, Kurtaran A, Li M, Traub-Weidinger T, Kienast O, Schima W, Angelberger P, Virgolini I, Raderer M, Dudczak R (2003) 111In-DOTA-dPhe1-Tyr3-octreotide, 111In-DOTA-lanreotide and 67Ga citrate scintigraphy for visualisation of extranodal marginal zone B-cell lymphoma of the MALT type: a comparative study. Eur J Nucl Med Mol Imaging 30:1087-1095

Lister-James J, Virgolini I, Nelson CA, Pearson DA, Leimer M, Moyer BR, Wilson DM, Dean RT (1998) Tc-99 m 1666: development of a technetium-99m-labeled VIP-receptor imaging agent. J Nucl Med 39:225A

Lowe V, Fletcher J, Gobar L et al (1998) Prospective investigation of positron emission tomography in lung nodules. J Clin Oncol 16:1075-1084

Lugtenburg PJ, Löwenberg B, Eljkemans MJC, Habbema JDF, Lamberts R, Valkema R, Krenning EP (1998) Somatostatin receptor scintigraphy in limited Hodgkin's disease: clinical impact and cost-effectiveness analysis. J Nucl Med 39:39A

Lugtenburg PJ, Krenning EP, Valkema R, Oei HY, Lamberts SW, Eijkemans MJ, van Putten WL, Loewnberg B (2001) Somatostatin receptor scintigraphy useful in stage I-II Hodgkin´s disease: more extended disease identified. Br J Haematol 112:936-944

Lutz EM, Sheward WJ, West KM, Fink G, Harmar AJ (1993) The VIP2 receptor: molecular characterization of a cDNA encoding a novel receptor for vasoactive intestinal peptide. FEBS Lett 334:3-8

Mailleux P, Vanderhaeghen JJ (1990) Cholecytochinin receptors of A type in the human dorsal medulla oblongata and meningenomas, and og B type in small cell lung cancer. Nature 316:823-825

Maina T, Stolz B, Albert R, Bruns C, Koch P, Maecke H (1994) Synthesis, radiochemistry and biological evaluation of a new somatostatin analogue (SDZ 219–387) labeled with technetium-99 m. Eur J Nucl Med 21:437-444

Maina T, Nock B, Nikolopoulou A et al (2002) [^{99m}Tc]Demotate, a new ^{99m}Tc-based [Tyr^3]octreotate analogue for the detection of somatostatin receptor-positive tumours: synthesis and preclinical results. Eur J Nucl Med Mol Imaging 29:742-753

Markwalder R, Reubi JC (1999) Gastrin-releasing peptide receptors in the human prostate: relation to neoplastic transformation. Cancer Res 59:1152-1159

Maoret JJ, Pospai D, Rouyer-Fessard C, Couvinnneau A, Laboisse C, Voisin T, Laburthe M (1994) Neurotensin receptor and its mRNA are expressed in many human colon cancer cell lines but not in normal colonic epithelium: binding studies and RT-PCR experiments. Biochem Biophys Res Commun 30:465-471

Mather SJ, Ellison D (1994) Technetium-99 m labeled hybrid receptor binding peptides. J Nucl Med Biol 38:480-481

Mazella J, Zsurger N, Navarro V, Chabry J, Kaghad M, Caput D, Ferrara P, Vita N, Gully D, Maffrand JP, Vincent JP (1998) The 100-kDa neurotensin receptor id gp95/sortilin, a non-G protein-coupled receptor. J Biol Chem 273:26273-26276

Miller GM, Alexander JM, Bikkal HA, Katzenelson L, Zervas NT, Klibanski A (1995) Somatostatin receptor subtype gene expression in pituitary adenomas. J Clin Endocrinol Metab 80:2974-2979

Moertel CG (1987) Karnovsky memorial lecture: an odyssee in the land of small tumors. J Clin Oncol 5:1503-1522

Moody TW, Leyton J, Unsworth E, John C, Lang L, Eckelman WC (1998) (Arg15, Arg21) VIP: evaluation of biological activity and localization to breast cancer tumors. Peptides 19:585-592

Moody TW, Chiles J, Casibang M, Moody E, Chan D, Davis TP (2001) SR48692 is a neurotensin receptor antagonist which inhibits the growth of small cell lung cancer cells. Peptides 22:109-115

Muehllechner P, Gabriel M, Decristoforo C, Kendler D, Heute D, Donnemiller E, Moncayo R (2003) Somatostatin receptor scintigraphy using 99mTc-EDDA-HYNIC-TOC in patients with medullary thyroid carcinoma. Eur J Nucl Med Mol Imaging 30:S285

Mundschenk J, Unger N, Schulz S, Hollt V, Schulz S, Steinke R, Lehnert H (2003) Somatostatin receptor subtypes in human pheochromocytoma; subcellular expression pattern and functional relevance for octreotide scintigraphy. J Clin Endocrinol Metab 88:5150-5157

Nagalla SR, Barry BJ, Crewick KC, Eden P, Taylor JT, Spindel ER (1995) Cloning of a receptor for amphibian [Phe13]bombesin distinct from the receptor for gastrin-releasing peptide: identification of a fourth bombesin receptor subtype (BB4). Proc Natl Acad Sci USA 92:6205-6209

Naruke T, Tsuchiya R, Kondo H, Asamura H, Nakayama H (1997) Implications of staging in lung cancer. Chest 112:242–248

National Cancer Institute (1991) Annual cancer statistics review 1973-1988. Department of Health and Human Services, Bethesda MD (NIH publication no 91–2789)

Nelson J, Donnelly M, Walkter B, Gray J, Shaw C, Murphy RF (1991) Bombesin stimulates proliferation of human breast cell cancer cells in culture. Br J Cancer 63:933-936

Nock B, Nikolopoulou A, Chiotellis E, Loudos G, Maints D, Reubi JC, Maina T (2003) (99mTc-Demobesin 1, a novel potent bombesin analogue for GRP receptor-targeted tumour imaging. Eur J Nucl Med Mol Imaging 30:247-258

O'Byrne K,J, Halmos G, Pinski J, Groot K, Szepeshazi K, Schally AV, Carney DN (1994) Somatostatin receptor expression in lung cancer. Eur J Cancer 30:1682-1687

Oka H, Jin L, Reubi J, Qian X, Scheithauer B, Fujii K, Kameya T, Lloyd R (1998) Pituitary adenylate-cyclase-activating polypeptide (PACAP) binding sites and PACAP / vasoactive intestinal polypeptide receptor expression in humam pituitary adenomas. Am J Pathol 153:1787-1796

O'Nilsson L, Kölby L, Wängberg B, Wigander A, Billig H, William-Olsson L, Fjälling M, Forssell-Aronsson E, Ahlman H (1998) Comparative studies on the expression of somatostatin receptor subtypes, outcome of octreotide scintigraphy and response to octreotide treatment in patients with carcinoid tumours. Br J Cancer 77:632-637

Otte A, Jermann E, Behe M, Goetze M, Bucher HC, Roser HW, Heppeler A, Mueller-Brand J, Meacke HR (1997) DOTA-TOC: a powerful new tool for receptor-mediated radionuclide therapy. Eur J Nucl Med 24:792-795

Otte A, Mueller-Brand J, Dellas S, Nitzsche EU, Herrmann R, Maecke HR (1998) Yittrium-90-labelled somatostatin-analogue for cancer treatment. Lancet 351:417-418

Pacini F, Fugazzola L, Basolo F et al (1994) Routine measurement of serum calcitonin in nodular thyroid diseases allows the preoperative diagnosis of unsuspected sporadic medullary thyroid carcinoma. J Clin Endocrinol Metab 78:826-829

Pallela VR, Chakdar S, Rattan S, Thakur ML (1998a) Tc-99 m labeled VIP receptor agonist: functional and pharmacokinetic studies. J Nucl Med 39:64A

Pallela VR, Reddy MVR, Senadhi VK, Thakur ML (1998b) Synthesis and evaluation of Tc-99m-labeled VIP as potential tumor imaging agents. J Nucl Med 39:226A

Pallela VR, Thakur ML, Chakder S, Rattan S (1998c) Tc-99 m labeled VIP receptor agonist: functional studies. J Nucl Med 40:352-360

Pangerl T, Peck-Radosavljevic M, Kaserer K, Niederle B, Gangl A, Virgolini I (1997) Somatostatin (SST)rand VIP receptor subtype gene expression in human tumors. Eur J Nucl Med 24:995A

Panetta R, Patel YC (1994) Expression of mRNA for all five human somatostatin receptors (hSSTR-1-5) in pituitary tumors. Life Sci 56:333-342

Patz EF, Lowe VJ, Hoffman JM et al (1994) Persistent or recurrent bronchogenic carcinoma: detection with PET and 2-[F-18] fluoro-2-deoxy-D-glucode. Radiology 191:379-382

Parker SL, Tong T, Bolden S, Wingo PA (1997) Cancer statistics 1997. Ca Cancer J Clin 47:5-27

Peck-Radosavljevic M, Yang Q, Leimer M, Bischof C, Virgolini I (1998) Thr somatostatin receptor (sstr) subtype 3 acts as an acceptor of vasoactive intestinal peptide (VIP). Gastroenterology 114:1172A

Pincus DW, DiCicco-Bloom EM, Black IB (1990) Vasoactive intestinal polypeptide regulates mitosis, differentiation and survival of cultured sympathetic neuroblasts. Nature 343:564-567

Plewe G, Beyer J, Krause U, Neufeld M, del Pozo E (1984) Long-acting and selective supression of growth hormon secretion by somatostatin analogue SMS 201–995 in acromegaly. Lancet 6:782-784

Poinot-Chazel C, Portier M, Bouaboula M, Vita N, Pecceu F, Gully D, Monroe JG, Maffrand JP, Le Fur G, Casellas P (1996) Activation of mitogen-activated protein kinase couples neurotensin receptor stimulation to induction of the primary response gene Krox-24. Biochem J 320:145-151

Postema PTE, de Herder WW, Reubi JC, Oei HY, Kwekkeboom DJ, Bruining HJ, van Toor H, Hennemann G, Krenning EP (1996) Somatostatin receptor scintigraphy in non-medullary thyroid cancer. Digestion 57:36-37

Raderer M, Becherer A, Kurtaran A, Angelberger P, Li S, Leimer M, Weinländer G, Kornel G, Kletter K, Scheithauer W, Virgolini I (1996) Comparison of iodine-123-vasoactive intestinal peptide receptor scintigraphy and indium-111-CYT-103 immunoscintigraphy. J Nucl Med 37:1480-1487

Raderer M, Pangerl T, Leimer T, Valencak J, Kurtaran A, Hamilton G, Scheithauer W, Virgolini I (1998a) Expression of human somatostatin receptor subtyp 3 in pancreatic cancer in vitro and in vivo. J Natl Cancer Inst 90:1666-1668

Raderer M, Kurtaran A, Yang Q, Susan Meghdadi, Vorbeck Friedrich, Heijn Michael, Angelberger P, Kornek G, Pidlich J, Scheithauer W, Virgolini I (1998b) Iodine-123-vasoactive intestinal peptide receptor scanning in patients with pancreatic cancer. J Nucl Med 39:1570-1575

Raderer M, Kurtaran A, Hejn M, Vorbeck T, Angelberger P, Scheithauer W, Virgolini I (1998c) ^{123}I-labelled vasoactive intestinal peptide receptor scintigraphy in patients with colorectal cancer. Br J Cancer 78:1-5

Raderer M, Valencak J, Pfeffler F, Drach J, Pangerl T, Kurtaran A, hejna M, Vorbeck F, Chott A, Virgolini I (1999) Somatostatin receptor expression in primary gastric versus non-gastric extranodal B-cell lymphoma of mucosa-associated lymphoid tissue type. J Natl Cancer Inst 21:716-718

Raderer M, Traub T, Formanek M, Virgolini I, Österreicher C, Fiebiger W, Penz M, Jäger U, Pont J, Chott A, Kurtaran A (2001) Somatostatin-receptor scintigraphy for staging and follow-up of patients with extraintestinal marginal zone B-cell lymphoma of the mucosa associated lymphoid tissue (MALT)-type. Br J Cancer 85:1462-1466

Rainhardt MJ, Moser E (1996) An update on diagnostic methods in the investigation of disease of the thyroid. Eur J Nucl Med 23:587-594

Rehfeld JF, van Solinge WW (1994) The tumor biology of gastrin and cholecytokinin. Adv Cancer Res 63:295-347

Reichlin S (1983) Somatostatin. N Engl J Med 309:1556-1563

Rettenbacher M, Reubi J (2001) Localization and characterization of neuropeptide receptors in human colon. Nauyn Schmiedbergs Arch Pharmacol 364:291-301

Reubi JC (1995) In vitro identification of vasoactive peptide receptors in human tumors: implications for tumor imaging. J Nucl Med 36:1846-1853

Reubi JC, Waser B (2003) Concomittant expression of several peptide receptors in neuroendocrine tumours: molecular basis for in vivo multireceptor tumour targeting. Eur J Nucl Med Mol Imaging 30:781-793

Reubi JC, Maurer K, von Werder K, Torhorst J, Klijn GM, Lamberts SWJ (1989) Somatostatin receptors in human endocrine tumors. Cancer Res 47:551-558

Reubi JC, Waser B, Sheppard M, Macaulay Y (1990) Somatostatin receptors are present in small-cell but not in non-small primary lung carcinomas: relationship to EGF-receptors. Int J Cancer 45:269-274

Reubi JC, Schaer JC, Waser B, Mengold G (1994) Expression and localization of somatostatin receptor SSTR1, SSTR2 and SSTR3 mRNAs in primary human tumors using in situ hybridization. Cancer Res 54:3455-3459

Reubi JC, Schaer JC, Waser B (1997) Cholecytochinin (CCK)-A and CCK-B/Gastrin receptors in human tumors. Cancer Res 60:3150-3112

Reubi JC, Waser B, Friess H, Buchler M, Laissue J (1998) Neurotensin receptors: a new marker for human ductal pancreatic adenocarcinoma. Gut 42:546-550

Reubi JC, Walser B, Schaer JC, Laissue JA (1999) Neurotensin receptors in human neoplasms: high incidence in Erwing´s sarcomas. Int J Cancer 82:213-218

Reubi JC, Schar JC, Waser B, Wenger B, Heppeler A, Schmitt JS, Macke HR (2000a) Affinity profiles for human somatostatin receptor subtypes SST1-5 of somatostatin radiotracers selected for scintigraphic and radiotherapeutic use. Eur J Nucl Med 27:273-282

Reubi JC, Läderach U, Waser B, Gebbers J-O, Robberecht P, Laissue JA (2000b) Vasoactive intestinal peptide/pituitary adenylate cayclase activating peptide receptor subtypes in human tumors and their tissues of origin. Cancer Res 60:3105-3112

Robberecht P, de Neef P, Gourlet P, Cauvin A, Coy DH, Christophe J (1989) Pharmacological characterization of the novel helodermin/VIP receptor present in human SUP-T1 lymphoma cell membranes. Regul Pept 26:117-126

Robberecht P, Vertongen P, Velkeniers B, de Neef P, Vergani P, Raftopoulos C, Brotchi J, Hooghe-Peters EL, Christophe J (1993) Receptors of pituitary adenylate cyclase activating peptides in human pituitary adenomas. J Clin Endocrinol Metab 77:1235-1239

Robberecht P, Woussen-Colle MC, Vertongen P, de Neef P, Hou X, Salmon I, Brotchi J (1994) Expression of pituitary ade-

nylate cyclase activating polypeptide (PACAP) receptors in human glial cell tumors. Peptides 15:661-665

Rogers BE, Bigott HM, McCarthy DW, Della Manna D, Kim J, Sharp TL, Welch MJ (2003) MicroPET imaging of a gastrin-releasing peptide receptor-positive tumor in a mouse model of human prostate cancer using a 64Cu labeled analogue. Bioconjug Chem 14:756-763

Rohrer L, Raulf F, Bruns C, Buetter R, Hofstaedter F, Schüle R (1993) Cloning and characterization of a fourth human somatostatin receptor. Proc Natl Acad Sci USA 90:4196-4200

Rosenberg L, Brown RA (1991) Sandostatin in the management of nonendocrine gastrointestinal and pancreatic disorders: a preliminary study. Cancer J Surg 34:223-229

Said SI, Foloona GR (1975) Elevated plasma and tissue levels of vasoactive intestinal peptide in the watery diarrhea syndrome. N Engl J Med 293:155-158

Said SI, Mutt V (1970) Polypeptide with broad biological activity. Isolation from small intestine. Science 169:1217-1218

Saurin JC, Rouault JP, Abello J, Berger F, Remy L, Chayvialle JA (1999) High gastrin releasing peptide receptor mRNA level is related to tumour differentiation and lymphatic vessel invasion inhuman colon cancer. Eur J Cancer 35:125-132

Scheithauer W, Rosen H, Kornek GV, Sebesta C, Depisch D (1993) Randomised comparison of combination chemotherapy plus supportive care with supportive care alone in patients with metastatic colorectal cancer. Br Med J 306:752-755

Schaer JC, Waser B, Mengold G, Reubi JC (1997) Somatostatin receptor subtypes sst1, sst2, sst5 expression in human pituitary, gastroentero-pancreatic and mammary tumors: comparison of mRNA analysis with receptor autoradiography. Int J Cancer 70:530-537

Schillaci O, Spanu A, Scopinaro F, Falchi A, Corleto V, Danieli R, Marongiu P, Pisu N, Madeddu G, Delle Fave G, Madeddu G (2003a) Somatostatin receptor scintigraphy with 111In-pentreotide in non-functioning gastroenteropancreatic neuroendocrine tumors. Int J Oncol 23:1687-1695

Schillaci O, Spanu A, Scopinaro F, Falchi A, Danieli R, Marongiu P, Pisu N, Madeddu G, Delle Fave G, Maddedu G (2003b) Somatostatin receptor scintigraphy in liver metastases detection from gastroenteropancreatic neuroendocrine tumors. J Nucl Med 44:359-368

Schlag P, Lehner B, Strauss LG, Georgi P, Herfarth C(1989) Scar or recurrent rectal cancer. Positron emission tomography is more helpful for diagnosis than immunoscintigraphy. Arch Surg 124:197-200

Schmidt M, Fischer E, Dietlein M, Nichel O, Weber K, Moka D, Stennert E, Schicha H (2002) Clinical value of somatostatin receptor imaging in patients with suspected head and neck paragangliomas. Eur J Mucl Med Mol Imaging 29:1571-1580

Schulz S, Helmholz T, Schmitt J, Franke K, Otto HJ, Weise W (2002) True positive somatostatin receptor scintigraphy in primary brest cancer correlates with expression of sst2A and sst5. Breast Cancer Res Treat 72:221-226

Scopinaro F, Varvarigou AD, Ussof W, de Vincentis G, Sourlingas TG, Evangelatos GP, Datsteris J, Archimandritis SC (2002) Technitium labeled bombesin-like peptide: preliminary report on breast cancer uptake in patients. Cancer Biother Radiopharm 17:327-335

Scopinaro F, De Vincentis G, Varvarigou AD, Laurenti C, Iori F, Remediani S, Chiarini S, Stella S (2003a) 99mTc-bombesin detects prostate cancer and invasion of pelvic lymph nodes. Eur J Nucl Med Mol Imaging 30:1378-1382

Scopinaro F, de Vincentis G, Corazziai E, Osti MF, Covotta A, Pallotta S, Remedianin S, Prosperi D, Monteleone F, Varvarigou A (2003b) Detection of colon cancer and invaded nodes with 99mTc-Bombesin. Preliminary data. Eur J Nucl Med Mol Imaging 30:P16

Seethalakshmi L, Mitra SP, Dobner PR, Menon M, Carraway RE (1997) Neurotensin receptor expression in prostatic cancer cell line and growth effect of NT at physiological concentrations. Prostate 31:183-192

Seidman H, Mushnick MH, Gelb SK, Silverberg E (1985) Probability of eventually developing or dying of cancer: United States. CA Cancer J Clin 35:36-56

Shirzad M, Leimer M, Lister-James J, Moyer BR, Angelberger P, Virgolini I (1998) Preclinical characterization of a 99m-technetium labeled vasoactive intestinal peptide (VIP) receptor imaging peptide. Eur J Nucl Med 25:977A

Siegelman S, Khouri N, Leo F, Fishman EK, Braverman RM, Zerhouni EA (1986) Solitary pulmonary nodules: CT assessment. Radiology 160:307-312

Smith-Jones P, Bischof C, Leimer M, Gludovac D, Angelberger P, Pangerl T, Peck-Radosavljevic M, Hamilton G, Kaserer K, Steiner G, Schlagbauer-Wadl H, Mäcke H, Virgolini I (1998) "MAURITIUS" a novel somatostatin analog for tumor diagnosis and therapy. J Nucl Med 39:223A

Smith-Jones P, Bischof C, Leimer M, Gludovacz D, Angelberger P, Pangerl T, Peck-Radosavljevic M, Steiner G, Virgolini I (1999) "MAURITIUS": a novel tumor diagnostic and therapeutic somatostatin analog. Endocrinology 140:5136-5148

Spindel ER, Giladi E, Brehm P, Goodman RH, Sgerson TP (1990) Cloning and functional characterization of a complementary DANN encoding the murine fibroblast bombesin/gastrin-releasing peptide receptor. Mol Endocrinol 4:1956-1963

Sreedharan SP, Kodama KT, Peterson KE, Goetzl EJ (1989) Distinct subjects of somatostatin receptors on cultured human lymphocytes. J Biol Chem 264:949-952

Sreedharan SP, Robichon A, Peterson KE, Goetzl EJ (1991) Cloning and expression of the human vasoactive intestinal peptide receptor. Proc Natl Acad Sci USA 88:4986-4990

Stiefel F, Morant R (1993) Vapreotide, a new somatostatin analogue in the palliative management of obstructive ileus in advanced cancer. Supp Care Cancer 1:57-58

Stokkel MP, Reigman HI, Verkooijen RB, Smith JW (2003) Indium-111-Octreotide scintigraphy in differentiated thyroid carcinoma metastases that do not respond to treatment with high-dose I-131. J Cancer Res Clin Oncol 129:287-294

Sun B, Halmos G, Schally AV, Wang X, Martinez M (2000) Pesence of receptors for bombesin/gastrin-releasing peptide and mRNA for three receptor subtypes in human prostate cancer. Prostate 42:295-303

Svoboda M, Tastenoy M, van Rampelsbergh J, de Neef P, Waelbroeck M, Robberecht O (1994) Molecular cloning and functional characterization of a human VIP receptor from sup-T1 lymphoblasts. Biochem Biophys Res Commun 205:1617-1624

Taucher S, Kurtaran A, Leimer M, Angelberger P, Pangerl T, Beck M, Gnant M, Jakesz R, Virgolini I (1996) Validation of VIP and somatostatin receptor scanning in primary breast cancer. Eur J Nucl Med 23:1094A

Tenenbaum F, Lumbroso J, Schlumberger M, Caillou B, Fragu P, Parmentier C (1995) Radiolabeled somatostatin analog scintigraphy in differentiated thyroid carcinoma. J Nucl Med 36:807-810

Thakur ML, Kolan H, Li J, Wiaderkiewicz, Pallela VR, Duggaraju R, Schally AV (1997) Radiolabeled somatostatin analogs in prostate cancer. Nucl Med Biol 24:105-113

Thakur ML, Marcus CS, Saeed S, Pallela V, Minami C, Diggles L, Le Pham H, Ahdoot R, Kalinowski EA (2000) ^{99m}TC-labeled vasoactive intestinal peptide analog for rapid localization of tumors in humans. J Nucl Med 41:107-110

Thomas F, Brambrilla E, Friedmann A (1994) Transcription of somatostatin receptor subtype 1 and 2 genes in lung cancer. Lung Cancer 11:111-114

Traub T, Petkov V, Ofluoglu S, Pangerl P, Raderer M, Fueger B, Schima W, Kurtaran A, Dudczak R, Vrgolini I (2001) 111In-DOTA-lanreotide scintigraphy in patients with tumors of the lung. J Nucl Med 42:1309-1315

Ullrich CD, Holtmann Martin, Miller LJ (1998) Secretin and vasoactive intestinal peptide receptors: members of a unique family of G protein-coupled receptors. Gastroenterology 114:382-397

Usdin TB, Bonner TI, Mezey E (1994) Two receptors for vasoactive intestinal polypeptide with similar specificity and complementary distributions. Endocrinology 135:2662-2680

Vallabhajosula S, Moyer BR, Lister-James J, McBride BJ, Lipszyc H, Lee H, Bastidas D, Dean RT (1996) Preclinical evaluation of technetium-99m-labeled somatostatin receptor-binding peptides. J Nucl Med 37:1016-1022

Van der Wiele C, Dumont F, Vanden Broecke R, Oosterlinck W, Cocquyt V, Serreyn R, Peers S, Thornback J, Slegers G, Dierckx RA (2000) Technetium-99m RP527, a GRP analogue for visualisation of GRP receptor expressing malignancies: a feasibility study. Eur J Nucl Med 27:1694-1699

Van de Wiele C, Dumont F, Dierckx RA et al (2001) Biodistribution and dosimetry of ^{99m}Tc-RP527, a gastrin-releasing peptide (GRP) agonist for the visualization of GRP receptor-expressing malignancies. J Nucl Med 42:1722-1727

Van Dyke JA, Stanley RJ, Berland LL (1985) Pancreatic imaging. Ann Intern Med 102:212-217

Van Eijck CHJ, Krenning EP, Bootsma A, Oei HY, van Pel R, Lindemans J, Jeekel J, Reubi JC, Lamberts SWJ (1994) Somatostatin-receptor scintigraphy in primary breast cancer. Lancet 343:640-643

Vaudry D, Gonzalez BJ, Basille M, Yon L, Fournier A, Vaudry H (1997) Pituitary adenylate cyclase-activating peptide and ist receptors: from structure to function. Pharmacol Rev 50:265-324

Verner JV, Morrison AB (1958) Islet cell tumor and a syndrome of refractory watery diarrhea and hypokalemia. Am J Med 25:374-380

Vertongen P, Devalck C, Sariban E, De Laet MH, Martelli H, Paraf F, Helardot P, Robberecht P (1996) Pituitary adenylate cyclase activating peptide and ist receptors are expressed in human neuroblastomas. J Cell Physiol 167:36-46

Vikic-Topic S, Raisch KP, Kvols L, Vuk-Pavlovic S (1995) Expression of somatostatin receptor subtypes in breast carcinoma, carcinoid tumors, and renal cell carcinoma. J Clin Endocrinol Metab 80:2974-2979

Vincent JP, Mazella J, Kitabgi P (1999) Neurotensin and neurotensin receptors. Trends Pharmacol Sci 20:302-309

Vinik AI, McLeod MK, Fig LM, Shapiro B, Lloyd RV, Cho K (1989) Clinical features, diagnosis, and localization of carcinoid tumors and their management. Gastroenterol Clin North Am 18:865-896

Virgolini I (1997) Mack Forster Award Lecture: receptor nuclear medicine: somatostatin receptor scintigraphy for diagnosis and treatment of tumor patients. Eur J Clin Invest 27:793-800

Virgolini I, Yang Q, Li S, Angelberger P, Neuhold N, Niederle B, Scheithauer W, Valent P (1994a) Cross-competition between vasoactive intestinal peptide and somatostatin for binding to tumor cell membrane receptors. Cancer Res 54:690-700

Virgolini I, Raderer M, Kurtaran A, Angelberger P, Banyai S, Yang Q, Li S, Banyai M, Pidlich J, Niederle B, Scheithauer W, Valent P (1994b) Vasoactive intestinal peptide (VIP) receptor imaging for the localisation of intestinal adenocarcinomas and endocrine tumors. N Engl J Med 331:1116-1121

Virgolini I, Kurtaran A, Raderer M, Leimer M, Angelberger P, Havlik E, Li S, Scheithauer W, Niederle B, Valent P, Eichler HG (1995) Vasoactive intestinal peptide receptor scintigraphy. J Nucl Med 36:1732-1739

Virgolini I, Angelberger P, Li S, Yang Q, Kurtaran A, Raderer M, Neuhold N, Kaserer K, Leimer M, Peck-Radosavljevic M, Scheithauer W, Niederle B, Eichler HG, Valent P (1996a) In vitro and in vivo studies of three radiolabelled somatostatin analoges: ^{123}I-octreotide (OCT), ^{123}I-Tyr-3-OCT and ^{111}In-DTPA-D-Phe-1-OCT. Eur J Nucl Med 23:1388-1399

Virgolini I, Pangerl T, Bischof C, Leimer M, Yang Q, Peck-Radosavljevic M, Kaserer K, Niederle B, Angelberger P, Gangl A, Valent P (1996b) Somatostatin (SST) and vasoactive intestinal peptide (VIP) receptor (R) subtype gene expression. Eur J Nucl Med 23:1101A

Virgolini I, Raderer M, Kurtaran A, Angelberger P, Yang Q, Radosavljevic M, Leimer M, Kaserer K, Li S, Kornek G, Hübsch P, Niederle B, Pidlich J, Scheithauer W, Valent P (1996c) ^{123}I-Vasoactive intestinal peptide (VIP) receptor scanning: update of imaging results in patients with adenocarcinomas and endocrine tumors of the gastrointestinal tract. Nucl Med Biol 23:685-692

Virgolini I, Pangerl T, Bischof C, Smith-Jones P, Peck-Radosavljevic M (1997) Somatostatin receptor subtype expression in human tissues: a prediction for diagnosis and treatment of cancer? Eur J Clin Invest 27:645-647

Virgolini I, Leimer M, Hirschmaker H, Lastoria S, Bischof C, Muto P, Pangerl T, Gludovacz D, Peck-Radosavljevic M, Lister-James J, Hamilton G, Kaserer K, Valent P, Dean R (1998a) Somatostatin receptor subtype specificity and in vivo binding of a novel tumor tracer, ^{99m}Tc-P829. Cancer Res 58:1850-1859

Virgolini I, Kurtaran A, Leimer M, Kaserer K, Peck-Radosavljevic M, Angelberger P. Hübsch P, Dvorak M, Valent P, Niederle B (1998b) Location of a VIPoma by iodine-123-vasoactive intestinal peptide scintigraphy. J Nucl Med 39:1575-1579

Virgolini I, Szilvasi I, Angelberger P, Raderer M, Havlik E, Vorbeck F, Bischof C, Leimer M, Dorner G, Kletter K, Niederle B, Scheithauer W, Smith-Jones P (1998c) Indium-111-DOTA-lanreotide: biodistribution, safety and tumor dose in patients. J Nucl Med 39:1928-1936

Virgolini I, Smith-Jones P, Moncayo R, Kurtaran A, Wenger M, Raderer M, Havlik E, Angelberger P, Szilvaszi I, Zoboli S, Paganelli G, Riccabona G (1998d) 111-In/90-Y-DOTA-lan-

reotide scintigraphy and therapy: initial clinical results of "Mauritius". Eur J Nucl Med 25:884A

Virgolini I, Traub T, Ofluoglu S, Kurtaran A, Raderer M, Peck M, Leimer M, Angelberger P, Li S, Novotny C, Havlik E, Dudczak R, Lister-James J (1999) 99mTc-P1666 vasoactive intestinal peptide (VIP) receptor scintigraphy: clinical efficacy, biodistribution and safety. Eur J Nucl Med 26:1154

Virgolini I, Patri p, Novotny C, Traub T, Leimer M, Fuger B, Li SR, Angelberger P, Raderer M, Wogritsch S, Kurtaran A, Kletter K, Dudczak R (2001)Comparative somatostatin receptor scintigraphy using In-111-DOTA-lanreotide and In-111-DOTA-Tyr3-octreotide versus F-18-FDG-PET for evaluation of somatostatin receptor-mediated radionuclide therapy. Ann Oncol 12 [Suppl 2]:41-45

Virgolini I, Britton K, Buscombe J, Moncayo R, Paganelli G, Riva P (2002) 111In- and 90Y-DOTA-Lanreotide: Results and implications of the MAURITIUS trail. Semin Nucl Med 32:148-155

Vural G, Unlu M, Atasever T, Özur I, Özdemir A, Gökcora N (1997) Comparison of indium-111 octreotide and thallium-201 scintigraphy in patients mammographically suspected of having breast cancer: preliminary results. Eur J Nucl Med 24:312-315

Wada E, Way J, Shapira H, Kusano K, Lebacq-Verheyden AM, Coy D, Jensen R, Battey J (1991) cDNA cloning, characterization and brain region-specific expression og a neuromedin-B preferring bombesin receptor. Neuron 6:421-430

Walsh JH (1994a) Gastrointestinal hormones. In: Johnson LR (ed) Physiology of the gastrointestinal tract, 3rd edn. Raven Press, New York, pp 1-28

Walch JH (1994b) Gastrin. GUT peptides: biochemistry and physiology. In: Walch JH, Dockray GJ (eds) Physiology of the gastrointestinal tract, 3rd edn. Raven Press, New York, pp 75-121

Wang QJ, Knezetic JA, Schally AV, Pour PM, Adrian TE (1996) Bombesin stimulate proliferation of human pancreatic cancer cells through an autocrine pathway. Int J Cancer 68:528-534

Wang KP, Kelly SJ, Britt JE (1988) Percutaneous needle aspiration biopsy of chest lesions. New instrument and new technique. Chest 9:993-997

Wang L, Friess H, Zhu Z, Graber H, Zimmermann A, Korc M, Reubi JC, Buchler MW (2000) Neurotensin receptor-1 mRNA analysis in normal pancreas and pancreatic disease. Clin Cancer Res 6:566-571

Wank SA, Pisegna JR, de Weerth A (1992) Brain and gastrointestinal cholecytochinin receptor family: structure and functional expression. Proc Natl Acad Sci USA 89:8691-8695

Warshaw AL, Fernandez-del Castillo C (1992) Pancreatic carcinoma. N Engl J Med 326:455-465

Wester HJ, Schottelius M, Scheidhauer K, Meisetschlager G, Herz M, Rau FC, Reubi JC, Schweiger M (2003) PET imaging of somatostatin receptors: design, synthesis and preclinical evaluation of a novel 18F-labelled, carbohydrated analogue octreotide. Eur J Nucl Med Mol Imaging 30:117-122

World Health Organization (1981) Histologic typing of lung cancer, 2nd edn. WHO, Geneva

Wraight EP, Bard DR, Maughan TS, Knight CG, Page-Thomas DP (1992) The use of a chelating derivate of a á melanocyte stimulating hormone for the clinical imaging of malignant melanoma. Br J Radiol 65:112-118

Yamada Y, Post SR, Wang K, Tager HS, Bell GI, Seino S (1992a) Cloning and functional characterization of a family of human and mouse somatostatin receptors expressed in brain, gastrointestinal tract and kidney. Proc Natl Acad Sci USA 89:251–255

Yamada Y, Reisine S, Law SF, Ihara Y, Kubota A, Kagimoto S, Seino M, Seino Y, Bell I, Seino S (1992b) Somatostatin receptors, an expanding gene family: cloning and functional characterization of human SSTR3, a protein coupled to adenylyl cyclase. Mol Endocrinol 6:2136-2142

Yamada Y, Kagimoto S, Kubota A, Yasuda K, Masuda K, Someya Y, Ihara Y, Li Q, Imura H, Seino S, Seino Y (1993) Cloning, functional expression and pharmacological characterization of a fourth (hSSTR4) and fifth (hSSTR5) human somatostatin receptor subtypes. Biochem Biophys Res Commun 195:844-852

Yamada M, Yamada M, Lombet A, Forgez P, Rostène W (1998) Distinct function characteristics of levobastine sensitive rat neurotensin NT2 receptor expressed in Chinese hamster ovary cells. Life Sci 62:375-380

Yasuda K, Res-Domiano S, Breder CA, Law SF, Saper C, Reisine T, Bell GI (1992) Cloning of a novel somatostatin receptor, SST3, coupled to adenylate cyclase. J Biol Chem 267:20422-20428

Zia H, Hida T, Jakowlew S, Birrer M, Gozes Y, Reubi JC, Fridkin M, Gozes I, Moody TW (1996) Breast cancer growth is inhibited by vasoactive intestinal peptide (VIP) hybrid, a synthetic VIP receptor antagonist. Cancer Res 56:3486-3489

11 FDG-PET Imaging in Oncology

Christiaan Schiepers and Carl K. Hoh

CONTENTS

11.1 Introduction

The advances in medical imaging technology pose a challenge to both the imaging specialist and the clinician. In the field of oncology, the goals of diagnostic imaging are to: (i) help establish the patient's diagnosis, (ii) streamline patient management, and (iii) monitor patients on established and experimental treatment protocols. Improved patient outcome may be expected, if these goals are achieved. Various modalities are available for this purpose, anatomical imaging such as radiography, computed tomography (CT), magnetic resonance (MR) imaging, ultrasonography (US), and molecular imaging such as positron emission tomography (PET), single photon imaging (planar and SPECT), and MR spectroscopy.

PET is based on the imaging of biochemical processes in vivo, and creates images similar to other tomographic imaging modalities such as CT and MR. PET is unique because it generates tomographic images reflecting the biochemical or metabolic activity of the underlying tissue processes. Although PET imaging has been in existence since the 1960s, it did not gain clinical acceptance until the 1990s.

The basics of positron emission are beyond the scope of this book. Phelps et al. (1986) is a standard text for the interested reader. Radiopharmaceuticals, instrumentation and image formation will be dealt with in the basic science section of this book (Chaps. 15–17). Here we will focus on the clinical applications of PET and the comparison with conventional radiological techniques, i.e., CT, MR and US. The advancements of dual modality imaging (PET/CT) will be discussed in Chaps. 12 and 13. The place of PET in stratifying patients and in the work-up of clinical problems is the topic of this chapter. PET as a complementary imaging modality rather than a single competitive modality is an important concept in building the synergistic diagnostic strengths of various imaging modalities in the clinical management of patients.

A few published reports have addressed the issue of the cost of PET imaging in patient care. Generally, algorithms that include a whole body PET appear cost effective when compared to a more conventional approach with multiple CT or MR scans of specific body areas. The main advantage of PET in oncology is that with one injection the whole body can be imaged in a tomographic mode. Multiple CT scans covering the head, chest, abdomen, and pelvis are usually more expensive than a single whole body PET scan. For the interested reader we refer to articles of Valk et al. (1996), and Gambhir et al. (1996) for the USA and the PLUS study for the EU (Verboom et al. 2003).

C. Schiepers, MD, PhD
Department of Molecular and Medical Pharmacology, David Geffen School of Medicine at UCLA, 10833 Le Conte Avenue, AR-144 CHS, Los Angeles, CA 90095-6942, USA
C. K. Hoh, MD
Department of Radiology, UCSD Medical Center, 200 W Arbor Drive, San Diego, CA 92103, USA

11.2 Methods

In order to perform PET imaging there are three essential technological components:

- Administration of a tracer with a positron emitting nuclide (see Chap. 15)
- Dedicated camera for detection of the tracer distribution (see Chap. 16)
- Computers and displays with all the necessary hardware and software (see Chap. 17)

11.2.1 Tracers and Uptake Mechanism

A wide variety of positron emitting tracers is available, permitting imaging and quantification of physiologic parameters such as perfusion, metabolism or receptor density of normal and abnormal tissues. The potential variety of radiopharmaceuticals, which may be developed for PET imaging, is unlimited. New tracers will evolve and empower nuclear medicine with a unique adaptive feature in the future of molecular imaging.

The most commonly used PET radiopharmaceutical in oncological applications is the glucose analogue 2-^{18}F-fluoro-2-deoxy-D-glucose (FDG). The ability to non-invasively image glucose utilization is important, since high rates of glycolysis are found in many malignant tumor cells (Warburg 1931, 1956). Malignant cells have increased membrane glucose transporters and upregulated hexokinase enzymes (Wahl 1997a). This chapter concentrates on the role of FDG as PET radiopharmaceutical in oncology (Conti et al. 1996; Rigo et al. 1996; Brock et al. 1997). The uptake of FDG varies greatly for different tumor types; however, high uptake is usually associated with a high number of viable tumor cells and high expression of GLUT-1 (glucose transporter 1). Lung cancer has among the highest expressions of GLUT-1, and therefore is readily detectable, whereas renal cell cancers show the opposite trend (Wahl 1997ab; Brown and Wahl 1993; Miyauchi et al. 1996).

Increased FDG uptake is by no means specific for neoplasms. Inflammatory processes also have increased uptake, and false positive results in the diagnostic setting have been reported for: tuberculosis, fungal infections, sarcoidosis, non-specific granulomas, suture granulomas, benign fibrous mesotheliomas, acute post-operative and radiation changes, abscesses, pancreatitis and fractures. Kubota et al. (1991, 1992) have studied the uptake of FDG in macrophages and granulation tissues and have discussed the accumulation of FDG in tumors (Kubota et al. 1993). Higashi et al. (1993a,b) have studied the relation of FDG uptake to proliferation rate and viable cell number after radiation treatment.

11.2.2 Acquisition

Dedicated PET scanners are true volumetric imaging devices with detectors surrounding the full 360° around a patient (see Chap. 16). Multiple image planes are acquired simultaneously in a 10- to 25-cm axial span. PET image acquisitions can be performed in three modes: (i) dynamic, (ii) static, and (iii) whole body. In the dynamic mode, the image acquisition is initiated at the same time the dose is injected into the patient. The blood pool and tissue accumulation of the radiopharmaceutical are recorded in a rapid sequence of image frames. The dynamic image can also be processed on a voxel basis over time to generate parametric images of the net FDG uptake rate. In the static acquisition mode, images are typically acquired after an uptake period (60–90 min after injection), to allow tracer clearance from the blood pool and sufficient tracer uptake in the target tissues. The final volumetric images are first reconstructed into multiple axial image planes, which can then be resliced and reformatted in coronal and sagittal planes for display on the monitor.

The whole body imaging mode was introduced in the late 1980s by UCLA, and subsequently became the standard for PET imaging in oncology (Dahlbom et al. 1992; Hoh et al. 1993, 1997a). In this mode of scanning, acquisitions are performed sequentially along the length of the patient's body, thereby extending the axial field of view to that of the entire body. The intuitive advantage of the whole body technique is that many cancers are systemic diseases requiring imaging of the entire body. In addition to axial, coronal and sagittal planes, planar projections are created, in which the total activity distribution is viewed from different angles around the patient. To generate the rotating whole body cine, either raw sinogram data or maximum intensity projections (MIP) from the reconstructed axial images can be used. Although these non-tomographic images have a lower lesion to background contrast, there is no image reconstruction artifact when using the raw

sinogram data, which may obscure tumor foci near bright objects such as the bladder.

Varying amounts of tissue attenuation in the body will determine the final number of photons that reach the PET detectors during emission scan with FDG. This tissue attenuation effect can be corrected for by the acquisition of a separate transmission scan. This can be done with positron emitting sources (Ge-68), high-energy single photon emitters (Cs-137), or CT (see Chaps. 12, 13, 16). Without attenuation correction, only visual interpretation is possible and quantitative analysis cannot be performed. Correction for attenuation is not necessary for image interpretation. No difference in lesion detection was found between corrected and non-attenuation corrected images for a variety of tumors (Bengel et al. 1997). However, attenuation and scatter corrected images are a more realistic representation of the concentration of radiopharmaceutical in the tissues, and are preferred for image interpretation.

The spatial resolution of a PET system is not the only factor for detecting abnormalities. The difference in metabolic activity of the lesion and its surroundings (target-to-background ratio) or the "contrast resolution" is also important. Metabolically active lesions of 5 mm have been detected with FDG-PET.

11.2.3 Quantification

Dynamic imaging with PET provides the ability to measure the concentration of a radiotracer as a function of time. When the pathway of the tracer molecule is known, mathematical models can be used to describe the in-vivo processes and absolute quantitative values such as blood flow (in ml/min) and glucose utilization (in mg/min/g) can be calculated from the acquired data. For a discussion of dynamic imaging and kinetic modeling, the reader is referred to the literature (Phelps et al. 1986, 2004).

Many clinical studies are analyzed semi-quantitatively by using the standardized uptake value (SUV) (Zasadny and Wahl 1993; Hamberg et al. 1994; Kim et al. 1994; Keys 1995), also known as the differential uptake ratio (DUR) or differential absorption ratio (DAR). The SUV is the ratio of the measured radioactivity concentration in a lesion to the calculated radioactivity concentration distributed in the entire body. The concentration of radioactivity is assumed to be a uniform distribution throughout the body. Another assumption is that tumors achieve their peak concentration around 1–2 h after FDG administration. In addition to proper calibration of the PET scanner, accurate pre- and post-injection FDG syringe activity and accurate FDG uptake periods need to be followed before SUV data between institutions can be compared. The SUV offers a more objective index in reporting the magnitude of metabolic activity than visual interpretation alone. The SUV technique appears satisfactory for clinical purposes such as staging and therapy monitoring. For other applications, the distinction between benign and malignant lesions is less clear and absolute quantification or a different radiotracer may be required (Wahl 1997a; Hoh et al. 1997a; Brock et al. 1997).

11.2.4 Patient Preparation and Diagnostic Protocol

The ideal metabolic state in a patient undergoing an FDG-PET scan is low insulin level and therefore low glucose utilization in the normal tissues. Malignant tissues are less dependent on insulin regulation, and thus will have higher uptake when compared to the surrounding normal tissues. This dietary state can be induced by prolonged fasting.

The scanning duration of a PET oncology protocol is dependent on the type of equipment and may vary from 15–75 min. About 7.7 MBq/kg (0.21 mCi/kg) FDG is the dose administered intravenously. After an uptake period of 45–75 min, the patient is asked to void and positioned in the scanner. Scanning from feet to head has the advantage of lower initial bladder activity after voiding.

Since FDG is filtered but not reabsorbed by the glomerulus, high FDG activity may be present in the urinary tract. Bowel uptake is variable, as is bone marrow metabolism in patients after chemotherapy. No consensus currently exists regarding possible interventions in oncological PET imaging protocols.

11.3 Objective

In a review of Brock et al. (1997), PET applications were discussed from the oncologist perspective, which focused on grading and staging of tumors and determining extent of disease involvement. It

appears that magnitude of FDG uptake in a tumor does not correlate very well with tumor grade. However, FDG in PET imaging appears very effective in staging newly diagnosed disease or detecting relapse or recurrence of disease. If PET finds unexpected lesions, anatomical imaging is indicated to delineate the structural involvement.

Husband (1995, 1996) has argued that imaging of treated tumors is becoming more important because of the increasing incidence of cancer and scientific progress in imaging and therapy. He distinguished two strategies, imaging for: (1) clinical service, and (2) research. He observed two referral patterns: (i) for patients with curable disease and treated according to an established protocol and (ii) imaging employed for individual patient management. The number of patients studied in protocols in which PET has a key function in triage or monitoring is increasing. In our opinion, PET has matured and reached the level of an essential imaging modality in clinical diagnostic algorithms. Input from the surgical, medical and radiation oncologist, as well as the imaging specialist in a multi-disciplinary setting, will provide the greatest benefit in the management of cancer patients.

As has been pointed out by Valk (1996), the reference standard in comparing modalities is imperfect, because full validation of findings with biopsy and histology is not feasible. Thus, there are no truly double blinded studies available comparing the performance of whole-body PET to conventional imaging in the majority of cancers. In the typical clinical context, on the other hand, it is not meaningful to evaluate the assumed 'separate' contribution of each imaging modality. The development of dual modality imaging (PET/CT, see Chap. 12 and 13) underscores the synergy attained by combining anatomic and functional imaging.

The purpose of imaging is to help establish the diagnosis, which will prompt the oncologist to wait and watch, or to start treatment. In this chapter, we will present an overview for three diagnostic imaging criteria: (i) diagnosis or detection of neoplasms, (ii) staging and re-staging of disease, and (iii) therapy monitoring. This diagnostic imaging scheme implicitly assumes a normal patient work-up with history, physical exam, routine labs and serum tumor markers, supplemented with standard radiographic imaging, mammography, CT, MR, US, or NM. A selection of oncological applications follows hereafter, in which FDG-PET has been shown to have merit. We have chosen the topographical presentation, common in radiology. In addition, we have pooled data for the four most common cancers, i.e., lung, colorectal, breast, and prostate (Tables 11.1–11.5).

11.4 Topographical Overview

11.4.1 Brain

FDG-PET has been most extensively studied for primary brain neoplasms. This is mainly due to pioneering work of Di Chiro and collaborators (1982, 1987a,b, 1988). The main applications are in: (i) grading of cerebral neoplasms, (ii) distinguishing tumor recurrence from radiation necrosis, (iii) assessing extent of disease for therapy management, and (iv) selecting the optimum site for biopsy. Other investigators have corroborated their results (Doyle et al. 1987; Alavi et al. 1988).

Table 11.1. Characterization of solitary pulmonary nodules

Author (year)	Country	Patient number	PET sensitivity (%)	PET specificity (%)	PET PPV (%)	PET NPV (%)
Scott et al. (1994)	USA	62	94	80	94	80
Dewan et al. (1995)	USA	76	100	78	93	100
Gupta et al. (1996)	USA	61	93	88	95	82
ICP[a] (1993)	USA	237	96	90		
Lowe et al. (1997)	USA	197	96	77	86	92
Lowe et al. (1998)	USA	89	92	90		
Gould et al. (2001)	Meta-analysis	403	94	86		

[a]The ICP data are a multi-center trial in the USA (unpublished data); most of the other data are incorporated in this series.
PPV, positive predictive value; NPV, negative predictive value.

Table 11.2. Staging of non-small cell lung cancer

Author (year)	Country	Patients	CT sensitivity (%)	CT specificity (%)	PET sensitivity (%)	PET specificity (%)
Chin et al. (1995)	USA	30	56	86	78	81
Valk et al. (1995)	USA	76	63	73	83	94
Sasaki et al. (1996)	Japan	29	65	87	76	98
Bury et al. (1996)	Belgium	50	72	81	90	86
Guhlmann et al. (1997)	Germany	46	50	75	80	100
Steinert et al. (1997)	Switzerland	47	57	94	89	99
Vansteenkiste et al. (1998)	Belgium	105	79	54	89	86
Pieterman et al. (2000)	Netherlands	102	75	66	88	91
Dwamena et al. (1999)	Meta-analysis	514	60[a]	77[a]	79	91

[a] *n*=2226, 29 CT studies.

Table 11.3. Breast cancer (all studies used biopsy or surgery to obtain the final diagnosis)

Author (year)	Country	Patients	PET sensitivity (%)	PET specificity (%)
Primary cancer detection				
Avril et al. (1996)[a]	Germany	51	92	97
Scheidhauer et al. (1996)	Germany	30	90	
Palmedo et al. (1997)	Germany	20	92	86
Axillary staging				
Utech et al. (1996)	USA	124	100	75
Adler et al. (1997)	USA	52	95	66
Crippa et al. (1998)	Italy	68	85	91
Smith et al. (1998)	USA	50	90	97
Greco	Italy	167	94	86
Schirrmeister	Germany	117	79	92
Multi-center trial				
Wahl et al. (2004)	USA	308	61	80

Table 11.4. Colorectal cancer

Author (year)	Country	Patients	CI sensitivity (%)	CI specificity (%)	PET sensitivity (%)	PET specificity (%)
Primary cancer						
Abdel-Nabi et al. (1998)	USA	48	37	83	100	43
Recurrent tumor						
Schiepers et al. (1995)	Belgium	74	71	88	94	97
Delbeke et al. (1997)	USA	52	81		91	
Ruhlmann et al. (1997)	Germany	59			100	67
Ogunbiyi et al. (1997)	USA	58	68		95	
Valk et al. (1999)	USA	115	71	85	68	90
Whiteford 2000)	USA	70	71	85	90	90
Huebner (2000)	Meta-analysis	281			97	76

CI, conventional imaging: CT/US/MR.

Table 11.5. Prostate cancer

Author (year)	Country	Patients	PET sensitivity (%)
Primary tumor			
Yeh et al. (1996)	USA	11	20
Effert et al. (1996)	Germany	48	19
Metastasis			
Shreve et al. (1996)	USA	34	65

In contrast to many other tumors, high-grade gliomas have high FDG uptake. Similarly, a high FDG uptake is associated with a poorer prognosis, although there is considerable overlap. An inherent difficulty concerns the high uptake of normal gray matter. PET is not sensitive in detecting low-grade gliomas because their uptake can be low relative to the normally high metabolism of the cortex. For this reason low grade tumors as well as metastatic tumors in the brain are frequently missed by PET. Use of a different tracer, e.g., methionine, tyrosine, dopamine or thallium, usually shows higher tumor to background uptake. F-DOPA appears useful even in low-grade gliomas (Chen et al., in press).

Because of tumor heterogeneity, PET may reveal areas with higher metabolic activity, which can be used to guide the optimum site for biopsy (Pirotte et al. 1995). The same principle can be applied in sequential studies, by detecting abnormal foci in a lesion that heralds the transformation of a low grade to high-grade glioma (Delbeke et al. 1995).

Edema is easily diagnosed on CT and MR, but the diagnostic challenge in distinguishing early recurrence of tumor is well known (Di Chiro 1988; Doyle et al. 1987). Even a metabolic imaging modality as MR spectroscopy may miss the diagnosis. Metabolic imaging with FDG can be helpful in differentiating recurrent tumor from radiation necrosis in lesions demonstrating contrast enhancement on MR. This is only applicable if the tumor was visible on FDG-PET prior to treatment.

PET with FDG may be useful in primary brain tumors, but the data on metastases is limited. A London group claimed in a study of 273 patients that routine screening for cerebral metastasis has a low yield (1.5%) and may not be clinically useful (Larcos et al. 1996). For the reasons mentioned above, lesions close to the cortex may be difficult to detect. MR imaging with contrast remains the imaging modality of choice for detecting brain metastases.

11.4.2 Head and Neck

The neck is notoriously difficult for imaging, due to the small size of anatomic structures and proximity of vessels, nodes and nerves. Various groups have shown a correlation between high metabolic activity and poor prognosis. The correlation between tumor grade and FDG uptake was not high (Lindholm et al. 1993). Haberkorn and coworkers (1991a,b) have shown that tumor perfusion did not correlate with proliferation rate. It should be stressed that the number of patients studied was small (Reisser et al. 1993).

FDG-PET has utility for accurate staging of head and neck cancers. Diagnostic accuracy was higher than anatomical methods for recurrent head and neck cancer (Rege et al. 1993a,b; Jabour et al. 1993; Laubenbacher et al. 1995a; Anzai et al. 1996; Benchao et al. 1996). Other reports show similar numbers for the sensitivity of primaries (>85%) and affected nodes (>80%) (Bailet et al. 1992; Wong et al. 1997). Although the accuracy of PET is higher than MR and/or CT, correct anatomical localization of the abnormal PET foci is necessary for treatment. The optimal diagnostic modality may be a fusion image showing the abnormal metabolic lesions superimposed on the anatomical locations (see Chap. 12). PET is able to stratify patients into those who will benefit from surgery and others who will not by accurate staging (Kau 1999; Stuckensen et al. 2000; Kresnik 2001). A large series on recurrent head and neck cancer was reported by Wong et al. (2002). They studied 143 patients with an overall sensitivity of 96% and specificity of 72%. The lower specificity was related to false positives at the site of the primary. Excluding these, the specificity elsewhere in the neck increased to 96% (Wong et al. 2002). This confirmed earlier reports that the specificity for nodal disease is over 90% (Bailet et al. 1992; Wong et al. 1997).

It is well known that well-differentiated thyroid tumors take up iodide, which is the foundation of radioactive iodine treatment. The more dedifferentiated tumors lose their ability to trap iodide and show increasing avidity for FDG. Thyroid tumors, which are iodine negative but FDG positive, tended to be more aggressive. Subsequent work has shown that well-differentiated, low-grade, thyroid cancers are iodide avid and not FDG avid (Adler and Bloom 1993; Bloom et al. 1993; Sisson et al. 1993; Feine et al. 1996; Grunwald et al. 1997). Both tracers have their place in the work-up and assessment of recurrence.

Neck metastases from an unknown primary (also called carcinoma of unknown primary), is another useful application of FDG-PET. This was reviewed by Schoder and Yeung (2004). Of the 11 studies with 253 patients reviewed, PET detected the primary in 30%. The typical scenario for PET is a neck mass and a non-diagnostic FNA (Braams et al. 1997).

11.4.3 Lung

The first well-established application of PET in lung cancer was the characterization of solitary pulmonary nodules and/or chest masses. CT cannot reliably distinguish benign from malignant nodules (Kunstaetter et al. 1985; Cummings et al. 1986; Keogan et al. 1993). The utility of FDG-PET in indeterminate lung nodules has been extensively evaluated (Table 11.1) and yields sensitivities over 90% as reported by various institutions (Knight et al. 1996). In general, false positive lesions can be easily identified through conventional radiography, therefore FDG-PET is best performed after conventional imaging for further lesion characterization. The reproducibility of quantitative measurements is high (Minn et al. 1995).

A report on 197 patients from Duke University [Lowe et al. (1997); see Table 11.1) revealed a somewhat lower specificity, which the authors contributed to a "verification bias", i.e., the referring physicians no longer chose biopsy to verify 'negative' PET studies. A proposed cost effective diagnostic algorithm for solitary pulmonary nodules consists of chest radiography, followed by an FDG-PET scan, which if positive, then proceeds to a CT guided biopsy. A meta-analysis on SPN was published in 2001 (Gould et al. 2001), which revealed a sensitivity of 94% and specificity of 86% for FDG-PET (Table 11.1). A clinical example is illustrated in Fig. 11.1.

The staging of nodes in the mediastinum is very important in stratifying patients for surgery, its relevance being related to the close correspondence between disease involvement and prediction of prognosis. In a meta-analysis (Dales et al. 1990) it was argued that non-invasive detection of lymph node metastasis must await an approach fundamentally different from the node size determination. In the prospective NIH sponsored trial of the RDOC (Webb et al. 1991), both CT and MR imaging had a sensitivity around 50% and a somewhat higher specificity around 65%. These results are expected since anatomical size of a node may not be directly related to the presence or absence of tumor. For example in about one third of resected nodes between 2–4 cm, no tumor cells were detected by histopathology. Similar reports on the relative insensitivity of CT have been reported (McLoud et al. 1992; Dillemans et al. 1994).

It is well established that metabolic imaging with FDG-PET is considerably more accurate than CT in staging mediastinal involvement with non-small cell lung cancer (NSCLC; Table 11.2). The available literature reveals that PET has a sensitivity of about 85% and specificity of 90%, which compares favorably to CT with 60% and 80%, respectively, in the same groups of patients.

The meta-analysis reported by Dwamena et al. (1999) pooled the data of 14 studies with 514 patients.

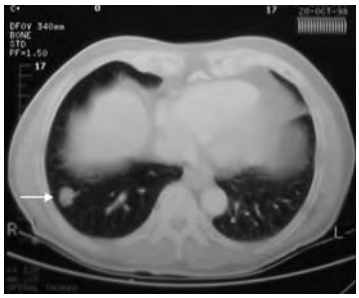

a

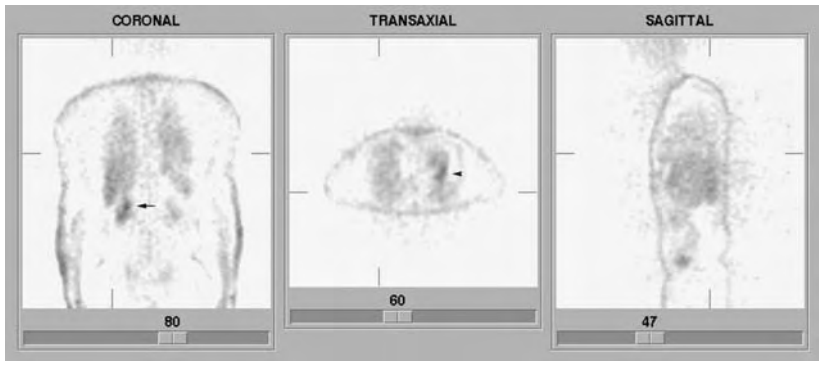

b

Fig. 11.1a,b. Solitary pulmonary nodule. **a** Transverse CT image shows a nodule in the right lung base (*arrow*). **b** Transverse, coronal, and sagittal PET images do not reveal increased metabolic activity in this area. This 63-year-old white male had a positive skin test, and the lesion was thought to be a tuberculoma. No biopsy was performed and conservative treatment selected with repeat CT. Note the physiologic uptake in the right renal pelvis (*arrow on coronal image*), and myocardium (*arrow on transaxial image*). Cross sectional CT slice of 8 mm obtained with a PQ 5000 system (Picker, Cleveland, OH). PET slices of 10 mm from ECAT ART system (CTI, Knoxville, TN) reconstructed without attenuation correction

They found a mean sensitivity of 79% and mean specificity of 91% for PET. The numbers for CT (Table 11.2) are from pooled CT data, comprising 29 studies with 2226 patients. Direct comparison of PET to CT for each patient was not performed in this meta-analysis.

A study from the Netherlands with meticulous sampling of mediastinal nodes corroborated these findings. For mediastinal staging of NSCLC, this group found an accuracy of 87%, sensitivity of 91%, and specificity of 86% for FDG-PET (Pieterman et al. 2000). The newer generation multi-slice CT scanners will perform with higher accuracy than the studies in Table 11.2, but the size criteria for calling a lymph node abnormal remain, with its inherent problems. The WBPET technique is not only able to evaluate the primary lesion and mediastinum, but is especially suited for detection of occult metastases and/or distant lesions (Schiepers 1997). The various series report an incidence of 10%–15% for occult metastases. Figure 11.2 shows an example of initial staging of lung cancer.

Gambhir et al. (1996) have performed a study on cost-effectiveness of FDG-PET in NSCLC staging and management. By using rigorous decision tree analysis, they were able to show that CT plus PET was theoretically the most economical way to work up primary lung cancer, with a marginal increase in patient life expectancy when compared to staging by CT alone. Frank et al. (1995) have also proposed a decision logic for treatment. Based on the evidence above, it is warranted to conclude that PET has a place in pre-operative staging of NSCLC. These results were corroborated in a large multicenter trial in the Netherlands, the PLUS study (Van Tinteren 2002; Verboom 2003).

11.4.4 Breast

A group from Milano reviewed imaging in breast cancer (Bombardieri et al. 1997), and summarized

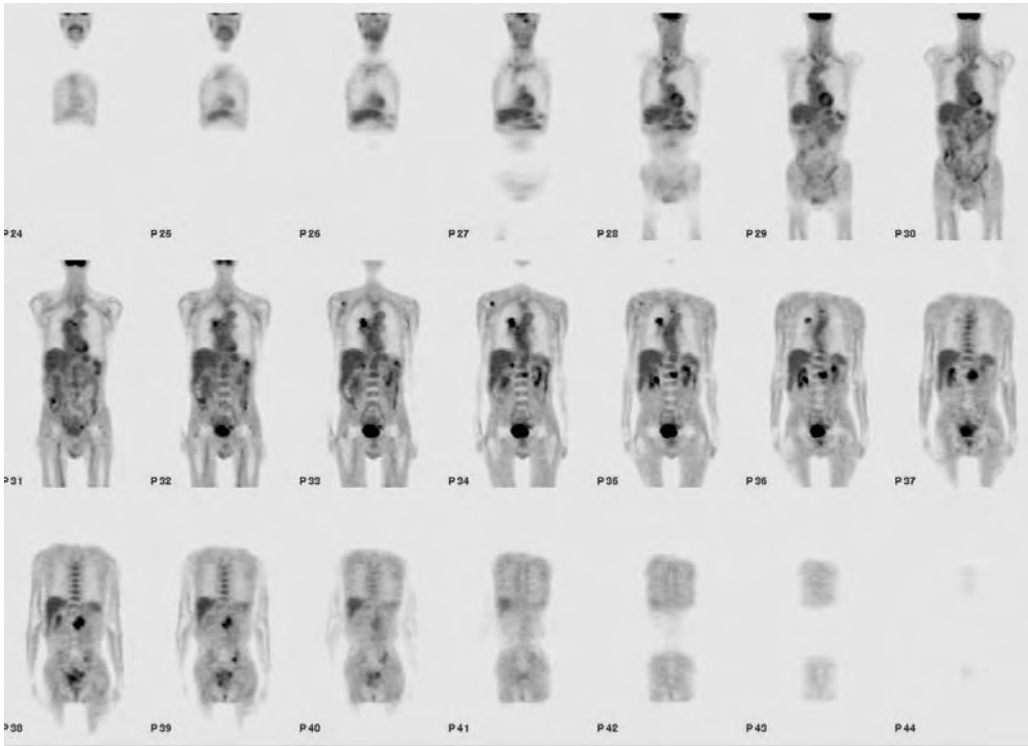

Fig. 11.2. Coronal PET images of a 70-year-old man with newly diagnosed non-small cell lung cancer of the right lung. The CT showed the primary tumor in the right upper lobe, near the superior aspect of the hilum, with borderline mediastinal lymphadenopathy, and negative adrenal glands. PET images are corrected for attenuation, and show intense hypermetabolism in the primary tumor (*P32–P36*), with a lesion medially of this tumor (*P34*), consistent with a malignant lymph node. An additional soft tissue lesion is seen in the right adrenal gland (*P33–P44*) and right lower neck (*P28*). Foci are seen in the right scapula (*P33–P34*), L2 (*P34–P37*) and L3 vertebral bodies (*P37–P38*), and in the left sacrum (*P38–P39*) consistent with bone metastasis. Imaging was performed 1 h after 15.2 mCi FDG, on an ECAT EXACT system (CTI, Knoxville, TN). Coronal slice thickness was 10 mm

the developments in mammography (MX). Although it is not a three-dimensional volumetric technique, it is the screening modality of choice for breast cancer. In women with dense breasts MX may be non-diagnostic and it may be difficult to detect tumors in fibrocystic disease. Nuclear medicine techniques may be helpful in providing parameters on vascularity, metabolic activity and receptor status. In general, a good sensitivity of PET with FDG has been reported for primary lesions (Wahl et al. 1991; Adler et al. 1993; Nieweg et al. 1993). A weakness of the FDG method concerns the false positives, since both neoplastic and inflammatory lesions have increased uptake (Hoh and Schiepers 1999).

Axillary staging is feasible with PET and various studies have shown high specificity (Table 11.3). Bombardieri et al. (1997) have argued that it could replace staging by axillary lymph node dissection. Since the dissection is currently done for prognosis only, the associated morbidity may be avoided in these patients. More studies are needed to confirm the high sensitivity and specificity of axillary staging with FDG-PET in stage I–II breast cancer.

In a WBPET study from our institution, 57 patients were imaged with a history of breast cancer and referred for suspicion of recurrence (Moon et al. 1998). Patients were followed for at least 6 months, so that positive or negative diagnoses could be confirmed by biopsy, or follow-up procedures. On a patient based analysis, the sensitivity and specificity were 93% and 79%, respectively. On a lesion based analysis, the sensitivity and specificity of WBPET for detecting breast cancer foci was 85% and 79%, respectively. There were six false negative lesions

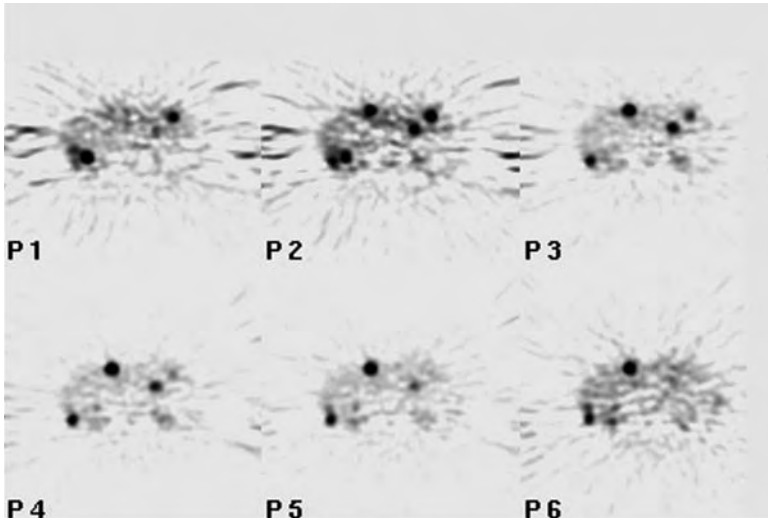

Fig. 11.3. Re-staging of breast cancer. Extensive liver metastasis was found in this 49-year-old white female. CT revealed two metastases in the left liver lobe. Six consecutive slices of 10 mm, P1–P6 (ECAT ART PET system)

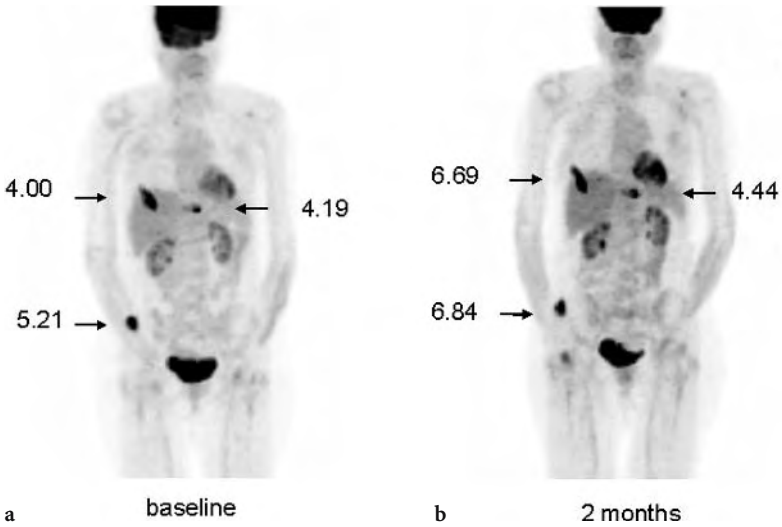

Fig. 11.4a,b. Whole body FDG-PET projection images of a patient with breast cancer prior to therapy (baseline) (**a**) and 2 months after therapy (**b**) with Navelbine and Xeloda. The standardized uptake values of the metastatic bone lesions show no significant decrease in FDG uptake consistent with no response to therapy

and 18 false positive lesions. More extensive metastasis on PET than CT was disclosed in Fig 11.3. The application of FDG-PET in monitoring of breast cancer is shown in Fig 11.4.

Table 11.3 represents the literature of adequately sized studies. In short, for screening purposes there is no indication for PET. In primary breast cancer, PET may be helpful to characterize indeterminate findings on MX. For axillary staging, the results of the prospective multicenter study were disappointing (Wahl et al. 2004). For newly diagnosed breast cancer, staging of the axilla had a sensitivity of 61%, specificity of 80%, PPV of 62%, and NPV of 79%. The authors concluded that FDG-PET cannot be recommended for routine staging of the axilla in patients with newly diagnosed breast cancer.

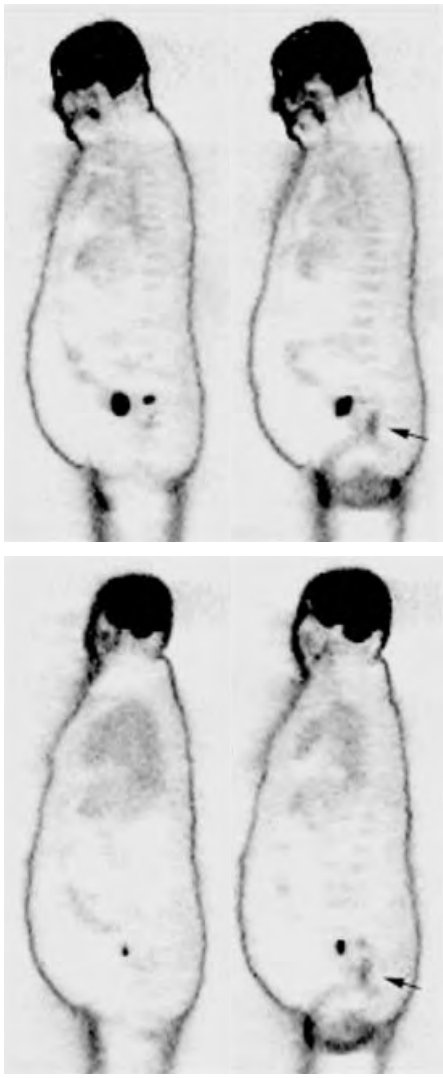

Fig. 11.5a,b. A 70-year-old white male with rectal cancer. cT3N1M0 disease on CT. Sagittal slices before (**a**) and after (**b**) radiation therapy. This whole body PET detected two affected lymph nodes superior of the tumor, which were outside the field of view of 101 mm on the dynamic scan. Note the decrease in metabolic activity of both the tumor (*arrow*) and lymph nodes. Average tumor glucose utilization was 178 ng/min/ml before (**a**) and 72 ng/min/ml after radiation therapy (ECAT 931 PET system)

11.4.5 Colorectal

FDG-PET has no established role in the diagnosis of primary colon cancer (Table 11.4). The surgical treatment of recurrent colorectal cancer remains problematic, despite the advancement of MR, helical CT, intra-operative US, serum tumor markers, or radiolabeled probes (radio-immuno guided surgery, RIGS). Proper selection of patients for secondary surgery with curative intent involves identifying all regional, abdominal and distant tumor foci. This objective is not easily achieved with non-invasive imaging because of lesion size and characterization, and occult disease. Tumor markers such as CEA have a low sensitivity to detect recurrence (around 60%). The aim of the pre-surgical work-up is to distinguish isolated resectable disease, i.e., local recurrence or liver metastasis, from advanced disease. By correct staging, patients with widespread metastasis may be identified in whom surgery is not an option. This will not only improve the cost–benefit ratio, but also spare the patient extensive surgery with its associated morbidity. The actual selection of patients with recurrent cancer results in 5-year survival rates of only 20%–30% after secondary 'curative' surgery (Strauss et al. 1989; Haberkorn et al. 1991a,b; Keogan et al. 1997). In Fig. 11.5 a scan with nodal involvement is shown.

Table 11.3 supplies the data on colorectal cancer recurrence. An early series with 76 patients comparing PET to conventional imaging was reported by Schiepers et al. (1995). The study was prospective, had surgical confirmation in 63% of patients and evaluated disease in three 'surgical' zones: local pelvic recurrence, hepatic involvement and distant metastasis. A high accuracy was obtained for PET, 95% for local disease, and 98% for hepatic metastasis. Unexpected advanced disease was diagnosed in 15% of patients. The study of Valk et al. (1996) provided similar results. Delbeke et al. (1997) reported on liver metastasis from colorectal origin. Since all 52 had suspected recurrence on CT, they utilized a lesion-based analysis, which furnished an accuracy of 92% for PET compared to 80% for conventional imaging. The main

difference in their protocol with the other two series was the longer image duration of 10 min per bed position and correction for attenuation effects.

Several reports were published about the impact of PET on patient management, which varied from 28% in the series of Delbeke et al. (1997), 29% in Lai et al. (1996), to 40% in Beets et al. (1994). Presently acknowledged PET indications for colorectal cancer are:

1. Differentiation of a pelvic mass as tumor recurrence vs. post-operative fibrosis
2. Assessment of hepatic metastasis
3. Establishment of disease in case of elevated tumor markers and negative conventional imaging
4. Disclosure of occult metastases and (re)staging of disease

11.4.6 Other Gastrointestinal Tumors

Several papers have been published on the use of FDG-PET for the characterization of pancreatic masses with indeterminate CT findings (Inokuma et al. 1995; Ho et al. 1996; Reske et al. 1997). In a study with 73 patients by Stollfuss et al. (1995) the SUV threshold for malignancy was set at 1.5 resulting in both sensitivity and specificity of 93% for lesion detection. Visual interpretation gave a slightly higher sensitivity of 95% but lowered specificity to 90%. With either method for FDG-PET interpretation, the results were better than abdominal CT, which had a sensitivity and specificity of 80% and 74%, respectively. Similar results were obtained in an earlier study by Bares et al. (1994), where PET was compared with abdominal CT, abdominal US, and endoscopic US in 46 patients. Less encouraging results were found when FDG-PET was used to differentiate pancreatic carcinoma from mass-forming pancreatitis. The problem of increased FDG uptake in intense inflammatory lesions (e.g., retroperitoneal fibrosis and chronic pancreatitis) will require further studies. False positive results due to inflammation have occurred in other types of lesions evaluated by PET, emphasizing the non-specific nature of FDG. PET may obviate further invasive diagnostic procedures in many patients with benign disease and only patients with abnormal FDG activity will need CT guided biopsies. There is no consensus on the indications for pancreas cancer.

In esophageal cancer, FDG PET imaging has been found to be very sensitive in detecting the primary tumor (100%) (Ogunbiyi 1997). In detecting nodal metastatic disease in esophageal cancer, PET had a sensitivity of 72% and specificity of 82% as compared to CT's sensitivity of 28% and 73%, respectively. In another study (Kole 1998), both PET and CT had high sensitivity in detecting the primary lesion, 96% and 81%, respectively; however, both imaging techniques failed to accurately assess the depth of esophageal wall invasion. A prospective study showed that PET was useful in detecting distant metastatic disease; however, it did not significantly change the clinical decision of resectability in these patients compared to using other conventional diagnostic procedures (Kneist 2004). PET may have clinical utility in esophageal cancer when used for distinguishing a responder to preoperative chemoradiation therapy SUV<4.0, versus a non-responder SUV$\geq$4.0 (Swisher 2004).

11.4.7 Prostate

The results of FDG-PET imaging with prostate cancer are mixed (Table 11.5). FDG-PET helped identify osseous and soft-tissue metastases of prostate cancer with a high positive predictive value but had a limited sensitivity (65%) compared to that of routine bone scintigraphy (Shreve et al. 1996). Yeh et al. (1996) also found a low sensitivity (20%) for osseous metastases. Laubenbacher et al. (1995b) and Effert et al. (1996) found that the SUV is relatively low in prostate carcinoma. One observation of Effert et al. (1996) was that in a subgroup of patients with metastases having SUVs in excess of 5, all had rapid progression of disease and did not respond well to subsequent hormone deprivation or radiation therapy. The relatively low FDG uptake by prostate carcinoma may reflect a characteristic of a slow growing or indolent neoplasm; however, an abnormal FDG-PET scan has a high positive predictive value (98%) for the presence of tumor (Shreve et al. 1996). The ability to determine the presence, extent, and metabolic activity of metastatic disease may be important in clinical management decisions concerning hormonal therapy or the institution of experimental therapies. In patients with advanced disease, an abnormal FDG PET has a high positive predictive value for presence of tumor.

Imaging of the primary tumor in the prostate will be technically challenging due to the relatively low FDG uptake in the tumor in the early stages of disease and due to the intense bladder activity, which may obscure the detection of a small tumor focus.

Lesions with low FDG uptake will be a diagnostic challenge for differentiation of an indolent but malignant tumor from an active but benign tumor or inflammatory lesion. Due to the proximity of the bladder and frequent problems with micturition and retention, significant artifacts may result. Not all of these can be overcome easily. Currently, there is no established utility of FDG-PET in this common cancer, both for primary and recurrent disease.

11.4.8 Other Genitourinary Tumors

Several studies have applied FDG-PET to renal cell carcinoma (RCC). In the study by Bachor et al. (1996) 29 patients with solid renal masses were scanned prior to surgery. In 20 of 26 patients, FDG-PET scans detected the histologically confirmed RCC and failed in six patients to detect the tumor focus. In three patients with benign lesions, falsely positive results were obtained. In another three patients, FDG-PET was able to detect regional lymph node metastases suggesting a role for staging of RCC. Bender et al. (1997) had similar results.

Goldberg et al. (1997) performed 26 FDG-PET studies in 21 patients. They evaluated the ability of FDG-PET to characterize solid renal masses (ten patients), indeterminate renal cysts (11 patients) as malignant or benign. PET correctly classified solid lesions as malignant in nine of ten histologically confirmed tumors (six RCC, three lymphomas). One patient with bilateral RCC was false negative. PET correctly classified indeterminate renal cysts as benign in seven of eight patients confirmed by surgery or needle aspiration. PET was false negative in one patient with a 4-mm papillary neoplasm. The authors suggested that a positive FDG-PET scan in the appropriate clinical setting might obviate the need for cyst aspiration in indeterminate renal masses. These early studies with a limited number of patients revealed that FDG-PET had a high positive predictive value, suggesting its utility for non-invasive characterization of indeterminate renal masses in patients in whom surgical resection or biopsy is not feasible.

Kang et al. (2004) reported a large retrospective study with 99 scans in 66 patients. The sensitivity for primary RCC was 60%, and the specificity 100%. The authors concluded that PET with FDG is limited due to the low sensitivity.

To investigate the reason why some patients with RCC had negative FDG PET scans, Wahl (1997a) compared several biological characteristics. They demonstrated that patients with positive PET scans at the primary tumor site had higher tumor grades and higher GLUT-1 expression than patients with negative PET scans. Since GLUT-1 is the key transporter for FDG, with low expression in RCC, most renal cancers are less well seen. The significance of FDG uptake relative to the prognostic outcomes is unknown.

In an Australian study, the effect of staging on patient management was investigated (Ramdave et al. 2001). The authors concluded that PET had a similar accuracy as CT (94%) and changed patient management in 40%.

Safaei et al. (2002) of our institution, assessed the utility of FDG-PET for restaging 36 patients with advanced RCC. In this retrospective study, the additional value of whole body PET to conventional imaging was demonstrated. The patient-based analysis revealed that FDG-PET correctly classified the clinical stage in 32 of 36 patients (89%) and was incorrect in four patients (11%). The lesion-based analysis showed that metabolic imaging correctly classified 21 of 25 lesions (81%), subsequently verified by surgical biopsy. This resulted in a sensitivity of 82%, specificity of 88%, and accuracy of 81% for lesion detection.

Majhail et al. (2003) reported on the evaluation of distant metastases in 24 patients with RCC. The sensitivity was 64%, the specificity 100%, and the positive predictive value 100%. They found that the false negative results were all related to lesions less than 1 cm in size. Similar results were published by Jadvar et al. (2003), demonstrating a modest accuracy for restaging of RCC. In 25 patients, they found a sensitivity of 71%, specificity of 75%, and accuracy of 72%. With a negative predictive value of 33% and a positive predictive value of 94%, these authors concluded that a negative study does not exclude disease, whereas a positive study is suspicious for malignancy. Kang et al. (2004) arrived at the same conclusion by finding a sensitivity of 75% and specificity of 100% for lymph node metastasis from RCC. In general, FDG-PET suffers from limited sensitivity in RCC. This is partially related to the low glucose utilization of renal tumors (low GLUT-1 expression). The fact that small lesions (< 1 cm) are missed is in part related to the spatial resolution of the PET systems used and, therefore, not specific for RCC.

In the few studies reported on patients evaluated for recurrent ovarian carcinoma and confirmed by second look laparotomy, PET had a sensitivity over

90%, whereas CT and US had sensitivities ranging from 33% to 85% (Hubner et al. 1993; Casey et al 1994). The specificity of PET was 80% and CT 50%. There was a good correlation between PET and histological findings so that patient management will benefit from PET by identifying occult foci that are not apparent on morphological imaging studies (Karlan et al. 1993). More studies are needed to define the clinical role of PET in the management of ovarian cancer.

The value of PET imaging for testicular cancers is still under investigation (Stephens et al. 1996; Nuutinen et al. 1997; Reinhardt et al. 1997). For initial staging after orchiectomy, PET may have a role in detecting metastases not seen by conventional imaging although this has not been proven in the studies completed to date. Following chemotherapy, PET may be able to differentiate viable carcinoma from scar tissue but preliminary findings indicate that it cannot differentiate scar tissue from mature teratoma. PET and for that matter any imaging technology will miss micro-foci of viable germ cell tumor. Focal areas of abnormal FDG uptake that are detected within extensive residual radiographic abnormalities may allow a more directed and possibly more limited surgical resection, especially in high risk patients who have had recurrence following previous medical and surgical treatment. Another application of PET is the patient with a rising tumor marker following chemotherapy and/or retroperitoneal lymph node dissection, but without evidence of residual mass on conventional imaging. The location of abnormal FDG uptake may be helpful in guiding anatomical imaging, surgical exploration, and tumor resection.

In general, both primary seminomas and malignant teratomas have avid FDG uptake, whereas differentiated teratomas and necrotic or fibrotic tissue have normal uptake. Except for Germany, where it has been incorporated in monitoring therapy, there is no consensus on the role of PET in testicular cancer.

11.4.9 Lymphoma

The same diagnostic questions as in lung cancer or colorectal cancer pertain to lymphoma: (i) determine the tumor stage at initial presentation, (ii) characterize a residual mass post treatment as scar or tumor, and (iii) assess response after therapy. These questions cannot be appropriately addressed with current anatomical imaging methods (Okada et al. 1991, 1992; Leskinen-Kallio et al. 1991). Moreover, gallium scintigraphy is not sensitive enough in low-grade lymphomas, whereas FDG is (Paul 1987). The accuracy of FDG-PET imaging in thoracic-abdominal lymphoma compared to that of CT was studied in 11 patients (Newman et al. 1994). All lesions were detected by PET, and five were missed by CT. No difference was found between low- and intermediate-grade lymphomas. In a study from our institution in 18 patients, both CT and PET detected 33 out of 37 lesions, although not all lesions were the same (Hoh et al. 1997a). Staging using WBPET was concordant with conventional staging in 14/17 patients, better than conventional staging in three and worse in one patient. For an analysis of cost effectiveness, the reader is referred to the original article (Hoh et al. 1997a). In a study of 24 patients by De Wit et al. (1997), PET correctly predicted all patients in complete remission after therapy, there were no false negatives. These investigators concluded that PET performed for evaluation of residual mass after treatment of lymphoma has a high predictive value.

A limited number of studies address primary staging of lymphoma, whereas the majority evaluates the ability of FDG-PET to accurately monitor therapy. In primary staging, most of the publications compare PET to anatomic imaging with CT. Moog et al. (1997) concluded from their study of 60 consecutive patients with HD and NHL that FDG-PET was more accurate for detecting lymph node involvement than CT. In these 60 untreated patients staged for nodal involvement, PET found 25 additional lesions, of which 16 remained unresolved. CT showed an additional six lesions, of which three were false positive and three were unresolved Moog et al. (1997). Stumpe et al. (1998) arrived at a similar conclusion when they compared the accuracy of FDG-PET to that of CT. The diagnostic sensitivity did not differ between PET and CT. However, the specificity of PET was 96% for Hodgkin's disease and 100% for non-Hodgkin's lymphoma while the corresponding values were only 41% and 67% for CT. This low specificity for CT is quite in contrast to other studies, which report high specificities for both CT and PET in lymphoma. The study of Stumpe et al. (1998) had a preponderance of patients referred for re-staging and had a retrospective design, which helps explain these unusual findings. An example of a responder to chemotherapy is provided in Fig 11.6.

Jerusalem et al. (2001) evaluated PET performance in different anatomical regions, and found

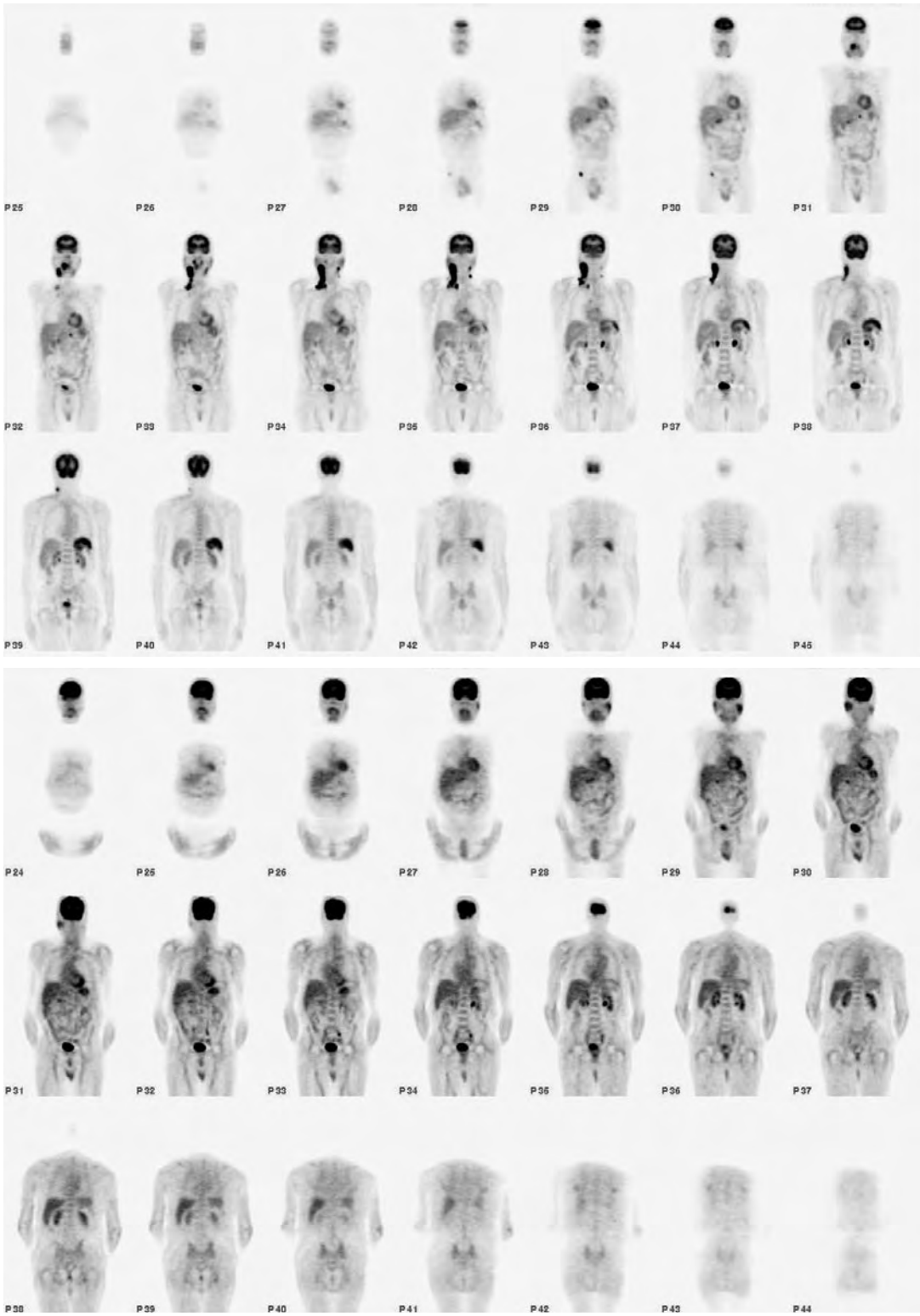

Fig. 11.6. Coronal slices of PET studies in a 73-year-old male with non-Hodgkin lymphoma; baseline study (**a**) and after four courses of chemotherapy (**b**). The baseline images show the primary neck mass on the right (*P34–P36*), involvement of contralateral nodes (*P35–P36*), an epigastrial node left of the midline (*P31–P32*), and a right inguinal node (*P29–30*). The high uptake in the spleen suggests splenic involvement. The scan after therapy shows resolution of the right neck mass and other nodal involvement. The spleen now has normal FDG uptake. Prominent uptake is seen in the parotid gland bilaterally and stomach

the highest PET sensitivity in the thorax (91%), and the lowest in the abdomen/pelvis (75%). Peripheral disease involvement was diagnosed with a sensitivity of 83%. The variations are larger for PET between the different body regions than CT, which has a sensitivity of 80%–85% across the various body regions. The somewhat lower sensitivity of PET for infra-diaphragmatic lesions was also reported by Buchmann et al. (2001), who showed that PET is only superior to CT for supra-diaphragmatic lesions and not different from CT for infra-diaphragmatic sites.

A major problem concerns the systemic nature of lymphoma and its treatment, which is usually not surgery. Thus, individual lesions observed on PET or CT cannot be compared to the reference standard. WBPET has a significant impact on staging of lymphoma, since biopsy of all lesions is impossible and characterization of abnormalities has been shown to be cost effective.

11.4.10 Melanoma

In two small studies for staging of metastatic melanoma, PET imaging had an overall accuracy of 100%, detecting all metastatic lesions (intra-abdominal, visceral, and lymph nodes) and correctly predicting all negative lymph node regions (Gritters et al 1993; Wagner et al 1997). In a study of 33 patients, Steinert et al. (1995) found a sensitivity of 92%. With blinded reading the specificity was 77%, which could be increased to 100% when clinical information was provided. In a large Australian study of 100 patients, the sensitivity was 93% for detection of metastatic lesions (Damian et al. 1996). Small metastatic foci were seen only on follow-up CT several months later. The sensitivity of the PET technique for detecting small pulmonary lesions was lower than CT, attributed to respiratory motion or prior cancer therapy.

From the studies available, it appears that PET is a sensitive and highly specific test for detecting lymph node metastasis in melanoma; however, the detection of microscopic disease in a lymph node draining the primary site will still be performed by the sentinel node technique. For very small tumor lesions (<5 mm), PET is not as sensitive as CT. Therefore an algorithm can be proposed for melanoma similar to that of lung and colorectal cancer, in which PET is performed to detect distant metastatic disease and to categorize the patient as potentially unresectable.

11.5 Conclusions

The unique imaging capabilities of PET enable physicians to detect disease in vivo, and to monitor treatment from a metabolic perspective. FDG-PET in oncologic imaging has been applied for characterizing lesions, differentiating recurrent disease from treatment effects, and staging. Future developments may utilize PET in basic drug development, and in monitoring or evaluating the eligibility of patients for new therapy protocols.

The goal in any staging method is to detect small tumor foci with the highest sensitivity and specificity. Excellent results are obtained for instance with MR of the brain, CT of the neck or liver, and mammography, but the anatomical modalities generally lack specificity. The limiting factor for PET sensitivity will be its resolution, whereas PET's strength will be in the development of even more specific radiopharmaceuticals for tumor imaging. An inherent difficulty in analyzing and comparing various imaging modalities is that, for ethical reasons, the identified lesions cannot always be confirmed histologically. Clinically oriented "reference standards" will have to be developed to assess the utility of PET. These include rigorous follow-up of patients to measure progression of disease, disease free survival, and prognosis. Improved categorization of patients into their correct stages, will result in improved patient outcome. In the future, the role of clinical imaging may be quite different due to the rapid developments in molecular biology and genetics. The management of cancer patient in the future may require very specific in-vivo tumor characteristic, which may be only measurable with molecular imaging techniques. Even if no effective therapy exists for a particular malignancy, PET and other quantitative imaging techniques may play an important role in the understanding of the underlying etiology, pathogenesis and in-vivo biology of that disease. In addition, PET may assist in the development of new therapies. In the end, the proper combination of imaging technologies in well-defined algorithms will provide the most accurate diagnostic information for optimal clinical management and patient outcome.

References

Abdel-Nabi H, Doehr RJ, Lamonica M, et al. (1998) Staging of primary colorectal carcinomas with fluorine-18 fluoro-

deoxy-glucose whole body PET: correlation with histopathologic and CT findings. Radiology 206:755–760
Adler LP, Bloom AD (1993) Positron emission tomography of thyroid masses. Thyroid 3:195–200
Adler LP, Crowe JP, al-Kaisi NK, Sunshine JL (1993) Evaluation of breast masses and axillary lymph nodes with [18F] 2-deoxy-2-fluoro-D-glucose PET. Radiology 187:743–750
Adler LP, Faulhaber PF, Schnur KC, Al-Kasi NL, Shenk RR (1997) Axillary lymph node metastases: screening with 18F-FDG PET. Radiology 203:323–327
Alavi JB, Alavi A, Chawluk, et al. (1988) PET in patients with glioma Cancer 62:1074–1078
Anzai Y, Carroll WR, Quint DJ, Bradford CR, Minoshima S, Wolf GT, Wahl RL (1996) Recurrence of head and neck cancer after surgery or irradiation: prospective comparison of 2-deoxy-2-[18F]fluoro-D-glucose PET and MR imaging diagnoses. Radiology 200:135–141
Avril N, Dose J, Janicke F, et al. (1996) Metabolic characterization of breast tumors with positron emission tomography using F-18 fluorodeoxyglucose. J Clin Oncol 14:1848–1857
Bachor R, Kotzerke J, Gottfried HW, et al. (1996) Positron emission tomography in diagnosis of renal cell carcinoma. Urology 35:146–150
Bailet JW, Abemayor E, Jabour BA, et al. (1992) Positron emission tomography: a new precise imaging modality for detection of primary head and neck tumors and assessment of cervical adenopathy. Laryngoscope 102:281–288
Bares R, Klever P, Hauptmann S, Hellwig D, Fass J, Cremerius U, Schumpelick V, Mittermayer C, Bull U (1994) F-18 fluorodeoxyglucose PET in vivo evaluation of pancreatic glucose metabolism for detection of pancreatic cancer. Radiology 192:79–86
Beets G, Penninckx F, Schiepers C, Filez L, Mortelmans L, Kerremans R, Aerts R, De Roo M (1994) Clinical value of whole-body positron emission tomography with [18F]fluorodeoxyglucose in recurrent colorectal cancer. Br J Surg 81:1666–1670
Benchaou M, Lehmann W, Slosman DO, et al. (1996) The role of FDG-PET in the preoperative assessment of N-staging in head and neck cancer. Acta Oto-Laryngologica 116:332–335
Bender H, Schomburg A, Albers P, Ruhlmann J, Biersack HJ (1997) Possible role of FDG-PET in the evaluation of urologic malignancies. Anticancer Research 17:1655–1660
Bengel FM, Ziegler SI, Avril N, et al. (1997) Whole body PET in clinical oncology: comparison between attenuation corrected and uncorrected images. Eur J Nucl Med 24:1091–1098
Bloom AD, Adler LP, Shuck JM (1993) Determination of malignancy of thyroid nodules with positron emission tomography. Surgery 114:728–734
Bombardieri E, Crippa F, Maffioli L, Greco M (1997) Nuclear medicine techniques for the study of breast cancer. Eur J Nucl Med 24:809–824
Braams JW, Pruim J, Kole AC, et al. (1997) Detection of unknown primary head and neck tumors by positron emission tomography. Int J Oral Maxillofac Surg 26:112–115
Brock CS, Meikle SR, Price P (1997) Does F-18 fluorodeoxyglucose metabolic imaging of tumours benefit oncology ? Eur J Nucl Med 24:691–705
Brown RS, Wahl RL (1993) Overexpression of Glut-1 glucose transporter in human breast cancer. An immunohistochemical study. Cancer 72:2979–2985
Buchmann I, Reinhardt M, Elsner K, Bunjes D, Altehoefer C, Finke J, et al. (2001) 2-(Fluorine-18)fluoro-2-deoxy-D-glucose positron emission tomography in the detection and staging of malignant lymphoma. A bicenter trial. Cancer 91:889–899
Bury T; Dowlati A; Paulus P, et al. (1996) Staging of non-small-cell lung cancer by whole-body fluorine-18 deoxyglucose positron emission tomography. Eur J Nucl Med 23:204–206
Casey MJ, Gupta NC, Muths CK (1994) Experience with positron emission tomography (PET) scans in patients with ovarian cancer. Gyn Onc 53:331–338
Chen et al 2005 (in press)
Chin R Jr, Ward R, Keyes JW, Choplin RH, Reed JC, Wallenhaupt S, Hudspeth AS, Haponik EF (1995) Mediastinal staging of non-small-cell lung cancer with positron emission tomography. Am J Respir Crit Care Med 152:2090–2096
Conti PS, Lilien DL, Hawley K, Keppler J, Grafton ST, Bading JR (1996) PET and [18F]-FDG in oncology: a clinical update. Nucl Med Biol 23:717–735
Crippa F, Agresti R, Seregni E, et al. (1998) Prospective evaluation of fluorine-18-FDG PET in presurgical staging of the axilla in breast cancer. J Nucl Med 39:4–8
Cummings SR, Lillington GA, Richard RJ (1986) Estimating the probability of malignancy in solitary pulmonary nodules. A Bayesian approach. Am Rev Respir Dis 134:449–452
Dahlbom M, Hoffman EJ, Hoh CK, Schiepers C, Rosenqvist G, Hawkins RA, and Phelps ME (1992) Whole-body positron emission tomography: Part I. Methods and performance characteristics. J Nucl Med 33:1191–1199
Dales RE, Stark RM, Raman S (1990) Computed tomography to stage lung cancer: approaching a controversy using meta-analysis. Am Rev Respir Dis 141:1096–1101
Damian DL, Fulham MJ, Thompson E, Thompson JF (1996) Positron emission tomography in the detection and management of metastatic melanoma. Melanoma Res 6:325–329
De Wit M, Bumann D, Beyer W, Herbst K, Clausen M, Hossfeld DK (1997) Whole-body positron emission tomography (PET) for diagnosis of residual mass in patients with lymphoma. Ann Oncol 8:57–60
Delbeke D, Meyerowitz C, Lapidus R, et al. (1995) Optimal cut-off levels for 18F-FDG uptake in the differentiation of low-grade from high-grade brain tumors with PET. Radiology 195:47–52
Delbeke D, Vitola J, Sandler MP, et al. (1997) Staging recurrent metastatic colorectal carcinoma with PET. J Nucl Med 38:1196–1201
Dewan NA, Gupta NC, Redepenning LS, Phalen JJ, Frick MP (1993) Diagnostic efficacy of PET-FDG imaging in solitary pulmonary nodules. Potential role in evaluation and management. Chest 104:997–1002
Dewan NA, Reeb SD, Gupta NC, Gobar LS, Scott WJ (1995) PET-FDG imaging and transthoracic needle lung aspiration biopsy in evaluation of pulmonary lesions. A comparative risk–benefit analysis. Chest 108:441–446
Di Chiro G (1987) Positron emission tomography using [18F]fluorodeoxyglucose in brain tumors – a powerful diagnostic and prognostic tool. Invest Radiol 22:360–371
Di Chiro G, De la Paz RL, Brooks RA, et al. (1982) Glucose utilization of cerebral gliomas measured by 18F-fluorodeoxyglucose and PET. Neurology 32:1323–1329
Di Chiro G, Hatazawa J, Katz DA, Rizzoli HV, De Michele DJ (1987) Glucose utilization by intracranial meningiomas as

an index of tumor aggressivity and probability of recurrence: a PET study. Radiology 164:521–526
Di Chiro G, Oldfield E, Wright DC, et al. (1988) Cerebral necrosis after radiotherapy and/or intra-arterial chemotherapy for brain tumors: PET and neuropathologic studies. AJR 150:189–197
Dillemans B, Deneffe G, Verschakelen J, Decramer M (1994) Value of computed tomography and mediastinoscopy in preoperative evaluation of mediastinal nodes in non-small cell lung cancer. Eur J Cardio-Thorac Surg 8:37–42
Doyle WK, Budinger TF, Valk PE, et al. (1987) Differentiation of cerebral radiation necrosis from tumor recurrence by 18F-FDG and 82Rb PET. J Comput Assist Tomogr 11:563–570
Dwamena BA, Sonnad SS, Angobaldo JO, Wahl RL (1999) Metastases from non-small cell lung cancer: mediastinal staging in the 1990s – meta-analytic comparison of PET and CT. Radiology 213:530–536
Effert PJ, Bares R, Handt S, et al. (1996) Metabolic imaging of untreated prostate cancer by positron emission tomography with [18F]fluorine-labeled deoxy-glucose. J Urol 155:994–998
Feine U, Lietzenmayer R, Hanke JP, et al. (1996) Fluorine-18-FDG and iodine-131-iodide uptake in thyroid cancer. J Nucl Med 37:1468–1472
Frank A, Lefkowitz D, Jaeger S, et al. (1995) Decision logic for retreatment of asymptomatic lung cancer recurrence based on positron emission tomography findings. Int J Rad Oncol Biol Physics 32:1495–1512
Gambhir SS, Hoh CK, Phelps ME, Madar I, Maddahi J (1996) Decision tree sensitivity analysis for cost effectiveness of FDG-PET in the staging and management of non-small-cell lung carcinoma. J Nucl Med 37:1428–1436
Goldberg MA, Mayo-Smith WW, Papanicolaou N, Fischman AJ, Lee MJ (1997) FDG PET characterization of renal masses: preliminary experience. Clin Radiol 52:510–515
Gould MK, Maclean CC, Kuschner WG, Rydzak CE, Owens DK (2001) Accuracy of positron emission tomography for diagnosis of pulmonary nodules and mass lesions: a meta-analysis. Jama 285:914–924
Greco M, Crippa F, Agresti R, Seregni E, Gerali A, Giovanazzi R et al. (2001) Axillary lymph node staging in breast cancer by 2-fluoro-2-deoxy-D-glucose-positron emission tomography: clinical evaluation and alternative management. J Natl Cancer Inst 93(8):630–635.
Gritters LS, Francis IR, Zasadny KR, Wahl RL (1993) Initial assessment of positron emission tomography using 2-fluorine-18-fluoro-2-deoxy-D-glucose in the imaging of malignant melanoma. J Nucl Med 34:1420–1427
Grunwald F, Menzel C, Bender H, et al. (1997) Comparison of 18FDG-PET with 131iodine and 99mTc-sestamibi scintigraphy in differentiated thyroid cancer. Thyroid 7:327–335
Guhlmann A, Storck M, Kotzerke J, et al. (1997) Lymph node staging in non-small cell lung cancer: evaluation by [18F]FDG positron emission tomography (PET). Thorax 52:438–441
Gupta NC, Maloof J, Gunel E (1996) Probability of malignancy in solitary pulmonary nodules using fluorine-18-FDG and PET. J Nucl Med 37:943–948
Haberkorn U, Strauss LG, Dimitrakopoulou A, et al. (1991a) PET studies of fluorodeoxyglucose metabolism in patients with recurrent colorectal tumors receiving radiotherapy. J Nucl Med 32:1485–1490
Haberkorn U, Strauss LG, Reisser C, et al. (1991b) Glucose uptake, perfusion, and cell proliferation in head and neck tumors: relation of positron emission tomography to flow cytometry. J Nucl Med 32:1548–1555
Haberkorn U, Strauss LG, Dimitrakopoulou A, et al. (1993) Fluorodeoxyglucose imaging of advanced head and neck cancer after chemotherapy. J Nucl Med 34:12–17
Hamberg LM, Hunter GJ, Alpert NM, et al. (1994) The dose uptake ratio as an index of glucose metabolism: useful parameter or oversimplification? J Nucl Med 35:1308–1312
Higashi K, Clavo AC, Wahl RL (1993a) Does FDG uptake measure proliferative rate of human cancer cells? In vitro comparison with DNA flow cytometry and tritiated Thymidine uptake. J Nucl Med 34:414–419
Higashi K, Clavo AC, Wahl RL (1993b) In vitro assessment of 2-fluoro-2-deoxy-D-glucose, L-methionine and thymidine as agents to monitor the early response of a human adenocarcinoma cell line to radiotherapy. J Nucl Med 34:773–779
Ho CL, Dehdashti F, Griffeth LK, Buse PE, Balfe DM, Siegel BA (1996) FDG-PET evaluation of indeterminate pancreatic masses. J Comput Assist Tomogr 20:363–369
Hoh CK, Hawkins RA, Glaspy JA, et al. (1993) Cancer detection with whole-body PET using 2-[18F]fluoro-2-deoxy-D-glucose. J Comput Assist Tomogr 17:582–589
Hoh CK, Glaspy J, Rosen PJ, et al. (1997a) Whole body FDG PET imaging for staging of Hodgkin's disease and lymphoma. J Nucl Med 38:343–348
Hoh CK, Schiepers C, Seltzer MA, et al. (1997b) PET in oncology: will it replace the other modalities? Semin Nucl Med 27:94–106
Hoh CK, Seltzer MA, Franklin J et al., (1998) Positron emission tomography (PET) in urologic oncology. J Urol 159:347–356
Hoh CK, Schiepers C (1999) 18FDG imaging in breast cancer. Semin Nucl Med 29:49–56
Hubner KF, McDonald TW, Niethammer JG et al. (1993) Assessment of primary and metastatic ovarian cancer by positron emission tomography (PET) using 2-[18F]deoxyglucose (2-[18F]FDG). Gyn Onc 51:197–204
Huebner RH, Park KC, Shepherd JE, Schwimmer J, Czernin J, Phelps ME et al. (2000) A meta-analysis of the literature for whole-body FDG PET detection of recurrent colorectal cancer. J Nucl Med 41(7):1177–1189
Husband JES (1995) Imaging of treated cancer. Brit J Radiol 68:1–12
Husband JE (1996) Monitoring tumour response. Eur Radiol 6:775–785
Inokuma T, Tamaki N, Torizuka T, Magata Y, Fujii M, Yonekura Y, Kajiyama T, Ohshio G, Imamura M, Konishi J (1995) Evaluation of pancreatic tumors with positron emission tomography and F-18 fluorodeoxyglucose: comparison with CT and US. Radiology 195:345–352
Jabour BA, Choi Y, Hoh CK, et al. (1993) Extracranial head and neck: PET imaging with 2-[18F]fluoro-2-deoxy-D-glucose and MR imaging correlation. Radiology 186:27–35
Jadvar H, Kherbache HM, Pinski JK, Conti PS (2003) Diagnostic role of [F-18]-FDG positron emission tomography in restaging renal cell carcinoma. Clin Nephrol 60:395–400
Jerusalem G, Beguin Y, Fassotte MF, Najjar F, Paulus P, Rigo P, et al. (2001) Whole-body positron emission tomography using 18F-fluorodeoxyglucose compared to standard procedures for staging patients with Hodgkin's disease. Haematologica 86:266–73

Kang DE, White RL, Jr., Zuger JH, Sasser HC, Teigland CM (2004) Clinical use of fluorodeoxyglucose F 18 positron emission tomography for detection of renal cell carcinoma. J Urol 171:1806–1809

Karlan BY, Hawkins R, Hoh C, et al. (1993) Whole-body positron emission tomography with 2-[18F]fluoro-2-deoxy-D-glucose can detect recurrent ovarian carcinoma. Gyn Onc 51:175–181

Kau RJ, Alexiou C, Laubenbacher C, Werner M, Schwaiger M, Arnold W (1999) Lymph node detection of head and neck squamous cell carcinomas by positron emission tomography with fluorodeoxyglucose F 18 in a routine clinical setting. Arch Otolaryngol Head Neck Surg 125:1322–1328

Keogan MT, Tung KT, Kaplan DK, et al. (1993) The significance of pulmonary nodules detected on CT staging for lung cancer. Clin Radiology 48:94–96

Keogan MT, Lowe VJ, Baker ME, McDermott VG, Lyerly HK, Coleman RE (1997) Local recurrence of rectal cancer: evaluation with F-18 fluorodeoxyglucose PET imaging. Abdom Imaging 22:332–337

Keys JW (1995) SUV: standard uptake or silly useless value? J Nucl Med 36:1836–1839

Kim CK, Gupta NC, Chandramouli B, Alvi A (1994) Standardized uptake values of FDG: body surface area correction is preferable to body weight correction. J Nucl Med 35:164–167

Kneist W, Schreckenberger M, Bartenstein P, Menzel C, Oberholzer K, Juginger T (2004) Prospective evaluation of positron emission tomography in the preoperative staging of esophageal carcinoma. Arch Surg 139:1043–1049

Knight SB, Delbeke D, Stewart JR, Sandler MP (1996) Evaluation of pulmonary lesions with FDG-PET. Comparison of findings in patients with and without a history of prior malignancy. Chest 109:982–988

Kole AC, Plukker JT, Nieweg OE, Vaalburg W (1998) Positron emission tomography for staging of oesophageal and gastroesophageal malignancy. Br J Cancer 78:521–527

Kresnik E, Mikosch P, Gallowitsch HJ, Kogler D, Wiesser S, Heinisch M, et al. (2001) Evaluation of head and neck cancer with 18F-FDG PET: a comparison with conventional methods. Eur J Nucl Med 28:816–821

Kubota K, Matzuzawa T M, Fujiwara et al. (1988) Differential diagnosis of solitary pulmonary nodules with PET using C-11 methionine. J Comput Assist Tomogr 12:794–796

Kubota K, Ishiwata K, Kubota R, et al. (1991) Tracer feasibility for monitoring tumor radiotherapy: a quadruple tracer study with 18F-fluoro-deoxy-glucose or 18F-fluoro-deoxyuridine, L-methyl-[14C]-methionine, 6-[3H]-thymidine and gallium-67. J Nucl Med 32:2118–2123

Kubota K, Yamada S, Kubota R, et al. (1992) Intratumoral distribution of 18F-fluoro-deoxy-glucose in vivo: high accumulation in macrophages and granulation tissues studied by micro-autoradiography. J Nucl Med 33:1972–1980

Kubota K, Kubota R, Yamada Y (1993) FDG accumulation in tumor tissue (editorial). J Nucl Med 34:419–421

Kunstaetter R, Wolkove N, Kreisman H, Cohen C, Frank H (1985) The solitary pulmonary nodule. Decision analysis. Med Decis Making 5:61–75

Laubenbacher C, Saumweber D, Wagner-Manslau C, et al. (1995a) Comparison of fluorine-18-fluorodeoxyglucose PET, MRI and endoscopy for staging head and neck squamous-cell carcinomas. J Nucl Med 36:1747–1757

Laubenbacher C, Hofer C, Avril N, Block T, Ziegler S, Herz M, Kruschke C, Hartung R, Schwaiger M (1995b) F-18 FDG PET for differentiation of local recurrent prostate cancer and scar. J Nuc Med 36:198P

Lai DT, Fulham M, Stephen MS, Chu KM, Solomon M, Thompson JF, Sheldon DM, Storey DW (1996) The role of whole-body positron emission tomography with [18F]fluorodeoxyglucose in identifying operable colorectal cancer metastases to the liver. Arch Surg 131:703–707

Larcos G, Maisey MN (1996) FDG-PET screening for cerebral metastases in patients with suspected malignancy. Nucl Med Commun 17:197–198

Leskinen-Kallio S, Ruotsalainen U, Nagren K, et al. (1991) Uptake of carbon-11-methionine and fluorodeoxyglucose in non-Hodgkin's lymphoma: a PET study. J Nucl Med 32:1211–1218

Lindholm P, Leskinen-Kallio S, Minn H, et al. (1993) Comparison of fluorine-18-fluorodeoxyglucose and carbon-11-methionine in head and neck cancer. J Nucl Med 34:1711–1716

Lowe VJ, Duhaylongsod FG, Patz EF, et al. (1997) Pulmonary abnormalities and PET data analysis: a retrospective study. Radiology 202:435–439

Lowe VJ et al. (1998) J Clin Oncol. 1998 Mar; 16(3):1075–1084

Majhail NS, Urbain JL, Albani JM, Kanvinde MH, Rice TW, Novick AC, Mekhail TM, Olencki TE, Elson P, Bukowski RM (2003) F-18 fluorodeoxyglucose positron emission tomography in the evaluation of distant metastases from renal cell carcinoma. J Clin Oncol 21:3995–4000

McLoud TC, Bourgouin PM, Greenberg RW, et al. (1992) Bronchogenic carcinoma: analysis of staging in the mediastinum with CT by correlative lymph node mapping and sampling. Radiology 182:319–323

Minn H, Zasadny KR, Quint LE, Wahl RL (1995) Lung cancer: reproducibility of quantitative measurements for evaluating 2-[F-18]-fluoro-2-deoxy-D-glucose uptake at PET. Radiology 196:167–173

Miyauchi T, Wahl RL (1996) Regional 2-[18F]fluoro-2-deoxy-D-glucose uptake varies in normal lung. Eur J Nucl Med 23:517–523

Moog F, Bangerter M, Diederichs CG, et al. (1997) Lymphoma: role of whole-body FDG-PET in nodal staging. Radiology 203:795–800

Moon DH, Hoh CK, Silverman DS, et al. (1998) Accuracy of whole body FDG PET for the detection of recurrent or metastatic breast carcinoma. J Nucl Med 39:431–435

Newman JS, Francis IR, Kaminski MS, Wahl RL (1994) Imaging of lymphoma with PET with 2-[18F]fluoro-2-deoxy-D-glucose: correlation with CT. Radiology 190:111–116

Nieweg OE, Kim EE, Wong WH, et al. (1993) Positron emission tomography with fluorine-18-deoxy-glucose in the detection and staging of breast cancer. Cancer 71:3920–3925

Nuutinen JM, Leskinen S, Elomaa I, Minn H, et al. (1997) Detection of residual tumours in postchemotherapy testicular cancer by FDG-PET. Eur J Cancer 33:1234–1241

Ogunbiyi OA, Flanagan FL, Dehdashti F, et al. (1997) Detection of recurrent and metastatic colorectal cancer: comparison of positron emission tomography and computed tomography Ann Surg Oncol 48:613–620

Okada J, Yoshikawa K, Imazeki K, et al. (1991) The use of FDG-PET in the detection and management of malignant lymphoma: correlation of uptake with prognosis. J Nucl Med 32:686–691

Okada J, Yoshikawa K, Itami M, et al. (1992) Positron emis-

sion tomography using fluorine-18-fluorodeoxyglucose in malignant lymphoma: a comparison with proliferative activity. J Nucl Med 33:325–329

Palmedo H, Bender H, Grunwald F, et al. (1997) Comparison of fluorine-18 FDG PET and technetium-99m MIBI scintimammography in the detection of breast tumours. Eur J Nucl Med 24:1138–1145

Paul R (1987) Comparison of fluorine-18-2 fluorodeoxyglucose and gallium 67 citrate imaging for detection of lymphoma. J Nucl Med 28:288–292

Phelps ME, Mazziotta JC, Schelbert HR (eds) (1986) Positron emission tomography and autoradiography: principal applications for the brain and the heart. Raven Press, New York

Pieterman RM, van Putten JW, Meuzelaar JJ, Mooyaart EL, Vaalburg W, Koeter GH, et al. (2000) Preoperative staging of non-small-cell lung cancer with positron-emission tomography. N Engl J Med 343:254–261

Pirotte B, Goldman S, Bidaut LM, et al. (1995) Use of PET in stereotactic conditions for brain biopsy. Acta Neurochir 134:79–82

Price P (1997) Is there a future for PET in oncology ? Eur J Nucl Med 24:587–589

Ramdave S, Thomas GW, Berlangieri SU, Bolton DM, Davis I, Danguy HT, Macgregor D, Scott AM (2001) Clinical role of F-18 fluorodeoxyglucose positron emission tomography for detection and management of renal cell carcinoma. J Urol 166:825–830

Rege SD, Chaiken L, Hoh CK, et al. (1993a) Change induced by radiation therapy in FDG uptake in normal and malignant structures of the head and neck: quantitation with PET. Radiology 189:807–812

Rege SD, Hoh CK, Glaspy JA, et al. (1993b) Imaging of pulmonary mass lesions with whole-body positron emission tomography and fluorodeoxyglucose. Cancer 72:82–90

Reinhardt MJ, Muller-Mattheis VG, Gerharz CD, et al. (1997) FDG-PET evaluation of retroperitoneal metastases of testicular cancer before and after chemotherapy. J Nucl Med 38:99–101

Reisser C, Haberkorn U, Strauss LG (1993) The relevance of positron emission tomography for the diagnosis and treatment of head and neck tumors. J Otolaryng 22:231–238

Reske SN, Grillenberger KG, Glatting G, et al. (1997) Overexpression of glucose transporter 1 and increased FDG uptake in pancreatic carcinoma. J Nucl Med 38:1344–1348

Rigo P, Paulus P, Kaschten BJ, et al. (1996) Oncological applications of positron emission tomography with fluorine-18 fluorodeoxyglucose. Eur J Nucl Med 23:1641–1674

Ruhlmann J, Schomburg A, Bender H, et al. (1997) Fluorodeoxyglucose whole-body positron emission tomography in colorectal cancer patients studied in routine daily practice. Dis Colon Rectum 40:1195–204

Safaei A, Figlin R, Hoh CK, Silverman DH, Seltzer M, Phelps ME, Czernin J (2002) The usefulness of F-18 deoxyglucose whole-body positron emission tomography (PET) for restaging of renal cell cancer. Clin Nephrol 57:56–62

Sasaki M, Ichiya Y, Kuwabara Y, Akashi Y, Yoshida T, Fukumura T, Murayama S, Ishida T, Sugio K, Masuda K (1996) The usefulness of FDG positron emission tomography for the detection of mediastinal lymph node metastases in patients with non-small cell lung cancer: a comparative study with X-ray computed tomography. Eur J Nucl Med 23:741–747

Scheidhauer K, Scharl A, Pietrzyk U, et al. (1996) Qualitative [18F]FDG positron emission tomography in primary breast cancer: clinical relevance and practicability. Eur J Nucl Med 23:618–623

Schiepers C, Penninckx F, De Vadder N, et al. (1995) Contribution of PET in the diagnosis of recurrent colorectal cancer: comparison with conventional imaging. Eur J Surg Oncol 21:517–522

Schiepers C (1997) Role of positron emission tomography in the staging of lung cancer. Lung Cancer 17:S29–S35

Schirrmeister H, Kuhn T, Guhlmann A, Santjohanser C, Horster T, Nussle K et al. (2001) Fluorine-18 2-deoxy-2-fluoro-D-glucose PET in the preoperative staging of breast cancer: comparison with the standard staging procedures. Eur J Nucl Med 28(3):351–358.

Schoder H, Yeung HW (2004) Positron emission imaging of head and neck cancer, including thyroid carcinoma. Semin Nucl Med 34:180–197

Scott WJ, Schwabe JL, Gupta NC et al. (1994) PET of lung tumors and mediastinal lymph nodes using FDG. Ann Thorac Surg 58:698–703

Shreve PD, Grossman HB, Gross MD, Wahl RL (1996) Metastatic prostate cancer: initial findings of PET with 2-deoxy-2-[18F]fluoro-D-glucose. Radiology 199:751–756

Sisson JC, Ackermann RJ, Meyer MA, Wahl RL (1993) Uptake of 18-fluoro-2-deoxy-D-glucose by thyroid cancer: implications for diagnosis and therapy. J Clin Endo and Metab 77:1090–1094

Smith IC, Ogston KN, Whitford P, et al. (1998) Staging of the axilla in breast cancer: accurate in vivo assessment using positron emission tomography with 2- fluorine-18-fluoro-2-deoxy-D-glucose. Ann Surg 228:220–227

Steinert HC, Huch Boni RA, Buck A, et al. (1995) Malignant melanoma: staging with whole-body PET and FDG. Radiology 195:705–709

Steinert HC, Hauser M, Allemann F, et al. (1997) Non-small cell lung cancer: nodal staging with FDG PET versus CT with correlative lymph node mapping and sampling. Radiology 202:441–446

Stephens AW, Gonin R, Hutchins GD, Einhorn LH (1996) Positron emission tomography evaluation of residual radiographic abnormalities in postchemotherapy germ cell tumor patients. J Clin Oncol 14:1637–1641

Stollfuss JC, Glatting G, Friess H, Kocher F, Berger HG, Reske SN (1995) 2-(Fluorine-18)-fluoro-2-deoxy-D-glucose PET in detection of pancreatic cancer: value of quantitative image interpretation. Radiology 195:339–344

Strauss LG, Clorius JH, Schlag P, et al. (1989) Recurrence of colorectal tumors: PET evaluation. Radiology 170:329–323

Stuckensen T, Kovacs AF, Adams S, Baum RP (2000) Staging of the neck in patients with oral cavity squamous cell carcinomas: a prospective comparison of PET, ultrasound, CT and MRI. J Craniomaxillofac Surg 28:319–324

Stumpe KD, Urbinelli M, Steinert HC, Glanzmann C, Buck A, von Schulthess GK (1998) Whole-body positron emission tomography using fluorodeoxyglucose for staging of lymphoma: effectiveness and comparison with computed tomography. Eur J Nucl Med 25:721–728

Swisher SG, Maish M, Erasmus JJ, Correa AM, Ajani JA, Bresalier R, Komaki R, Macapinlac H, Munden RF, Putnam JB, Rice D, Smythe WR, Vaporciyan AA, Walsh GL, Wu TT, Roth JA (2004) Utility of PET, CT, and EUS to identify pathologic responders in esophageal cancer. Ann Thoracic Surg 78:1152–1160

Utech CI, Young CS, Winter PF (1996) Prospective evaluation of fluorine-18 fluorodeoxyglucose positron emission tomography in breast cancer for staging of the axilla related to surgery and immunocytochemistry. Eur J Nucl Med 23:1588–1593

Valk PE, Pounds, TR, Hopkins DM, et al. (1995) Staging lung cancer by PET imaging. Ann Thor Surg 60:1573–1581

Valk PE (1996) Sense and sensitivity: issues in technology assessment [editorial]. J Nucl Med 37:1436–1437

Valk PE, Pounds TR, Tesar RD, Hopkins DM, Haseman MK (1996) Cost-effectiveness of PET imaging in clinical oncology. Nucl Med Biol 23:737–743

Valk PE, Abella-Columna E, Haseman MK, Pounds TR, Tesar RD, Myers RW, Greiss HB, Hofer GA (1999) Whole-body PET imaging with [18F]fluorodeoxyglucose in management of recurrent colorectal cancer. Arch Surg 134:503-511

Vansteenkiste JF, Stroobants SG, De Leyn PR, et al. (1998) Lymph node staging in non-small-cell lung cancer with FDG-PET scan: a prospective study on 690 lymph node stations from 68 patients. J Clin Oncol 16:2142–2149

Vansteenkiste JF, Mortelmans LA (1999) FDG-PET in the Locoregional Lymph Node Staging of Non-small Cell Lung Cancer. A Comprehensive Review of the Leuven Lung Cancer Group Experience. Clin Positron Imaging 2(4):223–231.

van Tinteren H, Hoekstra OS, Smit EF, van den Bergh JH, Schreurs AJ, Stallaert RA, et al. (2002) Effectiveness of positron emission tomography in the preoperative assessment of patients with suspected non-small-cell lung cancer: the PLUS multicentre randomised trial. Lancet 359:1388–1393

Verboom P, van Tinteren H, Hoekstra OS, Smit EF, van den Bergh JH, Schreurs AJ, et al. (2003) Cost-effectiveness of FDG-PET in staging non-small cell lung cancer: the PLUS study. Eur J Nucl Med Mol Imaging 30:1444–1449

Wagner JD, Schauwecker D, Hutchins G, Coleman JJ 3rd (1997) Initial assessment of positron emission tomography for detection of non palpable regional lymphatic metastases in melanoma. J Surg Oncol 64:181–189

Wahl RL, Cody RL, Hutchins G, Mudgett E (1991) Positron emission tomographic scanning of primary and metastatic breast with the radiolabeled glucose analogue 2-deoxy-2[18F]fluoro-D-glucose [letter]. N Engl J Med 324:200

Wahl RL, Quint LE, Greenough RL, Meyer CR, White RI, Orringer MB (1994) Staging of mediastinal non-small cell lung cancer with FDG PET, CT, and fusion images: preliminary prospective evaluation. Radiology 191:371–377

Wahl RL (1997a) Clinical oncology update: the emerging role of PET: Part I. Update to: DeVita VT, Hellman S, Rosenberg SA (eds) Cancer: principles and practice of oncology, vol. 11(1). Lippincott-Raven, Philadelphia, pp 1–18

Wahl RL (1997b) Clinical oncology update: the emerging role of PET: part II. Update to: DeVita VT, Hellman S, Rosenberg SA (eds) Cancer: principles and practice of oncology, vol. 11(2). Lippincott-Raven, Philadelphia, pp 1–24

Wahl RL, Siegel BA, Coleman RE, Gatsonis CG (2004) Prospective multicenter study of axillary nodal staging by positron emission tomography in breast cancer: a report of the staging breast cancer with PET Study Group. J Clin Oncol 22:277–285

Warburg O (1931) The metabolism of tumors. Richard R. Smith, Inc.; New York, pp 129–169

Warburg O (1956) On the origins of cancer cells. Science 123:309–314

Webb WR, Gatsonis C, Zeerhouni EA et al. (1991) CT and MR imaging in staging non-small cell bronchogenic carcinoma: report of the Radiological Diagnostic Oncology Group. Radiology 178:705–713

Wong WL, Chevretton EB, McGurk M, et al. (1997) A prospective study of PET-FDG imaging for the assessment of head and neck squamous cell carcinoma. Clin Otolaryngol 22:209–214

Wong RJ, Lin DT, Schoder H, Patel SG, Gonen M, Wolden S, et al. (2002) Diagnostic and prognostic value of [(18)F]fluor odeoxyglucose positron emission tomography for recurrent head and neck squamous cell carcinoma. J Clin Oncol 20:4199–4208

Yao WJ, Hoh CK, Hawkins RA, et al. (1995) Quantitative PET imaging of bone marrow glucose metabolic response to hematopoietic cytokines. J Nucl Med 36:794–799

Yeh SD, Imbriaco M, Larson SM, et al. (1996) Detection of bony metastases of androgen-independent prostate cancer by PET-FDG. Nucl Med Biol 23:693–697

Zasadny KR, Wahl RL (1993) Standardized uptake values of normal tissues at PET with 2-[18F]-fluoro-2-deoxy-D-glucose: variations with body weight and a method for correction. Radiology 189:847–850

12 PET/CT in Lung, Head and Neck Cancer

Hans C. Steinert, Gerhard Goerres, and Gustav K. von Schulthess

CONTENTS

12.1 General Aspects of PET/CT

12.1.1 Clinical Protocols of PET/CT

As PET/CT is a novel technology, the clinical protocols in PET/CT are subject to fast evolution. At our institution we routinely give diluted bowel contrast agent 1 h prior to scanning (Dizendorf et al. 2002) followed by supine FDG injection and patient rest of at least 45 min. After bladder voiding just prior to scanning, we first perform a low-dose CT scan at 40 mAs (Hany et al. 2002a). This covers 100 cm of axial field of view in less than 30 s with a slice thickness of 4.5 mm, which is matched to the PET slice thickness. The CT scanner is a state of the art four-slice CT (GE Medical Systems, Milwaukee, Wisconsin) with a gantry rotation of 0.5" minimum. Extensive evaluation of the CT breath hold breathing pattern best matching the free breathing pattern of PET data acquisition, has led us to conclude that an unforced end-expiratory state is best during the period where the CT images the regions adjacent to the diaphragm (Goerres et al. 2002a). Thus patients are instructed to expire and hold their breath when the CT scanner scans this body region. CT scanning is accomplished in less than 30 s. Subsequently, PET scanning is started from the pelvis up. PET scanning is performed using six to seven table positions. As the PET scanner covers an axial field of view of around 15 cm with 32 slices per table position, roughly 90–105 cm of the patient is covered, which includes the anatomic regions from the brain to the upper thighs in almost all patients. With table position imaging times of 3–4 min, typical scan length of a PET/CT partial body scan covering the patient from the head to the mid upper thighs is 20–30 min.

After this "baseline" PET/CT data acquisition, additional standard CT protocols can be run depending upon the clinical requirements. It is desirable in some settings to also perform a CT scan enhanced with intravenous contrast, which can better delineate the lesions in relation to vascular structures. The overall protocol design for such all-encompassing PET/CT examinations is not defined and the next years will have to tell where and when additional contrast enhanced CT scanning is useful. Other groups have advocated the use of i.v. contrast enhanced CT scans from the beginning and as only CT scan. It is our opinion, that this is less than optimal for two reasons. First, in many settings, CT contrast is not needed, as FDG is mostly a much better "contrast agent" than the contrast agents used in CT. Second, vascular contrast, which for vessel delineation is dense and transient, causes the CT data not to be ideal attenuation maps for the subsequent PET scan. It has to be emphasized that iodinated contrast behaves in such a way that it can be difficult to use

H. C. Steinert, MD; G. Goerres, MD;
G. K. von Schulthess, MD, PhD
Nuclear Medicine, Department of Medical Radiology,
University Hospital of Zurich, 8091 Zurich, Switzerland

a scan enhanced with intravenous contrast agent for attenuation correction (Dizendorf et al. 2003). Iodine looks like bone at 80–140 keV, but like soft tissue at 511 keV. Thus, the Hounsfield Unit transformation used for attenuation correction of the PET scan may not work consistently without segmenting the vessels out of the CT and replacing the vessels with soft tissue density on the CT data.

12.1.2 Critical Appraisal of Clinical PET/CT

Clinical experience with PET/CT is currently limited. However, after performing approximately 5000 clinical scans, we can confidently appraise at least some aspects of clinical PET/CT.

PET/CT is easy to use and in the overwhelming number of patients, image co-registration is excellent. This is probably due to the fact that oncology patients, who represent the major patient group imaged, are generally cooperative. To our surprise, routine availability of an anatomic reference frame has led to the identification of various pitfalls not fully appreciated in PET prior to the introduction of PET/CT. The superimposition of an FDG avid focus onto an anatomically identifiable structure makes the image interpreter more confident of what he sees and reduces interobserver variability. This also applies to the use of PET/CT data in radiation planning. The software infrastructure has now been developed which permits transfer of PET and CT data into the planning environment of radiation oncologists by DICOM standard formats.

Viewing PET and CT images next to each other is not adequate for lesion localization once lesions are below 1.5 cm, and it is particularly in such lesions, where PET excels and where standard morphological criteria of malignancy in CT no longer are very useful. Thus co-registration and fusion or linked cursor viewing are mandatory. All currently available data suggest that the software approach is at least logistically difficult and obviously does not provide easily accessible data for attenuation correction.

Any new modality has also new artifacts and pitfalls. The most relevant artifact identified so far is misregistration around the diaphragm (Goerres et al. 2002a). This can lead to abdominal lesions apparently located in the supradiaphragmatic lung zones and a photon deficit of variable importance overlying the diaphragmatic domes and looking like "bananas" on the coronal CT attenuation corrected PET scans. A second artifact, which may be more prominent in CT corrected PET scans than PET scans corrected with the standard transmission scan methods, is that arising around metallic implants (Goerres et al. 2002b; Kamel et al. 2003a). Slight misregistrations can lead to overcorrections, which then result in focal or linear regions of apparently increased FDG uptake. The last artifact comes from major misregistration due to patient motion between the acquisition of the two scans.

12.2 PET/CT in Lung Cancer

The majority of PET imaging work has been done in non-small cell lung cancer. It has been shown that FDG PET is highly accurate in classifying lung nodules as benign or malignant. Whole-body PET improves the rate of detection of mediastinal lymph node metastases as well as extrathoracic metastases when compared to conventional imaging methods, such as CT, MR, ultrasound or bone scan. Since commercial PET scanners provide nominal spatial resolution of 4.5–6 mm in the center of the axial field of view, even lesions less than 1 cm with an increased FDG uptake can be detected. This represents a critical advantage of PET over CT and MR. Integrated PET/CT enables the exact matching of focal abnormalities on PET to anatomic structures on CT. First clinical results show, that integrated PET/CT enables the exact matching of focal abnormalities on PET to anatomic structures on CT resulting in an increased diagnostic accuracy (Lardinois et al. 2003; Bar-Shalom et al. 2003; Antoch et al. 2003a).

12.2.1 Solitary Lung Nodule

The ability of PET to separate between benign and malignant lesions is high, but not perfect. For benign lesions, a high specificity for FDG PET has been demonstrated. It has been shown that FDG PET is highly accurate in differentiating malignant from benign solitary pulmonary nodules (0.6–3 cm) when radiographic findings were indeterminate (Gupta et al. 1996). In a series of 61 patients, PET had a sensitivity of 93% and a specificity of 88% for detecting malignancy. However, FDG PET may show negative results for pulmonary carcinoid tumors and bronchioloalveolar lung carcinoma. Lesions with increased FDG

uptake should be considered malignant, although false-positive results have been reported in cases of inflammatory and infectious processes, such as histoplasmosis, aspergillosis, or active tuberculosis. PET is clinically useful in patients with a solitary pulmonary nodule less than 3 cm in diameter, especially where biopsy may be risky or where the nodule carries a low risk for malignancy based on patients' history or radiographic findings. With integrated PET/CT an additional certainty to the presence or absence of FDG uptake in the pulmonary nodule can be achieved.

12.2.2 T Staging

Without image fusion, the use of PET in T staging lung cancer is limited. Recently, it has been shown that integrated PET/CT is superior to CT alone, PET alone, and visual correlation of PET and CT in T staging of patients with non-small cell lung cancer (Lardinois et al. 2003). Due to the exact anatomic correlation of the extent of FDG uptake, the delineation of the primary tumor can be defined precisely. Therefore the diagnosis of chest wall infiltration and the mediastinal invasion by the tumor is improved. Lesions with chest wall infiltration are classified as stage T3 and are potentially resectable. Integrated PET/CT provides important information on mediastinal infiltration too. However, PET/CT imaging is unable to distinguish contiguity of tumor with the mediastinum from the direct invasion of the walls of mediastinal structures. It has been shown that FDG PET is a useful tool for the differentiation between tumor and peritumoral atelectasis. This is particularly important for the planning of radiotherapy in patients with lung cancer associated with an atelectasis. The information provided by FDG PET results in a change in the radiation field in approximately 30%–40% of patients (Nestle et al. 1999).

12.2.3 N Staging

PET has proven to be a very effective staging modality for mediastinal nodal staging (Steinert et al. 1997; Vansteenkiste et al. 1998; Dwamena et al. 1999; Pieterman et al. 2000; Hellwig et al. 2001). CT and MR imaging are limited in depicting small mediastinal lymph node metastases. Several studies have demonstrated that FDG PET is significantly more accurate than CT in determination of nodal status. In our own study, PET assigned the correct N stage in 96% of cases, CT was correct in 79% of cases (Lardinois et al. 2003). A meta-analytic comparison of PET and CT in mediastinal staging of NSCLC was performed (Dwamena et al. 1999). The mean sensitivity and specificity (±95% CI) were 0.79±0.03 and 0.91±0.02, respectively, for PET and 0.60±0.02 and 0.77±0.02, respectively, for CT. These results were confirmed in another meta-analysis with a total of more than 1000 patients (Hellwig et al. 2001).

Even if mediastinoscopy remains the gold standard for mediastinal staging, not all mediastinal lymph nodes can be routinely accessed by mediastinoscopy, particularly in the para-aortic region and in aorto-pulmonary window. The limited view through the scope and the single direction in which biopsies can be carried out prevents 100% accuracy. The accuracy of mediastinoscopy is approximately 90% and is surgeon dependent (Patterson et al. 1987). It has been demonstrated that PET is useful to assist mediastinoscopy (Fig. 12.1). Due to the knowledge from the PET scan, mediastinoscopy revealed additional mediastinal disease in 6% of patients (Kerstine et al. 2002).

Exact allocation of focal abnormalities on PET to specific lymph nodes is difficult or even impossible due to the poor anatomic information provided by PET alone. The presence and site of lymph node metastases should be recorded according to the revised American Thoracic Society lymph node station-mapping system (Mountain and Dresler 1997). In patients with bulky mediastinal disease or multilevel nodal involvement the assessment of N stage is easy. However, the exact localization of lymph node metastases in the hilum is difficult. Lymph nodes distal to the mediastinal pleural reflection and within the visceral pleura are classified as N1 nodes. Lymph nodes within the mediastinal pleural envelope are classified as N2 nodes. Because the pleura is visible neither in CT nor in PET the exact classification of a hilar lesion as a N1 node or N2 node remains difficult. The difficulty of PET is the localization of small single nodes, particularly in patients with a mediastinal shift due to atelectasis or anatomical variants. In our experience, integrated PET/CT imaging will become the new standard of mediastinal staging. The high reliability of integrated PET/CT in the exact localization of extrathoracic vs. intrathoracic and mediastinal vs. hilar lymph nodes might have very important therapeutic implications.

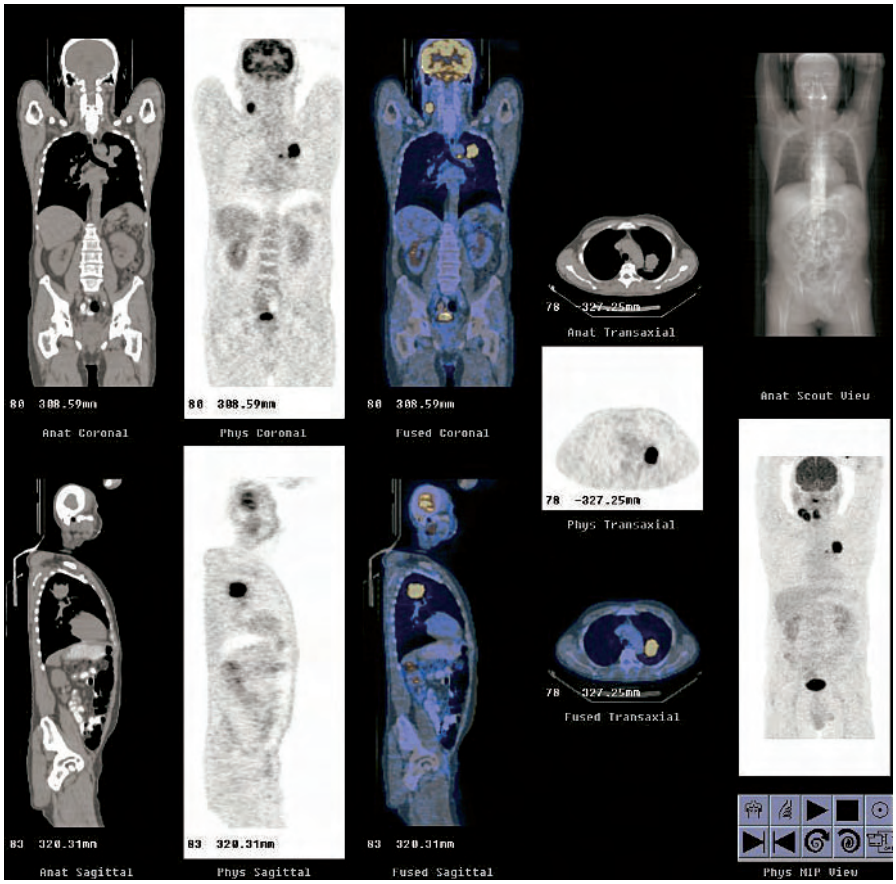

a

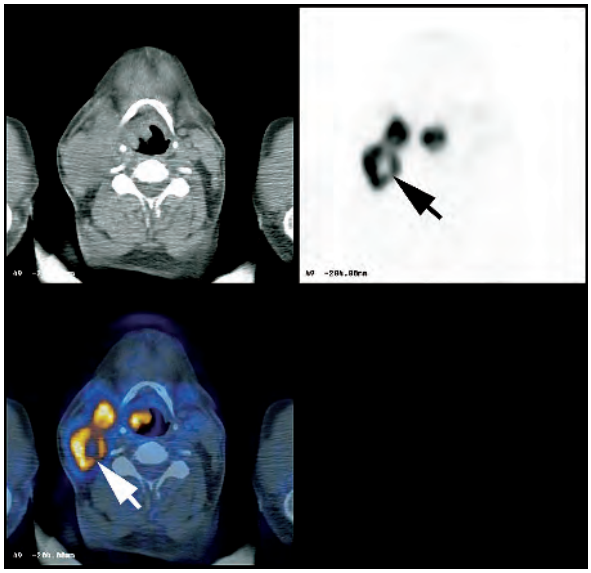

b

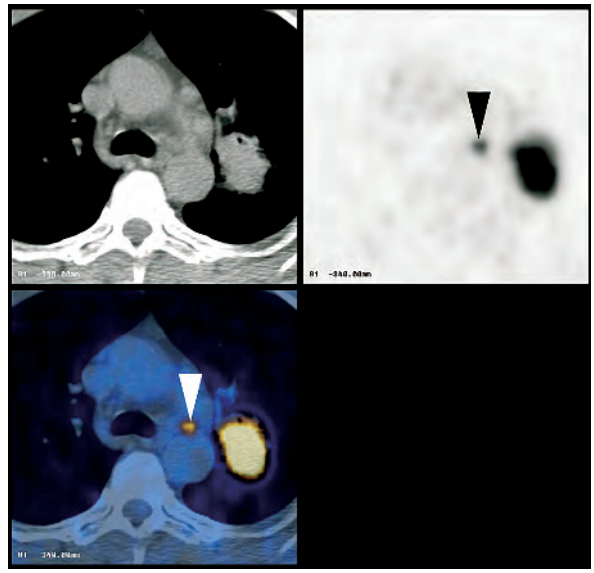

c

Fig. 12.1a–c. Whole-body PET/CT examination of a 50-year-old male patient who had been suffering hoarseness and a swallowing disorder for 6 weeks. Full screen with maximum intensity projection, CT, PET, and PET/CT scans (**a**). PET/CT reveals a supraglottic laryngeal cancer with ipsilateral lymph node metastases. There is central necrosis in an enlarged lymph node (**b**; *white* and *black arrows*). This was a G1 cT2 N2b squamous cell carcinoma. The patient underwent supraglottic partial laryngectomy with radical neck dissection. In the same PET/CT examination a bronchogenic cancer was found with ipsilateral lymph node metastasis in the aortic-pulmonary window (**c**; *white* and *black arrowheads*). This was a pT2 pN2 squamous cell carcinoma of the left upper lung lobe. The patient underwent resection of the upper lung lobe and mediastinal lymph nodes 3 weeks later. After surgery the patient was scheduled for subsequent combined radiation and chemotherapy

Until now, our group used non-enhanced CT scans for integrated PET/CT imaging. We could not ethically justify the use of vascular contrast material because all patients had a conventional contrast enhanced CT for staging before the PET/CT. In non-enhanced CT scans delineation of vessels was considerably poorer than with contrast enhancement or impossible. However, in our patient series non-enhanced PET/CT scans are sufficient for planning surgery in approximately 80% of patients. Further evaluation is necessary to define conditions in which the application of intravascular contrast material might have an additional diagnostic impact in integrated PET/CT imaging. However, regarding infiltration of hilar and mediastinal vessels, a relatively low sensitivity, specificity, and accuracy (68%, 72%, and 70%, respectively) of conventional CT scan with contrast enhancement has been observed (Rendina et al. 1987).

Microscopic foci of metastases within very small lymph nodes cannot be detected with any imaging modality. If there is no increased FDG uptake in PET, integrated PET/CT will not provide further information based on FDG accumulation. It has been reported that FDG PET after induction therapy is less accurate in mediastinal staging than in staging of untreated NSCLC (Akhurst et al. 2002). PET over-staged nodal status in 33% of patients, understaged nodal status in 15%, and was correct in 52%. Future studies are required to correlate FDG PET before and after treatment.

12.2.4 M Staging

Whole-body FDG PET is an excellent method to screen for extrathoracic metastases (Weder et al. 1998). In a meta-analysis of 581 patients, sensitivity, specificity, and accuracy of FDG PET were 94%, 97% and 96%, respectively (Hellwig et al. 2001). Current imaging methods are inadequate for accurate M staging of patients. PET detects unexpected extrathoracic metastases in 10%–20% of patients and changes therapeutic management in about 20% of patients. FDG PET is more accurate than CT in the evaluation of adrenal metastases (Erasmus et al. 1997). Marom et al. (1999) compared the accuracy of FDG PET to conventional imaging in 100 patients with newly diagnosed NSCLC. Comparing bone scintigraphy and FDG PET in detecting bone metastases, the accuracy was 87% and 98%, respectively. All hepatic metastases were correctly identified with PET and CT. With CT, however, benign liver lesions were over-staged as metastases, thus accuracy of PET was superior to CT in the diagnosis of liver metastases.

The clinical significance of a single focal abnormality on PET remains unclear, especially when no morphological alterations occur on CT images. The advantage of integrated PET/CT imaging is the exact localization of a focal abnormality on PET. This was the case in 20% of all patients with extrathoracic metastases in our study on the value of integrated PET/CT (Lardinois et al. 2003).

12.2.5 Recurrent Lung Cancer

A very high accuracy of FDG PET in distinguishing recurrent disease from benign treatment effects has been shown. If PET images demonstrate areas of tumor viability, they can direct biopsy for pathologic confirmation. Patients should be evaluated a minimum of 2 months after completion of therapy. Otherwise post-therapeutic healing processes or radiation pneumonitis may result in false positive PET findings. These abnormal findings return to normal at variable times without further intervention. In the experience of Inoue et al. (1995) a curvilinear contour of increased FDG accumulation was seen mostly in inflammatory lesions, while focal nodular uptake was seen mostly in recurrent tumors. Their data suggest that FDG PET can be clinically used for selecting biopsy sites because of its high sensitivity in detecting recurrent lung cancer.

12.2.6 Pitfalls

False negative FDG PET results have been reported in pulmonary carcinoid tumors and in bronchiolo-alveolar carcinomas. Some active infectious or inflammatory lesions may have an increased FDG uptake. Tuberculosis, eosinophilic lung disease, histoplasmosis, aspergillosis and other infections may have a significant uptake of FDG (Strauss 1996). Furthermore, sarcoid shows a typical bilateral relatively symmetric hilar uptake pattern. Therefore, lesions with an increased FDG accumulation should be histologically confirmed. However, most chronic inflammatory processes do not significantly take up FDG.

It is well known that active muscles accumulate FDG. In some patients with lung cancer an intense focal FDG accumulation is seen in the lower anterior neck just lateral to the midline. Co-registered PET/

CT images revealed that the focal FDG uptake was localized in the internal laryngeal muscles (Kamel et al. 2002). This finding is a result of compensatory laryngeal muscle activation caused by contralateral recurrent laryngeal nerve palsy due to direct nerve invasion by lung cancer of the left mediastinum or lung apices (Hany et al. 2002).

FDG accumulation in brown adipose tissue can easily be identified and discriminated from muscle uptake or a soft tissue mass using co-registered PET-CT.

12.2.7 Small Cell Lung Cancer

The staging procedures for SCLC do not differ from those for NSCLC. The primary role of imaging is to separate accurately limited disease (LD) from extended disease (ED). Based upon the widespread dissemination of SCLC, a battery of imaging tests is performed such as CT of the chest and abdomen, CT or MRI of the brain and a bone scan. Recently, it has been shown that whole-body FDG PET is a useful tool for staging SCLC (Kamel et al. 2003b). FDG PET is superior to conventional staging in the detection of all involved sites, and particularly in the assessment of mediastinal lymph node metastases. Our first experience demonstrated that integrated PET/CT imaging in SCLC is a highly valuable tool for planning radiation treatment. It is useful for accurate target definition by reducing the probability of overlooking involved areas.

12.2.8 Malignant Pleural Mesothelioma

Similarly to lung cancer, excellent FDG uptake in malignant pleural mesothelioma (MPM) has been previously described (Marom et al. 2002). Schneider et al. (2000) demonstrated that PET is particularly valuable for distinguishing between benign and malignant pleural processes. FDG is not taken up in pleural fibrosis, thus differential diagnosis of the pleural lesions is possible. PET imaging is useful in localizing the areas involved with MPM. However, PET and CT are unable to differentiate MPM from pleural adenocarcinoma, so that histology is needed for confirmation.

The role of PET is to document the extent of pleural disease, to establish mediastinal lymph node involvement, to evaluate tumor invasion, and to diagnose recurrence. Our experience demonstrates that integrated PET/CT imaging is an excellent method for staging patients with MPM. With the co-registration of anatomic and metabolic information, the extent of the tumor can be precisely defined. Small mediastinal lymph node metastases can be detected and precisely localized. Integrated PET/CT imaging is helpful to identify the optimal biopsy site thereby increasing diagnostic accuracy of the histological examination.

12.3 PET/CT in Head and Neck Cancer

In head and neck oncology, precise identification and localization of a lesion is frequently decisive, as many patients undergo surgical treatment after the PET and CT examinations. Therefore, availability of co-registered images is useful and sometimes critical. The combination of PET and CT is helpful for staging and treatment planning as shown in recent reports (Giraud et al. 2001; Kluetz et al. 2000).

12.3.1 Staging

In most patients with squamous cell carcinoma of the head and neck (HNSCC) a staging PET examination will be done after having obtained cytological/ histological proof of the cancer. In many patients the extent of a lesion can be reliably assessed with clinical evaluation. In most regions of the head and neck the T stages T1, T2, and T3 describe lesions with increasing size. In all regions a T4 stage describes a carcinoma invading into adjacent structures such as bone, cartilage, deep muscles, or vessels and nerve sheaths.

It has been questioned whether PET alone is suitable for routine evaluation of head and neck cancer patients, because of the lack of anatomic information (Keyes et al. 1997). T staging needs anatomic information and the possibility to exactly measure tumor size. Furthermore, the precise identification, localization, and delineation of size and anatomic extent of a primary lesion is very important to correctly plan surgical interventions and radiation treatment. Based on our experience in many patients the information obtained by a PET scan read side-by-side together with a separate spiral contrast-enhanced CT scan is equivalent to the information obtained from a co-registered PET/CT scan without intravenous contrast. Some primaries or lymph node metastases will be missed on PET images due to the low resolution of

PET cameras and partial volume effects. Therefore, small lesions and lesions with a superficial growth pattern may be missed (Goerres et al. 2002c, 2004a). Some of these lesions will be identified with structural imaging methods. On the other hand, a primary can be missed with CT or MRI when located in an area with metal induced artifacts. Furthermore, it might be overlooked due to a small size and location in an anatomical area difficult to assess. However, early publications have shown that with image co-registration of PET with CT or MRI, one can better evaluate HNSCC (Chisin et al. 1993; Wong et al. 1996).

Because HNSCC mainly spreads regionally, the correct lymph node staging is the key to an optimal treatment strategy. In patients treated for oral cavity cancer and an N0 neck the 5-year survival will be 73%, in patients with pathologically positive lymph nodes 50%, and in patients with extracapsular spread of lymph node involvement 30% (Myers et al. 2001). For the assessment of loco-regional lymph node status, numerous publications have shown that PET has a higher sensitivity and specificity than contrast enhanced CT or MRI. However, contrast-enhanced CT, sonography, or MRI are routinely used for lymph node assessment, because precise anatomical localization of lesions is important for the planning of surgical treatment and radiation therapy. Therefore, the CT information facilitates the identification and correct localization of lymph nodes with an increased FDG uptake.

Patients with HNSCC have a high risk of developing secondary cancers in the head and neck, esophagus or lung. Léon et al. (1999) reported an incidence to develop a second neoplasm of 4% per year. The incidence of distant metastases depends on the primary site of the lesion and the stage of disease at the time of first diagnosis. An advantage of the PET/CT technique is the ability to provide whole-body scanning in one imaging session. Several studies have suggested that imaging of the whole-body can have an impact on further treatment decisions by detecting distant metastases or secondary cancers (Goerres et al. 2003; Kitagawa et al. 2002; Schwartz et al. 2003; Stokkel et al. 1999; de Bree et al. 2000). Most secondary cancers observed in HNSCC patients, such as bronchogenic cancer and carcinomas of the esophagus, show a high FDG uptake (Fig. 12.1). Therefore, whole-body PET is a good imaging tool to also identify these secondary malignancies. Whole-body PET or PET/CT for screening of distant metastases seems to be most useful in patients with advanced stage HNSCC. Because secondary carcinomas are not only a problem at initial staging but may arise during the later disease course, whole-body imaging can be recommended for follow-up examinations.

12.3.2 Treatment Planning

PET/CT data have been shown to improve staging and treatment planning (Hany et al. 2002a; Kluetz et al. 2000). The co-registration of PET and CT data sets as acquired with routine clinical PET/CT studies is precise enough for the pre-surgical and pre-radiotherapeutic evaluation of patients. Intravenous contrast is important to assess the extension of a tumor and invasion into adjacent structures such as vessels. CT and MRI are currently acquired with intravenous contrast enhancement. However, small tumors and superficial mucosal lesions can be overlooked with morphological and functional imaging and some lesions may remain undetected on CT without intravenous contrast enhancement. Therefore, it is prudent to perform PET/CT with intravenous contrast enhancement if no additional CT scan is available. However, if the PET/CT data shall be used for radiation treatment planning, the CT scan has to be acquired without intravenous contrast enhancement and with a high enough mAs to reliably define attenuation values of the different tissues for dose calculations. The patient has to be positioned in exactly the same way during PET/CT as for the radiation treatment. With the co-registration PET information the radiation oncologist can better define the metabolically active tissue and adapt the target volume of the radiation field. It seems that this PET information influences the accuracy of target volume definition. However, to date no studies are available showing that adaptations of radiation therapy planning based on the area of increased FDG uptake improves local cancer control and outcome of the patient.

12.3.3 Follow-Up

At re-staging the most important question is to find out whether a patient can still be treated for example with salvage surgery for a locoregional problem or if the disease has spread systemically. Early after radiation treatment, edema and other post-therapeutic changes of the soft tissues can render the clinical evaluation of a patient difficult. Therefore,

structural imaging is most important in the follow-up of patients with HNSCC. Post-therapeutic soft tissue alterations may influence FDG uptake in the neck muscles and uptake in brown adipose tissue generating an asymmetric appearance. A common finding in patients undergoing follow-up PET/CT for HNSCC is the tracheotomy. It is important to insert a plastic tube before scanning to avoid metal induced artifacts in such patients. An increased FDG uptake at the borders of the tracheotomy due to inflammatory (post surgical) reaction is not uncommon and therefore additional clinical and other imaging information is needed for image interpretation in patients with suspected malignancy at this site (Goerres et al. 2002d). Common post-radiotherapy changes include inflammatory reactions of the mucosal membrane in the upper aerodigestive tract leading to increased FDG uptake. Such a reaction has usually normalized within a few weeks after the end of treatment. However, esophagitis and pharyngitis can be caused by fungal infection leading to increased FDG uptake (Goerres et al. 2002d). Some authors recommend waiting 4 months after completion of radiation treatment before scanning patients to identify residual cancer/early recurrence (Greven et al. 1994). However, it has been shown that already 6–8 weeks after the end of a combined chemotherapy and radiation treatment a reliable assessment of residual viable cancer tissue is possible with >90% sensitivity and specificity (Goerres et al. 2004b).

In difficult areas such as the base of the skull and in the paranasal sinuses with a wide range of morphological variants it is necessary to reliably co-register functional findings onto the structural findings in an individual patient. For imaging evaluation of the base of the skull MRI is often the first choice. However, future studies should clarify whether PET/CT has superior accuracy compared to MRI for the assessment of patients with carcinomas at the base of the skull and in the paranasal sinuses.

12.3.4 The Pros and Cons of PET/CT in Head and Neck Oncology

The ability to co-register PET data onto structural information facilitates the reading of images and speeds up image interpretation, because a lesion is reliably allocated to the correct anatomic region. For example, in a patient with muscle uptake, it is still possible to reliably identify FDG uptake in adjacent lymph nodes, because the lymph node is also anatomically delineated. FDG uptake facilitates the detection of cancer in non-enlarged lymph nodes or in lymph nodes which would have been missed on the CT image. Additionally, enlarged lymph nodes are often found on the CT but show no increased FDG uptake. Therefore, the correct localization of a lesion is easier with co-registered PET/CT than with PET read together with a separate CT. Physiological FDG accumulations such as in brown adipose tissue can easily be identified and discriminated from muscle uptake or a soft tissue mass, because on the co-registered CT image, this uptake will be localized within normal appearing fatty tissue (Hany et al. 2002b). Additionally, physiologic FDG uptake in normal lymphatic tissue of Waldeyer's ring and in the salivary glands may render interpretation of PET images difficult (Goerres et al. 2002d). PET/CT allows for the exact delineation of viable cancer tissue even in large lesions with necrotic areas. PET information may be used to guide interventions and improve planning of further treatment. The problems generated with the co-registration of data sets obtained by different devices at different time points such as patient repositioning can be overcome by using an integrated PET/CT scanner (Beyer et al. 2000). This is especially important when for example a lesion adjacent to the midline has to be assessed and it is not clear if this lesion crosses the midline or not. In this situation a reader may feel more confident with PET/CT images than with PET and contrast enhanced CT images read together side by side, because the area of edema around a lesion or contrast medium enhancement, respectively, may not correspond to the area of increased FDG uptake.

It has been shown that co-registered PET/CT improves whole-body staging of oncologic patients (Antoch et al. 2003b). Furthermore, a readers' confidence in image interpretation is improved and the number of equivocal findings decreases with PET/CT. More lesions will be judged either as positive or negative and the discrimination of benign from malignant lesions and thus the specificity is improved. However, based on our experience PET/CT and PET read together with (contrast enhanced) CT will identify an equal number of malignant lesions as long as FDG avid regions are examined.

Another important issue is the work-up time and patient scheduling. Because HNSCC are cancers that may grow very fast, it is very important to perform the different diagnostic steps efficiently. In busy centers patients often have to wait between the CT-

or MRI-scan and the PET examination. This supports the use of PET/CT for shortening the work-up of HNSCC patients.

The use of CT data for attenuation correction of PET emission scans has been established (Kinahan et al. 1998; Burger et al. 2002). CT based attenuation corrected PET scans can show some PET/CT specific artifacts in the head and neck area. Movement of the head between the PET and CT acquisition will lead to erroneous measurement of attenuation data with mistaken correction of PET emission data. Additionally, such movement will lead to misregistration ranging from slight to very severe image deterioration (Goerres et al. 2002d). However, the "intrinsic hardware" co-registration of both image data sets and the relatively fast acquisition provide high fusion accuracy. Co-registration of PET and CT data sets in the head and neck is possible to within only a few millimeters even in patients undergoing scanning without a face mask (Goerres et al. 2004c). However, in routine head and neck PET/CT imaging the major image quality degradation is due to metallic dental implants (Goerres et al. 2002b; Kamel et al. 2003a). Therefore, all artificial dentures and metal parts should be removed before scanning if possible.

12.4 Conclusion

In patients with HNSCC the combination of PET and anatomic information is indispensable. PET/CT offers many advantages in this patient group: it facilitates the interpretation of PET information and can offer adequate anatomic information to plan surgical interventions and radiation treatment. At staging and restaging, PET/CT improves identification of a lesion, allocation to the correct anatomic site and definition of the extension of a primary lesion. This is crucial in the complex anatomical situation of HNSCC patients especially in suspected recurrence.

The confidence of image interpretation is increased and images are read faster. Whole-body imaging can detect distant metastases and secondary tumors and, thus, influence patient management. However, future studies have to elucidate: (a) whether the CT portion of the PET/CT examination should always be done with a contrast agent, (b) the role of PET/CT for radiation treatment planning, and (c) if PET/CT can be cost-effective in defined patient groups.

References

Akhurst T, Downey RJ, Ginsberg MS et al (2002) An initial experience with FDG-PET in the imaging of residual disease after induction therapy for lung cancer. Ann Thorac Surg 73:259-266

Antoch G, Stattaus J, Nemat AT et al (2003a) Non-small cell lung cancer: dual modality PET/CT in preoperative staging. Radiology 229:526-533

Antoch G, Vogt FM, Freudenberg LS et al (2003b) Whole-body dual-modality PET/CT and whole-body MRI for tumor staging in oncology. JAMA 290:3199-3206

Bar-Shalom R, Yefremov N, Guralnik L et al (2003) Clinical performance of PET/CT in evaluation of cancer: additional value for diagnostic imaging and patient management. J Nucl Med 44:1200-1209

Beyer T, Townsend DW, Brun T et al (2000) A combined PET/CT scanner for clinical oncology. J Nucl Med 41:1369-1379

Burger C, Goerres G, Schoenes S, Buck A, Lonn AHR, von Schulthess GK (2002) PET attenuation coefficients from CT images: experimental evaluation of the transformation of CT into PET 511-keV attenuation coefficients. Eur J Nucl Med 29:922-927

Chisin R, Pietrzyk U, Sichel JY et al (1993) Registration and display of multimodal images: applications in the extracranial head and neck region. J Otolaryngol 22:214-219

De Bree R, Deurloo EE, Snow GB, Leemans CR (2000) Screening for distant metastases in patients with head and neck cancer. Laryngoscope 110:397-401

Dizendorf EV, Treyer V, von Schulthess GK, Hany TF (2002) Application of oral contrast media in co-registrated positron emission tomography-CT. Am J Roentgenol 179:477-481

Dizendorf E, Hany TF, Buck A, von Schulthess GK, Burger C (2003) Cause and magnitude of the error induced by oral CT contrast agent in CT-based attenuation correction of PET emission studies. J Nucl Med 44:732-738

Dwamena BA, Sonnad SS, Angobaldo JO, Wahl RL (1999) Metastases from non-small cell lung cancer: mediastinal staging in the 1990s - meta-analytic comparison of PET and CT. Radiology 213:530-536

Erasmus JJ, Patz EF, McAdams HP et al (1997) Evaluation of adrenal masses in patients with bronchogenic carcinoma using 18F-fluorodeoxyglucose positron emission tomography. AJR 168:1357-1362

Giraud P, Grahek D, Montravers F et al (2001) CT and (18)F-deoxyglucose (FDG) image fusion for optimization of conformal radiotherapy of lung cancers. Int J Radiat Oncol Biol Phys 49:1249-1257

Goerres GW, Kamel E, Heidelberg TN et al (2002a) PET-CT image co-registration in the thorax: influence of respiration. Eur J Nucl Med 29:351-60

Goerres GW, Hany TF, Kamel E, von Schulthess GK, Buck A (2002b) Head and neck imaging with PET and PET/CT: artefacts from dental metallic implants. Eur J Nucl Med 29:367-370

Goerres GW, Stoeckli SJ, von Schulthess GK, Steinert HC (2002c) FDG PET for mucosal malignant melanoma of the head and neck. Laryngoscope 112:381-385

Goerres GW, von Schulthess GK, Hany TF (2002d) Positron emission tomography and PET CT of the head and neck: FDG uptake in normal anatomy, in benign lesions, and in changes resulting from treatment. AJR 179:1337-1343

Goerres GW, Schmid DT, Gratz KW, von Schulthess GK, Eyrich GK (2003) Impact of whole body positron emission tomogra-

phy on initial staging and therapy in patients with squamous cell carcinoma of the oral cavity. Oral Oncol 39:547-551
Goerres GW, Schmid DT, Eyrich GK (2004a) Do hardware artifacts influence the performance of head and neck PET scans in patients with oral cavity squamous cell cancer? Dentomaxillofac Radiol 32:365-371
Goerres GW, Schmid DT, Bandhauer F et al (2004b) Positron emission tomography in the early follow-up of advanced head and neck cancer. Arch Otolaryngol Head Neck Surg 130:105-109
Goerres GW, von Schulthess GK, Steinert HC (2004c) Why most PET of lung and head-and-neck cancer will be PET/CT. J Nucl Med 45 [Suppl 1]:66S-71S
Greven KM, Williams DW, Keyes JW et al (1994) Positron emission tomography of patients with head and neck carcinoma before and after high dose irradiation. Cancer 74:1355-1359
Gupta NC, Maloof J, Gunel E (1996) Probability of malignancy in solitary pulmonary nodules using flurine-18-FDF and PET. J Nucl Med 37:943-948
Hany TF, Steinert HC, Goerres GW, Buck A, von Schulthess GK (2002a) Improvement of diagnostic accuracy of PET imaging using a high performance in-line PET-CT system: preliminary results. Radiology 225:575-581
Hany TF, Gharehpapagh E, Kamel EM, Buck A, Himms-Hagen J, von Schulthess GK (2002b) Brown adipose tissue: a factor to consider in symmetrical tracer uptake in the neck and upper chest region. Eur J Nucl Med 29:1393-1398
Hellwig D, Ukena D, Paulsen F, Bamberg M, Kirsch CM (2001) Metaanalyse zum Stellenwert der Positronen-Emissions-Tomographie mit F-18-Fluorodesoxyglukose (FDG-PET) bei Lungentumoren (in German). Pneumologie 55:367-377
Inoue T, Kim E, Komaki R et al (1995) Detecting recurrent or residual lung cancer with FDG-PET. J Nucl Med 36:788-793
Kamel E, Goerres GW, Burger C, von Schulthess GK, Steinert HC (2002) Detection of recurrent larygeal nerve palsy in patients with lung cancer using PET-CT image fusion. Radiology 224:153-156
Kamel EM, Burger C, Buck A, von Schulthess GK, Goerres GW (2003a) Impact of metallic dental implants on CT-based attenuation correction in a combined PET/CT scanner. Eur Radiol 13:724-728
Kamel EM, Zwahlen D, Wyss MT et al (2003b) Whole-body 18F-FDG PET improves the management of patients with small-cell lung cancer. J Nucl Med 44:1911-1917
Kernstine KH, McLaughlin KA, Menda Y et al (2002) Can-FDG PET reduce the need for mediastinoscopy in potentially resectable nonsmall cell lung cancer? Ann Thorac Surg 73:394-402
Keyes JW Jr, Watson NE Jr, Williams DW 3rd, Greven KM, McGuirt WF. (1997) FDG PET in head and neck cancer. AJR 169:1663-1669
Kinahan PE, Townsend DW, Beyer T, Sashin D (1998) Attenuation correction for a combined 3D PET/CT scanner. Med Phys 25:2046-2053
Kitagawa Y, Nishizawa S, Sano K et al (2002) Whole-body (18)F-fluorodeoxyglucose positron emission tomography in patients with head and neck cancer. Oral Surg Oral Med Oral Pathol Oral Radiol Endod 93:202-207
Kluetz PG, Meltzer CC, Villemagne VL et al (2000) Combined PET/CT Imaging in Oncology. Impact on Patient Management. Clin Positron Imaging 3:223-230
Lardinois D, Weder W, Hany TF et al (2003) Staging of non-small-cell lung cancer with integrated positron-emission tomography and computed tomography. N Engl J Med 348:2500-2507
Leon X, Quer M, Diez S, Orus C, Lopez-Pousa A, Burgues J (1999) Second neoplasm in patients with head and neck cancer. Head Neck 21:204-210
Marom EM, McAdams HP, Erasmus JJ (1999) Staging non-small cell lung cancer with whole-body PET. Radiology 212:803-809
Marom EM, Erasmus JJ, Pass HI, Patz EF Jr (2002) The role of imaging in malignant pleural MPM. Semin Oncol 29:26-35
Mountain CF, Dresler CM (1997) Regional lymph node classification for lung cancer staging. Chest 11:1718-1723
Myers JN, Greenberg JS, Mo V, Roberts D (2001) Extracapsular spread. A significant predictor of treatment failure in patients with squamous cell carcinoma of the tongue. Cancer 92:3030-3036
Nestle U, Walter K, Schmidt S, Licht N et al (1999) 18F-deoxyglucose positron emission tomography (FDG-PET) for the planning of radiotherapy in lung cancer: high impact in patients with atelectasis. Int J Radiat Oncol Biol Phys 44:593-597
Patterson GA, Ginsberg RJ, Poon PY et al (1987) A prospective evaluation of magnetic resonance imaging, computed tomography, and mediastinoscopy in the preoperative assessment of mediastinal node status in bronchogenic carcinoma. J Thorac Cardiovasc Surg 94:679-684
Pieterman RM, van Putten JWG, Meuzelaar JJ et al (2000) Preoperative staging of non-small-cell lung cancer with positron-emission tommography. N Engl J Med 343:254-261
Rendina EA, Bognolo DA, Mineo TC et al (1987) Computed tomography for the evaluation of intrathoracic invasion by lung cancer. J Thorac Cardiovasc Surg 94:57-63
Schneider DB, Clary-Macy C, Challa S et al (2000) Positron emission tomography with F18-fluorodeoxyglucose in the staging and preoperative evaluation of malignant pleural MPM. J Thorac Cardiovasc Surg 120:128-133
Schwartz DL, Rajendran J, Yueh B et al (2003) Staging of head and neck squamous cell cancer with extended-field FDG-PET. Arch Otolaryngol Head Neck Surg 129:1173-8
Steinert HC, Hauser M, Allemann F et al (1997) Non-small cell lung cancer: nodal staging with FDG PET versus CT with correlative lymph node mapping and sampling. Radiology 202:441-446
Stokkel MP, Moons KG, ten Broek FW, van Rijk PP, Hordijk GJ (1999) 18F-fluorodeoxyglucose dual-head positron emission tomography as a procedure for detecting simultaneous primary tumors in cases of head and neck cancer. Cancer 86:2370-2377
Strauss LG (1996) Fluorine-18 deoxyglucose and false-positive results: a major problem in the diagnosis of oncological patients. Eur J Nucl Med 23:1409-1414
Vansteenkiste JF, Stroobants SG, De Leyn PR et al (1998) Lymph node staging in non-small cell lung cancer with FDG PET scan: a prospective study on 690 lymph node stations from 68 patients. J Clin Oncol l16:2142-2149
Weder W, Schmid R, Bruchhaus H, Hillinger S, von Schulthess GK, Steinert HC. (1998) Detection of extrathoracic metastases by positron emission tomography in lung cancer. Ann Thorac Surg 66:886-893
Wong WL, Hussain K, Chevretton E et al (1996) Validation and clinical application of computer-combined computed tomography and positron emission tomography with 2-[18F]fluoro-2-deoxy-D-glucose head and neck images. Am J Surg 172:628-632

13 PET/CT Imaging in Breast Cancer, Gastrointestinal Cancers, Gynecological Cancers and Lymphoma

Martin Allen-Auerbach, Johannes Czernin, and Christiaan Schiepers

CONTENTS

13.1 Introduction

The advantages of PET/CT over PET are discussed in Chaps. 6, 12, and 15. In brief, PET/CT Imaging combines simultaneous high quality molecular (PET) with anatomical information (CT) (Townsend et al. 2004). Because the CT data are used for attenuation correction, imaging time is reduced by at least 50% (Halpern et al. 2004a). Thus, almost all patients can be imaged in arms-up position, which reduces motion artifacts.

The information provided by CT is important for several reasons. Hypermetabolic foci can be localized to specific anatomical structures. In addition, primary or metastatic lesions with low or no glucose metabolic activity might only be detectable by anatomic imaging. Areas of mildly and focally increased FDG uptake can result in ambiguous PET interpretations. Finally, misinterpretation of asymmetrical benign physiological activity in muscle or brown adipose tissue can be avoided (Goerres et al. 2003a; Cohade et al. 2003a). Because PET/CT provides the anatomical localization of mild or asymmetric hypermetabolic foci, images can be interpreted with a higher level of confidence, resulting in a reduced rate of false positive and false negative findings (Lardinois et al. 2003).

Since PET/CT only emerged as a clinical tool at the beginning of this millennium, studies evaluating the added value of PET/CT over PET are still limited. However, initial studies suggest that PET/CT improves the accuracy of staging in lung cancer, colorectal cancer, head/neck cancer and lymphoma (Lardinois et al. 2003; Cohade et al. 2003b; Schoder et al. 2004; Freudenberg et al. 2003).

This chapter reviews currently implemented PET/CT imaging protocols and the current state and specific impact of PET/CT on the most common oncological indications other than head/neck and lung cancer (discussed in Chap. 12).

13.2 Imaging Protocols

13.2.1 PET/CT

No firm consensus regarding the optimal PET/CT acquisition and processing protocols has been established. Specific protocols depend upon several factors. Firstly, differences in PET detector technology determine the duration of PET emission scanning. For instance, because of its high sensitivity and light output (see Chap. 15) the LSO detector technology allows for very short imaging sequences (Halpern et al. 2004a). Similarly, the CT component determines whether high quality, diagnostic CT studies can be performed. Multi-detector CT scanners are now standard in the radiology community. PET is a whole body imaging technique while CT traditionally provides limited views of head/neck, chest, and

M. Allen-Auerbach, MD; J. Czernin, MD;
C. Schiepers, MD, PhD
Department of Molecular and Medical Pharmacology, David Geffen School of Medicine at UCLA, 10833 Le Conte Avenue, AR-144 CHS, Los Angeles, CA 90095-6942, USA

abdomen/pelvis. Since CT is used for attenuation correction a whole body CT needs to be acquired in each patient. Whereas a low dose CT is sufficient for attenuation correction, its diagnostic quality is limited. Therefore, most institutions acquire a higher dose CT, i.e. 130 kVp and 120 mAs, resulting in diagnostic quality images.

Based on studies in more than 4000 patients we believe that PET/CT imaging should not only include diagnostic PET but also diagnostic CT images for several reasons. Whereas FDG-PET is highly sensitive and quite specific for malignancy (Antoch et al. 2004) the anatomic information undoubtedly adds to the diagnostic accuracy, probably most importantly by improving the specificity of PET imaging. In a group of 169 patients referred for staging of a mixture of neoplasms, we found a 12% improvement by PET/CT imaging over PET alone (Schiepers et al. 2003). Maximizing the information obtained by a single PET/CT scan will eventually lead to acceptance of PET/CT as the comprehensive cancer-imaging tool of choice.

13.2.2 CT with Contrast Enhancement

Diagnostic CT studies frequently include intravenous and oral contrast, which significantly enhance the quality of the CT images. Intravenous contrast results in improved definition of anatomical structures, increased sensitivity for pathological lesion detection and better lesion characterization. The PET/CT community is divided as to whether and how much contrast is necessary for optimizing PET/CT imaging. Intravenous contrast certainly increases the complexity of patient scheduling, preparation and throughput. Furthermore, considerable skills are required from technologists to simultaneously perform high quality PET and contrast CT scans. Frequently cited problems with attenuation correction secondary to the high density of the contrast material can lead to attenuation artifacts (Antoch et al. 2002; Halpern et al. 2004b). Thus, intravenous contrast studies require that interpreting physicians recognize these artifacts (Fig. 13.1).

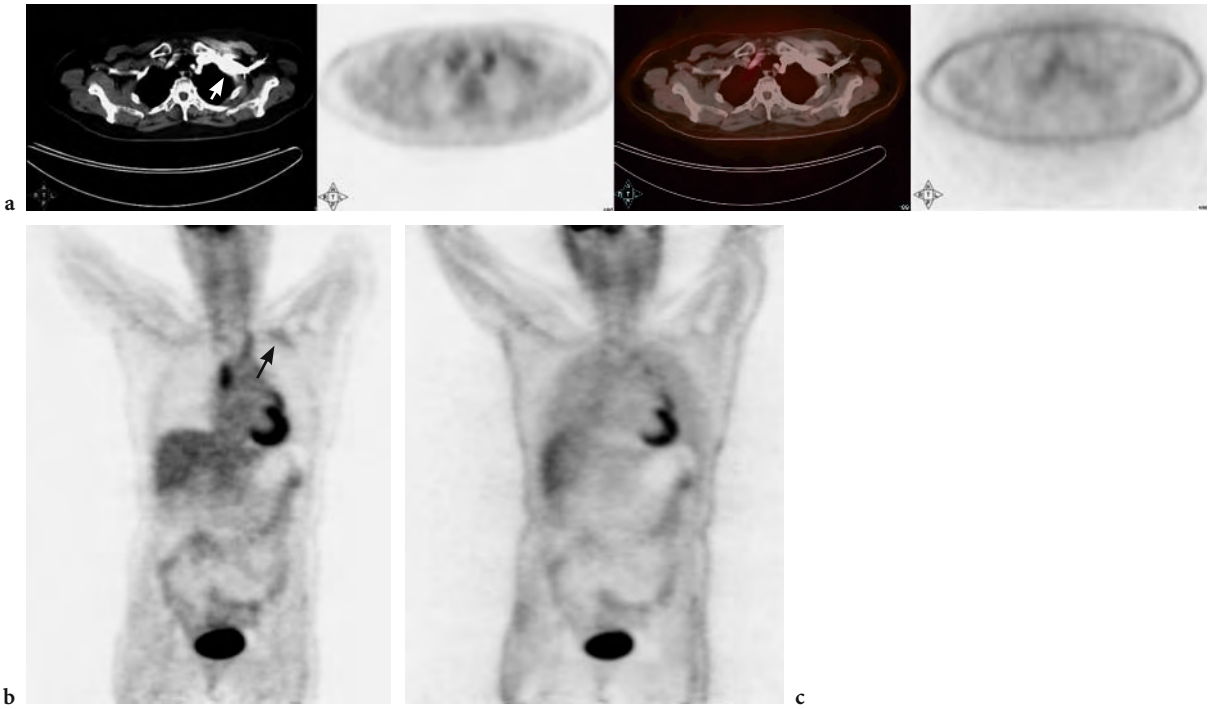

Fig. 13.1. a Axial images of a 67-year-old female referred for re-staging of colon cancer, 2 years after curative resection. *Left panel*, CT image in the soft tissue window, with intra-venous contrast in the left subclavian region (*white arrow*). *Second panel left*, PET image with mildly increased uptake in the left subclavian area, related to over-estimation of the attenuation coefficients due to the contrast. *Second panel from right*, fused axial images, CT in gray scale and PET in color. *Right panel*, PET image not corrected for attenuation shows normal uptake in the left subclavian region. **b** Coronal PET image shows the mildly increased uptake (pseudo FDG uptake) in the left subclavian region (*black arrow*). **c** In the uncorrected image this is not present, indicating that the "uptake" is an attenuation correction artifact

At our institution, a joint read out of PET/CT images by radiologists and nuclear medicine physicians has been established. Most academic institutions have sub-specialties in radiology, and several radiologists are needed to report a whole body CT scan. Because of the requests of referring oncologists and interpreting radiologists, we are administering contrast to all patients in whom there is no contraindication.

Our intravenous contrast protocol consists of 120 ml of Omnipaque 350 administered at a rate of 1.5–2 ml/s with a 45-s delay. For oral contrast, we use 900 ml of READY-CAT® with 2.1% barium sulfate, administered in three portions PO during the hour prior to imaging. This protocol results in satisfactory contrast enhancement and good image quality for the different body regions. Specialized protocols (e.g. arterial and venous phase of the liver) cannot be obtained given the time constraints of scheduling and throughput. The advantage of having IV contrast enhancement is most apparent in patients with head and neck cancer, where the differentiation between normal and abnormal glucose metabolic activity as well as the delineation of abnormal from normal anatomical structures can be very difficult. In the thorax the addition of IV contrast significantly enhances the evaluation of mediastinal structures, allowing for precise localization of increased FDG activity into specific lymph nodes and nodal stations. The enhancement of gastrointestinal tract with oral contrast allows the separation of soft tissue from bowel thus greatly facilitating the differentiation of physiological bowel activity from potentially abnormal activity within lymph nodes or other abdominal and pelvic structures. In our experience the attenuation artifacts caused by contrast are few, in most cases easily recognizable and usually caused by a bolus of IV contrast within the large thoracic veins (Antoch et al. 2002). The availability of non-attenuation corrected images further diminishes the problems caused by attenuation artifacts (Fig. 13.2).

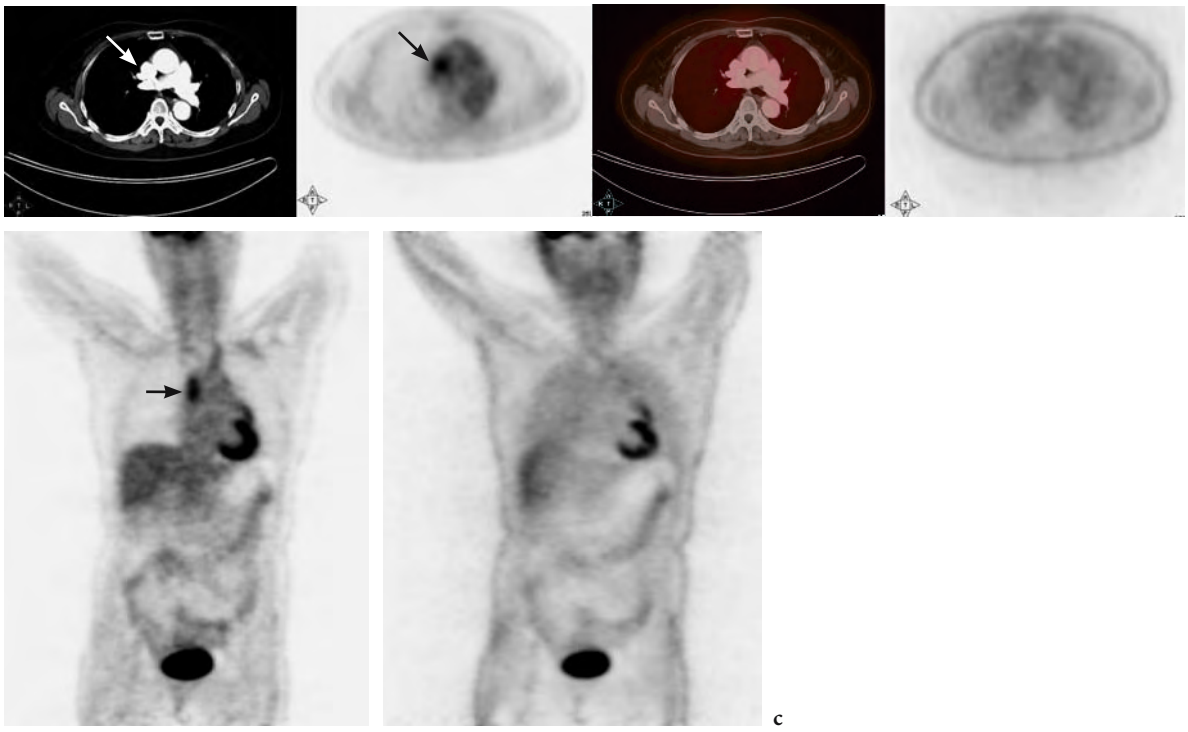

Fig. 13.2. a Same patient as in Fig. 13.1 with similar layout. Axial images at the level of the superior vena cava. Note the hot spot on PET (*black arrow* on second panel from left), corresponding to contrast on CT (*white arrow, left panel*). The uncorrected PET image is normal in this region (*right panel*). **b** Coronal PET images show that the hot focus in the superior vena cava region (*black arrow*) is induced by attenuation correction. **c** The uncorrected coronal image shows normal FDG uptake in this region of the thorax

13.2.3 Breathing Effects

Conventional CT imaging of the chest and abdomen is performed during breath hold at maximal inspiration to achieve optimal visualization of the lung parenchyma and to avoid artifacts of structures affected by diaphragmatic motion. The short scan times achieved with modern CT scanners allow for such breath hold studies in most patients. PET imaging requires much longer acquisition times. We have established a weight-based protocol with PET image acquisition times usually ranging from 1 to 4 min per bed position (Halpern et al. 2004a). This results in an average PET/CT acquisition time of about 15 min.

The chest usually encompasses two bed positions, and would require a breath hold of at least 2 min for PET. Since a breath hold over such an extended period of time is impossible, patients are imaged during shallow breathing. To achieve optimal fusion, the CT images are also acquired during shallow breathing. The image artifacts resulting from respiratory motion have been described (Beyer et al. 2003; Goerres et al. 2002, 2003b), are easily recognized and rarely cause significant problems for the interpretation of the studies. From a radiological point of view, the interpretation of the lung parenchyma and of structures adjacent to the diaphragm is significantly hampered by respiratory motion. Small sub-centimeter lung nodules are easily missed. Since sub centimeter lesions frequently are below the resolution of PET imaging (Crippa et al. 2000), significant findings can be missed. Several studies have addressed the quest for an ideal breathing protocol. Although some of the proposed protocols can reduce the artifacts produced by respiratory motion, none of the protocols allows for optimal imaging of the lung parenchyma. A promising approach for the future appears to be the implementation of respiratory gating which in theory could provide optimal fusion together with high quality CT images not compromised by respiratory motion artifacts (Boucher et al. 2004).

It is to date unknown whether all patients need a whole body diagnostic CT study with intravenous contrast. For instance, the accuracy of PET for staging and restaging of lymphoma is very high. The addition of non-contrast CT studies further enhances the diagnostic accuracy (Allen-Auerbach et al. 2004). Contrast CT might provide no or very limited additional diagnostic value (Schaefer et al. 2003).

13.3 Clinical Applications

13.3.1 Breast Cancer

Mammography is the screening modality of choice for the detection of breast cancer. However, in women with dense or scarred breasts, mammographic assessment is severely limited and its sensitivity has been reported to be as low as 30% (Mandelson et al. 2000). In addition, the specificity of mammography is low with more than 50% of biopsies performed for benign lesions (Orel et al. 1999). Given the fact that the overall sensitivity of PET and mammography are comparable (Noh et al. 1998; Scheidhauer et al. 1996) and that glucose metabolic activity of breast tissue is independent of breast density (Vranjesevic et al. 2003) PET can play an important role for screening women with dense or very dense, and scarred breasts.

The advent of PET/CT could provide additional information, by allowing precise anatomical localization of metabolic abnormalities and providing guidance for possible biopsy. FDG-PET is also helpful for detecting internal mammary node involvement and distant sites throughout the body (Schirrmeister et al. 2001). Nevertheless, certain problems remain. The sensitivity for staging of axillary lymph nodes with PET is unsatisfactory as was demonstrated in a multicenter trial by Wahl et al. (2004) and a prospective study by Fehr et al. (2004). PET/CT might be helpful in determining the precise number of axillary lymph nodes involved, an important prognostic marker, which cannot be accomplished by PET alone. Tatsumi et al. (2003) reported additional information with PET/CT compared to PET in 17 of 48 patients with breast cancer and abnormal PET findings. Additional information was however provided for only a single axillary lesion. At this point it seems unlikely that PET/CT will be able to replace sentinel lymph node biopsy and axillary lymph node dissection for axillary lymph node staging. In the same study (Tatsumi et al. 2003) PET/CT provided additional information for characterizing correctly four internal mammary, three mediastinal and seven bone lesions. Detection and differentiation of internal mammary nodes from mediastinal or lung metastases is important for staging of disease as well as guidance for possible biopsy procedures.

In the evaluation of bone metastasis, osteolytic and bone lesions of a mixed type are readily detected by FDG-PET. However, sclerotic bone lesions are frequently negative (Cook et al. 1998; Gallowitsch et

al. 2003). Fig. 13.3 illustrates the PET/CT images of such a patient. The identification of sclerotic bone lesions on the CT portion of the PET/CT might aid in directing further diagnostic imaging (bone scan, MRI) and treatment.

The overall effect of PET/CT on patient management was prospectively evaluated in a study by Buck et al. (2003) in 78 patients with suspected disease recurrence. As a result of improved detection and localization of lesions, PET/CT had a major impact on patient management in 36% of patients studied. The low sensitivity of PET for detection of breast cancer of the lobular and ductal in-situ type (Avril et al. 2001) is unlikely to be improved with the addition of CT since CT findings for these disease entities are non-specific and unlikely to improve overall sensitivity.

Data from our own institution by Fueger et al. (2004) in a group of 60 patients referred for staging and restaging of breast cancer demonstrated a considerable advantage of PET/CT over PET by correctly changing stage in 10% of patients (downstaging three patients and upstaging three). False negative PET studies were mostly due to sclerotic bone lesions. Whereas false positive PET studies in most cases were the result of non-specific muscle uptake as identified by PET/CT.

The role of PET/CT imaging in breast cancer is evolving. Clear advantages of PET/CT over PET alone have been demonstrated for restaging and for initial staging of axillary and internal mammary lymph node involvement, but not for primary diagnosis.

13.3.2 Gastrointestinal Cancer

The interpretation of FDG-PET images of the gastrointestinal tract is complicated by the frequently high

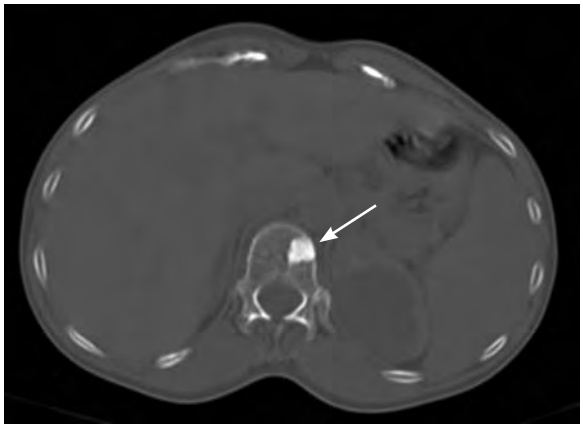

a

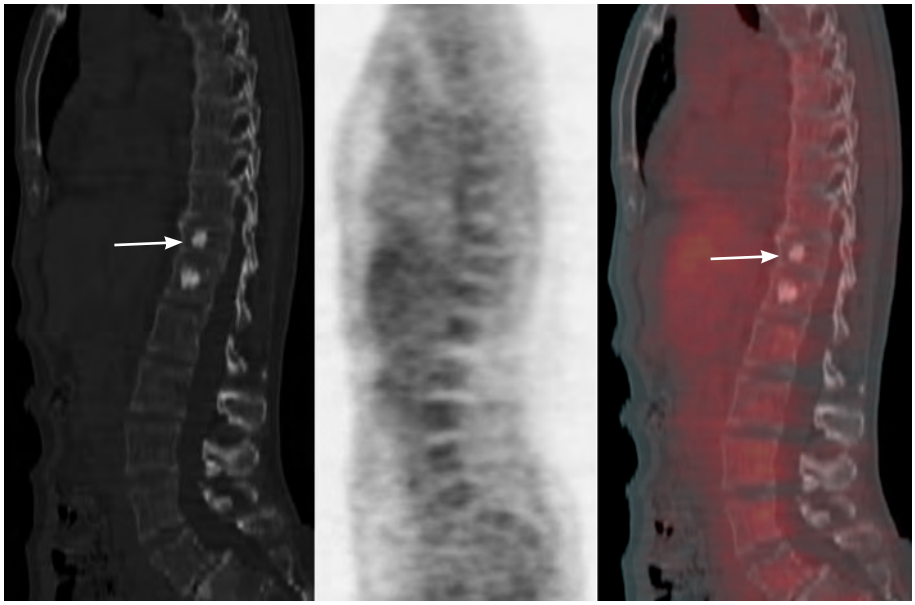

b

Fig. 13.3. a Axial CT slice (bone window), of a 53-year-old female with a history of breast cancer. Status post surgery and chemotherapy. Note the density in the vertebral body (*white arrow*), suspicious for metastasis. **b** Sagittal images show two lesions on CT in bone window (*left, white arrow* indicates T11), which have no increased uptake on PET (*middle panel*). The right panel shows the fused image, CT in gray and PET in color. This finding suggest sclerotic bone lesions

and sometimes focal physiological glucose metabolic activity of the bowel. These areas of increased FDG uptake represent normal gastrointestinal activity hypothesized to be either secondary to smooth muscle uptake related to peristalsis (Miraldi et al. 1998) or activity related to mucosal uptake (Jadvar et al. 1999). Normal ureteral and bladder activity can further complicate the assessment of FDG-PET scans of patients with gastrointestinal cancer. On the other hand, the evaluation with CT of patients previously treated with surgery or radiation can be difficult, because CT has a limited specificity in the characterization of soft tissue (such as presacral stranding) frequently representing scar tissue or necrotic residual masses.

Early PET literature suggests that the key advantage of PET imaging is related to its ability to determine extra-hepatic metastases (Schiepers et al. 1995; Rose et al. 1999). In addition, a superior performance of PET over CT with regards to identifying liver metastases has been reported (Schiepers and Hoh 2000). However, these studies were conducted when the CT technology was less advanced than it is now. Initial data assessing the performance of PET/CT over PET or CT alone are emerging.

Cohade et al. (2003c) reported an 11% increase in staging accuracy by PET/CT over PET alone in a retrospective study of 45 patients with colorectal cancer. Interestingly a positron emission source (^{68}Ge) instead of the available CT data was used for attenuation correction. Another study by Frances et al. (2003) comparing PET/CT to PET alone reported an impact on the surgical management in 24% of 21 patients with known colorectal cancer by PET/CT. In a study of 45 patients with recurrent colorectal cancer performed at our institution (Kim et al. 2004) PET/CT detected more lesions than PET alone, leading to a clinically relevant change of tumor stage in 9% of patients. A typical example of local recurrence is shown in Fig. 13.4.

Less information is available regarding the performance of PET/CT in patients with esophageal cancer. A study by Bar-Shalom et al. (2003) of 18 patients with esophageal cancer reported improved detection and characterization of 35% of suspicious sites in 89% of patients by PET/CT vs PET and CT.

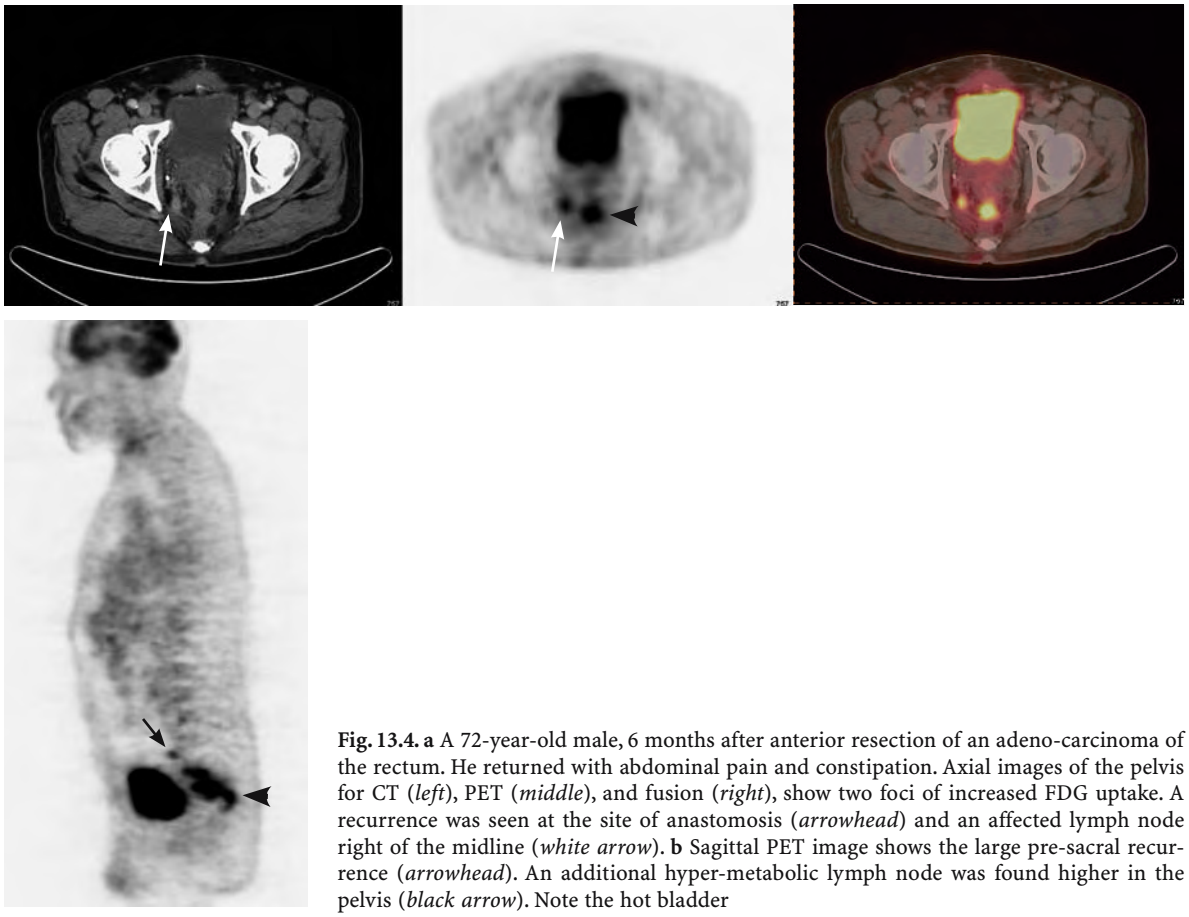

Fig. 13.4. a A 72-year-old male, 6 months after anterior resection of an adeno-carcinoma of the rectum. He returned with abdominal pain and constipation. Axial images of the pelvis for CT (*left*), PET (*middle*), and fusion (*right*), show two foci of increased FDG uptake. A recurrence was seen at the site of anastomosis (*arrowhead*) and an affected lymph node right of the midline (*white arrow*). **b** Sagittal PET image shows the large pre-sacral recurrence (*arrowhead*). An additional hyper-metabolic lymph node was found higher in the pelvis (*black arrow*). Note the hot bladder

Image fusion altered patient management in 22% of the study group.

Mucinous colorectal and pancreatic cancers frequently do not exhibit increased FDG uptake. It is therefore likely that lesions potentially missed by PET alone could be detected and better classified by PET/CT. In a study that included 16 patients with a pancreatic mass who were studied prior to surgery (Tann et al. 2003) PET/CT correctly reclassified five lesions interpreted as indeterminate by PET alone. However, the false negative rate in this study was not reduced by PET/CT.

The relatively high normal FDG activity in the liver frequently causes problems in the detection of malignant intrahepatic lesions. The availability of fused PET-CT images could help in the evaluation of patients with suspected hepatic malignancy since CT identifies hepatic lesions with a high sensitivity. However, the benefit of image fusion in patients with hepatocellular carcinoma is less clear, since hepatocellular carcinomas rarely demonstrate increased FDG uptake (Khan et al. 2000).

Few studies have evaluated the role and advantage of PET/CT over PET in the monitoring of treatment response for gastrointestinal malignancies. In patients with gastrointestinal stromal tumors (GIST) PET is superior to CT in detecting early metabolic changes that are indicative of tumor response (van den Abbeele et al. 2002). A study by Antoch et al. (2004) indicates that dual-modality PET/CT imaging compared to PET alone, or side-by-side PET and CT interpretation, detected more lesions on the baseline scans and demonstrated higher accuracy in determining tumor response after 1 month of treatment.

The role of PET/CT imaging of gastrointestinal malignancies can be summarized as follows. PET/CT improves the staging accuracy in colorectal cancer when compared to PET or CT alone. Initial studies suggest a similar advantage of PET/CT in patients with esophageal cancer while no clear benefits have been demonstrated for pancreatic and primary hepatic malignancies. The key advantage of PET/CT appears to be related to its increased specificity over PET alone.

13.3.2 Lymphoma

FDG-PET has proven to be a valuable tool for staging, restaging and prediction of response to chemotherapy in Hodgkin's disease (HD) and non-Hodgkin's lymphoma (NHL) (Cremerius et al. 1999; Kaplan 2002; Hoskin 2002; Bangerter et al. 1998; Jerusalem et al. 1999; Filmont et al. 2003; Spaepen et al. 2001). The limited anatomical resolution of PET can, however, result in difficulties in the localization of extranodal disease that frequently occurs in NHL.

Lymph node lesions mistakenly placed into bone or lung for example, would lead to significant upstaging of disease. Frequently encountered benign entities with increased uptake, such as brown fat or non-specific muscle activity, pose a particular challenge in patients with lymphoma. For instance, FDG uptake in brown fat occurs more frequently in younger patients, an age group with high incidence of lymphoma. Thus, benign patterns can easily be confused with malignant hypermetabolic foci in these patients. The anatomical detail provided by the CT portion has therefore the potential of significantly improving the specificity and hence accuracy of lymphoma staging. This, in turn, would allow for improved treatment monitoring and appropriate adjustments of subsequent treatment.

In a study of 27 patients with HD and NHL by Freudenberg et al. (2003) restaging was altered in 11 % of patients by FDG-PET/CT compared to FDG-PET imaging alone. The same study reported a change in disease stage by PET/CT in 14% of patients when compared to side-by-side interpretation of FDG-PET and CT images.

A study at our own institution involving 73 patients with HD and NHL demonstrated a significant change in disease stage in 10% of patients by PET/CT compared to PET alone (Allen-Auerbach et al. 2004). Figure 13.5 shows a patient with widespread disease involvement.

Several questions with regard to the role of PET/CT for imaging lymphoma are currently addressed. For instance, given the high sensitivity of FDG-PET for lymphoma assessment, how much intravenous contrast is needed for the CT portion of the study? Initial studies suggest that PET/CT could be performed without intravenous contrast in these patients. Given the frequently low glucose metabolic rate in low-grade lymphoma, is PET/CT more sensitive than PET alone? Is PET alone sufficient for therapy monitoring or is PET/CT the modality of choice? More studies in larger patient populations are needed to define the role of PET/CT in lymphoma.

13.3.2 Gynecological Malignancies

Some gynecological malignancies pose a considerable problem for PET imaging (Williams et al.

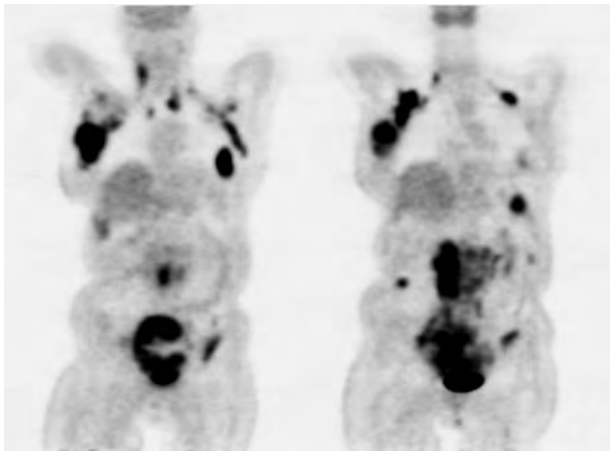

a

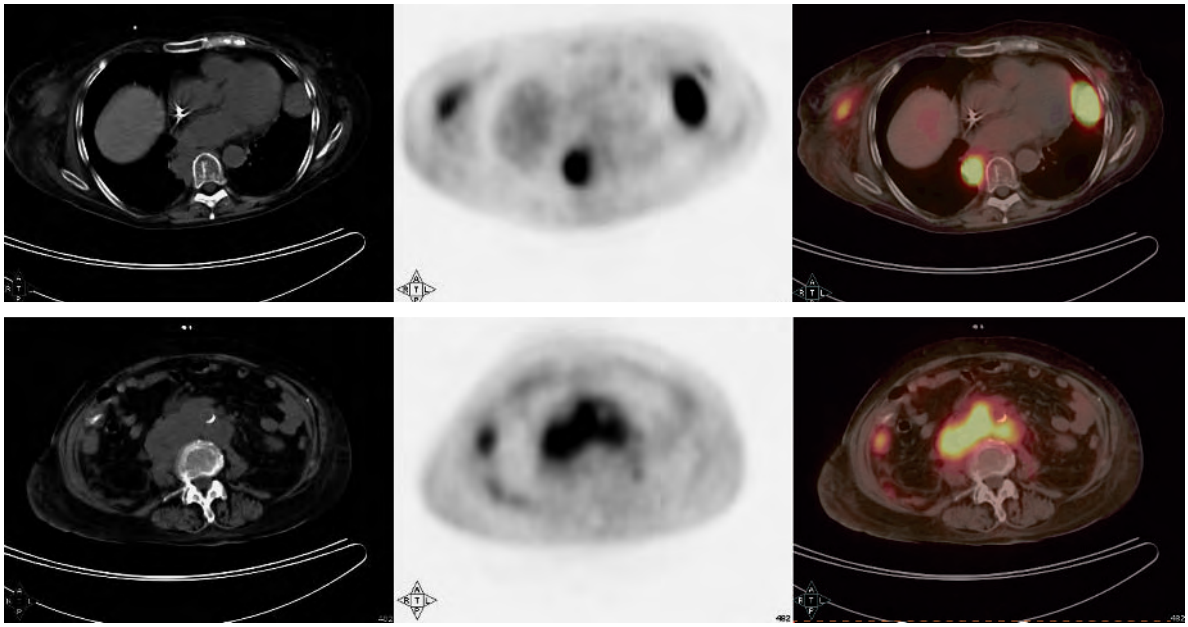

b

Fig. 13.5. a Extensive disease involvement in a 64-year-old woman with non-Hodgkin's lymphoma. Restaging exam after bone marrow transplant. The *left panel* shows a coronal image of the torso in a more anterior cross-section than the *right panel*, depicting a slice through the posterior mediastinum. **b** Axial images at the level of the dome of the diaphragm (*top row*) and pelvis at the level of L4 (*bottom row*). The left column shows the CT, middle column PET, and right column the fused images with PET in color and CT in gray scale. Note the intense foci of hyper-metabolism

2001). First, glucose metabolic activity can be low as is frequently the case for ovarian cancer. This is likely explained by the frequently cystic nature of these tumors in addition to special tumor features such as mucin production. Other tumors such as cervical cancer exhibit markedly increased FDG activity, but the close proximity to bowel, bladder and ureters can render the assessment of regional lymph node involvement difficult (Grigsby et al. 2001). It is important to realize that normal physiological activity is not only found in the urinary collecting system and bowel, but can also occur in the uterus and ovaries. As described by Lerman et al. (2004) premenopausal patients can demonstrate cycle dependent normal increase of FDG activity in the uterus and the ovaries. PET/CT provides a potential advantage by allowing the correct assignment of hypermetabolic activity to normal and abnormal anatomical structures. False positive lesions are always possible as is shown in Fig. 13.6.

The value of PET/CT for evaluating gynecologic malignancies was examined by Israel et al. (2003) in 57 patients with cervical cancer (n=38), ovarian cancer (n=13) and endometrial cancer (n=6). PET/CT led to management changes in 17 patients (30%) and added value to PET alone in 50% of the patients. No diagnostic benefit of PET/CT over PET alone was reported by Cohade et al. (2003b) in 46 clinical patients with ovarian cancer. The accuracy of PET was 80% while that of PET/CT was 83%. However, a significant impact of PET/CT in patients with endometrial cancer (n=15) was observed by the same group with 12 of 49 lesions (24.5%) misdiagnosed or anatomically incorrectly placed by PET alone.

Fig. 13.6. a Coronal image of a 38-year-old woman with a history of melanoma of the left conjunctiva. Status post resection, left neck dissection and left superficial parotidectomy. Referred for re-staging. An unsuspected focal hot spot was found in the left pelvis (*arrow*). **b** Axial images show the focus (PET, *middle panel*) to be related to a cystic structure (CT, *left panel*). The fusion image (*right panel*) demonstrates the exact location. Pelvic ultrasound and MRI confirmed that this lesion was a hemorrhagic ovarian cyst

a

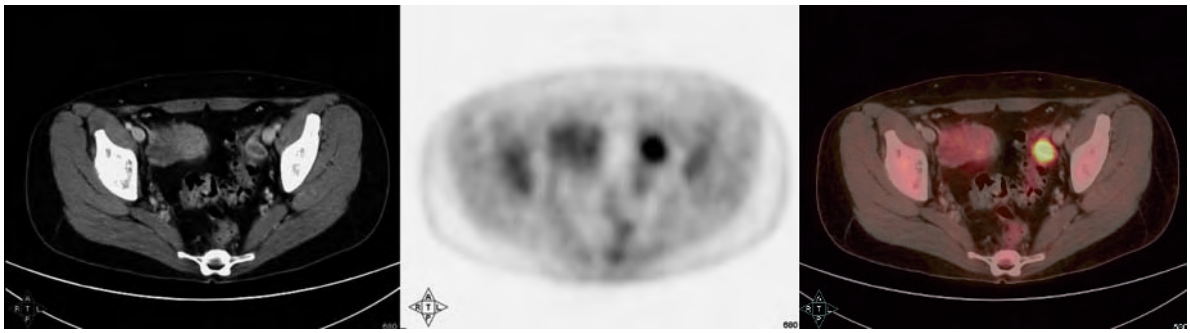

b

Larger studies remain to be conducted to determine advantages of PET/CT over PET for specific gynecological cancers. Initial data strongly suggest that PET/CT will improve the performance of PET in patients with gynecological malignancies.

As was outlined by Wahl (2004), imaging of abdominal and pelvic cancer in the future will be almost exclusively done by PET/CT. This was based on the experience of the Johns Hopkins PET Center, where over 2700 studies were performed in a 2-year period.

13.4 Conclusion

PET/CT is rapidly evolving as the standard imaging procedure in oncology. PET/CT has several established advantages over PET alone. Image duration is reduced by about 50% resulting in improved image quality due to reduced patient motion. A comprehensive "one stop shop" whole body survey for cancer is convenient for patients and interpreting physicians. Shortened image acquisition times also result in better utilization of the expensive equipment. Frequently these arguments are sufficiently compelling for the respective nuclear medicine and radiology departments to acquire this technology.

An increasing body of evidence is emerging that PET/CT leads to improved accuracy for detection, staging and restaging of cancer when compared to conventional PET.

Future studies will document the improved accuracy in larger and better defined patient populations.

Meanwhile the technology continues to develop at a rapid pace. PET/CT systems are now available whereby the number of CT detector slices varies from 1 to 64 and the PET technology ranges from standard to high – end systems. Improvements in PET detector technology will increase the sensitivity of PET for cancer detection. Respiratory gating will result in further improvements in image fusion and will permit exact identification of radiation targets. PET/CT will play an ever-increasing role in biopsy planning by delineating viable tumor from necrosis or scar.

Issues that need to be addressed are largely related to the PET/CT acquisition protocols. How

much CT is needed and how much intravenous contrast is required for diagnostic PET/CT? How can radiation exposure to patients be minimized? And finally and importantly, how should PET/CT studies be interpreted and reported? The need to have both radiologists and nuclear medicine specialists working jointly on PET/CT image protocols and interpretation to provide patients and their physicians with the best possible service, is becoming increasingly evident.

By the end of 2004, 80% of all PET sales were PET/CT with more than 350 systems installed worldwide. Thus, PET/CT is here to stay and training requirements for both nuclear medicine and radiology have to adapt to the new merger of molecular and anatomical imaging.

References

Allen-Auerbach M, Quon A, Weber WA, Obrzut S, Crawford T, Silverman DH et al (2004) Comparison between 2-deoxy-2-[18F]fluoro-D-Glucose positron emission tomography and positron emission tomography/computed tomography hardware fusion for staging of patients with lymphoma. Mol Imaging Biol 6:411–416

Antoch G, Freudenberg LS, Beyer T, Bockisch A, Debatin JF (2004) To enhance or not to enhance? 18F-FDG and CT contrast agents in dual-modality 18F-FDG PET/CT. J Nucl Med 45 [Suppl 1]:56S–65S

Antoch G, Freudenberg LS, Egelhof T, Stattaus J, Jentzen W, Debatin JF et al (2002) Focal tracer uptake: a potential artifact in contrast-enhanced dual-modality PET/CT scans. J Nucl Med 43:1339–1342

Antoch G, Kanja J, Bauer S, Kuehl H, Renzing-Koehler K, Schuette J et al (2004) Comparison of PET, CT, and dual-modality PET/CT imaging for monitoring of imatinib (STI571) therapy in patients with gastrointestinal stromal tumors. J Nucl Med 45:357–365

Avril N, Menzel M, Dose J, Schelling M, Weber W, Janicke F et al (2001) Glucose metabolism of breast cancer assessed by 18F-FDG PET: histologic and immunohistochemical tissue analysis. J Nucl Med 42:9–16

Bangerter M, Moog F, Buchman I, Kotzerke J, Griesshammer M, Hafner M et al (1998) Whole-body 2-[18F]-fluoro-2-deoxy-D-glucose positron emission tomography 9FDG-PET) for accurate staging of Hodgkin's disease. Ann Oncol 9:1117–1122

Bar-Shalom R, Leiderman M, Gaitini D (2003) The value of PET/CT using FDG in patients with esophageal cancer. J Nucl Med 44:21

Beyer T, Antoch G, Blodgett T, Freudenberg LF, Akhurst T, Mueller S (2003) Dual-modality PET/CT imaging: the effect of respiratory motion on combined image quality in clinical oncology. Eur J Nucl Med Mol Imaging 30:588–596

Boucher L, Rodrigue S, Lecomte R, Benard F (2004) Respiratory gating for 3-dimensional PET of the thorax: feasibility and initial results. J Nucl Med 45:214–219

Buck A, Wahl A, Eicher U, Blumstein N, Schirrmeister H, Helms G et al (2003) Combined morphological and functional imaging with FDG-PET/CT for restaging breast cancer-impact on patient management. J Nucl Med 44 [Suppl 5]

Cohade C, Mourtzikos K, Wahl R (2003a) "USA-Fat": prevalence is related to ambient outdoor temperature-evaluation with 18F-FDG PET/CT. J Nucl Med 44:1267–1270

Cohade C, Mourtzikos K, Pannu H, Leal J, Bristow R, Wahl R (2003b) Direct comparison of PET and PET/CT in the detection of recurrent ovarian cancer. J Nucl Med 44 [Suppl 5]:129P

Cohade C, Osman M, Leal J, Wahl R (2003c) Direct comparison of (18)F-FDG PET and PET/CT in patients with colorectal carcinoma. J Nucl Med 44:1797–1803

Cook GJ, Houston S, Rubens R, Maisey MN, Fogelman I (1998) Detection of bone metastases in breast cancer by 18FDG PET: differing metabolic activity in osteoblastic and osteolytic lesions. J Clin Oncol 16:3375–3379

Cremerius U, Fabry U, Kroll U, Zimny M, Neuerburg J, Osieka R et al (1999) Clinical value of FDG PET for therapy monitoring of malignant lymphoma – results of a retrospective study in 72 patients. Nuklearmedizin 38:24–30

Crippa F, Leutner M, Belli F, Gallino F, Greco M, Pilotti S et al (2000) Which kinds of lymph node metastases can FDG PET detect? A clinical study in melanoma. J Nucl Med 41:1491–1494

Fehr MK, Hornung R, Varga Z, Burger D, Hess T, Haller U et al (2004) Axillary staging using positron emission tomography in breast cancer patients qualifying for sentinel lymph node biopsy. Breast J 10:89–93

Filmont JE, Czernin J, Yap C, Silverman DH, Quon A, Phelps ME et al (2003) Value of F-18 fluorodeoxyglucose positron emission tomography for predicting the clinical outcome of patients with aggressive lymphoma prior to and after autologous stem-cell transplantation. Chest 124:608–613

Frances D, Visvikis D, Bomanji J, Costa D, Croasdale I, Taylore P et al (2003) The impact of FDG PET/CT in colorectal cancer-an outcome study. J Nuc Med 44 [Suppl 5]:26P

Freudenberg L, Antoch G, Mueller S, Goerges R, Bockisch A (2003) Whole body FDG-PET/CT in restaging of lymphoma. J Nucl Med 44 [Suppl 5]:83P

Fueger BJ, Quon A, Allen-Auerbach M, Halpern BS, Kim JH, Silverman DH et al (2004) FDG-PET, PET/CT and Software Fusion: diagnostic performance in re-staged breast cancer patients. J Nuc Med 45:86–87P

Gallowitsch HJ, Kresnik E, Gasser J, Kumnig G, Igerc I, Mikosch P et al (2003) F-18 fluorodeoxyglucose positron-emission tomography in the diagnosis of tumor recurrence and metastases in the follow-up of patients with breast carcinoma: a comparison to conventional imaging. Invest Radiol 38:250–256

Goerres GW, Kamel E, Heidelberg TN, Schwitter MR, Burger C, von Schulthess GK (2002) PET-CT image co-registration in the thorax: influence of respiration. Eur J Nucl Med Mol Imaging 29:351–360

Goerres GW, Schmid D, von Schulthess G, Hany T (2003a) FDG PET/CT improves the confidence of anatomic assignment of cancer lesions in the head and neck: a comparison with FDG PET and contrast enhanced CT. J Nucl Med 44 [Suppl 5]:128P

Goerres GW, Burger C, Schwitter MR, Heidelberg TN, Seifert B, von Schulthess GK (2003b) PET/CT of the abdomen: optimizing the patient breathing pattern. Eur Radiol 13:734–739

Grigsby PW, Siegel BA, Dehdashti F (2001) Lymph node staging by positron emission tomography in patients with carcinoma of the cervix. J Clin Oncol 19:3745–3749

Halpern BS, Dahlbom M, Quon A, Schiepers C, Waldherr C, Silverman DH et al (2004a) Impact of patient weight and emission scan duration on PET/CT image quality and lesion detectability. J Nucl Med 45:797–801

Halpern BS, Dahlbom M, Waldherr C, Yap CS, Schiepers C, Silverman DH et al (2004b) Cardiac pacemakers and central venous lines can induce focal artifacts on CT-corrected PET images. J Nucl Med 45:290–293

Hoskin PJ (2002) FDG PET in the management of lymphoma: a clinical perspective. Eur J Nucl Med Mol Imaging 29:449–451

Israel O, Keidar Z, Bar-Shalom R, Gaitini D, Beck D, Amit A (2003) Hybrid PET/CT imaging with FDG in management of patients with gynecologic malignancies. J Nuc Med 44 [Suppl 5]:129P

Jadvar H, Schambye RB, Segall GM (1999) Effect of atropine and sincalide on the intestinal uptake of F-18 fluorodeoxyglucose. Clin Nucl Med 24:965–967

Jerusalem G, Beguin Y, Fasotte M, Najjar F, Paulus P, Rigo P et al (1999) Whole body positron emission tomography using 18 F-fluorodeoxyglucose for post treatment evaluation in Hodgkin's disease and non-Hodgkin's Lymphoma has higher diagnostic and prognostic value than classical computed tomography scan imaging. Blood 94:429–433

Kaplan LD (2002) Fluorine-18 fluorodeoxyglucose positron emission tomography for lymphoma: incorporating new technology into clinical care. Am J Med 112:320–321

Khan MA, Combs CS, Brunt EM, Lowe VJ, Wolverson MK, Solomon H et al (2000) Positron emission tomography scanning in the evaluation of hepatocellular carcinoma. J Hepatol 32:792–797

Kim JH, Czernin J, Allen-Auerbach M, Quon A, Halpern BS, Fueger B et al (2004) Comparison between FDG-PET, inline PET/CT and Software Fusion for restaging of recurrent colorectal cancer. J Nuc Med 45:32P

Lardinois D, Weder W, Hany T, Ehab M, Korom S, Seifert B et al (2003) Staging of non-small-cell lung cancer with integrated positron-emission tomography and computed tomography. N Engl J Med 348:2500–2507

Lerman H, Metser U, Grisaru D, Fishman A, Lievshitz G, Even-Sapir E (2004) Normal and abnormal 18F-FDG endometrial and ovarian uptake in pre- and postmenopausal patients: assessment by PET/CT. J Nucl Med 45:266–271

Mandelson M, Oestreicher N, Porter P, White D, Finder C, Taplin S et al (2000) Breast density as a predictor of mammographic detection: comparison of interval-and screen-detected cancers. J Natl Cancer Inst 92:1081–1087

Miraldi F, Vesselle H, Faulhaber PF, Adler LP, Leisure GP (1998) Elimination of artifactual accumulation of FDG in PET imaging of colorectal cancer. Clin Nucl Med 23:3–7

Noh D, Yun I, Kim J, Kang H, Lee D, Chung J et al (1998) Diagnostic value of positron emission tomography for detecting breast cancer. World J Surg 22:223–228

Orel S, Kay N, Reynolds C, Sullivan D (1999) BI-RADS categorization as a predictor of malignancy. Radiology 211:845–850

Rose D, Delbeke D, Beauchamp R, Chapman WC, Sandler MP, Sharp K et al (1999) 18Fluorodeoxyglucose-positron emission tomography in the management f patients with suspected pancreatic cancer. Ann Surg 229:729–737

Schaefer N, Hany T, Taverna C, Goerres G (2003) FDG PET/CT versus contrast enhanced CT in aggressive non-Hodgkin lymphoma and Hodgkin's disease. J Nucl Med 44 [Suppl 5]:84P

Scheidhauer K, Scharl A, Pietrzyk U, Wagner R, Göhring U, Schomäker K et al (1996) Qualitative [18F] FDG positron emission tomography in primary breast cancer: clinical relevance and practicability. Eur J Nucl Med 23:618–623

Schiepers C, Hoh CK (2000) Clinical positron imaging in oncology, chap 10. In: Schiepers C (ed) Diagnostic nuclear medicine, 1st edn. Springer, Berlin Heidelberg New York, pp 159–176

Schiepers C, Penninckx F, de Vadder N, Merckx E, Mortelmans L, Bormans G et al (1995) Contribution of PET in the diagnosis of recurrent colorectal cancer: comparison with conventional imaging. Eur J Surg Oncol 21:517–522

Schiepers C, Yap CS, Quon A, Giuliano P, Silverman DH, Dahlbom M et al (2003) Added value of PET-CT for cancer staging and lesion localization. EJNM & MI 30

Schirrmeister H, Kühn T, Guhlman A, Santjohanser C, Hörster T, Nüssle K et al (2001) Fluorine-18 2-deoxy-2-fluoro-D-glucose PET in the preoperative staging of breast cancer: comparison with the standard staging procedures. Eur J Nucl Med 28:351–358

Schoder H, Yeung HW, Gonen M, Kraus D, Larson SM (2004) Head and neck cancer: clinical usefulness and accuracy of PET/CT image fusion. Radiology 231:65–72

Spaepen K, Stoobants S, Dupont P, van Steenweghen S, Thomas J, Vandenberghe P et al (2001) Prognostic value of positron emission tomography with fluorine-18 fluorodeoxyglucose ([18F]FDG) after first line chemotherapy in non-Hodgkin's lymphoma: is [18F]FDG-PET a valid alternative to conventional diagnostic methods? J Clin Oncol 19:414–419

Tann M, Fletcher J, McHenry L, Dewitt J, LeBlanc J, Howard T et al (2003) FDG-PET/CT in the evaluation of cystic pancreatic tumors: Comparison with endoscopic ultrasound fine needle aspiration. J Nucl Med 44 [Suppl 5]:24P

Tatsumi M, Cohade C, Mourtzikos K, Wahl R (2003) Initial experience with FDG-PET-CT in the evaluation of breast cancer. J Nucl Med 44 [Suppl 5]:394P

Townsend D, Carney J, Yap J, Hall N (2004) PET/CT Today and tomorrow. J Nucl Med 45S:4S–13S

Van den Abeele A, RD B (2002) Use of positron emission tomography in oncology and its potential role to assess response to imatinib mesylate therapy in gastrointestinal stromal tumors (GIST). Eur J Cancer 38 [Suppl 5]:S60–S65

Vranjesevic D, Schiepers C, Silverman DH, Quon A, Villalpando J, Dahlbom M et al (2003) Relationship between 18F-FDG uptake and breast density in women with normal breast tissue. J Nucl Med 44:1238–1242

Wahl RL (2004) Why nearly all PET of abdominal and pelvic cancers will be performed as PET/CT. J Nucl Med 45 [Suppl 1]:82S–95S

Wahl RL, Siegel BA, Coleman RE, Gatsonis CG (2004) Prospective multicenter study of axillary nodal staging by positron emission tomography in breast cancer: a report of the staging breast cancer with PET Study Group. J Clin Oncol 22:277–285

Williams AD, Cousins C, Soutter WP, Mubashar M, Peters AM, Dina R et al (2001) Detection of pelvic lymph node metastases in gynecologic malignancy: a comparison of CT, MR imaging, and positron emission tomography. AJR Am J Roentgenol 177:343–348

14 Pediatric Nuclear Medicine: A Coming of Age

Helen R. Nadel and Moira E. Stilwell

CONTENTS

14.1 General

Nuclear medicine studies contribute an integral part to the investigation of many disease processes in children. The standard studies of bone, renal, and tumor imaging with scintigraphy are still the backbone of any pediatric nuclear medicine department. Over the past decade we have seen the introduction and increased use of newer scintigraphic approaches in children. This chapter focuses on the use of scintigraphy in children for the assessment of *Helicobacter pylori* infection and inflammatory bowel disease and psychosocial, developmental, and traumatic brain disorders in children.

H. R. Nadel, MD, FRCPC;
M. E. Stilwell, MD, FRCPC
Department of Radiology, University of British Columbia, Children's and Woman's Health Center of British Columbia, 4480 Oak Street, Vancouver, B.C. V6H 3V4, Canada

A discussion of pediatric scintigraphic techniques would not be complete without mention of technical factors required due to the unique needs of imaging pediatric patients who range in age from birth to adulthood. Advances in radiopharmaceutical and instrumentation technology allow greater investigation of physiology as well as anatomy in this diverse group of patients.

14.1.1 Patient Preparation

It is routine in many departments to allow parents and/or siblings to remain in the imaging room to provide a sense of security and safety for the child. The presence of a favorite toy or a prized possession brought with them for the test can also be reassuring. Immobilization needs, which can be an important factor in producing high-quality studies in children, can be broken down by age. For neonates to age 2 years, bundling in a papoose-type holder, sleep deprivation, and feeding the child while on the imaging table are effective immobilization strategies. Videos, music, stories, or distraction techniques, such as bubble blowing, thus ensuring their cooperation, entertain children aged 4–5 years. It is also helpful to have dedicated pediatric nuclear medicine technologists who are secure in their dealings with the various age groups. A simple explanation of the involved procedure tailored to the age of the child will go a long way to gain a child's cooperation; however, some children still require sedation or general anesthesia. In particular, those children who are mentally retarded or have severe attention deficit problems, and often children between the ages of 2 and 4 years, fall into this category. If sedation is necessary, appropriate triage, monitoring, and discharge of the patient are now the standard of care (Weiss 1993; Pintelon et al. 1994). The use of a local anesthetic cream at an intravenous access site is also routine in many laboratories (Sherazi and Gordon 1996; Ljung 1997).

14.1.2 Radiation Safety Considerations

The use of ionizing radiation in the pediatric population is an ongoing issue frequently cited in the pediatric radiology literature and bears examination by all practitioners. Roebuck (1999) examines and re-examines a variety of related issues. He points out rightly that part of the job of the radiologist and/or nuclear medicine physician is to help ensure that the appropriate investigation is performed, and that use of radiation is justifiable. Knowledge of the approximate risk, and more importantly the ability to effectively communicate these to the referring physician and parent, is essential. Nuclear physicians and radiologists alike should be aware of new applications of nuclear medicine tests but remain skeptical (Roebuck 1999; Berdon 1999; Hall 1999). Discussions regarding the risks of radiation and what exactly they consist of are frequently misunderstood and misquoted even by the physicians using them. In a letter to the *Lancet*, Dixon and Dendy (1998) posed three valuable questions to be considered before performing a CT scan on a child. These questions can be rephrased for nuclear medicine tests: Can the same or better information be obtained by a method with a lower dose of radiation? Is the utilized technology functioning properly? Is the protocol optimized for the patient? Stabin and Gelfand (1998) have published tables for evaluating absorbed radiation doses for many pediatric nuclear medicine procedures. They used standard MIRD methodology and express absorbed dosimetry in mGy or rad for a body weight adjusted administered activity for each radiopharmaceutical.

14.2 Helicobacter pylori Infection in Children

The battle cry of pediatric medicine is that "children are not just small adults who suffer from small versions of adult diseases." Whereas this is true mainly in pediatric gastrointestinal disease, many entities that we commonly see in adults are seen in children and need to be considered when appropriate. One such entity is *Helicobacter pylori* (*H. pylori*) infection. *H. pylori* infection is endemic worldwide as an asymptomatic infection (Narla et al. 1999). The recent discovery and growing interest in this gram-negative bacterium as a gut pathogen has had and continues to have significant impact on the management of several gastrointestinal disorders. Peptic ulcer disease and gastritis have been closely linked to *H. pylori* infection, and this infection is implicated in a substantial percentage of cases of acute gastrointestinal bleeding. *H. pylori* has been classified as a type-I carcinogen by the World Health Organization (Narla et al. 1999). In addition, it has been impugned as a co-factor in other gastrointestinal diseases such as chronic diarrhea, protein-losing enteropathy, and gastric lymphoproliferative disease. Corrado et al. (1998) studied 90 patients and found a positive association between *H. pylori* infection and food allergy.

H. pylori appears to be acquired early in life with cross-sectional studies suggesting that infection is usually acquired before the age of 5 years, although the time, rate, and modus of colonization are not definitely defined (Bujanover et al. 1996). Maternal passive transfer of immunity via IgG antibodies appears to protect infants until approximately 6 months of age when infection of children with *H. pylori* is common in both developed and developing countries (Gold et al. 1997). There is correlation with socioeconomic and hygiene conditions such as overcrowding and lack of clean running water (Duggan et al. 1998; Vandenplas and Blecker 1998). The role of parental infection is not fully understood but is thought to play a role in transmission particularly in infected mothers of young children (Rothenbacher et al. 1999). *H. pylori* infection in children is thought to be affected by both the rate of acquisition and loss in different groups based on ethnicity. A study by Malaty et al. (1999) followed 212 children in a biracial community over 12 years from childhood to young adulthood and showed different rates for both acquisition and loss of infection in groups of black children compared with groups of white children. To illustrate, at 7–9 years of age, 19% of children in their population had *H. pylori* infection (40% of black children and 11% of white children). Twelve years later, 22% of the children were positive with the higher prevalence again noted to be present in the black children. Granström et al. (1997) studied a cohort of Swedish children from ages 6 months to 11 years of age measuring both IgG and IgA antibodies to *H. pylori*. They identified that 13.6% (40 of 294) of their children were infected at some time during the study. They noted that at 11 years of age only 3% of the children were seropositive suggesting that spontaneous resolution is common. In a study done in Germany, Hornemann et al. (1997) could not find evidence of *H. pylori* infection in infants less

than 4 years of age. After age 4 years, the seropositivity increased linearly with age.

H. pylori infection is a well-recognized cause of antral gastritis and a significant factor in peptic ulcer disease in the adult population. In children, peptic ulcer disease does occur, albeit less commonly (Stringer 1989; Hassall 1994; Huang et al. 1999). Peptic ulcer disease in children is mainly duodenal ulcer disease, and when *H. pylori* is the cause, antral gastritis is also present. *H. pylori* can cause isolated gastritis as well. When *H. pylori* induces antibodies and reacts with them in the gastric mucosa, chronic gastritis may result and it is thought that these mucosal changes play a role in the progression to gastric cancer in adults. Ieradi et al. (1998) found that autoreaction of gastric mucosa may be found in *H. pylori* gastritis of childhood. They postulated a role in progression to atrophy and possibly increased risk of late gastric cancer. Numerous properties of the bacteria itself are also suggested as being important, including the presence of the CagA protein and vacA alleles associated with cytotoxin production. *H. pylori* generally falls into one of two groups: a Cag-negative group which does not produce cytotoxin and a Cag-positive which does and is associated with peptic ulcer disease (Çelik et al. 1998). Çelik et al. (1998) confirmed that the Cag pathogenicity and toxin expression seen in adults is also seen in younger subjects with recurrent abdominal pain. Children and adolescents demonstrate 40% CagA positivity as compared with 80–100% of adults with duodenal ulcer and gastritis. Mitchell et al. (1999) also found that the presence of CagA is not a marker of specific disease in children. Furthermore, these investigators conclude that children do become persistently infected by *H. pylori* and few carry strains with the virulence properties seen in adults with gastrointestinal pathology. Whether these children should be treated to reduce risk of gastritis and gastric cancer is not clear at this time (Çelik et al. 1998). The current view holds that *H. pylori* is spread to children from close person-to-person contact and, because there is familial clustering seen with infection of children, it has been suggested that family treatment may decrease treatment failures due to increased compliance (Fall et al. 1997; Oderda et al. 1997).

H. pylori is responsible for approximately 80% of duodenal ulcer after other etiologies including Crohn's disease (CD), non-steroidal anti-inflammatory drug ingestion, and Zollinger-Ellison syndrome have been ruled out. In a retrospective review of pediatric gastroscopy carried out in Hong Kong, 88% of patients complaining of dyspepsia had positive histological findings. In this group 25% were positive for *H. pylori* (Ng et al. 1997). Heaney et al. (1998) have suggested that *H. pylori* infection status can be used as a criterion to select patients for gastroscopy when determining management of young dyspeptic patients. In this study 160 "young" patients (<45 years of age) were prospectively recruited when presenting with the complaint of epigastric pain and/or discomfort. Patients who were negative for *H. pylori* using the carbon-13 (^{13}C) urea breath test were reassured that they would likely have a normal gastroscopy. At this point they were given lifestyle advice and symptomatic therapy and then followed at intervals of 6 weeks, 3 months, and 6 months. If they were the same or worse at these intervals, they proceeded to gastroscopy. This management protocol resulted in a 42% reduction in the number of gastroscopy examinations in *H. pylori* patients.

Recurrent abdominal pain is a common presenting complaint in children. There is no substantial evidence to suggest that *H. pylori* has any role in recurrent abdominal pain or so-called non-ulcer dyspepsia in children. Wewer et al. (1998) assessed the IgG seroprevalence of *H. pylori* in children with recurrent abdominal pain compared with healthy children to investigate the presence or absence of related symptoms. IgG antibodies against low molecular weight *H. pylori* were assessed in a total of 438 children and 91 healthy controls. The seroprevalence in children with recurrent abdominal pain was 21%, against 10% in the controls with 46 of 66 of those positive by culture and histology. The presence of *H. pylori* was associated with both parents being born in a country with high prevalence of *H. pylori*, low socioeconomic class, and more pain related to meals but not related to low levels of hemoglobin, leukocytes, thrombocytes, weight, or height. No specific symptomatology was related to *H. pylori* positivity in children. In a case control study of Turkish children by Günel et al. (1998) no association was found between children with *H. pylori* infection, hypergastrinemia, and recurrent abdominal pain. *H. pylori* infection was as high in healthy children as in those with recurrent abdominal pain confirming the findings by Gottrand et al. (1997) that normal gastric histology can be associated with infection in children.

The wide interest in this bacterium has spawned many investigations of its relationships, if any, with other gastrointestinal diseases, with inflammatory bowel disease (IBD) being a case in point. The cause or causes of IBD remain incompletely understood

with infectious agents including several bacteria and viruses implicated. Since *H. pylori* infection causes changes in both permeability and immunological arrangements in the stomach similar to those seen in the colon in IBD, it is natural to wonder if there is a causal relationship. Currently, there is no epidemiological data to support that conclusion and while, interestingly, there is a low prevalence of *H. pylori* in inflammatory bowel disease, the clinical significance, if any, of *H. pylori* infection against the background of IBD is not yet clear (Nardone et al. 1998; Parente et al. 1997). Permanent colonization of the stomach in pediatric patients with IBD is unusual (Kolho et al. 1998). In a cross-sectional study with matching of patients with IBD and upper gastrointestinal lesions it is noted that the reduced *H. pylori* infection prevalence is due mainly to decreased frequency of colonization in patients with CD. The prior treatment of patients with sulfasalazine but not 5-aminosalicylic acid, steroids, or immune suppressants is associated with a reduced risk of infection in both patients with ulcerative colitis (UC) and CD. In the group of patients with CD (123 of 216), 10% had gastroduodenal localization of their disease while 15% had *H. pylori* negative gastritis on histological examination (Parente et al. 1997).

Celiac disease is a disorder frequently associated with gastritis. In a study performed to assess the prevalence and significance of *H. pylori* infection in children with celiac disease no increase in prevalence or clinical manifestations of *H. pylori* was found (Luzza et al. 1999). Recurrent abdominal pain was the only symptom that distinguished between *H. pylori* positive and negative children, but this symptom resolved on gluten withdrawal regardless of their *H. pylori* status.

As *H. pylori* is a causal agent for gastritis, the presence of *H. pylori* infection in gastric-body-type mucosa as is seen in Meckel's diverticulum may be pathogenic. Hill and Rode (1998) reported the case of a 25-year-old man who presented with rectal bleeding and a positive Meckel scan. Surgical pathology revealed a diverticulum with gastric-body-type mucosa with active chronic gastritis and positive immunohistochemistry for *H. pylori*. They found only one other case in a retrospective review at their hospital of 21 cases of proven Meckel's diverticulum.

In another line of investigation of gastritis, Salardi et al. (1999) looked at the prevalence of *H. pylori* in children with type-I diabetes mellitus. Children with diabetes are more susceptible to common acquired bacterial infections and chronic atrophic gastritis if they have longstanding disease. They concluded that, although children with diabetes do not differ from their healthy cohorts in terms of prevalence of *H. pylori* infection in the first few years of disease, they subsequently do have a higher *H. pylori* seroprevalence. They suggest that this could be the cause or one of the causes of chronic atrophic gastritis in children with longstanding diabetes. When Barrio et al. (1997) looked at a group of children and adolescents with diabetes, they found that 7% (12 of 177) of these patients had gastric parietal cell autoantibodies and 6 of 8 of those who had antral biopsies were found to have *H. pylori* infection leading them to suggest that diabetic children and adolescents should be screened for infection.

In a study looking at the role of *H. pylori* in diminished growth in children, three populations of children were studied including normal, diabetic, and hyposomic children (Vaira et al. 1998). They looked at the possible role of infection by differing strains of *H. pylori*. As infection with more cytotoxic strains, such as the so-called CagA or VacA strains, lead to more severe gastroduodenal infection, these authors looked for a possible role for these strains in children with decreased growth, but they did not find supportive data.

14.2.1 Diagnostic Tests

When *H. pylori* infection is diagnosed in children and thought to be the cause of the patient's morbidity, a course of double antibiotic therapy is recommended for 4–6 weeks' duration (Hassall 1994). *H. pylori* infection diagnosis can be achieved using invasive methods, such as endoscopy, to provide tissue samples for rapid urease tests, culture, and histological examination. Noninvasive testing can be performed by blood sampling for IgG antibody tests and urea breath testing using radioactive carbon-14 (^{14}C) or stable ^{13}C. Clinical guidelines for the diagnosis and treatment of *H. pylori* in children currently suggest a fairly limited use in the young age group. Ongoing research into its role in gastrointestinal disease and expanding use of nuclear medicine modalities in children may spur further utilization of these methodologies and knowledge of these for use in children will be valuable.

The noninvasive breath tests are painless and can be performed in children who are old enough to follow simple instruction for ingestion and blowing through a straw. Both ^{13}C and ^{14}C urea breath

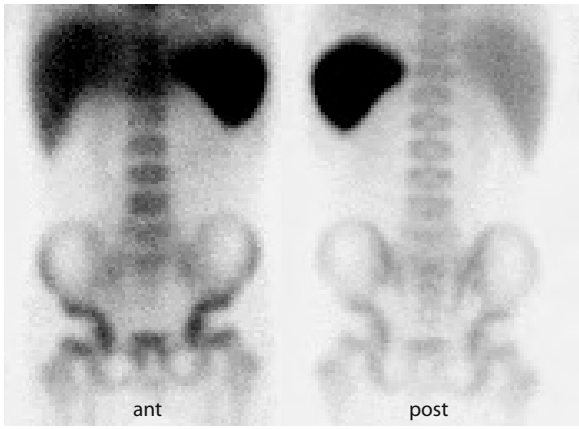

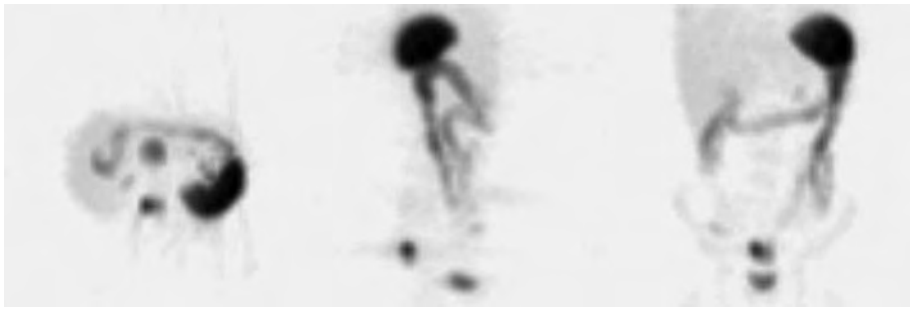

Fig. 14.1a,b. **a** Normal distribution of ^{99m}Tc-HMPAO labeled white blood cells in a child. Anterior view of the abdomen and pelvis. Note the prominent activity in the spleen, liver and bone marrow. **b** inflammatory bowel disease (IBD); diffuse involvement of the colon, including proximal ascending colon, transverse colon, splenic flexure, and descending colon to sigmoid colon in a 10 year old girl with Crohn's disease. Note the high uptake in the spleen in all three planes. MIP = maximum intensity projection image, i.e. a volume rendered summation of the maximal counts from the tomographic images, for the transverse, sagittal and coronal planes

tests for the diagnosis of *H. pylori* infection can be utilized (Cutler 1997). Both tests take advantage of the fact that *H. pylori* produces urease which is needed to break down labeled urea. Gastric urease activity can then be measured and used as an indicator of the presence of infection. Both tests rely on the measurement of labeled CO_2 exhaled by the patient after consuming a standard dose of labeled urea.

Urea breath tests have the ability to sample a larger area of the gastric mucosa than individual biopsies. In the ^{13}C breath test the patient is fed a high-carbohydrate, high-protein meal to slow gastric emptying and increase the residence time of ^{13}C-urea in the stomach. ^{13}C-urea is then ingested as a powder that is dissolved in water. Collection of breath samples occurs at baseline and at 30 min. Thirty minutes is the proposed collection time to avoid false-positive results due to urease in the mouth flora. A mass spectrometer is used for the measurement of ^{13}C.

In the ^{14}C-urea breath test the elimination of ^{14}C via exhaled air is measured with a liquid scintillation counting technique. The advantage of ^{14}C over ^{13}C is that smaller concentrations can be detected as radioactive substances are not routinely exhaled. Baseline breath samples are not required; and there is no need to slow gastric emptying. After a 4-h fast, the pediatric patients are given 0.055 MBq dose orally supplied as dissolvable capsules and samples of exhaled air are taken at as early as 10 min after oral administration with cumulative samples taken at 60 min. Caglar et al. (1999) have shown accurate results when comparing a single 10-min sample to 60-min cumulative excretion, thus improving cost-effectiveness and improving patient acceptance. The accepted upper limit of normal for excretion at 10 min is a specific activity of a breath sample corrected for body surface area of 0.3% (Henze et al. 1990; Debongie et al. 1991). An abnormal test result would be a cumulative value of greater than 2% excretion.

In all methodologies the accuracy of the results can be reduced if certain drugs have been taken by the patient. Antimicrobials should be discontinued a minimum of 4 weeks prior to testing; bismuth-containing compounds 1 month prior; proton pump inhibitors and sucralfate or similar compounds at least 1 week prior to the test; histamine (H2) receptor antagonists for 2 days prior; and antacids for 1 day prior. Histological method accuracy is reported to be reduced in the presence of an active or recently bleeding duodenal ulcer (Cutler 1997).

Although there is some controversy as to which of the available methods of diagnosis of *H. pylori* infection in the untreated patient is best, the urea breath

test is recognized as the method of choice to confirm *H. pylori* cure (Cutler 1997). Confirmation of eradication of *H. pylori* infection is most accurate when the breath test is performed a minimum of 4 weeks after the completion of therapy.

The ^{14}C-urea breath test is simple, easily performed, and inexpensive. It provides quantitative information regarding the total activity of the *H. pylori* bacterium in the stomach as reflected by urease activity and severity of gastritis and is a sensitive and specific method of confirming its presence in peptic ulcer disease (Henze et al. 1990; Debongie et al. 1991). The test has shown between 95 and 98% reproducibility when repeated after a 1-week interval in a series of children (Steen et al. 1995).

The ^{14}C isotope is radioactive and therefore raises considerations relevant to the use of ionizing radiation in the pediatric population . When ^{14}C-urea is used it is excreted in the breath as $^{14}CO_2$ or in the urine. Biokinetic models have been established to determine dosimetry in the pediatric population (Leide-Svegborn et al. 1999). Approximately 88% of the administered activity is excreted in the urine within 72 h of administration. Approximately 3% is exhaled within 20 days. The bladder wall receives the highest dose of radiation. In children aged 7–14 years this effective absorbed dose measures approximately 0.14–0.36 mGy/MBq. The effective total body dose in children is calculated therefore to be 0.9–2.5 μSv for an administered dose of 0.055 MBq. This is a minimal dose and therefore the use of this examination as a screening test and repeated examinations would be acceptable from a radiation burden standpoint.

14.3 Imaging of Inflammatory Bowel Disease

The demonstration of intra-abdominal sources of infection remains a challenging clinical problem. The front line imaging techniques of ultrasound, CT, and MRI provide structural detail but cannot always differentiate adequately treated residual morphological alterations. A variety of scintigraphic studies can provide physiological information not available through other means. This provides a significant contribution to the clinical problems of whether active infection exists in the abdomen, its location, extent, and response to therapy over time. Whereas gallium has a time-honored place in the visualization of infection, radiopharmaceutical innovations allow more specific and more sensitive delineation of infectious processes.

The use of radiolabeled autologous white blood cells (WBC) to assess intra-abdominal sites of infection is increasing. Labeled WBC will leave the circulation at sites of infection and migrate into the infected tissues as part of the normal host response. ^{99m}Tc-HMPAO as a practical label for autologous WBC offers high-quality images with favorable dosimetry. ^{111}In-WBC scanning is not recommended for children because of its unfavorable dosimetry (Gainey et al. 1988). ^{99m}Tc-HMPAO-labeled WBC are proving to be particularly helpful in pediatrics for the assessment of inflammatory bowel disease (Charron 1997; Barabino et al. 1998).

Normal distribution of labeled WBC occurs in the spleen, liver, and red bone marrow (Fig. 14.1), with some faint activity in submandibular glands, kidneys, and bladder. Transient WBC sequestration in the lungs can occur in the first few hours. The gallbladder can be seen in up to 10% of children, but this does not interfere with interpretation. Some activity in normal ascending colon can be seen at 4 h post injection. This activity is usually faint and less intense than iliac crest activity and has a diffuse pattern. This is thought to represent excretion of non-cell bound labeled secondary hydrophilic complexes (Charron 1997). Since imaging for the assessment of bowel inflammation is not usually obtained beyond 4 h, this does not decrease specificity.

No bowel preparation is required for this examination, unlike with gallium imaging. The administered dose is adjusted for body weight between a minimum–maximum dose of 185–740 MBq (5–20 mCi). Imaging protocol includes 0.5- to 1-h and 2- to 3-h static images in anterior and posterior projections and SPECT with low-energy high-resolution collimator. Tail on detector views can be used to help distinguish perianal and rectal disease from bladder activity. Upright anterior views of the abdomen can be helpful in separating liver activity from that in transverse colon. All imaging should be performed after the patient has voided. In children suspected of having CD, a view to include anterior chest and mouth can be used to assess for disease in the esophagus (Charron 1997). Charron et al. (1997) visually grade the inflammatory activity in each segment relative to the iliac crest bone marrow and liver activity: grade 0=no activity; grade 1=less than crest; grade 2=equal to crest; grade 3=greater than crest; grade 4=less than liver; grade 5=equal to liver; grade 6=greater than liver. Abnormal activ-

ity in keeping with inflammation appears bowel shaped, does not change configuration on the late scan, and increases in intensity temporally. The SPECT images reviewed in cine mode with maximal intensity can also increase sensitivity for detection of disease, although there may be some reduction in specificity.

Labeled WBC scintigraphy is particularly helpful for the assessment of small bowel disease. The demonstration of disease distribution influences the selection of therapeutic regimens and has prognostic implications. Labeled-WBC scintigraphy also has the ability to detect extra-intestinal sites of inflammation, such as abscess collections and fistulae (Fig. 14.2). The labeled-WBC scan has also been able to discriminate between continuous and discontinuous disease thereby effectively differentiating UC from CD (Charron et al. 1998). In a series of 106 patients with either UC or CD only 6 patients were classified incorrectly. Labeled-WBC scintigraphy allows for accurate assessment of the segmental distribution of disease when correlated with histology and endoscopy (Charron et al. 1998). This technique can be particularly helpful in identifying sites of inflammation when technical difficulties preclude this assessment with colonoscopy. Labeled-WBC scintigraphy is less invasive than barium follow-through examination or enteroclysis and is much better tolerated by children. Limitations of labeled-WBC scintigraphy include the inability to assess anatomical detail such as bowel strictures and prestenotic dilations. Fistulae may be difficult to detect. If the abnormal activity is focal, it may be difficult to distinguish large from small bowel due

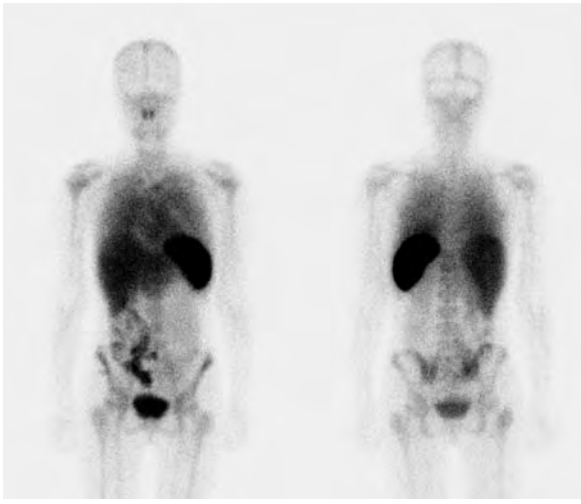

a

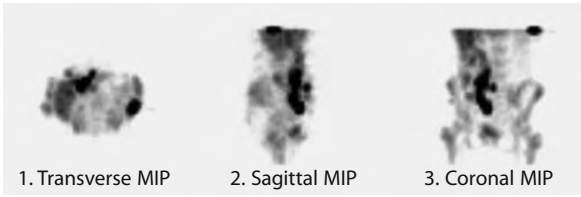

b

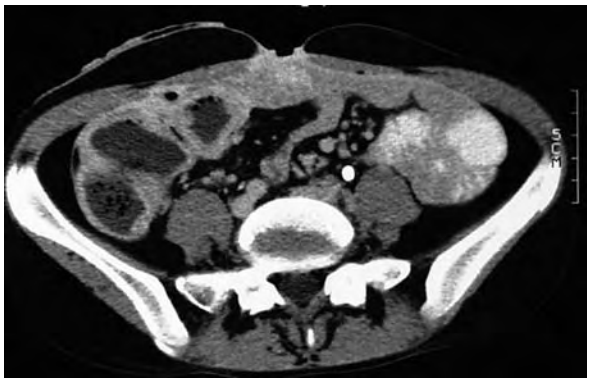

c

d

Fig. 14.2. 16 year old female with inflammatory bowel disease and previous partial colectomy with stoma in right iliac fossa and a fistulous skin tract in the anterior lower abdominal wall. CT showing extensive thick walled bowel in right lower quadrant (**c**). Surgical abdominal scar in the midline marked with a paper clip anteriorly, where the clinically identified skin fistula was noted. The CT scan does not clearly identify communication of the tract with bowel. ^{99m}Tc -HMPAO labeled-WBC scan shows extensive abnormal activity in the right lower abdomen with visualization of the transverse colon. There is abnormal activity to the anterior abdominal wall seen on the planar views (**a**) and SPECT MIP images (**b**). Fistulogram study showing contrast injected through a catheter placed through the skin fistula filling a connection to the colon in the right iliac fossa (**d**). This appearance is consistent with a colocutaneous fistula. MIP = maximum intensity projection image, see Fig. 14-1b

to insufficient anatomical landmarks. In the child who is actively bleeding there may be difficulty in scan interpretation (Charron et al. 1999). Overall accuracy of 93% with 90% sensitivity and 97% specificity has been reported (Charron et al. 1999; Del Rosario et al. 1999). Charron et al. (1999) report a positive predictive value for labeled-WBC scintigraphy of 97%. In the evaluation of 79 control subjects no false-positive results were obtained. Negative predictive value was 93%. The disease distribution can be underestimated in early CD and nonspecific colitis. When there is focal bowel involvement in the region of the cecum, appendicitis as well as involvement of the cecum with IBD must be included in the differential. Although endoscopy and biopsy are still the gold standards, labeled-WBC scintigraphy is helpful in the follow-up of IBD in detecting recurrence, monitor treatment, or plan surgery. This technique can reduce the need for repeated colonoscopies and barium examinations in these children.

14.4 Pediatric Neuronuclear Medicine

Just as there have been advances in the area of brain scintigraphy in adults, so too have there been advances in pediatric neuro-nuclear medicine. The advent of new radiopharmaceuticals for brain imaging has allowed scintigraphy to become a full-fledged member of the multidisciplinary team investigating neurological and psychological illness in the past decade. Cross-sectional imaging with CT and MRI revolutionized the treatment and diagnosis of neurological disease in adults and children; SPECT and PET imaging bring physiological and functional information to vastly improved morphological imaging modalities. This has opened new doors for medical care providers and scientists to study and learn more about neurological disease, neuropsychiatric disorders, brain development, and learning in childhood.

Advances in instrumentation and radiopharmaceuticals have made it easier to perform brain scintigraphy and to obtain more diagnostic information in children. The studies have focused mainly on regional cerebral blood flow, but new research is exploring metabolic and receptor imaging particularly in neuropsychiatric disease. The main indications for pediatric neurological nuclear scintigraphy include seizure disorders, assessment of brain development, evaluation of tumors, and trauma. Knowledge is growing rapidly and expanding our understanding of developmental and neuro-psychological disorders.

While heredity is a large contributor to brain structure and function, we know that development and learning after birth can and will have enormous impact on a child's ultimate motor sensory and intellectual potential and capabilities. When birth or early developmental experiences have a potentially negative impact, parents look anxiously to physicians and allied health personnel for aid. Neuroimaging can be performed to guide intervention, treatment, assessment, or prediction of ultimate outcome (Denays et al. 1990; Kerrigan et al. 1991; O'Tuama and Treves 1993; Kao et al. 1994; Yamada et al. 1995; Lee et al. 1998).

Radiopharmaceuticals used for PET have included ^{18}F-fluorodeoxyglucose (FDG), ^{11}C-L-methionine for tumor imaging, oxygen-^{15}O for cerebral blood flow assessment of intraventricular hemorrhage and infarction, and hypoxic ischemic encephalopathy in infants. SPECT radiopharmaceuticals include ^{99m}Tc-HMPAO and ^{99m}Tc-ECD or less commonly ^{123}I-iodoamphetamine or ^{133}Xe for regional cerebral blood flow assessment. Ligands labeled with ^{123}I or ^{11}C have been used in receptor imaging studies. ^{201}Tl has been used to differentiate recurrent disease from radiation necrosis in children with brain tumors.

Neuroimaging is also used in infants and children to learn about the normal and abnormal development of the brain. Neuroimaging is used more and more in the research and investigations of childhood psychiatric and behavioral disorders, which raises important questions about the value of these tests to children as a group and the individual and group attendant risks. Investigations using ionizing radiation are justified by using the calculation of the so-called risk/benefit ratio of the test. This ratio may not be calculable in the short term and certainly not for a particular child at a particular time in development, assuring that this debate will continue in the future. Ernst (1999) points out correctly that the risk/benefit ratio is essential to the conduct of research and requires the calculation of risks according to the ambiguous definition of "minimal risk." When discussing the risks of exposure to low-level radiation, it is helpful to compare the risk to everyday activities that the child might realistically expect to partake in, such as riding in a car, as well as risks which might be uppermost in the mind of children or their parents such as the risk of developing leukemia or other cancers and the risk of increased chromosomal abnormalities. In another review article assessing health hazards to children

of radiation exposure in the context of brain imaging research, the authors conclude that health risks from low-level radiation obtained by radiographic and scintigraphic diagnostic studies are not detectable above random events that occur in everyday life (Ernst et al. 1998).

Brain imaging research has huge potential benefits to society as a whole. Understanding its attendant risks to children is crucial to rational discussion of investigation of neurological and psychological disorders. Members of ethics and grant review boards, as well as individual researchers and practitioners, need to understand the risk of exposure to low-level radiation through research and diagnostic studies. This research needs the participation of both children who are abnormal and those who are normal. It is not unreasonable to assert that normal children will also benefit from further understanding of neurological and psychological dysfunction. PET studies in normal child volunteers have to date recorded very low acceptable radiation exposures (Ernst et al. 1998).

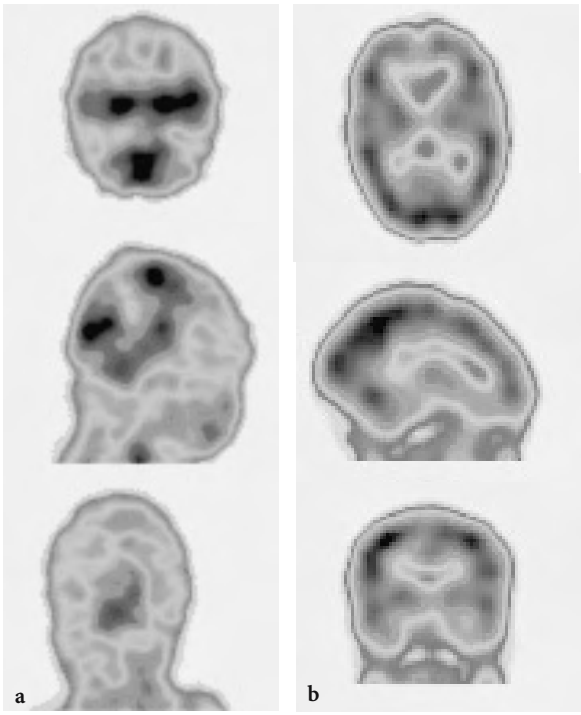

Fig. 14.3. ^{99m}Tc-HMPAO activity pattern in a normal newborn (**a**) and at 6 months of age (**b**). Note the initial lack of frontal activity, prominent brain stem and temporo-parietal perfusion, which increases over the first six months with more uniform cortical activity seen at 6 months

14.4.1 Scintigraphy in Brain Development

Brain development has been extensively studied using PET and FDG. Similarly SPECT radiopharmaceuticals have been used to assess changes in regional cerebral blood flow with brain development in the normal human infant (Chugani et al. 1987; Chiron et al. 1992; Chugani 1998; Kinnala et al. 1996; Schiepers et al. 1997; Rubinstein et al. 1989). Brain development is phylogenetic with developmentally older structures visualized before newer structures. At a gestational age less than 40 weeks, regional cerebral blood flow imaging shows prominent activity seen in the thalami with no parietal or occipital cortical activity and poor if any frontal activity. At 40 weeks or term gestational age, thalamic activity remains prominent. There is increase in activity in the parietal cortex, still low occipital activity and poor frontal activity (Fig. 14.3a). At 44 weeks of gestational age there is a prominent parietal cortex visualized, occipital activity is increasing, the thalami remain prominent, and there is still poor frontal activity. At 2 months of age there is predominance of parietal and occipital cortical activity with still low frontal activity. By 6 months of age there is marked cortical predominance. There is increase in frontal cortex activity but still considerably less than the corresponding parietal and occipital cortical activity (Fig. 14.3b). By 1 year of age all cortical areas show a significant increase in regional cerebral perfusion with either PET or SPECT.

Cerebral glucose metabolism matures through childhood until typical adult activity patterns are seen at approximately age 1 year (Chugani et al. 1987; Chugani and Phelps 1986). Cortical glucose metabolic rate measured with PET shows an increase until age 2–3 years which can exceed adult values. This remains high until 8–10 years of age and declines to normal adult values somewhere between 16–18 years of age. This period of rapidly increasing glucose utilization corresponds to a time of overproduction of nerve terminals and synapses. The plateau phase when glucose utilization remains stable but higher than that of adults represents overconnectivity followed by elimination of the excessive connectivity and corresponding reduction in cerebral glucose utilization to adult levels.

Takahashi et al. (1999) using PET have determined normal values for regional cerebral blood flow (rCBF), regional cerebral metabolic rate for oxygen ($rCRMO_2$), and regional oxygen extraction fraction

(rOEF). The children in their series ranged in age from 10 days to 16 years. In the neonatal period the rCBF and $rCRMO_2$ were lowest and increased during early childhood. A temporal sequence of rCBF and $rCRMO_2$ similar to that seen with glucose metabolism and brain SPECT findings was noted, likely reflecting physiological development within anatomical areas of the brain.

Chiron et al. (1992) studied 42 neurologically normal children of all ages (2 days to 19 years) with normal CT, EEG at time of study, and normal psychomotor development for 2 years post study using rCBF by SPECT with ^{133}Xe and compared the results to an adult reference group consisting of 32 subjects 19–29 years of age who were free of neuropathology. The mean rCBF was calculated for three age groups and the measurements showed effects of age in all cortical regions and on global blood flow. Global blood flow averaged 50 ml/min per 100 g at birth and increased in all age groups to a maximum at 5 years and decreased to adult levels after 19 years of age. Cortical regions all demonstrated lower perfusion at birth than in adulthood, and all regions peaked at around 5 years of age at levels 70% higher than adult levels. When studied on a relative basis, rCBF was at a lower level at birth than at maturity and increased in the first 2 years of life to plateau during the rest of childhood with less than 10% variation. In addition to refining reference values for large functional areas of the brain, this work reconfirmed the importance of the early years of life in neurological development.

Brain function assessed by regional glucose utilization and PET in the neonate is highest in the thalamic nuclei, brain stem, cerebellar vermis, and sensorimotor cortex which correlates with the dominance of subcortical activity at that age. Early physical examination of an infant elicits the basic reflexes such as rooting and the grasp reflex. As development progresses, the regional utilization of glucose continues to correlate with the development of function in corresponding anatomical regions and these are observed in PET studies in the parietal, temporal, and primary visual cortex, basal ganglia, and cerebellar hemispheres described as encephalization during 2–4 months of age (Chugani 1992).

While work in this area is ongoing, other efforts are aimed at using the neuroimaging techniques of SPECT and PET to attempt to study and, hopefully, predict outcome of neurological insult and catastrophe in the very young. One group of children in whom this would be helpful is the pre-term infant. These infants often have protracted courses in hospitals with superimposed serious illnesses which may conclude in death. Those who survive have often been subject to long periods of artificial ventilation with varying levels of low p_aO_2 and high p_aCO_2, low hematocrit, and low arterial blood pressure, all of which may negatively impact on development and growth. It has been reported that ventilation in neonates is associated with low CBF and specifically with hemorrhage and neurological deficit (Greisen 1986, 1990; Greisen and Pryds 1988; Allan and Volpe 1986; Altman et al. 1993). With respect to intracranial hemorrhage, cranial ultrasound is an effective investigation in the preterm infant for diagnosis and for predicting outcome. Hemorrhage tends to be less damaging to the very young infant than infarction into the periventricular white matter or periventricular leukomalacia. Infants born prior to 30–32 weeks gestational age are at risk due to the thin-walled vessels in those areas and combined factors of decreased cerebrovascular reserve and regulation. Baenziger et al. (1999) studied brain perfusion in these infants in an attempt to elucidate the predictive capacity of CBF measurements in this group. A total of 71 preterm infants (less than 1500 g birth weight and less than 34 weeks gestational age) were studied at three time intervals postnatally: between 2 and 36 h; between 36 and 108 h; and between 108 and 240 h respectively using ^{133}Xe and extracranial cadmium telluride detectors. Corresponding cranial ultrasound was performed. The surviving children were assessed for development at 18 months of age. There was a higher mean CBF and mental or motor development. Other studies in children with cerebral palsy have a spectrum of findings on brain SPECT studies which include absence of cerebral blood flow abnormality to thalamic hypoperfusion, diffuse hemispheric hypoperfusion, focal hypoperfusion in the contralateral hemisphere to an area of motor deficit, and cerebellar areas of hypoperfusion (Denays et al. 1990; Kao et al. 1994; Lee et al. 1998). Pryds et al. (1990) suggest that cerebral hyperperfusion in term asphyxiated infants who lose their ability to autoregulate may be an earlier indicator of cerebral hypoperfusion. There is no definitive pattern identified in children with birth asphyxia which can predict long-term sequelae, but cerebral blood flow imaging studies are helpful in the identification of CBF disturbances.

The brain and skull can be involved in a variety of syndromes or isolated insults in early infancy. Craniosynostosis is one such developmental anomaly. When there is premature fusion of multiple sutures

or involvement of only one suture, the result is brain compression which can lead to impaired cognitive development. Surgical correction can include cranial vault remodeling in severe cases and or strip craniectomy. Pre- and post-operative FDG PET studies in a small number of affected children have shown varying regional increases and decreases; however, more consistent postoperative increase in activity has been demonstrated in the posterior occiput in the region where visual development and visual–spatial coordination develops (David et al. 1999).

14.4.2 Language and Cognition

One of the main and best established uses of functional brain imaging is the localization of epileptogenic foci in children in whom surgical treatment is planned. When CT and MRI have ruled out a morphological abnormality, radionuclide perfusion imaging inter- and postictally offers a sensitive method for localization of the seizure activity. The finding of decreased regional perfusion at a focal area and increased perfusion at the same site during a seizure offers a sensitivity of approximately 95%, although this number falls if temporal lobe epilepsy is excluded (Gordon 1996). Nuclear physicians may be unaware that there are substantial considerations for these children regarding language problems and behavioral abnormalities which must be understood to allow the best possible treatment.

There are many language and behavioral manifestations associated with epilepsy and not infrequently these may be epileptic events which are erroneously ascribed to behavioral problems (Tuchman 1994). Although the anatomical basis linking seizure disorders to disorders of behavior, such as aggression, depression, and even schizophrenia, have been postulated, this is not yet universally accepted. These areas are fertile fields for functional imaging. The total effects of seizures on the brain are incompletely understood and still debated (Devinsky and Bear 1984; Holmes 1991; Lesser et al. 1986). In the 1950s Landau and Kleffner (1957) described a syndrome of acquired aphasia in epilepsy which has been followed by numerous other similar reports, although the exact pathogenesis and neuroanatomical basis for this is unclear. In a study designed to demonstrate the regional cerebral perfusion in Landau-Kleffner syndrome and its correlates with the EEG, O'Tuama et al. (1992) performed brain SPECT using ^{99m}Tc-HMPAO in five children with this syndrome and in three with other speech difficulties. They found perfusion asymmetry with decreased perfusion in the temporal lobes most marked in the perisylvian cortex. A PET-FDG study performed in three boys with this syndrome showed similar findings, mainly in the temporal lobe distribution. Neither study nor subsequent studies have yet defined the correspondence to EEG abnormalities (Maquet et al. 1990).

Congenital dysphasia has also been studied using SPECT. This is a clinical diagnosis of exclusion where deafness, mental retardation, speech pathology, and neurological and psychiatric causes have been ruled out. In a study of 14 affected children, SPECT demonstrated decreased activity in the left hemisphere, best localized near Broca's area in 2 patients with expressive aphasia. In 9 of 12 children with both expressive and comprehension problems there were two areas of abnormality best localized to the left temporo-parietal area and the right frontal lobe (Denays et al. 1989).

Children suffering from epilepsy have a higher risk of learning and behavioral disorders, which is multi-factorial and can be very complicated to investigate. Many of the important factors are not directly relevant to functional brain imaging; two of interest to nuclear medicine specialists are seizure activity and the location of the epileptogenic focus both of which have significant negative effects on cognition. Specifically, temporal lobe seizures are considered a definite risk factor for cognitive developmental problems and functional brain imaging studies have confirmed this through a suspected negative effect on verbal memory (Aldenkamp et al. 1990).

14.4.3 Brain Trauma and Brain Death

The determination of brain death relies on unequivocal clinical data indicative of irreversible cessation of brain function, specifically both cortical and brain stem functions. Supportive laboratory studies, most importantly two silent EEG studies separated by various time periods depending on legal jurisdiction, are desirable and often required. In cases of catastrophic injury of a child, the declaration of death can be a highly charged situation for the relatives and physicians involved in the child's care and for physicians involved in harvesting and transplanting organs into other ill children and adults. Not infrequently, an objective test provides comfort

for this task. Younger et al. (1989) claim that knowledge of medical and legal criteria for diagnosing death among physicians is surprisingly lacking. It is important that the contribution of nuclear brain scans be available, prompt, and knowledgeable.

Cerebral perfusion studies using tracers, such as ^{99m}Tc-HMPAO or ^{99m}Tc-ECD, are a quick and accurate alternative to traditional gold standard confirmatory four-vessel angiogram examination, to confirm absence of intracranial perfusion and help provide a timely diagnosis of brain death. These radiopharmaceuticals have advantages over the blood-brain barrier agents formerly used in that there is less difficulty in differentiating intra- and extracerebral activity and activity in the dural sinuses is not a potentially confusing picture. Technical aspects of bolus injection and timing of the study are less stringent and assessment of the posterior fossa using the ^{99m}Tc-lipophilic perfusion agents is far easier (Fig. 14.4; Laurin et al. 1989; Schiepers et al. 1997).

The absence of perfusion above the tentorium with preservation or persistence of blood flow in the cerebellum and/or brainstem contradicts the diagnosis of brain death, although it has a grave prognosis (Valle et al. 1993). The planar scintigraphy should include a lateral view and SPECT should be performed for the best evaluation of the posterior fossa. A prudent recommendation is to include views of the thyroid bed to confirm radiopharmaceutical quality. Views of the liver and heart also support radiopharmaceutical integrity and an estimation of viability of those organs (Wieler et al. 1993). Imaging can also be done with a portable camera in the ICU setting, if desirable. All patients showing absent brain uptake with these tracers are confirmed as brain dead uniformly in published series. Reported series include mainly adult patients (Larar and Nagel 1992; Wilson et al. 1993; Goodman et al. 1985). The diagnosis of brain death in children can be difficult and adult criteria are not necessarily sufficient or easy to obtain (Holzman et al. 1983). There are several series of pediatric patients which confirm that absence of intracerebral perfusion is a highly reliable aid in diagnosing of brain death (Fig. 14.4). This is particularly useful when the clinical criterion of silent EEG is complicated (Galaske et al. 1988).

Nonfatal head injury ranging from mild to severe has also been studied using lipophilic ^{99m}Tc-labeled brain agents and FDG. Both CT and MRI scans as the front line tools in the diagnosis of head injury can be less sensitive than nuclear medicine studies. Traumatic brain injury abnormalities in regional cerebral blood flow and glucose metabolism can be documented, more extensive, and detected earlier than with CT or MRI (Abu-Judeh et al. 1998). Evidence of ischemic injury is common and can be present in any region of the brain. It is attributed to diffuse or focal axonal shearing in the white matter in the absence of a structural abnormality on CT or MRI scan.

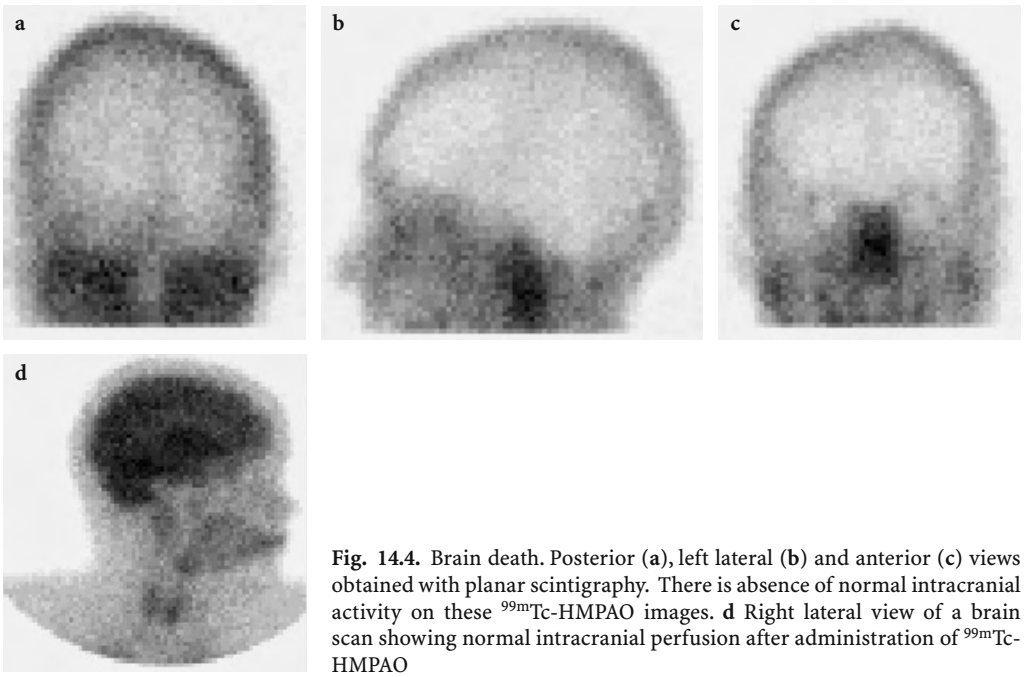

Fig. 14.4. Brain death. Posterior (**a**), left lateral (**b**) and anterior (**c**) views obtained with planar scintigraphy. There is absence of normal intracranial activity on these ^{99m}Tc-HMPAO images. **d** Right lateral view of a brain scan showing normal intracranial perfusion after administration of ^{99m}Tc-HMPAO

Regional hypoperfusion on SPECT can be concordant or discordant with reduced glucose metabolism on PET (Abu-Judeh et al. 1998; Yamaki et al. 1996). When the findings are discordant, it indicates a good prognosis which may be due to vasospasm and edema causing decreased perfusion which is temporary. Most studies demonstrate abnormalities in the temporal frontal or parietal lobes and correlate well with severity of injury generally described by duration, severity of coma, and length of retrograde amnesia (Jacobs et al. 1994; Gordon 1996). An initial negative SPECT examination within 4 weeks of a closed head injury is a robust predictor of full recovery, although a positive scan is of less use prognostically. The role of SPECT and PET brain studies in the clinical and medico-legal work-up and assessment of head injury and its sequelae has not been fully established. Efforts to gain a toe-hold are hampered by lack of knowledge and understanding of the usefulness and applicability by medical practitioners during the acute and chronic phases of head trauma evaluation (van der Kolk 1997). Furthermore, whereas early studies focusing on acute head trauma included patients in the pediatric age group, there are few studies exclusively of children. Studies focusing on the chronic sequelae of brain injury when relationship between the morphological findings may be difficult to confidently relate to the neurological, psychological, or behavioral findings, are also sparse. Goshen et al. (1996) published a series of 28 pediatric patients with chronic sequelae of traumatic brain injury. These patients were referred to the rehabilitation unit of the medical center. They ranged in age from 15 months to 16 years and were assessed using EEG, ^{99m}Tc-HMPAO scintigraphy, CT, and, when available, MRI following substantial head injury (Glasgow coma scale ratings of 3–10). Retrospective analysis showed that cerebral blood flow studies following brain trauma were more sensitive than the anatomical modalities for detection of abnormalities, particularly in the basal ganglia and cerebellum. These authors suggest that brain SPECT may play a role in children who have neurological sequelae in the follow-up of brain trauma.

14.5 Primary Neuro-Psychological Disorders in Childhood

Using the classification of O'Tuama et al. (1999) there are four primary categories of childhood neuro-psychiatric disorders: attention-deficit hyperactivity disorder (ADHD); mood disorders such as depression and obsessive–compulsive disorder (OCD); Tourette syndrome and related disorders; and infantile autism and autistic spectrum disorder. One of the most inspiring uses of functional brain imaging must be the study of neuro-psychological disorders in children. The definition, etiology, diagnosis, and treatment of many of these disorders can be difficult and controversial. Few would dispute the negative outcome on adult life nor deny the often alarming repercussions that many of these disorders have on emotional development and family relationships.

The ability to study cerebral perfusion and metabolism with radionuclides has inspired great hopes for better understanding of psychiatric and developmental disorders in children and adolescents. The hope has been to aid or substantiate the correlation of neuro-psychological deficits or behavioral abnormalities with specific morphological regions and metabolic abnormalities. However, as pointed out by Filipek (1999), behavioral problems in children provide a spectrum of disorders which encompass deficits or derangements in language, cognition, visual–spatial function, and socialization.

14.5.1 Attention Deficit Hyperactivity Disorder

Attention deficit hyperactivity disorder continues to receive enormous attention in the lay media and is a subject of great ongoing study and research. The diagnosis has evolved substantially in recent years in tandem with advances in genetic, cognitive, and pharmacological research among other factors. The American Psychiatric Association includes the following criteria as assessed by reports by parents and teachers: poor impulse control; hyperactivity; poor temper control; and poor attention span. This disorder is relatively common, affecting up to 5–6% of children, and its propensity for boys is well known. The syndrome manifests in adulthood and leads to substantial social problems and alienation. Affected children are generally further classified as predominantly inattentive, predominantly hyperactive, and a combination type. Research using neuroimaging is confounded by frequent overlay of other behavioral disorders, mood, and anxiety disorders, and learning disabilities. Although the exact mechanism for this is not certain, advances in cognitive research in this area consider the main impairment in ADHD to be the inability to inhibit a behavioral response. Multiple models exist in the literature pointing to an

arising focus of cognitive and genetic research, and neuroimaging (Tannock 1998).

Neuroimaging, specifically MRI, suggests that developmental abnormality involves the right hemisphere and basal ganglia (Tannock 1998; O'Tuama et al. 1999). Brain SPECT imaging neither confirms nor refutes global changes in cerebral perfusion and currently most convincingly presents hypoperfusion and, therefore, presumably decreased neuronal functioning in the striatal regions (Lou et al. 1989). More recent work using PET has demonstrated decreased glucose metabolism in the pre-frontal cortex (Tannock 1998). Experimental lesions in animals in both the striatal and prefrontal regions may cause hyperactivity (Lou et al. 1989). Although the available studies can be described as embryonic, at best, there is a clear indication that it is appropriate for nuclear brain imaging to join the research in this important disorder.

14.5.2 Mood Disorders: Depression and Obsessive–Compulsive Disorder

One of the most important advances in childhood neuropsychiatric disorders is simply the acknowledgement and understanding that mood and anxiety disorders do occur in young children and should be treated seriously when they exist. Functional brain imaging has shown great promise in the investigation of mood disorders. Decreased perfusion and metabolism has been demonstrated by SPECT and PET in the left prefrontal cortex and limbic areas, most notably in recurrent or chronic depression. In contrast, patients with transient or normal sadness demonstrate increased activity in the same areas when they are asked to recollect sad events (Risch 1997). This supports the theory that this activated circuitry in normals persists when it becomes chronic and ultimately burns out. Functional imaging in depression in adults most frequently demonstrates decreased perfusion in the temporal, frontal, and parietal areas. There is a significant shortage of studies in children in whom depression is now well recognized. Applying adult criteria to children may be completely erroneous as changes in brain activity may fluctuate during the course of an affective illness as well as during normal brain development (Risch 1997; O'Tauma et al. 1999).

The same caution applies to OCD which occurs in adults and children but has mainly been studied in adults. This disorder is not uncommon in children and teenagers and can be debilitating by virtue of intrusive and disturbing obsessive ideation and compulsive behaviors. As in other neuropsychiatric illnesses, a biologic or biochemical basis is suspected, although it is not known where this occurs or what its exact nature is. Functional brain imaging studies suggest involvement of the basal ganglia as well as the orbital–frontal cortex (Swedo et al. 1989; O'Tuama et al. 1999).

14.5.3 Tourette Syndrome

Tourette syndrome is a neuropsychiatric disorder that presents with motor and vocal tics most prominently along with frequent associations with ADHD, obsessive-compulsive disorder, and other disturbing behavioral symptoms. Both SPECT and FDG PET studies have demonstrated hypoperfusion in frontal and temporal lobes and basal ganglia regions (Lampreave et al. 1998; Sieg et al. 1993). As in the other conditions discussed herein, the ages of the patients can confound results with changes due to maturity and/or evolution of the disease with or without co-morbid features. Data from older age groups should not be assumed to apply to children in general, but they certainly suggest that theory-based studies applied to children may be helpful. As in other disorders the observed hypoperfusion is assumed to be linked to decreased neuronal activity. Improvement observed with neuroleptic treatment may be due to decreased hyperactivity in the dopaminergic system leading to clinical improvement (Lampreave et al. 1998).

14.5.4 Autism

Autism currently referred to as autistic spectrum or pervasive developmental disorders is a wide-ranging gamut of deficits involving verbal and nonverbal behaviors. Pervasive developmental disorders includes autistic disorder, Asperger syndrome, and Rett syndrome among others (O'Tuama et al. 1999; Filipek 1999).

Rett's syndrome is a well-known but rare neurodegenerative disorder which affects very young children, and is only seen in girls. In an effort to better understand the biological basis for this tragic disorder, PET studies have been performed using FDG and D2 receptors agonists, although conclusions are

hampered by the small number of subjects. Naidu et al. (1992) demonstrated decreased activity in the occipital cortex in association with slightly increased activity in the frontal cortex. Yoshikawa et al. (1991) studied six patients and suggest that impaired oxidative metabolism exists in Rett syndrome. Using $^{15}O_2$ PET they found that the cerebral metabolic rate of oxygen was decreased in five patients and oxygen extraction fraction in four when compared with three normal controls. Both measures declined with advancing age. The loss of hyperfrontality is also stressed in a study with 13 patients (Lappalainen et al. 1997). SPECT-ECD brain imaging confirms decreased perfusion in the frontal and fronto-parietal cortical areas (Burroni et al. 1997). These perfusion abnormalities become more marked in the later stages of the disease. In general, the perfusion abnormalities precede abnormal findings on MRI.

Gross brain anatomy in subjects with autism is generally normal and neuroimaging studies are inconsistent or inconclusive. The relationship of cortical migration abnormalities to this spectrum of disorders, if any, is not yet known. MRI studies in high functioning adults with autism, known as Asperger syndrome, have demonstrated abnormalities including polymicrogyria, macrogyria, and schizencephaly without a predilection for a particular region in the brain (Filipek 1999; Chakos et al. 1998). Findings from neuropathological and neuroimaging studies in groups of patients with autism can be generally summarized as: increased brain volume with patients demonstrating increased head circumference when compared both with normals and patients with other developmental abnormalities; impaired function at the corpus callosum; and impaired frontal lobe function and abnormalities in the areas of the mind where socialization responses and understanding occurs (Filipek 1999; Deb and Thompson 1998). Data from activation studies would be of potential value in investigating social responses. Data from SPECT and PET studies is only available for a small number of patients with autism many of whom are adults and are further hampered by lack of technical uniformity. Numerous findings are generally not reproduced in other studies (Müller et al. 1999)

Infantile autism is currently described as a developmental disorder for which no specific neurobiological or pathological correlate is defined. Schifter et al. (1994) evaluated retrospectively 13 children with the diagnosis of autism having dysfunctional social interaction skills, decreased or abnormal verbal abilities, and abnormally limited interests and abilities. Unlike other studies, they did not exclude those with significant other abnormalities such as seizure disorders and mental retardation. These children ranging in age from 4.5 to 11 years were studied using FDG PET and CT or MRI, and no common or uniform abnormality was found in the group. The most frequent abnormality found was decreased FDG uptake and for the most part this existed in patients with seizure disorders. The authors feel justified in excluding interictal foci as a cause of this finding due to the multiplicity and multifocal nature of the abnormalities. Furthermore, they conclude that the findings support other work impugning neuronal migration abnormalities, at least in part, as a significant feature. This study illustrates the myriad of technical and logistical difficulties in these and related types of disorders. The sensitivity and specificity of the various imaging studies, although interesting, are far from established but should not discourage ongoing efforts of nuclear physicians to better understand this disease and contribute potential solutions to it.

Functional neuroimaging in childhood disorders continues to be challenging and is complicated by the fact that only pooled data are available, which provides valuable albeit frequently inconsistent information. It is important to understand the large variety of issues to ensure that studies are performed in a manner most likely to enhance and complement ongoing advances in cognitive research, genetics, and therapies. Defining subject groups is difficult and made worse by frequent overlay of more than one disorder. Control groups are often not available in children and subject groups to date are very small. When radionuclide studies are performed, there is variation in scanning techniques, methods of analysis, and activation protocols. None of these factors should discourage informed investigators from further pursuing functional brain imaging research in children.

References

Abu-Judeh HH, Singh M, Masdeu JC, Abdel-Dayem HM (1998) Discordance between FDG uptake and technetium-99m HMPAO brain perfusion in acute traumatic brain injury. J Nucl Med 39:1357–1359

Aldenkamp AP, Alpherts WCJ, Dekker MJA, Overweg J (1990) Neuropsychological aspects of learning disabilities in epilepsy. Epilepsia 31:S9–S20

Allan WC, Volpe JJ (1986) Periventricular-intraventricular hemorrhage. Pediatr Clin North Am 36:47–63

Altman DI, Perlman JM, Volpe JJ, Powers WJ (1993) Cerebral oxygen metabolism in newborns. Pediatrics 92:99–104

Baenziger O, Mueller AM, Morales CG, Jaggi JL, Duc G, von

Siebenthal K, Bucher H-U (1999) Cerebral blood flow and neurological outcome in the preterm infant. Eur J Pediatr 158:138–143

Barabino A, Gattorno M, Cabria M, Sormani MP, Occhi M, Villavecchia G, Gandullia P, Buoncompagni A, Castellano E, Picco P (1998) 99mTc-white cell scanning to detect gut inflammation in children with inflammatory bowel diseases or spondyloarthropathies. Clin Exp Rheumatol 16:327–334

Barrio R, Roldán MB, Alonso M, Cantón R, Camerero C (1997) Helicobacter pylori infection with parietal cell antibodies in children and adolescents with insulin dependent diabetes mellitus. J Pediatr Endocrinol Metab 10:511–516

Berdon WE (1999) Editorial comment. Pediatr Radiol 29:721

Bujanover Y, Reif S, Yahav J (1996) *Helicobacter pylori* and peptic disease in the pediatric patient. Pediatr Clin North Am 43:213–234

Burroni L, Aucone AM, Volterrani D, Hayek Y, Bertelli P, Vella A, Zappella M, Vattimo A (1997) Brain perfusion abnormalities in Rett syndrome: a qualitative and quantitative SPET study with 99mTC-ECD. Nucl Med Commun 18:527–534

Caglar M, Belzberg AS, Spruston B, Sexsmith G (1999) Time-optimized carbon-14 breath test for *Helicobacter pylori* contamination of the stomach. Clin Nucl Med 9:674–677

Çelik J, Su B, Tirén U, Finkel Y, Thoresson A, Engstrand L, Sandstedt B, Bernander S, Normark S (1998) Virulence and colonization-associated properties of *Helicobacter pylori* isolated from children and adolescents. J Infect Dis 177:247–252

Chakos MH, Esposito S, Charles C, Lieberman JA (1998) Clinical applications of neuroimaging in psychiatry. MRI Clin North Am 6:155–164

Charron M (1997) Inflammatory bowel disease in pediatric patients. Q J Nucl Med 41:309–320

Charron M, del Rosario JF, Kocoshis S (1998a) Use of technetium-tagged white blood cells in patients with Crohn's disease and ulcerative colitis: is differential diagnosis possible? Pediatr Radiol 28:871–877

Charron M, Fernando del Rosario J, Kocoshis S (1998b) Distribution of acute bowel inflammation determined by technetium-labeled white blood cells in children with inflammatory bowel disease. Inflamm Bowel Dis 4:84–88

Charron M, del Rosario FJ, Kocoshis SA (1999) Pediatric inflammatory bowel disease: assessment with scintigraphy with 99mTc white blood cells. Radiology 212:507–513

Chiron C, Raynaud C, Maziere B, Zilbovicius M, Laflamme L, Masure MC, Dulac O, Bourguignon M, Syrota A (1992) Changes in regional cerebral blood flow during brain maturation in children and adolescents. J Nucl Med 33:696–703

Chugani HT (1992) Functional brain imaging in pediatrics. Pediatr Clin North Am 39:777–799

Chugani HT (1998) A critical period of brain development: studies of cerebral glucose utilization with PET (review). Prev Med 27:184–188

Chugani HT, Phelps ME (1986) Maturational changes in cerebral function in infants determined by [18]FDG positron emission tomography. Science 231:840–843

Chugani HT, Phelps ME, Mazziotta JC (1987) Positron emission tomography study of human brain functional development. Ann Neurol 22:487–497

Corrado G, Luzzi I, Lucarelli S, Frediani T, Pacchiarotti C, Cavaliere M, Rea P, Cardi E (1998) Positive association between *Helicobacter pylori* infection and food allergy in children. Scand J Gastroenterol 33:1135–1139

Cutler AF (1997) Diagnostic tests for *Helicobacter pylori* infection. Gastroenterologist 5:202–212

David LR, Genecov DG, Camastra AA, Wilson JA, Argenta LC (1999) Positron emission tomography studies confirm the need for early surgical intervention in patients with single-suture craniosynostosis. J Craniofac Surg 10:38–42

Deb S, Thompson B (1998) Neuroimaging in autism. Br J Psychiatry 173:299–302

Debongie JC, Pauwels S, Raat A, de Meeus Y, Haot J, Mainguet P (1991) Quantification of Helicobacter pylori infection in gastritis and ulcer disease using a simple and rapid carbon-14-urea breath test. J Nucl Med 32:1192–1198

Del Rosario MA, Fitzgerald JF, Siddiqui AR, Chong SK, Croffie JM, Gupta SK (1999) Clinical applications of technetium Tc 99m hexamethyl propylene amine oxime leukocyte scan in children with inflammatory bowel disease. J Pediatr Gastroenterol Nutr 28:63–70

Denays R, Tondeur M, Foulon M, Verstraeten F, Ham H, Piepsz A, Noel P (1989) Regional brain blood flow in congenital dysphasia: studies with technetium-99m HM-PAO SPECT. J Nucl Med 30:1825–1829

Denays R, Tondeur M, Toppet V, Ham H, Piepsz A, Spehl M, Rubinstein M, Noel P (1990) Cerebral palsy: initial experience with Tc-99m HMPAO SPECT of the brain. Radiology 175:111–116

Devinsky O, Bear D (1984) Varieties of aggressive behavior in temporal lobe epilepsy. Am J. Psychiatry 141:651–656

Dixon AK, Dendy P (1998) How much does radiation dose matter? The Lancet 352:1082–1083

Duggan AE, Usmani I, Neal KR, Logan RF (1998) Appendicectomy, childhood hygiene, *Helicobacter pylori* status, and risk of inflammatory bowel disease: a case control study. Gut 43:494–498

Ernst M (1999) PET in child psychiatry: the risks and benefits of studying normal healthy children. Prog Neuropsychopharmacol Biol Psychiatry 23:561–570

Ernst M, Freed ME, Zametkin AJ (1998) Health hazards of radiation exposure in the context of brain imaging research: special consideration for children. J Nucl Med 39:689–698

Fall CH, Goggin PM, Hawtin P, Fine D, Duggleby S (1997) Growth in infancy, infant feeding, childhood living conditions, and *Helicobacter pylori* infection at age 70. Arch Dis Child 77:310–314

Filipek PA (1999) Neuroimaging in the developmental disorders: the state of the science. J Child Psychol Psychiatry 40:113–128

Gainey MA, Siegel JA, Smergel EM, Jara BJ (1988) Indium-111-labeled white blood cells: dosimetry in children. J Nucl Med 29:689–694

Galaske RG, Schober O, Heyer R (1988) 99mTc-HM-PAO and 123I-amphetamine cerebral scintigraphy: a new, noninvasive method in determination of brain death in children. Eur J Nucl Med 14:446–452

Gold BD, Khanna B, Huang LM, Lee CY, Banatvala N (1997) *Helicobacter pylori* acquisition in infancy after decline of maternal passive immunity. Pediatr Res 41:641–646

Goodman JM, Heck LL, Moore BD (1985) Confirmation of brain death with portable isotope angiography: a review of 204 consecutive cases. Neurosurgery 16:492–497

Gordon I (1996) Cerebral blood flow imaging in paediatrics: a review. Nucl Med Commun 17:1021–1029
Goshen E, Zwas ST, Shahar E, Tadmor R (1996) The role of Tc-99m-HMPAO brain SPET in paediatric traumatic brain injury. Nucl Med Commun 17:418–422
Gottrand F, Cullu F, Turck D, Vincent P, Michaud L, Husson MO, Martin Delasalle E, Farriaux JP (1997) Normal gastric histology in *Helicobacter pylori* -infected children. J Pediatr Gastroenterol Nutr 25:74–78
Granström M, Tindberg Y, Blennow M (1997) Seroepidemiology of *Helicobacter pylori* infection in a cohort of children monitored from 6 months to 11 years of age. J Clin Microbiol 35:468–470
Greisen G (1986) Cerebral blood flow in preterm infants during the first week of life. Acta Paediatr Scand 75:43–51
Greisen G (1990) Cerebral blood flow in mechanically ventilated preterm neonates. Dan Med Bull 2:124–131
Greisen G, Pryds O (1988) Intravenous 133Xe clearance in preterm neonates with respiratory distress. Internal validation of CBF, as a measure of global cerebral blood flow. Scand J Clin Lab Invest 48:673–678
Günel E, Findik D, Caglayan O, Caglayan F, Topgaç Z (1998) *Helicobacter pylori* and hypergastrinemia in children with recurrent abdominal pain. Pediatr Surg Int 14:40–42
Hall E (1999) Commentary. Pediatr Radiol 29:721–722
Hassall E (1994) Clinical practise guidelines for suspected peptic ulcer disease in children. BC Med J 36:538–539
Heaney A, Collins JS, Tham TC, Watson PR, McFarland JR, Bamford KB (1998) A prospective study of the management of the young *Helicobacter pylori* negative dyspeptic patient – can gastroscopies be saved in clinical practice? Eur J Gastroenterol Hepatol 10:953–956
Henze E, Malfertheiner P, Clausen M, Burkhardt H, Adam WE (1990) Validation of a simplified carbon-14-urea breath test for routine use for detecting *Helicobacter pylori* noninvasively. J Nucl Med 31:1940–1944
Hill P, Rode J (1998) *Helicobacter pylori* in ectopic gastric mucosa in Meckel's diverticulum. Pathology 30:7–9
Holmes GL (1991) Do seizures cause brain damage? Epilepsia 32:S14–828
Holzman BH, Curless RG, Sfakianakis GN, Ajmone-Marsan C, Montes JE (1983) Radionuclide cerebral perfusion scintigraphy in determination of brain death in children. Neurology 33:1027–1031
Hornemann F, Nilius M, Malfertheiner P, Bartmann P (1997) Seroprevalence of *Helicobacter pylori* in German infants and children. Helicobacter 2:176–179
Huang FC, Chang MH, Hsu HY, Lee PI, Shun CT (1999) Long-term follow-up of duodenal ulcer in children before and after eradication of *Helicobacter pylori*. J Pediatr Gastroenterol Nutr 28:76–80
Ierardi E, Francavilla R, Balzano T, Negrini R, Francavilla A (1998) Autoantibodies reacting with gastric antigens in *Helicobacter pylori* associated body gastritis of dyspeptic children. Ital J Gastroenterol Hepatol 30:478–480
Jacobs A, Put E, Ingels M, Bossuyt A (1994) Prospective evaluation of technetium-99m HMPAO-SPECT in mild and moderate traumatic brain injury. J Nucl Med 35:942–947
Kao CH, Wang SJ, Yeh SH (1994) The relationship among the quantitative perfusion-defect indices in Tc-99m HMPAO brain SPECT, IQ test, and involved extremities in children with cerebral palsy due to perinatal asphyxia. Clin Nucl Med 19:309–313
Kerrigan JF, Chugani HT, Phelps ME (1991) Regional cerebral glucose metabolism in clinical subtypes of cerebral palsy. Pediatr Neurol 7:415–425
Kinnala A, Suhonen-Polvi H, Aarimaa T, Kero P, Korvenranta H, Ruotsalainen U, Bergman J, Haaparanta M, Solin O, Nuutila P, Wegelius U (1996) Cerebral metabolic rate for glucose during the first six months of life: an FDG positron emission tomography study. Arch Dis Child 74:F153–F157
Kolho KL, Rautelin H, Lindahl H, Savilahti E (1998) *Helicobacter pylori*-positive gastritis in pediatric patients with chronic inflammatory bowel disease. J Pediatr Gastroenterol 27:292–295
Lampreave JL, Molina V, Mardomingo MJ, Bittini A, Dominguez P, Almoguera I, Rubia FJ, Carreras JL (1998) Technetium-99m-HMPAO in Tourette's syndrome on neuroleptic therapy and after withdrawal. J Nucl Med 39:624–628
Landau WM, Kleffner FR (1957) Syndrome of acquired aphasia with convulsive disorder in children. Neurology 7:523–530
Lappalainen R, Liewendahl K, Sainio K et al (1997) Brain perfusion SPECT and EEG findings in Rett syndrome. Acta Neurol Scand 95:44–50
Larar GN, Nagel JS (1992) Technetium-99m-HMPAO cerebral perfusion scintigraphy: considerations for timely brain death declaration. J Nucl Med 33:2209–2213
Laurin NR, Dreidger AA, Hurwitz GA, Mattar AG, Powe JE, Chamberlain MJ, Zabel PL, Pavlovsky WF (1989) Cerebral perfusion imaging with technetium-99m HM-PAO in brain death and severe central nervous system injury. J Nucl Med 30:1627–1635
Lee JD, Kim DI, Ryu YH, Whang GJ, Park CI, Kim DG (1998) Technetium-99m-ECD brain SPECT in cerebral palsy: comparison with MRI. J Nucl Med 39:619–623
Leide-Svegborn S, Stenstrom K, Olofsson M, Mattsson S, Nilsson LE, Nosslin B, Pau K, Johansson L, Erlandsson B, Hellborg R, Skog G (1999) Biokinetics and radiation doses for carbon-14 urea in adults and children undergoing the *Helicobacter pylori* breath test. Eur J Nucl Med 26:573–580
Lesser R, Luders H, Wylie E et al (1986) Mental deterioration in epilepsy. Epilepsia 27:S105–S123
Ljung B (1997) The child in diagnostic nuclear medicine. Eur J Nucl Med 24:683–690
Lou HC, Henriksen L, Bruhn P, Borner H, Bieber Nielsen J (1989) Striatal dysfunction in attention deficit and hyperkinetic disorder. Arch Neurol 46:48–52
Luzza F, Mancuso M, Imeneo M, Mesuraca L, Contaldo A, Giancotti L, La Vecchia AM, Docimo C, Pensabene L, Strisciuglio P, Pallone F, Guandalini S (1999) *Helicobacter pylori* infection in children with celiac disease: prevalence and clinicopathologic features. J Pediatr Gastroenterol Nutr 28:143–146
Malaty HM, Graham DY, Wattigney WA, Srinivasan SR, Osato M, Berenson GS (1999) Natural history of *Helicobacter pylori* infection in childhood:12-year follow-up cohort study in a biracial community. Clin Infect Dis 28:279–282
Maquet P, Hirsch E, Dive D et al (1990) Cerebral glucose utilization during sleep in Landau-Kleffner syndrome: a PET study. Epilepsia 31:778–783
Mitchell HM, Hazell SL, Bohane TD, Hu P, Chen M, Li YY (1999) The prevalence of antibody to CagA in children is not a marker for specific disease. J Pediatr Gastroenterol Nutr 28:71–75
Müller RA, Behen ME, Rothermel RD, Chugani DC, Muzik O,

Mangner TJ, Chugani HT (1999) Brain mapping of language and auditory perception in high-functioning autistic adults: a PET study. J Autism Dev Disorders 29:19–31

Naidu S, Wong DF, Kitt C, Wenk G, Moser HW (1992) Positron emission tomography in the Rett syndrome: clinical, biochemical and pathological correlates. Brain Dev 14 [Suppl]: S75–79

Nardone G, Rocco A, Budillon G (1998) Does *Helicobacter pylori* play a role in inflammatory bowel disease? Ital J Gastroenterol Hepatol 30:134–137

Narla LD, Hingsbergen EA, Jones JE (1999) Adult diseases in children. Pediatr Radiol 29:244–254

Ng DK, Liu JH, Ho JC (1997) Paediatric upper gastrointestinal endoscopy: a 2-year review. Chin Med J (Engl) 110:587–589

Oderda G, Ponzetto A, Boero M, Bellis D, Forni M, Vaira D, Ansaldi N (1997) Family treatment of symptomatic children with *Helicobacter pylori* infection. Ital J Gastroenterol Hepatol 29:509–514

O'Tuama LA, Treves ST (1993) Brain single-photon emission computed tomography for behavior disorders in children (review). Semin Nucl Med 23:255–264

O'Tuama LA, Urion DK, Janicek MJ, Treves ST, Bjornson B, Moriarty JM (1992) Regional cerebral perfusion in Landau-Kleffner syndrome and related childhood aphasias. J Nucl Med 33:1758–1765

O'Tuama LA, Dickstein DP, Neeper R, Gascon G (1999) Functional brain imaging in neuropsychiatric disorders of childhood. J Child Neurol 14:207–221

Parente F, Molteni P, Bollani S, Maconi G, Vago L, Duca PG, Rembacken B, Axon AT, Bianchi Porro G (1997) Prevalence of Helicobacter pylori infection and related upper gastrointestinal lesions in patients with inflammatory bowel diseases. A cross-sectional study with matching. Scand J Gastroenterol 32:1140–1146

Pintelon H, Jonckheer MH, Piepsz A (1994) Paediatric nuclear medicine procedures: routine sedation or management of anxiety? Nucl Med Commun 15:664–666

Pryds O, Greisen G, Lou H, Friis-Hansen B (1990) Vasoparalysis associated with brain damage in asphyxiated term infants. J Pediatr 117:119–125

Risch SC (1997) Recent advances in depression research: from stress to molecular biology and brain imaging. J Clin Psychiatry 58:3–6

Roebuck DJ (1999) Risk and benefit in paediatric radiology. Pediatr Radiol 29:637–640

Rothenbacher D, Bode G, Berg G, Knayer U, Gonser T, Adler G, Brenner H (1999) *Helicobacter pylori* among preschool children and their parents: evidence of parent-child transmission. J Infect Dis 179:398–402

Rubinstein M, Denays R, Ham HR, Piepsz A, VanPachterbeke T, Haumont D, Noel P (1989) Functional imaging of brain maturation in humans using iodine-123 iodoamphetamine and SPECT. J Nucl Med 30:1982–1985

Salardi S, Cacciari E, Menegatti M, Landi F, Mazzanti L, Stella FA, Pirazzoli P, Vaira D (1999) *Helicobacter pylori* and type 1 diabetes mellitus in children. J Pediatr Gastroenterol Nutr 28:307–309

Schiepers C, Verbruggen A, Casaer P, De Roo M (1997) Normal brain perfusion pattern of technetium-99m-ethylcysteinate dimer in children. J Nucl Med 38:1115–1120

Schifter T, Hoffman JM, Hatten P, Hanson MW, Coleman E, DeLong GR (1994) Neuroimaging in infantile autism. J Child Neurol 9:155–161

Sherazi Z, Gordon I (1996) Quality of care: identification and quantitation of the process of care among children undergoing nuclear medicine studies. Nucl Med Commun 17:363–366

Sieg KG, Buckingham D, Gaffney GR, Preston DF, Sieg KG (1993) Tc-99m HMPAO SPECT brain imaging of Gilles de la Tourette's syndrome. Clin Nucl Med 18:255

Stabin MG, Gelfand MJ (1998) Dosimetry of pediatric nuclear medicine procedures. Q J Nucl Med 42:93–112

Steen T, Berstad K, Meling T, Berstad A (1995) Reproducibility of the 14 C urea breath test repeated after 1 week. Am J Gastroenterol 90:2103–2105

Stringer DA (1989) Pediatric gastrointestinal imaging. Decker, Philadelphia, Pa

Swedo SE, Schapiro MB, Grady CL, Cheslow DL, Leonard HL, Kumar A, Friedland R, Rapoport SI, Rapoport JL (1989) Cerebral glucose metabolism in childhood-onset obsessive-compulsive disorder. Arch Gen Psychiatry 46:518–523

Takahashi T, Shirane R, Sato S, Yoshimoto T (1999) Developmental changes of cerebral blood flow and oxygen metabolism in children. AJNR Am J Neuroradiol 20:917–922

Tannock R (1998) Attention deficit hyperactivity disorder: advances in cognitive, neurobiological, and genetic research. J Child Psychol Psychiatr 39:65–69

Tuchman RF (1994) Epilepsy, language, and behavior: clinical models in childhood. J Child Neurol 9:95–102

Vaira D, Menegatti M, Salardi S, Ali A, Altomare Stella F, Figura N, Landi F, Holton J, Farinelli S, Cuccaro V, Miglioli M, Cacciari E (1998) *Helicobacter pylori* and diminished growth in children: is it simply a marker of deprivation. Ital J Gastroenterol Hepatol 30:129–133

Valle G, Ciritella P, Bonetti MG, Dicembrino F, Perrone E, Perna GP (1993) Considerations of brain death on a SPECT cerebral perfusion study. Clin Nucl Med 18:953–954

van der Kolk BA (1997) The psychobiology of posttraumatic stress disorder (review). J Clin Psychiatry 58 [Suppl 9]:16–24

Vandenplas Y, Blecker U (1998) *Helicobacter pylori* infection in children. Acta Paediatr 87:1105–1112

Weiss S (1993) Sedation of pediatric patients for nuclear medicine procedures (review). Semin Nucl Med 23:190–198

Wewer V, Andersen LP, Paerregaard A, Gernow AB, Hart Hansen JP, Matzen P, Krasilnikoff PA (1998) The prevalence and related symptomatology of Helicobacter pylori in children with recurrent abdominal pain. Acta Paediatr 87:830-835.

Wieler H, Marohl K, Kaiser KP, Klawki P, Frossler H (1993) Tc-99m HMPAO cerebral scintigraphy. A reliable, noninvasive method for determination of brain death. Clin Nucl Med 18:104–109

Wilson K, Gordon L, Selby JB (1993) The diagnosis of brain death with Tc-99m HMPAO. Clin Nucl Med 18:428–434

Yamada K, Tsuzura S, Matsuda H (1995) Brain MRI and single photon emission computed tomography in severe athetotic cerebral palsy: a comparative study with mental and motor disorders (in Japanese). No To Hattatsu 27:269–275

Yamaki T, Imahori Y, Ohomori Y et al (1996) Cerebral hemodynamics and metabolism of severe diffuse brain injury measured by PET. J Nucl Med 37:1166–1170

Yoshikawa H, Fueki N, Suzuki H, Sakuragawa N, Masaaki I (1991) Cerebral blood flow and oxygen metabolism in Rett syndrome. J Child Neurol 6:237–242

Younger SJ, Landefeld CS, Coulton CJ, Jukialis BW, Leary M (1989) "Brain death" and organ retrieval. A cross-sectional survey

Basics of Scintigraphic Imaging

15 Radiopharmaceuticals: Recent Developments and Trends

Guy Bormans, Kristin Verbeke, and Alfons Verbruggen

CONTENTS

G. Bormans, PhD
K. Verbeke, PhD
A. Verbruggen, PhD
UZ Gasthuisberg, Radiopharmacy Department, Herestraat 49, 3000 Leuven, Belgium

15.1 Production of Radiopharmaceuticals, Quality Control and Availability

Radionuclides used in nuclear medicine are mostly artificial ones. They are primarily produced in a reactor or cyclotron and supplied by commercial companies to individual nuclear medicine departments and institutions. On the other hand, some radionuclides, in particular short-lived ones, are available at any time due to the availability of appropriate radionuclide generators. By far the most important generator in nuclear medicine is the ^{99}Mo/^{99m}Tc generator, which has led to the almost unlimited availability of ^{99m}Tc. Together with the excellent radiation characteristics of ^{99m}Tc and the commercial availability of efficient and licensed labeling kits, this generator lies at the base of contemporary nuclear medicine practice.

The very short-lived positron-emitting radionuclides used in clinical PET [^{11}C ($t_{½}$ = 20.38 min), ^{13}N ($t_{½}$ = 9.96 min) and ^{15}O ($t_{½}$ = 122.2 s)] are only available at or near institutions which have cyclotron facilities and can not be supplied to remote institutions or hospitals due to their rapid decay. Since facilities with a cyclotron and radiochemistry laboratory are expensive, they are not evenly spread worldwide, although their number has increased significantly in recent years.

A steadily growing number of PET centers performs clinical imaging but does not have a cyclotron. These sites are mostly limited to the use of radiotracers labeled with fluorine-18 ($t_{½}$ = 109.8 min), provided by nearby facilities. Currently, mainly ^{18}F-fluorodeoxyglucose (^{18}FDG) is produced in these facilities, increasingly under 'good manufacturing practice' (GMP) conditions, and dispensed to PET imaging facilities in the area. It can be foreseen that soon other fluorine-18 labeled PET radiopharmaceuticals will be distributed through the logistic channels that have been set up for ^{18}FDG distribution. There is a growing interest in using PET radiopharmaceuticals labeled with gallium-68, a radio-

nuclide available from a germanium-68/gallium-68 generator (Hoffend et al. 2004; Meyer et al. 2004; Nakayama et al. 2003).

Incorporation of the cyclotron-produced PET radionuclides into radiopharmaceuticals is performed using dedicated radiochemistry synthesis modules. These units are designed as closed systems to minimize radiation exposure, are computer controlled and operate fully automatically. Quality control of the end-products can be performed using radio GC or radio HPLC and should be carried out under the supervision of a qualified person.

15.2 Perfusion Agents

15.2.1 Myocardial Perfusion Imaging Agents

Mainly because of the nearly optimal physical properties of the radionuclide, ^{99m}Tc-labeled perfusion agents offer several advantages over ^{201}TlCl for myocardial perfusion imaging. Currently, ^{99m}Tc-labeled sestamibi and ^{99m}Tc-tetrofosmin are in routine clinical use. Each of these agents is a lipophilic monoionic cation (Fig. 15.1) and can be prepared in a nuclear medicine department using commercially available freeze-dried kits (Tables 15.1 and 15.2).

^{99m}Tc-sestamibi is a complex of Tc(I) with six molecules of 2-methoxy-2-isobutylisonitrile (MIBI). The labeling kit contains the isonitrile metal binding ligand as its Cu(I) complex to reduce toxicity, volatility and the foul odor of the isonitrile and allow lyophilization (Ramalingam 1989; Iqbal et al. 1989; Sachdev et al. 1990). The heating step during labeling is required to lower the oxidation state of Tc to +1, and to effect ligand exchange from [Cu(I)(MIBI)4]+ to [Tc(I)(MIBI)6]+. It has been shown (Crombez et al. 1991; Hung et al. 1991) that ^{99m}Tc-MIBI can also be prepared simply and efficiently by just heating the Cardiolite (DuPont Pharmaceutical, Medical Imaging Division, North Billerica, MA) vial for 10–13 s in a microwave oven after addition of the ^{99m}Tc generator eluate. However, extreme caution in applying this technique is required as incidents of breakage of ^{99m}Tc-MIBI vials during the micro-

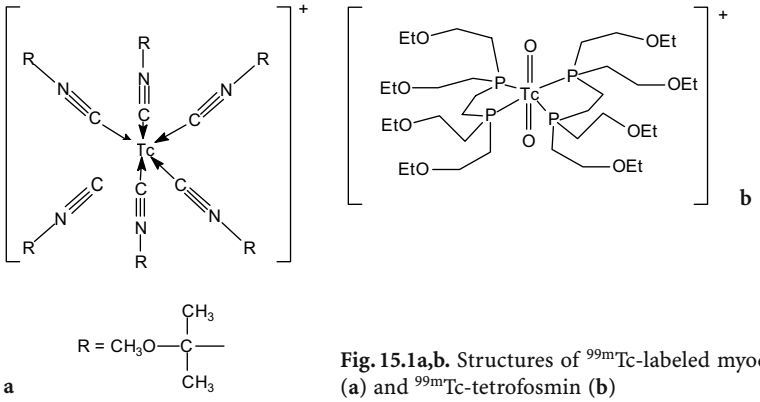

Fig. 15.1a,b. Structures of ^{99m}Tc-labeled myocardial perfusion imaging agents: ^{99m}Tc-MIBI (**a**) and ^{99m}Tc-tetrofosmin (**b**)

Table 15.1. Properties of the commercially available labeling kits for preparation of ^{99m}Tc-labeled myocardial perfusion imaging agents

Brand name of labeling kit	Cardiolite		Myoview	
Manufacturer	Bristol-Myers Squibb Medical Imaging		GE Healthcare (Amersham Health)	
Chemical name of the ligand	2-methoxy-2-isobutyl isonitrile (MIBI)		1,2-bis [bis(2-ethoxyethyl)-phosphino]ethane or tetrofosmin	
Other names of ^{99m}Tc-complex	^{99m}Tc-sestamibi ^{99m}Tc-hexamibi		^{99m}Tc-tetrofosmin	
Composition of labeling kit	$Cu(MIBI)_4BF_4$	1.0 mg	Tetrofosmin	0.23 mg
	$SnCl_2.2H_2O$	0.075 mg	$SnCl_2.2H_2O$	0.030 mg
	L-cysteine HCl H_2O	1.0 mg	Disodium sulfosalicylate	0.32 mg
	Sodium citrate $2H_2O$	2.6 mg	Sodium D-gluconate	1.0 mg
	Mannitol	20.0 mg	Sodium hydrogen carbonate	1.8 mg

Table 15.2. Guidelines for labeling and characteristics of ^{99m}Tc-labeled myocardial perfusion imaging agents

	^{99m}Tc-MIBI	^{99m}Tc-Tetrofosmin
Oxidation state of ^{99m}Tc	+1	+5
Charge of the complex	+1	+1
Incubation	10 min 100°C	15 min room temperature
Maximum activity	5.56 GBq	8.8 GBq
Volume	1–3 ml	4–8 ml
Eluate restrictions	None	Generator last eluted within 72 h Eluate not older than 6 h
pH after reconstitution	5.5	7.5–9.0
Stability after reconstitution	6 h	8 h

wave heating process have been reported (Hung and Gibbons 1992). The function of individual components in the Cardiolite kit formulation has not been described, but it can be assumed that citrate is present as a buffer, cysteine forms a temporary chelate with reduced technetium, and mannitol serves as a filler and 'accelerator' (Tweedle 1983).

^{99m}Tc-tetrofosmin is a ^{99m}Tc(V)dioxo-phosphine cation which can be prepared by simple addition of ^{99m}Tc generator eluate to the labeling vial. After incubation at room temperature for 15 min, the radiochemical purity (RP) of the labeled product exceeds 95% (Higley et al. 1993). Gluconate, present in the kit, is necessary to keep technetium in a +5 oxidation state after reduction by forming a relatively weak ^{99m}Tc-gluconate intermediary complex. Sulfosalicylic acid presumably accelerates ligand exchange from ^{99m}Tc(V)gluconate to ^{99m}Tc(V)dioxo-tetrofosmin. The radiopharmaceutical can be administered up to 8 h post-reconstitution (radiochemical purity >90%).

To assess the radiochemical purity of the ^{99m}Tc-labeled agents, simple quality control procedures (thin layer chromatography or separation on a SepPak-cartridge) are proposed by the manufacturers. Using the appropriate stationary and mobile phase (Table 15.3), the amounts of ^{99m}Tc-complex, $^{99m}TcO_4^-$ and $^{99m}TcO_2$ can easily and rapidly be determined.

Although the images obtained with these tracer agents are generally similar, there are differences in the myocardial kinetics and body distribution. Unlike ^{201}TlCl, the ^{99m}Tc-labeled perfusion agents accumulate in the myocardium by passive diffusion and are not transported by the Na^+-K^+-ATPase enzymatic pump and none of the ^{99m}Tc-labeled agents redistributes. Myocardial uptake for each of the tracer agents is proportional to blood flow and amounts at 60 min post injection to about 1.0 % of injected dose for ^{99m}Tc-MIBI (Wackers et al. 1989) and 1.2% for ^{99m}Tc-tetrofosmin (Higley et al. 1993) at rest and 1.4 % and 1.1 %, respectively, during exercise. Heart to lung and heart to liver ratios of the two ^{99m}Tc-labeled agents are presented in Table 15.4.

Whereas these ^{99m}Tc-labeled agents were originally developed as myocardial perfusion agents, they have been reported to be substrates for P-glycoprotein (Pgp), the product of the human multidrug resistance gene (MDR1), which confers resistance to drugs by transporting cytotoxic agents out of cells (Piwnica-Worms et al. 1993; Ballinger et al. 1996, 1997). As a consequence, they can be used for functional imaging of multidrug resistance in tumors.

Both ^{99m}Tc-MIBI (for this indication marketed under the brand name Miraluma; Bristol-Myers Squibb Medical Imaging, North Billerica, MA) and ^{99m}Tc-tetrofosmin (Myoview; GE Healthcare) have been found useful as a second line diagnostic radiopharmaceutical after mammography to assist in the evaluation of breast lesions in patients with an abnormal mammogram or a palpable breast mass (Cayre et al. 2004; Spanu et al. 2002). Uptake of these trac-

Table 15.3. Systems proposed by the manufacturer for rapid quality control of ^{99m}Tc-labeled myocardial perfusion imaging agents

	^{99m}Tc-MIBI	^{99m}Tc-Tetrofosmin
	TLC	TLC
Stationary phase	Baker-Flex aluminum oxide	Gelman ITLC/SG
Mobile phase	Ethanol	Acetone/dichloromethane (35/65)
^{99m}Tc-complex	Rf = 1	Rf = 0.2–0.8
^{99m}TcO4-	Rf = 0	Rf = 1
^{99m}TcO2	Rf = 0	Rf = 0

Table 15.4. Heart to lung and heart to liver activity ratios at rest and during exercise at different time points after injection of ^{99m}Tc-labeled myocardial perfusion imaging agents in humans

		^{99m}Tc-Tetrofosmin		^{99m}Tc-MIBI	
		Rest	Exercise	Rest	Exercise
15 min	H/lung	1.9 ± 0.2	1.9 ± 0.3	-	-
	H/liver	0.7 ± 0.1	1.2 ± 0.3	-	-
30 min	H/lung	2.0 ± 0.4	2.2 ± 0.5	2.2 ± 0.1	2.3 ± 0.2
	H/liver	1.0 ± 0.2	1.4 ± 0.3	0.5 ± 0.1	1.4 ± 0.2
60 min	H/lung	2.1 ± 0.3	2.1 ± 0.4	2.4 ± 0.1	2.4 ± 0.2
	H/liver	1.3 ± 0.4	1.6 ± 0.4	0.6 ± 0.1	1.8 ± 0.3

ers (low versus high) discriminates breast tumors with different histopathological characteristics and prognosis. The mechanism of localization of these cationic compounds in various types of breast tissue (e.g., benign, inflammatory, malignant, fibrous) has not been established.

15.2.2 Brain Perfusion Imaging Agents

Although in recent years no new radiopharmaceuticals for brain perfusion imaging have emerged, considerable efforts have been made in this field to improve some technical aspects regarding their preparation and stability and to ascertain and compare the individual value of the established radiopharmaceuticals, namely ^{99m}Tc-labeled d,l-HM-PAO and ^{99m}Tc-L,L-ECD (Fig. 15.2, Table 15.5).

^{99m}Tc-labeled d,l-HM-PAO (generic name = ^{99m}Tc-exametazime) can be prepared by reconstitution of the commercially available Ceretec kit (GE Healthcare) with generator eluate. However, to ensure adequate radiochemical purity of the resulting ^{99m}Tc-preparation, severe restrictions are imposed by the manufacturer on the volume, radioactivity concentration and age of the generator eluate and the total radioactivity added to the kit. Moreover, due to the chemical instability of ^{99m}Tc-d,l-HM-PAO (conversion of the lipophilic primary complex to a more hydrophilic secondary complex or directly to $^{99m}TcO_4^-$), the preparation should be administered within 30 min after reconstitution. Eluate age and radioactivity concentration influence the level of oxidants formed through radiolysis. Due to the low amount of stannous ion in the kit (7.6 μg $SnCl_2.2H_2O$ at the time of formulation of the kit), only very small amounts of oxidants can be tolerated. In addition, the primary complex is also susceptible to radiolysis (Tubergen et al. 1991) which explains the radioactivity concentration restrictions.

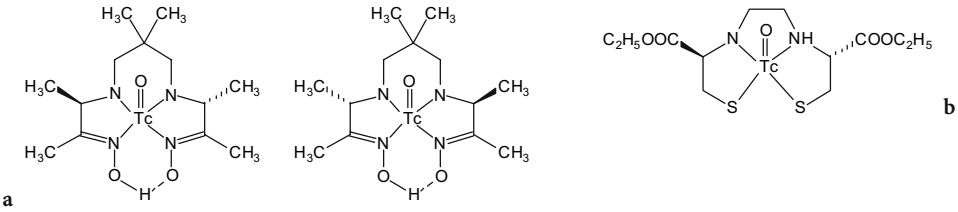

Fig. 15.2a,b. Structures of ^{99m}Tc-labeled brain perfusion imaging agents: ^{99m}Tc-d,l-HMPAO (mixture of D,D (=d) and L,L (=l) isomers) (**a**) and ^{99m}Tc-L,L-ECD (**b**)

Table 15.5. Properties of the commercially available labeling kits for preparation of ^{99m}Tc-labeled brain perfusion imaging agents

	d,l-HM-PAO	L,L-ECD
Brand name of kit	Ceretec	Neurolite
Manufacturer	GE Healthcare (Amersham Health)	Bristol-Myers Squibb Medical Imaging
Chemical name of ligand	[RR,SS]-4,8-diaza-3,6,6,9-tetramethylundecane-2,10-dione bisoxime	N,N'-2-ethylenediylbis-L-cysteine diethyl ester
Other names of ligand	Exametazime Hexamethyl propylene amine oxime d,l-HM-PAO	Bicisate L,L-ethylcysteinate dimer L,L-ECD
Composition of labeling kit	exametazime 0.5 mg $SnCl_2.2H_2O$ 7.6 μg NaCl 4.5 mg	A: ECD.2HCl 0.9 mg $SnCl_2.2H_2O$ 0.072 mg $Na_2EDTA.2H_2O$ 0.36 mg mannitol 24 mg B: Phosphate buffer pH 7.2–8.0

To overcome these severe restrictions, several procedures for stabilization of the primary ^{99m}Tc-d, l-HM-PAO complex have been reported (Hung et al. 1989; Ballinger and Gulenchyn 1991; Billinghurst et al. 1991; Sampson and Solanki 1991; Anon 1989; Lang et al. 1989). Two efficient stabilization methods merit special attention. Weisner et al. (1993) described a method for stabilizing 1.11 GBq-^{99m}Tc-d,l-HM-PAO preparations by addition of 200 µg cobalt chloride hexahydrate in 2 ml water shortly (within 2 min) after reconstitution of the kit with pertechnetate. In this way, a preparation is satisfactory up to 5 h after reconstitution. Mang'era et al. (1994) studied this method in more detail and found that also high activity preparations (up to 5.55 GBq) can be stabilized using this method. Radiochemical purity (% of primary lipophilic complex) exceeds 85% and clinical usefulness for both brain perfusion and white cell labeling is retained up to 6 h after reconstitution. As a consequence, it is possible to prepare a multi-dose preparation of ^{99m}Tc-d, l-HM-PAO.

In the US, the package insert of Ceretec kits prescribes stabilizing the reconstituted ^{99m}Tc-d,l-HM-PAO preparation with methylene blue and adjustment of the pH with phosphate buffer. For this purpose, a complete labeling set comprises the labeling vial with the exametazime ligand plus stannous chloride, a vial of methylene blue injection USP 1% and a vial of 0.003 M monobasic sodium phosphate USP and dibasic sodium phosphate USP in 0.9 % sodium chloride injection USP. Up to 2.00 GBq (54 mCi) ^{99m}Tc-pertechnetate may be used for reconstitution of the kit. For brain imaging when using the stabilizing protocol, generator eluate less than 30 min old should be used; for white blood cell labeling, generator eluate less than 2 h old should be used. The final radiopharmaceutical preparation with methylene blue stabilizer may be used up to 4 h after the time of reconstitution.

Unlike ^{99m}Tc-d,l-HM-PAO, ^{99m}Tc-labeled L,L-ethylene cysteine dimer (^{99m}Tc-L,L-bicisate) is a chemically stable ^{99m}Tc-complex which can be used up to 8 h after reconstitution of the commercially available Neurolite kit (Bristol-Myers Squibb). In the kit, ethylene cysteine dimer (ECD) is supplied in the form of the dihydrochloride for reasons of stability. Because a neutral pH is required to enable efficient labeling, a phosphate buffer pH 7.2–8.0 is supplied in a separate vial. The standard procedure for preparation of ^{99m}Tc-L,L-ECD, as described by the manufacturer, involves the following manipulations:

- Add 3.7 GBq generator eluate in 2 ml NaCl 0.9% to vial B (phosphate buffer)
- Add 3 ml NaCl 0.9% to vial A (containing ECD.2HCl + SnCl2.2H2O + additives) and mix
- Within 30 s, add 1 ml of the solution in vial A to vial B and mix
- Incubate for 30 min

The need for a rather long incubation period (30 min) is apparently caused by the formation of a weak intermediate complex between reduced ^{99m}Tc and mannitol which slowly converts to ^{99m}Tc-L,L-ECD (Mang'era et al. 1996). In order to shorten the preparation time, alternative procedures for preparation of ^{99m}Tc-L,L-ECD have been evaluated. Hung et al. (1997) found that a 97.4% ± 0.5% radiochemical purity (RCP) could be obtained after an 8–s microwave heating time at 300 W (solution temperature at 69°C) and an average RCP value of 96.4% was maintained throughout the 24–h evaluation period. To prevent the possibility of radioactivity spillage caused by either ejection of the rubber stopper or shattering of the glass vial (Hung and Gibbons 1992), an acrylic plastic container should be used or, alternatively, incubation in a water bath at 69°C can replace the microwave heating. However, in the latter case, the time gain is more limited.

Because of its higher stability, ^{99m}Tc-bicisate is the agent of choice for subtraction ictal SPECT coregistered with MRI (SISCOM) to localize the ictal onset zone after self-injection by patients with medically refractory epilepsy (Oliveira et al. 1999; van Paesschen et al. 2000; van Paesschen 2004).

15.2.3 Lung Ventilation Imaging Agents

Radioactive gases with suitable physical characteristics for use as ventilation imaging agents are limited to xenon-133 and krypton-81m. Aqueous aerosols of technetium-99m have been widely developed and refined as replacement for these gases, but suffer from practical limitations such as suboptimal particle size and specific activity. Burch et al. (1984, 1986a,b) developed a technique to produce an ultrafine dispersion of ^{99m}Tc-labeled carbon particles which can be considered as a pseudogas and is called Technegas. After inhalation, Technegas is distributed in the lungs in proportion to regional ventilation (Lemb et al. 1993). It does not show central deposition nor mucociliary clearance. Technegas is produced using a commercially available generator

by heating pertechnetate solution with high specific activity (2.6–4.0 GBq/ml) in a crucible of ultrapure (≥ 99.99%) graphite at 2500°C. During this heating step, argon is present (and is consequently inhaled by the patient) to provide a non-reactive, inert shield around the crucible. No evidence has been reported of any compound having been formed with argon under any circumstances.

When Technegas is prepared in a mixture of 97% argon and 3% oxygen, a pseudogas 'Pertechnegas' is formed. Whereas Technegas particles remain in the lungs for a long period of time, Pertechnegas rapidly disappears with a clearance half-life similar to that of pertechnetate aerosol (Tominaga et al. 1995; Burch and Browitt 1996; Scalzetti and Gagne 1995). Pertechnegas has been reported to be useful for examining the integrity of the alveolar capillary membrane (Monaghan et al. 1991) and for identifying individuals with opportunistic infection or other diffuse lung pathology.

The exact size and structure of the ultrafine carbon particles is difficult to determine. Some authors assume that Technegas might consist of small bucky balls (Burch et al 1986a; Mackey et al. 1994) compatible with the buckminsterfullerene model C60 in which ^{99m}Tc atoms are trapped. Most results suggest now that Technegas and Pertechnegas contain ^{99m}Tc-labeled agglomerated graphite particles in the size range of 60–160 nm.

In a comparison of Technegas, krypton-81m gas and a ^{99m}Tc labeled aerosol as lung ventilation tracer agents, Rizzo-Padoin et al. (2001) conclude that ventilation scintigraphy using krypon-81m clearly yields images with the highest quality, followed by Technegas scintigraphy, but the use of krypton-81m gas is only affordable in terms of cost if at least four patients are examined daily. In a similar comparison of ^{81m}Kr and Technegas, Hartmann et al. (2001) conclude that Technegas does not result in more false-positive V/Q lung scan results. The use of Technegas, however, increases the number of nondiagnostic V/Q lung scan results, which would increase the demand for further additional testing to confirm or refute pulmonary embolism.

15.3 Metabolism Agents

Metabolic imaging requires natural or exogenous radiolabeled substrates which participate in a metabolic process. The design of such tracers is based on physiological concepts such as turnover of oxygen, glucose, amino acids, fatty acids or DNA precursors.

Whereas labeling of candidate tracer agents with ^{11}C can result in an unchanged substrate, labeling with ^{18}F and especially with ^{123}I necessitates chemical changes (F for H, F for OH, alkyl fluoride for H, I for H, I for OH, I for CH_3) which can alter the physiological properties of the tracer molecule due to steric and electronic effects. For labeling with ^{99m}Tc, the necessity to incorporate a bifunctional chelating moiety renders it extremely difficult to predict preserved specificity for the metabolic process. As a consequence, examples of metabolic imaging with ^{99m}Tc-labeled tracer agents are rather scarce.

15.3.1 Glucose Metabolism

2-Fluoro-2-deoxy-D-glucose (2-^{18}F-FDG; Fig. 15.3), the work horse in clinical PET, is used for the evaluation of glucose metabolism. The energy metabolism of the brain is exclusively based on oxidation of glucose whereas the heart uses nonesterified fatty acids as primary substrate for energy production and only glucose in the case of low plasma levels of fatty acid. However, after feeding or glucose loading, glucose becomes the primary substrate. In addition, also tumor cells show a higher glucose consumption compared with normal tissues.

In most departments with dedicated radiochemistry facilities, ^{18}F-FDG is prepared by a nucleophilic displacement reaction of ^{18}F-fluoride on 1,3,4,6-tetra-O-acetyl-2-O-trifluoromethane-sulfonyl-β-D-mannopyranose followed by acidic or (now more frequently) alkaline hydrolysis of the acetyl esters (Hamacher et al. 1986).

After administration, FDG is taken up in the cells where it is phosphorylated by hexokinase to FDG-6-phosphate. FDG-6-phosphate is not a substrate for glycolysis and is not further metabolized but remains trapped in the cells for several hours. The blood clearance is triexponential with components

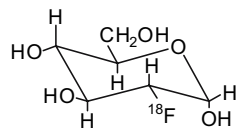

Fig. 15.3. Structure of ^{18}F-FDG

having half-lives of 0.2–0.3 min, 11.6±1.1 min, and 88±4 min (Phelps et al. 1978). The brain uptake in dogs is 2%–3.5% at 120 min (Gallagher et al. 1977) whereas the uptake in the myocardium is about 1%–4%.

Despite an intensive search (e.g. Henry et al. 1995; Dumas et al. 2001, 2003), at this moment no sugar derivative labeled with either ^{123}I or ^{99m}Tc is available as a SPET substitute for ^{18}F-FDG.

15.3.2 Amino Acid Metabolism

Radiolabeled amino acids could be important tools for the quantitative assessment of protein synthesis rate. This would allow diagnosis of various neurological diseases as well as tumor evaluation (diagnosis, tumor grading and prognosis and therapy monitoring). Radiolabeled amino acids pass the blood–brain barrier and are accumulated in tissues via a specific amino acid transport system. L-^{11}C-methyl-methionine (Fig. 15.4) is the most widely used labeled amino acid because of the ease, reliability and high yield of its preparation (Berger et al. 1979; Langström et al. 1987). However, in the cells, the labeled methyl group is transferred to a large number of non-protein acceptor molecules such as lipids and nucleic acids (Ishiwata et al. 1988). As a consequence, the non-protein metabolism is too complex to allow accurate calculation of protein synthesis rate.

It was found that the accumulation of amino acids in cells is dominated by their cellular transport by specific amino acid transporters and that irreversible trapping due to incorporation into proteins is of lesser importance (Wienhard et al. 1991). Therefore, also amino acid analogs which are a substrate for amino acid transporters but are not incorporated into proteins can be used for tumor visualization. In view of the longer half-life of fluorine-18, enabling distribution to satellite PET centers, several fluorine-18 labeled amino acid analogs have thus been evaluated as brain tumor tracers.

In a comparative study, the uptake of O-(2-[^{18}F]fluoroethyl)-L-tyrosine (FET) in brain tumors was found very similar to that of L-[^{11}C-methyl]-methionine (Weber et al. 2000). FET can be prepared in a high yield (40%) by nucleophilic substitution with [^{18}F]fluoride on ethylene glycol-1,2-tosylate, yielding [^{18}F]fluorethyltosylate, which is reacted with L-tyrosine (Wester et al. 1999). Alternatively, FET can be prepared by nucleophilic fluorination of O-(2-tosyloxyethyl)-N-trityl-L-tyrosine t-butylester, followed by removal of the trityl and ester protecting groups in acidic conditions (Hamacher and Coenen 2002).

For SPET studies, L-3-^{123}I-iodo-α-methyltyrosine (^{123}I-IMT) can be considered (Kloss and Leven 1979). There is evidence suggesting that IMT is also accumulated in the brain via a specific facilitating L-amino acid transport system. The carrier system for large neutral amino acids which also transports non-iodinated α-methyltyrosine is likely to be involved (Pardridge 1977). In analogy with FET, IMT is not incorporated into proteins (Langen et al. 1990) and its uptake only reflects amino acid transport (Kawai et al. 1991; Langen et al. 1991). IMT can be prepared by electrophilic substitution via in situ oxidation of ^{123}I-iodide by chloramine-T, hydrogen peroxide, iodogen or iodate with radiochemical yields of 70%–80%.

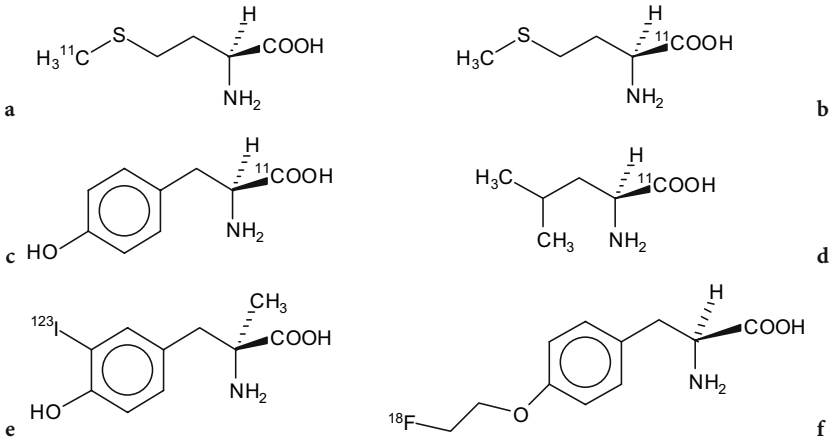

Fig. 15.4a-f. Structures of radiolabeled amino acids: L-^{11}C-methyl-methionine (**a**), L-[1-^{11}C]methionine (**b**), L-[1-^{11}C]tyrosine (**c**), L-[1-^{11}C]leucine (**d**), L-[3-^{123}I]iodo-α-methyltyrosine (**e**) and O-(2-[^{18}F]fluoroethyl)-L-tyrosine (**f**)

15.3.3 Nucleosides Metabolism

In analogy with FDG, nucleosides or nucleoside analogs can be transported across the cell membrane by selective transporters (either equilibrative or concentrative) and can then be phosphorylated intracellularly by specific kinases to the corresponding mono-, di- or triphosphate derivatives and ultimately they can be incorporated into DNA.

As thymidine kinase 1 (TK1) shows an S-phase dependent expression, the intracellular accumulation of labeled nucleosides that are substrates for TK1 reflects DNA synthesis and thus tumor proliferation.

Since incorporation of [^{3}H]thymidine ([^{3}H]TdR) is the gold standard for in vitro tumor cell proliferation, both methyl[^{11}C]thymidine and 2-[^{11}C]thymidine (Vander Borght et al. 1992) have been explored as PET tracers but they suffer from rapid in vivo degradation by thymidine phosphorylase in plasma, resulting in a number of labeled metabolites and a low tumor uptake. As the presence of a 2' or 3' fluorine atom prevents the degradation of nucleosides by thymidine phosphorylase, several fluorine substituted nucleosides have been evaluated (Fig. 15.5). Grierson et al. (2004) compared the uptake and retention characteristics of thymidine with those of ^{18}F-labelled FLT (3'-deoxy-3'-[^{18}F]fluorothymidine, FMAU (2'-arabino-fluoro-5-fluoromethyl-2'-deoxyuridine) and FIAU (2'-arabino-fluoro-5-iodo-2'-deoxyuridine). FLT lacks a hydroxyl group in the 2' position and is not incorporated into DNA in contrast to FMAU and FIAU which, however, have a lower affinity for TK1 resulting in a lower cellular retention compared to FLT. The uptake of FLT still remains a factor of 7 lower than that of thymidine.

FLT is transported in the cell by the equilibrative transporter hENT and in detailed analysis showed that FLT is initially retained in the cell as its monophosphate and at later time points as its mono- and triphosphate (Grierson et al. 2004).

Patient studies have shown that FLT shows uptake in bone marrow and liver and in a variety of tumors, although generally to a lower extent as compared to FDG (Mier et al. 2002). FLT can be synthesized by nucleophilic fluorination of different precursors including 5'-O-(4,4'-dimethoxytrityl)-2,3'-anhydrothymidine and 3-N-Boc-1-[5-O-(4,4'-dimethoxytrityl)-3-O-nosyl-2-deoxy-β-D-lyxofuranosyl]thymine followed by the removal of the protecting groups in acidic conditions (Martin et al. 2002).

Nucleoside derivatives that are selective substrates for herpes simplex virus thymidine kinase (HSVtk) have been developed for the in vivo visualization of transgene expression using the HSVtk gene as a reporter gene. Two classes of substrates were developed: radioiodine labeled uracil derivatives (e.g. 2'-fluoro-2'-deoxy-1-β-D-arabinofuranosyl-5-[^{124}I]iodouracil, FIAU) and fluorine-18 labeled acyclo guanosine derivatives (e.g. 9-(4-[^{18}F]fluoro-3-hydroxymethylbutyl)guanine, FHBG, Fig. 15.5.d).

FHBG is prepared by nucleophilic fluorination of N^2-monomethoxytrityl-9-[(4-(tosyl)-3-monomethoxytrityl-methylbutyl]guanine and subsequent deprotection of the methoxytrityl groups in acidic conditions (Shiue et al. 2001).

FIAU can be labeled with fluorine-18 (Mangner et al. 2003) or with radioiodine, for which both ^{131}I (Tjuvajev et al. 2002) and ^{124}I (β+ emitter, half life 4.15 days, Bengel et al. 2003) have been used.

15.3.4 Hypoxia Imaging

Whereas up to now perfusion agents were often used to identify tissues with reduced flow and hence, reduced delivery of oxygen, a marker of decreased intracellular oxygen tension would be an effective indicator of tissue that is viable but dysfunctional (hypoxic tissue). Visualization of hypoxia in tumors can be predictive for response to therapy. Most

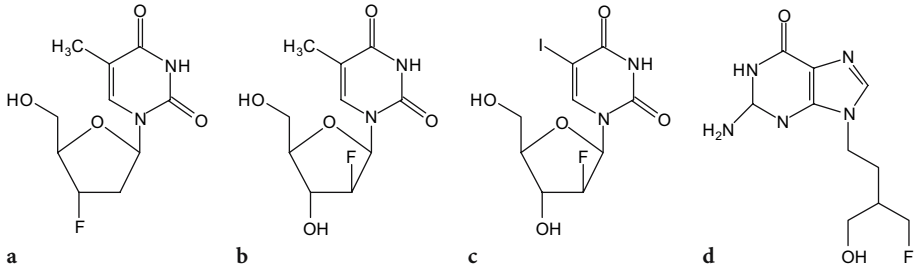

Fig. 15.5a-d. Structures of radiolabeled nucleosides and nucleoside analogs FLT (**a**), FMAU (**b**), FIAU (**c**) and FHBG (**d**)

hypoxia markers contain a nitroimidazole moiety as the reactive chemical species. Nitroimidazoles are reduced intracellularly in all cells, but in the absence of an adequate supply of oxygen, they undergo further reduction to more reactive products which bind to cell components. In this way, they are trapped in hypoxic tissue (for a review, see Ballinger 2001).

Fluoromisonidazole (FMISO, Fig. 15.6) is a fluorinated analogue of the chemical radiosensitizer misonidazole and is radiolabeled with ^{18}F by a nucleophilic fluorination on a tetrahydropyranyl protected tosyl precursor followed by acidic deprotection (Grierson et al. 1989; Lin and Berridge 1993). As [^{18}F]FMISO shows a slow blood clearance, more hydrophilic radiolabeled nitroimidazole derivatives have been developed such as [^{18}F]fluoroerythromisonidazole ([^{18}F]FETNIM, Yang et al. 1995; Fig. 15.6) and [^{18}F]fluoroazomycinarabinofuranoside ([^{18}F]FAZA, Sorger et al. 2003; Fig. 15.6). Direct comparison of [^{18}F]FMISO and [^{18}F]FAZA in a rat tumor model showed a higher tumor to muscle ratio for [^{18}F]FMISO at both 1 h and 3 h p.i. despite a faster clearance of [^{18}F]FAZA from muscle tissue (Sorger et al. 2003). Comparison of [^{18}F]FETNIM and [^{18}F]FMISO in an experimental mammary carcinoma model in rats showed similar tumor to muscle ratios which correlated with the oxygenation status in the tumors (Gronroos et al. 2004).

Several clinical studies aiming to visualize hypoxia in tumors in order to predict response to radiotherapy have been performed using both [^{18}F]FMISO (Bruehlmeyer et al. 2004) and FETNIM (Lehtiö et al. 2004).

Radiocopper-labeled diacetyl-bis(N_4-methylthiosemicarbazone) (Cu-ATSM, Fig. 15.6) does not contain a nitroimidazole group but also shows specific retention in hypoxic tissue (Lewis et al. 1999). Several clinical studies have been performed using copper-60 ($t_{1/2}$ = 24.5 min) labeled ATSM for visualization of tumor hypoxia (Dehdashti et al. 2003).

Although several ^{99m}Tc-based compounds including BMS181321, BMS194796 and ^{99m}Tc-HL91 have been designed and evaluated as tracer agents for imaging hypoxia, none of them is or has been commercially available.

Iodine-123 labeled iodoazomycin arabinoside (IAZA) has been validated in animal models and tested preclinically (Stypinksi et al. 2001), but no clinical studies with this agent have been reported so far.

15.4 Peptides and Proteins

15.4.1 Somatostatin Receptor Tracers

Radiolabeled natural somatostatin can not be used as a tracer agent for visualization of somatostatin receptors due to the very short plasma half-life of the peptide (2–4 min). Therefore, analogs have been developed which are more stable against the action of peptidases.

15.4.1.1 ^{111}In-Octreotide

One of the somatostatin analogs is octreotide, a cyclic octapeptide containing the physiologically active four-amino acid sequence (Phe-D-Trp-Lys-Thr). In order to enable labeling of octreotide with ^{111}In, a diethylenetriaminepentaacetic acid (DTPA) molecule has been conjugated to the α-NH_2 group of

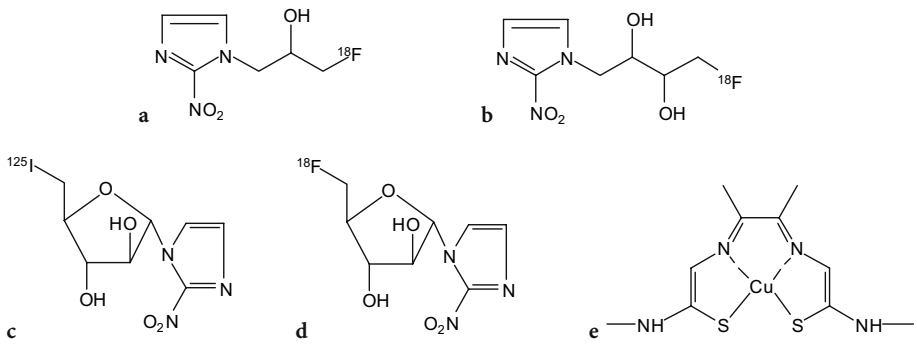

Fig. 15.6a-e. Structure of hypoxia imaging agents [^{18}F]MISO (**a**), [^{18}F]FETNIM (**b**), [^{125}I]IAZA (**c**), [^{18}F]FAZA (**d**) and Cu-ATSM (**e**)

the N-terminal D-Phe residue (Bakker et al. 1991a). The generic name of this conjugate is pentetreotide (Fig. 12.4). Labeling is performed using the commercially available Octreoscan 111 kit (Mallinckrodt-Tyco Healthcare, St. Louis, Mo.) which consists of two vials. ^{111}In-indium chloride (vial A) is added to vial B containing the lyophilized pentetreotide, after which the mixture is incubated for 30 min at room temperature. Labeling yield is higher than 97% and the preparation should be used within 2 h after reconstitution. The pH of the reconstituted product varies between pH 3.5–5.0.

After intravenous administration, ^{111}In-labeled pentetreotide is rapidly cleared from the blood (Krenning et al. 1992). Blood radioactivity decreases within 10 min to 33% of injected dose. Unlike the initially developed ^{123}I-octreotide, which is eliminated to a high degree via the hepatobiliary system (Bakker et al. 1991b), ^{111}In-pentetreotide is mainly excreted into the urine (50% of injected dose after 6 h, 85% after 24 h and 90% after 48 h). Up to 4 h after injection, radioactivity in plasma and urine is predominantly intact ^{111}In-pentetreotide. The relatively long residence time of ^{111}In-pentetreotide in the kidneys suggests that following glomerular filtration, part of the label is actively reabsorbed into the tubules (Bakker et al. 1991c).

Because pentetreotide only binds with high affinity to the somatostatin receptor subtype SSTR2, with moderate affinity to SSTR3 and SSTR5 and not to SSTR1 and SSTR4, research has continued to develop other somatostatin analogues, which also bind with high affinity to the other receptor subtypes. Lanreotide is an octapeptide which binds to SSTR2 through SSTR5 with high affinity and to SSTR1 with low affinity. This peptide is modified with DOTA (Fig. 15.7) and labeled with ^{111}In in a similar way as octreotide. The high-affinity binding of lanreotide to SSTR3 and SSTR4 makes it possible to visualize certain tumors such as intestinal adenocarcinomas which are not visualized by ^{111}In-pentetreotide scintigraphy (Virgolini et al. 1998).

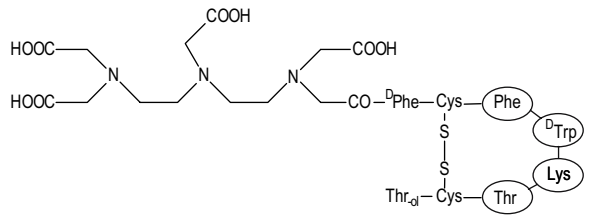

a

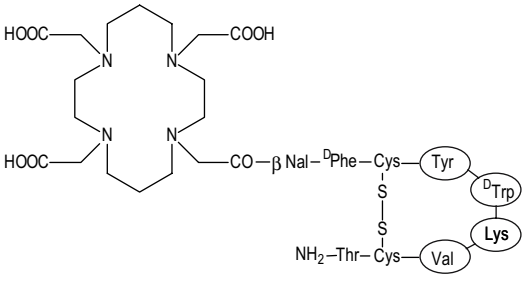

b (βNal = β-Naphtyl-alanine)

Fig. 15.7a,b. Structures of ligands for somatostatin receptor tracer agents: pentetreotide (**a**) and DOTA-lanreotide (**b**)

15.4.1.2 P587 and P829

Despite the encouraging results obtained with ^{111}In-labeled somatostatin analogs, a ^{99m}Tc-labeled SSTR-binding tracer agent is highly desirable for routine nuclear medicine procedures because ^{99m}Tc is considerably less expensive than ^{111}In. Also, ^{99m}Tc provides a higher photon flux per unit of absorbed radiation dose and better quality images.

Diatide Inc., now a division of Berlex laboratories (Londonderry, NH), developed a number of synthetic high-affinity SSTR-binding peptides, designed for labeling with technetium-99m. From these peptides, ^{99m}Tc-P587 and ^{99m}Tc-P829 (Fig. 15.8) were selected to enter clinical trials. These are peptides designed in a cyclic configuration which is not susceptible to reductive cleavage, in order to avoid the incompatibility of having a disulfide in a molecule that is to be radiolabeled with ^{99m}Tc in reducing conditions. In the peptides, a sequence is incorporated to provide a donor atom set which allows stable complexation of technetium-99m (Vallabhajosula et al. 1996). Labeling is performed by ligand exchange from ^{99m}Tc-glucoheptonate. Since the labeling sequence is in fact a diamide monoamine monothiolate chelator (P829), or a triamide thiolate chelator (P587), heat needs to be applied (15 min at 100 °C) to promote subtraction of the amide protons and afford stable ^{99m}Tc-complexes. In this way, labeling yields >90% can be obtained. A labeling kit for convenient preparation of ^{99m}Tc-P829 (which has as generic name technetium-99m depreotide) has been developed under the name NeoTect and clinical studies have been performed to establish the usefulness of the tracer agent (Blum et al. 2000). Imaging using ^{99m}Tc-depreotide was found to be useful for identifying somatostatin receptor bearing pulmonary masses in patients presenting with pulmonary

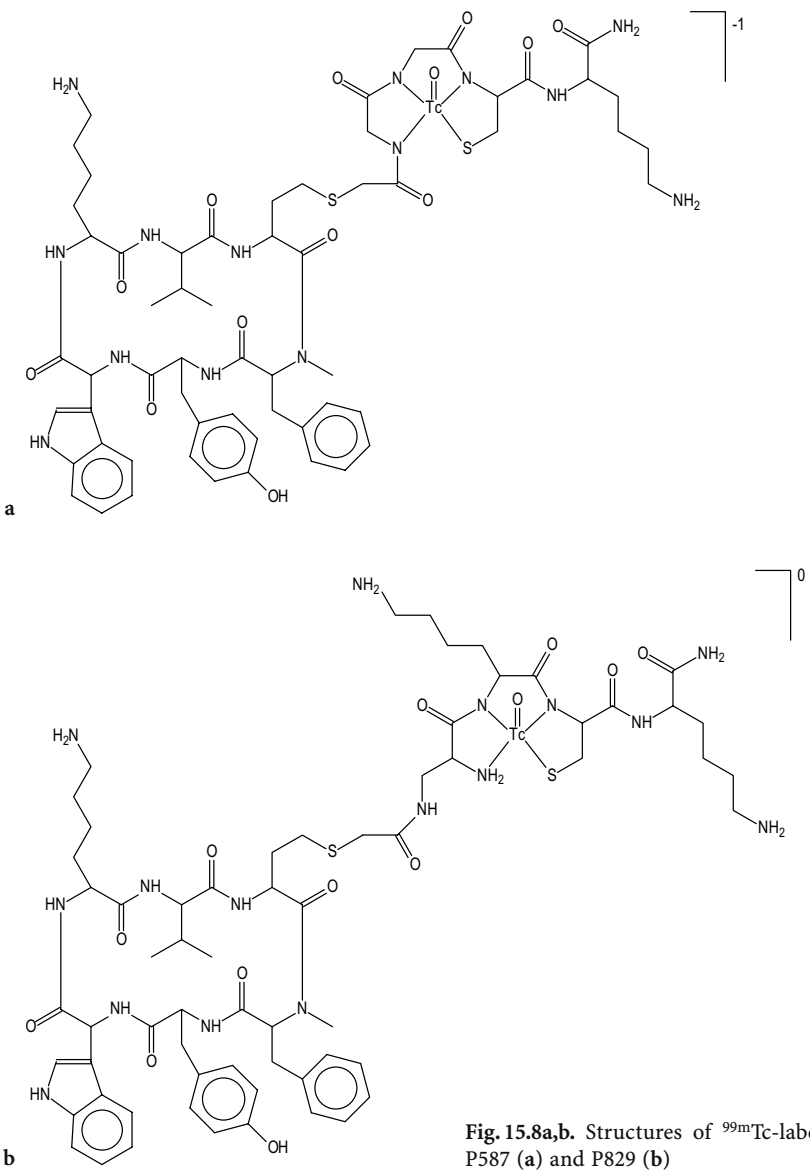

Fig. 15.8a,b. Structures of ^{99m}Tc-labeled somatostatin receptor tracer agents: P587 (**a**) and P829 (**b**)

lesions on CT and/or chest X-ray who have known malignancy or are highly suspect for malignancy.

15.4.2 Peptides for Thrombus Imaging

Platelet activation and deposition, the initial events in active thrombus formation, involve expression of the GPIIb/IIIa receptor, which recognizes proteins and peptides bearing the Arg-Gly-Asp (RGD) tripeptide sequence.

Lister-James and co-workers (1996; Pearson et al. 1996) at Diatide Inc. developed a ^{99m}Tc-labeled GPIIb/IIIa receptor antagonist for scintigraphic detection of deep venous thrombosis. P280 (now called bibapcitide) is a small oligopeptide, consisting of two identical, linked, cyclic 13-amino acid monomers (Fig. 15.9). Each monomer (called apcitide) contains a (S-aminopropyl)cysteine-Gly-Asp tripeptide sequence which mimics the RGD-sequence and a Cys(Acm)-Gly-Cys(Acm) tripeptide sequence, which forms after deprotection an N_2S_2 diamidedithiol type chelator for ^{99m}Tc-labeling. Because of the presence of protecting groups (acetamidomethyl, Acm) on the two thiol groups of the diamidedithiol and the presence of two amide protons, ^{99m}Tc-labeling of P280 requires heating at 100°C for 15 min during this heating step, bibapcitide is split and a ^{99m}Tc-apcitide complex is formed.

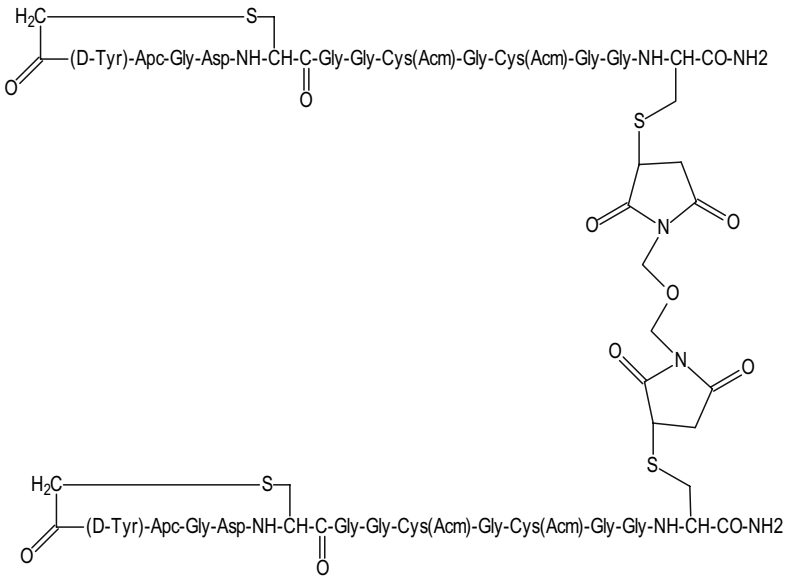

Fig. 15.9. Structure of the thrombus imaging peptide bibapcitide

^{99m}Tc-apcitide has been approved by the FDA and a kit for the preparation of ^{99m}Tc-apcitide has been developed (AcuTect®). Besides 100 µg bibapcitide, each vial contains 89 µg $SnCl_2.2H_2O$ for reduction of ^{99m}Tc-pertechnetate and 75 mg sodium glucoheptonate which forms an intermediary ^{99m}Tc-glucoheptonate complex which exchanges for apcitide upon heating. After administration, ^{99m}Tc-apcitide exhibits a fast plasma clearance and predominantly renal excretion which is favorable for rapid delineation of thrombi. It is indicated for scintigraphic imaging of acute venous thrombosis in the lower extremities in patients with signs and symptoms of acute blood clots.

15.4.3 Annexin V

Radiolabelled derivatives of Annexin V (Anx V) have been developed in order to enable in vivo imaging of apoptosis. Annexin V is a 36-kDa human protein which binds with high affinity (K_d = 7 nmol) to phosphatidylserine, a membrane-bound phospholipid which is redistributed from the inner to the outer leaflet of the plasma membrane, early in the apoptotic process (Reutelingsperger et al. 1988; Martin et al. 1995).

Up to now, three ^{99m}Tc-labelled Annexin V compounds, differing in the bifunctional chelating agent used for complexation of ^{99m}Tc, have been studied in humans. In ^{99m}Tc-i-Anx V (Mallinckrodt), Annexin V was derivatized with a monodentate n-1-imino-4-mercaptobutyryl side chain (Kemerink et al. 2001) but the radiochemical purity (82%±12%) and stability of the ^{99m}Tc-i-AnxV were found to be suboptimal.

In ^{99m}Tc-BTAP-Anx V (Apomate, Theseus Imaging Corp, Cambridge, MA) the protein is modified with an N2S2 bis(mercaptoacetyl)diaminopentan oyl group (Kemerink et al. 2001b), resulting in a stable and well-defined ^{99m}Tc-complex. However, ^{99m}Tc-BTAP-Anx V has to be prepared through a preformed chelate approach which is time-consuming and hardly applicable to routine use. In addition, after intravenous administration of the tracer agent, activity had already appeared in the bowel within a few hours, precluding imaging of apoptosis in the abdomen.

In ^{99m}Tc-Hynic-Anx V, the protein is modified with a hydrazino nicotinamide side chain (Blankenberg et al. 1998; Ohtsuki et al. 1999) after which labeling is performed by simple addition of Sn^{2+} ions and pertechnetate in the presence of tricine as coligand (Verbeke et al. 2003). Biodistribution studies in rats (Ohtsuki et al. 1999) and humans (Kemerink et al. 2003) indicated that ^{99m}Tc-Hynic-Anx V is mainly excreted through the kidneys, giving it a clear advantage over ^{99m}Tc-BTAP-Anx V.

More recently, a ^{18}F-labeled Annexin V derivative has been prepared using N-succinimidyl 4-[^{18}F]fluorobenzoate as the ^{18}F labeling reagent (Murakami et al. 2004). In rats, the accumulation of ^{18}F-Anx V and ^{99m}Tc-Anx V in the infarcted area was comparable whereas the uptake of ^{18}F-Anx V in liver, spleen and kidney was significantly lower

than that of ^{99m}Tc-Anx V. Data in humans are not yet available. An extensive review describing recently developed radiolabeled Annexin V derivatives which might have potential for in vivo use (including annexin V labeled with carbon-11, radioiodine, indium-111, copper-64 and radiogallium) has been published by Lahorte et al. (2004).

As Theseus Imaging Corp. has stopped its activities of developing radiolabeled Annexin derivatives, it is not clear at this moment whether or not further progress in this area may be expected.

15.4.4 Monoclonal Antibodies

Since the advent of hybridoma technology in 1975 (Kohler and Milstein 1975), an enormous effort has been put into the development of radiolabeled monoclonal antibodies (MoAbs), mainly to be used as in vivo tumor localizing agents. Only a few of these MoAbs have reached the point of proven clinical utility and have been approved for use in clinical diagnosis.

Capromab (Mab 7E11-C5.3) is a murine monoclonal antibody of the IgG_1K subclass which binds specifically to a prostate-specific membrane glycoprotein (PSMA), a cell surface antigen which is expressed only by prostatic epithelial cells (benign and malignant). The antibody is labeled with ^{111}In through site-specific modification of the oligosaccharide moiety of the molecule with a linker-chelator, glycyl-tyrosyl-(N,ε-diethylenetriaminepentaacetic acid)-lysine or GYK-DTPA (Rodwell et al. 1986). Therefore, the carbohydrate moieties of the MoAb are oxidized with sodium periodate and after purification, the aldehyde groups are reacted with the α-amino group of GYK-DTPA. The Schiff base formed in this way is further stabilized by reduction with sodium cyanoborohydride. The resultant MoAb 7E11-C5.3-GYK-DTPA is designated as CYT-356 or capromab pendetide. Because of the restricted localization of the glycosylation sites on immunoglobulins, this approach offers the advantage of modification of the antibody at a site distal to the antigen combining site resulting in modified antibodies with the same homogeneous antigen-binding property and affinity as the unmodified antibody. In addition, the antibodies can be labeled with a greater number of chelators without loss of antigen-binding capability.

The antibody conjugate is commercially available under the name ProstaScint (Cytogen Corp, Princeton, USA). It is provided in liquid form in 1-ml single dose vials at a concentration of 0.5 mg/ml. Before adding ^{111}In-chloride to the antibody solution, the isotope solution must be buffered with 0.5 M sodium acetate.

Indium-111 capromab pendetide is indicated for use in immunoscintigraphy in patients with biopsy-proven prostate carcinoma who are at high risk for pelvic lymph node metastases. It is also indicated in patients who have undergone a prostatectomy, and have rising prostate-specific antigen values and equivocal or no evidence of metastatic disease on standard metastatic evaluation, but in whom there is a high clinical suspicion of occult metastatic disease. Immunoscintigraphy using ^{111}In-capromab is not indicated as a screening test for carcinoma of the prostate or for readministration in order to assess response to treatment.

Arcitumomab is a Fab' fragment generated from IMMU-4, a murine IgG1 monoclonal antibody, by enzymatic digestion with pepsin to produce F(ab')2 fragments which are further reduced to Fab' fragments. It is directed against a 200-kDa carcinoembryonic antigen (CEA) that is expressed on the cell surface of numerous tumors, particularly of the gastrointestinal tract (Patt et al. 1994). The Fab' fragment is used rather than the whole antibody because of its more favorable pharmacokinetics (faster blood clearance and minimal liver uptake) and because it minimized the frequency of human anti-mouse antibody response. The rapid blood clearance of the Fab' fragment makes it compatible for labeling with a short-lived isotope such as ^{99m}Tc and allows imaging within 2–5 h after injection of the labeled antibody. The Fab' fragment does not require any further modification or derivatization before labeling and is able to bind up to 1.85 GBq of reduced ^{99m}Tc within 5 min (Hansen et al. 1990). After intravenous injection, blood levels were 63%, 23% and 7% at respectively 1 h, 5 h and 24 h after infusion. Because of its low molecular weight (54 kDa), elimination proceeds mainly through the kidneys with 28 % of the radiolabel excreted in the urine over the first 24 h after administration.

Arcitumomab is provided as a lyophilized formulation containing 1.25 mg of Arcitumomab and stannous chloride (CEA-scan, Immunomedics, Morris Plains, USA). Labeling with ^{99m}Tc is performed by simple reconstitution of the contents of the vial with 1 ml of a pertechnetate solution (1.1 GBq ^{99m}Tc) and incubation for 5 min at room temperature.

Imaging with ^{99m}Tc-arcitumomab, in conjunction with standard diagnostic modalities, e.g., com-

puted tomography, is indicated to detect, locate, and determine the extent of recurrent and/or metastatic colorectal carcinoma involving the liver and the extrahepatic abdominal and pelvic regions in patients with a histologically confirmed diagnosis of colorectal carcinoma. It also provides additional information in patients suspected of tumor recurrence or metastasis who have elevated or rising serum carcinoembryonic antigen (CEA) but no evidence of disease by standard diagnostic methods.

Antistage specific embryonic antigen-1 (anti-SSEA-1) is an IgM monoclonal antibody with a high specificity for a glycoprotein lacto-N-fucopentaeose-III which is expressed on human neutrophils, eosinophils and lymphocytes. The antigen is also known as CD15 (Barclay et al. 1990). Despite its high molecular weight of 900 kDa, this antibody shows a fast blood pool clearance which justifies labeling with the short lived ^{99m}Tc. In order to enable direct labeling with ^{99m}Tc, the antibody is reduced to generate sulfhydryl groups. The reduced antibody is lyophilized using maltose as a stabilizer and is commercially available as NeutroSpec (Mallinckrodt-Tyco Healthcare, St. Louis, Mo.). Labeling is performed by addition of 740–1480 MBq ^{99m}Tc in 0.20–0.35 ml generator eluate and incubation for 30 min at 37°C after which sufficient ascorbic acid solution (500 mg/ml, Cenolate) is added to make the final preparation volume up to 1 ml. Thakur et al. (1996) found that after intravenous injection of ^{99m}Tc-fanolesumab, 15%–50% of the administered dose was associated with polymorphonuclear neutrophils (PMNs) whereas the activity associated with lymphocytes, platelets and erythrocytes was generally low. This is considerably higher as compared to another ^{99m}Tc-labeled monoclonal antibody BW 250/183 where only 3%–10% of the administered dose was associated with PMNs. The high affinity of anti-SSEA-1 for human PMNs (K_d 10^{-11} M) together with the fast blood clearance may be the primary reason for the excellent image quality. ^{99m}Tc labeled fanolesumab is indicated for imaging equivocal appendicitis in patients 5 years or older.

15.5 Neurotransmitter Receptor and Transporter Tracers

Scintigraphic imaging and especially positron emission tomography (PET) are powerful non-invasive techniques in clinical research to detect, using suitable radioligands, functional receptors and binding sites at low (nM) concentrations. In this way, the relationship between changes in receptor or binding site occupancy or concentration and the progress of certain diseases can be elucidated. In current research, interest has been shown mainly in peptide receptor tracer agents (which have been discussed separately) and neuroreceptor and transporter radioligands.

15.5.1 Benzodiazepine Receptor Agents

Central benzodiazepine receptors have been studied in relation to diseases such as epilepsy (Savic et al. 1988), hepatic encephalopathy (Samson et al. 1987), Alzheimer's disease (Yamasaki et al. 1986), Huntington's disease (Hantraye et al. 1984) and chronic alcoholism (Litton et al. 1991).

Whereas diazepam and flunitrazepam were the first classical benzodiazepines to be labeled with carbon-11 in the N-methyl group (Mazière et al. 1980), [N-methyl-^{11}C]flumazenil and its iodinated analog ^{123}I-iomazenil (Fig. 15.10a,b) are currently the radioligands of choice for studies of central benzodiazepine receptors with PET, respectively SPET. They are high affinity benzodiazepine antagonists whereas they lack major intrinsic pharmacologic effects.

Radiosynthesis of [N-methyl-^{11}C]flumazenil involves N-methylation of N-*des*methyl-flumazenil with NCA [^{11}C]iodomethane or [^{11}C]methyl triflate. A recent report showed that no carrier added [^{18}F]flumazenil (Fig. 15.10c) can be synthesized by nucleophilic fluorination using a nitro-precursor (Krasikova et al. 2004). As an alternative 2'-[^{18}F]fluoroflumazenil ([^{18}F]FFMZ, Fig. 15.10d, Mitterhauser et al. 2004) has also been synthesized and showed a comparable affinity for the GABA receptor as flumazenil.

^{123}I-iomazenil is prepared with high specific activity [>185 TBq (5000 Ci)/mmol] by oxidative radioiodination of the tributylstannyl precursor (Beer et al. 1990).

After administration, the initial uptake of [N-methyl-^{11}C]flumazenil and ^{123}I-iomazenil in the brain is similar to the rCBF seen with ^{99m}Tc-HMPAO (Yamamoto et al. 1983; Bartenstein et al. 1991). Within 30 min post injection, unbound tracer agent is almost completely cleared from the brain and the distribution of both radioligands closely resembles the known biodistribution of benzodiazepine recep-

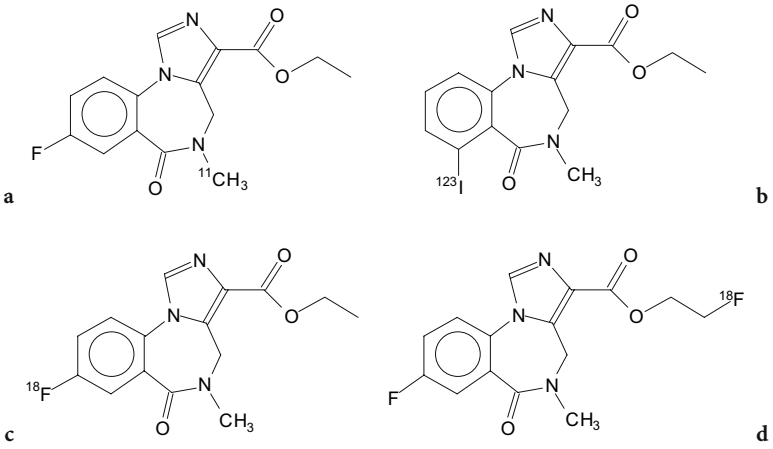

Fig. 15.10a-c. Structures of the benzodiazepine receptor agents [N-methyl-^{11}C]flumazenil (**a**), ^{123}I-iomazenil (**b**) and [^{18}F]fluoroflumazenil (**c**)

tors. As compared to [^{11}C]flumazenil, ^{123}I-iomazenil has a tenfold higher affinity for the neuronal type benzodiazepine receptor and a slower brain washout (Johnson et al. 1990).

15.5.2 Serotonergic (5-HT) Receptor Tracers

The in vivo investigation of brain serotonergic 5-HT receptors has been pursued for several years. There is evidence suggesting a role for the 5-HT system, in particular 5-HT$_2$ receptors in the regulation of a wide range of central mechanisms (Cowen 1991). Abnormalities in 5-HT$_2$ receptors have been proposed in several neuropsychiatric conditions including major depression, Alzheimer-type dementia, drug abuse and schizophrenia.

A great number of ligands have been prepared and evaluated for probing 5-HT receptors. At this moment, [^{18}F]setoperone (Mazière et al. 1988) and [^{18}F]altanserin (Lemaire et al. 1991) are the only radioligands used for PET-studies of 5-HT$_2$ receptors (Fig. 15.11). Both can be obtained by a direct one-pot nucleophilic substitution of the nitro-precursor by n.c.a. [^{18}F]fluoride. The binding affinity values for different neurotransmitter receptor sites have been reported by Leysen (1989) (Table 15.6). In rats, the frontal cortex-to-striatum activity ratio, which is a good index for ligand specificity (5-HT$_2$/D$_2$), reached 2.56 at 1 h post injection for [^{18}F]altanserin whereas this ratio did not exceed 1.18 for [^{18}F]setoperone. Hence, [^{18}F]altanserin appeared more selective for binding to 5-HT2 receptors than [^{18}F]setoperone.

For SPET studies, ^{123}I-5-I-R91150 ([^{123}I]-4-amino-N-[1-[3-(4-fluorophenoxy)-propyl]-4-methyl-4-piperidinyl]-5-iodo-2-methoxybenzamide) has been synthesized by Mertens et al. (1994) by electrophilic substitution on the 5-position of the methoxy benzamide group of R91150 (Fig. 15.12). It is a 5-HT$_2$ antagonist with high affinity and selectivity for the 5-HT$_{2A}$ receptor (the main subtype of 5-HT$_2$ receptors in the brain). The in vitro binding constant (K_i) for 5-HT$_2$ receptors is 0.2 nM whereas the selectivity to other neurotransmitter receptors (5-HTx, α_1, α_2, D_1 and D_2) is at least a factor of 50 (Terriere et al. 1995). The results obtained with this tracer agent up to now (e.g. Busatto et al. 1997; Peremans et al. 2003; Versijpt et al. 2003) indicate that this radioligand might be very useful for in vivo 5-HT$_{2A}$ receptor mapping, especially since SPET is cheaper and more accessible than PET.

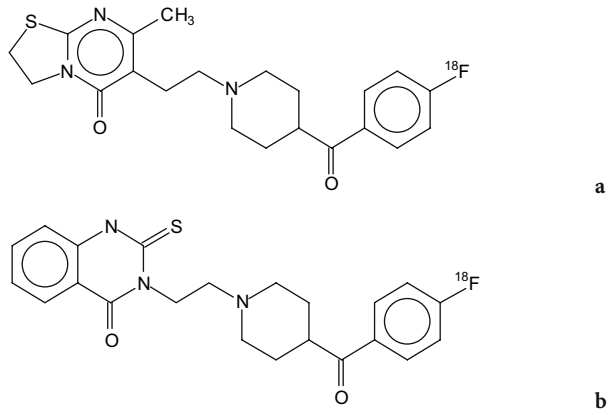

Fig. 15.11a,b. Structures of the 5-HT$_2$ receptor tracers [^{18}F]setoperone (**a**) and [^{18}F]altanserin (**b**)

Table 15.6. Binding affinity values (K_i, nM) of setoperone and altanserin for different neurotransmitter receptor sites

	5-HT_2 [^{3}H]ketanserin	D_2 [^{3}H]haloperidol	α_1 [^{3}H]WB-4101
Setoperone	0.37	25	13
Altanserin	0.13	62	4.55

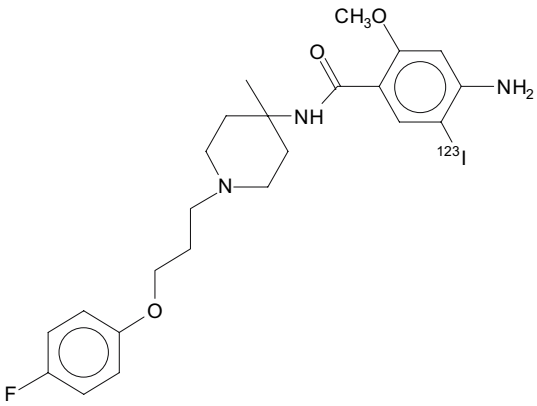

Fig. 15.12. Structure of the 5-HT_2 receptor tracer ^{123}I-5-I-R91150

Receptors of the 5-HT_1 family (5-HT_{1A} and 5-HT_{1D}) are distributed among several cortical and subcortical structures where they mediate neuronal hyperpolarization and inhibit the release of neurotransmitters (Hoyer et al. 1994). A selective ligand with high potency, high selectivity and pure antagonistic action of 5-HT_{1A} receptors is WAY-100635 (Fig. 15.13). The ligand can be radiolabeled with carbon-11 in the O-methyl as well as in the carbonyl position. In primates, it was found that the descyclohexane carbonyl analogue [O-methyl-^{11}C]WAY-100634 is a major radiolabeled metabolite of [O-methyl-^{11}C]WAY-100635 (Osman et al. 1996). WAY-100634 is known to have a high affinity for 5-HT_{1A} receptors and α1-adrenoreceptors, suggesting that this radioactive metabolite contributes to brain radioactivity in human PET-studies (Osman et al. 1996). Therefore, labeling of WAY-100635 with carbon-11 has been changed to the carbonyl position (Pike et al. 1996) to avoid formation of radioactive WAY-100634 or any other pharmacologically active metabolite.

[Carbonyl-^{11}C]WAY-1003635 is prepared by reaction of cyclohexane[carbonyl-^{11}C]chloride with WAY-100634 and is obtained in a 30%-50% decay-corrected radiochemical yield from trapped [^{11}C]carbon dioxide in 20 min from EOB. After semi-preparative reversed phase HPLC, radiochemical purity exceeds 99% (Pike et al. 1995).

Within 60 min after administration, the ratio of radioactivity uptake in receptor-rich medial temporal cortex to that in cerebellum reaches a value of 25, indicating the very low non-specific binding of this radioligand. Plasma analysis showed rapid metabolism but only to very polar radioactive compounds (most probably [^{11}C]cyclohexanecarboxylic acid and derivatives) which are not expected to enter the brain nor to be pharmacologically active.

15.5.3 Dopaminergic Receptor Tracers

The brain dopaminergic system lies in a well-defined region in the striatum and localization is relatively easy. Hence, a large number of ligands for the dopaminergic system, and in particular the D_2 receptor, have been studied so far. The most prominent reversible and high selective D_2 receptor ligands are the benzamides of the salicylamide type such as raclopride and FLB 457, eticlopride and fallypride (Fig. 15.14). The latter three compounds have a 30-fold higher affinity for the D_2-receptor than raclopride (Halldin et al. 1991; Mazière et al. 1992) and can be used to visualize the extrastriatal dopamine receptors (Olsson et al. 2004). For the four ligands, the (S)-enantiomer is the most potent form (Högberg et al. 1991). They can be radiolabeled with ^{11}C by O-methylation of the desmethyl precursor with ^{11}C-methyl iodide. In the case of eticlopride, two different O-methylated products are obtained

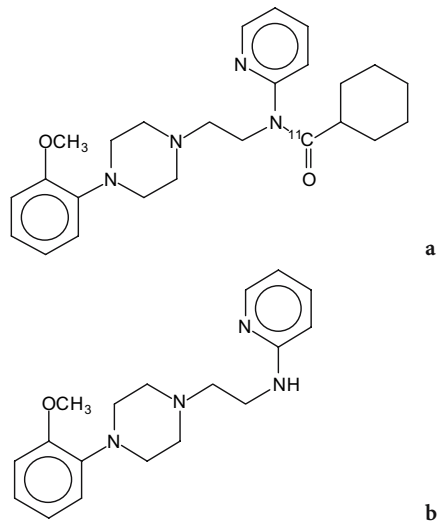

Fig. 15.13a,b. Structure of the 5-HT_1 receptor tracer [carbonyl-^{11}C]WAY-100635 (**a**) and its metabolite WAY-100634 (**b**)

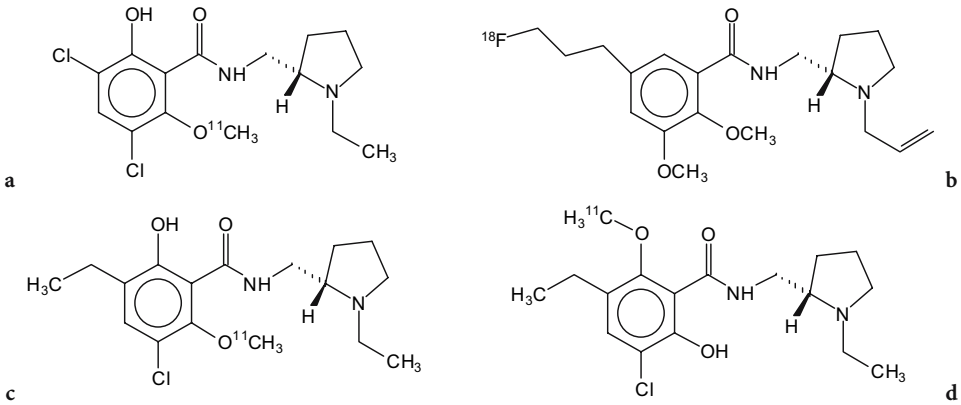

Fig. 15.14a-d. Structures of the dopaminergic tracer agents (S)-[O-methyl-^{11}C]raclopride (**a**), (S)-[6-O-methyl-^{11}C]eticlopride (**b**), (S)-[6-O-methyl-^{11}C]eticlopride (**c**) and [^{18}F]fallypride (**d**)

(Fig. 15.14) which have to be separated by HPLC. Alternatively, eticlopride can be labeled in the N-ethyl position as well. The fluorine-18 labeled analogs of eticlopride have also been prepared but show generally inferior binding properties.

The fluorine-18 labeled derivative of fallypride, however, has been used with success to visualize both striatal and extrastriatal D_2 receptors (Slifstein et al. 2004).

The favorable results obtained with these PET tracers stimulated the design of a ^{123}I-labeled analog for SPET, namely (S)-N-[(1-ethyl-2-pyrrolidinyl)]methyl-2-hydroxy-3-iodo-6-methoxybenzamide (^{123}I-IBZM, Fig. 15.15) (Kung et al. 1988). It can be prepared in high yield and with high specific activity by oxidative iodination of the enantiomerically pure BZM precursor with n.c.a. ^{123}I-iodide via in situ formation of peracetic acid (Bobeldijk et al. 1990). Biodistribution studies demonstrated that the agent is concentrated in the basal ganglia although some non-specific binding was noted in cerebral cortex and cerebellum (Kung et al. 1990). If receptor density or blockade is being quantified, it is necessary to correct for this non-specific binding.

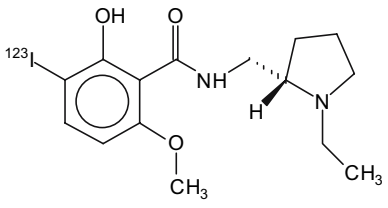

Fig. 15.15. Structure of the dopaminergic tracer agent ^{123}I-IBZM

15.5.4 Dopamine Transporter (DAT)

Dopamine reuptake sites can be visualized using radioligands binding to the dopamine transporter, a protein which plays an important role in the inactivation and recycling of dopamine released into the synaptic cleft. Measurement of decrease in the dopamine transporters may be a useful indicator of dopamine neuronal loss in Parkinson's and other neurodegenerative diseases (Kaufman and Madras 1991). Beta-carbomethoxy-3β-(4-iodophenyl)tropane (β-CIT, Fig. 15.16) is a more potent analog of the cocaine congener in the inhibition of dopamine uptake (Boja et al. 1990) and has been radiolabeled with ^{123}I for use in SPET imaging (Carroll et al. 1991). Alternatively, ^{11}C-β-CIT can be used for PET-imaging (Laihinen et al. 1995). In addition, the N-fluoroethyl (β-CIT-FE) and N-fluoropropyl analogs (β-CIT-FP) have been synthesized and radiolabeled with the relatively long-lived radionuclides ^{123}I and ^{76}Br. Due to the high proportion of homology between the dopamine transporter (DAT), the serotonin transporter (SERT) and the norepinephrine transporter (NET), these ligands are not selective for DAT (Amara and Kuhar 1993). Table 15.7 shows the K_i values of β-CIT, β-CIT-FE, β-CIT-FP and cocaine to inhibit the uptake of [^{3}H]dopamine, [^{3}H]serotonin and [^{3}H]1-norepinephrine (Okada et al. 1998).

Meegalla et al. (1997) have synthesized a tropane derivative, TRODAT-1, designed for labeling with ^{99m}Tc, by conjugation of an N_2S_2 diaminedithiol-type chelator with tropane at the 2β-position (Fig. 15.17). Labeling of the conjugate by ligand exchange from ^{99m}Tc-glucoheptonate yields a neutral, lipophilic

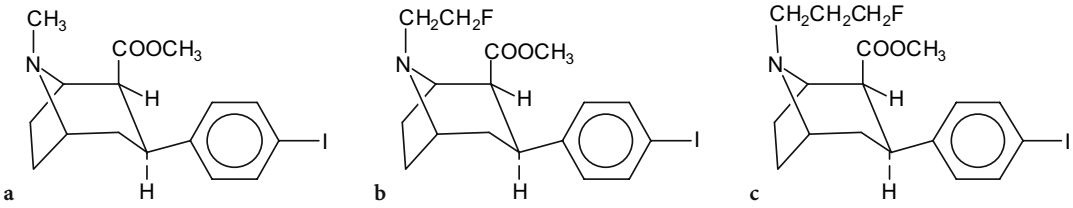

Fig. 15.16a-c. Structures of the dopamine reuptake tracer agents β-CIT (**a**) and its analogues β-CIT-FE (**b**) and β-CIT-FP (**c**)

Table 15.7. Ki values (nM) for inhibition of [^{3}H]dopamine, [^{3}H]serotonin or [^{3}H]1-norepinephrine uptake

	Dopamine transporter 45 nM [^{3}H]dopamine	Serotonin transporter 20 nM [^{3}H]serotonin	1-Norepinephrine transporter 50 nM [^{3}H]1-norepinephtine
β-CIT	6.34 ± 1.68	29.17 ± 6.40	32.77 ± 13.41
β-CIT-FE	90.88 ± 4.92	132.73 ± 31.90	130.45 ± 49.18
β-CIT-FP	27.97 ± 7.36	113.39 ± 63.77	70.42 ± 15.37

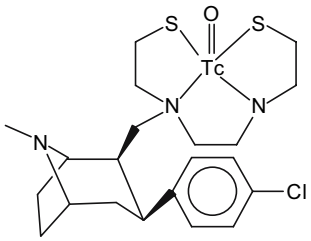

Fig. 15.17. Structure of the ^{99m}Tc-labeled dopamine reuptake tracer agent TRODAT-1

^{99m}Tc-TRODAT-1 complex in high yield (RCP > 93%). In vitro binding of the dopamine transporter was assessed using the surrogate Re-complex, Re-TRODAT-1, and a K_i value of 14 nM was obtained (Kung et al. 1997). As compared to iodinated receptor ligands, the ratio of specific to non-specific binding of ^{99m}Tc-TRODAT-1 appears to be lower than that of ^{123}I-β-CIT (1.66 vs 7). Nevertheless, animal studies and studies in normal humans (Kung et al. 1996; Chou et al. 2004; Huang et al. 2004) indicate that ^{99m}Tc-TRODAT-1 is a useful SPET imaging agent for localization of dopamine transporters.

15.5.5 Norepinephrine Transporter (NET)

The norepinephrine transporter has been associated with the pathophysiology of depression (Klimek et al. 1997). Several labeled derivatives of S,S-reboxetin ((S,S)-[^{11}C]MeNER (Schou et al. 2003), (S,S)-[^{18}F]FMeNER and (S,S)-[^{18}F]FMeNER-D-2 (Schou et al. 2004) have recently been reported to bind specifically to NET in the brain, The derivatives are obtained by respectively [^{11}C]methylation with [^{11}C]methyl triflate, [^{18}F]fluoromethylation with [^{18}F]fluoromethyl bromide or dideutero-[^{18}F]fluoromethyl bromide. The fluorine-18 labeled derivatives (S,S)-[^{18}F]FMeNER and (S,S)-[^{18}F]FMeNER-D-2 (Fig. 15.18) offer images with a better signal/noise ratio than carbon-11 labeled (S,S)-[^{11}C]MeNER. The dideutero derivative (S,S)-[^{18}F]FMeNER-D-2 showed reduced in vivo defluorination as compared to (S,S)-[^{18}F]FMeNER and therefore seems to be the tracer of choice for visualization of NET with PET.

15.5.6 Serotonin Transporter (SERT)

The most frequently used medication for treatment of depression are selective serotonin reuptake inhibitors (SSRI). Several radiotracers for the visualization of SERT with SPECT or PET have been described. Huang et al. (2002) compared the PET tracers [^{11}C]McN 5652, [^{11}C]ADAM, [^{11}C]DASB, [^{11}C]DAPA and [^{11}C]AFM in baboons. The authors concluded that [^{11}C]DASB and [^{11}C]AFM (Fig. 15.19) have superior characteristics over the other tracers for in vivo visualization of SERT as they provide images of SERT availability, in a shorter scanning time or with a better signal to noise ratio.

PET with [^{11}C]DASB has successfully been used for visualization of serotonin transporter occupancy after administration of different doses of several

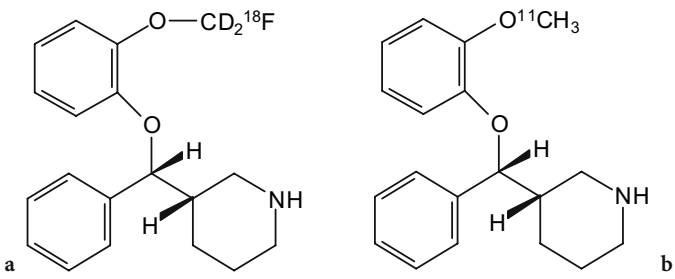

a b

Fig. 15.18a,b. Structure of Norepinephrine transporter [^{18}F]FMeNER-D-2 (**a**) and [^{11}C]MeNER (**b**)

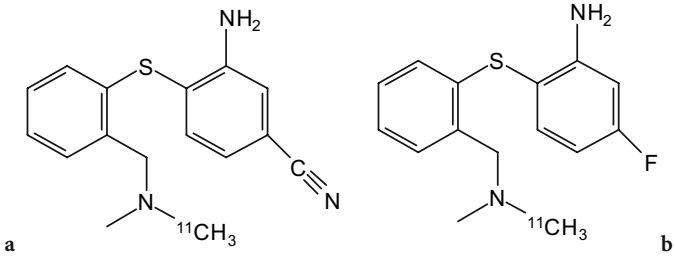

a b

Fig. 15.19a,b. Structure of serotonin transporter [^{11}C]DASB (**a**) and [^{11}C]AFM (**b**)

serotonin reuptake inhibitors in healthy volunteers (Meyer et al. 2004). In this study, an occupancy of 80% was observed at minimum therapeutic doses.

15.6 Amyloid Imaging

Alzheimer's disease (AD) is characterized by the presence of abundant senile plaques composed of amyloid-β (Aβ) peptides and neurofibrillary tangles formed by filaments of highly phosphorylated tau proteins (Selkoe 1999). In vivo assessment of the beta-sheet proteins deposited in amyloid plaques using a radiolabeled imaging agent with high affinity for Aβ would allow localization and quantification of senile plaques in a non-invasive way and possibly in an early stage of the disease.

Several derivatives of Congo red (this compound is being used for fluorescent staining of senile plaques in post-mortem brain sections of AD patients) and chrysamine G labeled with radioiodine or technetium-99m have been developed and evaluated as potential Aβ aggregate specific imaging agents (e.g., Han et al. 1996; Dezutter et al. 1999a,b; Link et al. 2001). Many of these compounds showed high in vitro binding affinity for amyloid fibrils, but their penetration through the blood–brain barrier and as a consequence their uptake in brain was very limited, as can be expected on the basis of their high molecular weight (> 700 Da) and the presence of very polar functional groups.

More promising radioactive compounds with smaller molecular size and increased lipophilicity, derived from the amyloid binding dye thioflavin T, have been reported. As thioflavin T contains a positively charged quaternary amine which likely will limit brain uptake, benzothiazoles which are uncharged at physiological pH were designed and tested for their amyloid-β binding properties and in vivo brain uptake.

Klunk and coworkers (2001) found attractive characteristics in a carbon-11 labeled benzothiazole, namely [N-methyl-^{11}C]6-Me-BTA-1 (Fig. 15.20). This compound enters the brain at levels comparable to commonly used neuroreceptor imaging agents (7.61% ID/g at 2 min post injection) and shows good clearance ($t_{½}$ = 20 min) of free and non-specifically bound radioactivity in normal rodent brain tissue. In addition, it shows a relatively high affinity for amyloid (K_i = 20.2 nM, being 45-fold that of thioflavin T) and has a specificity for staining plaques and neurofibrillary tangles in post-mortem AD brain. The octanol-buffer partition coefficient is 2290 (log P_{oct} = 3.36). These characteristics suggest that [N-methyl-^{11}C]6-Me-BTA-1 holds potential as an in vivo beta-sheet imaging agent for positron emission tomography, although its lipophilicity is rather high and its clearance from normal brain relatively slow.

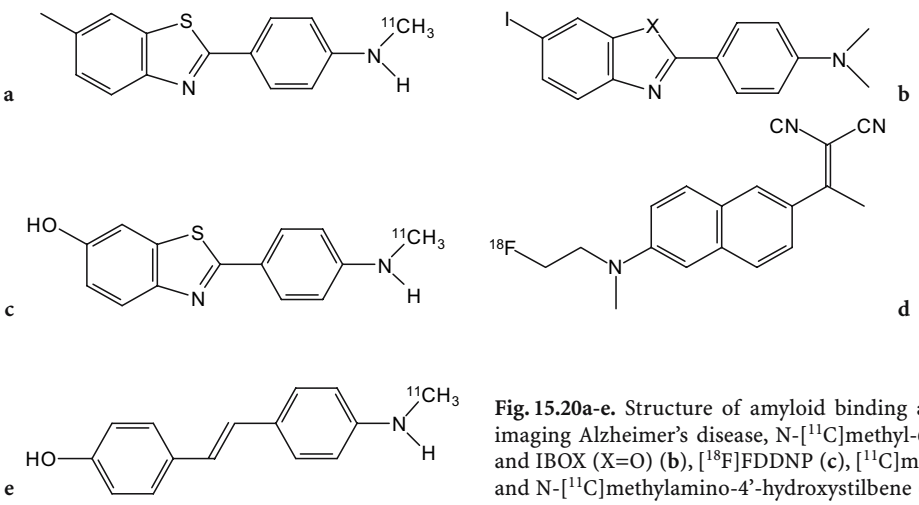

Fig. 15.20a-e. Structure of amyloid binding agents as potential tracers for imaging Alzheimer's disease, N-[^{11}C]methyl-6-Me-BTA-1 (**a**), TZDM (X=S) and IBOX (X=O) (**b**), [^{18}F]FDDNP (**c**), [^{11}C]methyl- 6-OH-BTA-1 (PIB-2) (**d**) and N-[^{11}C]methylamino-4'-hydroxystilbene (**e**)

For this reason, Mathis et al. (2003) developed more polar derivatives of which the 6-hydroxy analog ([^{11}C]6-OH-BTA-1, also called Pittsburg compound-B or PIB, Fig. 15.20) was found to have the most optimal pharmacokinetics. The first clinical studies using this tracer agent allowed to conclude that PET imaging with PIB can provide quantitative information on amyloid deposits in living subjects (Klunk et al. 2004).

Kung and coworkers (Zhuang et al. 2001a,b) developed a series of radioiodinated benzothiazoles of which TZDM and especially IBOX (Fig. 15.20) show the most promising properties. Octanol-buffer partition coefficients were 70 and 124 for TZDM and IBOX, respectively, and they were found to bind to Aß(1-40) aggregates with equal high potency (K_I = 1.9 nM and 0.8 nm, respectively). Both agents also showed excellent autoradiographic labeling of plaques in post-mortem brain sections of a confirmed AD patient. In normal mice, brain peak uptake was superior for ^{125}I-IBOX (2.08% of injected dose at 30 min post-injection versus 1.57% at 60 min for ^{125}I-TZDM) and its wash-out from brain was much faster.

Recent developments by the group of Kung led to the finding that a relatively simple carbon-11 labeled stilbene, (N-[^{11}C]methylamino-4-hydroxystilbene or [^{11}C]SB-13, Fig. 15.20) is an effective and favorable PET tracer for fibrillar Aß imaging in vivo, with similar performance to [^{11}C]PIB (Ono et al. 2003; Verhoeff et al. 2004).

In a different approach, Agdeppa and coworkers (2001a,b) developed a small but highly lipophilic (log P_{oct} = 3.92) fluorine-18 labeled compound, [^{18}F]FDDNP (Fig. 15.20) which crosses the blood–brain barrier and allows localization and determination of load of senile plaques in the living human brain with PET (Barrio et al. 1999; Agdeppa et al. 2001c). The tracer agent binds to two kinetically distinguishable binding sites on Aß(1-40) fibrils with apparent K_d values of 0.12 nM for the high-affinity binding site and 1.86 for the low-affinity binding site, as determined using fluorescence titrations. Specifically, the presence of the dicyano group in FDDNP appears critical for high-affinity binding. Detailed analysis of the distribution pattern in AD patients and normals (Shoghi-Jadid et al. 2002; Small et al. 2002) has led to the hypothesis that [^{18}F]FDDNP may be an in-vivo marker for neurofibrillary tangles as well as for diffuse and dense core Aß plaques. This could increase the potential ability of this tracer to detect AD presymptomatically, but it also suggests that [^{18}F]FDDNP is not solely an Aß-specific radiotracer, complicating its use in monitoring the effectiveness of Aß-reducing medication. A further intriguing finding is the fact that FDDNP competes with some, but not all, non-steroidal anti-inflammatory drugs for binding to Aß fibrils in vitro and to Aß plaques ex vivo (Agdeppa et al. 2003).

15.7 Newer Labeling Methods: ^{99m}Tc(I) Tricarbonyl Complexes

In view of the high stability and inertness of Tc(I) compounds, considerable efforts have been made to optimize methods for convenient synthesis of such ^{99m}Tc-complexes. Extensive research by the groups of Schubiger αnd Alberto (Alberto et al. 1998a) has resulted in the successful development

of a facile synthesis (30 min at 75°C) of the tricarbonyl complex of *fac*-$(Tc(I)[H_2O]_3[CO]_3)^+$ via the reduction of $Na^{99m}TcO_4$ with sodium borohydride at pH 11 under an atmosphere of carbon monoxide. This cationic species readily undergoes ligand exchange of coordinated water with a wide variety of donor ligands, of which the tridentate ligands such as histidine yield the most stable complexes (Abram et al. 1992; Schibli et al. 1998, 2000). The net charge of the final complex can be –1, 0 or +1 depending on the nature of the coordinating ligand. Moreover, these complexes can be formed with very small amounts of the ligand, resulting in preparations with extremely high specific activity. Recently, the preparation of the intermediary tri-aqua tricarbonyl Tc(I) core has been further optimized by using potassium boranocarbonate ($K_2BH_3CO_2$) as both a solid source of CO and the reductant for labeling with ^{99m}Tc (Dyszlewski et al. 2001). This has allowed the production of a kit formulation for the preparation of the tricarbonyl Tc(I) intermediate, which can then be further used for convenient production of a wide diversity of Tc(I) tricarbonyl compounds by ligand for water exchange. Examples of interesting biologically active agents labeled as a ^{99m}Tc(I) tricarbonyl complex include octreotate (Marmion et al. 2000), a 5-HT 1A receptor ligand (Alberto et al. 1998b), steroids (Wust et al. 1998), a cocaine derivative as ligand for the dopamine transporter (Hoepping et al. 1998), glucose (Dumas et al. 2001) and peptides and recombinant proteins containing C-terminal His_5-tag or His_6-tag (Waibel et al. 1999). This exciting chemistry thus can be assumed to allow technetium-99m labeling of any appropriately designed recombinant protein, synthetic peptide and a wide variety of organic synthetic compounds and holds a great potential for the development of a new generation of ^{99m}Tc-radiopharmaceuticals. First clinical studies using the Tc-tricarbonyl technique to label biomolecules (Buchegger et al. 2003) also revealed the potential clinical usefulness of such ^{99m}Tc-complexes. There remains, however, controversy about whether or not new radiopharmaceuticals on the basis of the Tc-tricarbonyl chemistry will be introduced into routine clinical use (Alberto and Welch 2003). Reasons for some skepticism are the fact that the key patent holder (Mallinckrodt) apparently is not actively pursuing new $^{99m}Tc(CO)_3$-radiopharmaceuticals, the shift of interest and research focus towards clinical PET and the regulatory hurdle and high costs associated with the approval of a new diagnostic drug as compared to the financial revenues.

15.8 Cell Labeling

15.8.1 Red Blood Cell Labeling

Several studies comparing the biological behavior of ^{99m}Tc-red blood cells (^{99m}Tc-RBCs) labeled via the in vitro, in vivo or modified in vivo method all revealed higher heart-to-background ratios and better subjective images with in vitro labeled RBCs (Hamilton and Alderson 1977; Hegge et al. 1978). A labeling kit for in vitro labeling of RBCs with ^{99m}Tc in whole blood has originally been developed at Brookhaven National Laboratory (Srivastava et al. 1983) and is commercially available under the brand name Ultra-Tag.

Each kit consists of three separate nonradioactive components with the following constituents:

1. Labeling vial: $SnCl_2.2H_2O$, 105 μg (50 μg stannous ion minimum); sodium citrate.$2H_2O$, 3.67 mg; dextrose, 5.50 mg; pH prior to lyophilization 7.1–7.2
2. Syringe I (to be protected from light): sodium hypochlorite, 0.6 mg; water for injection, 0.6 ml; pH 11–13
3. Syringe II: citric acid.H_2O, 8.7 mg; sodium citrate.$2H_2O$, 32.5 mg; dextrose, 12.0 mg; water for injection, 1.0 ml; pH 4.5–5.5

Red blood cell labeling is started by the addition of 1–3 ml of autologous whole blood, anticoagulated with heparin or anticoagulant citrate dextrose solution (ACD) to the labeling vial. In this vial, the citrate complex stannous ion and the dextrose is present to sustain red cell metabolism, which improves RBC viability. After an incubation period of 5 min, during which a portion of the stannous ion in the reaction vial diffuses across the RBC membrane and is bound intracellularly, the hypochlorite solution of syringe I is added to the vial to oxidize the extracellular stannous ion. To render the extracellular tin more readily available for oxidation by hypochlorite, the solution in syringe II is added. Finally, a pertechnetate solution (0.5–3 ml, 370–3700 MBq ^{99m}Tc) is added and the vial is incubated with occasional gentle mixing for 20 min.

A RBC labeling efficiency ≥95% is typically obtained using this in vitro labeling procedure. As the yield can decrease in the presence of excessive amounts of the long-lived daughter nuclide ^{99}Tc, the use of fresh (<24 h ingrowth time) generator eluate is recommended.

15.8.2 White Blood Cell Labeling

Radiolabeled autologous white cells offer the most widely accepted radioisotopic method for imaging infection and inflammation. Methods for labeling can be classified depending on the choice of the radionuclide (indium-111 or technetium-99m) and the choice of the cell preparation (pure granulocytes or mixed white cell populations).

Both mixed leukocytes and pure granulocytes have been labeled with ^{111}In. Although pure granulocytes offer the advantage of theoretically better sensitivity and specificity and avoid the risk of malignant transformations of lymphocytes, mixed leukocytes are more practical for routine use because they can be prepared easier and faster while having a comparative sensitivity in acute infections (Schauwecker et al. 1988). Hydroxyquinoline (oxine) was the first established and mostly used lipophilic chelating agent to transport ^{111}In into the cell (McAfee and Thakur 1976).

Because of the more favorable physical characteristics of ^{99m}Tc, many attempts have been made to develop methods for labeling leukocytes with it. The first approaches to label leukocytes with technetium-99m implied phagocytic engulfment of technetium-labeled colloid (Schroth et al. 1981; Pullman et al. 1986). However, this technique has not become established worldwide because, by deliberately inducing the cells to phagocytose, they become activated prior to injection (McAfee et al. 1984). Successful labeling of leukocytes with ^{99m}Tc was achieved in 1986 whit the use of ^{99m}Tc-HMPAO, like ^{111}In-oxine a neutral lipophilic chelate capable of penetrating blood cells (Peters et al. 1986; Roddie et al. 1988). Since ^{99m}Tc-HMPAO is relatively selectively taken up by granulocytes in mixed cell populations and elutes more rapidly from lymphocytes and monocytes than from granulocytes, labeling can be performed in a mixed white cell population which avoids the need for complex and lengthy cell purification (Frier 1994).

Leukocytes can be labeled with either ^{111}In or ^{99m}Tc by a variety of accepted procedures (Datz 1993, 1994; Thakur et al. 1977; Danpure et al. 1988; Dewanjee 1990; Mortelmans et al. 1989).

A major concern when preparing radiolabeled cells is the effect of the labeling procedure on granulocyte viability and function. In vitro tests examining chemotaxis, superoxide generation in response to activation and morphological changes can be used to assess granulocyte function. However, these tests cannot discriminate between cell damage and activation since the techniques themselves often activate the granulocytes.

The most sensitive and practical means of quality control of radiolabeled granulocytes are based on their in vivo distribution following injection. When radiolabeled granulocytes are damaged or activated, they are sequestrated in the lung microvasculature by a mechanism which is poorly understood. As a consequence, dynamic imaging over the lungs is a useful test. Alternatively, the radiolabeled granulocyte recovery, defined as the fraction of injected labeled granulocytes that are circulating in blood, can be determined. Normal recovery factors at 45 min p.i. are about 35% while these values fall to less than 5% when the cells are severely activated or damaged (Peters 1994). These tests need not be performed with every preparation but are useful when setting up a white cell labeling procedure.

The normal biodistribution of ^{99m}Tc-leukocytes is not fully identical to that of ^{111}In-labeled leukocytes. Whereas ^{111}In-leukocyte distribution at 18–24 h is primarily confined to the reticuloendothelial system of liver, spleen, bone marrow and major blood vessels (Seabold et al. 1997), non-specific bowel activity appears from about 3–4 h after administration of ^{99m}Tc-labeled white cells. This is due to elution of secondary hydrophilic ^{99m}Tc-HMPAO species which are excreted in the gut via biliary excretion and in the urine (Peters et al. 1988). As a consequence, imaging of inflammatory bowel disease (IBD) and intra-abdominal abscesses using ^{99m}Tc-labeled leukocytes needs to be performed within 2 h of injection.

References

Abram U, Abram S, Schibli R et al (1992) Synthesis and structures of technetium (I) and rhenium (I) tricarbonyl complexes with bis(diphenylthiophosphoryl)amide, {$M(CO)_3$[$Ph_2PS)_2N$](CH_3CN)}(M=Tc, Re). Polyhedron 17:1303–1309

Agdeppa ED, Kepe V, Flores-Torees S et al (2001a) In vitro binding characteristics of FDDNP and a new analog for synthetic [beta]-amyloid fibrils. J Nucl Med 42:64P

Agdeppa D, Kepe V, Liu J et al (2001b) Binding characteristics of radiofluorinated 6-dialkylamino-2-naphtylethylidene derivatives as positron emission tomography imaging probes for ß-amyloid plaques in Alzheimer's disease. J Neurosci 21:RC189 (1–5)

Agdeppa ED, Kepe V, Shogi-Jadid K et al (2001c) In vivo and in vitro labeling of plaques and tangles in the brain of an Alzheimer's disease patient: a case study. J Nucl Med 42:65P

Agdeppa ED, Kepe V, Petri A et al (2003) In-vitro detection of (S)-naproxen and ibuprofen binding to plaques in the

Alzheimer's brain using the positron emission tomography molecular imaging probe 2-(1-[6-[(2-[^{18}F]fluoroethyl)(methyl)amino]-2-naphthyl] ethylidene)malononitrile. Neuroscience 117:723–730

Alberto R, Welch MJ (2003) Tc(CO)(3)](+) chemistry: a promising new concept for SPET? For and Against. Eur J Nucl Med Mol Imaging 30:1299–1304

Alberto R, Schibli R, Egli A et al (1998a) Steps towards [(C_5Me_5)TcO_3] novel synthesis of [C_5Me_5)Tc(CO)$_3$] from [}{Tc(m^3-OH)(CO)$_3$}4] and oxidation of [(C_5Me)$_5$M(CO)$_3$] (M=Tc,Re) with Br_2. Polyhedron 17:1133–1140

Alberto R, Schibli R, Egli A et al (1998b) A novel organometallic aqua complex of technetium for the labeling of biomolecules: synthesis of [^{99m}Tc(OH$_2$)$_3$(CO)$_3$]$^+$ from [^{99m}TcO$_4$]$^-$ in aqueous solution and its reaction with a bifunctional ligand. J Am Chem Soc 120:7987–7988

Amara SG, Kuhar MJ (1993) Neurotransmitter transporters: recent progress. Annu Rev Neurosci 16:73–93

Anon (1989) In vitro stabilization of technetium-99m exametazime (HM-PAO). Res Discl 305:666

Bakker WH, Brunss AC, Breeman WAP et al (1991a) [^{111}In-DTPA-D-Phe^1]-octreotide, a potential radiopharmaceutical for imaging of somatostatin receptor-positive tumors: synthesis, radiolabeling and in vitro validation. Life Sci 49:1583–1591

Bakker WH, Krenning EP, Breeman WAP et al (1991b) In vivo use of radioiodinated somastatin analogue: dynamics, metabolism and binding to somatostatin receptor positive tumors in man. J Nucl Med 32:1184–1189

Bakker WH, Krenning EP, Reubi JC et al (1991c) In vivo application of [^{111}In- DTPA-D-Phe^1]-octreotide for detection of somatostatin receptor-positive tumors in rats. Life Sci 49:1593–1601

Ballinger JR (2001) Imaging hypoxia in tumors. Semin Nucl Med 31:321–329

Ballinger JR, Gulenchyn K (1991) Alternative formulations for technetium-99m HMPAO. Int J Appl Radiat Isotop 42:315–316

Ballinger JR, Banneman J, Boxen I et al (1996) Technetium-99m-tetrofosmin as a substrate for P-glycoprotein: in vitro studies in multidrug-resistant breast tumor cells. J Nucl Med 37:1578–1582

Ballinger JR, Muzzammil T, Moore MJ (1997) Technetium-99m-furifosmin as an agent for functional imaging of multidrug resistance in tumors. J Nucl Med 38:1915–1919

Barclay NA, Birkeland ML, Brown MH et al (eds) (1990) The leukocyte antigen facts book. Academic, New York, p 138

Barrio JR, Huang SC, Satyamurthy N et al (1999) PET imaging of tangles and plaques in Alzheimer disease with a highly hydrophobic probe. J Labelled Compd Radiopharm 42: S194–S195

Bartenstein P, Ludolph A, Schober O et al (1991) Benzodiazepine receptors and cerebral blood flow in partial epilepsy. Eur J Nucl Med 18:111–118

Beer HF, Blauenstein PA, Hasler PH et al (1990) In vitro and in vivo evaluation of iodine-123-Ro 16-0154: a new imaging agent for SPECT investigations of benzodiazepine receptors. J Nucl Med 31:1007–1014

Bengel FM, Anton M, Richter T et al (2003) Noninvasive imaging of transgene expression by use of positron emission tomography in a pig model of myocardial gene transfer. Circulation 108:2127–2133

Berger G, Mazière M, Comar D (1979) Automated synthesis of ^{11}C-labeled radiopharmaceuticals: imipramine, chlorpromazine, nicotine, methionine. Int J Appl Radiat Isot 30:393–399

Billinghurst MW, Abrams DN, Lawson MS (1991) Stabilization of [^{99m}Tc]HMPAO-1. Ethanolic preparation. Int J Appl Radiat Isotop 42:607–612

Blankenberg FG, Katsikis PD, Tait JF et al (1998) In vivo detection and imaging of phosphatidylserine expression during programmed cell death. Proc Natl Acad Sci USA 95:6349-6354

Blum J, Handmaker H, Lister-James J et al (2000) A multicenter trial with a somatostatin analog (99m)Tc depreotide in the evaluation of solitary pulmonary nodules. Chest 117:1219–1220

Bobeldijk M, Verhoeff NPLG, Vekemans JAJM et al (1990) A simple and high-yield synthesis of (S)-BZM, (R)-BZM and (S)-IBZM for the preparation of (S)-^{123}I-IBZM. J Labeled Compds Radiopharm 28:1247–1256

Boja JW, Carroll FI, Rahman MA et al (1990) New, potent cocaine analogs: ligand binding and transport studies in rat striatum. Eur J Pharm 184:329–332

Bruehlmeier M, Roelcke U, Schubiger PA et al (2004) Assessment of hypoxia and perfusion in human brain tumors using PET with [^{18}F]fluoromisonidazole and [^{15}O]H_2O. J Nucl Med 45:1851–1859

Buchegger F, Bonvin F, Kosinski M et al (2003) Radiolabeled neurotensin analog, ^{99m}Tc-NT-XI, evaluated in ductal pancreatic adenocarcinoma patients. J Nucl Med 44:1649–1654

Burch WM, Browitt RJ (1996) The transition from technegas to pertechnegas. J Nucl Med 37:1917–1918

Burch WM, Tetley IJ, Gras JL (1984) Technetium-99m 'Pseudogas' for diagnostic studies in the lung. Clin Phys Physiol Meas 5:79–85

Burch WM, Sullivan PJ, Lomas FE et al (1986a) Lung ventilation studies with technetium-99m pseudogas. J Nucl Med 27:842–846

Burch WM, Sullivan PJ, McLaren CJ (1986b) Technegas – a new ventilation agent for lung scanning. Nucl Med Commun 7:865–871

Busatto GF, Pilowsky LS, Costa DC et al (1997) Initial evaluation of ^{123}I-5-I-R91150, a selective 5-HT_{2A} ligand for single-photon emission tomography, in healthy human subjects. Eur J Nucl Med 24:119–124

Carroll FI, Rahman MA, Abraham P et al (1991) [^{123}I]3β-(4-iodophenyl)tropan-2β-carboxylic acid methyl ester (RTI-55), a unique cocaine receptor ligand for imaging the dopamine and serotonin transporters in vivo. Med Chem Res 1:289–294

Cayre A, Cachin F, Maublant J et al (2004) Does ^{99m}Tc-sestamibi uptake discriminate breast tumors? Cancer Invest 22:498–504

Chou KL, Hurtig HI, Stern MB et al (2004) Diagnostic accuracy of [^{99m}Tc]TRODAT-1 SPECT imaging in early Parkinson's disease. Parkinsonism Relat Disord 10:375–379

Cowen P (1991) Serotonin receptor subtypes: implications for psychopharmacology. Br J Psychiatry 159 [Suppl 12]:7–14

Crombez D, Van Nerom C, Bormans G et al (1991) Practical aspects of labeling and quality control of Tc-99m MIBI. In: Schmidt HAE, van der Schoot JB (eds) The state of the art of nuclear medicine in Europe. Schattauer, Stuttgart, pp 106–108

Danpure HJ, Osman S, Carroll MJ (1988) Development of a clinical protocol for radiolabeling of mixed leukocytes with ^{99m}Tc-hexamethylpropyleneamine oxime. Nucl Med Commun 9:465–475

Datz FL (1993) The current status of radionuclide infection imaging. In: Freeman LM (ed) Nuclear medicine annual. Raven, New York

Datz FL (1994) Indium-111-labeled leukocytes for the detection of infection: current status. Semin Nucl Med 24:92–109

Dehdashti F, Grigsby PW, Mintun MA et al (2003) Assessing tumor hypoxia in cervical cancer by positron emission tomography with 60Cu-ATSM: relationship to therapeutic response – a preliminary report. Int J Rad Oncol Biol Phys 55:1233–1238

Dewanjee MK (1990) The chemistry of ^{99m}Tc-labeled radiopharmaceuticals. Semin Nucl Med 20:5–27

Dezutter NA, De Groot TJ, Busson RH et al (1999a) Preparation of ^{99m}Tc-N2S2 conjugates of chrysamine G, potential probes for the beta-amyloid protein of Alzheimer's disease. J Labelled Compd Radiopharm 42:309–324

Dezutter NA, Dom RJ, De Groot TJ et al (1999b) ^{99m}Tc-MAMA- chrysamine G, a probe for beta-amyloid protein of Alzheimer's disease. Eur J Nucl Med 26:1392–1399

Dumas C, Petrig J, Schibli R et al (2001) Functionalisation of glucose for the labeling with ^{99m}Tc-tricarbonyl. J Labelled Compd Radiopharm 44:S57–S59

Dumas C, Schibli R, Schubiger PA (2003) Versatile routes to C-2- and C-6-functionalized glucose derivatives of iminodiacetic acid. J Org Chem 68:512–518

Dyszlewski ME, Bushman MJ, Alberto R et al (2001) Kit formulation and preliminary toxicity of $[^{99m}Tc(CO)_3]^+$ intermediate: a novel technetium radiopharmaceutical platform. J Labeled Compd Radiopharm 44:S483–S485

Frier M (1994) Leucocyte radiolabelling techniques: practical aspects. Scand J Gastroenterol 29 [Suppl]:32–35

Gallacher BM, Ansari A, Atkins H et al (1977) Radiopharmaceuticals XXVII. ^{18}F-labeled 2-deoxy-2-fluoro-d-glucose as a radiopharmaceutical for measuring regional myocardial glucose metabolism in vivo: tissue distribution and imaging studies in animals. J Nucl Med 18:990–996

Grierson IR, Link JM, Mathis CA et al (1989) A radiosynthesis of fluorine-18 fluoromisonidazole. J Nucl Med 30:343–350

Grierson JR, Schwartz JL, Muzi M et al (2004) Metabolism of 3'-deoxy-3'-[^{18}F]fluorothymidine in proliferating A549 cells: validations for positron emission tomography. Nucl Med Biol 31:829–837

Gronroos T, Bentzen L, Marjamaki P et al (2004) Comparison of the biodistribution of two hypoxia markers [^{18}F]FETNIM and [^{18}F]FMISO in an experimental mammary carcinoma. Eur J Nucl Med Mol Imaging 31:513–520

Halldin C, Farde L, Högberg T et al (1991) A comparative PET-study of five carbon-11 or fluorine-18 labelled salicylamides. Preparation and in vitro dopamine D-2 receptor binding. Nucl Med Biol 18:871–88

Hamacher K, Coenen HH (2002) Efficient production of the ^{18}F-labelled amino acid O-(2-[^{18}F]fluoroethyl)-L-tyrosine. Appl Rad Isot 57:853–856

Hamacher K, Coenen HH, Stöcklin G et al (1986) Efficient stereospecific synthesis of no-carrier-added 2-[^{18}F]-fluoro-2-deoxy-D-glucose using aminopolyether supported nucleophilic substitution. J Nucl Med 27:235–238

Hamilton RG, Alderson PO (1977) A comparative evaluation of techniques for rapid and efficient in vivo labeling of red cells with [^{99m}Tc]pertechnetate. J Nucl Med 18:1010–1013

Han G, Cho CG, Lansbury PT (1996) Technetium complexes for the quantitation of brain amyloid. J Am Chem Soc 118:4506–4507

Hansen HJ, Jones AL, Sharkey RM et al (1990) Preclinical evaluation of an "instant" ^{99m}Tc-labeling kit for antibody imaging. Cancer Res [Suppl] 50:794s–798s

Hantraye P, Kaijima M, Prenant C et al (1984) Central type benzodiazepine binding sites: a positron emission tomography study in the baboon's brain. Neuroscience Lett 48:115–120

Hartmann IJ, Hagen PJ, Stokkel MP et al (2001) Technegas versus ^{81m}Kr ventilation-perfusion scintigraphy: a comparative study in patients with suspected acute pulmonary embolism. J Nucl Med 42:393–400

Hegge FN, Hamilton GW, Larson SM et al (1978) Cardiac chamber imaging: a comparison of red blood cells, labeled with Tc-99m in vitro and in vivo. J Nucl Med 19:129–134

Henry C, Koumanov F, Ghezzi C et al (1995) Experimental models, protocols, and reference values for evaluation of iodinated analogues of glucose. Nucl Med Biol 22:875–885

Higley B, Smith FW, Smith T et al (1993) Technetium-99m-1,2 bis[bis(2-ethoxyethyl)phosphino]ethane: human biodistribution, dosimetry and safety of a new myocardial perfusion imaging agent. J Nucl Med 34:30–38

Hoepping A, Reisgys M, Brust P et al TROTEC-1 (1998) A new high-affinity ligand for labeling of the dopamine transporter. J Med Chem 41:4429–4432

Hoffend J, Mier W, Schmidt K et al (2004) In vivo characterization of gallium-68-DOTA-albumin, a generator-produced PET blood-pool tracer. Eur J Nucl Med Mol Imaging 31: S257–S258

Högberg T, Ström P, de Paulis T et al (1991) Potential antipsychotic agents. 9. Synthesis and stereoselective dopamine D-2 receptor blockade of a potent class of substituted (R)-N-((1-benzyl-2-pyrrolidinyl)methyl)benzamides. Relation to other side chain congeners. J Med Chem 34:948–955

Hoyer D, Clarke D, Fozard J et al (1994) International union of pharmacology classification of receptors for 5-hydroxytrypamine. Pharmacol Rev 46:157–203

Huang TY, Hwang DR, Narendran R et al (2002) Comparative evaluation in nonhuman primates of five PET radiotracers for imaging the serotonin transporters: [^{11}C]McN 5652. J Cereb Blood Flow Metab 22:1377–1398

Huang WS, Lee MS, Lin JC et al (2004) Usefulness of brain ^{99m}Tc-TRODAT-1 SPET for the evaluation of Parkinson's disease. Eur J Nucl Med Mol Imaging 31:155–161

Hung JC, Gibbons RJ (1992) Breakage of technetium-99m-sestamibi vial with the use of a microwave oven. J Nucl Med 33:176–178

Hung JC, Volkert WA, Holmes RA (1989) Stabilization of technetium-99m-d,l-hexamethylpropyleneamine oxime (^{99m}Tc-d,l-HM-PAO) using gentisic acid. Nucl Med Biol 16:675–680

Hung JC, Wilson ME, Brown ML et al (1991) Rapid preparation and quality control method for technetium-99m-2-methoxy isobutyl isonitrile (Technetium-99m-sestamibi). J Nucl Med 32:2162–2168

Hung JC, Chowdhury S, Redfern MG et al (1997) Rapid preparation method for technetium-99m-bicisate. Eur J Nucl Med 24:655–659

Iqbal T, Cain JH, Slosky JJ (1989) Tris(isonitrile)copper(I)

adducts for preparing radionuclide complexes for scintigraphy. PCT Int Appl WO 89 02,433

Ishiwata K, Vaalburg W, Elsinga PH et al (1988) Comparison of L-[1-^{11}C]methionine and L-methyl-[^{11}C]methionine for measurement of in vivo protein synthesis rate with PET. J Nucl Med 29:1419–1427

Johnson EW, Woods SW, Zoghbi SS et al (1990) Receptor binding characterization of the benzodiazepine radioligand ^{125}I-Ro 16-0154: potential probe for SPECT brain imaging. Life Sci 47:1535–1546

Kaufman MJ, Madras BK (1991) Severe depletion of cocaine recognition sites associated with the dopamine transporter in Parkinson's diseased striatum. Synapse 49:43–49

Kawai K, FujibayashiY, Saji H et al (1991) A strategy for the study of cerebral amino acid transport using iodine-123 labeled amino acid radiopharmaceutical: 3-iodo-alpha-methyl-L-tyrosine. J Nucl Med 32:819–824

Kemerink GJ, Liem IH, Dumont EA et al (2001a) Patient dosimetry of intravenously administered ^{99m}Tc-annexin V. J Nucl Med 42:382–387

Kemerink GJ, Boersma HH, Thimister PWL et al (2001b) Biodistribution and dosimetry of ^{99m}Tc-BTAP-annexin-V in humans. Eur J Nucl Med 28:1373–1378

Kemerink GJ, Liu X, Kieffer D et al (2003) Safety, biodistribution, and dosimetry of ^{99m}Tc-Hynic-Annexin V, a novel human recombinant Annexin V for human application. J Nucl Med 44:947–952

Klimek V, Stockmeier C, Overholser J et al (1997) Reduced levels of norepineprine transporters in the locus coeruleus in major depression. J Neurosc 17:8451–8458

Kloss G, Leven M (1979) Accumulation of radioiodinated tyrosine derivatives in adrenal medulla and in melanomas. Eur J Nucl Med 4:179–186

Klunk WE, Wang Y, Huang G et al (2001) Uncharged thioflavin-T derivatives bind to amyloid-beta protein with high affinity and readily enter the brain. Life Sci 69:1471–1484

Klunk WE, Engler H, Nordberg A et al (2004) Imaging brain amyloid in Alzheimer's disease with Pittsburgh Compound-B. Ann Neurol 55:306–319

Kohler G, Milstein C (1975) Continuous cultures of fused cells secreting antibody of predefined specificity. Nature 256:495–497

Krasikova RN, Ryzhikov NN, Gomzina NA et al (2004) One-step synthesis of n.c.a. [^{18}F]flumazenil and a preliminary evaluation in monkey by PET. Eur J Nucl Med Mol Imaging 31:S249

Krenning EP, Bakker WH, Kooij PPM et al (1992) Somatostatin receptor scintigraphy with indium-111-DTPA-D-Phe-1-octreotide in man: metabolism, dosimetry and comparison with iodine-123-Tyr-3-octreotide. J Nucl Med 33:652–658

Kung HF, Guoy Z, Billings D (1988) Preparation and biodistribution of [^{123}I]IBZM: a potential CNS D_2 dopamine receptor imaging agent. Nucl Med Biol 15:195–201

Kung HF, Alavi A, Chang W et al (1990) In vivo SPECT imaging of CNS D-2 dopamine receptors: initial studies with iodine-123-IBZM in humans. J Nucl Med 31:573–579

Kung HF, Kim H-J, Kung M-P et al (1996) Imaging of dopamine transporters in humans with technetium-99m TRODAT-1. Eur J Nucl Med 23:1527–1530

Kung M-P, Stevenson DA, Plössi K et al (1997) [^{99m}Tc]TRODAT-1: a novel technetium-99m complex as a dopamine transporter imaging agent. Eur J Nucl Med 24:372–380

Lahorte CMM, Vanderheyden J-L, Steinmetz N et al (2004) Apoptose-detecting radioligands: current state of the art and future perspectives. Eur J Nucl Med Mol Imaging 31:887–919

Laihinen AO, Rinne JO, Nägren K et al (1995) PET studies on brain monoamine transporters with carbon-11-β-CIT in Parkinson's disease. J Nucl Med 36:1263–1267

Lang J, Barbarics E, Lazar J et al (1989) Effects of labeling conditions and formulation of kit on in vitro stability of 99mTc-d,l-HM-PAO. Eur J Nucl Med 15:424

Langen K-J, Coenen HH, Roosen N et al (1990) SPECT studies of brain tumors wirh L-3-[^{123}I]iodo-α-methyl tyrosine: comparison with PET, ^{124}IMT and first clinical results. J Nucl Med 31:281–286

Langen K-J, Roosen N, Coenen HH et al (1991) Brain and brain tumor uptake of L-3-[^{123}I]iodo-α-methyl tyrosine: competition with natural L-amino acids. J Nucl Med 32:1225–1228

Langström B, Antoni G, Gullberg P et al (1987) Synthesis of L- and D-[methyl-11C]methionine. J Nucl Med 28:1037–1040

Lehtiö K, Eskola O, Viljanen T et al (2004) Imaging perfusion and hypoxia with PET to predict radiotherapy response in head-and-neck cancer. Int J Radiat Oncol Biol Phys 59:971–982

Lemaire C, Cantineau R, Guillaume M et al (1991) Fluorine-18-altanserin: a radioligand for the study of serotonin receptors with PET: radiolabeling and in vivo biologic behavior in rats. J Nucl Med 32:2266–2272

Lemb M, Oei TH, Eifert H et al (1993) Technegas: a study of particle structure, size and distribution. Eur J Nucl Med 20:576–579

Lewis JS, McCarthy DW, McCarthy TJ et al (1999) Evaluation of ^{64}Cu-ATSM in vitro and in vivo in a hypoxic tumor model. J Nucl Med 40:177–183

Leysen JE (1989) Use of 5-HT receptor agonists and antagonists for the characterization of their respective receptor sites. In: Boulton AB, Baker BG, Jurio AV (eds) Drugs as tools in neurotransmitter research. Humana Press, Clifton, NJ, pp 299–349 (Neuromethods, vol 12)

Lin JL, Berridge M (1993) An efficient radiosynthesis of [^{18}F]fluoromisonidazole. Appl Rad Isot 44:1085–1091

Link CD, Johnson CJ, Fonte V et al (2001) Visualization of fibrillar amyloid deposits in living, transgenic Caenorhabditis elegans animals using the sensitive amyloid dye, X-34. Neurobiol Aging 22:217–226

Lister-James J, Knight LC, Mauer AH et al (1996) Thrombus imaging with a technetium-99m-labeled activated platelet receptor-binding peptide. J Nucl Med 37:775–781

Litton J, Farde L, Neiman J et al (1991) Positron emission tomography of benzodiazepine receptor binding in alcoholics – equilibrium quantification. J Cerebr Blood Flow Metab 11 [Suppl]:617

Mackey DW, Jackson P, Baker RJ et al (1994) The observation of fullerenes in a Technegas lung ventilation unit. Nucl Med Commun 15:430–434

Mang'era KO, Vanbilloen HP, Schiepers CW et al (1995) Stabilisation of high-activity ^{99m}Tc-d,l-HMPAO preparations with cobalt chloride and their biological behaviour. Eur J Nucl Med 22:1163–1172

Mang'era KO, Vanbilloen HP, Bellande E et al (1996) Influence of a ^{99m}TcN core on the biological and physicochemical behavior of ^{99m}Tc complexes of L,L-EC and L,L-ECD. Nucl Med Biol 23:987–993

Mangner TJ, Klecker RW, Anderson L et al (2003) Synthesis of 2 ‘-deoxy-2 ‘-[^{18}F]fluoro-beta-D-arabinofuranosyl nucleosides, [^{18}F]FAU, [^{18}F]FMAU, [^{18}F]FBAU and [^{18}F]FIAU, as potential PET agents for imaging cellular proliferation - Synthesis of [^{18}F]labeled FAU, FMAU, FBAU, FIAU. Nucl Med Biol 30:215–224

Marmion ME, Bugaj JE, Schmidt MA et al (2000) Preparation and biological evaluation of ^{99m}Tc(I)-carbonyl labeled octreotate conjugates. J Nucl Med 41:156P

Martin SJ, Reutelingsperger CPM, McGahon AJ et al (1995) Early redistribution of plasma membrane phosphatidylserine is a general feature of apoptosis regardless of the initiating stimulus: inhibition by overexpression of Bcl-2 and Abl. J Exp Med 182:1545–1556

Martin SJ, Eisenbarth JA, Wagner-Utermann U et al (2002) A new precursor for the radiosynthesis of [^{18}F]FLT. N ucl Med Biol 29:263–273

Mathis CA, Wang Y, Holt DP et al (2003) Synthesis and evaluation of ^{11}C-labeled 6-substituted 2-arylbenzothiazoles as amyloid imaging agents. J Med Chem 46:2740–2754

Mazière M, Godot JM, Berger G et al (1980) High specific activity carbon-11 labelling of benzodiazepines: diazepam and flunitrazepam. J Radioanal Chem 56:229–235

Mazière B, Crouzel C, Venet M et al (1988) Synthesis, affinity and specificity of ^{18}F-setoperone, a potential ligand for in-vivo imaging of cortical serotonin receptors. Nucl Med Biol 15:463–468

Mazière B, Coenen HH, Halldin C et al (1992) PET radioligands for dopamine receptors and re-uptake sites: chemistry and biochemistry. Nucl Med Biol 19:497–512

McAfee JG, Thakur ML (1976) Survey of radioactive agents for in vitro labelling of phagocytic leukocytes. I. Soluble agents. J Nucl Med 17:480–487

McAfee JG, Subramanian JG, Gagne G (1984) Techniques of leucocyte harvesting and labeling: problems and perspectives. Semin Nucl Med 14:83–106

Meegalla SK, Plössi K, Kung M-P et al (1997) Synthesis and characterization of Tc-99m labeled tropanes as dopamine tansporter imaging agents. J Med Chem 40:9–17

Mertens J, Terriere D, Sipido V et al (1994) Radiosynthesis of a new radioiodinated ligand for serotonin-5HT2-receptors, a promising tracer for γ-emission tomography. J Labelled Compd Radiopharm 34:795–806

Meyer GJ, Macke H, Schuhmacher J et al (2004) Ga-68-labelled DOTA-derivatised peptide ligands. Eur J Nucl Med Mol Imaging 31:1097-1104

Meyer JH, Wilson A, Sagrati S et al (2004) Serotonin transporter occupancy of five selective serotonin reuptake inhibitors at different doses: an [^{11}C]DASB positron emission tomography study. Am J Psychiatry 161:826–835

Mier W, Haberkorn U, Eisenhut M (2002) [^{18}F]FLT; a portrait of a proliferation marker. Eur J Nucl Med Mol Imaging 29:165–169

Mitterhauser M, Wadsak W, Wabnegger L et al (2004) Biological evaluation of 2’-[^{18}F]fluoroflumazenil ([^{18}F]FFMZ), a potential GABA receptor ligand for PET. Nucl Med Biol 31:291–295

Monaghan P, Provan I, Murray C (1991) An improved radionuclide technique for the detection of altered pulmonary permeability. J Nucl Med 32:1945–1949

Mortelmans L, Malbrain S, Stuyck J et al (1989) In vitro and in vivo evaluation of granulocyte labeling with (^{99m}Tc)d,l-HMPAO. J Nucl Med 30:2022–2028

Murakami Y, Takamatsu H, Taki J et al (2004) ^{18}F-labelled annexin V: a PET tracer for apoptosis imaging. Eur J Nucl Med Mol Imaging 31:469–474

Nakayama M, Haratake M, Ono M et al (2003) A new Ge-68/Ga-68 generator system using an organic polymer containing N-methylglucamine groups as adsorbent for Ge-68. Appl Rad Isot 58:9–14

Ohtsuki K, Akashi K, Aoka Y et al (1999) Technetium-99m HYNIC-annexin V: a potential radiopharmaceutical for the in-vivo detection of apoptosis. Eur J Nucl Med 26:1251–1258

Okada T, Fujita M, Shimada S et al (1998) Assessment of affinities of beta-CIT, beta-CIT-FE, and beta-CIT-FP for monoamine transporters permanently expressed in cell lines. Nucl Med Biol 25:53–58

Oliveira AJ, da Costa JC, Hilario LN et al (1999) Localization of the epileptogenic zone by ictal and interictal SPECT with ^{99m}Tc-ethyl cysteinate dimer in patients with medically refractory epilepsy. Epilepsia 40:693–702

Olsson H, Halldin C, Farde L (2004) Differentiation of extrastriatal dopamine D2 receptor density and affinity in the human brain using PET. Neuroimage 22:794–803

Ono M, Wilson A, Nobrega J et al (2003) ^{11}C-labeled stilbene derivatives as Abeta-aggregate-specific PET imaging agents for Alzheimer’s disease. Nucl Med Biol 30:565–571

Osman S, Lundkvist C, Pike V et al (1996) Characterization of the radioactive metabolites of the 5-HT$_{1A}$ receptor radioligand [O-methyl-^{11}C]WAY-100635 in monkey and human plasma by HPLC-comparison of the behaviour of an identified radioactive metabolite with parent radioligand in monkey using PET. Nucl Med Biol 23:627–634

Pardridge WM (1977) Kinetics of competitive inhibition of neutral amino acid transport across the blood-brain barrier. J Neurochem 28:103–108

Patt YZ, Podoloff DA, Curley S et al (1994) Technetium-99m labeled IMMU-4, a monoclonal antibody against carcinoembryonic antigen, for imaging of occult recurrent colorectal cancer in patients with rising serum carcinoembryonic antigen levels. J Clin Oncol 12:489–495

Pearson DA, Lister-James J, McBride WJ et al (1996) Thrombus imaging using technetium-99m labeled high potency GPIIb/IIIa receptor antagonists. Chemistry and initial biological studies. J Med Chem 39:1372–1382

Peremans K, Audenaert K, Coopman F et al (2003a) Estimates of regional cerebral blood flow and 5-HT2A receptor density in impulsive, aggressive dogs with ^{99m}Tc-ECD and ^{123}I-5-I-R91150. Eur J Nucl Med Mol Imaging 30:1538–1546

Peremans K, Audenaert K, Coopman F et al (2003b) Regional binding index of the radiolabeled selective 5-HT2A antagonist ^{123}I-5-I-R91150 in the normal canine brain imaged with single photon emission computed tomography. Vet Radiol Ultrasound 44:344–51

Peters AM (1994) Quality control of radiolabelled white cells. In: Martin-Comin J, Thakur ML, Piera C, Roca M, Lomena F (eds) Radiolabeled blood elements. Recent advances in techniques and applications. Plenum, New York, pp 29–32

Peters AM, Danpure HJ, Osman S et al (1986) Preliminary clinical experience with ^{99m}Tc-HMPAO for labelling leucocytes and imaging inflammation. Lancet 2:946–949

Peters AM, Roddie ME, Danpure HJ et al (1988) ^{99m}Tc HMPAO labelled leucocytes: a comparison with In-111-tropolonate labelled granulocytes. Nucl Med Commun 9:449–463

Picwnica-Worms D, Chiu ML, Budding M et al (1993) Func-

tional imaging of multidrug-resistant P-glycoprotein with an organo-technetium complex. Cancer Res 53:977–984
Phelps ME, Hoffman EJ, Selin C et al (1978) Investigation of [^{18}F]-2-fluoro-2-deoxyglucose for the measure of myocardial glucose metabolism. J Nucl Med 19:1311–1319
Pike VW, McCarron J, Hume SP et al (1995) Preclinical development of a radioligand for studies of central 5-HT_{1A} receptors in vivo – [^{11}C]WAY-100635. Med Chem Res 5:208–227
Pike VW, McCarron J, Lamertsmaa A et al (1996) Exquisite delineation of 5-HT_{1A} receptors in human brain with PET and [carbonyl-^{11}C]WAY-100635. Eur J Pharmacol 301: R5–R7
Pullman W, Hanna R, Sullivan P et al (1986) ^{99m}Tc autologous phagocyte scanning: a new imaging technique for inflammatory bowel disease. Br Med J 293:171–174
Ramalingam K (1989) Facile synthesis of 2-methoxyisobutylisonitrile. Synth Commun 21:511–514
Reutelingsperger CPM, Kop JMM, Hornstra G et al (1988) Purification and characterization of a novel protein from bovine aorta that inhibits coagulation: inhibition of the phospholipid-dependent factor-Xa-catalyzed prothrombin activation, through a high-affinity binding of the anticoagulant to the phospholipids. Eur J biochem 173:171–178
Rizzo-Padoin N, Farina A, Le Pen C et al (2001) A comparison of radiopharmaceutical agents used for the diagnosis of pulmonary embolism. Nucl Med Commun 22:375–381
Roddie ME, Peters HM, Danpure HJ et al (1988) Imaging inflammation with ^{99m}Tchexamethyl propyleneamineoxime (HMPAO) labelled leucocytes. Radiology 166:767–772
Rodwell JD, Alvarez VL, Lee C et al (1986) Site-specific covalent modification of monoclonal antibodies: in vitro and in vivo evaluations. Proc Natl Acad Sci USA 83:2632–2636
Sachdev SS, Ramamoorthy N, Nayak UN et al (1990) Preparation and evaluation of ^{99m}Tc-t-butylisonitrile (^{99m}Tc-TBI) for myocardial imaging: a kit for hospital radiopharmacy. Nucl Med Biol 17:543–552
Sampson CB, Solanki C (1991) Stabilisation of Tc-99m-exametazine using ethanol and storage at low temperature. Eur J Nucl Med 18:532
Samson Y, Bernuau J, Pappata S et al (1987) Cerebral uptake of benzodiazepine measured by positron emission tomography in hepatic encephalopathy. N Engl J Med 316:414–415
Savic I, Roland P, Sedvall G et al (1988) In vivo demonstration of reduced benzodiazepine receptor binding in human epileptic foci. Lancet 16:863–866
Scalzetti EM, Gagne GM (1995) The transition from technegas to pertechnegas. J Nucl Med 36:267–269
Schauwecker DS, Burt RW, Park HM et al (1988) Comparison of purified indium-111 granulocytes and indium-111 mixed leukocytes for imaging of infections. J Nucl Med 29:23–25
Schibli R, Alberto R, Abram U et al (1998) Structural and ^{99}Tc NMR investigations of complexes with *fac*-[$Tc(CO)_3$]+ moieties and macrocyclic thioethers of various ring sizes: synthesis and x-ray structure of the complexes *fac*-[Tc(9-ane-S_3)$(CO)_3$]Br, *fac*-[Tc_2(tosylate)$_2$(18-ane-S_6)$(CO)_6$] and *fac*-[Tc_2(20-ane-S_6-OH)$(CO)_6$][tosylate]$_2$. Inorg Chem 37:3509–3516
Schibli R, La Bella R, Alberto R et al (2000) Influence of the denticity of ligand systems on the in vitro and in vivo behavior of ^{99m}Tc(I)-tricarbonyl complexes: a hint for the future functionalization of biomolecules. Bioconjug Chem 11:345–351
Schou M, Halldin C, Sóvágó J et al (2003) Specific in vivo binding to the norepinephrine transporter demonstrated with the PET radioligand, (S,S)-[^{11}C]MeNER. Nucl Med Biol 30:707–714
Schou M, Halldin C, Sóvágó J et al (2004) PET evaluation of novel radiofluorinated reboxetine analogs as norepinephrine transporter probes in the monkey brain. Synapse 53:57–67
Schroth HJ, Oberhausen E, Berberich R (1981) Cell labelling with colloidal substances in whole blood. Eur J Nucl Med 6:469–472
Seabold JE, Forstrom LA, Schauwecker DS et al (1997) Procedure guideline for indium-111-leukocyte scintigraphy for suspected infection/inflammation. J Nucl Med 38:997–1001
Selkoe DJ (1999) Biology of β-amyloid precursor protein and the mechanism of Alzheimer's disease. In: Alzheimer's disease. Lippincott, Williams and Wilkins, Philadelphia, pp 293–310
Shiue GG, Shiue CY, Lee RL et al (2001) A simplified one-pot synthesis of 9-[(3-[^{18}F]fluoro-1-hydroxy-2-propoxy)methyl]guanine ([^{18}F]FHPG) and 9-(4-[^{18}F]fluoro-3-hydroxymethylbutyl)guanine ([^{18}F]FHBG) for gene therapy. Nucl Med Biol 28:875–883
Shoghi-Jadid K, Small GW, Agdeppa ED et al (2002) Localization of neurofibrillary tangles and beta-amyloid plaques in the brains of living patients with Alzheimer disease. Am J Geriatr Psychiatry 10:24–35
Slifstein M, Hwang DR, Huang YY et al (2004) In vivo affinity of [^{18}F]fallypride for striatal and extrastriatal dopamine D-2 receptors in nonhuman primates. Psychopharmacology 175:274–286
Small GW, Agdeppa ED, Kepe V et al (2002) In-vivo brain imaging of tangle burden in humans. J Mol Neurosci 19:323–327
Sorger D, Patt M, Kumar P et al (2003) [^{18}F]Fluoroazomycin arabinofuranoside (^{18}FAZA) and [^{18}F]fluoromisonidazole (^{18}FMISO): a comparative study of their selective uptake in hypoxic cells and PET imaging in experimental rat tumors. Nucl Med Biol 30:317–326
Spanu A, Schillaci O, Meloni GB et al (2002) The usefulness of ^{99m}Tc-tetrofosmin SPECT scintimammography in the detection of small size primary breast carcinomas. Int J Oncol 21:831–840
Srivastava SC, Babich JB, Richards P (1983) A new kit method for the selective labeling of erythrocytes in whole blood with technetium-99m. J Nucl Med 24:128P
Stypinski D, McQuarrie SA, Wiebe LI et al (2001) Dosimetry estimations for ^{123}I-IAZA in healthy volunteers. J Nucl Med 42:1418–1423
Terriere D, Janssen PMF, Gommeren W et al (1995) Evaluation of radioiodo-4-amino-N-[1-[3-(4-fluorophenoxy)-propyl]-4-methyl-4-piperidinyl]-5-iodo-2-methoxybenzamide as a potential 5HT2 receptor tracer for SPE(C)T. Nucl Med Biol 22:1005–1010
Thakur ML Lavender JP, Arnot RN et al (1977) Indium-111-labeled autologous leukocytes in man. J Nucl Med 18:1014–1019
Thakur ML, Marcus CS, Henneman P et al (1996) Imaging inflammatory diseases with neutrophil-specific technetium-99m-labeled monoclonal antibody anti-SSEA-1. J Nucl Med 37:1789–1795
Tjuvajev JG, Doubrovin M, Akhurst T et al (2002) Comparison

of radiolabeled nucleoside probes FIAU, FHBG, and FHPG) for PET imaging of HSV1-tk gene expression. J Nucl Med 43:1072–1083

Tominaga S, Shimada T, Kawakami K (1995) Physicochemical characterization and lung clearance of pertechnegas. Kaku Ikagu 32:563–567

Tubergen K, Corlija M, Volkert WA et al (1991) Sensitivity of technetium-99m-d,l-HMPAO to radiolysis in aqueous solutions. J Nucl Med 32:111–115

Tweedle MF (1983) Accelerators for forming cationic technetium complexes useful as radiodiagnostic agents. World Patent 83 02:615

Vallabhajosula S, Moyer BR, Lister-James J et al (1996) Preclinical evaluation of technetium-99m-labeled somatostatin receptor-binding peptides. J Nucl Med 37:1016–1022

Vander Borght T, De Maeght S, Labar D et al (1992) Comparison of thymidine labeled in methyl group and in 2C-ring position in human PET studies. Eur J Nucl Med 19:578

Van Paesschen W (2004) Ictal SPECT. Epilepsia 45 [Suppl 4]:35–40

Van Paesschen W, Dupont P, Van Heerden B et al (2000) Self-injection ictal SPECT during partial seizures. Neurology 23:1994–1997

Verbeke K, Kieffer D, Vanderheyden J-L et al (2003) Optimization of the preparation of ^{99m}Tc-labeled Hynic-derivatized Annexin V for human use. Nucl Med Biol 30:771–778

Verhoeff NP, Wilson AA, Takeshita S et al (2004) In-vivo imaging of Alzheimer disease beta-amyloid with [^{11}C]SB-13 PET. Am J Geriatr Psychiatry 12:584–595

Versijpt J, van Laere KJ, Dumont F et al (2003) Imaging of the 5-HT2A system: age-, gender-, and Alzheimer's disease-related findings. Neurobiol Aging 24:553–561

Virgolini I, Szilvasi I, Kurtaran A et al (1998) Indium-111-DOTA-Lanreotide: biodistribution, safety and radiation absorbed dose in tumor patients. J Nucl Med 39:1928–1936

Wackers FJT, Berman DS, Maddahi J et al (1989) Technetium-99m hexakis 2-methoxyisobutyl isonitrile: human biodistribution, dosimetry, safety and preliminary comparison to thallium-201 for myocardial perfusion imaging. J Nucl Med 30:301–311

Waibel R, Alberto R, Willunda J et al (1999) Stable one-step technetium-99m labeling of His-tagged recombinant proteins with a novel Tc(I)-carbonyl complex. Nat Biotechnol 17:897–901

Weber W, Weste HJ, Grosu AL et al (2000) O-(2-[^{18}F]Fluoroethyl)-L-tyrosine and L-[methyl-^{11}C]methionine uptake in brain tumours: initial results of a comparative study. Eur J Nucl Med 27:542–549

Weisner PS, Bower GR, Dollimore LA et al (1993) A method for stabilising technetium-99m exametazime prepared from a commercial kit. Eur J Nucl Med 20:661–666

Wester HJ, Herz M, Weber W et al (1999) Synthesis and radiopharmacology of O-(2-[^{18}F]fluoroethyl)-L-tyrosine for tumor imaging. J Nucl Med 40:205–212

Wienhard K, Herholz K, Coenen HH (1991) Increased amino acid transport into brain tumors measured by PET of 2-[^{18}F]fluorotyrosine. J Nucl Med 32:1338–1346

Wust F, Carlson KE, Katzenellenbogen JA et al (1998) Synthesis and binding affinities of new 17 alpha-substituted estradiol-rhenium "n+1" mixed-ligand and thioether-carbonyl complexes. Steroids 63:665–671

Yamamoto YL, Meyer E, Menon D et al (1983) Regional cerebral blood measurement and dynamic positron emission tomography. In: Heiss WD, Phelps ME (eds) Positron emission tomography of the brain. Springer, Berlin Heidelberg New York, pp 78–84

Yamasaki T, Inoue O, Shinotoh H et al (1986) Benzodiazepine study in the elderly using PET and clinical application of a new tracer, C-11-α-methyl-N-methyl benzylamine. In: Kitane K (ed) Liver and aging, liver and brain. Elsevier, Amsterdam, pp 265–276

Yang DJ, Wallace S, Cherif A et al (1995) Development of ^{18}F labeled fluoroerythromisonidazole as a PET agent for imaging tumor hypoxia. Radiology 194:795–800

Zhuang ZP, Kung MP, Hou C et al (2001a) Radioiodinated styrylbenzenes and thioflavins as probes for amyloid aggregates. J Med Chem 44:1905–1914

Zhuang ZP, Kung MP, Hou C et al (2001b) IBOX (2-(4'-dimethylaminophenyl)-6-iodobenzoxazole): a ligand for imaging amyloid plaques in the brain. Nucl Med Biol 28: 887–894

16 Instrumentation and Data Acquisition

Sibylle I. Ziegler and Magnus Dahlbom

CONTENTS

16.1 Detectors and Imaging Systems

Nuclear medical images are formed by the detection of gamma-rays, X-rays or annihilation quanta (in the case of positron imaging). The camera detects the density of gamma rays per unit area, their energy and their direction of flight. If single photon emitters are used the direction of flight has to be determined by geometric collimation. In contrast, coincidence detection uses the unique feature of positron annihilation which results in two high-energy gamma rays simultaneously emitted back-to-back. The detection of both gamma rays within a very short time window defines the line of response in space and thus the direction of flight. Scintigraphic instrumentation consists of scintillation crystals to convert gamma-ray energy into visible light, suitable light sensors, readout electronics and image processing units.

S. I. Ziegler, PhD
Nuklearmedizinische Klinik und Poliklinik, Klinikum rechts der Isar der TU München, Ismaninger Str. 22, 81675 München, Germany
M. Dahlbom, PhD
Department of Molecular and Medical Pharmacology, David Geffen School of Medicine at UCLA, 10833 Le Conte Ave, AR-144 CHS, Los Angeles, CA 90095-6942, USA

16.1.1 Principles of Scintillation Detectors

Scintillators emit light after a gamma ray has deposited its energy in the crystal. The wavelength (UV, visible), the intensity and time distribution of the scintillation light are properties of the scintillating material. There are organic (plastic) and inorganic scintillators, each having some unique advantages or disadvantages for the detection of either charged particles or gamma- and X-rays. All clinical nuclear medicine cameras are built with inorganic scintillators because of their high detection efficiency for X-rays and gamma rays.

The search for new scintillation crystals which are suitable for nuclear medicine imaging is guided by the following requirements: the higher the density of the material and the higher the atomic number, the better is the detection efficiency for gamma rays. More scintillation light emitted in a shorter period of time allows the detection of events in short time intervals. Although there are numerous scintillation crystals available, NaI(Tl) (thallium activated sodium iodide) remains the crystal of choice for single photon detection with energies of 70–360 keV. This is mainly because of its high light output, reasonable decay time and inexpensive production in large quantities. One disadvantage of NaI(Tl) is that it is a hygroscopic material and needs to be sealed in airtight containers.

For efficient detection of high-energy gamma rays in positron imaging, requirements are even more stringent: if coincidence detection is used, detection efficiency is most important, since the total efficiency is the product of the individual detector sensitivities. High density and atomic number are essential for detection of photons at 511 keV. The

specific necessity of fast timing in coincidence measurements can be met by short decay times of scintillation light.

Although the energy resolution of a gamma camera is determined by the whole system, the light yield of the scintillation crystal is an important determinant. Better image contrast can be reached if the selection of accepted energy is improved. An energy resolution of less than 10% allows the choice of a narrow window with less loss in unscattered radiation (Kojima et al. 1993). Good energy resolution can be achieved with crystals of high light output. Additionally, luminous crystals provide improved event localization in a continuous detector.

Although the very first positron tomographs consisted of NaI(Tl) scintillation detectors, the most commonly used scintillator in positron emission tomography is bismuth germanate (BGO), which has high detection efficiency for annihilation quanta (Table 16.1). However, BGO has a low light yield and long light decay time, prohibiting short coincidence windows and high count rate capability. More recently, new scintillation materials became available specifically for coincidence detection. The most promising scintillator is cerium activated lutetium oxy-orthosilicate (LSO; Melcher and Schweitzer 1992). It has a similar detection efficiency as BGO, but a higher light yield and shorter light decay time. A high-resolution positron tomograph with this fast, luminous scintillation material is being constructed for brain research (Casey et al. 1997; Schmand et al. 1998a,b), and once large quantities of LSO can routinely be produced, it will substitute BGO most likely in clinical positron tomographs. These devices will perform at much higher count rates and will be less affected by random events in 3D mode (see below) since short coincidence windows can be implemented.

The light which is emitted by the scintillation crystal is detected by sensors coupled to the crystal. The coupling is achieved through a light pipe or directly on the entrance window of the light sensor. Photomultiplier tubes (PMT) are the light sensors which are in routine use. The photo-sensitive cathode of the PMT converts the impinging light into electrons, which are multiplied in the dynode structure of the PMT and read out as a pulse whose amplitude is proportional to the amount of light (Fig. 16.1). Semiconductor sensors may offer the advantage of very compact detector modules but are not yet implemented in commercial systems. First results in research imaging devices show their potential for the detection of signals from luminous, fast scintillators (Schmelz et al. 1995; Lecomte et al. 1996; Levin et al. 1997). In combination with PMTs, they offer novel designs for high-resolution detector modules (Huber et al. 1997).

Direct detection of gamma rays in semiconductor material such as cadmium-zinc-telluride (CdZnTe) has become more realistic since the production process and signal processing have been improved (Butler et al. 1998; Kipper et al. 1998). Future investigations will show if these devices will find widespread application in clinical systems.

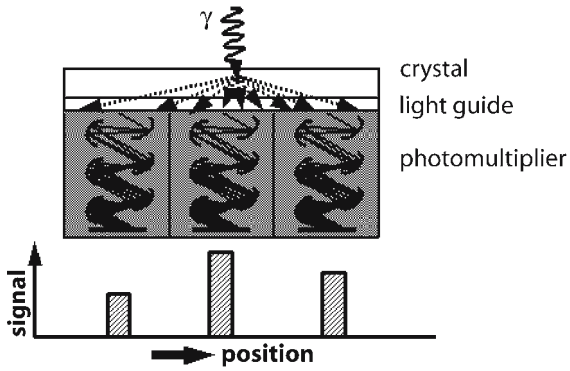

Fig. 16.1. Principle of the gamma camera. An incoming photon (γ) causes scintillations in the crystal which are guided to and amplified by photo multipliers. The position of the incoming photon is calculated from the signal intensity of the photomultiplier tubes

Table 16.1. Characteristics of scintillation crystals that are used in nuclear medicine. *NaI:Tl* Thallium activated sodium iodide, *BGO* bismuth germinate, *YSO:Ce* cerium activated yttrium oxy-orthosilicate, *LSO:Ce* cerium activated lutetium oxy-orthosilicate, *GSO:Ce* cerium activated gadolinium orthosilicate

	NaI:Tl	BGO	YSO:Ce	LSO:Ce	GSO:Ce
Light yield (% of NaI)	100	12	45	75	20
Wavelength (nm)	410	480	420	420	430
Light decay time (ns)	230	300	70	40	30-60
Attenuation length for 140 keV (mm)	004.2	0.8	7.7	1.0	1.1
Attenuation length for 511 keV (mm)	30	11	26	12	14

16.1.2 From Single-Head, Multi-Head and Ring Geometry to Hybrid Systems

Most nuclear medicine imaging is performed using a scintillation camera either in static or in dynamic acquisition mode. It consists of a single large area (typical 40×50 cm^2) NaI(Tl) scintillation crystal, which is read out by photomultiplier tubes (Fig. 16.1). A crystal of only 9.5 mm thickness has a detection efficiency of 90% for 140 keV gamma rays. Light sharing among the PMTs and centroid calculation of the light distribution is exploited for event localization on the detector head according to the scheme first proposed by Anger (1958). The technological improvements of this device which is in routine use since the 1960s, include higher spatial resolution, better uniformity and much higher count rate performance. Introduction of individual PMT-signal digitization resulted in new and better possibilities for the correction of system imperfections. In general, the Anger camera is optimized for imaging ^{99m}Tc-labeled compounds; thus performance is usually best for the detection of gamma rays of 140 keV.

Since the emission of gamma-rays from the patient is isotropic, collimation is needed to restrict data to gamma rays of certain, predefined directions. Most commonly used are parallel-hole collimators made of lead with very small holes separated by septa. The thickness and length of the septa are chosen such that for a given energy the gamma rays with inadequate direction are absorbed (Fig. 16.2). Obviously this leads to thicker septa for higher-energy gamma rays. Collimator design always is a compromise between spatial resolution and sensitivity: reducing the size of the holes or using longer septa improves spatial resolution but reduces sensitivity at the same time. This fact is the most important tradeoff in the imaging process using Anger cameras. The spatial resolution of a parallel-hole collimator decreases linearly with increasing distance between object and collimator (Fig. 16.2), whereas sensitivity stays approximately constant.

For transaxial tomography (single photon emission computed tomography, SPECT), the camera is rotated around the patient, acquiring multiple views from different angles. The transverse activity distribution is calculated from these projections using adequate reconstruction techniques (see chap. 14). The SPECT systems with two or three camera heads (Fig.-16.3) were developed to increase detection efficiency. Thus, for the same number of counts in the image, total scan duration can be reduced or higher-resolution collimators can be used.

Positron emission tomography (PET) utilizes the unique feature of two high-energy gamma rays emitted back-to-back after positron annihilation (Fig.-16.4). Detector pairs count all events which occur in both of them within a very short time interval (10–20-ns). From data along these lines of response, the distribution of radioactivity can be reconstructed by similar mathematical methods as are used in SPECT. The measured counts are the sum of true coincidences, belonging to a single positron decay, random events, which occur if two uncorrelated gamma rays are accidentally detected in a detector pair, and scattered events, in which at least one of the gamma rays lost its original direction of flight through Compton scattering in the patient (Fig. 16.5). Scattering is also responsible for the loss of counts along a given line of response if one of the gamma rays is scattered so that it does not reach the detector. This effect, the attenuation of counts, is much more pronounced in PET, as compared with SPECT, since both gamma

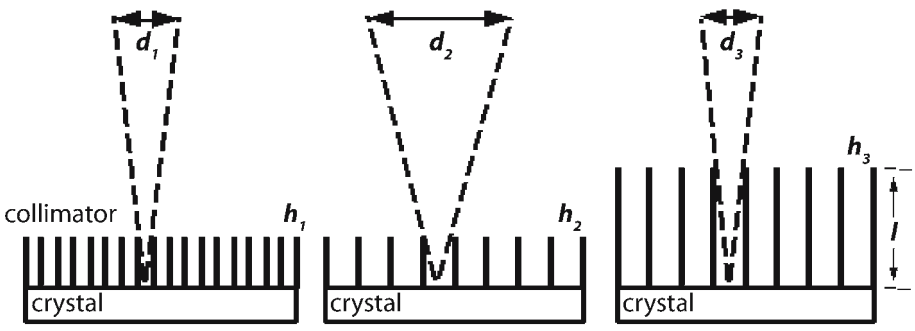

Fig. 16.2. Geometrical design of lead collimators defines the spatial resolution which can be achieved with a gamma camera. Septa length (l), thickness and hole width (h_1, h_2, h_3) define the blur in the image, represented by the visual field angle of the collimator (d_1, d_2, d_3). Spatial resolution degrades rapidly for larger distances

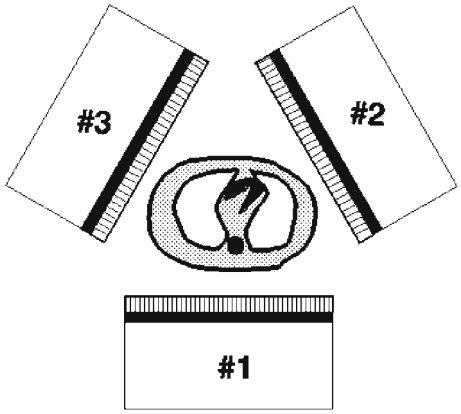

Fig. 16.3. Geometry of a triple-head SPECT system

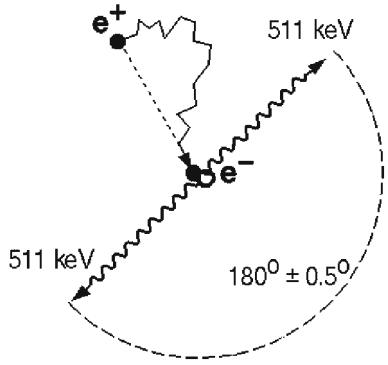

Fig. 16.4. Positron annihilation. Two high-energy gamma rays are emitted back-to-back, which can be used for "electronic collimation"

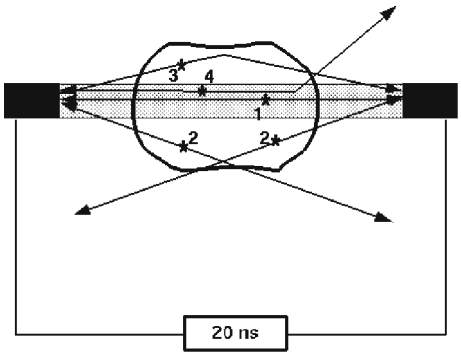

Fig. 16.5. Coincidence detector pair. True (*1*), random (*2*) and scattered (*3*) coincidence events, and attenuation (*4*). The *20 ns* is the time interval within which coincidence events occur for the 1-m distance between the detectors

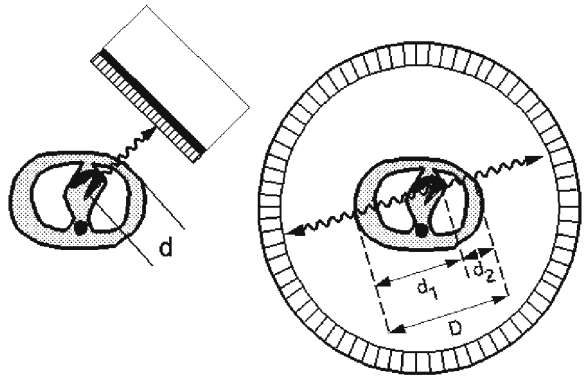

Fig. 16.6. Attenuation in SPECT (*left*) depends on the depth d of tissues in the body. In PET (*right*) one photon traverses d_1, and the other, d_2, which is the total length D through the body

quanta have to reach the detectors (Fig. 16.6). Attenuation causes artifacts in the reconstructed images which result in distortions or inhomogeneity. Heterogeneous attenuation in the thorax especially affects myocardial scans. Hardware and software approaches have been developed for both SPECT and PET imaging (Bacharach and Buvat 1995). In contrast to SPECT, attenuation in PET can precisely be corrected because the total length through the body determines the attenuation factor along a coincidence line. By doing so, quantitative information about the tracer distribution can be obtained. Compensation for count loss through attenuation can be achieved by individually measuring the attenuation factor for 511-keV gamma rays. This is routinely done by rotating positron (^{68}Ge/^{68}Ga) rod sources. The ratio of a reference (blank) scan without object in the field-of-view and the transmission data results in correction factors for the projection data. Measured integral attenuation factors can be reconstructed into two-dimensional attenuation images. While this reconstruction step is not necessarily needed for attenuation correction in coincidence imaging, it is essential in attenuation correction methods in SPECT. Limited count statistics in the transmission data is the reason for intensive research on optimizing measurement and processing in transmission acquisitions (Bailey 1998).

The main difference between single photon and coincidence measurements is the necessity of lead collimators for the definition of the angle of incidence, compared with electronic collimation in the case of positron imaging. The use of collimators results in a very low detection efficiency of approximately 10^{-4} times the emitted number of gamma rays. Positron imaging by coincidence counting is much more sensitive. For example, even a triple-

head SPECT system, designed to image Tc-99m-labeled tracers in the brain, is 15 times less sensitive than a positron tomograph if a 1-cm resolution is assumed in both systems (Budinger 1996). When imaging the body, this proportion becomes even less favorable (1:30).

The situation is even worse if annihilation quanta are detected in single photon mode by use of a ultra-high-energy collimator. The septa of such a collimator would cover more than half of the camera head. Taking into account that the efficiency of a 9.5 mm NaI(Tl) crystal is 50% lower at 511 than at 140 keV, the sensitivity for a SPECT system with 10-mm resolution would be 45 times less than a system for 140-keV and the same resolution (Budinger 1998). Therefore, the clinical potential of collimated detection of 511-keV single photons is found mainly in myocardial viability studies, where at the expense of spatial resolution (typically 2 cm FWHM) sensitivity is just 14 times lower than PET (van Lingen et al. 1992; Macfarlane et al. 1995; Chen et al. 1997).

Spatial resolution in coincidence detection is defined by the size of the detectors. Crystals were read out by individual PMTs in the first tomographs. Demands for higher resolution and closely packed channels led to the invention of the block detector (Casey and Nutt 1986). Most commercially available positron tomographs utilize this scheme. The small (4×4 cm) crystal blocks are segmented such that the light emitted from one block is distributed onto four photomultiplier tubes and Anger logic can be applied for segment identification, e.g. 64 segments. The function of a BGO block-detector therefore is very similar to a small gamma camera. The blocks are arranged in rings to cover the whole 360° around the patient and extend over 10–25 cm in the axial direction. The size of the sub-crystals in a block defines the intrinsic spatial resolution and thus is kept small.

Traditionally, PET acquisition is performed in transverse slices through the body, with inter-plane septa to reduce the scatter contribution (2D mode, Fig. 16.7a). In most of the current PET scanners, the septa can be retracted to allow three-dimensional data acquisition for enhanced sensitivity (Fig. 16.7b; Bendriem and Townsend 1998). Although this acquisition mode has a higher scatter and random fraction than a 2D tomograph, the gain in true coincidence counts in brain scans obviates the use of smooth filters in the reconstruction process, thus image contrast is noticeably improved. Acquisitions in the abdomen or whole body in 3D mode are more affected by scattered radiation and random events originating outside the axial coincidence field of view. This measurement situation needs to be further evaluated and normalization and correction methods for quantitative information have to be validated (Bendriem and Townsend 1998). To fully utilize the advantages of 3D acquisition, methods for scatter correction and random subtraction have to be implemented along with suitable reconstruction or rebinning algorithms.

Tomographs with full rings of BGO-, LSO- and GSO block detectors will remain the high performance PET scanners. However, clinical PET has gained much attention in the recent years, mostly triggered by the successes of using FDG in cancer diagnosis and treatment evaluation. Reducing the cost of PET instrumentation is the goal of new paths of scanner development: one being the introduction of positron tomographs with fewer or cheaper scintillation detectors, the other being hybrid dual head cameras offering SPECT as well as coincidence acquisition mode. The first category (dedicated positron imaging systems) is represented by a tomograph with large NaI(Tl) scintillation crystals arranged in a hexagon (UGM Quest, Philadelphia, Pennsylvania; ADAC C-PET, Milpitas, California). This is an intrinsically 3D system (Muehllehner and Karp 1986; Karp et al. 1990). From Table 16.1 it is clear that thicker NaI crystals are needed to improve coincidence detection efficiency. Thus, the crystals in this scanner are 25 mm thick. Since NaI(Tl) is less expen-

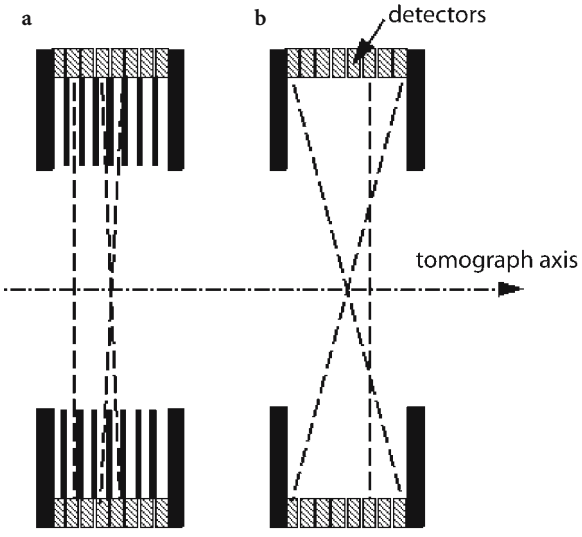

Fig. 16.7. a Two-dimensional PET uses inter-plane septa, restricting the events to direct slices and next neighbors. **b** In 3D PET septa are retracted, allowing all possible angles for coincidence detection

sive than BGO, the price for this tomograph is lower. This tomograph has very good spatial resolution, good contrast and detection efficiency, but low count rate efficiency. Further improvements of this type of tomograph are underway, one being the use of curved crystals for better homogeneity in spatial resolution.

Another design to reduce the cost is a 3D tomograph which consists of only two sectors with BGO block detectors (Siemens CTI ECAT ART, Siemens, Erlangen, Germany), continuously rotating around the patient to cover all projection angles (Townsend et al. 1993; Bailey et al. 1997). This scanner has a good spatial resolution, and a sensitivity comparable to a full ring BGO tomograph which is operated in 2D. The most important physical performance parameters of some commercial positron imaging systems are summarized in Table 16.2.

Various realizations of hybrid cameras are available; all consist of a dual-head NaI(Tl) camera operated in either SPECT or coincidence mode (Fig. 16.8). In coincidence mode the camera is operated without collimators, and events detected in both detectors within a narrow time window (15 ns) are assigned to one coincidence event. The exact location of the coincidence line is calculated by the coordinates of gamma radiation detection on the camera heads (equivalent to 3D operation). For each angular position of the heads, therefore, coincidence events in different directions are recorded, in contrast to a parallel-hole collimator, which only records the photons that appear at right angles to the camera head.

Because a dual-head coincidence camera is meant to be operated both in the coincidence mode and in the conventional SPECT mode, compromises must be made in the design since some requirements are contradictory. For example, a thin scintillation crystal (generally 9.5 mm) is required for SPECT so that the best possible spatial resolution can be achieved (Muehllehner 1979). However, if high-energy annihilation photons are to be recorded efficiently, thicker crystals must be used. With a 6.4-mm-thick NaI(Tl) crystal, only 7% of the photons deposit their entire energy (511 keV) in the crystal, and with double the crystal thickness the proportion is 17% (Anger and Davis 1964), resulting in a coincidence detection efficiency of 3%. Digital correction techniques are used in modern cameras; thus, despite increased crystal thickness, there is no resolution degradation in the detection of low-energy photons.

Since large-area camera heads are involved, events are also detected that have their origin outside the actual field of view of the camera and increase the singles count rate in the heads (Fig. 16.9). Similarly, the detectors are sensitive to photons that are scattered in the patient and reach the crystal. High singles count rates contribute to the background of random coincidences and, because of the open design, depend on the distribution outside the field of view, a fact that makes correction techniques more difficult or even impossible. The fraction of coincidence events is approximately 1–2% of all events, depending on crystal thickness. The singles count rates in a camera head during coincidence operation can be as high as 1 million/s. Compared with count rates of much less than 100 kcps, which normally occur in SPECT imaging, this imposes stringent demands on the camera's count rate performance. To solve the problem of a system that is less sensitive but may nevertheless be subjected to high count rates, pulse processing techniques become more important (Mankoff et al. 1990).

Although it provides a much higher sensitivity than a gamma camera equipped with an ultra-high-energy

Table 16.2. Performance parameters of dedicated ring tomographs (Siemens CTI ECAT EXACT47 and ART, Siemens, Erlangen, Germany; GE Advance and UGM Quest, General Electric Medical Systems, Milwaukee, Wis.; and a coincidence camera (ADAC Vertex MCD ADAC Laboratories, Milpitas, Calif.). *FWHM* full width at half maximum

	EXACT47		Advance		ART	Quest	MCD[c]
	2D[a]	3D[b]	2D[a]	3D[b]			
Axial field of view (cm)	16.2	16.2	15.2	15.2	16.2	25	38
Resolution in the center							
Transaxial FWHM (mm)	5.8	5.8	4.5	4.5	5.7	5.5	5.0
Axial FWHM (mm)	5.0	5.0	4.0	6.0	6.0	6.0	5.3
Sensitivity (cps/Bq per milliliter)[d]	5.8	40.5	5.7	30.4	7.5	12.2	3.2
Scatter fraction (%)[d]	17	48	10	34	37	28	32

[a] With tungsten septa
[b] Without tungsten septa
[c] Two energy windows (511 and 310 keV) 30% width, detector distance 62 cm
[d] Measured in a cylinder (20 cm diameter), homogeneously filled with ^{18}F

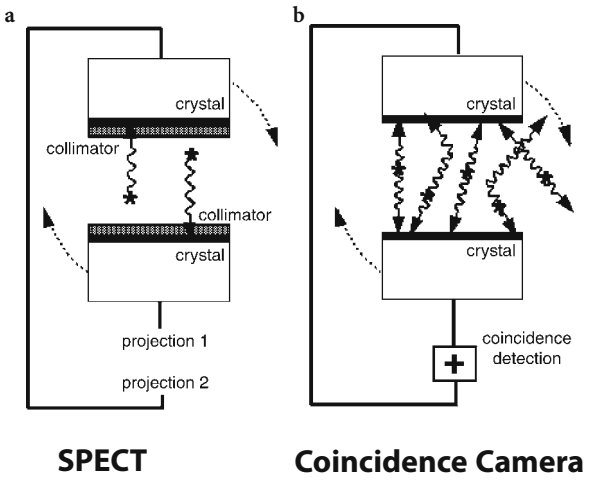

Fig. 16.8. Dual-head camera operated with collimators in **a** SPECT mode, and **b** without collimators in coincidence mode

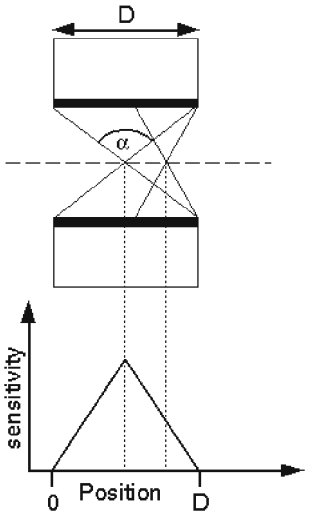

Fig. 16.9. The sensitivity profile in 3D imaging systems varies across the detector head *D,* depending on the axial acceptance angle α. The highest sensitivity is in the center

lead collimator, the dual-head coincidence camera is less sensitive than a full-ring PET scanner because of solid angle restrictions and lower detection efficiency at 511 keV in the NaI crystal. Therefore, a longer scan time is needed and the use of coincidence cameras is limited to the detection of ^{18}F labeled substances. Without attenuation correction, PET studies of the heart are not meaningful. Present implementations of coincidence cameras show a spatial resolution comparable to full-ring PET scanners, but with an increased scatter and random fraction (Table 16.2), causing the detectability of small lesions within background activity to be lower in coincidence cameras as compared with full-ring PET scanners (Shreve et al. 1998). These systems are still being improved. Thus, it is very important to know where the coincidence cameras are applicable – these areas may be different from dedicated PET scanners (Coleman 1997).

Attenuation correction in dual-head coincidence imaging is currently being developed either by measured attenuation factors or by including attenuation into iterative reconstruction algorithms. Together with random and scatter correction techniques, this will be the basis for potential quantitative information from dual-head coincidence imaging (see chap. 14).

Obviously, a scintillator with higher detection efficiency for gamma rays of 511 keV would greatly enhance the performance of a hybrid system. Cerium activated lutetium oxy-orthosilicate, the scintillator which is most promising for coincidence measurements, unfortunately has a disadvantage in single photon detection: the natural radioactivity in the material causes non-zero count rates at background levels. In positron imaging, these events are suppressed by the coincidence window. Therefore, a new hybrid system is being developed in which the combination of two scintillation materials in a type of sandwich geometry is used. Each scintillator is specially suited for the detection either of low-energy or high-energy photons. The SPECT technique can be performed with signals from the front layer, positron imaging with coincidence counting from the back layers. For the front layer yttrium oxy-orthosilicate (YSO; Dahlbom et al. 1997) or NaI(Tl) (Schmand et al. 1998a,b) were proposed in combination with a back layer made of LSO. The light decay constants of the two materials are different (Table 16.1); thus, pulse shape analysis can be used to discriminate which crystal was hit by the gamma ray. To meet the strict count rate requirements, the system consists of granulated detectors. The first cameras will merge SPECT and PET even closer.

16.2 Requirements of Imaging Systems

16.2.1 Fundamentals of Clinical Imaging Protocols and Technical Factors

The optimal use of any imaging system can only be provided if the technical parameters, such as resolution, sensitivity and scatter fraction, are evaluated in their influence on image quality.

Whereas spatial resolution is important for a realistic representation of the organ under study and quantitative information, it is not the only technical parameter determining image quality in terms of lesion detectability. Background due to septa penetration, scattered radiation or random coincidences affect contrast in the image. Thus, depending on the amount of background in the image, small lesions can get lost, even if the system resolution is the same.

For different imaging situations using gamma cameras, the most adequate collimator has to be chosen, depending on the energy of the incoming gamma ray, the size of the structures to be investigated and an acceptable scan duration for acquisition of sufficient count statistics. The highest-resolution collimator available for a given energy may be advantageous (Muehllehner 1985; Mueller et al. 1990), even if some sensitivity is lost.

In single-photon imaging, collimator resolution degrades rapidly with increasing distance from the collimator surface; therefore, the camera heads are kept as close as possible to the patient during acquisition. On the other hand, spatial resolution of coincidence detectors is almost independent of the position in-between the two detectors of a pair (Hoffman et al. 1982). However, coincidence sensitivity depends on the area of detector that is seen by each point in the object (solid angle), which is reduced with increased distance between the detector.

In camera systems utilizing lead collimators, performance is usually defined in terms of intrinsic (camera inherent properties) and extrinsic (including the collimator) system performance parameters. For patient imaging, the extrinsic values are more important since they reflect the actual clinical situation.

The system spatial resolution results from the combination of intrinsic detector resolution and resolution of the lead collimator. Measurement of the system spatial resolution is performed by imaging a ^{99m}Tc line source and using full width at half maximum (FWHM) and full width at tenth maximum (FWTM) as parameters of resolution. Whereas in most currently available gamma cameras the intrinsic spatial resolution is 4 mm FWHM, the limited resolution of the collimators degrades the system resolution to approximately 10 mm.

Intrinsic spatial resolution in camera-based systems is a result of PMT signal centroid-calculation (Fig. 16.1). Thus, it is affected by the statistical nature of scintillation light collection and random errors during conversion into electrons at the PMT cathode. Interaction of the 140-keV gamma ray, of ^{99m}Tc, produces more light in the scintillator and therefore less error in the positioning algorithm, than the 70–80 keV ray of ^{201}Tl. In order to detect a high-energy gamma ray efficiently, a thick crystal is favorable, but spread of light is more pronounced in thick crystals, causing the intrinsic spatial resolution to degrade in this situation.

It is important to eliminate image distortion by assuring spatial linearity; otherwise, images of line sources would not be straight. In modern gamma cameras, the digitized PMT signals are corrected before the event position is calculated (Muehllehner et al. 1980). Also, the event positioning in a gamma camera has to be independent of the total amount of light generated in the scintillation crystal. This is achieved by energy normalization of the centroid calculation.

One of the most important parameters is system sensitivity, describing the fraction of incoming gamma rays which are actually detected by the system. Single-photon devices suffer mainly from the low collimator efficiency needed to enhance spatial resolution. The total efficiency is also determined by the intrinsic gamma interaction probability in the crystal and the energy range selected.

The type of detection system in coincidence cameras permits 3D data acquisition with continuous sampling. The sensitivity of 3D systems strongly depends on the position within the field of view, both in axial and transaxial directions. The maximum acceptance angle for coincidence events defines the sensitivity profile. It has the shape of a pyramid or trapezoid (Fig. 16.9; Clack et al. 1984). This fact causes lesions to be detected with different statistical accuracy, depending on their location in the field of view.

Energy resolution, determined mainly by the crystal material, measures how well gamma rays with two different energies can be distinguished. Good energy resolution also provides a means of reducing the fraction of scattered gamma rays entering into the image, because a narrow energy window can be used. For instance, a 20% energy window accepts gamma rays of up to 52° scattering angle for an incident energy of 140 keV, visible as background events distributed across the image.

16.2.2 Acquisition Parameters and Procedural Factors

16.2.2.1 Sampling Requirements

The quality of scintigraphic images is influenced by several procedural parameters. Firstly, the projection data have to be acquired in agreement with the system

performance; thus, it is important to choose the pixel size of the acquisition matrix at approximately one half the size of the smallest structure to be resolved, which depends on the collimator. Gamma-camera images show variations in count density due to the limited number of photons which form the image. Therefore, detection of lesions depends on object contrast and size. Lesion contrast has to be much higher than noise levels in order to detect a lesion. A high number of counts reduces noise and smaller and/or lower-contrast lesions can be detected. For tomographic imaging the number of counts to detect a structure can be estimated, given the spatial resolution and the uncertainty with which the structure is to be imaged (Budinger et al. 1978).

Planar scintigraphy is performed by acquiring data with the gamma-camera viewing one direction of the patient. The data represent the projection of the tracer distribution; thus, overlapping structures result in summed signals and blurring in the image. Tomographic images, representing the activity distribution in a transaxial slice through the body, are generated from measured projections by the use of mathematical reconstruction algorithms. Full-ring dedicated positron tomographs collect all projections at once. Rotating single or multi-head gamma cameras acquire the data either during continuous motion or at a number of predefined angles (step-and-shoot). Depending on the duration of the gantry to rotate and switch between acquisition and motion, continuous rotation may be more efficient than step-and-shoot techniques. If, for instance, many angular steps with short measuring time per step are performed, continuous rotation is advantageous. In the case of larger angular steps, step-and-shoot acquisition should be preferred because of its higher angular precision and little loss in time.

To minimize resolution degradation in tomographic imaging, angular sampling should equal linear spatial sampling. Therefore, the number of angular views which are acquired in a 180° rotation (M_{180}) corresponds to the length of the arc of the selected rotation diameter (D), divided by the sampling distance Δl (Eq. 16.1; Huesman 1977):

$$M_{180} = \frac{\pi \times D}{2 \times \Delta l} \tag{16.1}$$

If this requirement is not met, image artifacts will show up in the reconstructed transverse slices. For a given system resolution, defined by the collimator in single-photon cameras, the pixel size in the matrix and the angular steps are defined. Patient tolerance restricts total imaging duration, limiting the count statistics. Thus, deviations from the ideal parameter set are common in clinical practice, mainly to reach a compromise between low counts in many views or high counts in fewer views, violating the sampling requirements. Since the strict requirement on count density from planar imaging does not necessarily apply to each individual projection image in a SPECT acquisition, protocols tend to favor a large number of angular steps. Resolution in the reconstructed SPECT image is not spatially invariant since the distance between detector and source organ varies between steps. Usually, SPECT resolution is worse than planar imaging. This is due in part to the fact that the camera head is farther away from the patient in SPECT. On the other hand, the limited number of events per view and the necessity to use smoothing filters in the reconstruction process further decrease the resolution. The main advantage of SPECT over planar imaging is the higher image contrast because overlapping structures are eliminated.

In PET scanners with BGO block detectors, the spatial resolution is defined by the size of the individual crystal; therefore, stationary rings cannot fulfill the sampling requirements. Although wobbling mechanisms had been developed to overcome this problem and increase sampling, these approaches have been abandoned in the recent designs, due mainly to the fact that in clinical situations the number of detected events is not high enough to fully utilize the finer sampling grid. Large-area crystals offer continuous sampling; thus, the binning process and subsequent sampling frequency have to meet the intrinsic spatial resolution (Karp et al. 1990).

16.2.2.2 Whole-Body Acquisition

A diagnostically valuable tool is the whole-body acquisition of ^{18}F labeled substances by sorting the sinogram data of a PET scanner into projection images, yielding images similar to planar body scans (Guerrero et al. 1990; Dahlbom et al. 1992). A stack of reconstructed transverse slices provides a volume data set which can be resliced into coronal and sagittal sections. Since most dedicated positron tomographs extend over 10 to 16 cm, numerous axial steps (or bed positions) have to be acquired in order to cover the whole body. Thus, acquisition duration per position has to be short (1–5 min), causing statistical noise in the reconstructed images. Despite the

short scan time, image quality can be improved by optimized sampling schemes (Dahlbom et al. 1992) and careful normalization of variations in detector efficiencies. Since the sensitivity of a tomograph drops at the edges of the axial field of view, adequate overlap of the neighboring bed positions needs to be applied to reduce artifacts due to variations in statistical quality of the data. Although currently not supported by commercial systems, a continuous axial motion may be advantageous in septumless, 3D PET acquisition (Cherry et al. 1992; Dahlbom et al. 1994). In addition to an increased scatter fraction, 3D whole-body acquisitions are specially affected by activity outside the axial field of view (Sossi et al. 1995). Scatter correction methods based on the information from within the field of view show deviations (Ferreira et al. 1998), causing some differences in quantitative information compared with 2D PET scanning. Numerous research groups are actively evaluating and improving this methodology.

Especially during acquisitions which involve rotating camera heads for sequential measurement of projection data (SPECT or dual-head coincidence cameras) it is important to minimize patient motion; otherwise, not only blurring but also distortions will be introduced in the reconstructed image. Therefore, it was suggested to fractionate scan times in order to reduce motion artifacts (Germano et al. 1994).

16.2.3.1 Attenuation Correction

Transmission measurements are frequently used as a basis for attenuation correction in nonhomogeneous objects. Whereas the projections can be precorrected in coincidence measurements, in SPECT imaging the measured transmission data are reconstructed and the attenuation maps are used as a basis in various correction methods, mostly applying iterative reconstruction methods (see chap. 17). Simultaneous transmission and emission scanning is most desirable so that misalignment is eliminated. This goal is achieved in SPECT imaging by using nuclides which emit gamma rays of different energy. Careful choice of transmission nuclides is important to minimize crosstalk effects and accurate determination of attenuation factors (Ficaro et al. 1994). ^{153}Gd and ^{241}Am have been implemented in clinical routine. Currently, scanning line sources for single and dual-head cameras (Tan et al. 1993), or stationary line sources in combination with fan-beam collimators in triple-head systems (Tung et al. 1992), are in use. Stationary multiple line sources are a new approach in overcoming the problem of count statistics in some areas of the body (Celler et al. 1998).

Despite the higher energy, attenuation factors for coincidence measurements are much higher than in SPECT, since the total path for both gamma rays is longer; thus, along certain coincidence lines, attenuation factors of more than 100 can occur. The transmission data in PET are routinely acquired in coincidence using rotating rod sources made of ^{68}Ge. Spatial windowing reduces the amount of scatter in the transmission data and the contamination of emission into transmission. Contrary to SPECT scanning, simultaneous acquisition is not performed clinically, since it requires low-activity transmission sources and therefore long scan times. Generally, count-rate limitations of full-ring BGO-ring tomographs do not allow the use of intense transmission sources in coincidence mode. Due to prolonged transmission measurements, misregistration of transmission and emission may result because of patient motion. To overcome this problem, singles acquisition was proposed using high activity of either a positron emitter or of ^{137}Cs (deKemp and Nahmias 1994; Karp et al. 1995; Yu and Nahmias 1995), which emits gamma rays with an energy of 662 keV. As in SPECT, the attenuation factors have to be scaled accordingly; however, the low-energy resolution of BGO crystals (>20%) results in high scatter fraction. NaI(Tl) systems have the advantage of intrinsically better energy resolution. The method has been implemented in a dual-head coincidence system using two collimated ^{137}Cs sources.

The clinical value of attenuation correction in whole-body PET imaging is discussed controversially (Bengel et al. 1997; Bedigian et al. 1998; Imran et-al. 1998). Up to 40% of the total scanning time has to be dedicated to transmission measurement for optimal noise characteristics in 3D total-body PET using ^{68}Ge/^{68}Ga transmission sources and coincidence measurement (Beyer et al. 1997). Reduced imaging time using strong ^{137}Cs sources and singles acquisition mode may offer the possibility of applying a short interleaved emission/transmission scan protocol (Karp et al. 1995; Smith et al. 1997). Thus, statistical quality of transmission data, which is a major obstacle in conventional transmission measurements, is improved and potential patient motion during the shorter scan is minimized. The results of ongoing investigations will show its clinical value.

The problem of the poor signal-to-noise ratio in the measured attenuation correction has to a great extent been solved with the introduction of combined PET-CT and SPECT-CT systems (Beyer et al. 1994; Hasegawa et al. 2002; Kalki et al. 1997; Townsend et al. 1998). These systems typically consist of a PET (or SPECT) scanner and a conventional CT scanner, combined in one single gantry. The primary function of the CT system is to provide anatomical information to the emission image. Since both the emission scan and CT scan are acquired sequentially on the same system, the two data sets are almost perfectly registered and can be fused to aid in localizing areas of abnormal uptake on the anatomical CT images.

Since the values in the CT image are proportional to photon attenuation, these can also be used to generate an attenuation correction for the emission data. However, since the CT images are reconstructed from data acquired using polychromatic X-rays of a relatively low energy, the image values (i.e., Hounsfield units) do not in general translate into attenuation values at the emission energy used (e.g., 511 keV for PET). Kinahan et al. (1998, 2003) have shown that an accurate attenuation correction can be derived from a CT image by classifying the image into two main tissue types (i.e., soft and bone tissue), which is accomplished by simple thresholding. Different scaling factors are then applied to the two tissue images, which convert the Hounsfield units into attenuation values at 511 keV. The two scaling factors are necessary due to the significant differences in mass attenuation coefficient between bone and soft tissue at low photon energies. The scaled images are combined and smoothed to generate the final attenuation map, which can subsequently be used to calculate the attenuation corrections that can be applied to the emission data. It has been found that a non-diagnostic, low dose CT (10–40 mA) usually provides images of adequate quality for the purpose of attenuation correction and anatomical localization.

The use of CT for attenuation correction is not without problems and has introduced a new set of image artifacts not seen with conventional correction methods (i.e., transmission sources). Due to the speed of a helical CT system, the images are not acquired over a number of respiratory cycles as in the case of the emission data. Therefore, there is a mis-registration between the CT and emission data that sometimes introduces streaking artifacts in the reconstructed emission images. This is commonly seen in areas where there is a large change in attenuation coefficients and significant respiratory motion (e.g., dome of the liver and base of the lung interface) (Goerres et al. 2003; Nehmeh et al. 2002). CT studies commonly involve the administration of contrast enhancing agents. In areas of increased contrast, the images have an appearance of increased attenuation, due to the higher absorption of the X-rays in the iodine. When a contrast enhanced image is used for attenuation correction, the attenuation coefficient for these regions is overestimated, and the result is an overcorrection of the emission data in these regions which sometimes can be mistaken for increased activity (pseudo-tracer uptake) (Bockisch et al. 2004; Townsend et al. 2004). A similar effect is seen in patients with metal implants, which produce a significant over-estimation of the attenuation coefficient (Goerres et al. 2002; Halpern et al. 2004; Beyer et al. 2004). To rule out these attenuation related artifacts, it is always important to review the non-attenuation corrected emission images in addition to the corrected images (Beyer et al. 2004).

16.2.3 Quality Control

Quality control of nuclear medicine instrumentation is essential to assure that the equipment functions within the known specifications and that image artifacts are avoided which could lead to misdiagnosis. There are recommendations of the manufacturers and medical physics society (NEMA 1986, 1994) on which camera parameters should be tested and how often this should be done according to a detailed protocol. The basis of quality control and action to be taken in cases of irregularities are the system performance parameters obtained during acceptance testing after the instrument has been installed in the department. These values are used as reference in the periodical checkout of the camera. Most vendors provide software tools for the routine quality control of modern digital cameras. It is important to be aware that any part in the imaging process can influence image quality, especially with automated tuning and correction processes implemented in the modern complex systems.

Besides the visual inspection of the camera, collimators and peripheral devices, certain measurements should be performed regularly. The results of these measurements have to be documented and reviewed to detect changes and obvious artifacts.

In camera-based systems, i.e. single-head planar, single- or multi-head SPECT and dual-head coincidence cameras, the basic quality control concerns the scintillation camera itself. Since the camera performance is dependent on the energy of the incident gamma ray, the implemented methods for correcting these differences have to be tested. Thus, every day before the first scan and each time a different nuclide is being used, the position and width of the energy window have to be checked. A point source in air and count rates below noticeable pileup yields the best results. This peaking of the camera is easily performed on the multi-channel display of the energy spectrum in modern systems. An evaluation of crystal, light pipe, photomultipliers, electronics and display system is achieved by the daily acquisition of a flood image. This is the most important check, yielding information on the global performance of the camera. The most convenient procedure is to measure the intrinsic uniformity. For this measurement the collimator is removed from the camera and the camera is irradiated by a point source (^{99m}Tc) which is positioned more than three times the camera diameter away. The total number of collected counts should be more than 1–3 million depending on the detector size. Comparison with the flood image taken after the last adjustment of the camera shows changes in the system, and in the case of obvious nonuniformities (e.g. defective PMT) the camera should not be used for clinical studies. Digital processing of the acquired flood images is used to quantify the nonuniformities in these images. Integral uniformity is defined as the maximum deviation of counts per pixel and differential uniformity measures the maximum change of count density over five neighboring pixels.

Nonuniformities can be produced by spatial nonlinearity, shifting events towards the center of the photomultiplier entrance window. In modern cameras this effect is reduced automatically by applying correction maps for linearity and multi-energy registration. Resolution and linearity should be checked on a weekly basis using a lead bar phantom on the camera without collimator, assessing nonlinearities and distortions in different areas of the camera. Also, the efficiency of the system can be determined weekly by calculating the ratio of counts per second in the uniformity test and the known activity in the point source which is placed at a fixed distance from the detector head. A fillable planar source (^{99m}Tc) or a ^{57}Co sheet source is needed for a monthly measurement of extrinsic uniformity, i.e. including the collimator.

Every 3 months the count rate performance and multienergy spatial registration should be checked according to the protocols used during acceptance testing. Special attention is needed for cameras used in whole-body imaging. Although they presently only need one scan covering the whole patient (older cameras with smaller fields of view needed two sweeps), alignment and electronic timing errors can severely affect the whole-body images, depending on the acquisition type. If a series of static images is acquired, misalignment between the individual images causes horizontal stripes in the image. During continuous head motion electronic timing errors will lead to areas of lower counts. A whole-body uniformity check shows these problems, which are not seen on normal flood images (O'Connor 1996).

Artefacts in planar images are propagated and even amplified in tomographic acquisitions. Linearity and uniformity are of primary importance in this context. Even small nonuniformities, not visible on the daily low-count flood images, cause artifacts in the tomographic images. Thus, quality control for SPECT systems includes some additional measurements. A weekly measurement of the extrinsic uniformity using a planar source and measurement times resulting in 10–30 million counts is incorporated in the data processing to eliminate even small nonuniformities in the camera which would cause concentric ring artifacts in the reconstructed SPECT image. Differential nonuniformity after applying the uniformity correction matrix should not exceed 1.0–2.5% to prevent ring artifacts in the tomographic image (O'Connor 1996). Especially in multi-head systems the uniformity measurement for each individual head is required. In addition, uniformity needs to be independent of the rotational position of the camera head. It is advisable to check this once per year. Careful alignment of the mechanical and electronic axis of rotation is required to prevent resolution loss or even distortion in the tomographic images. A difference of 0.5 pixel can cause serious distortions in a 128×128 image matrix. Most systems provide an automated procedure to detect deviations from the correct center of rotation (COR). In multi-head SPECT cameras, strict alignment of all axes of rotation has to be assured. Due to the improved stability of modern SPECT systems, the suggested test frequency of once per week may be prolonged. Once a month the mechanical head tilt in a SPECT system should be checked to avoid malpositioning of transaxial data. The pixel calibration, i.e. the number of pixels measured between two point sources of known

distance, should be measured every month. With point sources of different energy, the multi-energy spatial registration of the camera can be checked, which not only assures the same magnification but also the applicability of COR and nonuniformity corrections for different energies.

The global performance of the SPECT system is best monitored by regularly (every 3 months) performing an acquisition with a phantom containing structures (e.g. Jaszczak phantom) representing the system resolution.

The coincidence camera can be seen as a special type of multi-head SPECT system; therefore, all the aforementioned remarks are also valid. Currently, little experience is available in terms of which additional tests should be performed in what time interval. The available cameras differ in their implementation of pulse processing, coincidence event localization and coincidence circuitry including time window widths. Imaging a positron emitting line source (long lived ^{68}Ge/^{68}Ga can routinely be used) at a fixed geometry may be useful to detect gross nonuniformities or changes in sensitivity on a daily basis without adding too much time to the quality control procedures.

Quality control in dedicated PET scanners with BGO detectors arranged in a full ring is performed by a daily measurement of the relative line-of-response efficiency (corresponds to the flood images on scintillation cameras; Spinks et al. 1989). Data are acquired similar to a transmission scan using rotating rod sources. A defective block detector or electronics bank can easily be seen as a count-depressed line in the sinogram display of the data. The counts per block in the blank scan are compared with reference data. If there is a statistically significant deviation from the expected pattern, adjustment of the system, like tuning of a gamma camera, is needed.

If quantitative PET measurements are performed, the tomograph counts are related to the injected dose and careful cross-calibration between PET scanner and dose calibrator is essential. A cylindrical phantom of known volume is filled with positron activity and imaged. Calibration factors (cps/Bq per milliliter) are calculated for each plane from the counts in the reconstructed image and the known activity concentration in the phantom. This factor should be a constant.

Currently, the recommendations apply to full ring PET scanners with BGO block detectors. Standard procedures are being evaluated for rotating BGO, large area NaI full-ring tomographs, and dual-head coincidence cameras.

Independent of the acquisition system, patient-related quality control can be summarized as reduction in motion, choice of injection site relative to target organ, time of scan after injection (biokinetics) and positioning (truncation).

16.2.3.3 Attenuation Correction

The problem of the poor signal-to-noise ratio in the measured attenuation correction has to a great extent been solved with the introduction of combined PET-CT and SPECT-CT systems (Beyer et al. 1994; Townsend et al. 1998; Hasegawa et al. 2002; Kalki et al. 1997). These systems typically consist of a PET (or SPECT) scanner and a conventional CT scanner, combined in one single gantry. The primary function of the CT system is to provide anatomical information to the emission image. Since both the emission scan and CT scan are acquired sequentially on the same system, the two data sets are almost perfectly registered and can be fused to aid in localizing of areas of abnormal uptake on the anatomical CT images.

Since the values in the CT image are proportional to photon attenuation, these can also be used to generate an attenuation correction for the emission data. However, since the CT images are reconstructed from data acquired using polychromatic X-rays of a relatively low energy, the image values (i.e., Hounsfield units) do not in general translate into attenuation values at the emission energy used (e.g., 511 keV for PET). Kinahan et al. (Kinahan et al. 2003; Kinahan et al. 1998) have shown that an accurate attenuation correction can be derived from a CT image by classifying the image into two main tissue types (i.e., soft and bone tissue), which is accomplished by simple thresholding. Different scaling factors are then applied to the two tissue images, which convert the Hounsfield units into attenuation values at 511 keV. The two scaling factors are necessary due to the significant differences in mass attenuation coefficient between bone and soft tissue at low photon energies. The scaled images are combined and smoothed to generate the final attenuation map, which can subsequently be used to calculate the attenuation corrections that can be applied to the emission data. It has been found that a non-diagnostic, low dose CT (10–40 mA) most of the time provides images of adequate quality for the purpose of attenuation correction and anatomical localization.

The use of CT for attenuation correction is not without problems and has introduced a new set of image artifacts not seen with conventional correction methods (i.e., transmission sources). Due to the speed of a helical CT system, the images are not acquired over a number of respiratory cycles as in the case of the emission data. Therefore there is a mis-registration between the CT and emission data that sometimes introduce streaking artifacts in the reconstructed emission images. This is commonly seen in areas where there is a large change in attenuation coefficients and significant respiratory motion (e.g., dome of the liver and base of the lung interface) (Goerres et al. 2003; Nehmeh et al. 2002). CT studies commonly involve the administration of contrast enhancing agents. In areas of increased contrast, the images have an appearance of increased attenuation, due to the higher absorption of the X-rays in the iodine. When a contrast enhanced image is used for attenuation correction, the attenuation coefficient for these region is overestimated, and the result is an overcorrection of the emission data in these regions which sometimes can be mistaken for increased activity (pseudo tracer uptake) (Bockisch et al. 2004; Townsend et al. 2004). A similar effect is seen in patients with metal implants, which produce a significant over-estimation of the attenuation coefficient (Goerres et al. 2002; Halpern et al. 2004). To rule out these attenuation related artifacts, it is always important to review the non-attenuation corrected emission images in addition to the corrected images (Beyer et al. 2004).

16.3 Is There a Future for Dedicated Systems?

The historical division of nuclear medicine imaging into single-photon (traditionally nonquantitative) and positron imaging (quantitative) becomes more and more artificial as data processing and camera technology evolve, yielding devices capable of providing different acquisition modes and/or methodology for quantitative PET as well as SPECT. On the other hand, the imaging situation differs largely if, for example, brain or whole-body studies are performed; thus, high-performance instrumentation may have to be designed for its specific application. For instance, in single-photon detection it is indispensable to move the detector head as close as possible to the patient for optimal spatial resolution, but due to the design of the cameras this can sometimes not be accomplished. Therefore, in the past few years, investigators have concentrated on developing dedicated systems for imaging the breast or the brain.

Small, compact cameras which can be used in standard mammography systems may provide better image quality with reduced background as well as higher resolution and sensitivity than large-area conventional gamma cameras. The first feasibility studies (Levin et al. 1997; Gruber et al. 1998; Patt et al. 1998) point out that photodiode readout of luminous scintillators and the use of highly integrated electronics may be the most promising combination for this task. A prototype system showed excellent energy resolution (Patt et al. 1998) with pixelated CsI crystals and silicon photodiodes in combination with very high spatial resolution (1.5 mm). Once this technology is scaled up to a larger camera covering the whole breast, improved overall sensitivity and resolution in comparison with currently available large-area gamma cameras is expected. As important as the improvements in detector technology is the development of matched collimators for these cameras (Gruber et al. 1998).

The limitations of positron imaging in the breast are sought to be overcome with inexpensive, high-resolution dedicated systems with improved lesion detectability (Freifelder and Karp 1997). Flexible geometry will be one of the requirements for the successful clinical acceptance of these devices. The concept of just two opposing BGO detectors, mounted in an X-ray mammography gantry, is tested in two systems (Thompson et al. 1995; Weinberg et al. 1996). Owing to the position close to the breast, these systems provide much higher sensitivity than PET body scanners. Focal plane or limited-angle tomography is performed in the same geometry as X-ray imaging. Double-layer, finely pixelated BGO block detectors (Robar et al. 1997) are used in the prototype yielding a resolution of approximately 2 mm.

A high-resolution positron tomograph is being built for brain studies using LSO block detectors with two layers, providing depth-of-interaction information (Casey et al. 1997; Schmand et al. 1998a,b). This dedicated system will be the first complete tomograph utilizing this technology and is expected to yield brain images of unsurpassed quality. Cost will probably restrict the use of this tomograph type to research applications.

Clinical studies using these new dedicated imaging devices will reveal if they can improve patient care by cost-effective introduction of high-quality nuclear medical imaging.

References

Anger H (1958) Scintillation camera. Rev Sci Instr 29:27–33

Anger H, Davis D (1964) Gamma-ray detection efficiency and image resolution in sodium iodide. Rev Sci Instr 35:693–697

Bacharach SL, Buvat I (1995) Attenuation correction in cardiac positron emission tomography and single-photon emission computed tomography. J Nucl Cardiol 2:246–255

Bailey D (1998) Transmission scanning in emission tomography. Eur J Nucl Med 25:774–787

Bailey D, Young H, Bloomfield P et al. (1997) ECAT ART – a continuously rotating PET camera: performance characteristics, initial clinical studies, and installation considerations in a nuclear medicine department. Eur J Nucl Med 24:6–15

Bedigian M, Benard F, Smith R et al. (1998) Whole-body positron emission tomography for oncology imaging using singles transmission scanning with segmentation and ordered subsets-expecteation maximization (OS-EM) reconstruction. J Nucl Med 25:659–661

Bendriem B, Townsend D (1998) The theory and practice of 3D PET. Kluwer Academic, Dordrecht

Bengel F, Ziegler S, Avril N et al. (1997) Whole-body positron emission tomography in clinical oncology: comparison between attenuation-corrected and uncorrected images. Eur J Nucl Med 24:1091–1098

Beyer T, Antoch G, Muller S, Egelhof T, Freudenberg LS, Debatin J, Bockisch A (2004) Acquisition protocol considerations for combined PET/CT imaging. J Nucl Med 45[Suppl 1]:25S-35S

Beyer T, Kinahan P, Townsend D (1997) Optimization of transmission and emission scan duration in 3D whole-body PET. Trans Nucl Sci 44:2400–2407

Beyer T, Kinahan PE, Townsend DW, and Sashin D (1994) The use of X-ray CT for attenuation correction of PET data. Presented at Nuclear Science Symposium and Medical Imaging Conference

Bockisch A, Beyer T, Antoch G, Freudenberg LS, Kuhl H, Debatin JF, Muller SP (2004) Positron emission tomography/computed tomography – imaging protocols, artifacts, and pitfalls. Mol Imaging Biol 6:188-199

Budinger T (1996) Single photon emission computed tomography. In: Sandler M, Patton J, Coleman R et al. (eds) Diognostic nuclear medicine, vol 1. Williams and Wilkins, Baltimore, pp 121–138

Budinger T (1998) PET Instrumentation: what are the limits? Semin Nucl Med 28:247–267

Budinger T, Derenzo S, Greenberg W et al. (1978) Quantitative potentials of dynamic emission computed tomography. J Nucl Med 19:309–315

Butler J, Lingren C, Friesenhahn S et al. (1998) CdZnTe Solid-state gamma camera. IEEE Trans Nucl Sci 45:359–363

Casey M, Nutt R (1986) Multicrystal two dimensional BGO detector system for positron emission tomography. IEEE Trans Nucl Sci 33:460–463

Casey M, Eriksson L, Schmand M et al. (1997) Investigation of LSO crystals for high resolution positron emission tomography. IEEE Trans Nucl Sci 44:1109–1113

Celler A, Sitek A, Stoub E et al. (1998) Multiple line source array for SPECT transmission scans: simulation, phantom and patient studies. J Nucl Med 39:2183–2189

Chen E, MacIntyre W, Go R et al. (1997) Myocardial viability studies using fluorine-18-FDG SPECT: a comparison with fluorine-18-FDG PET. J Nucl Med 38:582–586

Cherry S, Dahlbom M, Hoffman E (1992) High sensitivity, total body PET scanning using 3D data acquisition and reconstruction. IEEE Trans Nucl Sci 39:1088–1092

Clack R, Townsend D, Jeavons A (1984) Increased sensitivity and field of view for a rotating positron camera. Phys Med Biol 29:1421–1431

Coleman R (1997) Camera-based PET: the best is yet to come. J Nucl Med 38:1796–1797

Dahlbom M, Cutler P, Digby W et al. (1994) Characterization of sampling schemes for whole body PET imaging. IEEE Trans Nucl Sci 41:1571–1576

Dahlbom M, Hoffman E, Hoh C et al. (1992) Whole-body positron emission tomography: part I. Methods and performance characteristics. J Nucl Med 33:1191–1199

Dahlbom M, MacDonald L, Eriksson L et al. (1997) Performance of a YSO/LSO detector block for use in a PET/SPECT system. IEEE Trans Nucl Sci 44:1114–1119

deKemp RA, Nahmias C (1994) Attenuation correction in PET using single photon transmission measurement. Med Phys 21:771–778

Ferreira N, Trebossen R, Bendriem B (1998) Assessment of 3-D PET quantitation: influence of out of the field of view radioactive sources and of attenuating media. IEEE Trans Nucl Sci 45:1670–1675

Ficaro EP, Fessler JA, Rogers WL et al. (1994) Comparison of americium-241 and technetium-99 m as transmission sources for attenuation correction of thallium-201 SPECT imaging of the heart. J Nucl Med 35:652–663

Freifelder R, Karp J (1997) Dedicated PET scanners for breast imaging. Phys Med Biol 42:2463–2480

Germano G, Kavanagh P, Kiat H et al. (1994) Temporal image fractionation: rejection of motion artifacts in myocardial SPECT. J Nucl Med 35:1193–1197

Goerres GW, Burger C, Schwitter MR, Heidelberg TN, Seifert B, von Schulthess GK (2003) PET/CT of the abdomen: optimizing the patient breathing pattern. Eur Radiol 13:734-739

Goerres GW, Hany TF, Kamel E, von Schulthess GK, Buck A (2002) Head and neck imaging with PET and PET/CT: artefacts from dental metallic implants. Eur J Nucl Med Mol Imaging 29:367-370

Gruber G, Moses W, Derenzo S et al. (1998) A discrete scintillation camera module using silicon photodiode readout of CsI(Tl) crystals for breast cancer imaging. IEEE Nucl Instr Methods 45:1063–1068

Guerrero T, Hoffman E, Dahlbom M et al. (1990) Characterization of a whole body imaging technique for PET. IEEE Trans Nucl Sci 37:676–679

Halpern BS, Dahlbom M, Waldherr C, Yap CS, Schiepers C, Silverman DH, Ratib O, Czernin J (2004) Cardiac pacemakers and central venous lines can induce focal artifacts on CT corrected PET images. J Nucl Med 45:290-293

Hasegawa BH, Wong KH, Iwata K, Barber WC, Hwang AB, Sakdinawat AE, Ramaswamy M, Price DC, Hawkins RA (2002) Dual-modality imaging of cancer with SPECT/CT. Technol Cancer Res Treat 1:449-458

Hoffman E, Huang S, Plummer D et al. (1982) Quantitation in positron emission computed tomography: effect of non-uniform resolution. J Comput Assist Tomogr 6:987–999

Huber J, Moses W, Derenzo S et al. (1997) Characterization of a 64 channel PET detector using photodiodes for crystal identification. IEEE Trans Nucl Sci 44:1197–1201

Huesman R (1977) The effects of a finite number of projection angles and finite lateral sampling of projections on

the propagation of statistical errors in transverse section reconstruction. Phys Med Biol 22:511–521
Imran M, Kubota K, Yamada S et al. (1998) Lesion-to-background ratio in nonattenuation-corrected whole-body FDG PET images. J Nucl Med 39:1219–1223
Kalki K, Blankespoor SC, Brown JK, Hasegawa BH, Dae MW, Chin M, Stillson C (1997) Myocardial perfusion imaging with a combined x-ray CT and SPECT system. J Nucl Med 38:1535-1540
Karp J, Muehllehner G, Mankoff D et al. (1990) Continuous-slice PENN-PET: a positron tomograph with volume imaging capability. J Nucl Med 31:617–627
Karp JS, Muehllehner G, Qu H et al. (1995) Singles transmission in volume-imaging PET with a 137 Cs source. Phys Med Biol 40:929–944
Kinahan PE, Hasegawa BH, Beyer T (2003) X-ray-based attenuation correction for positron emission tomography/computed tomography scanners. Semin Nucl Med 33:166-179
Kinahan PE, Townsend DW, Beyer T, Sashin D (1998) Attenuation correction for a combined 3D PET/CT scanner. Med Phys 25:2046-2053
Kipper M, Yeung D, Halpern S et al. (1998) Quality of planar images using a solid-state (CdZnTe) gamma camera, compared with conventional gamma scintillation cameras. J Nucl Med 39:P132
Kojima A, Matsumoto M, Takahashi M et al. (1993) Effect of energy resolution on scatter fraction in scintigraphic imaging: Monte Carlo study. Med Phys 20:1107–1113
Lecomte R, Cadorette J, Rodrigue S et al. (1996) Initial results from the Sherbrooke avalanche photodiode positron tomograph. IEEE Trans Nucl Sci 43:1952–1957
Levin C, Hoffman E, Tornai M et al. (1997) PSPMT and photodiode designs of a small scintillation camera for imaging malignant breast tumors. IEEE Trans Nucl Sci 44:1513–1520
Macfarlane D, Cotton L, Ackermann R et al. (1995) Triple-head SPECT with 2-[fluorine-18]fluoro-2-deoxy-D-glucose (FDG): initial evaluation in oncology and comparison with FDG PET. Radiology 194:425–429
Mankoff D, Muehllehner G, Miles G (1990) A local coincidence triggering system for PET tomographs composed of large-area positron-sensitive detectors. IEEE Trans Nucl Sci 37:730–736
Melcher CL, Schweitzer JS (1992) A promising new scintillator: cerium- doped lutetium oxyorthosilicate. Nucl Instr Methods 314:212–214
Muehllehner G (1979) Effect of crystal thickness on scintillation camera performance. J Nucl Med 20:992–993
Muehllehner G (1985) Effect of resolution improvement on required count density in ECT imaging: a computer simulation. Phys Med Biol 30:163–173
Muehllehner G, Karp J (1986) A positron camera using position-sensitive detectors: PENN-PET. J Nucl Med 27:90–98
Muehllehner G, Colsher J, Stoub E (1980) Correction for field nonuniformity in scintillation cameras through removal of spatial distortion. J Nucl Med 21:771–776
Mueller S, Foley Kijewski M, Moore S et al. (1990) Maximum-likelihood estimation: a mathematical model for quantitation in nuclear medicine. J Nucl Med 31:1693–1701
Nehmeh SA, Erdi YE, Ling CC, Rosenzweig KE, Squire OD, Braban LE, Ford E, Sidhu K, Mageras GS, Larson SM, Humm JL (2002) Effect of respiratory gating on reducing lung motion artifacts in PET imaging of lung cancer. Med Phys 29:366-371
NEMA (1986) Performance measurements of scintillation cameras, National Electrical Manufacturers Association
NEMA (1994) Performance measurements of positron emission tomographs, National Electrical Manufacturers Association
O'Connor M (1996) Instrument- and computer-related problems and artifacts in nuclear medicine. Semin Nucl Med 26:256–277
Patt B, Iwanczyk J, Tull C et al. (1998) High resolution CsI(Tl)/Si-PIN detector development for breast imaging. IEEE Trans Nucl Sci 45:2126–2131
Robar J, Thompson C, Murthy K et al. (1997) Construction and calibration of detectors for high-resolution metabolic breast cancer imaging. Nucl Instr Methods A 392:402–406
Schmand M, Dahlbohm M, Eriksson L et al. (1998a) Performance of a LSO/NaI(Tl) phoswich detector for a combined PET/SPECT imaging system. J Nucl Med 39:9P
Schmand M, Eriksson L, Casey M et al. (1998b) Detector design of a LSO based positron emission tomograph with depth of interaction capability for high resolution brain imaging. J Nucl Med 39:133P
Schmelz C, Bradbury SM, Holl I et al. (1995) Feasibility study of an avalanche photodiode readout for high resolution PET with nsec time resolution. IEEE Trans Nucl Sci 42:1080–1084
Shreve P, Steventon R, Deters E et al. (1998) Oncologic diagnosis with 2-[fluorine-18]fluoro-2-deoxy-D-glucose imaging: dual head coincidence gamma camera versus positron emission tomographic scanner. Radiology 207:431–437
Smith R, Karp J, Muehllehner G et al. (1997) Singles transmission scans performed post-injection for quantitative whole body PET imaging. IEEE Trans Nucl Sci 44:1329–1335
Sossi V, Barney J, Harrison R (1995) Effect of scatter from radioactivity outside of the field of view in 3-D PET. IEEE Trans Nucl Sci 42:1157–1161
Spinks T, Jones T, Heather J et al. (1989) Quality control procedures in positron tomography. Eur J Nucl Med 15:736–740
Tan P, Bailey DL, Meikle SR et al. (1993) A scanning line source for simultaneous emission and transmission measurements in SPECT. J Nucl Med 34:1752–1760
Thompson C, Murthy K, Picard Y et al. (1995) Positron emission mammography (PEM): a promising technique for detecting breast cancer. IEEE Trans Nucl Sci 42:1012–1017
Townsend DW, Beyer T, Kinahan PE, Brun T, Roddy R, Nutt R, and Byars LG (1998) The SMART scanner: a combined PET/CT tomograph for clinical oncology.
Townsend DW, Carney JP, Yap JT, Hall NC (2004) PET/CT today and tomorrow. J Nucl Med 45[Suppl 1]: 4S-14S
Townsend D, Wensveen M, Byars L et al. (1993) A rotating PET scanner using BGO block detectors: Design, performance and applications. J Nucl Med 34:1367–1376
Tung CH, Gullberg GT, Zeng GL et al. (1992) Non-uniform attenuation correction using simultaneous transmission and emission converging tomography. IEEE Trans Nucl Sci 39:1134–1143
van Lingen A, Huijgens PC, Visser FC et al. (1992) Performance characteristics of a 511-keV collimator for imaging positron emitters with a standard gamma-camera. Eur J Nucl Med 19(5):315–321
Weinberg I, Malewski S, Weisenberger A et al. (1996) Preliminary results for positron emission mammography: real-time functional breast imaging in a cenventional mammography gantry. Eur J Nucl Med 23:804–806
Yu S, Nahmias C (1995) Single-photon transmission measurements in positron emission tomography using ^{137}Cs. Phys Med Biol 40:1255–1266

17 Image Formation

Johan Nuyts and Dirk Bequé

CONTENTS

17.1 Introduction

In agreement with Moore's law, computer performance (or more precisely the number of transistors per chip) doubles about every 20 months. This is an exponential growth curve, and the cumulative gain is impressive: programs running for days 10 years ago, now require minutes. This allows algorithm designers to follow new strategies. A potential disadvantage is that beautiful design, ingenious mathematics and clever numerical analysis now must face competition from inefficient and ugly brute force computations (in agreement with Wirth's law). An important advantage is that problems, which cannot be solved analytically, can now be tackled with computation intensive numerical procedures.

A good example of this is reconstruction from projections. For a long time, reconstruction was almost exclusively done with filtered backprojection (FBP), a relatively fast, analytical method. The current proliferation of iterative reconstruction algorithms is a direct result of the increasing computer speed. Most of the algorithms applied today, have been around for several years, waiting for the computers to become sufficiently powerful. Many iterative algorithms have been proposed (Herman 1980; Schmidlin 1972) but, at least currently, the most successful for emission tomography is the maximum-likelihood expectation-maximisation (MLEM) algorithm (Rockmore and Mackovski 1976; Dempster et al. 1977; Shepp and Vardi 1982; Lange and Carson 1984), accelerated using the ordered subsets approach (Hudson and Larkin 1994). In part, this is due to the appealing theory behind it: the algorithm takes into account the statistical nature of the data, assuming that the data are Poisson distributed, which is exact or nearly exact in most cases. Convergence is guaranteed, and no tuning of mysterious parameters is required. Moreover, at least in emission tomography, it leads to a beautiful, simple mathematical expression which is very easy to program. To some extent, the success of MLEM is also due to historical reasons: it appeared at the right time, just when computers allowed application to real images in a reasonable time, and rapidly became the standard iterative method.

The literature on reconstruction from projections is extensive. Lewitt and Matej (2003) give an excellent overview of current methods for emission tomography.

J. Nuyts, PhD; D. Bequé, PhD
Department of Nuclear Medicine, University Hospital Gasthuisberg, Herestraat 49, 3000 Leuven, Belgium

17.2 Image Formation and Reconstruction Techniques

Here, we compare filtered backprojection (FBP) and maximum-likelihood expectation-maximisation (MLEM), and describe how more accurate reconstructions are obtained.

17.2.1 Filtered Backprojection

17.2.1.1 The Algorithm

The emission tomograph is unable to measure directly the tracer distribution in which we are interested. Instead, it measures some complex, but known transformation of that distribution. The mathematical model of this transformation has been given several names, including "the Radon transform", "a set of line integrals" or simply "the projection". Reconstruction from projections, then, is a series of computations required to undo this undesirable transformation.

We focus on the two-dimensional, discrete case: a finite set of sampled projections (i.e., all images acquired by the camera over 360 degrees around the patient) from a two-dimensional tracer distribution (i.e., a slice through the body of the patient) must be reconstructed into a discrete image.

Filtered backprojection consists of two steps: filtering and backprojecting. Backprojection is *not* the inverse of projection, it is its transpose. Taking the transpose of an operator roughly means that very similar computations must be carried out, but in reversed order. In a projection, pixels along projection lines in the image are summed and the resulting value is assigned to a projection pixel. Thus, every pixel in the projection is computed as a weighted sum of image pixels, possibly with a different weight in every image pixel. In the transpose operation, the backprojection, the whole computation is reversed: the image pixel is computed as a weighted sum of projection pixels, using exactly the same weights as in the projection. Consequently, image pixels that contribute little in the projection step, get little back in the backprojection step.

Since backprojection is not the inverse of projection, simple backprojection methods do not yield good reconstruction images. Indeed, the resulting image is a blurred version of the correct reconstruction. With some non-trivial mathematics, which are not discussed here, these images can be deblurred, such that an image of the original distribution is obtained. This is the filtering step. It does not matter whether filtering precedes or follows backprojection. In most implementations, first the projections are filtered, and then the filtered projections are backprojected. In the two-dimensional (2D) case, only the ramp filter can undo the blurring effect of the backprojection.

Filtered backprojection is an exact inverse of projection, when all possible line integrals of the two-dimensional tracer distribution are used. This implies an infinite number of angles, with an infinite number of pixel values for each angle, using a pixel size of zero. In reality, only a finite number of projection pixels for a finite number of angles is available. In addition, real SPECT or PET measurements are not true line integrals. Real projection lines have a finite and position dependent width, and the number of detected photons is not nicely proportional to the total activity along that "line" because of photon--electron interaction and Poisson noise. Consequently, FBP only produces an approximate image of the tracer distribution in the patient.

17.2.1.2 Regularisation

When FBP is applied to noisy projections, the noise propagates dramatically, resulting in very noisy reconstruction images. To suppress the noise, low-pass filtering (smoothing) is applied. Inevitably, smoothing also reduces the spatial resolution. For reasons of computational efficiency, one used to apply a one-dimensional smoothing filter on the projections, which results in smoothing within the transverse slice. The efficiency comes from the fact that the smoothing filter can be combined with the ramp filter into a single operation. However, computational speed and computer memory are no longer an issue, and for regular three-dimensional (3D) tomography it is preferable to apply a 2D smoothing filter on the projections. This is equivalent to 3D smoothing after FBP. The advantage of 3D smoothing is that the effect of the filter is isotropic. In addition, smoothing volumes is more effective than smoothing slices, because more pixels are involved for the same kernel size.

17.2.2 Maximum-Likelihood Expectation-Maximisation

17.2.2.1 Iterative Reconstruction as a Feed-Back Mechanism

With iterative inversion, one can compute the inverse of an operator numerically, if for some reason no analytical expression for that inverse operator is available. Iterative reconstruction algorithms start from an initial, arbitrary estimate of the unknown tracer distribution. This can be a very poor estimate, such as a completely homogeneous image. In every iteration, the algorithm checks the current estimate, and improves it based on that evaluation.

A key feature of iterative algorithms is that they are based on a feedback mechanism. Feedback mechanisms are very common in biological and man-made systems because of their robustness. The speed of a car is controlled by a feedback path, consisting of the speedometer and the eyes and brain of the driver, who compares the measured speed with the desired one. The feed-forward path, consisting of the driver's foot and the accelerator, is there to change the speed, until the feedback path is "satisfied". In MLEM, the feedback path is the projection of the current estimate of the tracer distribution, which is compared with the measurement. Comparison is done by computing the ratio of the measured and computed values in every projection pixel. If all these ratios are unity, then the current estimate must be excellent. If a particular ratio is higher (lower) than one, the measured photon count is higher (lower) than the estimated activity along the corresponding projection line, so the estimated activity must be increased (decreased) by the feed-forward path. In MLEM, the feed-forward path consists of multiplying the current estimate with the backprojection of the ratios. If all ratios are one, all backprojection pixels will also be equal to one. In this case, multiplication will not change anything, which is what we want, because the estimate is then perfect. The performance of a feedback mechanism is very sensitive to its feedback path, whereas it is less sensitive to the feed-forward path. As a result, virtually all iterative algorithms share the same feedback path, i.e., the computation of the projection; the differences are in the feed-forward path.

Iterative reconstruction algorithms converge towards the inverse of the operation in the feedback path. Consequently, the projector in the feedback path should be a good model of the acquisition process. If not, artefacts can be expected. In MLEM, the feed-forward path contains the transpose of the projection operator, which is the backprojection operator. As has been said before, deriving the transpose is usually not too difficult. If the projector takes into account blurring and attenuation, the backprojector should do likewise: a blurring and attenuating backprojector is required. Since projector and backprojector basically apply the same operations in a different order, the computation time is similar.

17.2.2.2 Theoretical Considerations

When applied to real measurements, the algorithm is not able to make all ratios equal to one. Because the measured photon count is subject to Poisson noise, it is almost always impossible to find a tracer distribution that corresponds perfectly to the measured values. One can show that in this case, MLEM produces the most likely tracer distribution, taking into account the characteristics of the Poisson distribution. In fact, this is the main difference between MLEM and other iterative reconstruction algorithms. Because we know that the number of measured photons is Poisson distributed, and because nice mathematical tools are available to deal with Poisson distributions, we can compute the probability of measuring what we actually did measure, assuming that the current estimate really represents the true tracer distribution. It seems logical to choose the estimate that maximises that probability as the reconstruction of the measurement.

Note that this probability is always extremely small, though. It is so small that it is zero in clinical practice. So we are in fact sure that the ML estimate is not the true distribution. We only select it because all other solutions are even less likely. In addition, we hope that the most likely solution is at least similar in many interesting features to the true distribution.

The MLEM algorithm maximises the likelihood function (ML). It does so by applying an iterative strategy, which belongs to a particular class of algorithms, named expectation maximisation (EM). The good thing about EM is that convergence is guaranteed; no step size or other parameter has to

be tuned (Dempster et al. 1977; Shepp and Vardi 1982; Lange and Carson 1984).

17.2.2.3 Regularisation

Many authors have reported noise deterioration in MLEM reconstruction from noisy projections. Noise levels do increase with increasing iteration numbers. At very high iteration numbers, i.e. close to the actual MLEM solution, the noise is often so high that the image is useless for visual inspection. The MLEM algorithm "knows" that the measurement is subject to Poisson noise, but it does not know whether a particular measured count rate is too high or too low due to that noise. The best guess is that it is correct, implying that as much noise as possible should be included in the reconstruction. The noise must be suppressed, or in mathematical language, regularisation is needed. Several effective approaches are available.

In MLEM, low spatial frequencies converge faster than high spatial frequencies. This means that image detail and noise only show up at higher iterations. So one can use the iteration number in much the same way as the cut-off frequency of the low-pass filter in FBP. This technique is often applied in clinical practice: it combines two advantages: the noise level remains acceptable and the computation time is minimised. The resulting so-called MLEM images are not really ML reconstructions. They are just "HL" images, where HL stands for high likelihood.

Stopping early is acceptable, but stopping too early is dangerous: convergence may be insufficient, resulting in large errors, both in absolute and relative quantification! The images do not warn for this: intermediate images from MLEM nearly always look nice, even at early iterations. Several authors have investigated stopping rules (Coakley and Llacer 1991; Falcon et al. 1998; Veklerov and Llacer 1987; Llacer and Veklerov 1989; Liow and Strother 1993).

In standard MLEM, any reconstruction pixel is treated as an independent variable, so it may end up with a value very different from that of the neighbours. Some authors propose to use overlapping bell-shaped functions (often called "blobs") instead of non-overlapping pixel values. If the size and shape of the blob is carefully chosen, it can suppress noise without loss of resolution (Daube Witherspoon et al. 2001). The width of the blob should not be larger than the resolution (the width of the point spread function) of the camera, to ensure that valuable information acquired by the camera can propagate into the reconstruction (Matej and Lewitt 1996). When used like that, the blob stops high frequency noise, but not the signal. Unfortunately, when one attempts to smooth more by using a wider blob, so-called edge artefacts or Gibbs overshoots result (Snyder et al. 1987). This artefact appears as soon as one tries to produce sharp edges without using high spatial frequencies. A possible solution is to use a blob of appropriate size, and in addition smooth the resulting reconstruction if it is still too noisy.

The very noisy ML image, obtained after many iterations, is not as useless as it seems. When filtered with a low-pass filter, an image with good visual and quantitative characteristics appears. An important advantage of this approach is that the risk of insufficient convergence is low (Beekman et al. 1998, Hutton and Lau 1998, Slijpen 1999), and that the resulting image has a predictable, and nearly object and position independent spatial resolution.

The MLEM algorithm can be extended to a maximum-a-posteriori (MAP) algorithm by including a-priori knowledge (the posterior is the product of the likelihood and the prior). This means that we not only ask the program to look at the data (by maximising the likelihood function), but also to judge the reconstruction (by maximising the prior). By using a prior function that is high for smooth images and low for noisy ones, we can encourage the program to look for smooth solutions. In these algorithms, there is almost always a parameter present, assigning a weight to the prior. With a low weight, the algorithm reduces to regular MLEM. With a high weight, only very smooth images are considered as a solution. The parameter must usually be tuned manually by a skilled observer in order to obtain a good compromise between smoothness and adherence to the measured projections.

These algorithms are also called "penalised-likelihood" algorithms: instead of encouraging smoothness with a prior, one can discourage non-smoothness with a penalty; from a mathematical point of view, there is no difference.

An important advantage of MAP or penalised likelihood is that no stopping rules are required because the noise is suppressed by the prior. If the weight of the prior is properly tuned, the program can be run until convergence, and no additional smoothing is necessary.

To encourage local smoothness, one often regards the image as a Markov random field and uses a Gibbs distribution as a prior. The mathematics of Markov

random fields have been studied extensively, because they are used in physics. This framework allows a wide variety of priors, including priors with edge-preserving characteristics (Mumcuoglu et al. 1996; Lalush and Tsui 1993; Nuyts et al. 2002). An alternative is to use a smoothed version of the current reconstruction estimate as a prior, as in the median root prior (Alenius and Ruotsolainen 1997; Hsiao et al. 2003). ML and MAP reconstruction has been compared to FBP using quantitative measures (Chatziioannou et al. 2000), numerical observers (Chan et al. 1997; Qi 2004) and human observers (LaCroix et al. 2000; Glatting et al. 2003), and most studies conclude that MAP is clearly superior to FBP. The differences between smoothed ML and MAP are more subtle and will be discussed below. If the patient has also undergone an anatomical study, such as MR or CT imaging, one can attempt to use that anatomical information to improve the reconstruction beyond what can be achieved with the emission data alone. This requires accurate registration of both datasets, and segmentation of the anatomical data, both of which are extended research areas of their own. The improvements aimed at are usually noise suppression and/or resolution recovery. The anatomical information can either be implemented as a post-processing technique, applied after reconstruction (Müller-Gärtner et al 1992), or as an MAP method, using the prior to impose the anatomical information (Ardekani et al. 1996; Bowsher et al. 1996; Comtat et al. 2002; Lipinski et al. 1997; Sastry et al. 1997; Rangarajan et al. 2000; Baete et al. 2004). In most implementations, the anatomy is used to define edges over which smoothing is forbidden in the functional image. Of course, this approach will be most effective in those cases were anatomical and functional boundaries tend to coincide.

17.2.3 Comparison of FBP and MLEM

17.2.3.1 Computation Time

Since backprojection is the dominating operation in FBP, and because backprojection and projection are of similar complexity, computing a single MLEM iteration takes about twice as long as computing the FBP reconstruction.

Typically at least several tens of iterations are required, and many researchers have studied techniques to accelerate MLEM (Kaufman 1987; Tanaka 1987). Currently, the most successful one is the use of ordered subsets (Hudson and Larkin 1994). A single MLEM iteration is computed using only a subset of the projections. For every iteration a different subset is used, so all projections still contribute to the final image. Acceleration factors of 10 and higher can be obtained, depending on the number of projections, the noise in the projections, the stopping rule, etc. However, the noise in the reconstruction tends to increase with increasing number of subsets. If that is to be avoided, one can use a scheme with a gradually decreasing number of subsets, or under-relaxation (Ahn and Fessler 2003). MLEM accelerated with ordered subsets is often called OSEM.

17.2.3.2 Noise Model

Without regularisation, noise in the projection data will be propagated into the reconstruction image for both the FBP and MLEM algorithms. Nevertheless, there is a marked difference in the way noise is treated by both algorithms and this influences the features of the reconstructed images. The MLEM approach is based on the true Poisson noise model of (uncorrected) emission data, while the FBP method was derived for an ideal noise-free reconstruction problem. This resulted in a noise model with equal (absolute) uncertainty for all measured pixel values. One can actually show that the FBP reconstruction is very similar to the solution of the unweighted linear least squares problem, which assumes Gaussian noise with the same variance for all measured count values. Since the Poisson model states that absolute uncertainty is related to the pixel value (larger value means larger absolute uncertainty), there is a considerable disagreement between the noise assumptions of the FBP algorithm and the true noise of emission data. This disagreement results in the often observed streak artefacts in FBP reconstructed emission tomography images. Note however, that it is not the FBP algorithm as such, but its implicitly assumed noise model that causes these problems. Consequently, similar problems can be expected in the hypothetical case where MLEM reconstruction is applied to projection data with Gaussian noise. This is illustrated in Fig. 17.1.

In Fig. 17.1, we simulated ideal projections of an object consisting of a disk of uniform background activity with a smaller high intensity disk inside it. Both Poisson and Gaussian noise realisations of the

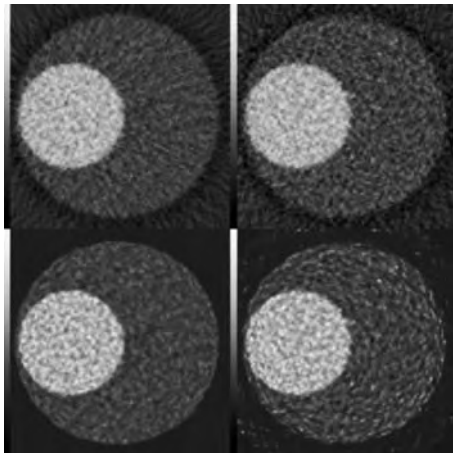

Fig. 17.1. FBP (*top*) and MLEM reconstruction (*bottom*) of projection data with Poisson (*left*) and Gaussian Noise (*right*). Simulated phantom consists of disk of uniform background activity with smaller high intensity disk inserted

ideal projections were simulated and used in both FBP and MLEM reconstructions. The FBP reconstruction of the Poisson noise projections shows the expected streak artefacts. They are pointing towards the high intensity disk, since FBP can easily deal with the "low noise" on the zero and low count data, but has great difficulty with the "exceptionally high" noise on the high count data. The MLEM reconstruction of the Gaussian noise projections shows streak artefacts as well, but they are pointing in all directions except towards the high intensity disk. The MLEM algorithm has little problems with the relatively low noise on the high count data, but is unable to deal with the noise on the low count data, which is larger than expected. The remaining two reconstructions are both contaminated with noise, but they show no streak artefacts, since their noise model corresponds to the noise in the projection data.

The above simulation clearly demonstrates the importance of a match between the noise model of a reconstruction algorithm and the noise on the data to which the method is applied. Emission data obey Poisson statistics, so the MLEM algorithm is the most appropriate reconstruction method, and care should be taken not to change the Poisson nature of the data by pre-processing.

17.2.3.3 Image Recovery and Resolution

Filtered backprojection is a linear and shift invariant algorithm. Consequently, FBP can be characterised by its point spread function, or equivalently, by its modulation transfer function. There is a direct relation between resolution and recovery. Recovery is the ratio of the reconstructed tracer concentration to the actual tracer concentration. If we know the size of an object, the resolution of the scanner and the low-pass filter used in FBP reconstruction, we can predict the recovery coefficient for that object. Furthermore, if the scanner has a space-invariant resolution, the image recovery will be space-invariant as well.

In contrast to FBP, MLEM and MAP algorithms are non-linear, which significantly complicates the specification of their performance. Their resolution and recovery capability cannot be explained by a simple point spread function. They depend on the position in the image and change in function of the iteration number. Nevertheless, it is possible to make some predictions about these characteristics (Qi et al. 2000; Wang et al. 1997; Fessler et al. 1996; Barret et al. 1994), but the calculations are complicated and only approximate.

Furthermore, FBP is designed under the assumption that both the projections and the tracer distribution are defined in continuous space. This means that FBP can only be applied to reconstruction problems where the number of projections and the number of pixels per projection is sufficiently large. In contrast, MLEM is specifically designed for digital data.

The difference in behaviour between the two algorithms can be shown with a few very simple simulations. In the first example, only two projections from a point source by a space-invariant projector are available (at 0^o and 90^o). Figure 17.2 (top) shows the true distribution, and the FBP and MLEM reconstructed images. FBP produces positive and negative streaks. The streaks cross near the point source, but the reconstruction is of poor quality. FBP fails because the number of projections is too low. The MLEM image is exact. Indeed, two projections are sufficient to find a single point source, provided that negative tracer uptakes are impossible as dictated by the Poisson nature of emission data.

In the bottom row of Fig. 17.2, the experiment was repeated, but now there were two point sources. Filtered backprojection reconstruction simply produces the cross-pattern twice. This was expected: FBP is linear and in this case also shift-invariant, so we should see the point spread function (that is, the response to a single point source) twice. In contrast, MLEM now shows four points, not two, clearly illustrating that MLEM is non-linear. This image is

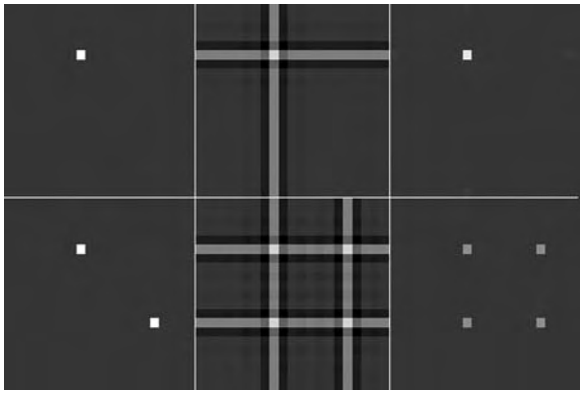

Fig. 17.2. True image (*left*), FBP (*centre*) and MLEM (*right*) reconstruction from two simulated perpendicular projections. *Top*, one point source; *bottom*, two point sources

not the exact reconstruction, and not the only solution either that produces exactly the same two perpendicular projections. These multiple solutions are possible, because the number of projections is too low.

Figure 17.3 shows images from a software phantom with two homogeneous regions and two identical point sources. MLEM images at iterations 40 and 200 are displayed. This figure also shows a horizontal profile intersecting the two point sources. It is clear that the isolated source converges much faster than the one surrounded by activity. In addition, there is no simple relationship between the width of the response in each point, and the recovery of that point. To further illustrate this, the right panel of the figure plots the full width at half maximum as a function of the maximum for subsequent iterations. For comparison, a similar plot for FBP was produced, by using different cut-off frequencies. The two MLEM curves converge to the same, exact reconstruction, but following different trajectories. The FBP curve shows a third relation between recovery and resolution, and does not reach the exact solution because of some residual blurring, caused by the violation of the continuity assumption about the image and its projections. Finally, the left panel of the figure shows that convergence can even be orientation dependent: in early iterations, the horizontal width of the hot spot at the left hand side is larger than its vertical width.

If position independent resolution is required, one could iterate until convergence is sufficient, and then smooth with a linear filter. Resolution will then be dominated by the filter, so the effective point spread function of the image would be the point spread function of the filter. (Note that in these examples, the resolution of the projections was ideal. In reality, the resolution of the reconstruction images is directly affected by the finite resolution of the measured projections).

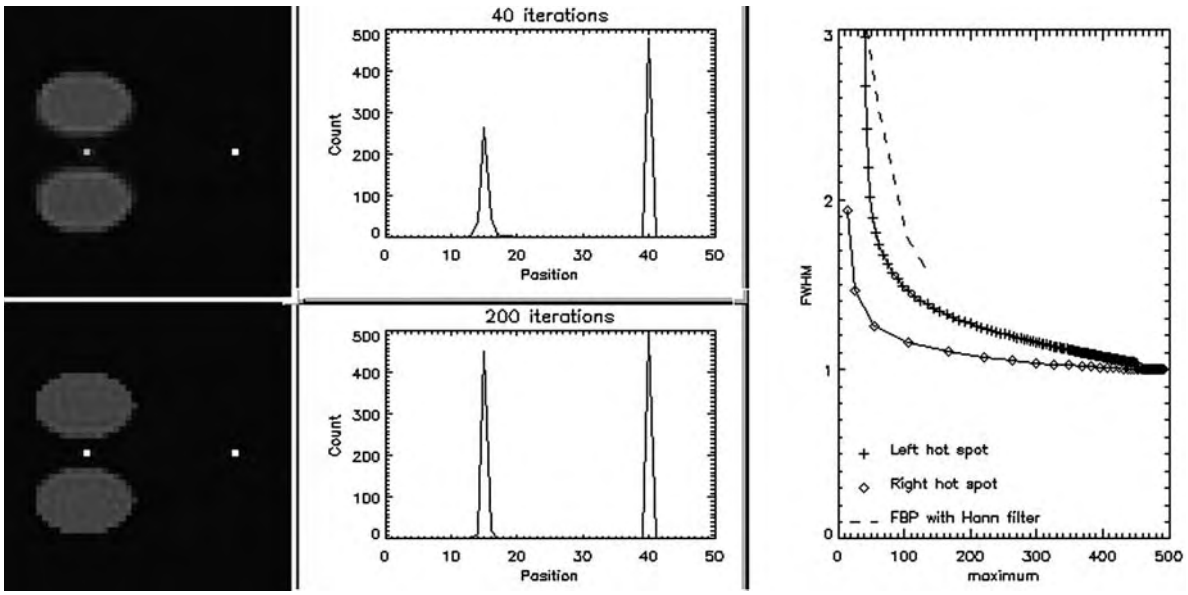

Fig. 17.3. *Left*, MLEM reconstruction after 40 (*top*) and 200 (*bottom*) iterations. *Centre*, the horizontal profile intersecting the two points. *Right*, the full width at half maximum as a function of the maximum pixel value for the two point sources. Each point corresponds to an iteration. The same relation is also shown for FBP (same curve for both point sources), by varying the cut-off frequency of the Hann low-pass filter

17.2.4 Comparison of MLEM and MAP

In the previous section it was shown that the convergence rate of MLEM is position dependent (Fig. 17.3). The reason is that the data provide only a limited amount of information, which is position and orientation dependent. The isolated point in Fig. 17.3 will be seen clearly separated in many projections. In contrast, the contribution of the other point will be masked in many projections by the surrounding activity. As a result, the data contain more information about the isolated point than about the other point. The likelihood is a measure of how well the information available in the data has been used in the reconstruction. If the isolated point is poorly reconstructed (as it is in the first iterations of MLEM), then the likelihood will be low. However, a similarly poor reconstruction of the other point has a much smaller effect on the likelihood. Consequently, the isolated point converges faster when the likelihood is maximised.

Similar effects are seen in MAP reconstruction. Usually, the prior is implemented as a function that penalises differences between neighbouring pixels, and its smoothing power is independent of position and orientation. In contrast, the likelihood provides information that does depend on position and orientation. Consequently, when they are combined in the posterior, the balance between the two is position and orientation dependent. If the likelihood contains more information about the activity at a certain position or along a certain orientation, the same prior will produce less smoothing. Consequently, the resolution and recovery coefficient is position and object dependent.

This position and object dependent resolution is undesirable for some applications, including (semi-) quantitative analysis (e.g. the computation of standard uptake values or SUV, see Chap. 11) or tracer kinetic modelling (see Chap. 2). In these applications, changes in reconstructed activity should reflect changes in tracer uptake, not changes of spatial resolution. For that reason, position dependent priors have been proposed that impose (approximately) position and object independent resolution (Stayman and Fessler 2004; Nuyts and Fessler 2003). Because they have to depend on the object, they are not true priors in Bayesian sense, so they are usually called penalties, applied in penalised-likelihood.

Thus, there are two ways to obtain uniform resolution with maximum-likelihood reconstruction: (1) apply many iterations of unconstrained MLEM and post-smooth, and (2) combine the likelihood with a carefully designed position dependent penalty, and iterate until convergence. It turns out that both procedures lead to virtually equivalent reconstructions (Stayman and Fessler 2004; Nuyts and Fessler 2003; Fessler 2004), i.e. at matched resolution, the noise characteristics are matched as well. The post-smoothed MLEM approach has the advantage of being simple; it can be implemented with existing software on most SPECT and PET systems. However, it requires a high amount of iterations (typically several hundreds, much more than common practice in clinical routine). In contrast, the penalised-likelihood approach allows faster converge (Stayman and Fessler 2004), but is more complex to implement.

In other applications, the resolution can be highly non-uniform. One example is the inclusion of anatomical information into the emission reconstruction: because smoothing over anatomical boundaries is discouraged, the resolution near these boundaries becomes very high. In contrast, the resolution within boundaries is still limited by the emission detector system. As before, two different approaches are available: (1) apply many iterations of the unconstrained MLEM algorithm, followed by post-processing based on anatomical data, and (2) apply a MAP algorithm, using a prior that is based on the anatomical data. We have some evidence that in this case, the MAP approach has superior noise properties (Nuyts et al. 2003).

17.2.5 Fully 3D Reconstruction

Originally, FBP and MLEM have been developed for the classical parallel beam geometry. However, both of them can be extended to other geometries. Gamma cameras equipped with fan beam collimators and PET systems with detector rings acquire data in a fan beam geometry. One can either rebin the fan beam data into parallel beam (as is common practice for PET), or adapt the FBP and MLEM algorithms to the fan beam geometry. For FBP, this involves changing the filter and the backprojection weights, for MLEM it suffices to replace parallel beam projection/backprojection with the fan beam counterparts.

Most current PET systems have either retractable septa or no septa. Fan beam, parallel beam and 2D PET data are 3D, and can be considered as a concate-

nation of independent 2D data sets, one set for each position along the symmetry axis. Each 2D data set is reconstructed into a 2D slice, a process often denoted as 2D reconstruction. In septa-less PET systems, the data are four dimensional, and there is no simple way to organise these data in separate 2D sets, with one set per slice. The most straightforward solution is to reconstruct the entire volume, hence the term "fully 3D" reconstruction. Extension of MLEM is straightforward, the projector and backprojector must be adapted to include all projection lines of the PET system (Chatziioannou et al. 2000; Leahy and Qi 2000). FBP has been extended as well (Kinahan and Rogers 1989; Defrise et al. 1994). However, Defrise et al. (1997) did find a way to reduce the dimensionality of the 4D data set into a 3D data set, while essentially preserving the statistical value of the data. This method, Fourier rebinning, allows applying the faster 2D methods to a fully 3D data set. Although the noise distribution is no longer Poisson after Fourier rebinning, the Poisson characteristics can be restored approximately by uncorrecting the rebinned data for attenuation (Lartizien et al. 2003).

17.2.5 Attenuation

17.2.5.1 Attenuation Correction

Filtered backprojection is the inverse of the projection operator. In practice, this operator is a poor model of the true radioactivity acquisition. Due to photon--electron interactions, many photons are lost, an effect usually called attenuation. Between 0.1 and 0.5 MeV, Compton scatter is the main cause of attenuation in tissue. Consequently, we need either the inverse (FBP) or the transpose (MLEM) of the attenuated projection operator.

In PET, the effect of attenuation can be separated from the projection, because all photon pairs contributing to the same projection pixel have undergone the same attenuation. Consequently, the acquisition can be modelled as the successive application of two independent operators: first projection, and then attenuation. The inverse operator is then easily obtained: attenuation compensation (a single correction factor in every projection pixel), followed by FBP. Further, the transpose operator consists of the same attenuation compensation, followed by backprojection. To make the MLEM algorithm correct for attenuation, it suffices to replace its non-attenuating projector and backprojector by the attenuating ones. The MLEM reconstruction could also be directly applied, like FBP, to the attenuation corrected projections. Note however that attenuation correction alters the Poisson nature of the noise in the projections. Therefore, the above MLEM approach (which is applied to the raw, uncorrected data) is preferable.

In SPECT, this separation is not possible: photons contributing to the same projection pixels have undergone different attenuation. Consequently, for reconstruction we need to invert the attenuated projection, where the attenuation is position dependent. In the case of a homogeneously attenuating object, this inverse can be computed analytically, leading to an adapted version of FBP (Bellini et al. 1979). For non-homogeneous attenuation, iterative algorithms are required (King et al. 1996). Extension of MLEM to attenuated projection is straightforward. In the feedback path, the projector is replaced with the attenuated projector. In the feed-forward path, the transpose operator must be inserted, which is attenuated backprojection.

17.2.5.2 Transmission Scan

Attenuation is supposed to be known. In some specific cases, it can be derived from the emission projections (Michel et al. 1989), in other cases a transmission measurement is needed. In PET, the raw transmission data can be used directly. In SPECT, they can be used to reconstruct an attenuation map with FBP, which is then inspected by the projector/backprojector pair of the MLEM algorithm to compute the effect of attenuation. However, both in PET and in SPECT, it is useful to compute an ML or MAP reconstruction of the transmission scan (Lange and Carson 1984; Mumcuoglu et al. 1996; Fessler et al. 1997), to reduce the contribution of the transmission noise to the final image. In SPECT, transmission measurements are often carried out with convergent beam configurations, leading to truncation problems because of the reduced field of view. It has been shown that the truncation artefacts are strongly reduced by ML or MAP, as compared to FBP (Manglos et al. 1993; Manglos et al. 1995; Case et al. 1995).

Figure 17.4 shows the FBP, the ML and a MAP reconstructed attenuation image from the same 1-min PET transmission sinogram, and the corre-

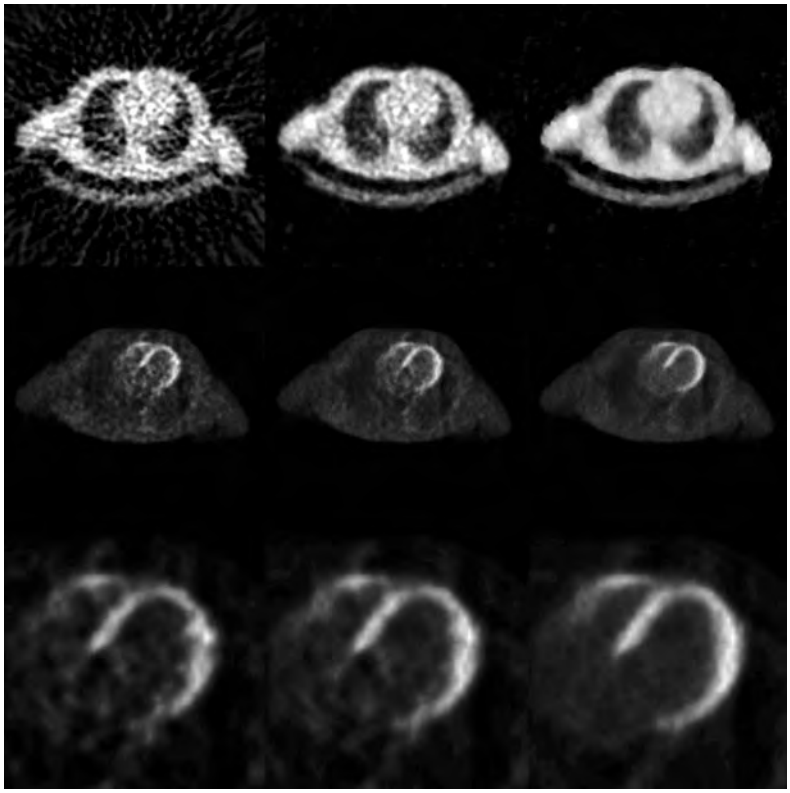

Fig. 17.4. *Top row*, reconstruction of the attenuation map from a short transmission scan with FBP (*left*), an ML algorithm (*centre*) and a MAP algorithm (*right*). Middle row, the corresponding attenuation corrected PET fluorodeoxyglucose images, produced with MLEM. *Bottom row*, zoomed images of the heart

sponding attenuation corrected MLEM reconstruction of the emission ^{18}F-fluorodeoxyglucose image. The ML and MAP transmission reconstructions were done with a gradient ascent algorithm (Nuyts et al. 1998). The figure also shows the emission MLEM images with attenuation correction based on the FBP, ML and MAP attenuation images. It is clear that short transmission scans may contribute significantly to the noise in the final attenuation corrected image, and that this contribution also depends on the attenuation correction method. MAP reconstruction can be regarded as a combination of reconstruction and (fuzzy) segmentation. Here, segmentation is the classification of pixels according to tissue type, such that appropriate attenuation coefficients can be assigned (lung, bone, soft tissue). Several authors have obtained significant noise reduction with the consecutive application of these operations: first reconstruction with FBP, then segmentation to reduce the noise (Meikle et al. 1993; Tai et al. 1996; Xu et al. 1996). However, combining everything in a single reconstruction procedure should, at least in principle, yield images with superior noise characteristics.

Some authors have investigated the alignment requirements of the transmission map with the emission reconstruction for SPECT (Matsunari et al. 1998) and PET (Chatziioannou and Dahlbom 1996; McCord et al. 1992). In SPECT, deviations of more than 1 cm can cause significant artefacts. In PET, appropriate alignment is even more delicate.

In Fig. 17.5, we simulated projections of an object with a small air bubble (zero activity, zero attenuation). They were reconstructed based on a transmission map, in which this region was labelled as tissue. Scatter and resolution effects were not simulated. As shown in this Fig. 17.5, the SPECT reconstruction shows a low activity in the region. The PET reconstruction, however, shows a marked hot spot in that region. The reconstructions were done with MLEM, but FBP shows the same artefacts. The clinical implication of this effect is that air bubbles in the colon, apparently, may cause artefactual hot spots in PET. A more general conclusion is that in PET, attenuation corrected images are very sensitive to the attenuation correction factors, even more so than in SPECT.

This may be one of the reasons why attenuation correction is often considered useful or even mandatory in PET, while it is often ignored in SPECT. In PET, attenuation correction is always applied in cardiac and brain applications. Its value in oncology

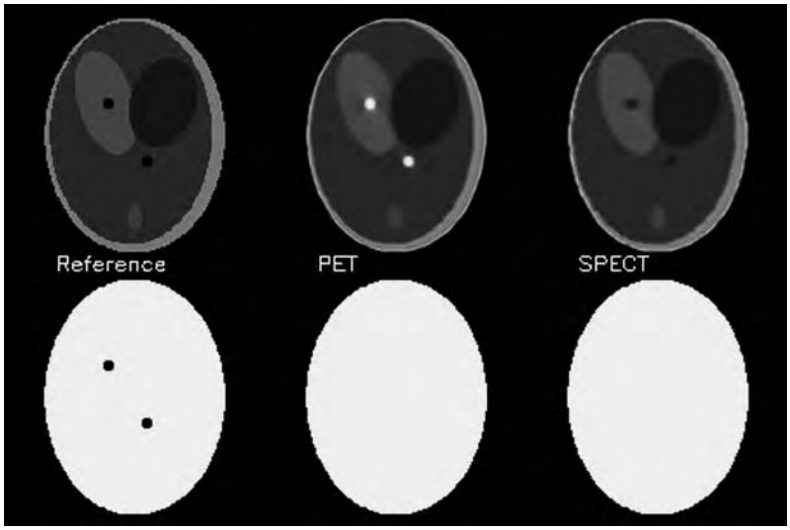

Fig. 17.5. Reconstruction artefact due to a region of zero attenuation and activity, which was missed in the transmission map: *Top*, reference image (*left*), reconstruction from PET (*centre*) and SPECT (*right*) projections. *Bottom*, the true attenuation map (*left*), and the maps used for attenuation correction in PET (*centre*) and SPECT (*right*) reconstruction

is less obvious. Although several studies reported no or only moderate improvement in tumour detection (Kotzerke et al. 1999; Lonneux et al. 1999), attenuation correction has become the standard procedure in oncology. The main reasons are that tumour localisation is much easier on attenuation corrected images, and that attenuation correction is mandatory for quantitative analysis. With carefully designed methods, images of excellent quality are obtained (Lartizien et al. 2003).

It is easy to show that attenuation correction dramatically improves quantification of tracer concentration and eliminates artefacts in SPECT (Nuyts et al. 1995), but this does not prove that diagnostic value has improved as well. In an ROC study, Jang et al. (1998) found that a group of physicists performed similar on attenuation corrected and uncorrected myocardial SPECT images, while a group of experienced physicians performed significantly worse on attenuation corrected images. This indicates that the long experience with non-attenuation corrected images may hamper the expert during the introduction of a new method. Similarly, Gilland et al. (1992) found in an ROC analysis based on simulated cardiac studies that attenuation correction had an adverse effect, and that MLEM was not statistically better than FBP. Hendel et al. (1999) studied the effect of attenuation and scatter correction in cardiac SPECT with ^{99m}Tc-sestamibi in a multicenter study, and Harel et al. (2001) evaluated the effect of correction for attenuation, scatter and collimator blurring in cardiac SPECT with ^{201}Tl. In both studies no impressive improvement was found. In contrast, LaCroix et al. (2000) compared FBP without attenuation correction with MLEM with non-uniform attenuation correction in myocardial SPECT with ^{99m}Tc-sestamibi, and they found MLEM to be significantly superior. It seems that, in particular for cardiac SPECT, it is not easy to improve the diagnostic value by making the images more quantitative. Possible reasons are: (1) the increase of the noise level by noise propagation from the transmission scan; (2) the reduction of familiar artefacts can be offset by the introduction of unfamiliar artefacts, if the physical models for attenuation, scatter or blurring are not sufficiently accurate; and (3) the effect of breathing, which is ignored in most reconstruction algorithms. Nevertheless, correction for attenuation, scatter and collimator blurring should be beneficial, and it seems that these corrections are becoming standard in clinical routine (Hendel et al. 2002). In brain SPECT, attenuation correction seems more effective and is more widely accepted already (Iida et al. 1998).

17.2.5.3 PET-CT

A relatively new and very successful development is multi-modality imaging with PET-CT, which combines a PET and a CT into a single device, therefore providing automatic registration between both modalities (Beyer et al. 2000). The main advantage is obviously the easy production of registered anatomical and functional images, which are particularly useful in oncology. Registration of multimodality images can also be done retrospectively, and

many sophisticated algorithms have been proposed (Pluim et al. 2003). The registration obtained with the PET-CT device is usually good but not perfect, so it is debatable whether that registration is superior to retrospective software registration (Vogel et al. 2004). However, there is no doubt that with the installation of these systems, the availability of registered images in clinical practice has been increased dramatically. Hopefully, this will lead to a faster transfer of research registration software into clinical routine.

CT scanning is fast, so the total acquisition time of the whole body PET protocol is reduced by replacing the traditional transmission scan (using a long lived isotope) with the CT scan. However, it is questionable if this faster procedure also yields improved attenuation correction. The advantage of CT is its speed and the very low noise amplitude. Disadvantages are more severe motion artefacts, artefacts due to breathing, and artefacts due to differences in photon energy. The traditional transmission scan uses the interleaved protocol, where a transmission and emission scan are acquired at each bed position. As a result, the time between emission and transmission scan is short, which reduces the probability and the impact of motion artefacts. In contrast, in PET-CT systems a whole body CT scan is followed by a whole body PET scan. Scanning is usually done from the hips towards the head, so the chance of motion artefacts in the upper thorax or head region is pretty high. Breathing causes problems because the fast CT scan takes a snapshot within the breathing cycle, while the slow PET scan averages over several cycles. Although the impact of breathing can be reduced by careful patient preparation (Goerres et al. 2002; Beyer et al. 2003), moderate to severe artefacts cannot be totally avoided (Chin et al. 2003; Sarikaya et al. 2003). Motion and breathing artefacts can often be identified by inspection of the non-attenuation corrected PET images. For that reason, it is strongly recommended to systematically compute both the corrected and non-corrected PET images. Finally, the difference in photon energy between CT and positron emitter causes problems, because attenuation is partly caused by Compton scatter and partly by photoelectric effect. Both contributions scale differently with energy, so the appropriate transformation from the CT energy (around 50--100 keV) to 511 keV depends on the material characteristics of the attenuator (Stonestrom et al. 1981). The standard procedure is to use a piecewise linear rescaling of the attenuation coefficients (Kinahan et al. 1998). This scaling is effective for living tissues: studies comparing CT-based and ^{68}Ge-based attenuation correction revealed small differences in SUV, which are statistically significant but probably not clinically relevant (Kamel et al. 2002). However, this scaling fails in the presence of contrast agents and metallic implants, causing considerable bias on tracer uptake values (Visvikis et al. 2003). Most authors studying these artefacts conclude that the attenuation corrected PET images are clinically useful, but that standard uptake values are not accurate in the presence of oral or intravenous contrast.

17.2.5 Scatter

Compton scatter not only prevents photons from being detected, it also deflects into the detector some photons that should not have been detected. This undesirable contribution to the projections is usually called scatter. Compton scatter can be modelled as an elastic collision between two particles of different mass, an electron and a photon. It follows that photons lose energy in the process. Fortunately, we know the energy of unscattered photons, and we can measure the energy of detected photons with the tomograph, so we can distinguish between scattered and unscattered photons. Unfortunately, the resolution of the energy measurement is limited, so the separation of photons based on measured energy is not very reliable. Consequently, many scattered photons pass the energy test, and further correction is required.

Many algorithms have been proposed, both for SPECT and PET. In SPECT, acquisition at energy levels just below and/or above the photo peak are often used to estimate the number of scattered photons that are accepted by the photo peak window (Jaszczak et al. 1984; Gagnon et al. 1989; Buvat et al. 1995; King et al. 1997; Ogawa et al 1991; Yang et al. 1997). Alternatively, the scatter can be estimated using a model. This can be a simple stationary convolution (Axelsson et al. 1984), a transmission scan dependent convolution model (Narita et al. 1997), or an attenuation map dependent model based on measurements (Hutton et al. 1996) or on the Klein-Nishina equation for Compton scatter (Walrand et al. 1994; Wells et al. 1997; Beekman et al. 2002).

For PET, energy based methods are less obvious because the energy resolution of most current PET systems is relatively poor, in particular for BGO systems. In septa-less PET scanning, the scatter contribution is very high, and if quantitative analysis

is desired, scatter correction is mandatory. Therefore, model based approaches have been developed (Ollinger 1996, Watson et al. 1997). With the introduction of scintillators with better energy resolution, such as LSO and GSO, the energy-based correction methods may also receive greater attention in PET.

When combined with FBP, the scatter is subtracted prior to reconstruction. When combined with MLEM, this approach is theoretically incorrect, since scatter subtraction destroys the Poisson nature of the data. It has been shown that superior images are obtained when the scatter model is correctly incorporated, although the differences are subtle in some cases (Welch and Gullberg 1997).

In simulations or phantom measurements, a perfect or at least excellent estimate of the scatter-free image can be obtained, which allows comparing the performance of different methods. Although differences in performance have been reported, these differences are usually not dramatic. Scatter correction definitely has an impact on quantification, but not necessarily on the diagnostic value of the images (deVries et al. 1997; Iida et al. 1998).

17.2.6 Detector Resolution

The projection of a point source should ideally be a point in the projections as well. After digitisation, it should be a single pixel in the projection matrix. In practice, however, the projection is always a blob consisting of multiple pixels.

In SPECT, this is due to the intrinsic resolution of the detector (typically 4 mm FWHM), and to the collimator (see Chap. 16). For parallel hole collimators, resolution is dominated by collimator blurring, and the FWHM is proportional to the distance to the collimator. Consequently, resolution in SPECT is significantly non-stationary. However, when projections over 360° are used, the blurring of opposite projections tends to average, and a relatively uniform resolution in the reconstructed image is observed.

In PET, resolution is limited by the positron range (less than 1 mm to several millimetres, depending on the isotope), the angle between the two photons (not exactly 180°), crystal penetration, depth of interaction and crystal geometry. Currently, these effects accumulate to about 4--6 mm in whole body scanners, and, when compared to SPECT, the resolution is fairly homogeneous over the entire field of view.

Resolution compensation is less difficult if stationary (i.e. position independent) resolution can be assumed, as in PET or sometimes in 360° SPECT. In this case, some resolution can be recovered using deconvolution techniques, such as Metz or Wiener filtering (King et al. 1986).

Position dependent resolution compensation for SPECT can be modelled using the frequency distance principle, which leads to a pre-correction approach (Glick et al. 1994; Xia et al. 1995). Alternatively, one can include the stationary or non-stationary spatial resolution in the projector and backprojector of the MLEM algorithm. An interesting approach for efficiently computing the position dependent collimator blurring is Gaussian diffusion (McCarthy and Miller 1991; Kohli et al. 1998).

Several authors have reported that resolution recovery in MLEM seems to have a beneficial effect on the noise characteristics as well (Kohli et al. 1998; Hutton and Lau 1998). This is not obvious, since resolution recovery in general is a somewhat ill-posed problem, and ill-posed problems require regularisation to prevent noise propagation. However, when the blurring is included in the projector, a larger fraction of the noise becomes inconsistent and cannot be incorporated in the reconstruction. More intuitively: if a single projection pixel has a higher count than it should because of noise, MLEM tries to "explain" that by inserting a hot spot in the reconstruction image. If blurring is ignored, projection of a hot spot is a hot spot, so hot spots (due to noise) in the projection will lead to hot spots in the reconstruction. However, if blurring is taken into account, the projection of a hot spot is a smooth blob, so hot spots in the projection cannot easily propagate into the reconstruction.

Figure 17.6 shows three reconstruction images of the same patient FDG scan, acquired with a PET system with retracted septa (3D mode). The first image is reconstructed with FBP, using the 3D FBP algorithm of Kanahan and Rogers (1989). The second image is obtained with MLEM with resolution recovery. The detailed protocol is as follows. The 4D projection data set was corrected for attenuation, detector sensitivity and scatter (Watson et al. 1997), and transformed in a series of parallel 2D data sets with Fourier rebinning (Defrise et al. 1997). Then the 2D data set was uncorrected for attenuation to approximately restore the Poisson characteristics (Lartizien et al. 2003), and the entire volume was reconstructed with MLEM, using a parallel beam projector/backprojector that included attenuation and a stationary blurring in the projections.

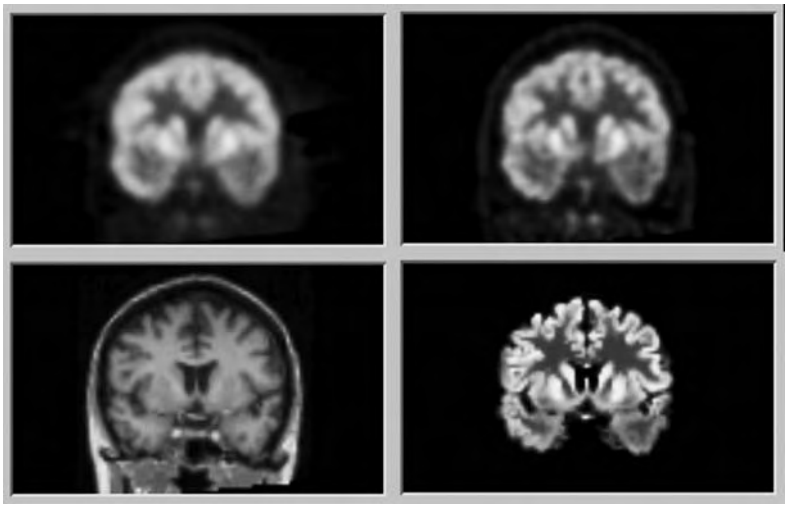

Fig. 17.6. Reconstructions of a brain FDG-PET scan. *Top left*, 3D FBP. *Top right*, FORE + 2.5-D MLEM with stationary resolution recovery. *Bottom left*, registered MR-image. *Bottom right*, FORE + 2.5-D MAP with an anatomical prior based on the MRI

The obtained resolution is markedly better than with 3D-FBP. The third image is obtained by MAP reconstruction, using an anatomical prior based on a registered MRI image (Baete et al. 2004). The MRI image was segmented to identify grey matter, white matter and CSF. The PET data were processed as before, but the MLEM algorithm was replaced with the MAP algorithm, using a prior that avoids smoothing over anatomical boundaries. The projector/backprojector uses the parallel beam geometry, treating the projections as a series of 2D sinograms. However, the blurring and prior operate in 3D, so the entire volume has to be reconstructed simultaneously. This approach is sometimes called "2.5-D" reconstruction (Obi et al. 2000). The figure shows an impressive improvement of the resolution, the sulci and gyri are now clearly visible in the PET image. However, the resolution is very non-uniform: it is very high perpendicular to anatomical boundaries, but within an anatomical region, similar as in the MLEM image. Nevertheless, it leads to improved lesion detection (Baete et al. 2004).

17.2.7 Motion Correction

Since SPECT and PET studies tend to be lengthy investigations, motion artefacts are very frequent and with the improvement in sampling and intrinsic resolution, especially in modern PET cameras, such artefacts are expected to become even more of a problem. Despite extensive study, motion correction still remains a topic of ongoing research, but recent progress for brain imaging applications yielded promising results for future introduction into clinical practice.

A first strategy consists in estimating the motion from the emission data itself. Motion correction and image reconstruction are then treated as a single (iterative) estimation problem, in which an intermediate reconstruction image serves to detect and identify motion, which in turn is then used to improve the reconstruction image. Such estimation approach is difficult, since more information has to be extracted from the emission data than in a regular reconstruction without motion correction. The technique is therefore most often applied under the assumption that the motion can be modelled as a simple translation in the projections (Matsumoto et al. 2001; Lee et al. 1998; Britten et al. 1998). Kyme et al. (2003) demonstrated potential clinical usefulness with a complete motion model for brain imaging. The technique implicitly assumes that all projections in the emission data are uncorrupted by motion, but it allows for different patient orientations in different projections. The approach is therefore specifically designed for SPECT imaging.

A second strategy for motion correction in SPECT and PET brain imaging consists in measuring patient motion by an independent motion tracking device. Several systems have been investigated, but the POLARIS (Northern Digital, Waterloo, Ontario, Canada) optical infrared tracking system is clearly the most popular in current research. The system itself is commercially available, but still has to be integrated with the camera system. The position of the patient's head is continuously monitored and communicated to the camera system, which separates the data acquired at different positions of the

patient's head. Motion correction is then generally performed by either (instantaneously) precorrecting the emission data (Bloomfield et al. 2003; Lopresti et al. 1999) or by incorporating the patient movement in the image reconstruction algorithm (Fulton et al. 1999).

Although motion correction may become available in the future, most researchers agree that the best strategy to avoid motion artefacts will still be to prevent motion. Consequently, the scan duration should be as short as possible. Since techniques such as post-injection transmission and maximum-a-posteriori reconstruction can be used to reduce scan times, they are expected to contribute significantly in avoiding motion artefacts.

17.3 Image Analysis

17.3.1 Diagnostic Value of an Image

There are two good reasons to apply all the corrections described above. First, the corrections eliminate artefacts, and second, the resulting images provide quantitative information (e.g., actual activity concentration in MBq per gram tissue).

For some applications, such as the computation of standard uptake values in therapy monitoring, the application of tracer kinetic modelling, or in dosimetry studies, quantification is very important. In many other applications, the image is produced for visual analysis and the main reason for applying the corrections is artefact removal.

To decide which of two images is the best, one must take into account the purpose of the images (Barrett et al. 1993): an image used for quantification does not have to look nice, an image used for visual inspection does not have to be quantitatively accurate. Evaluation of image quality is a research area of its own. The correct way to do it, is to produce many images using different methods, to ask blinded expert operators to interpret the images as they would in clinical practice, and analyse the results. Because sensitivity can be traded for specificity, the results are inconclusive if one method has higher sensitivity and the other has higher specificity. That problem is eliminated by designing the experiment such as to allow subsequent ROC analysis (Jang et al. 1998; De Vries et al. 1997). The main problem of such studies is that scoring of large image series by multiple observers is very time consuming. A solution would be to replace the human observer by a numerical observer. But until now, no numerical observer has been found that closely matches human performance in all situations. Currently, the most promising one seems to be the channelised Hotelling observer (Gifford et al. 2000; Abbey et al. 2001).

17.3.2 Region of Interest Analysis

When analysing images, we often compute the mean value of a region of interest (ROI), which is supposed to represent the regional tracer concentration. Intuitively, it seems a good idea to do this, because the mean of a region is probably a more robust estimate than an individual pixel value. However, we must keep in mind that even this mean ROI value has usually both limited precision and accuracy. Estimating bias and variance of that value is not easy.

If we acquire multiple images of a known distribution, and compute the mean value in the same ROI of all those images, we would obtain a set of different values. The mean of that set would usually be significantly different from the true mean tracer uptake, due to imperfect correction for Compton scatter, attenuation and collimator blurring. In real life situations, there is no way to estimate that bias. The set of values would be distributed about that biased mean, and we could compute the variance of that distribution. The most important cause of variance is Poisson noise. In real life, it is possible to compute that variance. The correct way to do that, is to take into account the Poisson noise of the projections and of all measured data that contribute to the final image, (measured randoms, scatter window images, transmission projections etc.), and to compute how this noise propagates during reconstruction (Huesman 1984; Barrett et al. 1994; Wilson et al. 1994). This approach is interesting but too elaborate for routine clinical application. Consequently, the variance is often estimated as the variance within the ROI. This is not correct, because the pixel values in the ROI are correlated, as a result of the reconstruction process and of low-pass filtering. Since the correlation decreases with inter-pixel distance, the estimate of the variance becomes less reliable with decreasing ROI size. Because of the low-pass filtering, neighbouring pixels tend to have positive correlation coefficients, which causes the variance within the region to be lower than the variance between repeated measurements.

Another important problem is the possible inhomogeneity of the regions. The regions can be inhomogeneous because of limited resolution and recovery (which causes blurring), and because we do not know where the true boundaries of homogeneous regions are. In earlier sections, some (partial) remedies have been mentioned: detector resolution can to some extent be compensated for, by including the detector characteristics in the reconstruction program. More accurate boundaries can be obtained from anatomical scans (CT, MR), and they can be incorporated during reconstruction by applying maximum-a-posteriori algorithms. Also differences in dynamic behaviour of the tracer concentration can be used to identify (and compensate for) tissue heterogeneity within the region of interest.

PET is often used for therapy follow-up in oncology, and one way to quantify is to report changes in SUV in the tumour. Because of the reasons mentioned above, the mean of a region is very dependent upon the region contour, and more so if the organ or lesion under study is smaller. As a result, the resulting mean SUV values tend to be very operator dependent. To problem can be reduced by using volumes of interest (VOI) rather than regions of interest (more voxels will be included), and by using software for (semi-) automated VOI definition. Although some (rather primitive) research and commercial VOI software exists, there is definitely a need for a more sophisticated tool, that could be accepted as a standard for the analysis of multi-centre studies.

17.3.3 Analysing Dynamic Images

A typical example of the analysis of dynamic images is the tracer kinetic modelling in PET, applied in order to determine the rate constants of a compartmental model (Huang and Phelps 1986). In the case of a myocardial study with $^{13}NH_3$, one of the rate constants represents the product of flow and extraction fraction. Assuming the latter is close to unity, this approach allows quantifying the flow in ml/(min g).

The standard approach is to define ROIs in the image. The mean value of an ROI as a function of time produces a time-activity curve (TAC). A region in the left ventricular cavity produces the input function, which is the tracer concentration in the vascular compartment. If the regional rate constants (i.e., diffusion rates between vascular, extra cellular and tissue compartments) were known, we could compute the tracer concentration in the other compartments, and predict the TAC in tissue regions. In reality, the TAC is known and the rate constants are not, so we calculate the rate constants between compartments by fitting the predicted TAC to the measured one.

Ideally, this function must be corrected for various factors, such as spillover, blood volume in the tissue, metabolites of the injected tracer, etc., so that it really represents freely diffusible tracer delivered to the tissue. This can be done based on measurements, or by including the unknown parameters and determining their value by fitting (Raylman et al. 1994).

Some authors propose automated procedures to eliminate the manual ROI definition, and the variability produced by that process. They use factorial analysis in order to extract the arterial blood component from the dynamic data set (Wu et al. 1996) or to identify different components in heterogeneous regions (Zhou et al. 1997). This approach not only eliminates manual intervention, it also minimises contributions from neighbouring regions due to spillover.

In principle, it is not required to reconstruct every frame. The projection data (or sinograms) contain the same information. One could reconstruct an image suitable for region drawing. The regions can then be forward projected into the sinograms to compute the activity in those regions as a function of time (Huesman 1984). This procedure eliminates a lot of computations. Of course, it also eliminates the possibility to look at the images in function of time. In addition, the values obtained with this approach are equivalent to FBP values, and there is some evidence that MLEM reconstruction may reduce noise on the estimated kinetic parameters (Schiepers et al. 1997).

One can go even further, and combine the kinetic modelling and the reconstruction tasks. Instead of reconstructing individual time frames, one can directly reconstruct dynamic behaviour from the projections (Meikle et al. 1998).

17.4 Future Developments

BGO was the dominating scintillator for PET. Currently, LSO and GSO are being used in commercial systems as well. These crystals have a higher light yield, a better energy resolution and a shorter scintillation time (see Table 16.1). This should lead to decreased randoms and scatter contamination, higher counting capabilities and higher resolution.

This may provoke new software developments, including energy-based scatter subtraction, and possibly the reconstruction using time-of-flight information. Moreover, other promising materials, such as Lanthanum scintillators, are being studied (Surti et al. 2003). For many applications, it is important that the sensitivity of the PET systems would be as high as possible. Thus, septa-less systems with a large axial extent are desired. With increasing axial extent, the contribution of scatters and randoms increases as well, and the resolution may decrease because of parallax problems. Probably, these problems can be overcome with the new scintillators: better energy resolution and shorter scintillation times will improve randoms and scatter rejection. The availability of different fast crystals with slightly different scintillation properties is used for depth of interaction encoding to suppress the parallax problem. The development of this new hardware will be a very interesting challenge for software researchers.

In SPECT, solid state detectors are receiving continuous attention, because they have superior characteristics when compared to NaI(Tl) (Eisen et al. 2002), but their introduction is still hampered by the high cost.

PET-CT has become a very popular device. Improvements are necessary to reduce the artefacts due to patient motion and breathing. Faster PET systems (due to larger field of view and higher sensitivity) and gated acquisition schemes may help. Hopefully, the success of PET-CT imaging will lead to further sophistication and clinical use of retrospective software registration. Such development would extend the applications to other modalities (PET-MR, SPECT-PET), and it would help avoid repeated CT scanning for registration purposes.

Emission tomography, and in particular PET, is being used increasingly in clinical multicenter trials. To maximise the statistical power of such studies, the image formation and subsequent analysis should be standardised. With the current diversity of systems and (powerful) reconstruction and analysis algorithms, this is not a trivial task.

References

Abbey CK, Barrett HH (2001) Human and model observer performance in ramp-spectrum noise: effects of regularization and object variability'. J Opt Soc Am A, 18:473–488

Ahn S, Fessler JA (2003) Globally convergent image reconstruction for emission tomography using relaxed ordered subsets algorithms. IEEE Trans Med Imaging 22:613–626

Ardekani BA, Braun M, Hutton BF et al. (1996) Minimum cross-entropy reconstruction of PET images using prior anatomical information. Phys Med Biol 41:2497–2517

Alenius S, Ruotsolainen U (1997) Bayesian image reconstruction for emission tomography based on median root prior. Eur J Nucl Med vol 24:pp 258–265

Axelsson B, Msaki P, Israelsson A (1984) Subtraction of Compton scattered photons in single-photon emission computed tomography. J Nucl Med 23:290–294

Baete K, Nuyts J, Van Paesschen W et al (2004) Anatomical based FDG-PET reconstruction for the detection of hypometabolic regions in epilepsy. IEEE Trans Med Imaging 23:510-519

Barrett HH, Wilson DW, Tsui BMW (1994) Noise properties of the EM algorithm: I. Theory. Phys Med Biol 39:833–846

Barrett HH, Yao J, Rolland JP et al. (1993) Model observers for assessment of image quality. Proc Natl Acad Sci USA 90:9758–9765

Beekman FJ, de Jong HWAM, van Geloven S (2002) Efficient fully 3-D iterative SPECT reconstruction with Monte Carlo-based scatter compensation. IEEE Trans Med Imaging 21:867–877

Beekman FJ, Slijpen ETP, Niessen WJ (1998) Selection of task-dependent diffusion filters for the post-processing of SPECT images. Phys Med Biol 43:1713–1730

Beyer T, Townsend DW, Brun T et al (2000) A combined PET/CT scanner for clinical oncology. J Nucl Med 41:1369–1379

Beyer T, Antoch G, Blodgett T et al (2003) Dual-modality PET/CT imaging: the effect of respiratory motion on combined image quality in clinical oncology. Eur J Nucl Med 30:588–596

Bellini S, Piacentini M, Cafforio C, Rocca F (1979) Compensation of tissue absorption in emission tomography. IEEE Trans. Acoustics Speech and Signal Processing 27:213–218

Bloomfield PM, Spinks JS, Reed J, et al. (2003) The design and implementation of a motion correction scheme for neurological PET. Phys Med Biol 48:959–978

Bowsher JE, Johnson VE, Turkington TG et al. (1996) Bayesian reconstruction and use of anatomical a Priori information for emission tomography. IEEE Trans Med Imaging 15:673–686

Britten AJ, Jamali F, Gane JN, and Joseph EA. (1998) Motion detection and correction using multi-rotation 180° single-photon emission tomography for thallium myocardial imaging. Eur. J. Nucl. Med. 25:1524–1530

Buvat I, Benali H, Todd-Pokropek A et al. (1995) Scatter correction in scintigraphy: the state of the art. Eur J Nucl Med 21:675–694

Case JA, Pan TS, King MA, Luo DS, Penney BC, Rabin MSZ (1995) Reduction of truncation artifacts in fan beam transmission imaging using a spatially varying gamma prior. IEEE Trans Nucl Sci 42:2260–2265

Chan MT, Leahy RM, Mumcuoglu EU et al. (1997) Comparing lesion detection performance in PET image reconstruction algorithms: a case study. IEEE Trans Nucl Sci 44:1558–1563

Chatziioannou A, Dahlbom M (1996) Detailed investigation of transmission and emission data smoothing protocols and their effects on emission images. IEEE Trans Nucl Sci 43:290–294

Chatziioannou A, Qi J, Moore A, et al (2000) Comparison of 3-

D maximum a posteriori and filtered backprojection algorithms for high-resolution animal imaging with microPET. IEEE Trans Med Imaging 19:507–512

Chin BB, Nakamoto Y, Kraitchman DL (2003) PET-CT evaluation of 2-deoxy-2-[^{18}F]fluoro-D-glucose myocardial uptake: effect of respiratory motion. Mol Imaging Biol 5:57–64

Coakley K, Llacer J (1991) The use of cross-validation as a stopping rule in emission tomography image reconstruction. SPIE Medical Imaging V:226–233

Comtat C, Kinahan PE, Fessler JA, et al (2002) Clinically feasible reconstruction of 3D whole-body PET/CT data using blurred anatomical labels. Phys Med Biol 47:1–20

Daube-Witherspoon ME, Matej S, Karp JS, Lewitt RM (2001) Application of the row action maximum likelihood algorithm with spherical basis functions to clinical PET imaging. IEEE Trans Nucl Sci 48:24–30

Defrise M, Geissbuler A, Townsend DW (1994) A performance study of 3D reconstruction algorithms for positron emission tomography. Phys Med Biol 39:305–320

Defrise M, Kinahan PE, Townsend DW, et. al (1997) Exact and approximate rebinning algorithms for 3D PET data. IEEE Trans Med Imag 16:145–158

Dempster AP, Laird NM, Rubin DB (1977) Maximum likelihood from incomplete data via the EM algorithm. J R Stat Soc Series B39:1–38

De Vries DJ, King MA, Soares EJ et al. (1997) Evaluation of the effect of scatter correction on lesion detection in hepatic SPECT imaging. IEEE Trans Nucl Sci 44:1733–1740

Eisen Y, Mardor I, Shor A (2003) NUCAM3-a gamma camera based on segmented monolithic CdZnTe detectors. IEEE Trans Nucl Sci 49:1728–1732

Falcon C, Juvells I, Pavia J, Ros D (1998) Evaluation of a cross-validation stopping rule in MLE SPECT reconstruction. Phys Med Biol 43:1271–1283

Fessler DU, Ficaro EP, Clinthorne NH, et al. (1997) Grouped-coordinate ascent algorithms for penalized-likelihood transmission image reconstruction. IEEE Trans Med Imaging 16:166–175

Fessler JA, and Rogers WL (1996) Spatial resolution properties of penalized-likelihood image reconstruction: space-invariant tomographs. IEEE Trans Im Proc 5:1346–1358

Fessler JA (2003) Analytical approach to regularization design for isotropic spatial resolution. Proc IEEE Nucl Sci Symp Med Im Conf 2003. To appear. 1343, M5–5

Fulton RR, Eberl S, Meikle SR, Hutton BF, Braun M (1999) A practical 3D tomographic method for correcting patient head motion in clinical SPECT. IEEE Trans Nucl Sci 46:667–672

Gagnon D, Todd-Pokropek A, Arsenault A et al. (1989) Introduction to holospectral imaging in nuclear medicine for scatter subtraction. IEEE Trans Med Imaging 8:245–250

Gifford HC, King MA, de Vries DJ (2000) Channelized Hotelling and human observer correlation for lesion detection in hepatic SPECT imaging. J Nucl Med 41:514–521

Gilland DR, Tsui BM, Metz CE et al. (1992) An evaluation of maximum-likelihood expectation maximization reconstruction for SPECT by ROC analysis. J Nucl Med 33:451–457

Glatting G, Werner C, Reske SV, Bellemann ME (2003) ROC analysis for assessment of lesion detection performance in 3D PET: influence of reconstruction algorithms. Med Phys 30:2315–2319

Glick SJ, Penney BC, King MA et al. (1994) Noniterative compensation for the distant-dependent detector response and photon attenuation in SPECT imaging. IEEE Trans Med Imaging 13:363–374

Goerres GW, Kamel E, Heidelberg TNH et al (2002) PET-CT image co-registration in the thorax: influence of respiration. Eur J Nucl Med 29:351–360

Hendel RC, Berman DS, Cullom SJ et al (1999) Multicenter clinical trial to evaluate the efficacy of correction for photon attenuation and scatter in SPECT myocardial perfusion imaging. Circulation 99:2742–2749

Hendel RC, Corbett JR, Cullom SJ et al (2002) The value and practice of attenuation correction for myocardial perfusion SPECT imaging: a joint position statement from the American Society of Nuclear Cardiology and the Society of Nuclear Medicine. J Nucl Cardiol 9:135–143

Herman GT (1980) Image reconstruction from projections, the fundamentals of computerized tomography. New York, NY, Academic Press

Hsiao IT, Rangarajan A, Gindi G (2003) A new convex edge-preserving median prior with applications to tomography. IEEE Trans Med Imaging 22:580–585

Huang SC, Phelps ME (1986) In: Phelps ME, Mazziotta JC, Schelbert HR (eds) Positron emission tomography and autoradiography. Raven Press, New York, pp 287–346

Hudson HM, Larkin RS (1994) Accelerated image reconstruction using ordered subsets of projection data. IEEE Trans Med Imaging 13:601–609

Huesman RH (1984) A new fast algorithm for the evaluation of regions of interest and statistical uncertainty in computed tomography. Phys Med Biol 29:543–552

Hutton BF, Lau YH (1998) Application of distance-dependent resolution compensation and post-reconstruction filtering for myocardial SPECT. Phys Med Biol 43:1679–1693

Hutton BF, Osiecki A, Meikle SR (1996) Transmission-based scatter correction of 180 degrees myocardial single-photon emission tomographic studies. Eur J Nucl Med 23:1300–1308

Iida H, Narita Y, Kado H et al (1998) Effects of scatter and attenuation correction on quantitative assessment of regional cerebral blood flow with SPECT. J Nucl Med 39:181–189

Jang S, Jaszczak RJ, Tsui BMW et al (1998) ROC evaluation of SPECT myocardial lesion detectability with and without single iteration non-uniform Chang attenuation compensation using an anthropomorphic female phantom. IEEE Trans Nucl Sci 45:2080–2088

Jaszczak RJ, Greer KL, Floyd CE et al (1984) Improved SPECT quantification using compensation for scattered photons. J Nucl Med:25:893–900

Kamel E, Hany TF, Burger C et al (2002) CT vs ^{68}Ge attenuation correction in a combined PET/CT system: evaluation of the effect of lowering the CT tube current. Eur J Nucl Med 29:346–350

Karp JS, Becker AJ, Matej S et al (1998) Data processing and image reconstruction methods for the HEAD PENN-PET scanner. Phys Med Biol 45:1144–1151

Kaufman L (1987) Implementing and accelerating the EM algorithm for positron emission tomography. IEEE Trans Med Imaging MI-6:37–51

Kinahan PE, Rogers JG (1989) Analytic three-dimensional image reconstruction using all detected events. IEEE Trans Nucl Sci NS-36:964–968

Kinahan PE, Townsend DW, Beyer T et al (1998) Attenuation correction for a combined 3D PET/CT scanner. Med Phys 10:2046–2053

King MA, de Vries DJ, Pan TS et al (1997) An investigation of the filtering of TEW scatter estimates used to compensate for scatter with ordered subset reconstructions. IEEE Trans Nucl Sci 44:1140–1145

King MA, Schwinger RB, Penney BC et al (1986) Digital restoration of indium-111 and iodine-123 SPECT images with optimized Metz filters. J Nucl Med 27:1327–1336

King MA, Tsui BMW, Pan TS et al (1996) Attenuation compensation for cardiac single-photon emission computed tomographic imaging: 2. Attenuation compensation algorithms. J Nucl Cardiology 3:55–64

Kohli V, King MA, Glick SJ et al (1998) Comparison of frequency-distance relationship and Gaussian-diffusion-based methods of compensation for distance-dependent spatial resolution in SPECT imaging. Phys Med Biol 43:1025–1037

Kotzerke J, Gulmann A, Moog F et al (1999) Role of attenuation correction for fluorine-18 fluorodeoxyglucose positron emission tomography in the primary staging of malignant lymphoma. Eur J Nucl Med 16:31–38

Kyme AZ, Hutton BF, Hatton RL, et al (2003) Practical aspects of a data-driven motion correction approach for brain SPECT. IEEE Trans Med Imag 22:722–729

LaCroix KJ, Tsui BMW, Frey EC, Jaszczak RJ (2000) Receiver operating characteristic evaluation of iterative reconstruction with attenuation correction in ^{99m}Tc-sestamibi myocardial SPECT images. J Nucl Med 41:502–513

Lalush DS, Tsui BM (1993) A generalized Gibbs prior for maximum a posteriori reconstruction in SPECT. Phys Med Biol 38:729–741

Lange K, Carson R (1984) EM reconstruction algorithms for emission and transmission tomography. J Comp Assist Tomogr 8:306–316

Lartizien C, Kinahan PE, Swensson R et al (2003) Evaluating image reconstruction methods for tumor detection in 3-dimensional whole-body PET oncology imaging. J Nucl Med 44:276–290

Leahy R, Qi J. (2000) Statistical approaches in quantitative positron emission tomography. Stat Comput 10:147–165

Lee KJ,and Barber DC (1998) Use of forward projection to correct for patient motion during SPECT imaging. Phys. Med. Biol. 43:171–187

Lewitt RM (1992) Alternatives to voxels for image representation in iterative reconstruction algorithms. Phys Med Biol 37:705–716

Lewitt RM, Matej S (2003) Overview of methods for image reconstruction from projections in emission computed tomography. Proceedings of the IEEE, 10:1588–1611

Liow JS; Strother SC (1993) The convergence of object dependent resolution in maximum likelihood based tomographic image reconstruction. Phys Med Biol 38:55–70

Lipinski B, Herzog H, Rota Kops E et al (1997) Expectation maximization reconstruction of positron emission tomography images using anatomical magnetic resonance information. IEEE Trans Med Imaging 16:129–136

Llacer J, Veklerov E (1989) Feasible images and practical stopping rules for iterative algorithms in emission tomography. IEEE Trans Med Imaging 8:186–193

Lonneux M, Borbath I, Bol A et al (1999) Attenuation correction in whole-body FDG oncological studies: the role of statistical reconstruction. Eur J Nucl Med 16:591–598

Lopresti BJ, Russo A, Jones WF et al (1999) Implementation and performance of an optical motion tracking system for high resolution brain PET imaging. IEEE Trans Nucl Sci 46:2059–2067

Manglos SH, Gagne GM, Bassano DA (1993) Quantitative analysis of image truncation in focal-beam CT. Phys Med Biol 38:1443–1457

Manglos SH, Gagne GM, Krol A, et al (1995) Transmission maximum-likelihood reconstruction with ordered subsets for cone beam CT. Phys Med Biol 40:1225–1241

Matej S, Lewitt RM (1996) Practical considerations for 3-D image reconstruction using spherically symmetric volume elements. IEEE Trans Med Imaging 15:68–78

Matsunari I, Boning G, Ziegler SI et al (1998) Effects of misalignment between transmission and emission scans on attenuation-corrected cardiac SPECT. J Nucl Med 39:411–416

Matsumoto N, Berman DS, Kavanagh PB, et al (2001) Quantitative assessment of motion artifacts and validation of a new motion-correction program for myocardial perfusion SPECT. J Nucl Med 42:687–694

McCarthy AW, Miller MI (1991) Maximum likelihood SPECT in clinical computation times using mesh-connected parallel computers. IEEE Trans Med Imaging 10:426–436

McCord ME, Bacharach SL, Bonow RO et al. (1992) Misalignment between PET transmission and emission scans: its effect on myocardial imaging. J Nucl Med 33:1209–1214

Meikle SR, Dahlbom M, Cherry SR (1993) Attenuation correction using count-limited transmission data in positron emission tomography. J Nucl Med 34:143–144

Meikle SR, Matthews JC, Cunningham VJ et al. (1998) Parametric image reconstruction using spectral analysis of PET projection data. Phys Med Biol 43:651–666

Michel C, Bol A, De Volder AG, Goffinet AM (1989) Online brain attenuation correction in PET: towards a fully automated data handling in a clinical environment. Eur J Nucl Med 15:712–718

Müller-Gärtner HW, Links JM, Prince JL, et al (1992) Measurement of radiotracer concentration in brain gray matter using positron emission tomography: MRI-based correction for partial volume effects. J Cereb Blood Flow Metab 12:571–583

Mumcuoglu EU, Leahy RM, Cherry SR (1996) Bayesian reconstruction of PET images: methodology and performance analysis. Phys Med Biol 41:1777–1807

Narita Y, Iida H, Eberl S et al (1997) Monte Carlo evaluation of accuracy and noise properties of two scatter correction methods for Tl-201 cardiac SPECT. IEEE Trans Nucl Sci 44:2465–2472

Nuyts J, De Man B, Dupont P et al (1998) Iterative reconstruction for helical CT: a simulation study. Phys Med Biol 4:729–737

Nuyts J, Dupont P, Van den Maegdenbergh V et al (1995) A study of the liver-heart artifact in emission tomography. J Nucl Med 36:133–139

Nuyts J, Bequé D, Dupont P, Mortelmans L (2002) A concave prior penalizing relative differences for maximum-a-posteriori reconstruction in emission tomography. IEEE Trans Nucl Sci 49:56–60

Nuyts J, Baete K, Dupont P (2003) Comparison between MAP and post-processed ML for incorporating anatomical knowledge in emission tomography. Proc IEEE Nuc Sci Symp Med Im Conf. To appear. 1271, M5–2

Nuyts J, Fessler JA (2003) A penalized-likelihood image reconstruction method for emission tomography, compared to

post-smoothed maximum-likelihood with matched spatial resolution. IEEE Trans Med Imaging 22:1042–1052
Obi T, Matej S, Lewitt RM, Herman GT (2000) 2.5-D simultaneous multislice reconstruction by series expansion methods from Fourier-rebinned PET data. IEEE Trans Med Imaging 19:474–484
Ogawa K, Harata Y, Ichihara T et al (1991) A practical method for position-dependent Compton scatter correction in single photon emission CT. IEEE Trans Med Imaging 10:408–412
Ollinger JM (1996) Model-based scatter correction for fully 3D PET. Phys Med Biol 41:153–176
Pluim JPW, Maintz JBA, Viergever MA (2003) Mutual-information-based registration of medical images: a survey. IEEE Trans Med Imaging 8:986–1004
Qi J, and Leahy R (1999) A theoretical study of the contrast recovery and variance of MAP reconstructions form PET Data. IEEE Trans Med Imag 18:293–305
Qi J (2004) Analysis of lesion detectability in Bayesian emission reconstruction with nonstationary object variability. IEEE Trans Med Imaging, to appear
Rangarajan A, Hsiao IT, Gindi G (2000) A Bayesian joint mixture framework for the integration of anatomical information in functional image reconstruction. J Math Imag Vision 12:119–217
Raylman RR, Hutchins GD, Beanlands RSB et al. (1994) Modeling of carbon-11-acetate kinetics by simultaneously fitting data from multiple ROIs coupled by common parameters. J Nucl Med 35:1286–1291
Rockmore AJ, Macovski A (1976) A maximum likelihood approach to emission image reconstruction from projections. IEEE Trans Nucl Sci NS-23:1428–1432
Sarikaya I. Yeung HWD, Erdi Y et al (2003) Respiratory artefact causing malpositioning of liver dome lesion in right lower lung. Clin Nucl Med 28:942–944
Sastry S, Carson RE (1997) Multimodality Bayesian algorithm for image reconstruction in positron emission tomography: a tissue composition model. IEEE Trans Med Imaging 16:750–761
Schiepers C, Nuyts J, Wu C et al. (1997) PET with F-18 fluoride: effects of iterative versus filtered backprojection reconstruction on kinetic modeling. IEEE Trans Nucl Sci 44:1591–1593
Schmidlin P (1972) Iterative separation of sections in tomographic scintigrams. Nuklearmedizin 11:1–16
Shepp LA, Vardi Y (1982) Maximum likelihood reconstruction for emission tomography. IEEE Trans Med Imaging MI-1:113–122
Slijpen ETP, FJ Beekman FJ (1999) Comparison of post-filtering and filtering between iterations for SPECT reconstruction. IEEE Trans Nucl Sci 46:2233–2238
Snyder DL, Miller MI (1985) The use of sieves to stabilize images produced with the EM algorithm for emission tomography. IEEE Trans Nucl Sci NS-32:3864–3872
Snyder DL, Miller MI, Thomas LJ et al (1987) Noise and edge artifacts in maximum likelihood reconstructions for emission tomography. IEEE Trans Med Imaging MI-6:228–238
Stayman JW, Fessler JA (2003) Compensation for nonuniform resolution using penalized-likelihood reconstruction in space-variant imaging systems. IEEE Trans Med Imaging, in press
Stonestrom JP, Alvarez RE, Macovski A (1981) A framework for spectral artifact corrections in X-ray CT. IEEE Trans Biomedical Engineering BME-28:128–141
Surti S, Karp JS, Muehllehner G et al (2003) Investigation of lanthanum scintillators for 3-D PET. IEEE Trans Nucl Sci 50:348–354
YC Tai, KP Lin, M Dahlbom, EJ Hoffman (1996) A hybrid attenuation correction technique to compensate for lung density in 3D total body PET. IEEE Trans Nucl Sci 43:323–330
Tanaka E (1987) A fast reconstruction algorithm for stationary positron emission tomography based on a modified EM algorithm. IEEE Trans Med Imaging MI-6:98–105
Veklerov E, Llacer J (1987) Stopping rule for the MLE algorithm based on statistical hypothesis testing. IEEE Trans Med Imaging; MI-6:313–319
Visvikis D, Costa DC, Croasdale I (2003) CT-based attenuation correction in the calculation of semi-quantitative indices of [[sup 18] F]FDG uptake in PET. Eur J Nucl Med Mol Imaging 30:344–353
Vogel WV, Oyen WJG, Barentsz OJ et al (2004) PET/CT: panacea, redundancy, or something in between? J Nucl Med 45:15S–24S
Walrand SHM, van Elmbt LR, Pauwels S (1994) Quantitation in SPECT using an effective model of the scattering. Phys Med Biol 39:719–734
Wang W, and Gindi G (1997) Noise analysis of MAP-EM algorithms for emission tomography. Phys Med Biol 42:2215–2232
Watson CC, Newport D, Casey ME et al (1997) Design and performance of collimated coincidence point sources for simultaneous transmission measurements in 3-D PET . IEEE Trans Nucl Sci 44:90–97
Welch A, Gullberg GT (1997) Implementation of model-based nonuniform scatter correction scheme for SPECT. IEEE Trans Med Imaging 16:717-726
Wells RG, Celler A, Harrop R (1997) Experimental validation of an analytical method of calculating SPECT projection data. IEEE Trans Nucl Sci 44:1283–1290
Wilson DW, Tsui BMW, Barrett HH (1994) Noise properties of the EM algorithm: II. Monte Carlo simulations. Phys Med Biol 39:833–846
Wu HM, Huang SC, Allada et al. (1996) Derivation of input function from FDG-PET studies in small hearts. J Nucl Med 37:1717–1722
Xia W, Lewitt RM, Edholm PR (1995) Fourier correction for spatially variant collimator blurring in SPECT. IEEE Trans Med Imaging 14:100–115
Xu M, Cutler PD, Luk WK (1996) Adaptive, segmented attenuation correction for whole-body PET imaging. IEEE Trans Nucl Sci 43:331–336
Yang JT, Yamamoto K, Sadato N et al (1997) Clinical value of triple-energy window scatter correction in simultaneous dual-isotope single-photon emission tomography with I-123-BMIPP and Tl-201. Eur J Nucl Med 24:1099–1106
Zhou Y, Cloughesy T, Hoh CK et al (1997) A modeling-based factor extraction method for determining spatial heterogeneity of Ga-68 EDTA kinetics in brain tumors. IEEE Trans Nucl Sci 44:2522–2527

Future Outlook

18 Imaging Gene Expression: Concepts and Future Outlook

Meike L. Schipper and Sanjiv Sam Gambhir

CONTENTS

M. L. Schipper, MD
S. S. Gambhir, MD, PhD, Director and Professor
Molecular Imaging Program at Stanford (MIPS), Department of Radiology and Bio-X Program, Division of Nuclear Medicine, The James H. Clark Center, 318 Campus Drive, East Wing, First Floor, E150A, Stanford, CA 94305-5427, USA

18.1 Introduction

Advances in molecular biology are making it possible to develop assays for imaging specific molecular processes, including those directly related to gene expression. Imaging gene expression entails determining the location(s) of those cells expressing a particular gene of interest, as well as monitoring the magnitude and persistence of gene expression. The gene of interest may be an endogenous gene or it may be an "exogenous" gene introduced into the organism/tissue(s) of interest. Imaging gene expression with generalized approaches applicable to any gene of interest has recently been reported. Conventional nuclear imaging techniques can be used to image gene expression if a radiolabeled substrate can be developed to interact with the protein of the gene of interest. However, more general methods are emerging to image gene expression without the need for developing new radiolabeled substrates for each new gene of interest.

In this chapter two general approaches for imaging gene expression are reviewed. The first approach uses an antisense oligodeoxynucleotide targeted towards the messenger ribonucleic acid (mRNA) of a gene of choice. The second approach uses a reporter gene to track the expression of an endogenous or exogenous gene. Methods to introduce genes into

target tissue(s) are presented. Principles and applications of assays for imaging gene expression in animals and in human clinical gene therapy trials are also presented and discussed.

18.2 Fundamentals of Gene Expression

The process of gene expression (Fig. 18.1) and the components of gene regulation are only partially understood and are reviewed in detail elsewhere (Lewin 1994). Not all genes are expressed in all cells, leading to a wide variety of cellular functions or phenotypes. Many phenomena, including cellular development, maturation, proliferation, and oncogenesis can be attributed to the differential expression of genes. As advances in molecular and cell biology lead to a better understanding of the mechanisms leading to altered cellular functions, imaging assays may be able to allow imaging of these alterations in living animals and humans.

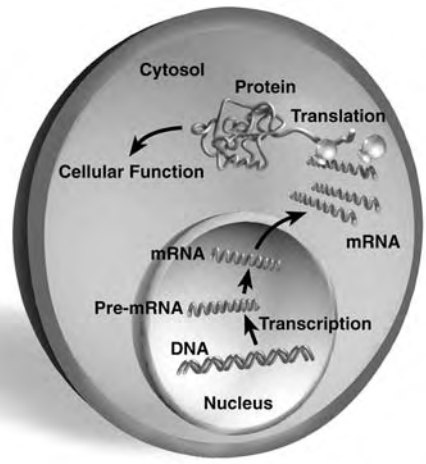

Fig. 18.1. Gene expression. Transcription of DNA in the nucleus leads to the synthesis of pre-messenger RNA (pre-mRNA), which is then processed into mRNA, transported into the cytoplasm, and translated into protein. The final protein product may serve as an enzyme, cell surface receptor, structural component, etc. Conventional targets for in vivo nuclear imaging have been aimed at the protein level. Newer targets for gene expression include mRNA through the use of small modified antisense oligodeoxynucleotides

18.2.1 Gene Promoters/Enhancers

Specific sequence motifs about 100 nucleotide bases from the transcription initiation start site are referred to as the promoter region of the gene. The promoter is directly involved in RNA polymerase (a RNA synthesizing enzyme) binding and the initiation of transcription. Eukaryotic promoters do not always function alone, but can be influenced by enhancers. The position of the enhancer can be quite variable and can be upstream or downstream from the location of the promoter, and sometimes the enhancer is located within the transcription unit itself. The enhancer can increase the efficiency of initiation or be involved in specific regulation of a given gene. A complex of proteins and RNA polymerase are involved in the transcription process, which begins by interactions with the promoter. For the purposes of imaging gene expression, two main types of promoters need to be described. Constitutive promoters can be used to produce continuous transcription of a gene, and inducible promoters can be used to provide external control for varying the levels of transcription. Constitutive promoters can be those of exogenous genes (e.g., cytomegalovirus, CMV) or those of endogenous genes (e.g., GAPDH, a protein made in all cells). Inducible promoters can also be those of exogenous genes (e.g., tetracycline regulable) or those of endogenous genes (e.g., c-jun).

18.3 Imaging Technology for Monitoring Gene Expression in Animals

The mouse has long been used by molecular biologists to study fundamental cellular events in vivo. The relatively small size of the mouse makes it difficult to image using conventional imaging technology. Noninvasive imaging of mice/rats in vivo is now possible using microPET technology recently developed at the Crump Institute for Biological Imaging (Cherry et al. 1997). This new PET scanner design facilitates imaging of small animals with a volumetric resolution of 2^3 mm^3 [a significant advantage over current systems with a resolution of $(4–6)^3$ mm^3]. The microPET system and others like it should significantly improve over the next several years, facilitating even better resolution and dynamic imaging capabilities. The next

generation of microPET technology has a goal of improving volumetric resolution by another factor of ~10. Anatomical imaging with MRI and combined PET and MRI imaging with joint PET/MRI systems (Shao et al. 1997), and animal SPECT systems (Kastis et al. 1998; Sharma et al. 2002) should also further facilitate the development of various imaging assays.

18.4 Targets for Imaging Gene Expression

In order to image gene expression, one could attempt to image: (1) whether transcription has occurred, or (2) whether transcription and translation have occurred. Potential targets for imaging gene expression include proteins on the cell surface, intracellular proteins, RNA (pre-mRNA, mRNA, other RNA) and least likely DNA (by targeting open transcription complexes). For both an endogenous gene and an administered (exogenous) gene, the same types of probes can be used to image gene expression. Targeting DNA is particularly difficult because of the limited number of copies present within a cell, as well as limited accessibility to the target DNA sequence. Targeting of RNA and proteins is possible and is discussed in detail in upcoming sections.

18.4.1 Conventional Probes Targeted for Proteins

Conventional radiotracer imaging methods have focused primarily on the final products of gene expression by utilizing radiolabeled substrates that interact with the proteins originating from specific genes. These interactions are based on either receptor-radioligand binding (e.g., binding of the dopamine 2 receptor to 3-(2'-[^{18}F]-Fluoro-ethyl)-spiperone [^{18}F]FESP) or enzyme mediated trapping of a radiolabeled substrate (e.g., [^{18}F]-2-fluoro-2-deoxyglucose ([^{18}F]FDG) phosphorylation by hexokinase). The fundamental limitation of a majority of these conventional approaches is that new substrates must be discovered and radiolabeled for each new protein to be targeted. Due to the difficulty of radiolabeling new substrates, and characterizing all their interactions in vivo, alternate methods are needed in order to develop new assays that can categorically image gene expression of any gene of interest.

18.4.2 Antibody and Antibody Fragments Targeted for Proteins

For imaging gene expression, one could potentially develop an antibody targeted against the protein product of the gene. The antibody could then be radiolabeled non-specifically using the same methodology, regardless of the antibody type. The antibody approach, however, is predominantly limited to genes whose products are proteins that have a component on the cell surface. Most genes lead to protein products that remain in the intracellular space, and would therefore be difficult to target with an antibody based approach. In addition, high background signal due to the slow clearance of antibodies from the blood pool, and an immune response to them, limits their overall utility (Goldenberg 1997). Newer molecularly engineered antibody fragments that are smaller in size, with rapid targeting and fast blood clearance, may help resolve existing problems with conventional antibody approaches. These antibody fragments can be constructed by retaining the active binding site of the antibody [e.g., Fab and F(ab')$_2$], and removing the Fc region leading to lower immunogenicity. A very small antibody fragment (e.g., a "minibody") has also been developed. An example of this category is an antibody fragment targeted against carcinoembryonic antigen (CEA) with useful in vivo properties of rapid targeting and fast blood clearance (Sundaresan et al. 2003). It has been shown to detect colon cancer in human subjects (Wong et al. 2004). So called diabodies, i.e. dimers of single chain Fvs, have also shown promise as imaging agents due to high affinity for target antigen, rapid, high-level accumulation in xenografts in murine models and quick clearance from the circulation resulting in high tumor to normal activity ratios, and potentially less immunogenicity than intact murine or even chimeric antibodies when administered to humans (Olafsen et al. 2004). If general labeling strategies can be applied to the various antibody fragments, then these engineered antibodies may be useful for imaging gene expression for those genes leading to protein products that have a component at the cell surface.

18.4.3 Oligodeoxynucleotide Antisense Probes Targeted for mRNA

In order to image transcription directly, one has to develop tracers that can interact with pre-mRNA or

mRNA. Assays for imaging mRNA levels are currently being investigated through the use of small (12–35 nucleobases long) modified radiolabeled "antisense" oligodeoxynucleotide (RASON) probes targeted toward a specific mRNA (Fig. 18.2). This RASON "antisense" probe is complementary to a small segment of target mRNA. RASON probes have the potential for imaging gene expression specifically at the transcription level. The RASON must be stable against degradation from nucleases, be able to enter and efflux from cells, and be of sufficient specific activity to detect relatively low levels of mRNA. The antisense method is a general approach, because the RASON probe sequence could easily be modified in order to target many mRNAs of interest. RASONs have the distinct advantage of easy modification (by changing the sequence of bases) in order to target a new mRNA.

The pharmaceutical industry has been investigating both DNA and mRNA as targets for antisense drugs for over a decade (Crooke and Lebleu 1993; Agrawal and Iyer 1997; Crooke 1997). DNA is an ideal target for a drug, because by binding of an antisense drug to a specific gene (via Hoogsteen base pairing in the major groove) one could theoretically prevent the production of mRNA, and therefore stop protein production. For diseases in which stopping the production of an aberrant protein is beneficial,

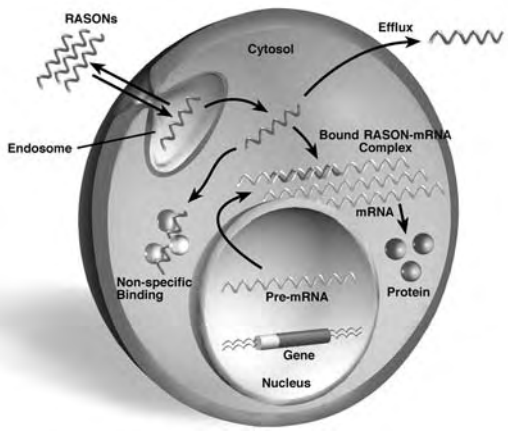

Fig. 18.2. Radioactive antisense oligodeoxynucleotides (RASONs) as probes for imaging gene expression. RASON probes can be designed to target a specific mRNA of a gene of interest. The RASON must be able to enter cells, hybridize to target mRNA. Intracellular RASONs are likely to be in endosomes, and must be able to leave the endosome prior to interaction with target mRNA. Non-specific interactions with proteins as well as efflux out of the cell are key processes which must be considered for developing RASONs as effective probes for imaging gene expression. The target mRNA may be that of an endogenous gene or an administered gene

this approach holds significant promise. Companies that focus specifically on the development and testing of antisense drugs (e.g., Isis Pharmaceuticals, Carlsbad, CA) targeted towards various mRNAs are now testing third-generation antisense drugs. However to date, clinical trials using antisense drugs have met with limited success (reviewed in Pirollo et al. 2003). Progress towards developing more stable antisense oligodeoxynucleotides with improved uptake, issues of cellular efflux, characterization of biodistribution, and the understanding of appropriate controls is important for developing RASON probes. Much of what may be possible with imaging applications utilizing RASON probes is dependent on the significant progress on antisense pharmaceuticals made by the pharmaceutical industry over the last decade.

Of the two choices, DNA and mRNA, only mRNA is a good target for developing an assay for imaging endogenous gene expression. Every cell has the DNA (gene) of interest, but only cells in which the gene has been transcribed have the mRNA of interest. Messenger RNA concentrations are typically in the range of 1–1000 pM (Hargrove et al. 1990). Messenger RNA molecules are ideal targets due to their ability to very specifically pair with antisense oligonucleotides through hydrogen bonds. The binding affinity of antisense drugs for mRNA is very high, but a single mismatch can drop the affinity by as much as 300-fold (Crooke and Lebleu 1993). It has been mathematically shown that a minimum of only 11–15 bases need to be targeted in order to hybridize uniquely to any mRNA in the human genome (Helene and Toulme 1989). This calculation is based on assuming that 0.5% of the human genome is expressed as mRNA. The two numbers correspond to the extreme cases where the oligonucleotide contains only C and G (n=11) or only A and T (n=15). Therefore, an antisense probe of relatively short length can be used to target a given mRNA (Fig. 18.3).

Messenger RNA molecules are typically several hundred to thousands of base pairs long, but not all of these bases are accessible to an antisense probe due to the secondary and tertiary structure of the mRNA molecule. Intracellular mRNA is invariably protein bound, and only a few sites are probably available for base pairing. The location of the best targets for the antisense mRNA approach has been pursued in detail (Goodchild 1989). The main findings are that in general, the best mRNA locations are the 5' cap or initiation codon (AUG) regions. There are, however, exceptions to this rule and the tertiary

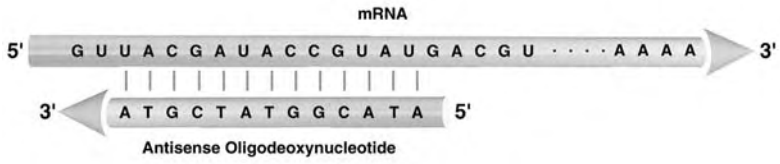

Fig. 18.3. Hybridization of an antisense oligodeoxynucleotide probe with a target mRNA. The antisense probe has a very high specificity for a target mRNA sequence. Although the mRNA can contain hundreds to thousands of bases, an antisense probe of small length (11–15 bases) can uniquely target any mRNA. *A*, adenine; *T*, thymidine, *G*, Guanine; *C*, cysteine

structure of the mRNA must be considered in order to predict potential binding sites. It is important not to generalize mRNA regions that are useful for targeting; instead for each mRNA careful studies must be performed in order to identify good target sites.

Since mRNA-antisense probe interaction is stoichiometric, and therefore equivalent to a receptor-ligand interaction, one can attempt to answer questions about the minimal levels of mRNA that can be detected by a given antisense probe. Variables such as the concentration of target mRNA, binding affinities of receptor and ligand, antisense probe specific activity, free intracellular antisense tracer concentration, sensitivity of detection (typically only 0.5%–2% of annihilation events are detected by PET), and target to background levels all play key roles. Based on these parameters it has been estimated that mRNA concentrations as low as 1 pM tissue can probably be imaged with PET, using RASON probes with specific activities of ~1,000–10,000 Ci/mmol (Pan et al. 1998).

Oligonucleotides are readily cleaved by nucleases in vivo (Wickstrom 1986). A non-hydrolysable analogue of an oligonucleotide is therefore required so that sufficient amounts can reach the target in effective concentrations. Oligodeoxynucleotides are more stable in vivo when compared with oligoribonucleotides (Wickstrom 1986), and are therefore the probes of choice. Various investigators have investigated modified oligodeoxynucleotides (e.g., phosporothioates) for greater stability against degradation (Matsukura et al. 1978; Murakami et al. 1985; Agrawal and Iyer 1997) (Fig. 18.4). Additional modifications that confer stability are alpha oligodeoxynucleotides, as well as 2' modified moieties (Crooke 1997), such as 2`O-Methyl oligoribonucleotides, which are more resistant to nucleases and are efficient at dimerizing with their RNA counterparts. 3' end modifications may be particularly useful in preventing exonuclease-based degradation. For a more comprehensive review of modifications, please refer to Kurreck (2003). Polypeptide nucleic acids (PNAs) (Good and Nielsen 1997), in which nucleobases are attached to a pseudopeptide, have also been explored as potential drugs, but they may suffer from little to no cellular uptake. PNAs do however have improved stability against nucleases, and may even have enhanced sequence selectivity for target mRNA. PNAs have been successfully employed for imaging gene expression in the brain (Shi et al. 2000; Lee et al. 2002). Targeting to brain tumors was achieved by conjugating the PNA to antibodies directed against the transferrin receptor, which is abundantly expressed both on the brain capillary endothelium, which forms the blood–brain barrier, and tumor cell membranes (Suzuki et al. 2004). Non-viral gene delivery systems such as cationic liposomes, charged lipids, synthetic polymers, or non-viral vectors are being evaluated to increase extracellular stability and cellular uptake of oligonucleotides (Shoji and Nakashima 2004)and will be discussed below.

Uptake of oligonucleotides by cells appears to occur via several mechanisms. The surprising and essential feature is that oligonucleotides are readily taken up by many different cells. This uptake is critical to insure that a probe can be delivered to the intracellular target mRNA by injection into the venous plasma space. Most oligonucleotides (except methylphosphonates) are polyanionic and do not passively diffuse across cell membranes. Transport mechanisms include receptor mediated endocytosis, adsorptive endocytosis, as well as fluid-phase pinocytosis (Loke et al. 1989; Wu-Pong et al. 1992, 1994; Cotten et al. 1993). There is a fast component as well as a slow component of uptake. A ~80-kD protein has also been isolated from several cell types that seems to be responsible for oligodeoxynucleotide binding and possible internalization (Loke et al. 1989; Cotton et al. 1993). The exact transport mechanism seems to be different for various cell types. There have been some preliminary attempts to model oligonucleotide cell transport (Wu-Pong et al. 1992), but no mathematical model is currently available. It is likely that non-diffusible oligodeoxynucleotides end up in cellular endosomes, but it is

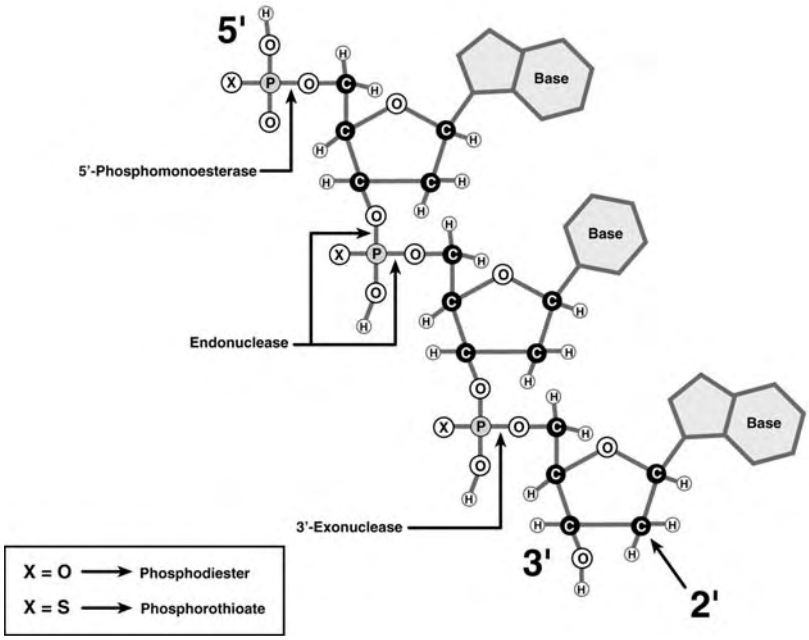

Fig. 18.4. Structure of an oligodeoxynucleotide. Shown is a trimer. The ribose sugars are interlinked through a backbone composed of phosphodiester bonds. The backbone can be modified in order to achieve greater stability against degradation from nucleases. Phosphorothioates have significant increased stability as compared to phosphodiesters. 2′ modification of the ribose can also lead to more stable oligodeoxynucleotides. Degradation sites are as indicated

not clear how they leave the endosomes or the efflux rate from endosomes. Several groups have shown that exogenously administered oligonucleotides appear to localize readily in the nucleus, mitochondria or both (Wu-Pong et al. 1992). The degree of controversy surrounding uptake mechanism and subcellular fate of oligonucleotides likely indicates the presence of several different complex pathways, depending, on cell type, oligonucleotide composition, and potentially further factors (Thierry et al. 2003).

The oligonucleotide, once inside the cell, must be able to bind to the target mRNA, and excess unhybridized oligonucleotide must also be able to leave cells during the time in which the oligonucleotide and target mRNA complex is stable. Charged oligonucleotides can nonspecifically interact with intracellular proteins. This may lead to nonspecific binding, and the potential inhibition of oligonucleotide internalization (Loke et al. 1989). To obtain sufficient specificity of the image signal, the rates of exocytosis and mRNA binding must exceed the rate of nonspecific binding. Exocytosis follows a multi-compartmental model, with a rapid phase (half-life of 10 min) as well as a slower phase (half-life of 30 min) in some cases, but varies depending on the cell type and the type of oligodeoxynucleotide. Truncated fragments as well as chain extension products efflux from cells. Some studies have reported desired pharmacological effects of a decrease in protein production with non-antisense oligodeoxynucleotides; this may be due to interaction of the drug with proteins. It is important that a true antisense mechanism be demonstrated by using controls with sequentially increasing number of nucleobase mismatches, before proceeding with in vivo studies. As the number of mismatches in bases increases, the binding to target mRNA should decrease. Without these appropriate controls, it is possible that non-specific binding of oligodeoxynucleotide to protein(s) is leading to a desired effect (e.g., reduction in protein production).

Numerous investigators have explored the use of antisense oligonucleotides, both in vitro and in vivo, as therapeutic agents for decreasing protein production (Stein and Cheng 1993). For the first time, an antisense oligonucleotide drug has been approved by the FDA, targeting CMV retinitis in patients with HIV (2002). Also, the number of clinical trials including phase 3 trials has increased steeply in the last years. Approaches include targeting the 35S RNA of the Rous sarcoma virus (Zamecnik and Stephenson 1978), various mRNAs for use against HIV (Zamecnik et al. 1986), as well as many oncogene mRNA's including c-myc, bcl-2, Raf-1, H-Ras, and many others. Preclinical studies involve telomerases, MDM2, Her-2, and IGF-IR [for review of antisense oligonucleotide therapy, please refer to Pirollo et al. (2003)]. Diseases targeted by antisense therapy approaches include cancer (Kalota et al. 2004), renal (Tomita et al. 2004), CNS (Jaeger and Banks 2004), and cardiovascular disease (Tomita and Morishita 2004). Most of this work has shown

that antisense oligonucleotides can work effectively in suppressing mRNA translation. After binding of oligodeoxynucleotide to target mRNA, the mRNA can be digested by ribonuclease H. Direct translation inhibition can also occur. In either case, the net result is a direct decrease in translation of mRNA and production of protein product.

Biodistribution of oligodeoxynucleotides in normal animals has been reported (Crooke 1995). Phosphorothioate oligonucleotides, for example, bind to serum proteins (~400 μM dissociation constant for albumin). The plasma disappearance is extremely rapid, and is well described by a two-compartment model. A large volume of distribution (~20 ml with a dose of 3.6 mg/kg) is observed for phosphorothioates demonstrating a widespread distribution to many tissues in vivo. Peaks of blood activity occur within 2–4 h after bolus injection. The kidneys and liver have the greatest concentrations, with no significant penetration across the blood–brain-barrier. Natural phosphodiester oligonucleotides are very rapidly degraded to monomers in vivo, and would probably have limited use for targeting gene expression. Animal whole-body autoradiography has also been used to assess the biodistribution of various radiolabeled oligodeoxynucleotides (see for example: Phillips et al. 1997). Biodistribution studies based on noninvasive PET imaging of ^{18}F and ^{68}Ga labeled antisense oligonucleotides were published (Tavitian et al. 1998; Roivainen et al. 2004). However, biodistribution of oligonucleotides depends on the composition of the backbone and on the labeling method (Zhang et al. 2000). One cannot, thus, generalize findings from single biodistribution studies to the pharmacokinetics of other oligonucleotides.

Although much can be learned from the development and use of antisense oligodeoxynucleotides as drugs, several distinctions must be kept in mind for using them as imaging probes. First, any isotope labeling modification to the oligodeoxynucleotide must not significantly decrease its stability as well as its cellular influx, efflux, specific interaction, or hybridization ability. Second, the relative rate of hybridization to target mRNA must exceed the net effect of the non-specific interactions and efflux rates. Also, the efflux rate must dominate if no target mRNA is expressed, so as to lead to minimal background signal. The isotope half-life, biological half-life, and specific activity of the RASON are also important parameters to consider when attempting to target a specific mRNA in vivo.

The first RASON probe to be developed specifically for nuclear imaging was an Indium-labeled oligodeoxynucleotide targeted against the amplified c-myc oncogene (Dewanjee et al. 1994). A 15-mer oligonucleotide sequence was synthesized, amino linked (sense and antisense phosphodiester and monothioester) and bound with diethylenetriamine pentaacetate (DTPA) containing ^{111}In. Subsequently, oligodeoxynucleotides labeled with ^{99m}Tc (Hnatowich et al. 1995), ^{131}I, ^{123}I, ^{125}I (Cammilleri et al. 1996), ^{11}C (Younes et al. 2002), and ^{76}Br (Kuhnast et al. 2000), have been reported. Fluorine labeled oligodeoxynucleotides for use with PET (Pan et al. 1998; Tavitian et al. 1998) have been synthesized. As described earlier, it is essential that high specific-activity probes be developed for targeting the lowest possible levels of mRNA. ^{18}F labeling may achieve high specific activities of 1,000–10,000 Ci/mmol, but has the disadvantage of a relatively short isotope half-life of 110 min. ^{68}Ga labeling of oligonucleotides targeting activated human K-ras has been described (Roivainen et al. 2004). In this study, Roivainen et al. analyzed tracer pharmacokinetics in tumor and major organs non-invasively with PET and found considerable variations depending on the oligonucleotide backbone employed.

18.4.4 mRNA Imaging Based on Pre-mRNA Splicing

A novel alternative method of mRNA imaging involves pre-mRNA trans-splicing. This is a pre-mRNA splicing process involving the spliceosome, which occurs naturally in trypanosomes, flatworms and nematodes. This process has been shown to be introducible into mammalian cells (Puttaraju et al. 1999). For review of the mechanism of pre mRNA trans-splicing, see Garcia-Blanco (2003). Briefly, short mRNA molecules are introduced into the cell, which contain the mRNA of an effector or reporter gene and an artificial intron sequence, which recognizes the intron of the gene of interest. If the effector gene mRNA is desired 5' of the mRNA of the target, an artificial intron would be designed which recognizes and binds to the intron of the target in the 5' splice site region. At the same time, the artificial intron offers an alternative 5' splice site to the spliceosome. During the splicing process, the reporter exon is spliced at its 5' splice site to the "natural" 3' splice site of the target mRNA. The resulting mRNA is a hybrid of a 5' effector, or reporter gene, and a 3' target gene mRNA. Transcription of this mRNA will lead to a hybrid protein that may be used for imaging. There

are two major advantages in this technique. First, only a small but likely constant fraction of the pre-mRNA will be trans-spliced. Thus, the danger of disturbing cellular function by mRNA imaging is comparatively low relative to conventional antisense techniques. Second, the reporter mRNA can code for an enzyme, such as firefly Luciferase or HSV1-thymidine kinase (see below). In this case, every hybrid reporter protein is capable of producing multiple molecules of signaling reporter probe, resulting in a strong amplification with multiple signals per targeted mRNA molecule. This will be of special interest when targeting mRNA, which is transcribed at low levels and might not be detectable by conventional antisense oligonucleotides, which only produce one signal per targeted mRNA. This concept has recently been validated in vivo by bioluminescence imaging of renilla luciferase (see below) which was translated from a mRNA resulting from a trans splicing event (Bhaumik et al. 2004). This proof-of-principle study did not image an endogenous mRNA, but imaged the repair of the renilla Luciferase reporter gene. However, it sets the way for true imaging of an endogenous mRNA through trans-splicing.

A second novel approach involves autocatalytic RNA, or so called group I introns. First discovered in the intron of the *Tetrahymena* large (26S) rRNA subunit I, this catalytic RNA, or ribozyme, was shown to catalyze a two step trans-esterification reaction resulting in joining of the two rRNA exons and release of the intron (Rossi 1998). Hasegawa et al. have used this principle in an interesting in vitro imaging application (Hasegawa et al. 2003). The reporter gene beta-lactamase was used to report splicing activity in single living cells and perform high-throughput screening with flow cytometry. By inserting the self-splicing *Tetrahymena thermophila* group I intron ribozyme into the open reading frame of the beta-lactamase mRNA, splicing activity in single living cells could be detected quantitatively and visualized. This was initially done with flow cytometry to screen for mutations with higher splicing efficiency in vitro. However, while *Tetrahymena* ribozyme is cis-splicing, the same concept is applicable to trans-splicing ribozymes as well, as was recently shown (Hasegawa et al. 2004). The method can likely be used for molecular imaging and potentially a variety of other applications, including gene therapy.

While an entirely comprehensive description of the state of the art in antisense technologies is beyond the scope of this chapter, we recommend the following reviews for further reading: Crooke (2004) and Tavitian (2003).

18.4.5 Oligodeoxynucleotide (Aptamer) Probes Targeted for Proteins

Small oligodeoxynucleotide probes can also be used to target proteins in addition to targeting RNA. In this case, the affinity between mRNA and the target molecule is mediated not by nucleotide base pairing, but by three-dimensional steric interactions between the partners. Dissociation constants are in the micromolar to low picomolar range, which is comparable to those of antibody-antigen interactions. In vitro selection, or systematic evolution of ligands by exponential enrichment (SELEX), has been used both to characterize the interaction of natural nucleic acids with proteins and to generate novel nucleic acid-binding species, or aptamers (Conrad et al. 1995; Buerger and Groner 2003; Tavitian 2003). Large libraries of potential aptamers can be screened in order to arrive at a high affinity probe targeted towards a specific protein of interest. Depending on the selection process, aptamers can recognize single or multiple intra- or extracellular targets, including specific proteins, small molecules, or even complex heterogeneous targets such as cells or tissues. Since many aptamers can in theory be transported into the cell, the products of many genes can potentially be targeted. The use of an aptamer targeted towards neutrophil elastase (a surface protein) for in vivo inflammation imaging with a gamma camera has been reported (Charlton et al. 1997). A rat reverse passive Arthus reaction model for inflammation was utilized. The aptamer achieved a peak target-to-background ratio of ~4 in 2 h, with fast blood clearance of the aptamer. More research in this important arena may lead to other imaging applications in which proteins can be targeted with aptamers. This could allow for imaging endogenous gene expression, by developing aptamers targeted towards the protein of the gene of interest. Aptamers have been labeled with ^{99m}Tc for imaging purposes and to investigate aptamer pharmacokinetics (Hicke and Stephens 2000). In a recent study, these authors labeled an aptamer directed against Tenascin C, an extracellular stroma protein present in tumor and neovasculature, with different radiometal chelators and fluorescent reporters for in vivo imaging and biodistribution studies. Due to a long tumor half life and fast clearance from the rest of the body,

^{99m}Tc-labeled aptamers yielded a tumor to blood ratio of 50 at 3 h, and clearly imaged U251 and MDA-MB-435 using a gamma camera (Hicke et al. 2005). The aptamer approach is a potentially exciting new avenue of research and other aptamers specific for targets of interest will now likely be imaged.

18.5 Gene Delivery

For some applications a gene has to be introduced into the organism of interest. Prior to the introduction of any gene, a decision must be made as to what promoter to couple to the gene to drive its transcription. As described in Sect. 18.2.1, the choices include constitutive or inducible promoters based on the intended application.

Ex vivo gene delivery in which target cells are first removed from the host, transfected with a specific gene, and then re-delivered to the host are one possible mechanism for some gene delivery applications. Alternatively, gene delivery can be preformed in vivo by using one of several vectors to deliver the gene into some specific tissue(s) of interest.

Introduction of genes into animals can be accomplished by one of two general methods. Transgenic animals can be made in which every cell in the animal carries the gene of interest (Haider et al. 1998). The transgene can be driven by a constitutive or inducible promoter. Only certain tissues can be made to express this gene, depending on the type of promoter used. Alternatively, a wide variety of non-viral (Rolland 1998) and viral vectors (Miller and Vile 1995) can be used to introduce a gene of interest into target somatic tissue.

Delivery of genes into humans continues to remain a challenge for a wide variety of investigations, and is reviewed in detail elsewhere (Smith 1995). Although not sufficient, a necessary condition for the success of gene therapy in humans will be efficient delivery of the gene(s) of interest into the appropriate target tissue(s). The use of a plasmid (an autonomously replicating DNA molecule) in vivo has been investigated, but is limited by a poor efficiency of transfer into cells. Plasmid vectors can also be delivered by the use of cationic liposomes or lipids, which enhance transfer of genetic material into the cell. The use of adenoviral vectors, retroviral vectors, adeno-associated vectors, and most recently lentiviral vectors are all being pursued and are discussed in upcoming sections. For further reading on gene transfer and therapy, we recommend: De and Gambhir (2002) and Biswal and Gambhir (2004).

When two genes need to be introduced into the same tissue (e.g., a therapeutic gene and a reporter gene for monitoring human gene therapy), it is then preferable to have a system in which a fixed relationship holds between the expressions of both genes. Such fixed expression of two genes is possible through the use of an internal ribosomal entry site (IRES) (Gallardo et al. 1997; Levenson et al. 1998). In this case a single mRNA containing both genes is transcribed (driven by a common promoter of choice), and translation produces both protein products from the same transcript because of the IRES (Fig. 18.5).

18.5.1 Transgenics

Animals in which a specific new or altered gene (driven by a promoter of choice) has been introduced into every cell of the entire organism are referred to as transgenics. The recombinant gene (transgene) is introduced into the fertilized ovum of an animal at the two-cell stage of development. The fertilized ovum is reimplanted into a surrogate female (a pseudo-pregnant mouse primed for implantation), and animals that are born which contain the transgene can be identified. Green et al. (2000) indirectly showed albumin gene expression in transgenic mice, which expressed the herpes

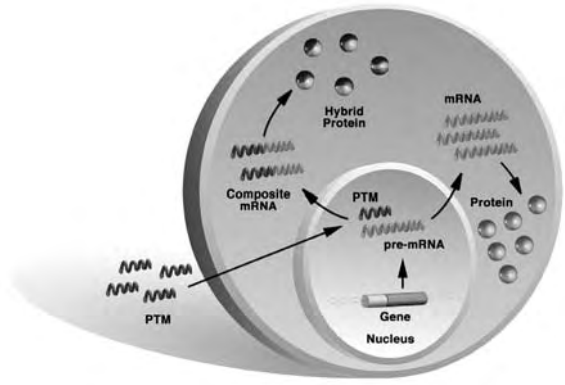

Fig. 18.5. Pre-mRNA tans-splicing. The pre-mRNA trans-splicing molecule (PTM), a short mRNA fragment with a reporter gene and an artificial intron sequence recognizing the intron of the gene of interest, enters the cell. The artificial intron offers an alternative 5' splice site to the spliceosome. The reporter exon is spliced at its 5' splice site to the "natural" 3' splice site of the target mRNA. Transcription of the hybrid mRNA leads to a hybrid protein which is used for imaging

simplex virus-1 thymidine kinase (HSV1-TK, see below) PET reporter gene under the control of the albumin promoter. PET imaging showed uptake of the reporter probe, FHBG, in the liver, going from medium values to basically absent to high values as mice went through dietary phases of medium protein, no protein, and high protein diet. The mouse model has been the most frequently used in transgenics, but other animal models are also possible. More work is still needed to study other endogenous genes using transgenic models carrying one or more reporter genes. Quantitation issues of relating the endogenous gene expression to the reporter gene expression must be pursued in detail.

18.5.2 Non-viral Vectors

DNA containing a gene of interest and its promoter can be injected directly into the blood stream, but as discussed in Sect. 18.4.3, breakdown of DNA by nucleases, immune response to certain DNA sequences, lack of delivery across cell membranes, and, once inside the cell, preferred transport into lysosomes and poor nuclear localization severely limit this approach. The use of a plasmid (an autonomously replicating DNA molecule) in vivo has been investigated, but is limited by the same factors. Plasmid vectors can also be delivered by the use of cationic liposomes, or lipids (Iyer et al. 2002). Like other cationic compounds such as polylysine, polyethyleneimine (PEI), or PEGylated PEI, they enhance stability of the DNA in the extracellular compartment and transfer of genetic material into the cell. Hildebrandt et al. (2003) showed that expression of a firefly luciferase reporter gene was significantly stronger in tumor as compared to normal organs after gene transfer with PEGylated PEI or a transferrin targeted PEI than with PEI alone. Signal from in vivo imaging correlated well with ex vivo enzyme activity measurements (Hildebrandt et al. 2003). These vectors lead to only transient expression of the delivered gene, and are limited in their utility by several factors, as reviewed by Wiethoff and Middaugh (2003).

18.5.3 Adenoviral Vectors

Adenoviral vectors are relatively large (38 Kb) DNA viral vectors. The wild-type adenovirus can be modified by deleting one or more early genes (e.g., E1a, E2, and E3), which are responsible for activation of other genes. Through deletion of one or more of these genes, one can incorporate a segment of DNA that can then be delivered into cells capable of being infected by the adenovirus. The E1a gene is needed for viral replication, but the E2 and E3 genes are not. Additional genes can also be deleted to increase the packaging capacity if needed.

Since the adenoviral vector with the E1a gene deleted cannot replicate, the isolation of high titers of adenovirus requires cells, which express the E1a gene. A total of 293 human kidney cell lines, which constitutively express the E1a protein, can be used to grow an adenovirus in which the E1a gene is replaced by a gene of interest. Standard purification techniques can be used to isolate relatively high titers (10^{11} pfu/ml) of the desired adenoviral vector.

Adenoviral vectors like the wild-type adenovirus are capable of transducing both replicating and non-dividing cells. These vectors can transfect a wide variety of cells, with respiratory airway epithelium being particularly susceptible. The adenoviral vectors do not integrate their DNA into host DNA, but do lead to an immune response. The immune response can be particularly worsened by repeated administration of the viral vector. Adenoviral vectors lead to a transient level of gene expression, primarily due to host response to viral proteins in transduced cells. Future research may lead to adenoviral vectors with a decreased immune response, and improved specificity for the tissue(s) of choice. So-called "gutless" adenoviruses (Hardy et al. 1997) have been developed which lack all viral coding regions. They can be used to transfer large amounts of message, up to 35 kb, whereas the capacity of "normal" adenoviruses is typically around 6–8 kb. While being highly efficient gene carriers, gutless adenoviruses also have low toxicity and immunogenicity (Sakhuja et al. 2003). These gutless systems incorporated with therapeutic and reporter genes may prove to be an active area of research for the molecular imaging community in the next several years.

18.5.4 Retroviral Vectors

Retroviruses have a RNA genome, which is converted into DNA in the infected cell followed by its integration into host DNA. Entry of the retrovirus into target cells is critically dependent on appropriate receptors on the cell surface. Packaging cell lines

which are capable of generating retroviruses of a variety of host ranges have been used to combat this problem. Also, mitosis of the target cells is necessary for proviral integration to occur. The retroviral genome is composed of three genes termed gag, pol, and env which are flanked by long terminal repeats (LTRs), and a packaging sequence (Ψ) which allows viral RNA to be distinguished from other RNAs in the cell. The LTRs serve to control expression of the viral genes, and also define the beginning and end of the viral genome. Viral genes can be replaced with a gene of interest (transgene) to deliver this gene into host cells. The transgene can be under the control of the LTRs or a promoter which is a part of the transgene. Packaging cells can be used that allow production of high titers of replication-deficient recombinant virus. Retroviruses are primarily limited by their ability to integrate only into replicating cells, and their relative lability as compared to other viruses.

18.5.5 Adeno-associated Viral Vectors

Adeno-associated virus (AAV) is a single-stranded DNA virus that is capable of infecting non-replicating cells. It can integrate into host genome at a specific site on chromosome 19. AAV is a small virus which is relatively difficult to propagate in vitro and can only be purified in low titers. AAV vectors have low packaging ability (4 Kb) because of their small size, but have the advantage of a decreased host immune response because of their structural similarity.

18.5.6 Lentiviral Vectors

Lentiviruses belong to the retrovirus family and are capable of infecting both dividing and non-dividing cells. The human immunodeficiency virus (HIV) is an example of a lentivirus. A disabled HIV virus has been developed and could be used for in vivo gene delivery. A portion of the viral genome which encodes for accessory proteins can be deleted without affecting production of the vector and efficiency of infection. The lentiviral vectors have been produced in small scale ($>10^9$ virus particles per ml). Lentiviruses integrate themselves into the host genome, and consequently, transgene delivery into various rodent tissues shows sustained expression for up to 6 months. Furthermore, there seems to be little or no immune response with these vectors. In a recent study, a bicistronic lentivirus was used for transfer of two reporter genes, a mutant HSV1-TK (see below), and firefly luciferase (see below). Both genes were expressed in a highly correlated fashion, and imaging signal from optical and PET imaging also was well correlated (De et al. 2003). Reporter gene encoding lentiviruses have since been employed to image tumor-specific lymphocytic migration by both microPET scan and bioluminescence imaging (Kim et al. 2004), prostate specific gene expression (Iyer et al. 2004), and islet cell survival after transplantation (Lu et al. 2004).These lentiviral vectors hold a lot of promise for in vivo gene delivery and are likely to play a greater role in future imaging and gene therapy applications.

18.6 Reporter Gene Imaging

18.6.1 Fundamental Principles of Reporter Genes

Molecular biologists have used reporter genes both in vitro and in vivo for over a decade to monitor gene expression. Reporter genes are used to study promoter/enhancer elements involved in gene expression, inducible promoters to investigate the induction of gene expression, and endogenous gene expression through the use of transgenes containing endogenous promoters fused to the reporter gene. In all of these cases transcription of the reporter gene can be tracked and therefore gene expression can be studied.

Specific examples of reporter genes include the bacterial gene chloramphenicol acetyl transferase (CAT), and the lacZ gene which codes for β-galactosidase. Autoradiography of a chromatogram (when using CAT) or enzyme assay (when using lacZ) can then be used to assay cell extracts for the product of the reporter gene (Lewin 1994). For tissue specimens, the same reporter genes can also be used, with the use of immuno-histochemistry or histochemical staining. In these types of studies, the introduction of a chimeric fusion gene (a gene coupled to some endogenous or exogenous promoter) into the target tissue has to be accomplished. A reporter gene (e.g., alkaline phosphatase) which can lead to a protein product secreted into the blood stream can also be used, thereby allowing monitoring in living animals

(Fig. 18.6). However, the location(s) of the reporter gene are not able to be determined in this case, because only the blood can easily be sampled.

Conventional reporter gene methods are relatively limited by their inability to determine the location(s) of gene expression in living animals. Approaches using light producing fluorescent green fluorescent protein (GFP) (Chalfie et al. 1994; Misteli and Spector 1997) and bioluminescent firefly or renilla luciferase (Jacobs et al. 1993; Bhaumik and Gambhir 2002) as reporter genes whose products directly interact with light, allow for localization in small living animals. Animals that are transparent to light can be imaged with simple video cameras because of the ability of these reporter genes to produce products that interact with visible light. However, these imaging techniques are limited because of their lack of generalizability (e.g., GFP would not be transferable to humans, as tissue penetration of excitation and emission light is in the range of 1–5 mm in mammalian tissues). Also, detailed tomographic resolution is currently lacking, despite advances towards imaging of deeper lying structures by fluorescence-mediated tomography (Ntziachristos et al. 2003). In this approach, several light sources emit wave or pulsed light in an imaging chamber, whereas emitted light is captured by detectors arranged in a spatially defined order. However, the system is still in its infancy, requiring extensive mathematical validation prior to routine implementation. Radionuclide imaging techniques offer the possibility of monitoring the location, magnitude, and persistence of reporter gene expression (with potentially a very high sensitivity) for in vivo use in animals and humans. Figures 18.7 and 18.8 show approaches in which a reporter gene which encodes for a enzyme and receptor respectively can lead to trapping of

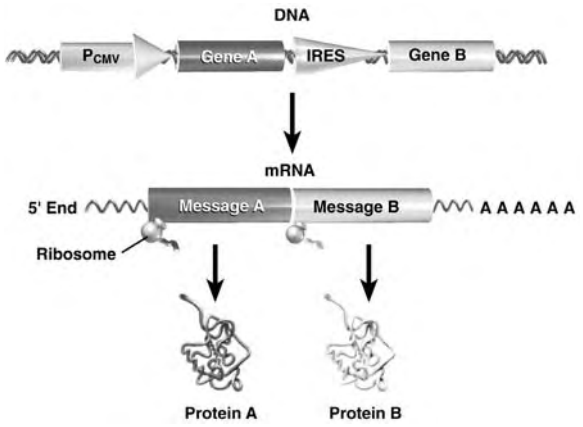

Fig. 18.6. A bicistronic vector with an internal ribosomal entry site (*IRES*). In applications in which two genes (*A* and *B*) need to be jointly expressed through a common promoter, an IRES can be used. A single mRNA (containing both genes) is transcribed, but translation of this single transcript leads to two distinct proteins. Ribosomes can enter at the IRES leading to only translation of message B, and production of protein B

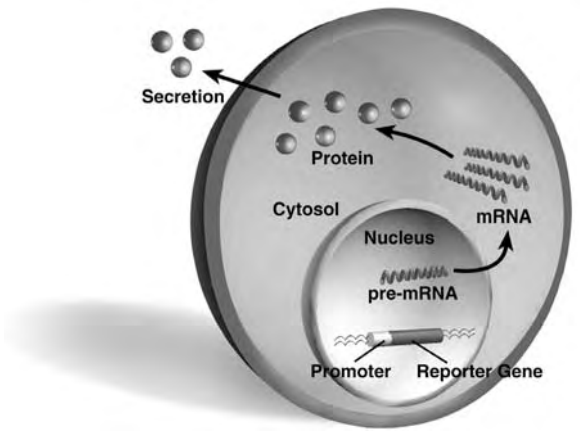

Fig. 18.7. The reporter gene concept for in vivo applications. A reporter gene driven by a promoter of choice must first be introduced into the cell(s) of interest. If the reporter gene is transcribed, a protein product is eventually made which can be secreted into the blood and therefore detected. Sampling the blood will not reveal the location(s) where the reporter gene is active, but it will reveal that it is being transcribed and translated. Changes in magnitude of protein product may also allow for the determination of the degree to which the promoter is actively driving the gene of interest

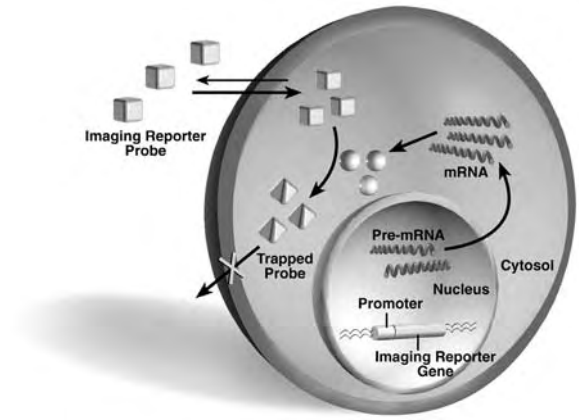

Fig. 18.8. An imaging reporter gene with enzyme mediated trapping of the imaging reporter probe. An imaging reporter gene driven by a promoter of choice must first be introduced into the cell(s) of interest. If the reporter gene is transcribed, a enzyme product (spheres) is eventually made which can lead to the trapping (tetrahedrons) of the imaging reporter probe (cubes). The imaging reporter probe must be able to enter cells. Signal amplification by accumulation of trapped imaging reporter probe leads to the ability to determine the location(s), magnitude, and persistence of reporter gene expression

an imaging probe, thereby allowing the imaging of reporter gene expression.

18.6.2 Properties of the Ideal Reporter Gene for Imaging

The ideal reporter gene/reporter probe imaging system would have the following characteristics: (a) The reporter gene should be present in mammalian cells, but not expressed (this will prevent an immune response). (b) When expressed, the reporter gene protein should produce specific reporter probe accumulation only in those cells in which it is expressed. (c) When the reporter gene is not expressed, there should be no significant accumulation of reporter probe in cells. (d) There should be no significant immune reaction to the reporter gene product. (e) The reporter probe should be stable in vivo and not be converted to peripheral metabolites that complicate the development of a quantitative assay. (f) The reporter probe should be rapidly cleared from the blood and non-specific sites in tissues, and preferably have an elimination route that does not interfere with the detection of specific signal. (g) The reporter probe should be conveniently radiolabeled with a variety of radionuclides without significant change in its properties, and should be labeled with an appropriate specific activity. (h) The reporter probe or its metabolites should not be cytotoxic at the concentrations used. This is likely to be the case for most tracer applications, which are based on very low concentrations of tracer. (i) The size of the reporter gene and the promoter driving it should be small enough to fit in the delivery vehicle (e.g., for a conventional adenoviral vector the upper limit is ~ 7 Kb). This requirement can be relaxed for animal applications such as transgenics in which a delivery vehicle is usually not needed. (j) The reporter probe must be able to reach the area(s) of interest without transport across membranes being a significant limitation. (k) The reporter probe image signal should correlate well (over the range of concentration relevant to the study paradigm) with levels of reporter gene mRNA and protein in vivo. (l) The reporter gene assay should correlate well with levels of endogenous gene expression, if the reporter gene is being used to monitor endogenous gene expression. (m) A reporter gene working in any cellular compartment would be more versatile than reporter genes which are restricted to certain subcellular structures, e.g. receptor reporter genes are usually integral membrane proteins. (n) With view towards transferability to human uses, it is practical to work with reporter genes whose substrates are already approved by drug regulating agencies (e.g. in the case of octreotide, a commonly used nuclear medicine imaging agent, which is the substrate of the somatostatin receptor 2 reporter gene. Obtaining approval for substrates is a process which otherwise can take years and is extraordinarily expensive. (o) The reporter gene signal should be amplifiable if the original event which is imaged is rare (e.g. in the case of low copy number transcript mRNA imaging). (p) Imaging of signal should be possible with imaging modalities suitable both for in vitro and in vivo (large animal) imaging in order to streamline the development process. (q) Imaging should be cheap and convenient. (r) If events should be imaged in real time, the signal should occur quickly and disappear immediately after the event one is imaging is over.

No single reporter gene/reporter probe system currently meets all these criteria. It is likely that each reporter gene/reporter probe system will only meet some of the above criteria, and therefore different reporter systems will have to be chosen based on the intended application. The development of multiple reporter gene/reporter probe systems will help to provide a choice, based on their application of interest, for future investigators. Furthermore, by having multiple reporter gene assays, it should be possible to monitor the expression of more than one reporter gene in the same living animal or human.

18.6.3 Cytosine Deaminase Reporter Gene

Cytosine deaminase (CD) was one of the first reporter genes to be studied for imaging reporter gene expression. CD is found primarily in yeasts and bacteria and its expression is responsible for the deamination of cytosine to form uracil. Mammalian cells lack CD and therefore cannot convert cytosine to uracil. In those cells expressing CD, 5-fluorocytosine is converted to 5-fluorouracil which is cytotoxic. CD has been used in animal (Nishiyama et al. 1985) and human (Wallace et al. 1994) cancer therapy models with 5-fluorocytosine. The reporter probe 6-[^{3}H]-5-fluorocytosine has been studied in human glioblastoma cells stably transfected with the *Escherichia coli* CD reporter gene, because of its ability to be converted to 6-[^{3}H]-5-fluorouracil only in cells expressing CD (Haberkorn et al. 1996). Rapid cel-

lular efflux of 6-[^{3}H]-5-fluorouracil limits the utility of this reporter probe and further exploration of the CD reporter gene with 5-[^{18}F]-fluorocytosine and PET. Furthermore, very slow uptake of [^{3}H]-5-fluorocytosine, in part attributable to different transporters between prokaryotes and eukaryotes, is also a problem. Times of up to 48 h are needed to see differences in radioactivity accumulation between cells expressing CD and control cells. Alternative substrates for CD, which are rapidly transported, deaminated, and trapped intracellularly, may eventually allow the use of CD to develop an assay for imaging reporter gene expression.

18.6.4 Herpes Simplex Virus Type-1 Thymidine Kinase Reporter Gene

There are two known mammalian thymidine kinases – a mitochondrial and a cytosolic enzyme (Arner and Eriksson 1995). These kinases are responsible for catalyzing the transfer of the γ-phosphate from ATP to the 5'-terminus of deoxythymidine to form deoxythymidine monophosphate (dTMP). When cells are infected with the Herpes simplex virus, the viral thymidine kinase is expressed. The viral thymidine kinase has relaxed substrate specificity as compared to the mammalian thymidine kinases, and is capable of phosphorylating pyrimidine and purine nucleoside derivatives (de Clercq 1993), as well as deoxythymidine. These compounds, when phosphorylated, are trapped intracellularly.

The discovery that acyclovir (9-(2-hydroxyethoxymethyl)guanine) is specifically phosphorylated by the viral thymidine kinase resulted in one of the most successful approaches to the treatment of Herpes simplex virus infection (Elion 1993). Subsequent phosphorylation of acyclovir monophosphate by guanylate kinase to form acyclovir diphosphate, followed by phosphorylation by various cellular enzymes leads to the formation of acyclovir triphosphate. Acyclovir triphosphate leads to chain termination when it is incorporated into DNA, and acts as a more potent inhibitor of the viral DNA polymerases than of cellular polymerases. The DNA polymerases of HSV1 and HSV2 also use acyclovir triphosphate as a substrate and incorporate it into the DNA primer-template to a much greater extent than do the cellular enzymes. The viral DNA polymerase binds strongly to the acyclovir triphosphate-terminated template, and is thereby inactivated (Elion 1993). Multiple substrates for HSV1-TK including ganciclovir (9-[[2-hydroxy-1-(hydroxymethyl)ethoxy]methyl]guanine) and penciclovir (9-(4-hydroxy-3-hydroxymethylbutyl)guanine) have subsequently been synthesized and reported in the literature as antiviral agents (Alrabiah and Sacks 1996). Note that HSV1-tk denotes the gene and HSV1-TK denotes the enzyme. We have reported the generation of a mutant HSV1-tk (HSV1-sr39tk) with enhanced ganciclovir phosphorylation capabilities and less undesired thymidine phosphorylation, thus yielding higher and more specific signal (Gambhir et al. 2000).

There are two main categories of substrates for HSV1-TK/HSVsr39TK; pyrimidine nucleoside derivatives (e.g., 5-Iodo-2'-fluoro-2'-deoxy-1-β-D-arabinofuranosyl-5-iodouracil, FIAU), and acycloguanosine derivatives [e.g., 8-[^{18}F]-fluoroganciclovir ([^{18}F]FGCV) and 9-(4-fluoro-3-hydroxymethylbutyl)guanine (FHBG)], which are utilized as reporter probes for imaging HSV1-tk/HSV1-sr39tk reporter gene expression. These reporter probes are transported into cells, and trapped as a result of phosphorylation by HSV1-TK. HSV1-tk has been used as a reporter gene in many applications, the most pertinent of which are discussed next.

Tjuvajev et al. (1995) used a recombinant replication-deficient STK retrovirus containing HSV1-tk to transduce RG2 glioma cells in vitro and in vivo. HSV1-tk gene expression was then imaged using quantitative autoradiography of 2-[^{14}C]FIAU in an intracerebral tumor model in rats. Transduction of the RG2 tumor cells with the HSV1-tk gene in vivo resulted in tumors which accumulated 2-[^{14}C]FIAU and produced good autoradiographic images of gene expression. Imaging relatively late, at 24 h after the injection of 2-[^{14}C]FIAU, reduced the effects of background radioactivity by taking advantage of a long washout time. These authors also explored 8-[^{3}H]-ganciclovir in vitro, but it was not explored in vivo because it showed less accumulation in cell culture when compared to 2-[^{14}C]FIAU. In a subsequent study, Tjuvajev et al. (1996) used [^{131}I]FIAU and gamma camera/SPECT imaging. In this study, using rats, tumors were transduced in vitro with the HSV1-tk gene, and also in vivo using direct intratumoral injection of retroviral vector-producer cells. Animals were imaged with a gamma camera/SPECT 24-48 hours after injection of [^{131}I]FIAU. The authors concluded that "clinically relevant" levels of HSV1-tk gene expression can be imaged with [^{131}I]FIAU and gamma camera/SPECT. Studies with [^{124}I]FIAU and PET have also been reported (Tjuvajev et al. 1998) and demonstrate that tumors with

various levels of HSV1-tk expression can be distinguished by PET imaging at 30 h after injection of [^{124}I]FIAU. Good correlations between sensitivity of the transduced tumors to ganciclovir (IC_{50}) and the [^{124}I]FIAU %ID/g, as well as the incorporation constant (Ki) were shown.

Adenoviral-directed gene delivery has been used in which a replication-deficient adenovirus carrying the HSV1-tk reporter gene driven by the cytomegalovirus promoter delivers the HSV1-tk reporter gene primarily to the murine liver (Fig. 18.9) (Gambhir et al. 1998). Peripheral intravenous injection of adenovirus causes a predominant infection of the mouse liver (Stratford-Perricaudet et al. 1990; Herz and Gerard 1993). At 48 h after tail-vein injection of either control virus or virus carrying HSV1-tk, mice were injected with 8-[^{14}C]-ganciclovir and imaged 1 h later. Digital whole-body autoradiography was used to evaluate the specificity and sensitivity of this assay. Correlations in vivo between relative levels of HSV1-TK enzyme, HSV1-tk mRNA, and %ID/g, show the feasibility of quantitatively relating the in vivo imaging signal from the liver to the level of reporter gene expression. Preliminary microPET (Cherry et al. 1997) studies using the same murine model and [^{18}F]FGCV also show encouraging results (Fig. 18.10) (Gambhir et al. 1998). Further studies validating the use of [^{18}F]FGCV in vivo are currently being completed. 9-[(3-[^{18}F]Fluoro-1-hydroxy-2-propoxy)methyl]guanine [^{18}F]FHPG has also been preliminarily studied in primates in order to demonstrate the absence of catabolism and relative uptake into transduced cells (Alauddin et al. 1997; Bading et al. 1997).

Multiple candidate tracers have been developed for use with the HSV1-tk reporter gene, which are grouped into pyrimidine nucleoside derivatives, such as FIAU, and acycloguanosine derivatives, e.g., FHBG. There has been an amount of controversy concerning which tracer would be the most efficient for imaging purposes, and the answer depends on which type of thymidine kinase (mutant HSVsr39tk, or wild type HSV-tk) is being used, as well as which route of delivery (Adenoviral gene delivery vs. stable transfection) is being utilized for the transgene. Experiments performed in mammalian cells which were stably transfected with wild type HSV1-tk showed higher specific accumulation of FIAU than of the acycloguanosine derivatives FHBG and FHPG in vivo and in vitro (Brust et al. 2001; Tjuvajev et al. 2002). Alternate acycloguanosine derivative substrates, such as [^{18}F]PCV (Iyer et al. 2001a) or [^{18}F]FHBG, have been evaluated in an attempt to improve sensitivity (Iyer et al. 2000). [^{18}F]PCV resulted in a two- to three fold

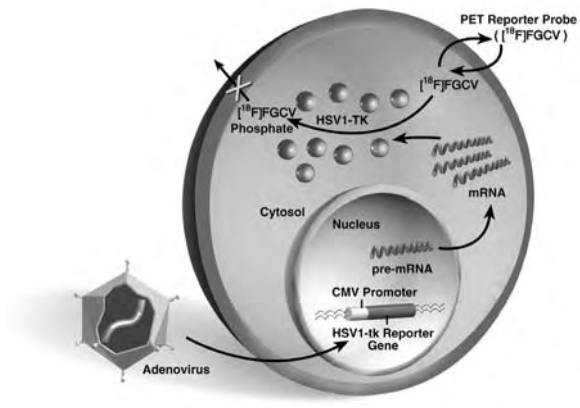

Fig. 18.9. An imaging reporter gene with receptor mediated trapping of the imaging reporter probe (a ligand). An imaging reporter gene driven by a promoter of choice must first be introduced into the cell(s) of interest. If the reporter gene is transcribed, a receptor protein (Y) is eventually made which leads to binding of the imaging reporter probe (cubes). Signal amplification by receptor-ligand interaction leads to the ability to determine the location(s), magnitude, and persistence of reporter gene expression. The receptor protein can be intracellular and/or at the cell surface. If the receptor protein is only intracellular, than the imaging reporter probe must be able to enter cells

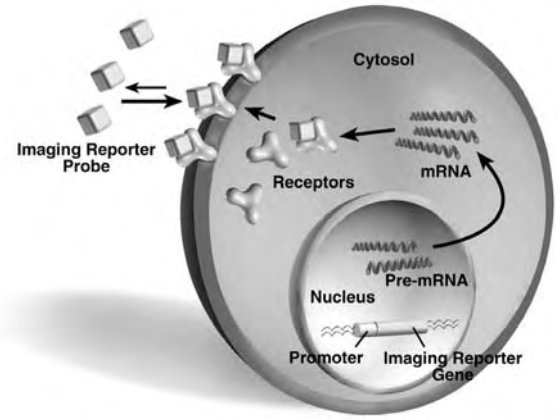

Fig. 18.10. Adenoviral mediated delivery of the Herpes simple type 1 virus thymidine kinase (*HSV1-tk*) reporter gene followed by subsequent 8-[^{18}F]-fluoroganciclovir (*[^{18}F]FGCV*) PET reporter probe trapping. An adenovirus carrying the HSV1-tk reporter gene has been used to deliver the HSV1-tk reporter gene [driven by a constitutive cytomegalovirus (*CMV*) promoter]. Transcription and translation of HSV1-tk lead to production of HSV1-TK enzyme which can phosphorylate and trap [^{18}F]FGCV. PET imaging can thereby detect the location(s), magnitude, and persistence of HSV1-tk reporter gene expression

greater sensitivity for detection of *HSV1-tk* expression compared with [^{18}F]GCV in cell culture and in vivo (Iyer et al. 2001a). In more recent studies, [^{18}F]FHBG and [^{14}C]FIAU were found to be superior to FPCV as reporter probes for monitoring *HSV1-tk* expression, and [^{18}F]FHBG may have an added advantage over [^{14}C]FIAU because of its significantly lower accumulation in cells not expressing *HSV1-tk*, resulting in a better target to background ratio (Iyer et al. 2000). Both FHBG and FIAU are all the more interesting as tracers since they were granted investigational new drug (IND) status by the US Federal Drug Administration, making them potential tracers for clinical studies. A mutant reporter gene, *HSV1-sr39tk*, with improved affinity for acycloguanosines and decreased affinity for the native substrate thymidine, has also been evaluated. Using FPCV as a reporter probe enhanced sensitivity by a factor of 2–4 (Gambhir et al. 2000). It was also observed that in cells infected with adenovirus encoding *HSV1-tk*, FHBG is a better probe than FIAU. One study compared the uptake characteristics of [^{18}F]FHBG, [^{3}H]PCV, and [^{14}C]FIAU in cell culture and in vivo using an adenoviral mediated gene transfer model and a stable tumor xenograft model. Further, the uptake of [^{18}F]FHBG, [^{3}H]PCV, and [^{14}C]FIAU in an *HSV1-tk* and *HSV1-sr39tk* expressing model were compared to assess the optimal reporter probe/reporter gene combination (Min et al. 2003). Results indicated that the mechanism of reporter gene introduction is an important variable for determining the optimal reporter gene/reporter probe combination. In *HSV1-tk* stably transfected cells, [^{14}C]FIAU accumulation was greater than that of [^{3}H]PCV and [^{18}F]FHBG ($p<0.001$), corroborating earlier results. However, after adenoviral gene transfer, [^{18}F]FHBG and [^{3}H]PCV accumulation was significantly greater than that of [^{14}C]FIAU ($p<0.01$). When the mutant HSV1-sr39-tk was used, [^{18}F]FHBG and [^{3}H]PCV accumulated to a significantly greater extent than [^{14}C]FIAU in C6 cells ($p<0.001$). These results were found similarly in the in vivo models. For adenoviral studies, the [^{18}F]FHBG/*HSV1-sr39tk* combination is more sensitive than the [^{14}C]FIAU/*HSV1-tk* combination, while for stable transfection experiments, the [^{14}C]FIAU/*HSV1-tk* combination appears to be ideal (Min et al. 2003). New studies which have also explored FEAU show it may have advantages over both FHBG and FIAU for both HSV1-tk and HSV1-sr39tk and needs further investigation (Alauddin et al. 2002; Buursma et al. 2003; Kang et al. 2005).

18.6.5 Dopamine 2 Receptor Reporter Gene

The dopamine 2 receptor (D2R) is primarily expressed in the brain striatum and in the pituitary glands. The D2R is a 415 amino acid protein with seven transmembrane domain topology (Bunzow et al. 1988). Ligand-activated D2R interacts with G proteins to inhibit adenylate cyclase (Strange 1990). Several PET D2R ligands (labeled with either ^{11}C and ^{18}F) for the D2R reporter gene have been well validated in animal and human applications (Wagner et al. 1983; Ehrin et al. 1985). 3-(2'-[^{18}F]-Fluoroethyl)spiperone ([^{18}F]FESP), a D2R antagonist is one of these ligands (Barrio et al. 1989). [^{123}I]Iodobenzamine is also potentially useful for imaging D2R expression with SPECT (Kessler et al. 1991).

A PET reporter gene/PET reporter probe assay based on D2R/[^{18}F]FESP has been developed by the UCLA Gene Imaging Consortium and investigated in nude mice using both an adenoviral-directed hepatic gene delivery system, and in tumors transfected with D2R ex vivo, then implanted in nude mice (MacLaren et al. 1999). The D2R reporter gene when expressed, leads to accumulation of [^{18}F]FESP by direct binding to D2R (cell membrane and intracellular). Good correlations ($r^2 > 0.88$) with PET image signal in vivo, and with GAPDH normalized levels of D2R mRNA and receptor concentrations, as quantified from tissue extracts in vitro were demonstrated.

Dopamine binding to the D2R can modulate cyclic AMP levels, potentially compromising the usefulness of the D2R as a reporter gene in vivo. To uncouple ligand-binding from G-protein-mediated inhibition of cAMP production, a mutant D2R was generated. A D2R80A mutation completely eliminated the ability of the D2R to suppress forskolin-stimulated cAMP accumulation in response to dopamine, while maintaining equivalent [^{3}H]spiperone binding activity. Moreover, hepatic FESP sequestration is equivalent, following intravenous injection of adenoviruses expressing D2R and D2R80A (Liang et al. 2001). The usefulness of D2R80A as a "pure" reporter gene without physiological function has recently been demonstrated in gene transfer experiments. To monitor activity of a therapeutic gene, D2R80R was expressed from a bicistronic adenoviral vector (Ad-CMV-D2R80a-IRES-HSV1-sr39tk) in which two reporter genes were linked by an internal ribosomal entry site (IRES). Both in vitro and in vivo, expression of the two genes was highly cor-

related, emphasizing that D2R80A is an ideal candidate reporter gene for monitoring gene therapy without having intrinsic physiologic actions itself (Liang et al. 2002; Chen et al. 2004).

18.6.6 Somatostatin 2 Receptor Reporter Gene

The somatostatin 2 receptor (SSTR2) is one of five known subtypes of human somatostatin receptors, G-protein coupled, internalizing 7 transmembrane domain receptors. It is physiologically expressed in pancreatic islets, spleen, germinal centers of the lymphoid tissues, and anterior hypopituitary gland (Reubi et al. 2001). SSTR2 is overexpressed in a number of human tumors of neuroendocrine origin, such as neuroendocrine gastroenteropancreatic (GEP) tumors, pheochromocytoma, medullary thyroid carcinoma, and small cell carcinoma of the lung, lymphoma, meningioma, and breast cancer. Tumors may be imaged using radiolabeled analogs of the peptide hormone somatostatin, such as ^{111}In-DTPA-D-Phe Octreotide. Radioligand therapy has been conducted in experimental studies with considerable success. Imaging employing physiologically expressed SSTR2 is covered in Chap. 10 of this book in more detail. The SSTR2 gene has been employed as a reporter gene to image tumors such as non small lung cancer and ovarian cancer in gamma cameras using ^{99m}Tc, ^{111}In, and ^{188}Re labeled somatostatin analogs (Rogers et al. 1999; Zinn et al. 2000; Chaudhuri et al. 2001). The major advantage of using the SSTR2 as an imaging reporter gene is that it has been used for imaging in its physiologic form for many years. Imaging of SSTR2 overexpressing malignancies is a standard procedure in nuclear medicine departments around the world, and different tracers have been developed, tested and approved for human use by the respective authorities. Since approval for human use is a key step in drug or imaging probe development, which takes enormous financial and time investments, this is a very important advantage. A second advantage of the SSTR2 is that no immune response is to be expected, since it is a human gene. However, there is some concern about whether SSTR2 gene transfer and imaging might result in unwanted activation of physiologic signal transduction pathways. To circumvent this problem, an epitope-tagged receptor was recently constructed in which the hemagglutinin (HA) sequence is fused to the extracellular N-terminus of the SSTR2 gene. FITC-labeled anti-HA antibody confirmed surface expression and absence of internalization in vitro. In a mouse tumor model, imaging detected increased tumor uptake of ^{99m}Tc-anti-HA after intratumoral injection of an adenovirus encoding the fusion gene as compared to tumors injected with the SSTR2 gene alone (Rogers et al. 2003). A second elegant method to uncouple SSTR2 receptor binding from signal transduction would be to mutate the transactivating domain as previously shown for the D2R (Liang et al. 2001). Since work has been carried out characterizing signal transducing and internalizing domains of the protein (Oomen et al. 2001), progress in this field may be expected.

An interesting study combined imaging of the SSTR2 with those of the HSV1-TK gene (Verwijnen et al. 2004). Glioma cell lines were transfected with an adenovirus carrying both genes. Uptake of 1-(2-fluoro-2-deoxy-b-D-ribofuranosyl)-5-[^{125}I] iodouracil (FIRU), a HSV1-TK substrate, and the somatostatin analog ^{111}In-DOTA-Tyr3-octreotate, which binds to the SSTR2, increased with time, with uptake of ^{111}In-DOTATyr3-octreotate being higher than that of ^{125}I-FIRU. Both genes may be used in a therapeutic as well as in an imaging approach, using DOTA-Tyr3-octreotate radiolabeled with ^{177}Lu or ^{90}Y for the SSTR2, and ^{131}I-FIRU or the prodrug ganciclovir for HSV1-TK.

18.6.7 Sodium Iodide Symporter Reporter Gene

The human sodium iodide symporter (NIS) is a 643 amino acid protein expressed mainly in thyroid, stomach, and salivary glands. It concentrates iodide and other negatively charged ions within cells in an energy dependent process which uses the Na^+ concentration gradient upheld by the Na^+/K^+-ATPase (see Dohan et al. 2003). NIS mediated radioisotope uptake has been used clinically for five decades in the diagnosis and therapy of thyroid disease (Eichler et al. 1951; Horst 1951; Klain et al. 2002; Lind 2002; Manders and Corstens 2002; Reiners and Schneider 2002; Dohan et al. 2003). The cloning of its cDNA has initiated efforts to employ NIS as a tool for gene therapy of a large variety of tumors, including hepatic (Faivre et al. 2004), prostate (Spitzweg et al. 1999), glioma (Carlin et al. 2000), lung (Boland et al. 2000), and as an imaging reporter gene for gamma camera imaging, SPECT, and PET. NIS gene transfer was mostly achieved by adenoviral transfection, and driven by the CMV promoter. Approaches towards

tissue- and tumor-targeted expression have successfully been taken. Among other examples, expression was targeted to neuroendocrine tumors by using the Chromogranin A promoter (Schipper et al. 2003), or to tumors in general by using the Glut1-Promoter (Sieger et al. 2004) and human telomerase RNA/reverse transcriptase promoter fragments (Groot-Wassink et al. 2004). Use of NIS as a reporter and gene therapeutic gene offers several advantages. As it is a human gene, there is no immune response to the gene product. Biodistribution, metabolism, and toxicity data of the most likely radiotracers, Iodide and Tc-pertechnetate, are well known from decades of clinical experience. In addition, NIS transports a wide range of other isotopes, which may be employed for many diagnostic and therapeutic purposes, including $^{123/124/131}$I, ^{99m}Tc, $^{188/186}$Re, and ^{211}At. It may be imaged using either PET (Groot-Wassink et al. 2002) (Groot-Wassink et al. 2004) or SPECT (Haberkorn 2001; Haberkorn et al. 2001). Despite lack of organification and fast externalization of radionuclides in monolayer cell culture, half lives in three dimensional systems as tumors in vivo are much longer owing to reuptake of externalized iodide (Schipper et al. 2003). This was recently confirmed by a study showing an effective half life of ^{131}I of 2.2 days in NIS transfected livers. When the competitive NIS inhibitor Sodium Perchlorate was administered, activity disappeared from the liver within 6 min (Faivre et al. 2004). Since NIS is both a therapeutic and an imaging reporter gene, it can be used to directly image therapeutic gene expression in therapy, thereby sidestepping potential problems which would be encountered when using a separate reporter gene, e.g. correlation of expression of the two genes. However, the combination of NIS as part of multimodality fusion reporters and combined therapeutic/reporter constructs has been reported, such as NIS in combination with a HSV1-tk-cytosin deaminase fusion gene (Barton et al. 2004), and a dual reporter in which NIS and fLuc were joined by an IRES (Shin et al. 2004). Since NIS is an integral membrane protein and is nonfunctional when in the cytoplasm, NIS fusion genes will function only if the second gene is selected so that this fact does not impair its activity.

18.6.8 Miscellaneous Reporter Genes

Like the sodium iodide transporter, the human norepinephrine transporter (NET) has been used in clinical nuclear medicine imaging for decades due to its ability to transport ^{131}I Meta-iodo-benzylguanidine (MIBG). NET rapidly removes Norepinephrine from the synaptic cleft after release from the presynaptic adrenergic neuron and is physiologically expressed in many tissues with adrenergic innervation, such as salivary glands and heart. It is used for imaging and treatment of tumors originating from the sympathetic nervous system, such as medulloblastoma and pheochromocytoma. As a molecular imaging reporter gene, the norepinephrine transporter gene has been used to image hepatoma and other tumors with ^{131}I MIBG (Altmann et al. 2003). Advantages of the NET as a reporter gene are the availability of clinically used radiotracers, PET radiotracers, and a favorable biodistribution with a long intratumoral retention of MIBG (Anton et al. 2004).

The dopamine transporter (DAT) gene is also physiologically expressed in the adrenergic central nervous system. It may be imaged using [^{99m}Tc]TRODAT-1, and has been used as a reporter gene in murine muscle (Anton et al. 2004). One of the advantages of both NET and DAT is that in addition to being human genes (and therefore, nonimmunogenic), high level expression is absent outside of the CNS, decreasing the likelihood of confusing reporter gene expression with physiologic expression.

The aromatic L-amino acid decarboxylase (AADC) has been used in a gene therapy and imaging setting with immediate clinical relevance. In Parkinson's disease, striatal levels of dopamine are decreased due to the degeneration of neurons which produce the neurotransmitter dopamine from its precursors. Administering the precursor L-Dopa decreases symptoms, but high systemic levels of the drug lead to unwanted side effects. In recent work (Bankiewicz et al. 2000; Eberling et al. 2003), *Macaca mulatta* monkeys with pharmacologically induced parkinsonian syndrome received local intracerebral infusions of an adenovirus expressing the AADC gene. Uptake of the AADC PET reporter probe 6-[^{18}F]fluoro-L-m-Tyrosine (FMT) was substantially increased as compared to before gene transfer, correlating well with immunohistochemical expression of the therapeutic/imaging gene and a marked clinical improvement of symptoms due to increased local conversion of L-Dopa to dopamine by the AADC.

A new approach to the design of reporter/probe pairs has been proposed in which theoretically any immunogenic low molecular weight probe can be

detected. The reporter is a cell surface-expressed single chain antibody variable fragment directed against the low molecular weight imaging probe. In this way, a probe with optimized pharmacokinetic properties can be chosen. In the initial study, a single chain antibody variable fragment directed against fluorescein and an imaging probe consisting of fluorescein isothiocyanate coupled to the chelator diethylene triamine penta-acetic acid labeled with the gamma-emitter ^{111}In were chosen. Specific uptake of the probe by tumors in vitro and imaging of tumors expressing the reporter in vivo were shown (Northrop et al. 2003).

18.6.9 Reporter Genes for Use with Magnetic Resonance Imaging

In order to be useful with MRI, a reporter gene would have to lead to a change in relaxivity of cells in which the reporter gene is expressed. Intrinsically, MRI has a sensitivity of ~10^{-4}–10^{-5} M, and does not compete well with PET where the sensitivity is ~10^{-10} M. Therefore a PET based approach would need much less accumulation of a reporter probe than would an MRI based approach for a given level of gene expression. However, an MRI based approach might have an advantage of improved spatial and temporal resolution which in part is based on signal strength. Reporter genes for use with MRI have been studied in vivo. An example of this approach is the use of the β-galactosidase reporter gene which when expressed can lead to the hydrolysis of a compound complexed with gadolinium ((1-(2-(b-galactopyranosyloxy)propyl)-4,7,10-tris(carboxymethyl)-1,4,7,10-tetraazacyclododecane)gadolinium (III), or EgadMe). When cleaved, water protons can interact with the chelated paramagnetic ion, which enhances MRI signal (Louie et al. 2000). Other approaches use the tyrosinase reporter gene leading to greater production of melanin, and subsequent trapping of heavy metals by melanin binding thereby changing cell relaxivity (Weissleder et al. 1997). Lastly, an engineered transferring receptor (ETR) has been used as a reporter gene which internalizes (super)paramagnetic TF-monocrystalline iron oxide nanoparticles (or MIONs) into cells and thereby increases MRI signal, to image gliosarcoma xenografts (Weissleder et al. 2000). Remarkably, the transferrin receptor is a recyclable receptor. Upon ligand binding, receptor mediated internalization is initiated. After release of the ligand from the endosome, the endosome containing the receptor travels back to the cell membrane and fuses with it. By multiple repetitions of this cycle, the amount of trapped probe inside the cell per molecule of reporter gene increases proportionally. While an extensive discussion of MRI reporter genes is beyond the scope of this chapter, more detailed reviews can be found in: Weissleder (2002); Massoud and Gambhir (2003).

18.6.10 Reporter Genes for Use with Optical Imaging

Optical reporter gene imaging is not fully generalizable in large animals or humans due to the limited tissue penetration of light. Its use is limited to areas near the surface or areas which can be reached by endoscopic imaging. However, optical reporter genes may be used to study gene expression in small animals in a convenient and economic way. In fluorescence imaging, a fluorescent protein such as *Aequorea victoria* green fluorescent protein GFP, or *Discosoma* red fluorescent protein (dsRED), is excited by external light of an appropriate wavelength. As it returns to its ground energy level, a photon of characteristic longer wavelength is emitted and can be detected at close to "real-time". Drawbacks include limited tissue penetration of light due to absorption by intrinsic chromophores such as hemoglobin and deoxyhemoglobin, melanin, and myoglobin, and autofluorescence of mammalian tissues. Autofluorescence is caused by intrinsic fluorophores in tissues, such as the aromatic amino acids tryptophan, tyrosine, and phenylalanine, crosslinking amino acids contained in collagen and elastin, such as lysyl pyridinoline and hydroxylysyl pyridinoline, NADH, FAD, heme precursors, such as protoporphyrin, pyridoxine and its metabolites, eosinophilic granules in eosinophils, and fluorescent lipopigments, such as lipofuscin and ceroid, which are associated with ageing and many pathologic processes (Richards-Kortum and Sevick-Muraca 1996). Depending on tissue content of any of these intrinsic fluorophores, there will be a degree of background fluorescence, which may lead to low signal to noise ratios in vivo. Red- or near infrared shifted fluorescent proteins with increased tissue penetration have been investigated (Ntziachristos et al. 2003).

Firefly luciferase is the most widely employed reporter gene for bioluminescence imaging. It catalyzes oxyluciferin from D-luciferin, leading to light production in the presence of oxygen, ATP, cofac-

tors, and Mg^{++} with a peak measurable at 562 nm wavelength. *Renilla* luciferase generates a 482 nm peak of light by oxidation of its substrate coelenterazine in an ATP independent process (Bhaumik and Gambhir 2002). Bioluminescence imaging has only minimal background signal, as there is no physiologic expression of bioluminescent proteins in mammals, resulting in superior signal to noise ratios when compared to fluorescence imaging. As a full discussion of optical imaging is beyond the scope of this chapter, we recommend the following for further reading: Bremer et al. (2003); Massoud and Gambhir (2003); Min and Gambhir (2004).

18.7 Signal Amplification for Imaging Gene Expression

Signal amplification is a key issue in imaging gene expression. Higher levels of imaging signal per unit level of gene expression lead to a higher sensitivity for any particular gene imaging assay. The antisense approach has the lowest concentration of the target (mRNA), and is the most challenging of the methods discussed in this respect. The receptor based reporter gene approach is better because one mRNA leads to many receptor proteins. The enzyme based reporter gene approach has the greatest signal amplification, because one mRNA leads to many enzyme molecules, and each enzyme molecule can lead to the trapping of a large number of reporter probe molecules. These differences must be kept in mind based on the imaging application desired prior to selecting an optimal approach.

18.8 Imaging Endogenous Gene Expression

18.8.1 Imaging Endogenous Gene Expression with Antisense Probes

In vivo imaging applications with antisense probes have been limited to date. Dewanjee et al. (1994) were the first to demonstrate the targeting of endogenous gene expression with antisense probes and gamma camera imaging using a tumor bearing model in mice. This study demonstrated rapid targeting to a tumor expressing the c-myc oncogene as compared to a control tumor with imaging performed at 2 h after injection. Control probes were used, but sequential mismatch probes were not studied. No subsequent applications have been reported, and no other laboratories have reported verification of these preliminary, but encouraging results. Tavitian et al. (1998) reported the biodistribution of antisense probes in baboons in vivo, using PET. 18-mer oligodeoxynucleotides labeled at the 3' end with ^{18}F (specific activity 1000-2000 Ci/mmol) were studied. Phosphodiester, phosphorothioate, and 2'-O-methyl oligodeoxynucleotides were each studied. The 18-mer sequence chosen was complementary to a murine virus with computer database verified lack of matches to any mammalian mRNA target. This study demonstrated that each of the three types of fluorine-18 labeled oligodeoxynucleotides studied behaved very differently in vivo (as expected), that the 3' labeling with ^{18}F did not affect the biodistribution of each probe, and that PET could be used to quantitate the biodistribution of oligodeoxynucleotides. This study focused on the in vivo pharmacokinetics of the RASONs, and did not attempt to target any particular mRNA, as would be needed for eventual application of imaging gene expression. In an application involving peptide nucleic acids, PNAs that were antisense to caveolin-1alpha (CAV) mRNA were labeled with ^{111}In with the help of a DTPA chelator and targeted with a biotin-streptavidin attached murine OX26 monoclonal antibody to the rat transferrin receptor. Brain glial tumors were selectively imaged ex vivo with the ^{111}In-CAV-PNA conjugated to SA-OX26 owing to upregulation of CAV gene expression in brain cancer (Suzuki et al. 2004). While most antisense imaging applications to date have been preliminary, Tc labeled aptamers directed against Tenascin C, were shown to clearly image U251 and MDA-MB-435 tumor xenografts in vivo using a gamma camera (Hicke et al. 2005). With further validation and continued exploration, antisense imaging applications should lead to reproducible assays for imaging gene expression.

18.8.2 Imaging Endogenous Gene Expression with a Reporter Gene

In most imaging applications to date, reporter genes driven by a constitutive promoter such as the CMV promoter have been used (Gambhir et al. 1998). This allows for continued transcription of the reporter gene (up to the cellular life-time of the

reporter gene), but does not allow for tracking of endogenous gene expression. Through the creation of a chimeric fusion gene, in which the promoter of an endogenous gene is coupled to the reporter gene, endogenous gene expression can be monitored (Fig. 18.11).

A reporter gene assay to specifically monitor endogenous gene expression in living animals through the use of a radiotracer imaging technique has not yet been reported. Because methods to image a reporter gene with a constitutive promoter have been demonstrated (see previous section), it should soon be possible to image endogenous gene expression while utilizing a reporter gene. This should allow for many new questions to be asked and answered in which repeated, noninvasive, imaging of endogenous gene expression is needed to monitor the location(s), magnitude, and persistence of endogenous gene expression. In order to use reporter methods for monitoring endogenous gene expression, levels of endogenous mRNA and reporter mRNA should be independently assayed in order to verify that reporter gene expression correlates with endogenous gene expression. There need not be a linear relationship between levels of reporter and endogenous gene mRNA if a reporter gene approach is used. This potential lack of linearity must be kept in mind, as one seeks to interpret and quantify assays for measuring endogenous gene expression.

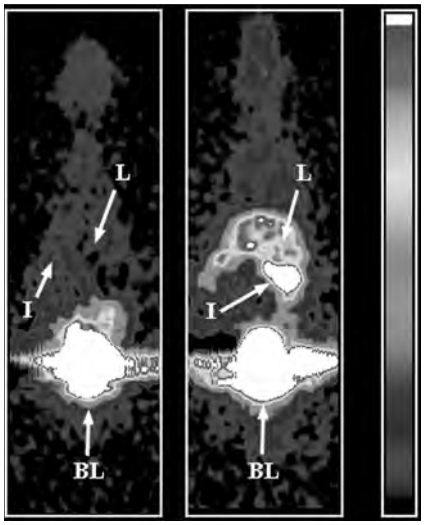

Fig. 18.11. Coronal microPET images from a mouse injected with control adenovirus (*left*) and adenovirus carrying the HSV1-tk gene (*right*). Each viral vector was injected 48 h prior to imaging. The images were obtained 1 h after the injection of 150 μCi of [^{18}F-]FGCV using eight bed positions and 8 min/bed. Each image is normalized to a common global maximum with thresholding and represents approximately 1 mm depth and an in-plane resolution of approximately 3 mm. The color white representing maximum counts. *L*, liver; *I*, intestine; *BL*, bladder. [Reproduced with permission from Gambhir et al. (1998)]

18.8.3 Signal Amplification for Imaging Endogenous Gene Expression with a Reporter Gene

For both imaging and gene therapeutic purposes, research efforts aim at amplifying gene expression from weak endogenous promoters. Significant progress has been made employing a two step transcriptional amplification (TSTA) strategy (Iyer et al. 2001b; Zhang et al. 2002). In this approach, a weak, endogenous, tissue specific promoter (the PSE, or prostate specific antigen promoter) does not drive expression of the imaging gene directly. Instead, it is used to drive expression of a fusion gene in which the DNA binding domain of the yeast GAL4 gene is fused to the strong HSV1 VP16 transcriptional transactivation domain (GAL4VP16) (first step). In the second step, this fusion protein then binds to GAL4 binding sites upstream of the actual reporter gene, and promotes expression of the true reporter (or, if desired, the therapeutic) gene. The TSTA system amplifies expression to up to 20-fold of the cytomegalovirus (CMV) enhancer, and could be varied over an 800-fold range, while retaining the tissue specificity and androgen inducibility of the original promoter. It has been used in a two plasmid version, where each of the two steps is encoded by a separate plasmid, or as a combined single plasmid version. It is a generalizable system, i.e. it may be used in any other investigation by merely exchanging the weak endogenous tissue specific promoter.

Secondly, the site specific recombination by the bacteriophage P1 encoded Cre-LoxP system has been adapted as a method to amplify imaging reporter signal from weak promoters. Cre-recombinase forms a DNA-protein complex at the specific recognition site loxP. When two loxP sites are on the same linear DNA molecule, Cre binds the two sites together to form a circular protein–DNA complex. It then unites the two loxP sites to form a single DNA strand lacking the part which was previously between the two loxP sites (site-specific recombination) (Hamilton and Abremski 1984). Lyons et al. (2003) have constructed a transgenic mouse line in which the fLuc gene is driven by the beta-actin promoter, a ubiquitous promoter. However, transcription is prevented by the insertion of an interfering

sequence between promoter and reporter gene, which is flanked by two loxP sites. By crossing these mice with transgenics which express Cre recombinase in a tissue or tumor specific way driven by an endogenous, specific promoter, fLuc expression can be selectively switched on in any organ or tumor of choice, as shown by the authors in a NSCLC model (Lyons et al. 2003). A similar transgenic strain was reported by Safran et al. (2003). As the generation of transgenic mice is a tedious, time consuming and expensive process, Sundaresan et al. (2004) have recently shown that Cre-loxP can be used with in vivo gene transfer. Mice with hepatic Cre expression were tail vein injected with an adenovirus carrying a loxP "silenced" HSV1-tk reporter. Upon recombination, strong signal was demonstrated in the liver using MicroPET, whereas control mice without hepatic Cre expression did not transcribe the gene.

18.9 Imaging Protein–Protein Interactions

To image protein–protein interactions in vivo, two major strategies have been devised. The first is an adaptation of the well known yeast two-hybrid system, and the second employs split reporter genes. The two-hybrid system was adapted for mammalian cells by Ray et al. (2002) and modified to be inducible. The *NF*-kappa*B* promoter, which may be modulated through TNF-alpha, drove expression of two fusion proteins, VP16-MyoD and GAL4-Id. The interaction of MyoD and Id led to transcriptional activation of *Fluc* reporter gene expression as described earlier for the TSTA amplification system. Protein–protein interaction in transiently transfected cells was shown in cell culture and imaged it in living mice. A similar strategy by Luker et al. (2002) involved interactions between the p53 tumor suppressor and the large T antigen of simian virus 40. This visualized tumor xenografts of stably transfected HeLa cells.

Compared to the yeast two-hybrid approach, the split reporter approach has the advantage that it may be used in any cellular compartment, whereas the two-hybrid system is restricted to the nucleus. Paulmurugan et al. (2002) and Paulmurugan and Gambhir (2003) showed that both complementation and intein-mediated reconstitution of fLuc and rLuc can be used to image protein–protein interactions in living mice. The system has been established for imaging of drug modulated protein–protein interactions, and for studying the interaction of homodimeric proteins (Massoud and Ramasamy 2004; Paulmurugan et al. 2004). Imaging interacting protein partners in living subjects may be a tool to investigate functional proteomics in whole animals and study new pharmaceuticals targeted to modulate protein–protein interactions.

18.10 Multi-modality Imaging

One of the most exciting areas evolving in molecular imaging is the use of several different reporter genes to answer more complex questions. Several techniques have been developed, the most simple being co-transfection. In this approach, two (or more) genes are encoded by different plasmids, but driven by identical promoters. Yaghoubi et al. (2001) demonstrated very good correlation in vitro and in vivo between two reporter genes using this method. In the dual promoter approach, two genes will be located on the same plasmid, but driven by two identical promoters. Bicistronic vectors contain only one vector, but two genes separated by an internal ribosomal entry site (IRES) derived from polio- or encephalomyelitis viruses (Jang et al. 1990). A single mRNA results from which two separate proteins are translated. Imaging signal of both genes correlates well, although the gene downstream of the IRES is often translated to a lesser degree than the one upstream (Liang et al. 2002). An early and widely used method is the use of fusion genes, in which different reporter genes are joined by linker amino acid sequences and expressed as a single protein from one promoter. Examples of the many different combinations published include HSV1-TK-GFP (Loimas et al. 1998), and fLuc-GFP-betaGal (Strathdee et al. 2000). While fusion reporter proteins must always translate the reporters at the same frequency, signal attenuation due to steric interactions between the partners remains a challenge to be solved. Also, several commonly used reporter genes are obligate dimers (e.g. HSV1-TK) or multimers (RFP), which further complicates matters. In addition, to localize fusion proteins to the desired cellular compartment, existing localization sequences may have to be interfered with or new ones introduced. An interesting new approach is the use of bidirectional transcription. In this system, a promoter of choice drives expression of a fusion protein containing a transactivation domain (VP16) and a DNA binding domain (rtetR). The fusion protein then

binds to a specific tetracycline responsive element (TRE) sequence, from which it enhances transcription of the two bidirectional reporter genes via two minimal CMV promoter elements (Sun et al. 2001).

The introduction of several reporter genes into a living organism by any of the methods mentioned may help to image expression of a given gene by different imaging modalities. This will greatly simplify and speed up the development of new models, as some reporter genes may be used to quickly assess gene expression in cell culture (e.g., using fluorescence), while others may serve better in the three dimensional imaging of gene expression in animals (or even humans) in vivo (e.g., using PET). Ray et al. (2004) recently reported the development of eight different trifusion reporter genes combining sets of three different reporter genes each, including HSV1-sr39tk, HSV1-tk, rLuc, fLuc, RFP, and eGFP, and their imaging in vivo. Trifusion reporters such as these may prove to be useful, generalizable, and highly versatile investigative tools for molecular imaging.

18.11 Human Gene Therapy Imaging

In human gene therapy trials physicians delivered a therapeutic, or a suicide, gene (a gene which can inhibit tumors such as the HSV1-tk gene). For the first time, imaging of the expression of either therapeutic or suicide genes has been reported (Voges et al. 2003).

18.11.1 Suicide Gene Therapy and Imaging

A suicide gene is a gene that, when delivered to cells, renders the cell susceptible to an administered pro-drug. Moolten (1986) first demonstrated the transfer of the HSV1-tk suicide gene into neoplasms. Subsequent systemic treatment with the pro-drug ganciclovir resulted in neoplasm reduction. The mechanism of ganciclovir trapping was described in Sect. 18.6.4. Cancer cells are unable to replicate leading to a decrease in tumor burden and tumor cell death. Multiple clinical trials in which the HSV1-tk suicide gene is being used are underway. Retroviral vector producer cells, adenoviral vectors, and convection enhanced stereotactic delivery of liposomal formulations directly into the tumor are being used. Most gene therapy trials using the suicide gene approach have employed the HSV1-tk gene. Brain tumors have been a preferred target of experimental gene therapy trials, as their prognosis is extremely poor and no satisfactory therapeutic option currently exists. Two studies have shown some effect of HSV1-tk therapy in brain tumors after administration of virus producing cells. Ram et al. (1997)

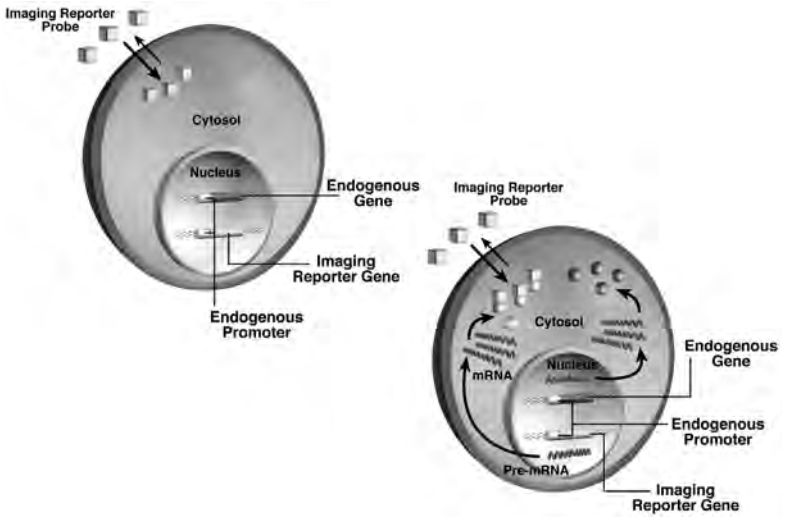

Fig. 18.12. Monitoring of endogenous gene expression through the use of a reporter gene. The endogenous gene and the reporter gene share the same promoter. If the endogenous gene is not transcribed, then the reporter gene is not transcribed, and there is no accumulation of the imaging reporter probe (cubes) (*upper left panel*). If the endogenous gene is transcribed, leading to transcription of the imaging reporter gene, then imaging reporter probe (cubes) is accumulated (*lower right panel*). The interaction of reporter gene protein and imaging reporter probe can be enzyme based or receptor-ligand based. Accumulation of imaging reporter probe allows for the potential indirect monitoring of the endogenous gene expression in vivo

injected cells stereotactically, and showed reduction of tumor volume in five of 18 patients despite low transduction efficiency (<0.17% of the tumor cells). Klatzmann et al. (1998) observed a median survival of 206 days, with 25% of patients surviving longer than 12 months following injection of virus producing cells into the surgical cavity margins after debulking. In order to investigate in vivo how factors such as distribution and expression of the therapeutic gene in vivo, or blood brain barrier (BBB) influence HSV1-tk suicide gene therapy, imaging of HSV1-tk in gene therapy will be of great value. A study by Yaghoubi et al. (2001) indicated that ^{18}F-FHBG should be a good reporter probe for HSV1-tk due to its high stability, fast blood clearance, low background, biosafety, and acceptable dosimetry, despite limited crossing of the BBB. Imaging of this gene with PET in humans using ^{124}I-FIAU has been reported in a trial treating glioblastoma multiforme with ganciclovir 4 days after convection enhanced liposomal delivery of HSV1-TK through a stereotactically implanted intratumoral catheter (Voges et al. 2003). However, FIAU uptake was only demonstrated in one of eight patients. The same authors had previously shown that ^{124}I-FIAU does not cross the BBB unless it is disrupted (Jacobs et al. 2001), and hypothesized that lack of specific ^{124}I-FIAU uptake in all but one patient was due to below threshold expression levels of HSV1-tk, since patients without uptake showed lower numbers of proliferating tumor cells in histology (Jacobs et al. 2001). These efforts recognize the need to determine the successful delivery and distribution of the therapeutic gene and optimal start time for ganciclovir therapy. Tumor metabolism in the glioblastoma therapy trial was monitored with PET using ^{18}F-FDG and ^{11}C-methionine, showing ^{18}F-FIAU uptake in an area of decreased ^{11}C-methionine uptake 8 weeks after therapy. During treatment with ganciclovir, the use of a reporter gene distinct from HSV1-tk would be useful because of the potential pharmacologic competition of ganciclovir with the PET reporter probe. It should be possible to use a construct in which both HSV1-tk (as a suicide gene) and a second gene (e.g., the D2R gene) serving as a reporter gene (through the use of an IRES) for imaging suicide gene expression. Jacobs et al. (2003) have investigated the use of HSV1-tk (as an imaging gene) in combination with CD (as a therapeutic gene), and GFP (for proof of principle and fast in vitro assay) either linked

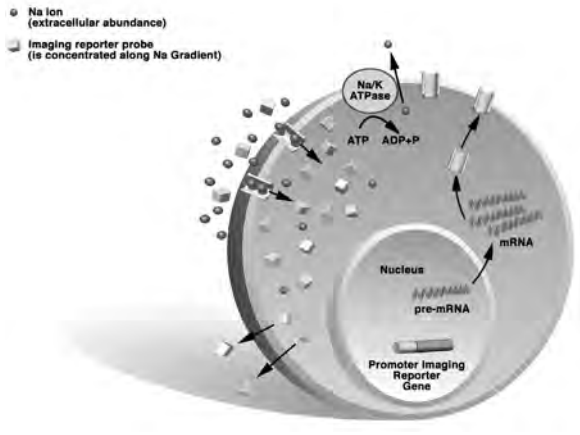

Fig. 18.13. An ion transporter type imaging reporter gene. The ion transporter type imaging reporter gene driven by a promoter of choice is introduced into the cell(s) of interest. An ion transporter, e.g. the sodium iodide symporter (NIS) is transcribed and targeted to the cell membrane. The imaging reporter probe (*cubes*) is concentrated inside the cell along an electrochemical gradient (Na ion, *spheres*), which is maintained by a separate process (Na/K ATPase). At the same time, the imaging reporter probe passively diffuses from the cell. Eventually, an equilibrium between uptake and externalization of the probe is reached. Signal intensity is thus dependent not only on the amount of reporter gene expression, but also on the rate of externalization from the cell, and factors influencing the electrochemical gradient and imaging reporter probe availability

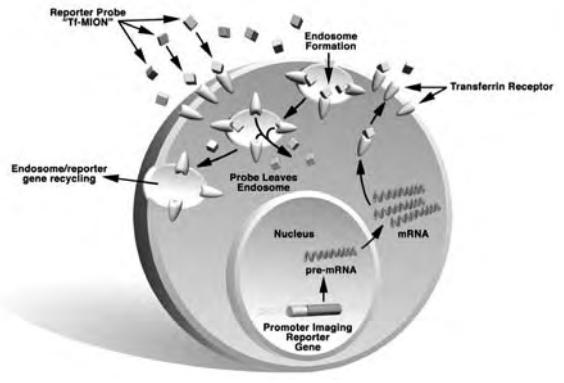

Fig. 18.14. An imaging reporter gene with trapping of imaging reporter probe by a recyclable cell surface receptor. Following the introduction of the imaging reporter gene and the promoter of choice into the cell, the gene coding for the recyclable cell surface receptor, e.g. the transferrin receptor, is transcribed, translated, and targeted to the cell surface. Upon binding of imaging reporter probe ("*Tf-MION*"), several receptors internalize by endosome formation. Once inside the cell, the reporter probe leaves the endosome by an unknown mechanism, thereby changing the relaxivity of the cell, and the endosome with the remaining empty recyclable receptor returns to the cell surface. The recycling process, and repeated cycles of imaging reporter probe deposition in the cell, results in an amplification of signal per reporter gene molecule transcribed

by an IRES, or as fusion proteins. In general, however, the success of suicide gene therapy, foremost in glioma patients, has been less encouraging than initially expected. Issues related to delivery across the blood–brain barrier (BBB) (for brain tumors) will need to be investigated further.

In another study, PET imaging using [^{18}F]FHBG was employed to monitor the expression of Herpes simplex virus thymidine kinase (HSV1-tk) in patients with hepatocellular carcinoma after intratumoral injection of a first generation recombinant adenoviral vector encoding this enzyme (AdCMVtk) (Penuelas et al. 2005). After the PET study the patients were placed on oral valganciclovir. Interestingly, all patients who had received 10^{12} viral particles or more showed [^{18}F]FHBG uptake in the treated lesions and no tumor progression at day 30, whereas all patients receiving lower doses showed no uptake and had progressive disease. This study of human imaging of gene therapy with AdCMVtk is very encouraging, as both patient response and tracer uptake in treated lesions are more common than in the brain tumor study and, above all, may correlate. Whether [^{18}F]FHBG-PET imaging reflects the transduction efficiency of the vector, and can be used as a non-invasive tool to predict the efficacy of gene therapy strategies, awaits confirmation in future trials.

18.11.2 Therapeutic Gene Therapy and Imaging

Currently, therapeutic gene therapy is being aimed only at somatic (non-reproductive) cells (Knoell and Yiu 1998). Specifically, hematopoietic stem cells are potentially an optimal target because transduction and transplantation of these cells would hopefully lead to continuous expression of the transgene during the life-time of the patient. The β-globin gene for β thalassemia and sickle cell anemia has been used for stem cell transduction with limited results. Therapeutic genes such as the low density lipoprotein receptor (LDL-R) targeted for expression in hepatocytes, and the cystic fibrosis transmembrane conductance regulator (CFTR) have also been investigated (Rosenfeld et al. 1992). In the case of human gene therapy with therapeutic genes (e.g., for treating cystic fibrosis), the use of a bicistronic vector with an IRES should make monitoring of the therapeutic gene through the use of an imaging reporter gene possible. Monitoring of the delivery of the therapeutic gene and the magnitude of its expression over time should help to determine the reasons why gene therapy is effective or not. It should also be possible to directly target the therapeutic gene mRNA through the use of antisense probes (see Sect. 18.4.3), thereby circumventing the need to introduce a reporter gene.

18.12 Future Outlook

Since the emergence of molecular imaging, significant progress has been made in developing assays for imaging gene expression in vivo. However, much work remains to be done in the development of practical, highly sensitive, and specific quantitative assays for in vivo applications. For antisense based imaging approaches researchers will need to resolve key issues including those related to stability of probes, minimization of non-specific interaction, and sufficient efflux of probes for minimizing the background. It is thus likely that these antisense based approaches will lag behind the reporter gene approaches. However, when successful (both for the pharmaceutical industry and for imaging applications) the antisense approach will provide a more general method to imaging gene expression, as well as to be able to identify the early changes in gene expression signaling the transformation of normal cellular function to that of an altered state of disease. Reporter approaches are currently one step ahead, having proven themselves in many preliminary animal applications and pilot human studies. Studies with transgenic animals, in vivo inducible expression, bicistronic vectors, and the monitoring of endogenous gene expression with a reporter gene, are all actively investigated and have produced interesting first results. Amplification of gene expression from weak endogenous promoters may open new approaches to imaging and gene therapy. Multimodality reporters and generalizable reporters/probes will enable researchers to greatly speed up and simplify the process from in vitro to in vivo and ultimately human studies and allow them to study more complex biological processes. There are exciting developments in human studies, especially in the imaging of gene therapy and cancer therapy, and we will hopefully see further development of these evolving technologies so that they may be harnessed to help the fight against human disease and suffering.

Acknowledgements
We thank Jim Strommer for graphical support and our many colleagues in the field of molecular imaging for making this a highly exciting research area.

References

Agrawal S, Iyer RP (1997) Perspectives in antisense therapeutics. Pharmacol Therapeut 76:151-160

Alauddin MM, Conti PS, Mazza SM, Hamzeh FM, Lever JR (1997) 9-[(3-[18F]-fluoro-1-hydroxy-2-propoxy)methyl]guanine ([18F]-FHPG): a potential imaging agent of viral infection and gene therapy using PET. Nucl Med Biol 23:787–792

Alauddin MM, Conti PS et al (2002) Synthesis of [18F]-labeled 2'deoxy-2'-fluoro-5-methyl-1-beta-D-arabinofuranosylur acil([18F]-FMAU). J Labelled Comp Radiopharm 45:583-590

Alrabiah FA, Sacks SL (1996) New Antiherpesvirus agents: their targets and therapeutic potential. Drugs 52:17-32

Altmann A, Kissel M et al (2003) Increased MIBG uptake after transfer of the human norepinephrine transporter gene in rat hepatoma. J Nucl Med 44:973-980

Anton M, Wagner B et al (2004) Use of the norepinephrine transporter as a reporter gene for non-invasive imaging of genetically modified cells. J Gene Med 6:119-126

Arner ES, Eriksson S (1995) Mammalian deoxyribonucleoside kinases. Pharmacol Therapeut 67:155-186

Bankiewicz KS, Eberling JL et al (2000) Convection-enhanced delivery of AAV vector in parkinsonian monkeys; in vivo detection of gene expression and restoration of dopaminergic function using pro-drug approach. Exp Neurol 164:2-14

Barrio JR, Satyamurthy N et al (1989) 3-(2'-[18F]fluoroethyl)spiperone: in vivo biochemical and kinetic characterization in rodents, nonhuman primates, and humans. J Cereb Blood Flow Metab 9:830-839

Barton KN, Xia X et al (2004) A quantitative method for measuring gene expression magnitude and volume delivered by gene therapy vectors GENIS: gene expression of sodium iodide symporter for noninvasive imaging of gene therapy vectors and quantification of gene expression in vivo safe use of acetaminophen effects of urea and trimethylamine N-oxide on fluidity of liposomes and membranes of an elasmobranch direct effects of 3,5,3'-triiodothyronine and 3,5-diiodothyronine on mitochondrial metabolism in the goldfish Carassius auratus lysine residues at positions 234 and 236 in yeast porin are involved in its assembly into the mitochondrial outer membrane. Mol Ther 9:625-631

Bhaumik S, Gambhir S (2002) Optical Imaging of Renilla luciferase reporter gene expression in living mice. Proc Natl Acad Sci USA 99:377-382

Bhaumik S, Walls Z et al (2004) Molecular imaging of gene expression in living subjects by spliceosome-mediated RNA trans-splicing. Proc Natl Acad Sci USA 101:8693-8698 Epub 25 May 2004

Biswal S, Gambhir SS (2004) Monitoring gene therapy in living subjects with molecular imaging technologies. Gene and cell therapy, vol 1. TNS. Dekker, New York, NY, pp 447-480

Boland A, Ricard M et al (2000) Adenovirus-mediated transfer of the thyroid sodium/iodide symporter gene into tumors for a targeted radiotherapy. Cancer Res 60:3484-3492

Bremer C, Ntziachristos V et al (2003) Optical-based molecular imaging: contrast agents and potential medical applications. Eur Radiol 13:231-243 Epub 13 Aug 2002

Brust P, Haubner R et al (2001) Comparison of [18F]FHPG and [124/125I]FIAU for imaging herpes simplex virus type 1 thymidine kinase gene expression. Eur J Nucl Med 28:721-729

Buerger C, Groner B (2003) Bifunctional recombinant proteins in cancer therapy: cell penetrating peptide aptamers as inhibitors of growth factor signaling. J Cancer Res Clin Oncol 129:669-675 Epub 11 Sep 2003

Bunzow JR, van Tol HH et al (1988) Cloning and expression of a rat D2 dopamine receptor cDNA (see comments). Nature 336:783-787

Buursma AR, Vaalburg W et al (2003) [18F]FEAU as a novel radiotracer for herpes simplex virus thymidine kinase (HSVtk) gene expression. J Label Compounds Radiopharmacol 46:S11

Cammilleri S, Sangrajrang S et al (1996) Biodistribution of iodine-125 dyramine transforming growth factor alpha antisense oligonucleotide in athymic mice with a human mammary tumor xenograft following intratumoral injection. Eur J Nucl Med 23:448-452

Carlin S, Cunningham SH et al (2000) Experimental targeted radioiodide therapy following transfection of the sodium iodide symporter gene: effect on clonogenicity in both two- and three-dimensional models. Cancer Gene Ther 7:1529-1536

Chalfie M, Tu Y et al (1994) Green fluorescent protein as a marker for gene expression. Science 263:802-805

Charlton J, Sennello J et al (1997) In vivo imaging of inflammation using an aptamer inhibitor of human neutrophil elastase. Chem Biol 4:809-816

Chaudhuri TR, Rogers BE et al (2001) A noninvasive reporter system to image adenoviral-mediated gene transfer to ovarian cancer xenografts. Gynecol Oncol 83:432-438

Chen IY, Wu JC et al (2004) Micro-positron emission tomography imaging of cardiac gene expression in rats using bicistronic adenoviral vector-mediated gene delivery. Circulation 109:1415-1420 Epub 8 Mar 2004

Cherry SR, Shao Y et al (1997) MicroPET: A high resolution PET scanner for imaging small animals. IEEE Trans Nucl Sci 44:1161-1166

Conrad RC, Baskerville S et al (1995) In vitro selection methodologies to probe RNA function and structure. Mol Divers 1:69-78

Cotten M, Wagner E et al (1993) Receptor-mediated transport of DNA into eukaryotic cells. Methods Enzymol 217:618-644

Crooke ST (1995) Progress in antisense therapeutics. Hematol Pathol 9:59-72

Crooke ST (1997) Progress in antisense therapeutics discovery and development. Ciba Found Symp 209:158-164

Crooke ST (2004) Progress in antisense technology. Annu Rev Med 55:61-95

Crooke ST, Lebleu B (1993) Antisense research and applications. CRC Press, Ann Arbor, p 579

De A, Gambhir S (2002) PET in imaging gene expression and therapy. In: Valk P, Bailey DL, Townsend D, Maisey M (eds) Positron emission tomography: basic science and clinical practice. vol 1. Springer, Berlin Heidelberg New York, pp 845-868

De A, Lewis XZ et al (2003) Noninvasive imaging of lentivi-

ral-mediated reporter gene expression in living mice. Mol Ther 7:681-691
De Clercq E (1993) Antivirals for the treatment of herpesvirus infections. J Antimicrob Chemother 32 [Suppl A]:121-132
Dewanjee MK, Ghafouripour AK et al (1994) Noninvasive imaging of c-myc oncogene messenger RNA with indium-111-antisense probes in a mammary tumor-bearing mouse model. J Nucl Med 35:1054-1063
Dohan O, de la Vieja A et al (2003) The sodium/iodide Symporter (NIS): characterization, regulation, and medical significance. Endocr Rev 24:48-77
Eberling JL, Cunningham J et al (2003) In vivo PET imaging of gene expression in parkinsonian monkeys. Mol Ther 8:873-875
Ehrin E, Farde L et al (1985) Preparation of 11C-labelled Raclopride, a new potent dopamine receptor antagonist: preliminary PET studies of cerebral dopamine receptors in the monkey. Int J Appl Radiat Isotopes 36:269-273
Eichler O, Hess H et al (1951) Radioiodine therapy of thyroid carcinoma. Langenbecks Arch Klin Chir Ver Dtsch Z Chir 269:19-36
Elion GB (1993) Acyclovir: discovery, mechanism of action, and selectivity. J Med Virol [Suppl] 1:2-6
Faivre J, Clerc J et al (2004) Long-term radioiodine retention and regression of liver cancer after sodium iodide symporter gene transfer in wistar rats. Cancer Res 64:8045-8051
Gallardo HF, Tan C et al (1997) The internal ribosomal entry site of the encephalomyocarditis virus enables reliable coexpression of two transgenes in human primary T lymphyocytes. Gene Therapy 4:1115-1119
Gambhir SS, Barrio JR et al (1998) Imaging of adenoviral-directed herpes simplex virus type 1 thymidine kinase reporter gene expression in mice with radiolabeled ganciclovir. J Nucl Med 39:2003-2011
Gambhir SS, Bauer E et al (2000) A mutant herpes simplex virus type 1 thymidine kinase reporter gene shows improved sensitivity for imaging reporter gene expression with positron emission tomography. Proc Natl Acad Sci USA 97:2785-2790
Garcia-Blanco MA (2003) Messenger RNA reprogramming by spliceosome-mediated RNA trans-splicing. J Clin Invest 112:474-480
Goldenberg DM (1997) Perspectives on oncologic imaging with radiolabeled antibodies. Cancer 80 [Suppl 12]:2431-2435
Good L, Nielsen PE (1997) Progress in developing PNA as a gene-targeted drug. Antisense Nucleic Acid Drug Dev 7:431-437
Goodchild J(1989). Oligodeoxynucleotides. Antisense inhibitors of gene expression. Macmillan, London
Green L, Nyugen K et al (2000) Indirect monitoring of endogenous gene expressionby imaging PET reporter gene in transgenic mice. J Nucl Med 41:81P
Groot-Wassink T, Aboagye EO et al (2002) Adenovirus biodistribution and noninvasive imaging of gene expression in vivo by positron emission tomography using human sodium/iodide symporter as reporter gene. Hum Gene Ther 13:1723-1735
Groot-Wassink T, Aboagye EO et al (2004) Noninvasive imaging of the transcriptional activities of human telomerase promoter fragments in mice. Cancer Res 64:4906-4911
Haberkorn U (2001) Gene therapy with sodium/iodide symporter in hepatocarcinoma. Exp Clin Endocrinol Diabetes 109:60-62
Haberkorn U, Oberdorfer F et al (1996) Monitoring gene therapy with cytosine deaminase: in vitro studies using tritiated-5-fluorocytosine. J Nucl Med 37:87-94
Haberkorn U, Henza M, Altmann A, Jiang S, Morr I, Mahmut M, Peschke P, Kubler W, Debus J, Eisenhut M (2001) Transfer of the human NaI symporter gene enhances iodide uptake in hepatoma cells. J Nucl Med 42:317-325
Haider N, Iyer RR et al (1998) Topics in molecular biology. Techniques and methods. J Nucl Cardiol 5:343-354
Hamilton DL, Abremski K (1984) Site-specific recombination by the bacteriophage P1 lox-Cre system. Cre-mediated synapsis of two lox sites. J Mol Biol 178:481-486
Hardy S, Kitamura M et al (1997) Construction of adenovirus vectors through Cre-lox recombination. J Virol 71:1842-1849
Hargrove JL, Hulsey MG et al (1990) A computer program for modeling kinetics of gene expression. BioTechniques 8:654-660
Hasegawa S, Jackson WC et al (2003) Imaging tetrahymena ribozyme splicing activity in single live mammalian cells. Proc Natl Acad Sci USA 100:14892-14896 Epub 25 Nov 2003
Hasegawa S, Choi JW et al (2004) Single-cell detection of trans-splicing ribozyme in vivo activity. J Am Chem Soc 126:7158-7159
Helene C, Toulme JJ (1989) Oligodeoxynucleotides. In: Cohen JS (ed) Antisense inhibitors of gene expression. Macmillan, London, pp 137-172
Herz J, Gerard RD (1993) Adenovirus-mediated transfer of low density lipoprotein receptor gene acutely accelerates cholesterol clearance in normal mice. Proc Natl Acad Sci USA 90:2812-2816
Hicke BJ, Stephens AW (2000) Escort aptamers: a delivery service for diagnosis and therapy. J Clin Invest 106:923-928
Hicke BJ, Stephens AW et al (2005) Tumor targeting by an aptamer. J Nucl Med (in press)
Hildebrandt IJ, Iyer M et al (2003) Optical imaging of transferrin targeted PEI/DNA complexes in living subjects. Gene Ther 10:758-764
Hnatowich DJ, Winnard P Jr et al (1995) Technetium-99m labeling of DNA oligonucleotides. J Nucl Med 36:2306-2314
Horst W (1951) Radioiodine in hyperthyreosis therapy. Strahlentherapie 85:186-195
Iyer M, Bauer E et al (2000) Comparison of FPCV, FHBG, and FIAU as reporter probes for imaging Herpes Simplex Virus Type 1 thymidine kinase reporter gene expression. J Nucl Med 41 [Suppl 5]:80P-81P
Iyer M, Barrio JR et al (2001a) 8-[18F]Fluoropenciclovir: an improved reporter probe for imaging HSV1-tk reporter gene expression in vivo using PET. J Nucl Med 42:96-105
Iyer M, Wu L et al (2001b) Two-step transcriptional amplification as a method for imaging reporter gene expression using weak promoters. Proc Natl Acad Sci USA 98:14595-14600
Iyer M, Berenji M et al (2002) Noninvasive imaging of cationic lipid-mediated delivery of optical and PET reporter genes in living mice. Mol Ther 6:555-562
Iyer M, Salazar FB et al (2004) Noninvasive imaging of enhanced prostate-specific gene expression using a two-step transcriptional amplification-based lentivirus vector. Mol Ther 10:545-552

Jacobs A, Braunlich I et al (2001) Quantitative kinetics of [124I]FIAU in cat and man. J Nucl Med 42:467-475
Jacobs A, Voges J et al (2001) Positron-emission tomography of vector-mediated gene expression in gene therapy for gliomas. Lancet 358:727-729
Jacobs AH, Winkeler A et al (2003) Improved herpes simplex virus type 1 amplicon vectors for proportional coexpression of positron emission tomography marker and therapeutic genes. Hum Gene Ther 14:277-297
Jacobs WR Jr, Barletta RG et al (1993) Rapid assessment of drug susceptibilities of Mycobacterium tuberculosis by means of luciferase reporter phages (see comments). Science 260:819-822
Jaeger LB, Banks WA (2004) Antisense therapeutics and the treatment of CNS disease. Front Biosci 9:1720-1727
Jang SK, Pestova TV et al (1990) Cap-independent translation of picornavirus RNAs: structure and function of the internal ribosomal entry site. Enzyme 44:292-309
Kalota A, Shetzline SE et al (2004) Progress in the development of nucleic acid therapeutics for cancer. Cancer Biol Ther 3:4-12 Epub 18 Jan 2004
Kang KK, Min JJ et al (2005) Comparison of [14C]FMAU, [3H]FEAU, [14C]FIAU, and [3H]PCV for monitoring reporter gene expression of wild type and mutant herpes simplex virus type 1 thymidine kinase in cell culture. Mol Imaging Biol (in press)
Kastis GK, Barber HB et al (1998) High resolution SPECT imager for three-dimensional imaging of small animals. J Nucl Med 39 [Suppl 5]:9P
Kessler RM, Ansari MS et al (1991) High affinity dopamine D2 receptor radioligands. 1. Regional rat brain distribution of iodinated benzamides. J Nucl Med 32:1593-1600
Kim YJ, Dubey P et al (2004) Multimodality imaging of lymphocytic migration using lentiviral-based transduction of a tri-fusion reporter gene. Mol Imaging Biol 6:331-340
Klain M, Ricard M et al (2002) Radioiodine therapy for papillary and follicular thyroid carcinoma. Eur J Nucl Med Mol Imaging 29 [Suppl 2]:S479-S485 Epub 9 May 2002
Klatzmann D, Valery CA et al (1998) A phase I/II study of herpes simplex virus type 1 thymidine kinase "suicide" gene therapy for recurrent glioblastoma. Study Group on Gene Therapy for Glioblastoma. Hum Gene Ther 9:2595-2604
Knoell DL, Yiu IM (1998) Human gene therapy for hereditary diseases: a review of trials. Am J Health Syst Pharmacy 55:899-904
Kuhnast B, Dolle F et al (2000) General method to label antisense oligonucleotides with radioactive halogens for pharmacological and imaging studies. Bioconjug Chem 11:627-636
Kurreck J (2003) Antisense technologies. Improvement through novel chemical modifications. Eur J Biochem 270:1628-1644
Lee HJ, Boado RJ et al (2002) Imaging gene expression in the brain in vivo in a transgenic mouse model of Huntington's disease with an antisense radiopharmaceutical and drug-targeting technology. J Nucl Med 43:948-956
Levenson VV, Transue ED et al (1998) Internal ribosomal entry site-containing retroviral vectors with green fluorescent protein and drug resistance markers. Hum Gene Ther 9:1233-1236
Lewin B (1994). Genes V. Oxford University Press, New York
Liang Q, Satyamurthy N et al (2001) Noninvasive, quantitative imaging in living animals of a mutant dopamine D2 receptor reporter gene in which ligand binding is uncoupled from signal transduction. Gene Ther 8:1490-´1498
Liang Q, Gotts J et al (2002) Noninvasive, repetitive, quantitative measurement of gene expression from a bicistronic message by positron emission tomography, following gene transfer with adenovirus. Mol Ther 6:73-82
Lind P(2002) Strategies of radioiodine therapy for Graves' disease. Eur J Nucl Med Mol Imaging 29 [Suppl 2]:S453-S457 Epub 25 Jun 2002
Loimas S, Wahlfors J et al (1998) Herpes simplex virus thymidine kinase-green fluorescent protein fusion gene: new tool for gene transfer studies and gene therapy. Biotechniques 24:614-618
Loke SL, Stein CA et al (1989) Characterization of oligonucleotide transport into living cells. Proc Natl Acad Sci USA 86:3474-3478
Louie AY, Huber MM et al (2000) In vivo visualization of gene expression using magnetic resonance imaging. Nat Biotechnol 18:321-325
Lu Y, Dang H et al (2004) Bioluminescent monitoring of islet graft survival after transplantation. Mol Ther 9:428-435
Luker GD, Sharma V et al (2002) Noninvasive imaging of protein-protein interactions in living animals. Proc Natl Acad Sci USA 99:6961-6966
Lyons SK, Meuwissen R et al (2003) The generation of a conditional reporter that enables bioluminescence imaging of Cre/loxP-dependent tumorigenesis in mice. Cancer Res 63:7042-7046
MacLaren DC, Gambhir SS et al (1999) Repetitive, non-invasive imaging of the dopamine D2 receptor as a reporter gene in living animals. Gene Ther 6:785-791
Manders JM, Corstens FH (2002) Radioiodine therapy of euthyroid multinodular goitres. Eur J Nucl Med Mol Imaging 29 [Suppl 2]:S466-S470 Epub 18 Jun 2002
Massoud TF, Gambhir SS (2003) Molecular imaging in living subjects: seeing fundamental biological processes in a new light. Genes Dev 17:545-580
Massoud TF, Ramasamy P (2004) Molecular imaging of homodimeric protein-protein interactions in living subjects. FASEB J 18:1105-1107
Matsukura M, Shinozuka K et al (1978) Phosphorothioate analogs of oligodeoxynucleotides: novel inhibitors of replication and cytopathic effects of human immunodeficiency virus (HIV). Proc Natl Acad Sci USA 84:7706-7710
Miller N, Vile R (1995) Targeted vectors for gene therapy. FASEB J 9:190-199
Min JJ, Gambhir SS (2004) Gene therapy progress and prospects: noninvasive imaging of gene therapy in living subjects. Gene Ther 11:115-125
Min JJ, Iyer M et al (2003) Comparison of [18F]FHBG and [14C]FIAU for imaging of HSV1-tk reporter gene expression: adenoviral infection vs stable transfection. Eur J Nucl Med Mol Imaging 30:1547-1560 Epub 10 Jul 2003
Misteli T, Spector D (1997) Applications of the green fluorescent protein in cell biology and biotechnology. Nat Biotechnol 15:961-964
Moolten FL (1986) Tumor chemosensitivity conferred by inserted herpes thymidine kinase genes: paradigm for a prospective cancer control strategy. Cancer Res 46:5276-5281
Murakami A, Blake KR et al (1985) Characterization of sequence-specific oligodeoxyribonucleoside methylphos-

phonates and their interaction with rabbit globin mRNA. Biochemistry 24:4041-4046
Nishiyama T, Kawamura Y et al (1985) Antineoplastic effects in rats of 5-fluorocytosine in combination with cytosine deaminase capsules. Cancer Research 45:1753-1761
Northrop JP, Bednarski M et al (2003) Cell surface expression of single chain antibodies with applications to imaging of gene expression in vivo. Eur J Nucl Med Mol Imaging 30:1292-1298 Epub 25 Jun 2003
Ntziachristos V, Bremer C et al (2003) Fluorescence imaging with near-infrared light: new technological advances that enable in vivo molecular imaging. Eur Radiol 13:195-208 Epub 19 Jul 2002
Olafsen T, Cheung CW et al (2004) Covalent disulfide-linked anti-CEA diabody allows site-specific conjugation and radiolabeling for tumor targeting applications. Protein Eng Des Sel 17:21-27Oomen SP, Hofland LJ et al (2001) Internalization-defective mutants of somatostatin receptor subtype 2 exert normal signaling functions in hematopoietic cells. FEBS Lett 503:163-167
Pan D, Gambhir SS et al (1998) Rapid synthesis of a 5'-fluorinated oligodeoxy-nucleotide: a model antisense probe for use in imaging with positron emission tomography (PET). Bioorg Med Chem Lett 8:1317-1320
Paulmurugan R, Umezawa Y et al (2002) Noninvasive imaging of protein-protein interactions in living subjects by using reporter protein complementation and reconstitution strategies. Proc Natl Acad Sci USA 99:15608-15613
Paulmurugan R, Gambhir SS (2003) Monitoring protein-protein interactions using split synthetic renilla luciferase protein-fragment-assisted complementation. Anal Chem 75:1584-1589
Paulmurugan R, Massoud T. F et al (2004) Molecular imaging of drug-modulated protein-protein interactions in living subjects. Cancer Res 64:2113-2119
Penuelas I, Mazzolini G et al (2005) Positron emission tomography imaging of adenoviral-mediated transgene expression in liver cancer patients. Gastroenterology (in press)
Phillips JA, Craig SJ et al (1997) Pharmacokinetics, metabolism, and elimination of a 20-mer phosphorothioate oligodeoxynucleotide (CGP 69846A) after intravenous and subcutaneous administration. Biochem Pharmacol 54:657-668
Pirollo KF, Rait A et al (2003) Antisense therapeutics: from theory to clinical practice. Pharmacol Ther 99:55-77
Puttaraju M, Jamison SF et al (1999) Spliceosome-mediated RNA trans-splicing as a tool for gene therapy. Nat Biotechnol 17:246-252
Ram Z, Culver KW et al (1997) Therapy of malignant brain tumors by intratumoral implantation of retroviral vector-producing cells. Nat Med 3:1354-1361
Ray P, Pimenta H et al (2002) Noninvasive quantitative imaging of protein-protein interactions in living subjects. Proc Natl Acad Sci USA 99:3105-3110
Ray P, De A et al (2004) Imaging tri-fusion multimodality reporter gene expression in living subjects. Cancer Res 64:1323-1330
Reiners C, Schneider P (2002) Radioiodine therapy of thyroid autonomy. Eur J Nucl Med Mol Imaging 29 [Suppl 2]:S471-S478 Epub 18 Jul 2002
Reubi JC, Waser B et al (2001) Somatostatin receptor sst1-sst5 expression in normal and neoplastic human tissues using receptor autoradiography with subtype-selective ligands. Eur J Nucl Med 28:836-846
Richards-Kortum R, Sevick-Muraca E (1996) Quantitative optical spectroscopy for tissue diagnosis. Annu Rev Phys Chem 47:555-606
Rogers BE, McLean SF et al (1999) In vivo localization of [(111)In]-DTPA-D-Phe1-octreotide to human ovarian tumor xenografts induced to express the somatostatin receptor subtype 2 using an adenoviral vector. Clin Cancer Res 5:383-393
Rogers BE, Chaudhuri TR et al (2003) Non-invasive gamma camera imaging of gene transfer using an adenoviral vector encoding an epitope-tagged receptor as a reporter. Gene Ther 10:105-114
Roivainen A, Tolvanen T et al (2004) 68Ga-labeled oligonucleotides for in vivo imaging with PET. J Nucl Med 45:347-355
Rolland AP (1998) From genes to gene medicines: recent advances in nonviral gene delivery. Crit Rev Ther Drug Carrier Syst 15:143-198
Rosenfeld MA, Yoshimura K et al (1992) In vivo transfer of the human cystic fibrosis transmembrane conductance regulator gene to the airway epithelium. Cell 68:143-155
Rossi JJ (1998) Ribozymes to the rescue: repairing genetically defective mRNAs. Trends Genet 14:295-298
Safran M, Kim WY et al (2003) Mouse reporter strain for noninvasive bioluminescent imaging of cells that have undergone Cre-mediated recombination. Mol Imaging 2:297-302
Sakhuja K, Reddy PS et al (2003) Optimization of the generation and propagation of gutless adenoviral vectors. Hum Gene Ther 14:243-254
Schipper ML, Weber A et al (2003) Radioiodide treatment after sodium iodide symporter gene transfer is a highly effective therapy in neuroendocrine tumor cells. Cancer Res 63:1333-1338
Shao Y, Cherry SR et al (1997) Development of a PET detector system compatible with MRI/NMR systems. IEEE Trans Nucl Sci 44:1167-1171
Sharma V, Luker G. D et al (2002) Molecular imaging of gene expression and protein function in vivo with PET and SPECT. J Magn Reson Imaging 16:336-351
Shi N, Boado RJ et al (2000) Antisense imaging of gene expression in the brain in vivo. Proc Natl Acad Sci USA 97:14709-14714
Shin JH, Chung JK et al (2004) Noninvasive imaging for monitoring of viable cancer cells using a dual-imaging reporter gene. J Nucl Med 45:2109-2118
Shoji Y, Nakashima H (2004) Current status of delivery systems to improve target efficacy of oligonucleotides. Curr Pharm Des 10:785-796
Sieger S, Jiang S et al (2004) Tumor-specific gene expression using regulatory elements of the glucose transporter isoform 1 gene. Cancer Gene Ther 11:41-51
Smith AE (1995) Viral vectors in gene therapy. Annu Rev Microbiol 49:807-838
Spitzweg C, Zhang S et al (1999) Prostate-specific antigen (PSA) promoter-driven androgen-inducible expression of sodium iodide symporter in prostate cancer cell lines. Cancer Res 59:2136-2141
Stein CA, Cheng YC (1993) Antisense oligonucleotides as therapeutic agents – is the bullet really magical? Science 261:1004-1012
Strange PG (1990) Aspects of the structure of the D2 dopamine receptor. Trends Neurosci 13:373-378

Stratford-Perricaudet LD, Levrero M et al (1990) Evaluation of the transfer and expression in mice of an enzyme-encoding gene using a human adenovirus vector. Hum Gene Ther 1:241-256

Strathdee CA, McLeod MR et al (2000) Dominant positive and negative selection using luciferase, green fluorescent protein and beta-galactosidase reporter gene fusions. Biotechniques 28:210-212, 214

Sun X, Annala AJ et al (2001) Quantitative imaging of gene induction in living animals. Gene Ther 8:1572-1579

Sundaresan G, Paulmurugan R et al (2004) MicroPET imaging of Cre-loxP-mediated conditional activation of a herpes simplex virus type 1 thymidine kinase reporter gene. Gene Ther 11:609-618

Sundaresan G, Yazaki PJ et al (2003) 124I-labeled engineered anti-CEA minibodies and diabodies allow high-contrast, antigen-specific small-animal PET imaging of xenografts in athymic mice. J Nucl Med 44:1962-1969

Suzuki T, Wu D et al (2004) Imaging endogenous gene expression in brain cancer in vivo with 111In-peptide nucleic acid antisense radiopharmaceuticals and brain drug-targeting technology. J Nucl Med 45:1766-1775

Tavitian B (2003) In vivo imaging with oligonucleotides for diagnosis and drug development. Gut 52 [Suppl 4]:iv40-iv47

Tavitian B, Terrazzino S et al (1998) In vivo imaging of oligonucleotides with positron emission tomography. Nature Med 4:467-471

Thierry AR, Vives E et al (2003) Cellular uptake and intracellular fate of antisense oligonucleotides. Curr Opin Mol Ther 5:133-138

Tjuvajev JG, Stockhammer G et al (1995) Imaging the expression of transfected genes in vivo. Cancer Res 55:6126-6132

Tjuvajev JG, Doubrovin M et al (2002) Comparison of radiolabeled nucleoside probes (FIAU, FHBG, and FHPG) for PET imaging of HSV1-tk gene expression. J Nucl Med 43:1072-1083

Tomita N, Morishita R (2004) Antisense oligonucleotides as a powerful molecular strategy for gene therapy in cardiovascular diseases. Curr Pharm Des 10:797-803

Tomita N, Azuma H et al (2004) Application of decoy oligodeoxynucleotides-based approach to renal diseases antisense oligonucleotides as a powerful molecular strategy for gene therapy in cardiovascular diseases. Curr Drug Targets 5:717-733

Verwijnen SM, Sillevis Smith PA et al (2004) Molecular imaging and treatment of malignant gliomas following adenoviral transfer of the herpes simplex virus-thymidine kinase gene and the somatostatin receptor subtype 2 gene. Cancer Biother Radiopharm 19:111-120

Vitravene Study Group (2002) A randomized controlled clinical trial of intravitreous fomivirsen for treatment of newly diagnosed peripheral cytomegalovirus retinitis in patients with AIDS. Am J Ophthalmol 133:467-474

Voges J, Reszka R et al (2003) Imaging-guided convection-enhanced delivery and gene therapy of glioblastoma. Ann Neurol 54:479-487

Wagner HN Jr, Burns HD et al (1983) Imaging dopamine receptors in the human brain by positron tomography. Science 221:1264-1266

Wallace PM, MacMaster JF et al (1994) Intratumoral generation of 5-fluorouracil mediated by an antibody-cytosine deaminase conjugate in combination with 5-fluorocytosine. Cancer Res 54:2719-2723

Weissleder R (2002) Scaling down imaging: molecular mapping of cancer in mice. Nat Rev Cancer 2:11-18

Weissleder R, Cheng HC et al (1997) Magnetically labeled cells can be detected by MR imaging. J Magn Reson Imaging 7:258-263

Weissleder R, Moore A et al (2000) In vivo magnetic resonance imaging of transgene expression. Nature Med 6:351-355

Wickstrom E (1986) Oligodeoxynucleotide stability in subcellular extracts and culture media. J Biochem Biophys Methods 13:97-102

Wiethoff CM, Middaugh CR (2003) Barriers to nonviral gene delivery. J Pharm Sci 92:203-217

Wong JY, Chu DZ et al (2004) Pilot trial evaluating an 123I-labeled 80-kilodalton engineered anticarcinoembryonic antigen antibody fragment (cT84.66 minibody) in patients with colorectal cancer. Clin Cancer Res 10:5014-5021

Wu-Pong S, Weiss TL et al (1992) Antisense c-myc oligodeoxyribonucleotide cellular uptake. Pharmaceut Res 9:1010-1017

Wu-Pong S, Weiss TL et al (1994) Antisense c-myc oligonucleotide cellular uptake and activity. Antisense Res Dev 4:155-163

Yaghoubi SS, Wu L et al (2001) Direct correlation between positron emission tomographic images of two reporter genes delivered by two distinct adenoviral vectors. Gene Ther 8:1072-80

Younes CK, Boisgard R et al (2002) Labelled oligonucleotides as radiopharmaceuticals: pitfalls, problems and perspectives. Curr Pharm Des 8:1451-1466

Zamecnik PC, Stephenson ML (1978) Inhibition of Rous sarcoma virus replication and cell transformation by a specific oligodeoxynucleotide. Proc Natl Acad Sci USA 75:280-284

Zamecnik PC, Goodchild J et al (1986) Inhibition of replication and expression of human T-cell lymphotropic virus type III in cultured cells by exogenous synthetic oligonucleotides complementary to viral RNA. Proc Natl Acad Sci USA 83:4143-4146

Zhang L, Adams J. Y et al (2002) Molecular engineering of a two-step transcription amplification (TSTA) system for transgene delivery in prostate cancer. Mol Ther 5:223-232

Zhang YM, Liu N et al (2000) Influence of different chelators (HYNIC, MAG3 and DTPA) on tumor cell accumulation and mouse biodistribution of technetium-99m labeled to antisense DNA. Eur J Nucl Med 27:1700-1707

Zinn KR, Buchsbaum DJ et al (2000) Noninvasive monitoring of gene transfer using a reporter receptor imaged with a high-affinity peptide radiolabeled with 99mTc or 188Re. J Nucl Med 41:887-895

19 Quo Vadis?

Christiaan Schiepers

This book presents the status of nuclear medicine in the new millennium from the clinical, technical and gene imaging point of view. An update was provided of the progress in the last decade. Promising developments in receptor and metabolic imaging turned out to be important clinically, and attest that these radiopharmaceutical and technical developments are here to stay. The introduction of dual modality imaging with PET/CT caught on in record time, and over 90% of new equipment sold in 2004 was PET/CT. Applications in oncology were the main driving force behind this development. A few dedicated PET scanners of high resolution were installed for neuro-imaging.

Image quality improved due to complete digitization of cameras, multi-head detectors, and faster computers with advanced processing and reconstruction techniques. Adaptation of existing tests and imaging protocols by adding pharmacological interventions, common in nuclear cardiology, that were proposed for renal and hepatobiliary imaging, are now routine in the nuclear medicine clinic. A small number of new ^{99m}Tc-based radiopharmaceuticals was approved.

Metabolic imaging with FDG, introduced as the "new kid on the block" in the 1990s, is now commonplace and has propelled diagnostic imaging in oncology. FDG is still the most frequently used PET pharmaceutical. Networks have been set up both in the US and EU for the distribution of FDG over densely populated areas. The once heralded development of hybrid gamma camera systems (with coincidence detection) has stalled and no new applications were approved. Hybrid imaging now refers to dual-modality imaging with a multi-slice CT system and a whole-body PET system.

C. Schiepers, MD, PhD
Department of Molecular and Medical Pharmacology, David Geffen School of Medicine at UCLA, 10833 Le Conte Avenue, AR-144 CHS, Los Angeles, CA 90095-6942, USA

The future of nuclear medicine imaging is continuously being discussed and opinions encompass the whole spectrum from negative to positive. The demise of the field has been predicted on many an occasion, but every time nuclear medicine appears extremely adaptive. New radiopharmaceuticals and imaging systems lead to new tests, and the term "molecular imaging" is used more and more for our field. From the clinical section in this book, the progress in certain fields is obvious, and dual modality imaging with both PET/CT and SPECT/CT, has a bright future (Chaps. 11–13 and 16). Oncology is currently the main engine for this image integration, and will be followed by cardiac applications once the resolution of the multi-slice CT component of PET/CT is sufficiently high, both in the spatial and temporal domain. One of the great advantages of multimodality imaging is the ease of localization of lesions and abnormalities. The lack of landmarks or reference points in routine nuclear medicine images is thus circumvented. This allows for the development of very specific tracers, which disclose only those tissues that take up the radiopharmaceutical, whereas the anatomic modality provides the reference framework for localization of the lesions. Soon, multi-slice CT will provide sub-millimeter spatial resolution. Functional imaging is not up there, yet. Currently, the high-resolution neuro-PET scanners have a spatial resolution of 2.5 mm in the center of the field of view. The situation for SPECT is different and these devices still trail PET by a factor of three. Standard systems currently available (i.e. parallel hole collimators of ultra high resolution) yield a spatial resolution approaching 1 cm. To detect smaller lesions, specialized and dedicated equipment is necessary. Innovative designs are needed to bring SPECT within the same range of resolution as PET. This will be especially relevant for receptor imaging, which is highly specific but still suffers from low uptakes. The anatomic modality CT will again provide the reference frame for localization.

Presentation of multimodality images has great influence, not only on imaging specialists, but also

at hospital tumor boards, where surgical, medical, and radiation oncologists can directly appreciate anatomic and functional assessment of tumors and tissues. In joint discussion, they decide which therapy is best for the individual cancer patient. This approach appears effective and provides the patient with the optimal treatment plan available in a particular institution.

Merger and fusion are frequently encountered entities in our society. Mergers have happened between hospitals, health care organizations, telecommunication industries, media networks and other businesses. Academic disciplines are now doing the same. Nuclear medicine as a relatively small specialty will have to follow. At our own institution, UCLA, the integration of nuclear medicine with medical and molecular pharmacology is another example of bringing together basic science with clinical applications. The intention is to develop new diagnostic imaging products and manufacture new radiopharmaceuticals as well as equipment. Instruments such as micro-PET and micro-CT, combined CT-PET and MR-PET scanners, and optical imaging systems, are continuously being improved. These innovations will keep NM in the forefront of the imaging field and will result in new diagnostic strategies for work-up of patients.

Cost-effectiveness of diagnostic tests and combination of imaging modalities to arrive at the diagnosis in the shortest amount of time with an adequate balance between tests performed and costs incurred, was mentioned only sporadically. In the present environment of managed care and budget shortfalls, there is a need for objective assessment and evaluation of imaging strategies for specific clinical problems. At UCLA, a method based on decision tree analysis was used to evaluate such strategies. Models have been designed for staging of lung cancer (Gambhir 1996, Scott 1998), and management of solitary pulmonary nodules (Gambhir 1998). A combined model for detection and staging of lung lesions has also been proposed (Shepherd 1999). A decision model for the workup and staging of recurrent colorectal cancer was reported by Park (2001).

NM as a biological imaging modality will keep expanding and continuously evolving. NM as a molecular imaging modality is an active field, despite reservations in the eye of some beholders that it is an appendix of radiology. It has shown to be an adaptive imaging field, with enthusiastic clinicians, scientists, and scholars. The continuous input from scientists and interested clinicians from other fields is mandatory for progress. In addition, new ways of inter-disciplinary collaboration need to be explored to assemble the best team of experts that will arrive at the diagnosis in the shortest amount of time and provide the best treatment plan, without prohibitive costs of health care to society. In this way, the patient will benefit by being provided with optimum care.

References

Gambhir SS, Hoh CK, Phelps ME, Madar I, Maddahi J (1993) Decision tree sensitivity analysis for cost-effectiveness of FDG-PET in the staging and management of non-small-cell lung carcinoma. J Nucl Med 37:1428–1436

Gambhir SS, Shepherd JE, Shah BD, Hart E, Hoh CK, Valk PE, Emi T, Phelps ME (1998) Analytical decision model for the cost-effective management of solitary pulmonary nodules. J Clin Oncol 16:2113–2123

Park KC, Schwimmer J, Shepherd JE, Phelps ME, Czernin JR, Schiepers C, et al. (2001) Decision analysis for the cost-effective management of recurrent colorectal cancer. Ann Surg 233:310-9

Scott WJ, Shepherd J, Gambhir SS (1998) Cost effectiveness of FDG-PET for staging non-small cell lung cancer: a decision analysis. Ann Thorac Surg 66:1876–1885

Shepherd JE, Phelps ME, Czernin J, Gambhir SS (1990) Cost effectiveness analysis for the role of FDG-PET in lung carcinoma. J Nucl Med 40:56P

Glossar

Accuracy	probability that a test will yield the correct diagnosis
ACEI	angiotensin-converting enzyme inhibitor
AD	Alzheimer's dementia
ADHD	attention deficit hyperactivity disorder
Anion	electro negative ion, element or molecule
Antisense	in molecular genetics: strand of DNA having set of nucleotides complementary to the sense strand
Apoptosis	programmed cell death, suicidal pathway of cell stored in the genes
Aptamer	novel nucleic acid-binding species
BGO	bismuth germanate
Cation	electro positive ion, element or molecule
Chelate	chemical compound that sequesters and firmly binds a metallic ion into a ring, thus shielding the chemical effects of the metal
Chemotaxis	orientation of a cell along a chemical gradient, or movement in the direction of the gradient
Compartmental analysis	method of analyzing the data, in which the organ or system under study is represented as a set of compartments, e.g. intra-vascular, extra-cellular fluid (ECF), intra-cellular, and excretion compartments.
DAS	dynamic antral scintigraphy
DAT	Dopamine transporter
Deconvolution analysis	mathematical technique to reconstruct a function at time T from measurements at a later time.
DLBD	diffuse Lewy body disease
Dose, absorbed	radiation energy absorbed in the body, expressed in mSv (milli Sievert); 1 Sievert = 1 Gray · Q (Q is quality factor, which equals 1 for gamma and beta radiation); 1 Gray = 1 Joule/kilogram
Dose, administered	amount of radioactivity, e.g. mCi – (milli Curie), or Bq (Becquerel; 1 Bq is 1 disintegration per second); the prefix indicates the power of 10, e.g. M is mega for 10^6 and T is for tera or 10^{12}; 1 mCi = $3.7 \cdot 10^7$ Bq
Dose, exposed	amount of radiation emitted to the organ or system or body under study, expressed in Coulombs/kilogram in the current SI system, or mR (milli Roentgen) in the old system: 1 Roentgen = $2.58 \cdot 10^{-4}$ Coulombs/kilogram
Eluate	product of elution, i.e. separation by washing, such as freeing an enzyme from its absorbent
EOB	end of bombardment, i.e. of the target in a cyclotron
Epitope	antigenic determinant
ER	estrogen receptor (in breast cancer)

ETT	esophageal transit time, (in gastro-enterology); or exercise treadmill test (in cardiology)
FBP	filtered back-projection; reconstruction algorithm for tomography
FNA	fine- needle aspiration
FWHM	full width at half maximum
FWTM	full width at one tenth of the maximum
GB	gallbladder
GBEF	gallbladder ejection fraction
Genome	the full set of genes of an individual
GEP tumor	gastro-entero-pancreatic tumor
GFR	glomerular filtration rate
Glucose clamp	method to keep serum glucose within a specific range by infusing insulin and glucose simultaneously: originally developed for arterial glucose levels (invasive), but in most PET centers applied to keep venous glucose levels constant in myocardial metabolism studies
GLUT	glucose transporter: subtypes are indicated with an Arabic numeral
Glycolysis	breaking down of sugars into simpler compounds; specifically, the metabolic degradation path of glucose
Glycoprotein	conjugated protein, having protein(s) with a carbohydrate group
HAMA	human anti-mouse antibody
HPLC	high- pressure liquid chromatography
hSSTR	human somatostatin receptor
HSV1-tk	herpes simplex virus-1 thymidine kinase (gene)
HSV1-TK	herpes simplex virus-1 thymidine kinase (enzyme)
HU	Hounsfield unit, used for CT density
hVIPR	human vasoactive intestinal peptide receptor
Hydrophilic	having affinity for water
Hygroscopic	material that attract water or water vapors
IBD	inflammatory bowel disease
ICAM	intercellular adhesion molecule
IRES	internal ribosomal entry site
K_a	association constant of a chemical reaction, e.g. binding of an agonist or antibody to its receptor on the cell membrane
K_d	dissociation constant of a chemical reaction
keV	kilo electron Volt: energy an electron accumulates after acceleration over 1000 Volts
Ligand	molecule or compound active in biological processes, usually a small molecule that binds specifically to a larger one, e.g. antibody binding to an antigen, hormone or neurotransmitter binding to a receptor, substrate binding to an enzyme
Lipophilic	having affinity for fat
LSO	luthetium oxy-orthosilicate
LSO(Ce)	cerium- activated lutetium oxy-orthosilicate; high energy scintillator
LVEF	left ventricular ejection fraction
MDR	multidrug resistance

Micturition	voiding of bladder
MIRD	medical internal radiation dossimetry
MLEM	maximum-likelihood expectation -maximization
MoAB, MAB	monoclonal antibody
MSA	multi-system atrophy
NET	norepinephrine transporter
NIS	sodium iodide symporter
Normoxic	having normal oxygen tension
NPV	negative predictive value, likelihood that a negative test result indicates absence of disease
NSCLC	non-small- cell lung cancer
OCD	obsessive compulsive disorder
Oncogene	gene with properties for inducing cancer
Oncogenesis	the formation of cancer cells
OSEM	ordered subsets maximum-likelihood expectation -maximization; iterative reconstruction algorithm
PCR	polymerase chain reaction
PET	positron emission tomography: the term ET for emission tomography, combining both SPECT and PET, has not been generally accepted
Pgp	P-glycoprotein
PIOPED	Prospective Investigation of Pulmonary Embolism Diagnosis (study)
Plasmid	an autonomously replicating DNA molecule
PMT	photomultiplier tube
PNA	polypeptide nucleic acid
PPV	positive predictive value; likelihood that a positive test result indicates presence of disease
PR	progesterone receptor (of tumors)
PTCA	percutaneous transluminal coronary angioplasty
Radiolysis	decomposition of a radio-labeled compound by the radiation emitted by its own radioactive nuclide
Radionuclide	radio-active element:, formerly isotope
Radiopharmaceutical	biological compound or pharmaceutical labeled with a radioactive element to trace its pathway; used for diagnostic or therapeutic purposes
RASON	radiolabeled antisense oligodeoxynucleotide
RBF	renal blood flow
rCBF	regional cerebral blood flow
rCMR-Xx	regional cerebral metabolic rate of substance Xx
Rebinning	regrouping of data, for faster processing by computer algorithms
ROI	region of interest
Scintillator	substance that emits light after interaction with high- energy photons
Sensitivity	probability that a test will detect presence of disease
Specificity	probability that a test will determine absence of disease
SPECT (or SPET in Europe)	single photon emission computed tomography
SPM	statistical parametric mapping

SPN	solitary pulmonary nodule
SSTR	somatostatin receptor
SUV	standardized uptake value: ratio of measured activity in a certain area to the expected activity if the radioactivity were homogeneously distributed through the body
TCA cycle	tricarboxylic acid cycle
TER	tubular extraction rate
Transduction	transfer of DNA via a bacteriophage to another cell, thereby changing the constitution of the second organism, also called genetic recombination
Transfection	artificial infection of cells by nucleic acid isolated from virus or bacteriophage, resulting in production of mature virus or phage particles
Transgenic animal	animal in which every cell carries a specific new or altered gene of interest
TTNA	trans-thoracic needle aspiration
USP	United States Pharmacopoeia
YSO	yttrium oxy-orthosilicate; high- energy scintillator

Subject Index

List of Contributors

Martin Allen-Auerbach, MD
Department of Molecular and
Medical Pharmacology
David Geffen School of Medicine at UCLA
10833 Le Conte Avenue, AR-144 CHS
Los Angeles, CA 90095-6942
USA

Raffaele Barone, MD
Center of Nuclear Medicine
University Louvain Medical School
UCL 54.30
54, Avenue Hippocrate, 54
1200 Brussels
Belgium

Dirk Bequé, PhD
Department of Nuclear Medicine
University Hospital Gasthuisberg
Herestraat 49
3000 Leuven
Belgium

Chantal P. Bleeker-Rovers, MD
Department of Nuclear Medicine and
Department of Internal Medicine
University Medical Center Nijmegen
PO Box 9101
6500 HB Nijmegen
The Netherlands

Guy Bormans, PhD
UZ Gasthuisberg
Radiopharmacy Department
Herestraat 49
300 Leuven
Belgium

Roxana Campisi, MD
Department of Molecular and
Medical Pharmacology
David Geffen School of Medicine at UCLA
10833 Le Conte Avenue, AR-144 CHS
Los Angeles, CA 90095-6942
USA

Johannes Czernin, MD
Department of Molecular and
Medical Pharmacology
David Geffen School of Medicine at UCLA
10833 Le Conte Avenue
AR-144 CHS
Los Angeles, CA 90095-6942
USA

Magnus Dahlbom, PhD
Department of Molecular and
Medical Pharmacology
David Geffen School of Medicine at UCLA
10833 Le Conte Avenue, AR-144 CHS
Los Angeles, CA 90095-6942
USA

James J. Frost, MD
Departments of Radiology and Radiological Services
and Neuroscience
The John Hopkins University School of Medicine
JHOC 3225
601 North Carolina Stret
Baltimore, MD 21287
USA

Sanjiv Sam Gambhir, MD, PhD
Director, Molecular Imaging Program
at Stanford (MIPS)
Professor, Department of Radiology
and Bio-X Program
Head, Division of Nuclear Medicine
The James H. Clark Center
318 Campus Drive
East Wing, First Floor, E150A
Stanford, CA 94305-5427
USA

Gerhard Goerres, MD
Nuclear Medicine
Department of Medical Radiology
University Hospital of Zurich
8091 Zurich
Switzerland

David A. Hillier, MD, PhD
Division of Nuclear Medicine
Mallinckrodt Institute of Radiology
510 S. Kingshighway Blvd
Saint Louis, MO 63110, USA
USA

Carl Hoh, MD
Department of Radiology
UCSD Medical Center
200 W Arbor Drive
San Diego, CA 92103
USA

François Jamar, MD, PhD
Center of Nuclear Medicine
University Louvain Medical School
UCL 54.30
54, Avenue Hippocrate, 54
1200 Brussels
Belgium

Felix Y. J. Keng, PhD
Department of Molecular and
Medical Pharmacology
David Geffen School of Medicine at UCLA
10833 Le Conte Avenue, AR-144 CHS
Los Angeles, CA 90095-6942
USA

Giovanni Lucignani, MD
Unit of Molecular Imaging
Division of Radiation Oncology
European Institute of Oncology and
Institute of Radiological Sciences
University of Milan
Via Ripamonti 435
20141 Milan
Italy

Helen R. Nadel, MD, FRCPC
Associate Professor, Department of Radiology
University of British Columbia
Children's and Women's Health Center
of British Columbia
4480 Oak Street
Vancouver, B.C. V6H 3V4
Canada

Johan Nuyts, PhD
Department of Nuclear Medicine
University Hospital Gasthuisberg
Herestraat 49
3000 Leuven
Belgium

Wim J. G. Oyen, PhD
Professor, University Medical Center Nijmegen
Department of Nuclear Medicine (565)
PO Box 9101
6500 HB Nijmegen
The Netherlands

Huub J. J. M. Rennen, PhD
Department of Nuclear Medicine
University Medical Center Nijmegen
PO Box 9101
6500 HB Nijmegen
The Netherlands

Henry D. Royal, MD
Division of Nuclear Medicine
Mallinckrodt Institute of Radiology
510 S. Kingshighway Blvd.
Saint Louis, MO 63110
USA

Heinrich R. Schelbert, MD, PhD
Department of Molecular and
Medical Pharmacology
David Geffen School of Medicine at UCLA
10833 Le Conte Avenue, 23-148 CHS
Los Angeles, CA 90095-6942
USA

Christiaan Schiepers, MD, PhD
Department of Molecular and
Medical Pharmacology
David Geffen School of Medicine at UCLA
10833 Le Conte Avenue, AR-144 CHS
Los Angeles, CA 90095-6942
USA

Meike L. Schipper, MD
Molecular Imaging Program at Stanford (MIPS)
Department of Radiology and Bio-X Program
Division of Nuclear Medicine
The James H. Clark Center
318 Campus Drive, East Wing, First Floor, E150A
Stanford, CA 94305-5427
USA

Hans C. Steinert, MD
Professor, Nuclear Medicine
Department of Medical Radiology
University Hospital of Zurich
8091 Zurich
Switzerland

Moira E. Stilwell, MD, FRCPC
Clinical Assistant Professor
Department of Radiology
University of British Columbia
Children's and Women's Health Center
of British Columbia
4480 Oak Street
Vancouver, B.C. V6H 3V4
Canada

T. Traub-Weidinger, MD
Medical University of Innsbruck
Clinic of Nuclear Medicine
Anichstrasse 35
6020 Innsbruck
Austria

Mark Tulchinsky, MD, FACP, FACNP
Associate Professor and
Associate Chief of Nuclear Medicine Section
Department of Radiology
Penn State University
Milton S. Hershey Medical Center
500 University Drive, M.C. H066
P.O. Box 850
Hershey, PA 17033-0850
USA

Jean-Luc C. P. Urbain, MD, PhD
Chair, Department of Nuclear Medicine
St. Joseph's Health Centre
The University of Western Ontario
268 Grosvenor St.
London, Ontario N6A 4V2
Canada

Kristin Verbeke, PhD
UZ Gasthuisberg
Radiopharmacy Department
Herestraat 49
3000 Leuven
Belgium

Alfons Verbruggen, PhD
Professor, Radiopharmacy Department
UZ Gasthuisberg
Herestraat 49
3000 Leuven
Belgium

Irene Virgolini, MD
Professor of Internal Medicine
and Experimental Nuclear Medicine
Medical University of Innsbruck
Clinic of Nuclear Medicine
Anichstrasse 35
6020 Innsbruck
Austria

Gustav K. von Schulthess, MD, PhD
Professor and Director, Nuclear Medicine
Department of Medical Radiology
University Hospital of Zurich
8091 Zurich
Switzerland

Sibylle I. Ziegler, PhD
Priv.-Doz., Department of Nuclear Medicine
Nuclearmedizinische Klinik und Polyklinik
Klinikum rechts der Isar der TU München
Ismaninger Strasse 22
81675 Munich
Germany